Charles University in Prague
Faculty of Mathematics and Physics

HABILITATION THESIS

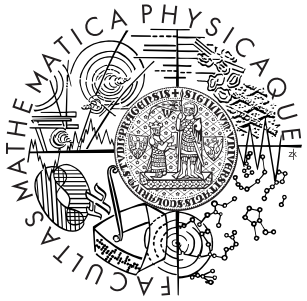

František Gallovič

Forward and inverse modeling of earthquake sources

Department of Geophysics

Field: Geophysics

Prague 2016

Contents

Preface

This Thesis represents a summary of 19 publications which I am an author or a co-author of. The papers consist of 18 papers published in international impacted journals and 1 extended conference abstract. They deal, in general, with forward and inverse kinematic modeling of earthquakes with particular emphasis on the earthquake source properties. The papers include development of new methods, assessment of their performance by means of synthetic test, and applications to real data. The main motivation driving the research is to gain better understanding of tectonic earthquakes, including their complexity. This topic is not only interesting from the academic point view, but it will eventually enable reliable physics-based estimation of ground shaking for seismic hazard assessment, which is now based predominantly on empirical data, and for engineering applications in seismic design in earthquake prone countries. Except for 1 publication, the papers of the Thesis use kinematic description of the earthquake source.

Seismological research including earthquake source physics are driven by observed data. Thus this work would not be possible without the endeavor of people responsible for the data measurement and collection. Thanks to the broadly accepted open-data policy researches from around the world (including myself) can download and interpret high-quality ground motion recordings. This makes seismology truly international and collaborative branch of science, which I enjoy to be part of. In particular, strong ground motion data from near fault and near regional distances are employed in this Thesis. The quality and quantity of those data have improved dramatically during the last decades in Europe, Japan and the United States. Moreover, new types of data, mostly based on satellite measurements (Global Navigation Satellite Systems and Synthetic Aperture Radars) have led to better constrained earthquake source models and have enabled studies of previously unknown phenomena such as afterslip and slow slip, making the extent of the earthquake source complexity truly amazing. It is also to emphasize that the data not only drive the development of new methods, but limit it too. Indeed, even mostly sophisticated inversion methods cannot substitute missing and/or poor quality data. In similar sense, limited knowledge of the crustal structure restricts the capabilities of even the most enhanced source inversion methods. Therefore, in the papers of this Thesis I put strong emphasis on understanding the limitations of the methods for proper interpretation of the results.

The work has been performed mostly at my home institution at the Charles University in Prague, Faculty of Mathematics and Physics, Department of Geophysics. I also benefited from stays and cooperations at INGV in Milano, Laboratorio di Sismologia at the Universita' degli Studi "Federico II" di Napoli, ITSAK in Thessaloniki, Dept. of Earth and Environmental Sciences at the Ludwig-Maximilians-University in Munich, Dept. of Physics of the Earth and Planets at the Comenius University in Bratislava,

and Disaster Prevention Research Institute at the Kyoto University. The papers of the Thesis were written in collaboration with many devoted seismologists. To start with, I have learned a lot from enjoyable cooperations with J. Zahradník, whose productivity and enthusiasm are admirable, very inspirational and always motivating. I also enjoyed cooperation with E. Sokos, whose endeavor in data collection in Greece and concern in earthquake source interpretations have led to many interesting results. I am particularly thankful to W. Imperatori and M. Käser for performing 3D wave propagation modeling, which were essential in our common publications. Among many other collaborators I would like to mention (in alphabetical order) G. Ameri, J.-P. Ampuero, A. Emolo, H. Igel, M. Lancieri, M. Mai, F. Pacor, A. Zollo. I have also benefited from numerous discussions with my former advisor J. Brokešová, J. Burjánek, M. Causse, G. Cultrera, G. Festa, V. Plicka, R. Puglia, S.-G. Song, and many others. I am grateful to my PhD students for smooth collaborations that have broadened the scope of my studies, namely M. Halló, F. Kostka, and Ľ. Valentová.

Last but not least, I would like to express my thanks to my beloved wife, two sons and my parents for providing me with endless background support and understanding.

Chapter 1

Introduction

Earthquake source physics is a well-established branch of seismology. During last decades it continuously improves our knowledge about the physical processes that control the occurrence of earthquakes and drive the earthquake rupture propagation. The viable approaches that contribute to this endeavour range from frictional laboratory experiments, dynamic modeling of earthquake ruptures and interpretation of observed seismograms by means of forward and inverse kinematic modeling.

The spatial-temporal complexity of large earthquakes is broadly recognized. For example, strike-slip faults with significant surface ruptures are often composed of distinct segments with complex rupture propagation, including partial rupture arrests on fault bends, varying rupture velocities, etc. On smaller scales, in terms of observations, the situation is much less clear. Laboratory experiments present evidences of rupture delays at barriers (*Latour et al.*, 2013), fault bends (*Kato et al.*, 1999), or on faults with branches (*Biegel et al.*, 2007). The ruptures can switch from subshear to supershear under favorable conditions (*Mello et al.*, 2014). Also dynamic source simulations can model smaller-scale temporal and geometrical complexities (*Kato et al.*, 1999; *Biegel et al.*, 2007; *Bhat et al.*, 2007). The dynamic source complexity (slip reactivation, rupture jump, change of direction of rupture propagation, rupture delay, etc.) may originate from frictional and stress heterogeneity (*Ripperger et al.*, 2007), surface reflections and/or from complex friction law (*Goto et al.*, 2012; *Kaneko et al.*, 2008; *Kanamori and Heaton*, 2000). However, these models are still based on rather speculations, simplifications and/or unknown input parameters. Therefore, constraints on the smaller-scale behavior from slip inversions are necessary.

Practical earthquake source analysis requires several steps that iteratively improve the image of the source rupture process. Typically, the analysis starts with point-source interpretations, i.e. earthquake location and centroid moment tensor (CMT) inversion. The former provides information about the location of rupture nucleation from rather high-frequency data, while the latter represents a low-frequency point-source approximation of the complete rupture providing timing, location and mechanism of the overall slip. The CMT, possibly with other source of information based on, e.g., geodetic measurements, can be used to identify the causative fault. Afterwards, more details about the rupture propagation and spatial slip distribution may be inferred by means of slip inversion. It is noteworthy that, in principle, all of these steps are associated with uncertainties that should be considered during the eventual interpretation of the rupture process. In the papers of this Thesis we present several examples of earthquake source analysis, which comprises all the discussed steps supplemented in some

cases by strong motion modeling. We emphasize the importance of the uncertainty estimate to prove or disprove source features identified by the inversions.

In section 1.1 I first overview kinematic representation of an earthquake source. I explain source approximations and their range of validity, which are necessary for the iterative improvement of the source details. Section 1.2 shortly discusses the calculation of seismograms and section 1.3 then overviews the basic ideas behind the iterative analysis of the earthquake source.

1.1 Earthquake source representation

Here I briefly overview basic equations that are used in the present Thesis when describing introduced methods. More details can be found in the respective publications or general books on theoretical seismology (e.g., *Aki and Richards*, 2002).

1.1.1 Representation theorem

Kinematic seismic source and its radiation is a well investigated theoretical problem in elastodynamics (see, e.g., *Aki and Richards*, 2002). We consider that tectonic earthquake can be described as purely shear slip (discontinuity of displacement) $\Delta\boldsymbol{u}(\boldsymbol{\xi},t)$ describing the rupture propagation along fault $\Sigma(\boldsymbol{\xi})$. Such a source can be represented by the seismic moment tensor density,

$$m_{jk}(\boldsymbol{\xi},t) = \mu(\boldsymbol{\xi})\Delta u(\boldsymbol{\xi},t)\left[n_j(\boldsymbol{\xi})\nu_k(\boldsymbol{\xi}) + n_k(\boldsymbol{\xi})\nu_j(\boldsymbol{\xi})\right], \tag{1.1.1}$$

where μ is the medium rigidity, and $\boldsymbol{\nu}$ and $\boldsymbol{n}$ are the unit normal to the fault and the unit vector in the slip direction, respectively. The moment tensor can be understood as a double-couple force system. Then displacement $\boldsymbol{u(r,t)}$ measured at position $\boldsymbol{r}$ caused by the slip is given by the representation theorem (*Aki and Richards*, 2002),

$$u_i(\mathbf{r},t) = \iint_{\Sigma} G_{ij,k}(\boldsymbol{r},t;\boldsymbol{\xi}) * m_{jk}(\boldsymbol{\xi},t)d\boldsymbol{\xi}, \tag{1.1.2}$$

where $*$ denotes the time convolution and comma in the subscript means spatial derivative. G_{ij} is the Green's tensor composed of solutions of elastodynamic equation in terms of displacement in direction i for force impulse acting at position $\boldsymbol{\xi}$ in direction j.

Introducing impulse response $H_i(\boldsymbol{r},t;\boldsymbol{\xi})$ of the medium to a point double couple dislocation,

$$H_i(\boldsymbol{r},t;\boldsymbol{\xi}) = \mu(\boldsymbol{\xi})n_j(\boldsymbol{\xi})\nu_k(\boldsymbol{\xi})\left[G_{ij,k}(\boldsymbol{r},t;\boldsymbol{\xi}) + G_{ik,j}(\boldsymbol{r},t;\boldsymbol{\xi})\right], \tag{1.1.3}$$

the representation integral (1.1.2) reads

$$u_i(\boldsymbol{r},t) = \iint_{\Sigma} H_i(\boldsymbol{r},t;\boldsymbol{\xi}) * \Delta u(\boldsymbol{\xi},t)d\boldsymbol{\xi}. \tag{1.1.4}$$

Equation (1.1.4) is the basic formula used for the earthquake source analyses. Indeed, considering that the crustal model, fault plane geometry and slip direction (rake) is considered to be known a priori (i.e. impulse responses $\boldsymbol{H}$ are known), (1.1.4) represents a linear relationship between the slip distributed

along the fault and the displacement observed at a receiver. Since, typically, slip rates $\Delta\dot{u}$ are preferred as model parameters in slip inversions, (1.1.4) can be alternatively expressed as

$$u_i(\boldsymbol{r},t) = \iint_{\Sigma} \tilde{H}_i(\boldsymbol{r},t;\boldsymbol{\xi}) * \Delta\dot{u}(\boldsymbol{\xi},t)d\boldsymbol{\xi}, \tag{1.1.5}$$

where $\tilde{H}_i$ represent temporal integrals of the impulse responses H_i, i.e. $\tilde{H}_i(\boldsymbol{r},t;\boldsymbol{\xi}) = \int_0^t H_i(\boldsymbol{r},\tau;\boldsymbol{\xi})d\tau$.

1.1.2 Point source approximation

To simplify the parameterization of the seismic source it is useful to introduce its point approximation. As discussed by *Aki and Richards* (2002), if receivers are located at distances larger than several times the size of the fault, Green's tensor derivatives $G_{ij,k}$ do not change much along the fault in shape, so that their spatial dependence on the position on the fault can be approximated only by means of a time shift, i.e.

$$G_{ij,k}(\boldsymbol{r},t;\boldsymbol{\xi}) \approx G_{ij,k}\left(\boldsymbol{r},t-\left(T(\boldsymbol{r},\boldsymbol{\xi})-T(\boldsymbol{r},\boldsymbol{\xi_0})\right);\boldsymbol{\xi_0}\right). \tag{1.1.6}$$

The difference $T(\boldsymbol{r},\boldsymbol{\xi}) - T(\boldsymbol{r},\boldsymbol{\xi_0})$ represents station-dependent temporal shift of the Green's tensor with respect to some (optimal) point on the fault, $\boldsymbol{\xi_0}$. Then, Equation (1.1.2) simplifies to

$$u_i(\mathbf{r},t) \approx G_{ij,k}(\boldsymbol{r},t;\boldsymbol{\xi_0}) * M_{jk}(\boldsymbol{r},t),$$

where time-dependent moment tensor $M_{jk}(\boldsymbol{r},t)$ reads

$$M_{jk}(\boldsymbol{r},t) = \iint_{\Sigma} m_{jk}\left(\boldsymbol{\xi},t-\left(T(\boldsymbol{r},\boldsymbol{\xi})-T(\boldsymbol{r},\boldsymbol{\xi_0})\right)\right)d\boldsymbol{\xi}. \tag{1.1.7}$$

Typically, $M_{jk}(\boldsymbol{r},t)$ is considered to have the same time dependence for all components,

$$M_{jk}(\boldsymbol{r},t) = M_{jk}\Omega(\boldsymbol{r},t), \tag{1.1.8}$$

where $\Omega(\boldsymbol{r},t)$ is denoted as the apparent moment time function, whereas its time derivative $\dot{\Omega}(\boldsymbol{r},t)$ is called the apparent source time function (ASTF), which has a pulse-like shape. ASTFs contain information about how the rupture propagation appears to the individual stations. Since the propagating rupture front can be considered as a moving source of radiation, ASTFs are affected by the Doppler-like effect, called directivity effect in seismology. Generally speaking, the directivity effect leads to apparently shorter duration of the ASTF for station located in the direction of the rupture propagation, associated with increased maximum amplitude. Consequently, in the frequency domain, the (apparent) corner frequency of the apparent source pulse is shifted towards higher values and the amplitudes at higher frequencies are amplified accordingly (for more details see section 2.3.3).

Even stronger simplification of the earthquake source description can be obtained if one considers frequencies much lower than reciprocal of the rupture duration. In such a case the ASTFs become effectively delta-functions at time t_0, leading to

$$u_i(\mathbf{r},t) \approx G_{ij,k}(\boldsymbol{r},t;\boldsymbol{\xi_0}) * M_{jk}\delta(t-t_0) = M_{jk}G_{ij,k}(\boldsymbol{r},t-t_0;\boldsymbol{\xi_0}), \tag{1.1.9}$$

in which t_0 is called the centroid time. The equation (1.1.9) can be used to obtain time-independent moment tensor (MT) parameters describing the faulting mechanism (strike and dip angle of the fault orientation, and rake angle of the slip direction, see *Aki and Richards*, 2002) by means of fitting observed low-frequency seismograms. Note that MT is a symmetric tensor and thus contains equivocal information about the fault plane orientation (so-called nodal planes). In addition, position $\boldsymbol{\xi_0}$ represents also a free parameter when interpreting real data. Its optimal position is called centroid and the MT inferred at that location is denoted as the centroid moment tensor (CMT). In principle, causative fault plane should cross centroidal position and coincide with one of the MT nodal planes.

1.2 Green's functions

In the publications of this Thesis only regional, near-regional and local seismic data are considered (i.e., teleseismic data are not considered). Almost exclusively full wavefield synthetic Green's functions (GFs) are considered. No stochastic GFs were used due to their loose physical background.

In case of considering a 1D velocity model composed of homogeneous layers, GFs are calculated by the discrete wavenumber method (DWN; *Coutant*, 1989; *Bouchon*, 1981; *Kennett and Kerry*, 1979). We typically use a regional 1D model or several such models to study the dependence of the results on the choice of the crustal model. If available, in broadband ground motion simulations we consider 1D crustal models with site-specific subsurface structures to approximate the site effects.

For example, 1D velocity model derived from the model proposed by *Bianchi et al.* (2010) was used to simulate the 2009 L'Aquila main shock in [P13] with upper-most shear wave velocity of 1700 m/s. Although this model was appropriate to reproduce the overall wave propagation in the study area, it caused underestimation of the high-frequency amplitude of the ground motion at rock sites. Indeed, in central Italy sedimentary rocks are generally weathered and fractured, therefore very hard rock sites with shallow shear wave velocity of 1700 m/s are hardly expected (Gruppo di Lavoro MS-AQ, 2010). In order to simulate 1D site effects at generic rock stations, we substituted the uppermost 160m of the regional crustal model by 60m superficial layer with shear wave velocities of 800 m/s above another 100 m thick layer with velocity of 1200 m/s. The velocity of the first layer (800 m/s) is the value prescribed for seismic bedrock by the Italian seismic code (NTC08) and similar values have been measured at several rock stations in central Italy. The site-specific subsurface soil-profiles were available for some strong-motion stations collected in the Italian accelerometric archive ITACA.

In papers [P8] and [P15] we used Green's functions calculated in 3D velocity models. In particular, in [P15] we used second-order finite-difference code WPP (*Nilsson et al.*, 2007), which is based on summation-by-part stencils, featuring efficient absorbing boundaries, vertical mesh refinement and visco-elastic attenuation (*Petersson and Sjögreen*, 2012). In addition to heterogeneous Earth models, the code also handled complex topography by means of curvilinear grid meshing. In [P8] the 3D numerical simulations were carried out by the highly accurate ADER-Discontinuous Galerkin scheme (ADER-DG) using Arbitrary high order DERivatives (*Dumbser and Käser*, 2006; *Käser and Dumbser*, 2006). It solves the heterogeneous elastic wave equations formulated as a linear hyperbolic system (velocity–stress formulation) with arbitrary high order of accuracy in space and time on 3-D unstructured tetrahedral meshes. The main idea of the ADER approach is a Taylor expansion in time, in which all time deriva-

tives are replaced by space derivatives using Cauchy–Kovalewski procedure (*Titarev and Toro*, 2002).

In the broadband simulations, we adopted the 'kappa' factor (κ), introduced by *Anderson and Hough* (1984) to properly describe the high-frequency spectral decay as observed in the real data. We adjust the κ value for stations with subsurface velocity profile, while we fix $\kappa = 0.01$s for the generic rock stations.

1.3 Iterative improvement of the seismic source model

Obtaining details of rupture propagation along a fault by means of slip inversion and broadband ground motion modeling may be considered as the final goals of the earthquake source analysis. However, they both cannot be performed without a prior (at least approximate) knowledge of the fault plane position. Therefore, in several papers of this Thesis (see section 3.1.1) we follow a self-consistent chain of operations how to study an earthquake source, which relies mainly on seismological data:

- ▷ *Point-source parameters.*
  - The centroid moment tensor including its location is determined using low-frequency recordings from distant stations (regional to near-regional) in order to satisfy the assumptions of the point source approximation.
  - Earthquake hypocenter is relocated using as much stations as possible. I note that rather high-frequency waveforms are used to pick the P and/or S wave arrivals, so that the hypocenter and CMT can be considered as being obtained from independent data.

- ▷ *Identification of the causative fault plane (section (2.1)).* The fault plane can be constrained from aftershock distribution, geodetic observations such as satellite interferometry, and/or surface fault trace if the rupture reaches the surface. Nevertheless, this does not need to be always possible, e.g., when dealing with events with scarce aftershock production, or with deep events with weak geodetic signal and no or just secondary surface expression. Other alternative is its seismological identifications from the CMT solution. However, even in such case the situation is not ideal due to the uncertainty of the CMT solution and the ambiguity of the double-couple nodal planes. Joint interpretation of hypocenter and centroid (so-called H-C method introduced in [P3]) proved to be useful in cases of deep events and/or for a quick analysis before the satellite data and/or aftershocks are collected.

- ▷ *Slip inversion (section 2.2).* Once the fault geometry is identified, data from shorter distances can be added, maximum inverted frequency can be increased and more detailed information about the earthquake source can be retrieved by means of slip inversion. The fault plane position and mechanism can be optimized by means of performing the slip inversion repeatedly for varying fault location and mechanism.

- ▷ *Broadband ground motion modeling (section 2.3).* The slip inversion result represents a low-frequency approximation of the earthquake source. The slip inversion result can be enriched by a high-frequency (synthetic or empirical) component and broadband strong ground motion

modeling may be performed. Such modeling can provide additional constraints on the earthquake source.

As discussed in section 3.1.1, the full cascade of operations as described above was applied to the 2011 Mw 7.1 Van, Turkey ([P14]). The analyses of the 2009 Mw 6.3 Movri Mountain, Greece, earthquake and the 2014 doublet of Mw 6 earthquakes in Cephalonia, Greece, included all the steps but the broadband ground motion modeling. All other events of this Thesis were analyzed only in terms of some particular aspect as detailed in section 3.1.

Chapter 2

Methods

Here we describe methods developed within the papers of this Thesis. The methods cover most of the areas that are necessary for interpretation of the observed seismograms in terms of earthquake source process. In particular, section 2.1 describes a method to reveal rupture fault plane by means of collocating the hypocenter and centroid. Sections 2.2 and 2.3 are devoted to slip inversion methods and broadband ground modeling approaches, respectively.

2.1 Identification of causative fault by collocating hypocenter and centroid (H-C method)

Seismologists have limited possibilities how to constrain geometry of the fault. Obviously, it is due to the fact that most of the slip takes place at large depths. Only for some earthquakes the rupture reaches the surface, creating primary fault traces. Nevertheless, even in such a case one can learn only about the strike of the fault because the fault trace does not necessarily have to be the direct continuation of the main fault rupture, and thus the dip angle cannot be easily inferred. Indeed, major faults are characterized by so-called flower structure of minor subsurface faults, upon which the slip may be just triggered by the main rupture. The apparently straightforward case, where an earthquake occurs at or close to a geologically well-known fault, also benefits from an independent check, because the "known" fault may have a complex tectonic structure at depth.

The fault plane can sometimes be well "mapped" (constrained) by the spatial distribution of numerous early aftershocks (see, e.g., [P8]). However, this technique has serious limitations. One of them is the fact that in sparsely instrumented regions, accurate location of weak aftershocks is impossible. Moreover, some events lack numerous aftershocks at the mainshock fault plane altogether (this is typical of intermediate-depth earthquakes). In other cases, when a large network of faults is activated in a seismic sequence, the aftershocks exhibit a diffused pattern without any clear expression of a planar structure. This was observed, e.g., for the 2014 Cephalonia sequence discussed in [P16] and section 3.1.5, where we had to adopt fault geometry constrained by geodetic data (GPS, InSAR), which represent another possible way to infer the fault geometry. However, these data are sensitive to shallow slip only, which limits their application in fault plane determination. As a purely seismological alternative, estimations of the directivity of the rupture in terms of rupture vector (e.g., *Warren et al.*,

2015) or second-order spatial moments (e.g., *Chen et al.*, 2010; *Adamová and Šílený*, 2013) can be used to constrain the causative fault.

In [P3] we introduced a simple method to identify the fault plane, which is immediately applicable (under favorable conditions) when a reliable earthquake location and its CMT are available. Location, based on travel times, provides the hypocenter position (H), the place at which the rupture propagation initiated. The CMT solution from relatively long-period waveforms provides the centroid (C), which is the point-source approximation of the dominating slip region(s) on the fault. The CMT solution also gives two nodal planes passing through C defined by the strike and dip angles of the moment-tensor solution. Assuming a planar fault, the fault plane can be identified as that one among the two nodal planes that encompasses the hypocenter. This is what we call as H-C method. Its great potential is in simple linking of the independent pieces of short- and long-period seismic information. [P3] discusses the favorable conditions in terms of the mutual position of H and C, and presents an example application on the deep Mw 6.2 2008 Leonidio, Greece, earthquake. The preferred fault plane was later linked with the "storm" of earthquakes in Greece that took place in 2008 by *Durand et al.* (2014). In particular, they associated the event with breakup of the subducting African plate (below the Aegean-Anatolian plates). The fault plane we suggested agrees with the geometry of a preexisting normal or thrust fault in the slab.

We note that the H-C method is particularly useful for quick identification of the earthquake fault plane. Such information would be important for fast simulation of strong ground motions (Shake Maps) for post-event emergency services. I point out that in practical applications the best approach is to combine all constraints on the fault plane stemming from various datasets. In our slip inversions we also perform grid-search over fault parameters to further refine the fault plane geometry and slip direction ([P14, 16, 18]).

2.2 Earthquake slip inversions

Finite fault slip inversions play a crucial role in understanding earthquake rupture phenomenon. In particular, inferred source models are used to develop dynamic rupture models, providing constraints on stress state and frictional properties of faults (*Ide and Takeo*, 1997; *Day et al.*, 1998; *Dalguer et al.*, 2002; *Zhang et al.*, 2003, etc.), to study earthquake source scaling and determine the earthquake slip heterogeneity (*Causse et al.*, 2010; *Mai and Beroza*, 2002; *Somerville et al.*, 1999, etc.). Source inversion results are also used to conduct post-seismic stress-change calculations for seismic hazard assessment (e.g., *Nalbant et al.*, 2013), to analyze possible fault segment reactivations (*Vallée and Satriano*, 2014, and references therein) and instability of asperities of repeating earthquakes (e.g., *Custódio and Archuleta*, 2007). Quick slip inversions have the potential to improve community products such as ShakeMaps for fast response (e.g., *Cultrera et al.*, 2013).

Since the 70-80's many slip inversion methods have been introduced (e.g., *Custódio et al.*, 2009; *Dreger and Kaverina*, 2000; *Ji et al.*, 2002b; *Monelli and Mai*, 2008; *Piatanesi et al.*, 2007; *Hartzell et al.*, 2007, and references therein). They basically differ in how the rupture model is parameterized and which regularizations or constraints are applied. Some methods are utilized even routinely for large earthquakes and published online (see, e.g., the USGS website). However, there is currently no consen-

sus about which of the slip inversion methods is preferable, and there are doubts about the reliability of the inferred source models due to the inherent non-uniqueness (i.e. ill-conditioning) of the inverse problem (*Hartzell et al.*, 2007; *Shao and Ji*, 2012). As a consequence, the slip inversion results for individual events as obtained by various authors may differ (e.g., *Clévédé et al.*, 2004). Moreover, using various data (near-field, teleseismic, regional, static co-seismic) and their combination can provide also different models (e.g., *Delouis et al.*, 2002). This makes slip inversions a subject of still active research.

2.2.1 Overview of slip inversion methods

Depending on the rupture parameterization we can distinguish several basic classes of slip inversion methods:

- Linear inversion techniques (usually called multi-time window) are based on a discretized version of the representation theorem (Eq. (1.1.5)). The slip rate functions are parametrized by elementary functions (overlapping narrow triangles, delta-like, etc.) at several or many time windows. The windows span various time intervals ranging from relatively small fraction of the source duration (e.g., *Delouis et al.*, 2002; *Hartzell and Heaton*, 1983) up to the total rupture duration (e.g., *Frankel and Wennerberg*, 1989; *Das and Kostrov*, 1994; *Olson and Anderson*, 1988; [P7, 11, 15, 16, 17, 18]). After proper spatial discretization of the fault, this formulation typically results in relatively large number of model parameters (thousands) to be inverted. Those are related linearly to the wavefield. The inversion is usually performed in L1 or L2 norm considering regularization by means of smoothing and positivity constraint (*Hartzell et al.*, 1991). The result then represents the slip rate functions along the fault. Those might be post-processed to obtain kinematic parameters, such as rupture time and rise time, peak and static slip, etc. Although the linear inversion is very fast and recently possible on a common PC, any practical uncertainty analysis is prohibited due to the overwhelming number of model parameters. Thus the methods can be assessed only by means of synthetic tests, such as those presented in [P15, 17].

- Another class of inversion methods, so called nonlinear (or parametric), utilizes the representation theorem as well, but the shape of the slip rates is prescribed a priori. This way, the source model is parametrized by means of kinematic quantities (typically rupture time and rise time, peak slip rate, etc.) that are, generally, nonlinearly related to the wavefield. The major advantage of the parametric (nonlinear) inversions is that they deal with much lower number of parameters (hundreds), thus allowing for an uncertainty analysis by means of, e.g., Monte Carlo sampling of posterior probability density function (*Razafindrakoto and Mai*, 2014; *Monelli et al.*, 2009; *Cirella et al.*, 2012). A special subclass of nonlinear methods is represented by models, which are parametrized by relatively small number of parameters. For example, *Vallée and Bouchon* (2004) consider one or two elliptical slip patches, over which the rupture propagates at a constant speed. The authors then grid search for the location and geometry of the ellipses and the rupture speeds. *Twardzik et al.* (2012) introduced a similar model using rupture dynamics with slip-weakening friction law. In this model the source is composed of elliptical cracks, dynamic parameters of which are also grid-searched. The main advantage is that such models have very small amount of rupture parameters (tens), allowing for (almost) full sampling of the parametric space and

thus very simple and efficient uncertainty analyses. The inversion approach introduced in [P12] is similar to that of *Vallée and Bouchon* (2004), allowing slightly more general source description to capture more complex rupture models, while still keeping the number of model parameters low.

In the following sections 2.2.2 and 2.2.3 I describe slip inversion methods that were introduced, tested and applied in the papers of this Thesis. Sections 2.2.2.4 and 2.2.2.5 deal with uncertainties and artifacts in the linear slip inversion methods related to the imprecise knowledge of the velocity medium and detailed rupture location and geometry. Section 2.2.4 overviews the international benchmarking experiment Source Inversion Validation and describes my contributions to this effort including newly proposed method for comparison of the inferred source models.

2.2.2 Linear inversion methods

Linear inversion approaches have recently regained attention for its a-priori unconstrained source parametrization. This is especially important if rupture propagation complexities are expected. Indeed, linear inversions, especially when using long time windows, have the advantage of very general description of the source model. The result of the inversion are slip rates as a function of fault position without any prescribed nucleation point, shape of slip rate, rupture speed, etc. Therefore, linear inversion has the potential to infer even unexpected complex features of the rupture evolution, such as delays, slip reactivation (multiple rupturing), rupture-propagation reversals, etc. The formulation allows also to correctly capture the supershear rupture propagation including the associated trailing Rayleigh pulse (*Dunham and Archuleta*, 2004; *Mello et al.*, 2014).

Linear inversion methods are based on the representation integral (1.1.5) discretized in time and space. Typically the spatial discretization is considered smooth enough to achieve its continuum limit (*Spudich and Archuleta*, 1987; *Beresnev*, 2003). In [P7, 11, 12, 14, 15, 16, 17, 18] we considered spatial and temporal sampling with equidistant steps ΔL, ΔW, and Δt, respectively. Moreover, the temporal duration of the slip rates is the same everywhere on the fault, covering the whole time interval between the rupture onset and its considered arrest.

After the discretization of the spatial and temporal integrals in (1.1.5), the representation theorem can then be expressed in a matrix form as

$$\boldsymbol{d} = \mathbf{G}\boldsymbol{m}, \tag{2.2.1}$$

where vector $\boldsymbol{d}$ (size N) contains the displacement wavefields $\boldsymbol{u}$ of all stations and components considered, vector $\boldsymbol{m}$ (size M) encompasses model parameters in terms of the spatial and temporal samples of the slip rates (i.e. space-time amplitudes of the slip rates). Matrix $\mathbf{G}$ (size $N \times M$) contains the responses to point-source excitations by the individual elementary spatial-temporal elementary subfaults of model vector $\boldsymbol{m}$.

Inverse problem requires regularization. In the next subsections we discuss possible ways how to constrain the inverse solution.

2.2.2.1 Iterative linear slip inversion

In [P7] we propose to solve the inverse problem by means of the conjugate-gradient technique. Assuming L2 norm of the difference between the data and synthetics (see Eq. (2.2.1)), the misfit is

$$M(\boldsymbol{m}) = \frac{1}{2} \left(\boldsymbol{d} - \mathbf{G}\boldsymbol{m}\right)^{\boldsymbol{T}} \left(\boldsymbol{d} - \mathbf{G}\boldsymbol{m}\right), \tag{2.2.2}$$

where **T** represents matrix transpose. The derivative of the misfit with respect to the model parameters (i.e. samples of the slip rate functions) is

$$\frac{\partial M}{\partial \boldsymbol{m}} = \mathbf{G}^{\boldsymbol{T}} \left(\boldsymbol{d} - \mathbf{G}\boldsymbol{m}\right). \tag{2.2.3}$$

In Eq. (2.2.3) the term in parenthesis corresponds to residual seismograms for given model $\boldsymbol{m}$, and the matrix multiplication represents correlations of the residuals with with impulse responses of the medium, or convolutions of the residuals with time-reversed impulse responses (for a detailed derivation see the electronic appendix of [P7]). In other words, the misfit derivative is given by the back-propagation of the residual seismograms towards the source, which makes the approach similar to the adjoint tomographic inversions. Positivity constraint on the slip rate samples is achieved by means of switching to logarithms of the model parameters (see [P7]). The formulation can be also supplemented by constraint on the total seismic moment.

For the conjugate-gradient technique a good initial source approximation is necessary. In [P7] we consider a smooth slip patch located at the centroid. The resulting iterative approach then reveals the spatio-temporal evolution of the earthquake rupture process as we illustrate on a synthetic test. The method was applied to investigate a line-source model of the damaging Mw 6.3 2008 Movri Mountain earthquake in Greece ([P7]).

2.2.2.2 Truncated singular value decomposition

Olson and Apsel (1982) were the first to utilize Singular Value Decomposition (SVD) to the linear slip inversion. Detailed presentations of the role of the SVD in understanding the properties of linear-inverse problems can be found in textbooks on inverse problems (e.g., *Press et al.*, 1992; *Lawson and Hanson*, 1995; *Menke*, 2012), or, for example, *Olson and Apsel* (1982) and [P11, 17] in the context of the slip inversions. The SVD approach implicitly assumes as the misfit function the L2 norm of data residuals with respect to model predictions (2.2.2).

The SVD of matrix **G** is

$$\mathbf{G} = \mathbf{U}\mathbf{\Lambda}\mathbf{V}^{\mathbf{T}}, \tag{2.2.4}$$

in which **U** and **V** are orthonormal matrices ($\mathbf{U}^{\mathbf{T}}\mathbf{U} = \mathbf{I}$, $\mathbf{V}^{\mathbf{T}}\mathbf{V} = \mathbf{I}$) of size $N \times N$ and $M \times M$, respectively, and $\mathbf{\Lambda}$ is a diagonal matrix of size $N \times M$ consisting of positive singular values λ_i, $i = 1..\min(M, N)$, sorted in a descending order. The columns $\boldsymbol{V}_i$ of matrix **V** are called right-singular vectors. They are also eigenvectors of matrix $\mathbf{G}^{\mathbf{T}}\mathbf{G}$ (size $M \times M$), forming an orthonormal basis system in the model space and are associated with eigenvalues λ_i^2. The columns $\boldsymbol{U}_i$ of matrix **U** are called left-singular vectors, and represent orthogonal basis in the data space. The first $\min(M, N)$

vectors $\boldsymbol{U}_i$ are projections of vectors $\boldsymbol{V}_i$ from the model space to the data space:

$$\boldsymbol{U}_i = \mathbf{G}\boldsymbol{V}_i/\lambda_i, \quad i = 1..\min(M,N), \tag{2.2.5}$$

that is, normalized seismograms generated by the individual model-space singular vectors.

The generalized solution of the inverse problem considering the L2 norm (2.2.2) is defined as $\tilde{\boldsymbol{m}} = \mathbf{G}^{\#}\boldsymbol{d}$, in which $\mathbf{G}^{\#} = \mathbf{V}\mathbf{\Lambda}^{\#}\mathbf{U}^{\mathbf{T}}$ is the pseudo-inverse of $\mathbf{G}$, where $\mathbf{\Lambda}^{\#}$ is formed by replacing every nonzero diagonal entry of $\mathbf{\Lambda}$ by its reciprocal and transposing the resulting matrix. This is equivalent to expressing $\tilde{\boldsymbol{m}}$ as a linear combination of basis vectors $\boldsymbol{V}_i$,

$$\tilde{\boldsymbol{m}} = \sum_{i=1..\min(M,N)} \tilde{m}_i \boldsymbol{V}_i, \tag{2.2.6}$$

in which the ith spectral component of the singular vector expansion of the model vector is given by

$$\tilde{m}_i = \boldsymbol{U}_i \cdot \boldsymbol{d}/\lambda_i, \quad i = 1..\min(M,N), \tag{2.2.7}$$

where the centered dot represents the scalar product. Similarly, the data vector can be expressed as $\boldsymbol{d} = \sum_{i=1..\min(M,N)} \tilde{d}_i \boldsymbol{U}_i$, in which the ith spectral component of the data vector is $\tilde{d}_i = \boldsymbol{U}_i \cdot \boldsymbol{d}$. The first $\min(M,N)$ spectral components of the data and model vectors are thus related by $\tilde{d}_i = \lambda_i \tilde{m}_i$. From the latter expression it follows that the smaller is the singular value, the less sensitive is the data component to a given change of the corresponding model component; in other words, the singular value bears information about the sensitivity of the data to the particular basis function in the model space. Moreover, the relation $\tilde{m}_i = \tilde{d}_i/\lambda_i$ shows that noise in a data component associated with small λ_i is amplified by the inversion; the singular value thus also bears information about the sensitivity of the model to additive data noise.

Olson and Apsel (1982) divided the inversion solution into two parts: stable and unstable, which are associated with larger and small singular values, respectively. The singular vectors than form so-called co-image and (effective) null subspaces in the model space. A possible regularization of the inverse solution is obtained by using only singular vectors from the co-image space to form the solution. The so-called truncated solution $\boldsymbol{m}_T$ is thus defined as

$$\boldsymbol{m}_T = \sum_{i=1..K} \tilde{m}_i \boldsymbol{V}_i, \tag{2.2.8}$$

in which K is the index of the smallest singular value larger than λ_c considered as the separation between the co-image and null spaces.

We note that for a given fault position the shapes of the singular vectors are determined by distribution of stations and crustal structure. This information is independent of the actual rupture model and data (seismograms). In [P11] we show examples of singular vectors for a realistic configuration of near-regional stations for example application to the 2008 Mw 6.3 Movri Mountain, Greece, earthquake. Starting with the analysis of singular vectors for individual stations, the first singular vectors are shown to have the character of smooth inclined strips with angles given by the station azimuths with respect to the fault strike. When the whole station network is considered, more complex shapes

appear, being combination of the individual station strips. Such a smooth ('low-frequency') character of the singular vectors is advantageous because, typically, synthetic Green's functions are more reliably estimated in the low-frequency band. The singular vectors with lower data sensitivity (associated with small singular values) have more complex ('high-frequency') shapes, being more vulnerable to Green's function imperfections and/or noise in the data. More on this issue can be found in section 2.2.2.4.

In [P12] we supplemented the TSVD method by the positivity constraint on the slip velocity using the non-negative least-square (NNLS) approach (*Lawson and Hanson*, 1995). To be able to truncate while using NNLS, the augmented matrix approach is used (*Olson and Apsel*, 1982). This way, a new set of equations is thus added to the problem to minimize the contribution from the truncated singular vectors in the NNLS solution.

2.2.2.3 Linear slip inversion with prior covariance

In [P15] we propose to consider a prior covariance function as a smoothing constraint and constrain scalar seismic moment M_0 of the earthquake. In such a case, the L2 misfit function reads

$$M(\boldsymbol{m}) = \frac{1}{2}\left(\boldsymbol{d}-\mathbf{G}\boldsymbol{m}\right)^{\mathrm{T}}\mathbf{C}_{\mathbf{D}}^{-1}\left(\boldsymbol{d}-\mathbf{G}\boldsymbol{m}\right)+\frac{1}{2}\left(\boldsymbol{m}-\boldsymbol{m_A}\right)^{\mathrm{T}}\mathbf{C}_{\mathbf{M}}^{-1}\left(\boldsymbol{m}-\boldsymbol{m_A}\right)+\frac{1}{2\sigma_{M0}}\left(\boldsymbol{E}\,.\,\boldsymbol{m}-M_0\right)^2, \tag{2.2.9}$$

where $\mathbf{C_D}$ and $\mathbf{C_M}$ denote the data and prior covariance matrices, σ_{M0} is the weight of the seismic moment constraint, and $\boldsymbol{E}$ is a vector of seismic moments of the elementary subfaults i, $E_i = \mu_i \Delta L \Delta W \Delta t$. We assume $\sigma_{M0} = M_0$ and $\boldsymbol{m_A} = \mathbf{0}$.

In order to apply the non-negativity constraint on the slip rates, we write a system of equations, misfit function of which is the same as in Eq. (2.2.9),

$$\begin{pmatrix} \mathbf{U}_{\mathbf{D}}^{-\mathrm{T}}\mathbf{G} \\ \mathbf{U}_{\mathbf{M}}^{-\mathrm{T}} \\ \frac{1}{\sigma_{M0}}\boldsymbol{E} \end{pmatrix} \boldsymbol{m} = \begin{pmatrix} \mathbf{U}_{\mathbf{D}}^{-1}\boldsymbol{d} \\ \mathbf{0} \\ \frac{1}{\sigma_{M0}}M_0 \end{pmatrix}. \tag{2.2.10}$$

In Eq. (2.2.10) matrices $\mathbf{U_D}$ and $\mathbf{U_M}$ are (upper) triangular matrices obtained by Cholesky decomposition $\left(\mathbf{C} = \mathbf{U}^{\mathrm{T}}\mathbf{U}\right)$ of $\mathbf{C_D}$ and $\mathbf{C_M}$, respectively. The augmented matrix and augmented data vector in (2.2.10) are inputs to the fast NNLS subroutine by *Luo and Duraiswami* (2011) that takes advantage of the efficient multi-core Intel Math Kernel Library.

Let me remark that *Fan et al.* (2014) formulated the linear inverse problem in frequency domain, which, however, prevented them from applying the positivity constraint. I also note that the present approach could be converted to the more classical one with spatial smoothing by means of a Laplace operator applied on $\boldsymbol{m}$ (e.g., *Hartzell and Heaton*, 1983; *Sekiguchi et al.*, 2000) by substituting matrix $\mathbf{U}_{\mathbf{M}}^{-\mathrm{T}}$ in Eq. (2.2.10) by a discretized version of the Laplacian.

In [P15] we consider $\mathbf{C_M}$ to be composed of discretized prior covariance function $\sigma_M^2 c_M(\tau, x, y)$ with temporal lag τ, and with spatial lags x (along strike) and y (along dip), where σ_M is the marginal standard deviation of the model parameters (c_M itself is considered to have unit variance). We assume further that the Fourier spectrum of c_M (i.e. slip-rate power spectral density) is proportional to

$$c_M(f, k_x, k_y) \propto \left(\frac{1}{1 + (k_x L)^2 + (k_y W)^2} \right)^2 , \tag{2.2.11}$$

where f is frequency, and k_x and k_y are wavenumbers in the along-strike and along-dip directions, respectively. Since c_M in (2.2.11) is independent of f, the prior model parameters are considered to be statistically independent of time. From (2.2.11) it also follows that the slip rates are considered to have k^{-2} amplitude spectrum in the spatial domain (with radial wavenumber $k = \sqrt{k_x^2 + k_y^2}$). The particular choice of the spectral decay in Eq. (2.2.11) follows theoretical (*Andrews*, 1980; *Herrero and Bernard*, 1994; *Gallovič and Brokešová*, 2004) and observational (*Somerville et al.*, 1999; *Mai and Beroza*, 2002) studies on spatial properties of earthquake slip distributions. Note that the covariance function controls the spectral decay (i.e. smoothness) of the solution.

The developed suite of codes for linear slip inversions and resolution analysis has been made publicly available under the name LinSlipInv at `https://github.com/fgallovic/LinSlipInv`.

2.2.2.4 Analysis of slip inversion uncertainty and artifacts

Let us first review some general properties of a linear slip inversion. The minimization of L2 misfit function (2.2.2) is implicitly controlled by the condition number of matrix $\mathbf{G^T G}$. We note that matrix $\mathbf{G}$ of the forward problem is composed of Green's functions (GFs), and thus $\mathbf{G^T G}$ contains cross correlations of the GFs along the fault. Therefore, the performance of linear slip inversion is determined by the variability of the GFs along the fault. Due to the necessity of fine fault sampling to accurately compute the representation integral, for each station the adjacent GFs are alike and hence strongly correlated. This effectively lowers the rank of $\mathbf{G^T G}$, and thus the matrix becomes generally not invertible. To correct for this, regularization by smoothing or inclusion of a prior covariance matrix must be employed (section 2.2.2.3). In particular, in case of distant (near-regional) receivers, the difference between neighboring GFs is merely a time shift, leading to strong spatial-temporal trade-offs (P[9, 11]). In the extreme case of using only direct S waves, modeled as rays in the Fraunhoffer approximation, the forward problem becomes equivalent to the Radon transform with a well-defined kernel in the space-time domain even for continuous station coverage, implying that, in principle, some slip models cannot be recovered (e.g., *Menke*, 1985; *Bindi and Caponnetto*, 2001).

Olson and Apsel (1982) divided the inversion solution by means of SVD into two parts: stable and unstable. The stable part is demanded by the data, while the unstable part is unrecoverable by the data alone. Thus the key question to be addressed is whether the stable part reflects at least the major features of the true model. If not, the inversion is said to contain artifacts. Possible artifacts of the seismic slip inversion were investigated in [P9] considering a near-regional station distribution. The main concept of seismic source tomography, i.e. the projection lines (along which the observed signals are back-projected to the fault) was extended to complete wavefields. The so-called "dynamic projection strips" (DPSs) were defined, and a method to construct the strips from waveforms was described. In this way, each individual station role in the inversion can be better understood. Synthetic models with two asperities (two unilateral and one bilateral rupture scenarios) were considered as examples. They were analyzed using two independent slip inversion methods, both resulting in a biased rupture speed for all scenarios and a strong false asperity in the middle of the bilateral fault. The artifacts can be

explained by the DPS analysis as a result of inherent non-uniqueness of the inverse problem due to the joint effect of the two true asperities. Removal of some slip artifacts by imposing various constraints was also discussed. The ideas were applied to the Movri Mountain earthquake in Greece, Mw 6.3, June 8, 2008. Few equivalent non-smooth models, all fitting near-regional waveforms equally well, were illustrated.

Contrary to the above mentioned intuitive, physically-based approach, in [P11] we complemented the analysis of artifacts by a mathematically-based approached exploiting the SVD approach (see section 2.2.2.2). When inverting waveforms for the slip velocity image, the sum over singular vectors is truncated, preserving only the so-called leading singular vectors. Keeping only a few leading singular vectors works seemingly as smoothing due to the smooth character of the singular vectors themselves. However, such regularizations (although providing a stable solution) may also have a negative effect on the inversion. For example, in [P11] we demonstrate that truncation of the symmetric bilateral rupture with little slip at the hypocenter discussed above results in a model with the strong asperity at the hypocenter. Thus, the truncated solution not only limits the resolution, but in some problems even simple and stable structures in the parameter space may differ from the true ones. Note that this does not mean that the stable structures are incorrect. It is a correct part of the solution of the inverse problem, however, it is an incomplete representation (approximation) of the true solution. Therefore, generally speaking, the success of the inversions depends on how well the true (unknown) slip model can be decomposed into the leading singular vectors.

From the above discussion it follows that it is important to have the singular vectors with a 'rich' space-time pattern, which happens in case of near-field stations with good azimuthal coverage. This is demonstrated in [P12, 15, 17] on the L'Aquila earthquake applications, where we deal with near-source data in a 1-D layered and 3-D complex structures. In such case the wavefield is inherently more complex even at relatively low frequencies (< 0.5 Hz), comprising strongly spatially variable near-field and intermediate-field terms (consisting of both P and S waves) and free surface effects. Therefore, the GFs are much more variable along the fault plane with respect to the near-regional case discussed in P[9, 11], making $\mathbf{G^T G}$ better conditioned and the inversion better constrained. Nevertheless, I stress that even in such a case it is still important to first properly understand the effects of smoothing and the role of imperfect GFs before application to real data.

2.2.2.5 Limitations due to the complexity of the wave propagation

The performance of the slip inversion is limited by the presence of errors in the data and the quality of the waveform modeling. The data error may be due to instrumental or ambient noise effects. However, in most source inversion studies including those of this Thesis the signal-to-noise ratio is rather high and data corrupted by strong instrumental disturbances (e.g., *Zahradník and Plešinger*, 2010; *Vackář et al.*, 2015) are typically omitted. The second source of errors is related to the imperfections of the Green's functions (GFs) due to the inaccuracy of the crustal model considered. A third source is related to the uncertainty of the fault location and its precise geometry, which can be to some extent considered as equivalent to the previous one.

In literature many synthetics tests of slip inversions were documented, most of them being performed using the nonlinear inversion techniques (*Konca et al.*, 2013; *Shao and Ji*, 2012; *Razafindrakoto*

and Mai, 2014). The message regarding the inversion performance is typically optimistic. The problem is that such 'positive' tests are typically performed under conditions that are far from those met in real-data applications. For example, *Shao and Ji* (2012) demonstrated on the SPICE source inversion validation test BlindTest1 that the nonlinear inversion performs well considering frequency range 0-2Hz, precise Green's functions and fault location, and almost perfect station coverage. In some cases the authors 'simulate' the real conditions, e.g., by introducing imperfections in the Green's functions (*Graves and Wald*, 2001; *Ji et al.*, 2002a; *Piatanesi et al.*, 2007; *Konca et al.*, 2013; *Razafindrakoto and Mai*, 2014) or data, such as by adding uncorrelated Gaussian noise to the 'observed' data (*Shao and Ji*, 2012; *Sekiguchi et al.*, 2000; *Ji et al.*, 2002b; *Cohee and Beroza*, 1994; *Bernauer et al.*, 2014). The stability of the inverted slip models in these synthetic tests is in contradiction with differences found in models obtained by various authors using various inversion methods and/or datasets. For example, *Clévédé et al.* (2004) compare models of the Izmit earthquake inverted by various authors and various techniques, some of them being characterized by rupture complexities, and some not.

To understand the inversion performance properly, one needs to perform synthetic tests under conditions that are as realistic as possible. Therefore, in [P15] we performed a series of synthetic tests to understand the behavior of the linear slip inversion with prior covariance, positivity constraint and a long time window (section 2.2.2.3) in terms of stability and sensitivity to 3D crustal structure. In particular, we discussed the effect of smoothing and the use of imperfect Green's functions. All the tests are performed under realistic conditions corresponding to the Mw 6.3 L'Aquila earthquake by considering i) real station distribution, ii) the same frequency range as used in the real data case, iii) the test crustal model being based on 3D tomography and including topography and realistic random velocity variations. In the inversion tests we consider a smooth target model as well as a point dislocation model to analyze the inversion resolution in detail. In particular, we analyzed how neglecting 3D heterogeneous earth crust properties (velocities and topography) affect source imaging results. With this aim we created a set of synthetics using complex 3D crustal model and topography and inverted them in a flat 1D structural model, considering various strengths of the smoothing constraint. We found that time of the slip-rate peak is the least affected source parameter and that imprecise Green's functions can introduce artificial slip-rate multiples especially at shallow depths. We concluded that the inversion result cannot be taken as it is, but it must be interpreted taking into account the lessons learned from the synthetic tests. Only this way one can conclude which of the model features are convincing and which of them are doubtful, having several possible explanations.

2.2.3 Multiple-Finite Extent (MuFEx) source model

As discussed above, the linear slip inversions are highly vulnerable to occurrence of artifacts especially in unfavorable conditions (see section 2.2.2.4). Moreover, the abundant number of model parameters prevents from any uncertainty analysis. Therefore, in some applications it is advantageous to restrict ourselves to more simple source models with lower number of parameters to overcome these issues.

In [P12] we introduced a simple source model composed of Multiple Finite-Extent (MuFEx) subsources of rectangular shapes. The slip amplitude, rupture velocity, rake and rise time are assumed to be constant within each subsource. The rise time is assumed smaller than the reciprocal of the maximum investigated frequency, so that the slip rate function corresponds effectively to an impulse function.

The size and location of the MuFEx subsources have to be inferred independently by other method(s), e.g., a linear slip inversion, or the iterative multiple-point source deconvolution by the ISOLA package (*Sokos and Zahradník*, 2008, 2013).

Each MuFEx subsource is characterized by an individual set of trial nucleation points, rupture velocities and nucleation times. The inversion is performed by means of grid search. For each combination of these parameters, the slip values of the subsources are determined by the least-squares approach. Each model is then characterized by its fit with observed data in terms of variance reduction VR. Neglecting all models with negative slip values and considering minimum acceptable VR, we end up with a set of plausible rupture models. This procedure thus not only provides a best-fitting model, but also a whole range of acceptable models, allowing for a straightforward uncertainty analysis. Examples of the application of this method can be found in sections 3.1.3 and 3.1.4, and papers [P12, 14]

2.2.4 Comparison of slip inversion results by exploiting the eigenstructure of the inverse problem

An important step in understanding the variability of the inverse solutions obtained by various methods and/or inversion setups is to characterize the similarities and differences of the inverted models. For example, *Clévédé et al.* (2004) demonstrated that slip models of the 1999 Izmit earthquake inverted by various authors agree in terms of the second order moment tensor properties. *Zhang et al.* (2015) and *Razafindrakoto et al.* (2015) developed and calibrated advanced comparison techniques and presented example applications to models from synthetic tests. Moreover, the latter comparison approach has been also applied to published rupture models of the 2011 Tohoku earthquake. However, those methods were used only for comparing the final slip distribution.

In [P17] we propose an alternative approach to compare the complete space-time evolution of inferred rupture models. The method is based on a spectral decomposition of the forward operator using SVD (see section 2.2.2.2), providing basis functions (singular vectors) $\boldsymbol{V}_i$ in the model space. These can be divided into those lying in either the co-image space or the null space, associated to large and small (or even zero) singular values, respectively. One can then decompose any source model into two parts made of linear combinations of singular vectors lying in the co-image and in the (effective) null space. It is desirable for any slip inversion method to reveal correctly those model features that are resolvable, i.e. those lying in the co-image space. The inversion results obtained by different methods may then differ in their null space contributions, which are implicitly determined by the particular choices of source model parameterization and regularization of each method. I point out that since matrix $\mathbf{G}$ has, in general, smoothly decaying spectrum without a clear boundary between the co-image and the null space, the choice of a cut-off singular value that separates co-image and null spaces is not obvious. In [P17] we proposed an objective criterion to define the cut-off singular value in practice, which is based on the Discrete Picard criterion, a fundamental condition for stability of regularized solutions of the inverse problem, which requires the spectral amplitudes of the data to decay faster than the singular values *(e.g., Hansen, 2010).*

In [P17] we illustrate the proposed comparison technique through an example from an international synthetic benchmark experiment conducted under the Source Inversion Validation (SIV) initiative (*Mai et al.*, 2016), which aims to characterize and understand the performance of slip inversion methods

(http://equake-rc.info/SIV/). Up to now, four benchmark test cases have been proposed, some of which were conducted as blind tests. The benchmarks differ in the properties of the target models and in the amount of information provided to the modelers. In the benchmark problem SIV2a considered in [P17] the crustal model is known exactly and the fault plane location is given with some uncertainty. Modelers are asked to download synthetic data calculated at an array of receivers, perform their inversion and eventually upload their model on the website. For the SIV2a benchmark, 10 slip models have been uploaded so far, including updates of the individual solutions. I have contributed by uploading solution obtained by the linear inversion approach with slip-rate positivity constraint and smoothing by means of the prior k^{-2} covariance functions assuming several strengths of the smoothing constraint. *Mai et al.* (2016) ranks my solution "gallovic2" of the INV1 benchmark second best among the uploaded slip models based on the comparison metric of *Razafindrakoto et al.* (2015). For the SIV2a benchmark, *Mai et al.* (2016) demonstrates that good waveform-fitting can be achieved despite remarkably different rupture models obtained by various participants. Using the comparison metric of *Razafindrakoto et al.* (2015) to these solutions, *Mai et al.* (2016) find that only four models fall in the category "good", but it is clear that solutions "asano" and "gallovic1" clearly outperform the other solutions.

In [P17] we compare selected models inferred by various authors using various techniques (see Table 2.1). The models show significant differences, which can be ascribed to i) different model parametrization (linear, nonlinear, nonlinear with very few parameters, etc.), ii) different inversion setup (choice of frequency ranges, filter types, station/component weights, smoothing constraints, etc.), and iii) different GFs (slightly differing fault plane position and orientation, different rake angle, numerical issues, etc.). The tests performed in [P17] utilizing the Picard condition and the comparison of the inverted models indicate that due to the use of imperfect Green's functions the effective rank of $\mathbf{G}$ is 637, corresponding to the subspace associated to singular values larger than $1/10$ of the maximum singular value λ_{MAX}. The source models obtained by various modelers using different inversion methods for the SIV2a problem (see Table 2.1) agree well with each other when the comparison is restricted to the well-resolved part of the true model, i.e. to the effective range of $\mathbf{G}$. The models thus mainly differ in their respective contribution from the null space, which is determined by the particular priors implied by their choices of regularization or parameterization and affected by the imperfections of the GFs.

We note that although the truncated models capture the overall rupture propagation, their final slip distributions are biased, showing distinct spurious peaks below the stations lying above the rupture. This suggests that although the overall characteristics of the rupture propagation can be retrieved relatively well, the static slip distribution is not very well constrained. Hence, each station has enhanced sensitivity in its vicinity. This example highlights the abstract nature of the co-image subspace: a truncated model, although robust, may display source patterns that are not directly amenable for physical interpretation, which was already pointed out in Sec. 2.2.2.4.

The comparison of SIV2a benchmark solutions presented here suggests that the linear methods perform better than the nonlinear ones. That might be true in this particular case where the fault-plane geometry and the GFs are almost exact. However, nonlinear methods can be potentially less sensitive to imperfections in the GFs, thus providing more robust (albeit less precise) solutions. They can also work with other objective functions than the L2 norm considered here, putting emphasis on different aspects of the wavefield and potentially leading to different solutions (*Hartzell et al.*, 1991). Moreover,

Model name *Method*	Description	Data processing
Gallovic0.01 *[P15]*	Linear multi-time window inversion approach with long duration of slip rate functions (equal to the assumed duration of the rupture process). Constraints: i) smoothing by means of a prior k^{-2} covariance functions, ii) positivity of the slip rate function. The smoothing weight is relatively small (perhaps not applicable in real-data application).	Bandpass Butterworth filter in range of 0.05-0.5 Hz (4 poles, causal).
Gallovic0.1 *[P15]*	Same as Gallovic0.01, but with more severe smoothing (similar to that used in real data applications).	Same as Gallovic0.01.
Hoby *(Razafindrakoto and Mai, 2014)*	Parametric (single-time window) inversion assuming triangular slip rate function. Parameters: rupture times, rise times, peak slip rates. Metropolis algorithm is used to optimize the parameters considering L2-norm.	Butterworth bandpass in range of 0.01-1 Hz.
CedricT3 *(Twardzik et al., 2012)*	Simplified source model considering two elliptical slip patches, triangular slip rate function and constant rupture velocities along the patches. Parameters: location and size of the ellipses, rupture velocities, onset times of the subfault patches. Neighborhood algorithm is used to find the best fitting parameters considering L2-norm.	Butterworth bandpass filter in range of 0.1 - 1.0 Hz (4 poles, 2 passes - acausal).
Asano *(Sekiguchi et al., 2000)*	Multi-time window linear inversion with spatiotemporal smoothing constraint. Weight of smoothing is determined by minimizing the Akaike's Bayesian Information Criterion (ABIC).	Bandpass filter in range of 0.05 - 1.0 Hz.

Table 2.1: List of the inverted models of the SIV2a benchmark with brief explanation of the applied inversion techniques. Adopted from [P17].

the nonlinear methods have the advantage of working with generally lower number of parameters, which enables effective uncertainty analysis (e.g., *Cirella et al.*, 2009).

We note that it is not straightforward to compare the performance of linear slip inversion to the non-linear slip inversions and to transfer lessons learned in one of the methods to the other. Such generalization requires further considerations. We present here an analogy with the problem of spectral estimation. In our understanding, linear approach to slip inversion can be seen as "nonparametric" approach in spectral estimation (i.e. nonparametric spectral estimators). In nonlinear inversions the rupture is parameterized assuming some shape of slip rate function, rupture propagation, etc., which would correspond to "parametric" spectral estimators. It is well known that the parametric spectral estimators have higher resolution than their nonparametric counterparts due to the use of a model to explain the observed signal. Thus, in analogy considered here, the parametric (nonlinear) inversions could be able to resolve parameters more precisely due to the use of a rupture propagation model. However, the higher resolution in the parametric estimations is appropriate only when the adopted model is correct, which is of course very hard to prove (especially in the seismic source analysis when we are not very sure about exact behavior of the rupture process). In similar sense, it is not simple to extend our conclusions to the so-called dynamic slip inversions (e.g., *Peyrat and Olsen*, 2004), where the source model is described by a friction law and a stress state.

2.3 Broadband strong ground motion modeling

Modeling realistic time histories of displacement, velocity and acceleration in broad frequency range in the vicinity of a fault is of great importance for seismic engineers in determining the structural response and in damage estimation. Physics-based strong ground motion simulations can provide a realistic representation of site-specific ground motions through a detailed modeling of the seismic source process, waves propagation and local site response. Especially at short fault distances the simulations require physically plausible earthquake source model. Such model must be compatible with basic characteristics observed in earthquake source studies of real events and with properties suggested by earthquake source dynamics. Moreover, the method must be able to provide ω-square source spectrum in a broad frequency range, which is commonly observed in the real data (*Aki*, 1967).

The simplest ω-square amplitude spectrum of the source time function introduced by *Brune* (1970) reads

$$|\Omega_0(f)| = \frac{M_0}{1 + (f/F_c)^2}, \tag{2.3.1}$$

where M_0 and F_c are the seismic moment and corner frequency of the target event, respectively. The acceleration spectrum is then characterized by a plateau described as:

$$\lim_{f\to\infty} (2\pi f)^2 \, |\Omega_0(f)| = (2\pi)^2 M_0 F_c^2. \tag{2.3.2}$$

The corner frequency of the target event can be converted to standard Brune stress drop $\Delta\sigma$ (*Keilis-Borok*, 1959; *Brune*, 1970) using formula $F_C = 49\beta(\Delta\sigma/M_0)^{1/3}$, β being the shear wave velocity (3.5km/s in our application). Stress drop $\Delta\sigma$ can be determined through the fit with the observed

high-frequency seismograms.

A summary and comparison of some of the finite-extent broadband kinematic models are given by, e.g., *Hartzell et al.* (1999). Let us distinguish the models into *integral* and *composite*, according to the source representation.

- In the *integral* approach (*Bernard et al.*, 1996; *Gallovič and Brokešová*, 2004; *Liu et al.*, 2006; *Schmedes et al.*, 2012; *Gusev*, 2012; *Song*, 2016, etc.), the source process is described by a spatial-temporal distribution of slip function over the fault. Strong ground motions generated by such source model are calculated by means of evaluating the representation integral along the fault (see Eq. (1.1.2)). Numerically, the fault is discretized on a fine grid and the representation integral is substituted by a sum, so that the finite extent source is represented as a coherent superposition of point sources distributed regularly along the fault. The spatial spacing must be small enough to avoid numerical problems in the integral evaluation (*Spudich and Archuleta*, 1987). It is clear that this procedure could require much numerical effort at high frequencies due to the necessity of dense discretization and evaluation of large number of Green's functions. On the other hand, it is straightforward to implement such source model to numerical codes for wave propagation modeling with almost no additional computational burden. Note that some methods combine the integral approach with stochastic Green's functions by means of tapering broadband correlated noise with ω-square spectrum by a low-frequency envelope obtained by the integral approach (e.g., *Pacor et al.*, 2005).

- The idea of *composite* models (*Hartzell*, 1978; *Irikura and Kamae*, 1994; *Zeng et al.*, 1994; *Frankel*, 1995; *Beresnev and Atkinson*, 1997) is based on assumption that the modeled event can be seen as a discrete sequence of individually-rupturing subevents that are typically treated in the point-source approximation (*Brune*, 1970). The source time function of each subsource is characterized by its spectral shape, corner frequency, seismic moment, etc. Contributions of subevents are summed in order to get proper seismic moment and spectral shape of the source function corresponding to the whole fault. This approach is often used together with stochastic Green's functions (e.g., *Motazedian and Atkinson*, 2005), the empirical Green's function method (e.g., *Irikura and Kamae*, 1994), but synthetic Green's function can be used as well (e.g., *Zeng et al.*, 1994).

- *Hybrid* combination of the above approaches are perhaps the most widely used. In particular, the integral and composite approaches are used for low- and high-frequency bands, respectively, and then they are combined by means of cross-over filtering (e.g, *Graves and Pitarka*, 2010; *Irikura and Miyake*, 2010; *Gallovič and Brokešová*, 2007). However, in some of the methods the integral and composite models in the hybrid approach are unrelated (e.g, *Graves and Pitarka*, 2010), which might lead to sometimes tricky spectral matching in the cross-over frequency zone.

Below I overview two kinematic methods, which were introduced and utilized in broadband ground motions simulations of past events and also in the ground motion prediction in the papers of this Thesis (see also Chapter 3). In particular, section 2.3.1 describes so-called Hybrid Integral Composite (HIC) method of *Gallovič and Brokešová* (2007) with related low- and high-frequency source models. In section 2.3.2 I briefly overview the main properties of the so-called Ruiz Integral Kinematic (RIK) source

model originally introduced by *Ruiz et al.* (2013) and tuned in [P18]. The main difference between the various broadband source models is in how they treat the directivity effect at high frequencies. Since the correct approach is still a subject of debate, I devote section 2.3.3 to this issue. Last section 2.3.4 discusses the treatment of the radiation pattern at high frequencies.

2.3.1 Hybrid integral composite (HIC) method

HIC model introduced by *Gallovič and Brokešová* (2007) is developed for earthquake ground-motion simulations following ω-squared source model, see Eq. (2.3.1). The modeling technique is based on previous works by *Andrews* (1980), *Herrero and Bernard* (1994), *Zeng et al.* (1994) and *Gallovič and Brokešová* (2004). The faulting process is decomposed into slipping on individual, formal, overlapping subsources of various sizes, distributed randomly along the fault.

The subsources have number-size distribution with fractal dimension $D = 2$. For simplicity, the subsources are assumed rectangular with length and width given by integer fractions of the fault length L and width W, i.e., of sizes $l_k = L/n$ and $w_k = W/n$, where the level $n = 2 \dots N$. For the particular number-size distribution the number of subsources at level n equals to $2n - 1$. The variable size of subsources is advisable in composite source modeling as it overcomes problems with the definition of the size of the subsources and related deficiency in radiation at mid frequencies (*Irikura and Kamae*, 1994). We assume that the subsources radiate Brune source time functions being described by seismic moment m_0^k and corner frequency f_c^k with the complex Fourier spectrum

$$\Omega^k(f) = \frac{m_0^k}{\left(1 + if/f_c^k\right)^2}, \tag{2.3.3}$$

where i is the imaginary unit.

Assuming that slip is proportional to the subsource length (the constant stress drop scaling), the subsource seismic moment and corner frequency depend on the size of the subsource as $m_0^k = c_1 \mu l_k^2 w_k$ and $f_c^k = c_2 v_r / l_k$, respectively, where μ is the shear modulus and v_r the rupture velocity. Constant of proportionality c_1 for the seismic moment is such that the sum of seismic moments of all subsources is equal to the target seismic moment, i.e.

$$c_1 = \frac{M_0}{\mu \sum_{k=1}^{N} l_k^2 w_k}. \tag{2.3.4}$$

Assuming incoherent summation of the subsource contributions, constant of proportionality c_2, related to corner frequency f_c^k, is such that the target acceleration power-spectrum plateau matches the plateau of the sum of the subsource acceleration power spectral plateaus, i.e.,

$$c_1 = \frac{M_0 F_c^2}{\mu \sqrt{\sum_{k=1}^{N} \left(l_k^2 w_k\right)^2 \left(v_r / l_k\right)^4}} = \frac{M_0 F_c^2}{\mu v_r^2 \sqrt{\sum_{k=1}^{N} w_k^2}}. \tag{2.3.5}$$

Let us point out that although the subsources share the same stress drop, its particular value is not the same as the target stress drop. This is so because it is theoretically impossible to create a fully self-similar source model, where both seismic moment and high-frequency plateau of the target ω-squared spectrum would be fitted by subsources following constant stress drop scaling and having

ω-squared spectrum (*Frankel*, 1991). Therefore, the decomposition of the source model into subsources is to be considered just as a formal representation to introduce a complex ω-squared source radiation. We emphasize that the important physical feature of our model is that the fractal decomposition of the source model implies k^{-2} slip distribution (as demonstrated by *Gallovič and Brokešová*, 2007 or *Ruiz et al.* (2011) and *Ruiz et al.* (2013)) and, consequently, k^{-1} stress distribution. The latter spectral fall-off was shown to be physically plausible on the basis of theoretical considerations by *Andrews* (1980).

Since the subsources provide k^{-2} slip distribution, we can use in the HIC model the same set of subsources both in the integral (low-frequency) and composite (high-frequency) calculations. Indeed, at low frequencies we employ the representation theorem assuming the k^{-2} slip distribution (obtained by composing subsources slip contributions). At high frequencies, the composite approach, based on the summation of ground motion contributions from the subsources treated as individual point sources, is used. In the cross-over frequency range we apply weighted averaging of the real and imaginary parts of the integral and composite parts of the spectrum.

2.3.2 Ruiz Integral Kinematic (RIK) model

Ruiz et al. (2011) introduced an advanced kinematic model (hereafter denoted as Ruiz Integral Kinematic, RIK, model), which can be understood as an extension of the HIC model. The main difference is that the RIK utilizes the representation integral in the whole frequency band (no composite modeling is needed), while providing ω-squared source spectral decay at high frequencies. The other advantage of the RIK model is that it does not need any cross-over filtering required in the hybrid techniques, which is typically performed ad-hoc. In [P18, 19] we simplified some aspects of the original method for better efficiency and introduced several specific features required by our particular applications (such as the depth-dependence of the rupture velocity and randomized rupture velocity).

As in the HIC model, the RIK model is composed of randomly distributed subsources with fractal number-size distribution with dimension $D = 2$. In this case the subsources attain circular shape. Unlike in the HIC model where the subsources are treated as point sources at high frequencies, the RIK subsources have prescribed kinematic properties (including the rupture propagation) to each of the subsources individually, and thus each subsource is characterized by its own slip rate functions along its areal extent. The total slip rates of the RIK model are eventually evaluated on a regular discretization grid along the fault by summing up slip rate contributions from all the subsources (following the representation integral). Therefore, RIK subsources are not treated as extended sources, taking fully into account rupture propagation along them.

The subsource radii R are integer fractions of the fault width W, i.e. $R = W/n$. For the particular number-size distribution, the number of subsources at level n is $2n - 1$. The subsources are distributed randomly along the fault. In the scenario modeling we consider uniform distribution, but in the real data modeling we use slip distribution obtained from inversion of low-frequency data as a spatial probability density (PDF). The individual subsources have the crack-model slip distributions, i.e.

$$\Delta u^R \propto \sqrt{R^2 - \rho^2} \text{ if } \rho < R;\ \Delta u^R = 0 \text{ otherwise}, \tag{2.3.6}$$

where ρ is the distance from the subsource center. The constant of proportionality in (2.3.6) is deter-

mined so that the total seismic moment fits the prescribed scalar seismic moment of the target event M_0. As in the HIC model, this fractal decomposition of the source model implies that the slip decays with k^{-2} at high wavenumbers k (*Ruiz et al.*, 2007; *Gallovič and Brokešová*, 2007), which implies physically plausible k^{-1} spectral decay of the stress distribution (*Andrews*, 1980).

The rupture is assumed to propagate in form of a slip pulse of width L_0 with the Brune's pulse (*Brune*, 1970) as the slip rate function, which has form equivalent to (2.3.3). If rise time was constant, the source spectrum would decay as ω-squared only up to the reciprocal of the rise time, decaying then faster due to the low-pass filtering effect of the slip rate function. To correct for this, *Bernard et al.* (1996) introduced the concept of the k-dependent rise time (see also *Gallovič and Brokešová*, 2004). In terms of the RIK subsources of various sizes, the rise time is considered to depend on subsource radius R as

$$\tau(R) = \tau_{max} = aL_0/v_r \text{ if } 2R > L_0;\ \tau(R) = a(2R)/v_r \text{ otherwise}, \tag{2.3.7}$$

where a is a free parameter (of the order of 1). Rupture speed v_r follows the S-wave velocity profile, keeping constant the rupture speed to S-wave velocity ratio, in order to avoid too fast (or even super-shear) rupture propagation close to the surface and thus enhanced source radiation. The dependence of the rise time on the subsource radii also implies a positive correlation between the slip and the rise time as it is observed in dynamic rupture simulations (e.g., *Schmedes et al.*, 2010).

In terms of the rupture propagation, *Ruiz et al.* (2011) introduced a concept of small- and large-scale rupture fronts. In particular, each point on subsources with radius $R > L_0$ starts to slip upon arrival of the macroscopic rupture front from the hypocenter. Contrarily, each smaller subsource has its own random point, from which a small-scale rupture is initiated after the random point is reached by the macroscopic rupture front. In other words, rupture time at a given point on the small subsource is a sum of the arrival time of the macroscopic rupture front to the random point and the time delay corresponding to the small-scale rupture propagation from the random point. This feature has a diminishing effect on the rupture directivity as discussed in the next section.

2.3.3 High-frequency directivity

In case of a unilateral rupture propagating at constant speed, the directivity can be parametrized by the well-known directivity coefficient $C_d = 1/(1 - \alpha\cos\theta)$, where α is the ratio between rupture and shear wave velocities, and θ is the angle between station position and the direction of rupture propagation (*Ben-Menahem*, 1961). While in theoretical models there is an agreement that the corner frequency is proportional to C_d, the amplification of the high frequency acceleration spectrum behind the corner frequency is subject of debate. Various models have been proposed, suggesting amplification by C_d^n with different powers n: ω-squared models with single corner frequency (e.g., k^{-2} model by *Herrero and Bernard*, 1994) suggest $n = 2$, models with two corner frequencies (e.g., the Haskell model with constant slip and rise time) suggest $n = 1$. More advanced models with inhomogeneous slip and rise time distributions (*Bernard et al.*, 1996; *Gallovič and Brokešová*, 2004; *Ruiz et al.*, 2011) and/or complex (incoherent) rupture propagation (*Zeng et al.*, 1994; *Gallovič and Brokešová*, 2007; *Ruiz et al.*, 2011) provide source radiation with frequency dependent n, typically decreasing from 1-2 to even 0 in

case of purely stochastic models. As explained further, the decay of n to 0 with increasing frequency is an implicit feature of the composite models (*Zeng et al.* 1994; *Pitarka et al.* 2000; *Gallovič and Brokešová* 2007; *Irikura and Miyake* 2010; etc.).

Let us discuss the two above described models, HIC and RIK, in terms of the directivity effect. In the integral part of the HIC model, the source spectral amplitudes above the (frequency dependent) corner frequency are proportional to C_d^2 (*Gallovič and Brokešová*, 2004). Contrarily, the spectral amplitudes of the composite modeling, when the subsources are treated as points sources with no directivity effect, the subsource contributions are summed up incoherently, providing isotropic ($C_d^0 = 1$) radiation. In the RIK model the situation is slightly more complicated. The source spectral amplitudes are proportional to C_d^2 between roughly the corner frequency and the reciprocal of the maximum rise time ($1/\tau_{max}$). As discussed by *Bernard et al.* (1996) and *Gallovič and Brokešová* (2004), at frequencies larger than $\sim 1/\tau_{max}$, the directivity effect is reduced to C_d^1, while preserving the ω-squared spectral decay. Introducing the concept of small- and large-scale rupture fronts, where the first one propagates from a randomly chosen points on the subsource, the directivity effect is weakened even further.

Unfortunately, observational data do not allow us to easily test various directivity models. Generally, wave propagation phenomena mask the source directivity effect due to complex crustal properties both along the path and close to the receivers (so-called path and site effects, respectively). Observations of strongly directive large earthquakes are sparse with, moreover, rather poor azimuthal station coverage. Well known examples are two recordings of the (predominantly unilateral) Mw 7.3 1993 Landers earthquake at Lucerne and Joshua Tree stations, which are clearly affected by forward and backward directivity effect, respectively. *Somerville et al.* (1997) pointed out that the strength of the directivity effect diminution with increasing frequency, which they supported also by empirical analysis of more events. Similar behavior of the frequency dependent directivity effect was observed by *Day et al.* (2008) in laboratory foam rubber experiments simulating earthquake with unilateral rupture propagation.

In [P1] we compared two common approaches to strong ground motion simulations due to finite extent seismic sources: a fully integral with impulse slip rate function and a composite approach. We showed that the former model provides larger scatter of peak ground acceleration than empirical models (ground motion prediction equations), which is explained by the overestimated directivity effect. Contrarily, the composite modeling resulted in more realistic scatter. In [P18] I have tested various strengths of the directivity using the RIK model, showing that the weakest directivity model fits near-field recordings particularly well (see also section 3.1.6). These results perhaps explain why methods utilizing composite models at high frequencies are generally very successful in modeling real data of large magnitude earthquakes.

Nevertheless, the observation of large earthquakes is sparse and the source effects are masked by complex site and path effects due to the large source area. Analysis of more abundant small events with better station coverage is thus appealing. Authors of such studies analyze the source directivity effect on either peak values (*Boatwright*, 2007) or duration of apparent source time functions (*Kane et al.*, 2013; *Courboulex et al.*, 2013; *Tan and Helmberger*, 2010). *Chen et al.* (2014) considered standard point-source model by *Brune* (1970), showing azimuthal variations of its corner frequency. *Tan and Helmberger* (2010) found evidence for directivity up to 7Hz for $M_w < 5$ events in the Big Bear sequence. However, in those studies the authors do not consider possible frequency dependence of the directivity effect.

In *Pacor, Gallovič, et al.* (submitted) present clear observations of directivity effects for small events (magnitudes 3-4) utilizing 261 events from the Abruzzo region, Central Italy, composed of mostly aftershocks of the Mw 6.3 2009 L'Aquila earthquake. Apparent source spectra of these events revealed by means of removing path and site effects using standard Generalized Inversion Technique (*Pacor et al.*, 2016) were used to evaluate spectral residuals (differences between the apparent source spectra and their mean) at selected frequencies. Those were investigated in terms of azimuthal and frequency dependence. Considering only 10 strongly directive events with very good azimuthal coverage, we observe a remarkable decrease of the directivity amplification at high frequencies (in particular at frequencies greater than roughly ~5 times the corner frequency of the respective event). This suggests that that the vanishing source directivity effect observed in large earthquakes (see above) holds also for small events, stemming perhaps from the self-similar character of earthquakes.

Note that the directivity effect could be weakened also by the wave propagation effects, such in random 3D scattering medium. However, simulations of such effects by *Imperatori and Mai* (2012) suggest that this effect is rather weak. We point out that in our above-mentioned study we observe very weak distance dependence of the directivity, similarly to *Somerville et al.* (1997). We demonstrate that the diminution of the directivity is related to the earthquake source effects, since it is observed at sites located both close and far from the epicenters. Therefore, we rule out the possibility that the path effect would be responsible for the observed directivity effect reduction.

2.3.4 Radiation pattern at high frequencies

Broadband ground motion simulations method seem to yield synthetic strong motion seismograms of realistic appearance in most cases. However, sometimes the synthetics have one component with amplitude much smaller than the other components, which is not observed in real data. To suppress the radiation pattern at high frequencies, *Zeng and Anderson* (1995) suggested prescribing random variation of the rake angle. In accordance with the studies of non-planar fault radiation by [P2] and [P8], we assume ±30° random variations of the strike, dip and rake angles of the subsources that are smaller than one half of the fault dimension when using the HIC model ([P5, 6, 10, 13, 14]). Due to the scaling of the source time functions of the subsource, the reduction of the radiation pattern is efficient only at high frequencies (at high frequencies the subsource wavefield contribution is proportional to the subsource size, in contrast to low frequencies, where it is proportional to its third power).

In [P8] we studied the applicability of deterministic strong ground motion simulations at near-fault distances on the example of the 2004 M6 Parkfield, California, earthquake. Theoretical modeling under the assumption of a planar rupture and 1D medium shows that, as a consequence of the S-wave radiation pattern, the particle motion should be almost linear in the fault-normal (F-N) direction, having fault-parallel (F-P) and vertical (V) components almost zero valued. However, in practice this is not the case. We numerically investigated this effect, considering a non-planar fault, a three-dimensional (3D) heterogeneity of the medium, and the non-planar Earth's surface topography. We found that just the 3D velocity model is crucial to obtain realistic estimates of ground motions at near-fault distances, i.e., the crustal heterogeneity seems to better explain the observed particle motions than the detailed fault geometry or surface topography. I note that this problem is rather localized to a narrow vicinity of faults (so-called fault zones). Indeed, I have not observed such problems in the modeling of the Napa

earthquake ([P18]) although the event had also strike-slip mechanism, but the nearest stations were approximately 5km away from the fault.

Chapter 3

Applications

In addition to synthetic tests, any newly introduced method requires extensive assessment of its performance by means of applications on real data to identify its practical limitations. In particular, slip inversions are mainly limited by our ability to evaluate Green's functions correctly, which is complicated by our rather poor knowledge of the Earth structure and also imprecise knowledge of the true fault plane location and geometry (see section 2.2.2.5). This limits the usable frequency range, which, in turn, limits the resolution of slip inversions. I emphasize that the "loss of resolution" can be appraised correctly only by means of synthetic tests as presented in sections 2.2.2.4 and 2.2.4. Only lessons learned from the synthetic tests may help the interpreter to carefully assess, which of the individual features of revealed source models are well constrained and which are not.

In the present chapter, I describe in section 3.1 the real-data applications, putting emphasis on the interesting features of the earthquake source that were revealed when combining selected methods described in Chapter 2. Section 3.2 is devoted to applications of strong ground motion simulations. In particular, I discuss scenario modeling, which are of interest for seismic hazard assessment, and applications to assess the performance of earthquake early warning systems.

3.1 Applications to real events

3.1.1 Overview of events analyzed in the collected publications

The tools developed within the papers of the present Thesis were applied on, in total, 10 earthquakes with magnitudes ranging from 5.7 to 7.1. The events are shown on maps in Fig. 3.1.1 and listed in Tab. 3.1. The table also briefly describes which methods were applied to each of the events. I point out that each event has its own characteristics and brings new lessons when interpreting the revealed source image in detail.

In the following sections I describe analysis of selected events.

3.1.2 Mw 6.3 2008 Movri Mountain (Greece) earthquake

On June 8, 2008 (12:25 UTC) a Mw 6.3 strike-slip earthquake occurred in the north-western Peloponnese (Greece) at 20km depth without any clear relation to mapped faults, but as close as 30 km from Patras, the third major city of Greece (*Ganas et al.*, 2009). Two victims were reported, along with hundreds

Earthquake Date	**Location [Lat., Long.]**	**Depth [km]**	M_w	**References (Methods)**
Athens, Greece 1999/09/07	38.08°, 23.58°	10	5.9	[P1]: SM prediction with emphasis on directivity (HIC).
Leonidio, Greece 2008/01/06	37.11°, 22.75°	70	6.2	[P3]: Fault plane identification (H-C).
Irpinia, Italy 1980/11/23	41.76°, 15.31°	10	6.9	[P5]: SM prediction for EEW testing (HIC). [P10]: Modeling of SM data, GM scenario (HIC).
Gubbio, Italy 1984/04/29	43.23°, 12.56°	6	5.7	[P6]: Modeling of SM data, variability of GM parameters (HIC).
Movri Mountain (Andravida), Greece 2008/06/08	37.94°, 21.52°	20	6.3	[P7]: Cascade analysis (IterLSI). [P9], [P11]: Analysis of slip inversion uncertainty and artifacts (IterLSI, TSVD).
Parkfield, USA 2004/09/28	35.82°, -120.37°	8	6.0	[P8]: 3D near-fault GM modeling.
L'Aquila, Italy 2009/04/06	42.34°, 13.38°	9	6.3	[P12]: Slip inversion (MuFEx). [P13]: SM data modeling (HIC). [P15]: Slip inversion with 3D GFs (LSI).
Van, Turkey 2011/10/23	38.72°, 43.41°	8	7.1	[P14]: Full cascade analysis (H-C, MuFEx, HIC)
Cephalonia doublet, Greece 2014/01/26 and 2014/02/03	38.15°, 20.39° 38.27°, 20.43°	15 6	6.1 6.0	[P16]: Cascade analysis (H-C, LSI).
South Napa, USA 2014/08/24	38.22°, -122.31°	10	6.0	[P18]: Slip Inversion (LSI) and SM data modeling with emphasis on directivity (RIK). [P19]: SM data modeling and GM scenario simulations (RIK).

Abbreviations: EEW – Earthquake Early Warning, SM – Strong ground motions, GM – Ground motion, GF – Green's function.
Methods: HIC – Hybrid Integral Composite SM model (*Gallovič and Brokešová*, 2007; Sec. 2.3.1), H-C – Hypoceter-Centroid collocation method ([P3], Sec. 2.1), MuFEx – Multiple Finite-Extent source inversion method ([P12], Sec. 2.2.3), IterLSI – Iterative linear slip inversion ([P7], Sec. 2.2.2.1), TSVD – Linear slip inversion using Truncated singular value decomposition approach ([P11], Sec. 2.2.2.2), LSI – Linear slip inversion method with prior k^{-2} covariance function and nonnegativity constraints ([P15], Sec. 2.2.2.3), RIK – Ruiz Integral Kinematic SM model (*Ruiz et al.*, 2011, [P18], Sec. 2.3.2).

Table 3.1: Events analyzed in publications appended to this habilitation Thesis. For map locations and focal mechanisms of the events see Fig. 3.1.1. Cascade analysis comprises of hypocenter relocation, centroid moment tensor inversion, fault plane identification and slip inversion. In addition, the full cascade analysis includes also modeling of strong ground motion data as the last step.

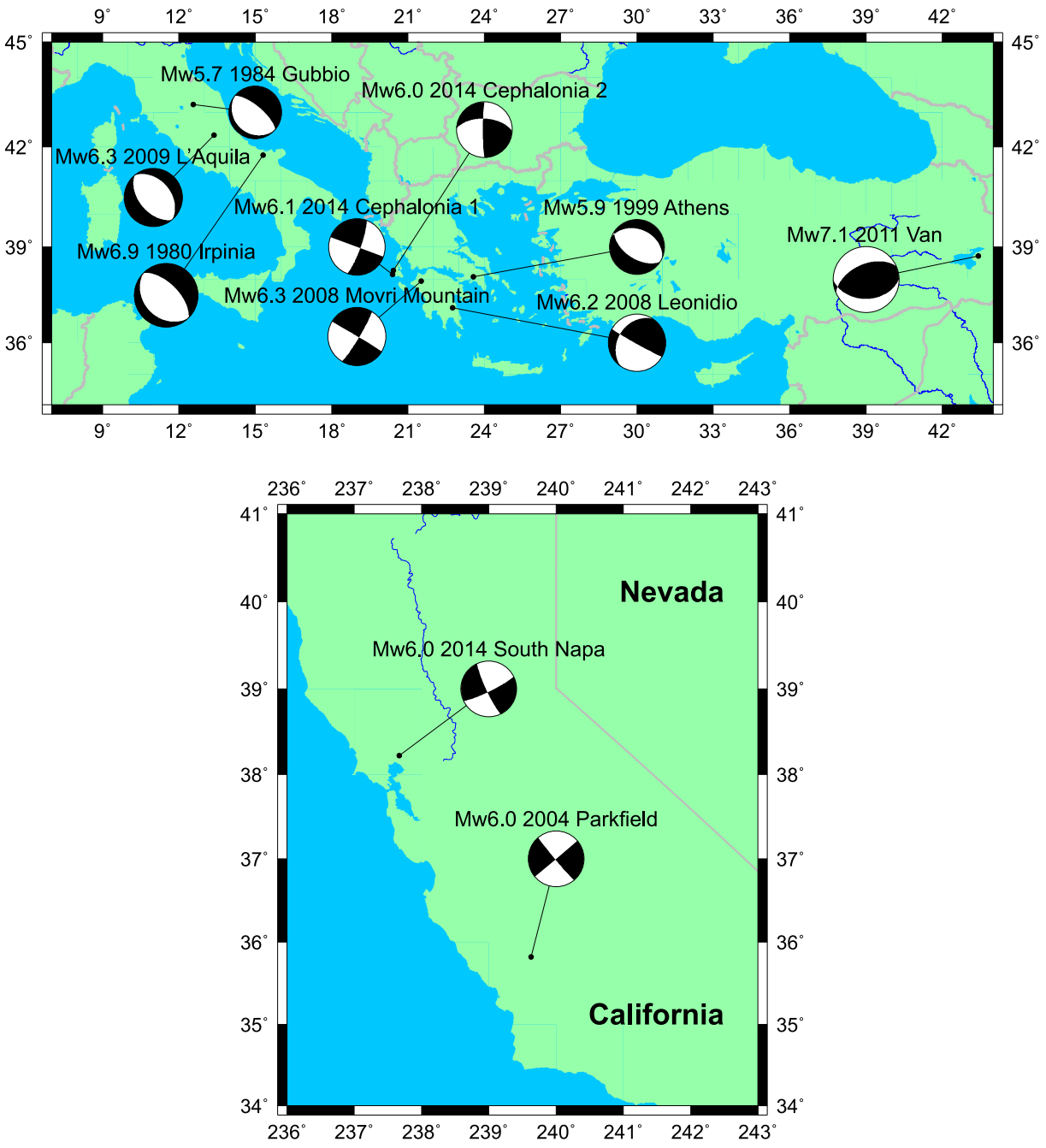

Figure 3.1.1: Map view of events analyzed in papers of this Thesis. For more parameters on the events and methods applied see Tab. 3.1.

of injuries and extensive damage, mainly in non-reinforced buildings. Although strong earthquakes are common in western Greece, this event took place in a region free of strong events throughout the historic observation period. The earthquake was followed by aftershock sequence with an irregular distribution, composed of at least two clusters.

In [P7] we applied the iterative slip inversion approach (section 2.2.2.1) to reveal the spatio-temporal evolution of the earthquake rupture process from near-regional data in frequency range (0.01-0.2Hz). It revealed the predominantly unilateral rupture propagation toward north-east direction, with two or three main slip patches. One of them was significantly delayed, thus indicating a temporary rupture arrest. The largest slip coincided with the region of the least abundant (double-difference relocated) aftershocks (almost a gap) located between the hypocenter and centroid. Similar conclusion was drawn when applying the truncated singular value decomposition (TSVD) in [P11]. Unfortunately, we were unable to obtain any more details being limited by the near-regional stations.

In [P7] we also noted that the north-east and south-west clusters of aftershocks differed in several aspects. The former group comprised events up to M 4.4, the latter contained only smaller magnitudes (M < 3.3). Moreover, first event of M 3 occurred in the south-western group as late as 13 hours after the mainshock, while, during the same period, there were more than 30 such events in the northeastern group. We speculated that the north-eastern aftershocks might have been dynamically boosted by the predominantly unilateral north-east rupture propagation.

Based on our results among others, *Serpetsidaki et al.* (2014) speculated that the activated blind fault belongs to a growing strike-slip fault system driven by a well-developed NNE striking shear zone within the uppermost mantle, marking at depth the southward propagation of the northern branch of the North Anatolian fault. They also related the possible immature character of this large crustal fault with the high variability of focal mechanisms and of fault geometries deduced from aftershock clusters in the strike direction.

3.1.3 Mw 6.3 2009 L'Aquila (Central Italy) earthquake

On April 6, 2009, at 1:32 GMT, a Mw 6.3 earthquake struck the L'Aquila city, one of the largest urban centers in the Abruzzo region (central Italy) with about 70,000 inhabitants, causing 308 casualties and vast destruction in the town and surrounding villages. This event represents the third largest earthquake recorded by strong-motion instruments in Italy, namely after the Mw 6.9 1980 Irpinia and the Mw 6.4 1976 Friuli earthquakes. The earthquake occurred along a NW-SE trending normal fault, approximately 20 km long, dipping about 45° SW. The hypocenter depth was estimated at 9.5 km, and the epicenter at less than 5 km SW of the town center (*Chiarabba et al.*, 2009). The earthquake has been recorded by relatively large number of digital strong-motion stations. Such a dataset is unique in Italy in terms of number and quality of records, azimuthal coverage and presence of near-fault recordings (*Ameri et al.*, 2009). Several studies on low-frequency source inversion showed that the rupture followed a complex pattern with a slip distribution composed by at least two asperities and a variable rupture velocity over the fault plane possibly including a temporal rupture stop (e.g., *Cirella et al.*, 2012).

The L'Aquila earthquake was recorded by 56 digital strong-motion stations (*Ameri et al.*, 2009) belonging to the Italian National strong-motion network (RAN). All the records are available in the Italian Accelerometric Archive (ITACA, http://itaca.mi.ingv.it/). In particular, there are 17 records with

Joyner-Boore distances (RJB) smaller than 50 km and five records with RJB = 0. Three of these RJB = 0 stations are part of an array deployed in the upper Aterno-river valley (AQG, AQA and AQV) whereas the other two (i.e., AQK and AQU) are in downtown L'Aquila.

In [P12] we performed slip inversion using the MuFEx source model (see Sec. 2.2.3), using band-pass filtered (0.06-0.3 Hz) accelerograms, double integrated to ground displacement time histories. The high-pass filtering at 0.06 Hz was applied to avoid of long-period instrumental noise present in the data. The low-pass filtering frequency is partially due to the simplicity of the 1D velocity model considered, limiting the quality of the Green's functions at higher frequencies.

In the MuFEx model we considered three subsources based on preliminary TSVD slip inversion (see section 2.2.2.2) and multiple-point source inversion by ISOLA (*Sokos and Zahradník*, 2008, 2013). After grid-searching over all parameters of the MuFEx source model (see section 2.2.3) we examined all models with VR larger or equal to 95% of the best model. We found that the inversion was very weakly sensitive to the actual rupture velocity inside the subsources, perhaps due to the relatively low frequency range in the present application. We note that the large uncertainty is the consequence of a strong trade-off among parameters, which is hardly detectable in the linear slip inversion approaches due to overwhelming number of parameters prohibiting to investigate such trade-offs. In this sense, a reasonably limited number of the MuFEx parameters is advantageous. In spite of the considerable uncertainty of the finite-fault model, there three important features proved stable: i) the shallow asperity located up-dip from the hypocenter was reached by the rupture front relatively quickly after the earthquake origin, ii) the south-east deep slip asperity awas characterized by a large seismic moment, and iii) the deep asperity was considerably delayed by 3–4 s. We also observed indication for lower rupture velocity close to the surface.

In [P13] (companion paper to [P12]) we attempted to extend the low-frequency source model to higher frequencies using the HIC approach (*Gallovič and Brokešová*, 2007, see also section 2.3.1) to simulate observed strong ground-motions in a broad frequency range (0.05-10Hz). We constrained the basic features of the kinematic rupture model according to the low-frequency inversion from [P12]. In particular, the rupture delay of the southern asperity by approximately 3s was included in the model. We tested different rupture velocities and set the final values in the bottom and top part of the fault equal to $V_r = 3$km/s and $V_r = 2$km/s, respectively. We also added shallow subsurface velocity layers to the individual stations if available (see section 1.2).

The simulated seismograms match the observed waveforms well both in terms of acceleration and velocity (see [P13]). Neglecting stations dominated by the site effects, the overall results indicate that the spatial broadband ground-motion variability (both in frequency and time domain) is in the epicentral area controlled by the rupture kinematic properties. We illustrated this in [P13] by performing simulations, where the individual source features constrained by the low-frequency kinematic inversion were altered to explore their effect on the broadband ground motion synthetics. In particular, (i) the two slip asperities in the rupture model were necessary to explain the ground motion at the closest sites, where two distinct wave groups were clearly visible on recorded waveforms (e.g., AQ_, GSA stations). (ii) The rupture delay of the southeastern asperity and the along-strike rupture propagation were essential to reproduce the CLN, GSA and CSO records. (iii) The up-dip rupture propagation correctly explained the ground motion at the GSA station; tests regarding the effect of rupture velocity

distribution on ground motion at this site showed that the decrease of rupture velocity from 3 to 2 km/s in the shallow part of fault was required to correctly fit its velocity waveforms (larger rupture velocity overestimated the observed amplitudes). (4) The near-fault AQ_ records were mainly controlled by the early phases of the rupture propagation that were responsible for the velocity pulses, which was also later concluded by *Tinti et al.* (2014). The southeastern asperity characterized by the larger slip generated the smaller later arrivals at those stations.

In [P15] we performed a more detailed slip inversion of the 2009 L'Aquila earthquake using the linear slip inversion technique with prior covariance for slip rate functions and non-negativity constraint (see Sec. 2.2.2.3). We extended the low-pass filtering frequency up to 0.5Hz and considered Green's functions calculated in the 3D tomographic velocity model by *Di Stefano et al.* (2011). The accelerometric data were supplemented by displacement waveforms from high-rate GPS recordings adopted from *Avallone et al.* (2011) including static displacements. Taking into account the lessons learned from extensive inversion tests described in [P15] and Sec. 2.2.2.5, we interpreted result of the real-data inversion. Besides confirming the above described complex rupture propagation, we identified also another interesting feature, where the co-seismic rupture circumvented a patch corresponding to a (later occurring) large afterslip inferred by *Gualandi et al.* (2014). Nevertheless, we admit that this feature is rather not well constrained by the inversion. Dynamic modeling of this distinct feature might help to resolve this issue.

3.1.4 Mw 7.1 2011 Van (Eastern Turkey) earthquake

The Mw 7.1 Van earthquake occurred on 23 October 2011 in eastern Turkey, close to the towns of Van and Erciş, causing more than 600 casualties and widespread damage. Basic parameters of the earthquake were reported soon after the earthquake occurrence on websites of the United States Geological Survey (USGS) and European–Mediterranean Seismological Center (EMSC). The earthquake ruptured a 60–70 km long northeast–southwest fault with a thrust mechanism, which is in agreement with the regional tectonic stress regime. Preliminary analysis suggested that the rupture was confined to the depths of 8-20km ([P14], *Konca*, 2015).

The only data, which could be utilized in the slip inversion were recorded at near-regional distances ($\sim$ 100 km) and almost exclusively in a single southwest quadrant. Our analysis of the Van earthquake in [P14] showed that the uncertainty of its slip model was rather large due to such unfavorable station distribution. Indeed, as I described in section 2.2.2.4 (see also P[9, 11]), the slip inversion may suffer from strong artifacts in such cases. In particular, the resulting model could overestimate the rupture propagation toward the stations. In other words, rupture propagation in the opposite direction and/or possible up-dip propagation is not well pronounced in the observed data, and thus it cannot be easily retrieved.

To overcome this at least partially, we adopted the MuFEx source model for the slip inversion (section 2.2.3, [P12]), assuming three finite-extent subsources. The MuFEx inversion ended with a database of plausible models that varied significantly in terms of all aspects of the rupture propagation. Therefore, we decided to perform strong ground motion modeling using the HIC approach (section 2.3.1, *Gallovič and Brokešová*, 2007) to better constrain the source model by means of modeling the only one available near-fault station Muradiye in a broad frequency band (0.1–10 Hz). We considered several

MuFEx models to initiate the HIC model. We showed that the long duration of the closest station, consisting of 2–3 distinct wave packages in the observed accelerometric record, can be reproduced only when models with complex rupture propagation (such as a delayed rupture of shallow asperities) are considered. I point out that such rupture complexity would not be possible to identify from the near-regional data without the uncertainty analysis performed using the MuFEx source model.

3.1.5 Mw 6 2014 Cephalonia (Greece) earthquake doublet

An earthquake sequence occurred at the Cephalonia Island (Ionian Sea, Greece) in January-February 2014. The sequence started on January 26, 2014 with an Mw 6 and culminated on February 3 to another Mw 6 event. The island of Cephalonia has been the locus of many catastrophic earthquakes in the past. The most characteristic example is the 1953 earthquake sequence that devastated Cephalonia, Ithaki and Zakynthos islands, causing death of more than 450 people. This event was the startup point for the Hellenic Antiseismic Code whose provisions for the constructions in the Ionian Islands are the strictest over Greece.

The 2014 Cephalonia earthquake sequence was complicated since it included three large events that occurred within few days. Earthquake 'twins' (doublets), i.e. two large events following each other within a few days, represent a characteristic complexity feature of the regional seismicity (*Lekkas et al.*, 1997).

In [P16] we used weak and strong motion waveforms from local and regional stations to constrain kinematic rupture models of the two major events. In particular, we paid careful attention to the determination and consistency of their hypocenters, centroid moment tensors (location and faulting parameters), and fault plane geometries. In [P16] we discuss the two largest events not only in terms of their source properties, but also in terms of the difficulties encountered during their source inversions due to, especially, the relatively poor data coverage. In particular, for the waveform inversions we used waveforms from strong motion stations, lying at local distances (within 40km). Only one station for each event is located very close to the source (DMLN and CHV1 for the 1st and 2nd event, respectively), see [P16] for more details.

Below I summarize the main results as well as problems met during the interpretation of the earthquake recordings. For brevity, I denote the January 26 and February 3 earthquakes as the 1st and 2nd event, respectively.

- 1st event: The CMT solutions were inferred by the ISOLA software package (*Sokos and Zahradník*, 2008, 2013), including 3D search for optimal centroid location. The inferred solution agreed well with those reported by various world agencies. The CMT solution from near-regional seismic waveforms was thus a good proxy for the fault plane position. We chose the nodal plane striking at ~20° as the fault plane because it is almost parallel to the nearby Cephalonia Transform Fault. To further refine the source geometry and mechanism, we repeated slip inversions of near-fault stations (0.05-0.20Hz) assuming variations in both fault location and strike, dip and rake angles. The optimal fault agreed with the (independently relocated) hypocenter. The slip inversion revealed major slip area covering almost the whole fault with maximum slip situated close to the nearest (DMLN) station. We point out that such result could be merely an artifact as suggested by

synthetic tests showing that slip peaks occur preferentially "below" the stations (see the synthetic tests in [P15] and [P17]). Nevertheless, the maximum slip was only ~6 km NNE from the centroid position and still within the area of the preferred CMT locations, which can be considered as an independent observation because the CMT solution did not involve the DMLN station. We noted that although this earthquake had a relatively large hypocentral depth (10 km), the slip reached shallow depths, inducing presumably surface ruptures identified by *Valkaniotis et al.* (2014). The synthetic seismograms showed good agreement with the observed data (variance reduction 0.83), but especially the closest station DMLN was not fitted perfectly. Therefore, we cannot exclude the possibility that the rupture process along the whole fault had a more complex fault geometry and/or variable focal mechanism. However, inference of such a model is under resolution power considering the frequency range of the data and the sparse station coverage.

- ▷ 2nd event: The grid search over centroid location using ISOLA revealed largely variable CMT solutions with very low DC percentage (29%). Although the data were fitted almost equally well as in the case of the 1st event, the spatial variability of CMT and the low-DC solutions near the best-fitting trial source points issued a warning against any straightforward interpretation. In such a situation designing a reasonable fault plane for the slip inversion is very difficult. Indeed, we performed slip inversions considering various fault planes and mechanisms corresponding to the MT uncertainty, but the obtained space-time slip distributions were doubtful. Fortunately, the fault plane of the 2nd event is well constrained by DInSAR data (*Merryman Boncori et al.*, 2015), suggesting one or two segments with pronounced slip. The larger segment was consistent with the relocated hypocenter. We performed the slip inversion considering both fault segments simultaneously using the velocity waveforms at the five near stations in the frequency range of 0.05-0.2 Hz. The results showed that the 2nd event could be understood as an almost simultaneous rupture process on the two fault segments. We also tested slip inversion considering just the larger segment 1. The rupture propagation was very similar to that obtained along segment 1 in the above mentioned two-segment inversion, while the fit deteriorated only slightly (Figure S4c, variance reduction 0.70). Therefore, we admitted that it was impossible to strictly prove the existence of the rupture propagating along segment 2 based on the available data. In any case, similarly as for the first event we speculated that the surface ruptures of *Valkaniotis et al.* (2014) were related to the large shallow slip at the larger fault segment.

The difficulties met when interpreting the Cephalonia doublet illustrate how hard is to reveal rupture source characteristics in some cases. Some of the problems are related to the relatively poor station coverage. However, this cannot explain the difficulties with identification of the fault geometry of the 2nd event using seismological data only because the quality of the station coverage for the 1st and the 2nd event is rather similar. I point out that this issue is also related to the fact that the moment tensor solutions, as reported by different agencies, are quite alike for the 1st event, whereas those reported for the 2nd event vary significantly, exhibiting also large non-DC components.

The first obvious possibility how to explain the MT variability is related to a complicated fault geometry of the 2nd event. However, adding the second segment improved the fit of the DInSAR data only marginally, leaving the existence of the second segment rather uncertain. As mentioned

above, even the slip inversion provided similar fit with the recorded seismograms for both the single- and double-segment fault model. The other possibility is simply related to the source shallow depth. Based on the analysis of theoretical MT resolvability (*Zahradník and Custódio*, 2012), in [P16] we show that shallow hypothetical sources inverted in the same setting (station network, velocity model, same low-frequency range, etc.) are characterized by much more uncertain MT solution including its DC percentage than deeper sources. *Henry and Das* (2002) related this issue to vanishing Green's functions related to the $M_{r\theta}$ and $M_{r\phi}$ components of MT at the free surface, which in turn leads to ambiguous focal mechanisms solutions (see also *Bukchin et al.*, 2010). The same shallow-source effect most likely caused the large variation of the MT agency reports of this event.

To conclude, in [P16] we demonstrate that a remarkable feature of the sequence is that the events occurred on-land, activating a network of minor mapped faults over the whole Cephalonia Island. This is independently supported by the rather diffuse pattern of the (relocated) aftershocks, not delineating any single fault structure.

3.1.6 Mw 6 2014 Napa earthquake

The South Napa earthquake occurred on 24 August 2014 at 10:20:44 UTC in California, 6km NW of American Canyon and 9km SW of Napa, causing one fatality and damaging many older buildings in the Napa area (*Brocher et al.*, 2015). The earthquake was recorded by 10 stations within 30km distance from the fault. Basic parameters of the event (location and centroid moment tensor) were inferred by world agencies and are summarized at, e.g., the U.S. Geological Survey (USGS) website. The event ruptured the previously recognized West Napa Fault belonging to the San Andreas Fault system.

[P18] presented a slip inversion of the South Napa earthquake utilizing method from [P15] and the near-fault stations. The inferred source model is in general agreement with other models published so far (e.g., *Dreger et al.*, 2015; *Ji et al.*, 2015; *Melgar et al.*, 2015; *Wei et al.*, 2015), showing a unilateral northward rupture propagation towards the city of Napa, having significant asperity at shallow depths (<5 km) with longer rise times at the place where 40-46cm slip was observed at the surface (*Brocher et al.*, 2015).

Such a unilateral event is expected to exhibit strong source directivity effect, amplifying the ground motions in the direction of the rupture propagation (northwards) and broadening of velocity pulses especially at the fault-normal (F-N) components (e.g., *Somerville et al.*, 1997). Interestingly, recordings of the strong motions at the near-fault stations suggest that the source directivity effect is reduced at higher frequencies. For example, *Baltay and Boatwright* (2015) analyzed residuals of the South Napa earthquake observed data with respect to ground-motion prediction equations (GMPEs), showing that while the residuals of pseudospectral acceleration (PSA) at 3s the residuals exhibit clear amplification due to the directivity effect, those at 0.3s and the peak ground accelerations (PGAs) do not. At mid-frequencies, the residuals of PSA at 1s and PGVs show indeed a less pronounced directivity effect, being also perhaps overlaid by a fault-zone-guided wave effect (*Baltay and Boatwright*, 2015). Instrumental intensity ShakeMaps (obtained by interpolating recorded ground motion) do not exhibit clear manifestation of the northward source directivity effect, being characterized only by elongation due to the finite extent of the fault. I emphasize that this in contradiction with the classical source directivity models that predict amplification of the motion up to 5-10 times at all frequencies larger than the corner

frequency (see section 2.3.3), which is definitely not observed for this particular event. Although wave propagation effects could have contributed to some extent to the amplification of the ground shaking south from the event (e.g., station NHC is situated in deeper sediments than N019B), it is very likely that also the source effect had to contribute in the almost full 'removal' of the directivity effect at high frequencies. Since the event was recorded by such relatively large number of stations with very good azimuthal coverage, it is a unique opportunity to test source models with various directivity strengths.

In [P18] we used the RIK source model (section 2.3.2) to simulate ground motions at all the receiver sites. For the wave propagation modeling I use a modification of the 1-D layered velocity model GIL7 (*Stidham et al.*, 1999), with two additional layers with subsurface velocity representing soft-rock site properties. Full wavefield 1D Green's functions (GFs) were calculated using the discrete wavenumber technique; no stochastic GFs were used throughout the whole study (see section 1.2).

The advantage of the RIK model is that it has adjustable strength of the directivity effect including its frequency dependence by considering the rupture propagation more (or less) coherent (see section 2.3.2). In particular, I considered three models with weak, moderate and strong directivity effects. The first two models are characterized by decreasing strength of the directivity effect with increasing frequency. The weak directivity model includes the stochastic rupture propagation at small scales, which decreases the coherency of the rupture front and thus effectively weakens the high-frequency directivity effect. The weak and moderate directivity models are shown to best fit the observed velocity waveforms both in the temporal domain (Figure 4) including the peak values (Figure 5b) and in terms of the response spectra (Figure 6). Those two models explain the observed data with both the smallest modeling bias and modeling variance (variability of the bias over stations). This is particularly important since any mismodeling of the directivity effect of this unilateral event would introduce a systematic azimuthally dependent variability in the modeling bias, thus increasing the modeling variance. In this sense, the weak directivity model fitted the data slightly better than the moderate directivity model. Due to the very large modeling variance the strong directivity model can be considered as unrealistic with confidence.

3.2 Ground motion prediction for future events

3.2.1 Scenario simulations

Any simulation method requires specifications of source parameters, most of which are generally unknown a-priori. For example, kinematic finite-extent source models (see sections 2.3.1, 2.3.2) require the specification of parameters describing the rupture evolution, such a nucleation point position, rupture velocity, shapes of slip-rate functions, etc. These parameters are sought when one is interested in reproducing strong-motion records associated with an occurred earthquake (section 3.1). On the contrary, for seismic hazard assessment the parameters describing the rupture evolution need to be varied in order to produce a large number of scenario events. This approach is supported by the fact that it is not possible to predict which rupture scenario will occur on a seismogenic fault. In this way, various possible rupture processes, occurring on the same fault, are simulated and synthetic seismograms for each of them are computed.

One of the key ingredients in seismic hazard assessment is the prediction of ground-motion pa-

rameters, assuming occurrence of specific earthquakes. This goal may be easily pursued using ground-motion prediction equations (GMPEs) that provide the probability distribution of earthquake ground motion at a given site as a function of several basic parameters, such as magnitude, distance, site condition, fault mechanism, etc. Although they are retrieved through the analysis of recorded strong motion data, the GMPEs account only for the average characteristics of the earthquake source and wave-propagation processes. In general, at distances comparable with the fault dimensions, the complexity and heterogeneity of the source rupture process strongly influence the ground motion, especially in the case of moderate-to-large earthquakes (e.g., *Archuleta and Hartzell*, 1981, [P13, 18]). Such features are crudely accounted for by GMPEs due to the simplistic source parameterization adopted in their functional forms, and to the paucity of strong-motion data recorded at near-source distances for large magnitudes. An alternative approach to predict earthquake ground motions is represented by the strong ground motion simulations of synthetic accelerograms.

Many scenarios for engineering use were calculated by the HIC method by *Gallovič and Brokešová* (2007), see also section 2.3.1. For example, in [P6] we investigated the M5.7 1984 Gubbio, Italy, earthquake by this technique, comparing results with independent method of *Pacor et al.* (2005). In [P10] we compared three ground-motion simulation techniques including the HIC technique and investigated their performances in near-fault strong-motion modeling. The test case focused on the Mw 6.9 1980 Irpinia, Italy, earthquake, which occurred in the Potenza urban area. Important engineering parameters were analyzed, such as PGA, PGV and spectral accelerations including their variability. The seismograms generated in [P10] were later used by *Chiauzzi et al.* (2012) to estimate the damage levels of the residential buildings located in the urban area of Potenza.

In [P19] I extended the real data modeling of the 2014 Mw 6.0 South Napa, California, earthquake ([P18]) by performing scenario simulations for this event. I considered random variations of the rupture speed following k^{-1} distribution instead of a constant rupture velocity. Considering a nucleation point, the rupture times were calculated using the solver of the eikonal equation by *Podvin and Lecomte* (1991). To estimate the ground-motion variability due to the a-priori unknown rupture scenario, I assumed the following variations of the source parameters: two mean rupture speeds, six positions of the nucleation point on the fault and six slip distributions, i.e. 72 rupture scenarios in total. For the wave propagation modeling I used a modification of the 1-D layered velocity model GIL7 (*Stidham et al.*, 1999), with two additional layers with subsurface velocity representing soft-rock site properties. Full wavefield Green's functions (GFs) were calculated using the discrete wavenumber technique in the complete frequency range (see section 1.2).

The resulting Napa-earthquake-like scenario seismograms were explored in terms of PGV and PGA values. The synthetics agree well with the existing ground motion prediction equations (GMPEs) by *Boore et al.* (2014). I also explored the spatial distribution of the simulated PGV and PGA values in terms of their mean and standard deviations (in natural log units). The mean values have elongated shape following the geometry of the fault. In the along strike direction at larger distances the mean values are larger than in the perpendicular direction. Similarly, the standard deviation (also called single-station between-event sigma) have also spatially inhomogeneous distributions. Indeed, the corresponding maps have fan-like shape with the largest values located in the along the directions of the fault. This is due to the directivity effect, which is mostly pronounced in the along-fault direction.

Therefore, the variability is lowest in the directions perpendicular to the fault, where the ground motions are not much affected by the direction, in which the rupture front propagates.

In the scenario simulations of [P19] single-station between-event standard deviations range from 0.35 to 1.1 with root-mean-square value (over all stations) of 0.7, which is larger than the between-event standard deviations of GMPEs (0.35). I note that the standard GMPEs take into account only the distance dependence of the observed motion, and thus do not capture the systematic azimuthal dependence of the ground motion variability as suggested by the simulations. The simulations will help to introduce new types of functional forms of GMPEs that would take into account the ground motion variability due to the source effect.

3.2.2 Constraining the nucleation point of aftershocks using the rate-and-state friction law

As mentioned above in sections 3.2.1 and 2.3.3, the directivity effect plays an important role in the strong ground motion simulations. Therefore, prior knowledge of the nucleation point location would decrease considerably the uncertainty of ground motion predictions, which would be, in turn, important in seismic hazard analysis. In [P4] I have analyzed whether such a constrain cannot be earned in the case of aftershock prediction by means of calculations of Coulomb stress (CS) changes, which are used to assess places of increased aftershock probabilities after strong events (e.g., *Stein et al.*, 1997; *Stein*, 1999; *Steacy et al.*, 2005).

In [P4] the problem of stress loading was addressed using a 3D fault model with rate-and-state friction (*Dieterich*, 1979). I tested how the 3D fault behavior is modified under homogeneous or heterogeneous (i.e. non-constant along the fault) Coulomb stress load. In agreement with the 2D modeling by *Perfettini et al.* (2003) I found that the Coulomb stress increase may lead to both advanced or even delayed earthquake occurrence. The new finding of [P4] is that if the earthquake is triggered relatively soon after the loading (within months), the nucleation point position is located within the Coulomb stress load zone. Later on, the stress becomes redistributed along the fault in such a way that the nucleation point may appear anywhere on the fault, even outside of the loaded area.

Simulations in [P4] thus suggest that the rate-and-state fault model can help in constraining the aftershock hazard calculations. Let us assume that a strong earthquake occurred, causing Coulomb stress increase on some part of a nearby active fault. One may expect that within the next two months the nucleation point will be located in the strike extent of the CS increase area, independently on the CS load amplitude. Such constraint may significantly modify the (time-dependent) hazard maps due to, e.g., pronounced directivity effect. After this 'favorable' period of the two months, the anticipated fault will produce an earthquake later, but in this case it can nucleate anywhere. Nevertheless, I emphasize that these results must be considered as exploratory and suggestive to seek evidences in real triggering sequences. Unfortunately, such analysis has not yet been performed and thus this issue remains open.

3.2.3 Assessing the performance of Earthquake Early Warning System (EEWS)

In [P5] we used synthetic ground motion scenarios calculated by the HIC approach to test the performance of an EEWS in the Irpinia region of southern Italy. The deployment of the seismic network

ISNet started in 2005 with the aim to implement a regional EEWS for Civil Protection purposes. The ISNet network and the implemented EEWS methods are described by *Satriano et al.* (2011). In particular, the so-called PRESTo methodology utilizes an evolutionary algorithm for estimating the location and magnitude of an on-going event.

In general, methodologies for earthquake early warning assume a point source model of the earthquake and thus isotropic wave amplitude attenuation. Indeed, early portions of the P- and S-wave signals are used to estimate the earthquake location and magnitude and to predict ground motions using a isotropic GMPEs. To test an EEWS the best approach would be to use recordings of past strong earthquakes acquired at the stations and investigate the system capabilities to estimate the source parameters and to predict the peak motion at distant sites through an off-line analysis. This was not possible in southern Apennines due to the recent implementation of our EEWS and to the relatively low seismicity rate in the moderate to large magnitude range (M > 6). Therefore, in [P5] we adopted a different strategy utilizing synthetic seismograms simulated at the ISNet stations for a large number of M 6.9 and 6.0 earthquake scenarios, with events occurring inside and at the border of the network. The main purpose of the study was to investigate the effects of a complex rupture process for moderate to large earthquakes on real-time measurements and early warning methodologies.

The EEWS performance is evaluated through Effective Lead-Time (ELT), and Probability of Prediction Error (PPE) evaluated at a regional scale. The former was defined as the time interval between the arrival of first S-wave and the time at which the location and magnitude estimations stabilizes, while the latter provides a measure of the PGV prediction error at a regional scale. The ELT evaluated in [P5] is almost isotropically distributed with weak azimuthal anomalies, mainly controlled by the focal mechanism and directivity. The areal distribution of PPE is instead strongly heterogeneous, showing that systematic errors in the predictions may occur for sites located in or close to the S-wave nodal planes, where observations are generally overestimated. We note that directivity effects are still present at the borders of the faults, although only half of the scenarios are on average directive, while the other half are anti-directive. The results thus indicate that the capability of the EEWS to accurately predict the observed peak ground motion strongly depends on distance and azimuth from the fault. This might be improved if the distance definition used for early warning was substituted by the fault distance as a better representation of the distance.

Assuming that the latency of telemetry is constant, we found negative ELTs inside the network, suggesting that the real-time characterization of the on-going event requires acquirement of enough data, preventing from issuing warning before the S-waves arrival in this area. For the densely populated Naples urban area, ELT ranges between 8s and 16s, and PPE between 50% and 60%. This indicates that some mitigation actions could be effectively initiated before S-waves reach potential targets. The uncertainty of the PGV prediction is similar to that of the GMPEs.

Chapter 4

Conclusions

In the papers of this Thesis I introduced or contributed to introduction of several methods for earthquake source forward and inverse modeling. The methods range from low-frequency (0.05-0.5 Hz) slip inversions to broadband (0-10 Hz) strong ground motion modeling. In particular, the proposed slip inversion methods were tested on synthetic tests in realistic setting to mimic real data applications. Both the slip inversion methods and the broadband simulation methods were applied to recordings of crustal earthquakes with magnitudes 6-7, which occurred worldwide. The strong ground motion modeling was also used for earthquake scenario simulations and testing of the Earthquake Early Warning System in the Irpinia region (southern Italy).

Our slip inversion studies suggest that synthetic testing should be broad and should be performed in parallel with real data applications. Indeed, slip inversions are jeopardized by our inability to model correctly Green's functions due to imperfect knowledge of the velocity structure and the geometry of the fault. This generally limits the usable frequency range of the data and makes it necessary to apply regularization constraints in the inverse process. In particular, the commonly used spatial smoothing was shown in our papers to be able to introduce persisting artifacts in the inferred models especially if the data coverage is not perfect (larger distances, incomplete azimuthal coverage). Indeed, serious problems were met when interpreting events with insufficient station coverage (see, e.g., the Van, Cephalonia, Movri Mountain earthquakes). The possible artifacts include false strong asperity or exaggerated rupture propagation towards some station(s). We introduced ways how to overcome such issues (see, e.g., the MuFEx source model). Nevertheless, still the resulting source features exhibit large uncertainty due to the strong non-uniques of the inverse solution.

Contrarily, in case of well recorded earthquakes (see, e.g., the Napa and L'Aquila earthquakes) when stations lay very close to the fault and/or even above the fault plane, the slip inversions can reveal more constrained details of the source processes. Nonetheless, even in such cases it is important to keep in mind lessons learned from synthetic tests when interpreting the inferred source images in terms of rupture complexity. It should be also noted that, interestingly, in our applications we did not observe that a 3D model would considerably improve the inversions. Perhaps the models used so far are still not well constrained for such applications. Determination of more realistic velocity models suitable for slip inversions thus represent a challenging task for the future.

Results of real data applications were carefully interpreted in terms of earthquake source properties.

We identified several interesting features of the sources that document complexity of real earthquake ruptures. For example, in case of the L'Aquila earthquake when we combined accelerometric and high-rate GPS data including static displacements recorded just above the fault, the inferred model suggested that, after the initial fast up-dip propagation of the co-seismic rupture, it seemed to circumvent a patch of large afterslip in the along-strike direction. As for the Napa earthquake, we observed in accord with other studies that the event propagated to shallow depths and unilaterally northwards.

The strong ground motion modeling methods utilized in the papers of this Thesis represent vital approaches to model observed data in broad frequency range. Indeed, if some general source process characteristics are known a-priori from a preceding slip inversion, the broadband source model can be adjusted to replicate main characteristics of the recordings in both time and frequency domains (if site effects are nor very strong). This was demonstrated mainly on the two well-recorded events, L'Aquila and Napa. In particular, we succeeded to reproduce velocity waveforms of the Napa earthquake using a model with frequency-dependent directivity effect, where the best-fitting model yielded weakening directivity amplification with increasing frequency. Interestingly, such diminution of the directivity effect has been also observed independently in the low-magnitude events in the paper by *Pacor, Gallovič, et al.* (submitted), supporting thus the idea of self-similarity of rupture behavior between large and small events.

Validated broadband ground motion simulations methods can be utilized for earthquake scenario simulations to estimate ground motions including their variability due to an a-priori unknown rupture process of a future event for seismic hazard assessment. In our applications we analyzed predicted uncertainties, showing that without any prior information on the rupture process (except for the fault position and mechanism), the simulated ground motion variability is comparable to (or even larger than) the empirical one derived from ground motion prediction equations (GMPEs). Nevertheless, such simulations are still important especially at distances smaller than the fault dimensions where the complexity and heterogeneity of the source rupture process strongly influence the ground motions. Indeed, such features are crudely accounted for by GMPEs due to the simplistic source parameterization adopted in their functional forms, and to the paucity of strong-motion data recorded at near-source distances for large magnitudes. At larger distances the simulations will help to introduce new types of functional forms of GMPEs taking into account the spatial (mainly azimuthal) ground motion variability due to the source effects. For such purpose, however, the ground motion models must be carefully validated by means of modeling more real earthquake data. In that case, the simulations could also estimate realistic limits of extreme ground motions close to earthquake ruptures. The ground motion modeling could also provide a series of synthetics for dynamic analysis of engineering structures.

There are many directions in which the research presented in this Thesis will continue. To name a few, we need to implement more objective estimations of inversion uncertainties based on estimated uncertainty of Green's functions using a fully Bayesian approach (e.g., *Yagi and Fukahata*, 2011; *Duputel et al.*, 2012, 2015). This approach should include also objective determination of stations weights and appropriate testing both on synthetic and real data. In the framework of Source Inversion Validation benchmarks we will develop an ultimate slip inversion test, which will mimic a possible scenario on a blind fault beneath Los Angeles and will involve complex fault geometry (multiple segments), rupture evolution and random velocity model perturbations for an ultimate quasi-realistic setting. We also need

to test and perhaps adapt our broadband source models to simulate M>7 earthquakes including those happening on subduction zone megathrust faults. Regarding the latter, such source models will have to take into account the observed depth-dependent rupture characteristics observed for the subduction earthquakes (e.g., *Lay et al.*, 2012). Challenging is also adaptation of the forward and inverse modeling methods for real-time applications.

To conclude, the methods for earthquake source analysis developed and applied in the papers of this Thesis complement those already utilized at my home institution, the Department of Geophysics, Faculty of Mathematics and Physics at Charles University in Prague. Altogether the tools range from earthquake location, centroid moment tensor determination, fault identification, and slip inversion to broadband ground motion simulations. In my view, mastering and developing such broad suite of tools at our department is rather uncommon worldwide. It allows us to efficiently analyze data from significant earthquakes, putting emphasis on events in Greece where the department maintains stations with broadband, strong-motion and GNSS instruments. To me it is a challenge for the future to further extend our abilities in order to gain better understanding of earthquakes and their tectonic context.

Acknowledgement

I acknowledge financial support from the Czech Science Foundation grant GACR-14-04372S.

Bibliography

Adamová, P., and J. Šílený (2013), Disputable non-double-couple mechanisms of several strong earthquakes: Second-degree moment approach, *Bull. Seism. Soc. of Am.*, *103*(5), 2836–2849, doi:10.1785/0120130014.

Aki, K. (1967), Scaling law of seismic spectrum, *J. Geophys. Res.*, *72*(4), 1217–1231, doi:10.1029/JZ072i004p01217.

Aki, K., and P. G. Richards (2002), *Quantitative Seismology*, University Science Books, Sausalito, California.

Ameri, G., et al. (2009), The 6 April 2009 Mw 6.3 L'Aquila (central Italy) earthquake: Strong-motion observations, *Seismol. Res. Lett.*, *80*(6), 951–966, doi:10.1785/gssrl.80.6.951.

Anderson, J. G., and S. E. Hough (1984), A model for the shape of the Fourier amplitude spectrum of acceleration at high frequencies, *Bull. Seismol. Soc. Am.*, *74*(5), 1969–1993.

Andrews, D. J. (1980), A stochastic fault model 1. Static case, *J. Geophys. Res.*, *85*, 3867–3877.

Archuleta, R. J., and S. H. Hartzell (1981), Effects of fault finiteness on near-source ground motion, *Bull. Seismol. Soc. Am.*, *71*(4), 939–957.

Avallone, A., et al. (2011), Very high rate (10 Hz) GPS seismology for moderate-magnitude earthquakes: The case of the M w 6.3 L'Aquila (central Italy) event, *J. Geophys. Res.*, *116*(B2), B02,305, doi:10.1029/2010JB007834.

Baltay, A. S., and J. Boatwright (2015), Ground-Motion Observations of the 2014 South Napa Earthquake, *Seismol. Res. Lett.*, *86*(2A), 355–360, doi:10.1785/0220140232.

Ben-Menahem, A. (1961), Radiation of seismic surface-waves from finite moving sources, *Bull. Seismol. Soc. Am.*, *51*(3), 401–435.

Beresnev, I. A. (2003), Uncertainties in Finite-Fault Slip Inversions: To What Extent to Believe? (A Critical Review), *Bull. Seismol. Soc. Am.*, *93*(6), 2445–2458, doi:10.1785/0120020225.

Beresnev, I. A., and G. M. Atkinson (1997), Modeling finite-fault radiation from the ω^n spectrum, *Bull. Seismol. Soc. Am.*, *87*(1), 67–84.

Bernard, P., A. Herrero, and C. Berge (1996), Modeling directivity of heterogeneous earthquake ruptures, *Bull. Seismol. Soc. Am.*, *86*(4), 1149–1160.

Bernauer, M., A. Fichtner, and H. Igel (2014), Reducing nonuniqueness in finite source inversion using rotational ground motions, *J. Geophys. Res.*, *119*(6), 4860–4875, doi:10.1002/2014JB011042.

Bhat, H. S., M. Olives, R. Dmowska, and J. R. Rice (2007), Role of fault branches in earthquake rupture dynamics, *J. Geophys. Res.*, *112*(B11), doi:10.1029/2007JB005027, b11309.

Bianchi, I., C. Chiarabba, and N. Piana Agostinetti (2010), Control of the 2009 L'Aquila earthquake, central Italy, by a high-velocity structure: A receiver function study, *J. Geophys. Res.*, *115*(B12), doi:10.1029/2009JB007087, b12326.

Biegel, R. L., C. G. Sammis, and A. J. Rosakis (2007), Interaction of a dynamic rupture on a fault plane with short frictionless fault branches, *Pure Appl. Geophys.*, *164*(10), 1881–1904, doi:10.1007/s00024-007-0251-2.

Bindi, D., and A. Caponnetto (2001), Tomographic imaging of the earthquake source: numerical validation in two-dimensional approximation, *J. Geophys. Res.*, *106*(2000), 6643–6656.

Boatwright, J. (2007), The persistence of directivity in small earthquakes, *Bull. Seismol. Soc. Am.*, *97*(6), 1850–1861, doi:10.1785/0120050228.

Boore, D. M., J. P. Stewart, E. Seyhan, and G. M. Atkinson (2014), NGA-West2 equations for predicting PGA, PGV, and 5% damped PSA for shallow crustal earthquakes, *Earthq. Spectra*, *30*(3), 1057–1085, doi:10.1193/070113EQS184M.

Bouchon, M. (1981), A simple method to calculate Green's functions for elastic layered media, *Bull. Seism. Soc. Am.*, *71*, 959–971.

Brocher, T. M., et al. (2015), The Mw 6.0 24 August 2014 South Napa Earthquake, *Seismol. Res. Lett.*, *86*(2A), 309–326, doi:10.1785/0220150004.

Brune, J. N. (1970), Tectonic stress and the spectra of seismic shear waves from earthquakes, *J. Geophys. Res.*, *75*(26), 4997–5009.

Bukchin, B., E. Clévédé, and A. Mostinskiy (2010), Uncertainty of moment tensor determination from surface wave analysis for shallow earthquakes, *J. Seismolog.*, *14*(3), 601–614, doi:10.1007/s10950-009-9185-8.

Causse, M., F. Cotton, and P. M. Mai (2010), Constraining the roughness degree of slip heterogeneity, *J. Geophys. Res.*, *115*(B5), B05,304, doi:10.1029/2009JB006747.

Chen, P., T. H. Jordan, and L. Zhao (2010), Resolving fault plane ambiguity for small earthquakes, *Geophys. J. Int.*, *181*(1), 493–501, doi:10.1111/j.1365-246X.2010.04515.x.

Chen, Y., J. Letort, F. Cotton, and S. Drouet (2014), High-frequency directivity effects: evidence from analysis of the Les Saintes records, *J. Seismol.*, *18*, 457–466, doi:10.1007/s10950-014-9419-2.

Chiarabba, C., et al. (2009), The 2009 L'Aquila (central Italy) Mw 6.3 earthquake: Main shock and aftershocks, *Geophys. Res. Lett.*, *36*(18), L18,308, doi:10.1029/2009GL039627.

Chiauzzi, L., A. Masi, M. Mucciarelli, M. Vona, F. Pacor, G. Cultrera, F. Gallovič, and A. Emolo (2012), Building damage scenarios based on exploitation of Housner intensity derived from finite faults ground motion simulations, *B. Earthq. Eng.*, *10*(2), 517–545, doi:10.1007/s10518-011-9309-8.

Cirella, A., A. Piatanesi, M. Cocco, E. Tinti, L. Scognamiglio, A. Michelini, A. Lomax, and E. Boschi (2009), Rupture history of the 2009 L'Aquila (Italy) earthquake from non-linear joint inversion of strong motion and GPS data, *Geophys. Res. Lett.*, *36*(19), L19,304, doi:10.1029/2009GL039795.

Cirella, A., A. Piatanesi, E. Tinti, M. Chini, and M. Cocco (2012), Complexity of the rupture process during the 2009 L'Aquila, Italy, earthquake, *Geophys. J. Int.*, *190*(1), 607–621, doi:10.1111/j.1365-246X.2012.05505.x.

Clévédé, E., M.-P. Bouin, B. Bukchin, A. Mostinskiy, and G. Patau (2004), New constraints on the rupture process of the 1999 August 17 Izmit earthquake deduced from estimates of stress glut rate moments, *Geophys. J. Int.*, *159*(3), 931–942, doi:10.1111/j.1365-246X.2004.02304.x.

Cohee, B. P., and G. C. Beroza (1994), A comparison of two methods for earthquake source inversion using strong motion seismograms, *Ann. Geophys.*, *XXXVII*, 1515–1538.

Courboulex, F., A. Dujardin, M. Vallee, B. Delouis, C. Sira, A. Deschamps, L. Honore, and F. Thouvenot (2013), High-frequency directivity effect for an Mw 4.1 earthquake, widely felt by the population in southeastern France, *Bull. Seismol. Soc. Am.*, *103*(6), 3347–3353, doi:10.1785/0120130073.

Coutant, O. (1989), Program of numerical simulation AXITRA, *Tech. rep.*, Lab. de Geophys. Interne et Tectonophys., Grenoble, France.

Cultrera, G., G. Ameri, A. Sarao, A. Cirella, and A. Emolo (2013), Ground-motion simulations within ShakeMap methodology: application to the 2008 Iwate-Miyagi Nairiku (Japan) and 1980 Irpinia (Italy) earthquakes, *Geophys. J. Int.*, *193*(1), 220–237, doi:10.1093/gji/ggs074.

Custódio, S., and R. J. Archuleta (2007), Parkfield earthquakes: Characteristic or complementary?, *J. Geophys. Res.*, *112*(B5), 1–10, doi:10.1029/2006JB004617, b05310.

Custódio, S., M. T. Page, and R. J. Archuleta (2009), Constraining earthquake source inversions with GPS data: 2. A two-step approach to combine seismic and geodetic data sets, *J. Geophys. Res.*, *114*(B1), 1–20, doi:10.1029/2008JB005746.

Dalguer, L. A., K. Irikura, W. Zhang, and J. D. Riera (2002), Distribution of dynamic and static stress changes during 2000 Tottori (Japan) earthquake: Brief interpretation of the earthquake sequences; Foreshocks, mainshock and aftershocks, *Geophys. Res. Lett.*, *29*(16), 5–1–5–4, doi:10.1029/2001GL014333.

Das, S., and B. Kostrov (1994), Diversity of solutions of the problem of earthquake faulting inversion; application to SH waves for the great 1989 Macquarie Ridge earthquake, *Phys. Earth Planet. Inter.*, *85*(3-4), 293–318, doi:10.1016/0031-9201(94)90119-8.

Day, S. M., G. Yu, and D. J. Wald (1998), Dynamic stress changes during earthquake rupture, *Bull. Seismol. Soc. Am.*, *88*(2), 512–522.

Day, S. M., S. H. Gonzalez, R. Anooshehpoor, and J. N. Brune (2008), Scale-model and numerical simulations of near-fault seismic directivity, *Bull. Seismol. Soc. Am.*, *98*(3), 1186–1206, doi:10.1785/0120070190.

Delouis, B., D. Giardini, P. Lundgren, and J. Salichon (2002), Joint inversion of InSAR, GPS, teleseismic, and strong-motion data for the spatial and temporal distribution of earthquake slip: Application to the 1999 Izmit mainshock, *Bull. Seismol. Soc. Am.*, *92*, 278–299.

Di Stefano, R., C. Chiarabba, L. Chiaraluce, M. Cocco, P. De Gori, D. Piccinini, and L. Valoroso (2011), Fault zone properties affecting the rupture evolution of the 2009 (M w 6.1) L'Aquila earthquake (central Italy): Insights from seismic tomography, *Geophys. Res. Lett.*, *38*(10), L10,310, doi:10.1029/2011GL047365.

Dieterich, J. H. (1979), Modeling of rock friction 1. Experimental results and constitutive equations, *J. Geophys. Res.*, *84*(9), 2161–2168.

Dreger, D., and A. Kaverina (2000), Seismic remote sensing for the earthquake source process and near-source strong shaking: a case study of the October 16, 1999 Hector Mine earthquake, *Geophys. Res. Lett.*, *27*(13), 1941–1944.

Dreger, D. S., M.-H. Huang, A. Rodgers, T. Taira, and K. Wooddell (2015), Kinematic finite-source model for the 24 August 2014 South Napa, California, earthquake from joint inversion of seismic, GPS, and InSAR data, *Seismol. Res. Lett.*, *86*(2A), 327–334, doi:10.1785/0220140244.

Dumbser, M., and M. Käser (2006), An arbitrary high-order discontinuous Galerkin method for elastic waves on unstructured meshes - II. The three-dimensional isotropic case, *Geophys. J. Int.*, *167*(1), 319–336, doi:10.1111/j.1365-246X.2006.03120.x.

Dunham, E. M., and R. J. Archuleta (2004), Evidence for a supershear transient during the 2002 Denali fault earthquake, *Bull. Seismol. Soc. Am.*, *94*(6), 256–268.

Duputel, Z., L. Rivera, Y. Fukahata, and H. Kanamori (2012), Uncertainty estimations for seismic source inversions, *Geophys. J. Int.*, *190*(2), 1243–1256, doi:10.1111/j.1365-246X.2012.05554.x.

Duputel, Z., et al. (2015), The iquique earthquake sequence of april 2014: Bayesian modeling accounting for prediction uncertainty, *Geophys. Res. Lett.*, *42*(19), 7949–7957, doi:10.1002/2015GL065402, 2015GL065402.

Durand, V., M. Bouchon, M. a. Floyd, N. Theodulidis, D. Marsan, H. Karabulut, and J. Schmittbuhl (2014), in Greece following the breakup of the slab, *Geophys. Res. Lett.*, *41*, 7129–7134, doi:10.1002/2014GL061408.

Fan, W., P. M. Shearer, and P. Gerstoft (2014), Kinematic earthquake rupture inversion in the frequency domain, *Geophys. J. Int.*, *199*(2), 1138–1160, doi:10.1093/gji/ggu319.

Frankel, A. (1991), High-frequency spectral falloff of earthquakes, fractal dimension of complex rupture, b value, and the scaling of strength on faults, *J. Geophys. Res.*, *96*(B4), 6291–6302, doi: 10.1029/91JB00237.

Frankel, A. (1995), Simulating strong motions of large earthquakes using recordings of small earthquakes: the Loma Prieta mainshock as a test case, *Bull. Seismol. Soc. Am.*, *85*(4), 1144–1160.

Frankel, A., and L. Wennerberg (1989), Rupture process of the Ms 6.6 Superstition Hills, California, earthquake determined from strong-motion recordings: application of tomographic source inversion, *Bull. Seismol. Soc. Am.*, *79*(2), 515–541.

Gallovič, F., and J. Brokešová (2004), On strong ground motion synthesis with k^{-2} slip distributions, *J. Seismol.*, *8*, 211–224.

Gallovič, F., and J. Brokešová (2007), Hybrid k-squared source model for strong ground motion simulations: Introduction, *Phys. Earth Planet. Inter.*, *160*(1), 34–50, doi:10.1016/j.pepi.2006.09.002.

Ganas, A., E. Serpelloni, G. Drakatos, M. Kolligri, I. Adamis, C. Tsimi, and E. Batsi (2009), The Mw 6.4 SW-Achaia (western Greece) earthquake of 8 June 2008: Seismological, field, GPS observations, and stress modeling, *J. Earthq. Eng.*, *13*(8), 1101–1124, doi:10.1080/13632460902933899.

Goto, H., Y. Yamamoto, and S. Kita (2012), Dynamic rupture simulation of the 2011 off the Pacific coast of Tohoku Earthquake: Multi-event generation within dozens of seconds, *Earth Planets Space*, *64*(12), 1167–1175, doi:10.5047/eps.2012.06.002.

Graves, R., and D. Wald (2001), Resolution analysis of finite fault source inversion using one- and three-dimensional Green's functions. I- Strong motions, *J. Geophys. Res.*, *106*(2000), 8745–8766.

Graves, R. W., and A. Pitarka (2010), Broadband Ground-Motion Simulation Using a Hybrid Approach, *Bull. Seismol. Soc. Am.*, *100*(5A), 2095–2123, doi:10.1785/0120100057.

Gualandi, A., E. Serpelloni, and M. E. Belardinelli (2014), Space-time evolution of crustal deformation related to the Mw 6.3, 2009 L'Aquila earthquake (central Italy) from principal component analysis inversion of GPS position time-series, *Geophys. J. Int.*, *197*(1), 174–191, doi:10.1093/gji/ggt522.

Gusev, A. A. (2012), High-Frequency Radiation from an Earthquake Fault: A Review and a Hypothesis of Fractal Rupture Front Geometry, *Pure Appl. Geophys.*, doi:10.1007/s00024-012-0455-y.

Hansen, P. (2010), *Discrete Inverse Problems*, Society for Industrial and Applied Mathematics, doi:10.1137/1.9780898718836.

Hartzell, S., S. Harmsen, A. Frankel, and S. Larsen (1999), Calculation of broadband time histories of ground motion: Comparison of methods and validation using strong-ground motion from the 1994 Northridge earthquake, *Bull. Seismol. Soc. Am.*, *89*(6), 1484–1504.

Hartzell, S. H. (1978), Earthquake aftershocks as Green's functions, *Geophys. Res. Lett.*, *5*(1), 1–4, doi: 10.1029/GL005i001p00001.

Hartzell, S. H., and T. H. Heaton (1983), Inversion of strong ground motion and teleseismic waveform data for the fault rupture history of the 1979 Imperial Valley, California, earthquake, *Bull. Seismol. Soc. Am.*, *73*(6), 1553–1583.

Hartzell, S. H., G. S. Stewart, and C. Mendoza (1991), Comparison of L1 and L2 norms in a teleseismic waveform inversion for the slip history of the Loma Prieta, California, earthquake, *Bull. Seismol. Soc. Am.*, *81*(5), 1518–1539.

Hartzell, S. H., P. Liu, C. Mendoza, C. Ji, and K. M. Larson (2007), Stability and Uncertainty of Finite-Fault Slip Inversions: Application to the 2004 Parkfield, California, Earthquake, *Bull. Seismol. Soc. Am.*, *97*(6), 1911–1934, doi:10.1785/0120070080.

Henry, C., and S. Das (2002), The Mw 8.2, 17 February 1996 Biak, Indonesia, earthquake: Rupture history, aftershocks, and fault plane properties, *J. Geophys. Res.*, *107*(B11), ESE 11–1–ESE 11–16, doi:10.1029/2001JB000796, 2312.

Herrero, A., and P. Bernard (1994), A kinematic self-similar rupture process for earthquakes, *Bull. Seismol. Soc. Am.*, *84*(4), 1216–1228.

Ide, S., and M. Takeo (1997), Determination of constitutive relations of fault slip based on seismic wave analysis, *J. Geophys. Res.*, *102*(B12), 27,379, doi:10.1029/97JB02675.

Imperatori, W., and M. P. Mai (2012), Broad-band near-field ground motion simulations in 3-dimensional scattering media, *Geophys. J. Int.*, *192*(2), 725–744, doi:10.1093/gji/ggs041.

Irikura, K., and K. Kamae (1994), Estimation of strong ground motion in broad-frequency band based on a seismic source scaling model and an empirical Green's function technique, *Ann. di Geofis.*, *XXXVII*, 1721–1743.

Irikura, K., and H. Miyake (2010), Recipe for Predicting Strong Ground Motion from Crustal Earthquake Scenarios, *Pure Appl. Geophys.*, *168*(1-2), 85–104, doi:10.1007/s00024-010-0150-9.

Ji, C., D. Wald, and D. V. Helmberger (2002a), Source description of the 1999 Hector Mine, California, earthquake, part II: Complexity of slip history, *Bull. Seismol. Soc. Am.*, *92*(4), 1208–1226.

Ji, C., D. Wald, and D. V. Helmberger (2002b), Source description of the 1999 Hector Mine, California, earthquake, part I: Wavelet domain inversion theory and resolution analysis, *Bull. Seismol. Soc. Am.*, *92*(4), 1192–1207.

Ji, C., R. J. Archuleta, and C. Twardzik (2015), Rupture history of 2014 Mw 6.0 South Napa earthquake inferred from near-fault strong motion data and its impact to the practice of ground strong motion prediction, *Geophys. Res. Lett.*, *42*(7), 2149–2156, doi:10.1002/2015GL063335, 2015GL063335.

Kanamori, H., and T. H. Heaton (2000), *Microscopic and Macroscopic Physics of Earthquakes*, pp. 147–163, American Geophysical Union, doi:10.1029/GM120p0147.

Kane, D. L., P. M. Shearer, B. P. Goertz-Allmann, and F. L. Vernon (2013), Rupture directivity of small earthquakes at Parkfield, *J. Geophys. Res. Solid Earth*, *118*(1), 212–221, doi:10.1029/2012JB009675.

Kaneko, Y., N. Lapusta, and J.-P. Ampuero (2008), Spectral element modeling of spontaneous earthquake rupture on rate and state faults: Effect of velocity-strengthening friction at shallow depths, *J. Geophys. Res.*, *113*(B9), 1–17, doi:10.1029/2007JB005553.

Käser, M., and M. Dumbser (2006), An arbitrary high order discontinuous Galerkin method for elastic waves on unstructured meshes I: The two-dimensional isotropic case with external source terms, *Geophys. J. Int.*, *166*(2), 855–877.

Kato, N., T. Satoh, X. Lei, K. Yamamoto, and T. Hirasawa (1999), Effect of fault bend on the rupture propagation process of stick-slip, *Tectonophysics*, *310*(1-4), 81–99, doi:10.1016/S0040-1951(99)00149-3.

Keilis-Borok, V. (1959), On estimation of the displacement in an earthquake source and of source dimensions, *Annals of Geophysics*, *12*, 205–214.

Kennett, B. L. N., and N. J. Kerry (1979), Seismic waves in a stratified half space, *Geophysical Journal of the Royal Astronomical Society*, *57*(3), 557–583, doi:10.1111/j.1365-246X.1979.tb06779.x.

Konca, A. (2015), Rupture process of 2011 Mw7.1 Van, Eastern Turkey earthquake from joint inversion of strong-motion, high-rate GPS, teleseismic, and GPS data, *J. Seismol.*, *19*(4), 969–988, doi:10.1007/s10950-015-9506-z.

Konca, O. A., Y. Kaneko, N. Lapusta, and J.-P. Avouac (2013), Kinematic inversion of physically plausible earthquake source models obtained from dynamic rupture simulations, *Bull. Seismol. Soc. Am.*, *103*(5), 2621–2644, doi:10.1785/0120120358.

Latour, S., C. Voisin, F. Renard, E. Larose, S. Catheline, and M. Campillo (2013), Effect of fault heterogeneity on rupture dynamics: An experimental approach using ultrafast ultrasonic imaging, *J. Geophys. Res. Solid Earth*, *118*, 1–15, doi:10.1002/2013JB010231.

Lawson, C., and R. Hanson (1995), *Solving Least Squares Problems*, *Classics in Applied Mathematics*, vol. 15, SIAM, Philadelphia.

Lay, T., H. Kanamori, C. J. Ammon, K. D. Koper, A. R. Hutko, L. Ye, H. Yue, and T. M. Rushing (2012), Depth-varying rupture properties of subduction zone megathrust faults, *J. Geophys. Res.*, *117*, B04,311, doi:10.1029/2011JB009133.

Lekkas, E., G. Danamos, and G. Mavrikas (1997), Geological structure and evolution of cefallonia and ithaki islands, *Bull. Geol. Soc. Greece*, *34*(1), 11–17.

Liu, P., R. J. Archuleta, and S. H. Hartzell (2006), Prediction of broadband ground-motion time histories: Hybrid low/high- frequency method with correlated random source parameters, *Bull. Seismol. Soc. Am.*, *96*(6), 2118–2130, doi:10.1785/0120060036.

Luo, Y., and R. Duraiswami (2011), Efficient parallel nonnegative least squares on multicore architectures, *SIAM J. Sci. Comput.*, *33*(5), 2848–2863, doi:10.1137/100799083.

Mai, P., and G. Beroza (2002), A spatial random field model to characterize complexity in earthquake slip, *J. Geophys. Res.*, *107*, 2308, doi:10.1029/2001JB000588.

Mai, P. M., et al. (2016), Earthquake early warning system in southern Italy: Methodologies and performance evaluation, *Seismol. Res. Lett.*, p. submitted.

Melgar, D., J. Geng, B. W. Crowell, J. S. Haase, Y. Bock, W. C. Hammond, and R. M. Allen (2015), Seismogeodesy of the 2014 Mw6.1 Napa earthquake, California: Rapid response and modeling of fast rupture on a dipping strike-slip fault, *J. Geophys. Res. Solid Earth*, *120*(7), 5013–5033, doi: 10.1002/2015JB011921.

Mello, M., H. Bhat, A. Rosakis, and H. Kanamori (2014), Reproducing the supershear portion of the 2002 Denali earthquake rupture in laboratory, *Earth Planet. Sci. Lett.*, *387*, 89–96, doi:10.1016/j.epsl.2013.11.030.

Menke, W. (1985), Imaging fault slip using teleseismic waveforms: analysis of a typical incomplete tomography problem, *Geophys. J. R. Astron. Soc.*, *81*, 197–204.

Menke, W. (2012), *Geophysical Data Analysis: Discrete Inverse Theory*, Academic Press, Boston, Massachusetts.

Merryman Boncori, J. P., et al. (2015), The February 2014 Cephalonia Earthquake (Greece): 3D Deformation Field and Source Modeling from Multiple SAR Techniques, *Seismol. Res. Lett.*, *86*(1), 124–137, doi:10.1785/0220140126.

Monelli, D., and M. P. Mai (2008), Bayesian inference of kinematic earthquake rupture parameters through fitting of strong motion data, *Geophys. J. Int.*, *173*(1), 220–232, doi:10.1111/j.1365-246X.2008.03733.x.

Monelli, D., M. P. Mai, S. Jónsson, and D. Giardini (2009), Bayesian imaging of the 2000 Western Tottori (Japan) earthquake through fitting of strong motion and GPS data, *Geophys. J. Int.*, *176*(1), 135–150, doi:10.1111/j.1365-246X.2008.03943.x.

Motazedian, D., and G. M. Atkinson (2005), Stochastic finite-fault modeling based on a dynamic corner frequency, *Bull. Seismol. Soc. Am.*, *95*(3), 995–1010, doi:10.1785/0120030207.

Nalbant, S., J. McCloskey, S. Steacy, M. NicBhloscaidh, and S. Murphy (2013), Interseismic coupling, stress evolution, and earthquake slip on the Sunda megathrust, *Geophys. Res. Lett.*, *40*(16), 4204–4208, doi:10.1002/grl.50776.

Nilsson, S., N. A. Petersson, B. Sjögreen, and H.-O. Kreiss (2007), Stable difference approximations for the elastic wave equation in second order formulation, *SIAM Journal on Numerical Analysis*, *45*(5), 1902–1936, doi:10.1137/060663520.

Olson, A. H., and J. G. Anderson (1988), Implications of frequency-domain inversion of earthquake ground motions for resolving the space-time dependence of slip on an extended fault, *Geophys. J. Int.*, *94*(3), 443–455, doi:10.1111/j.1365-246X.1988.tb02267.x.

Olson, A. H., and R. J. Apsel (1982), Finite faults and inverse theory with applications to the 1979 Imperial Valley earthquake, *Bull. Seismol. Soc. Am.*, *72*(6), 1969–2001.

Pacor, F., G. Cultrera, A. Mendez, and M. Cocco (2005), Finite fault modeling of strong ground motions using a hybrid deterministic-stochastic approach, *Bull. Seismol. Soc. Am.*, *95*(1), 225–240, doi:10.1785/0120030163.

Pacor, F., D. Spallarossa, A. Oth, L. Luzi, R. Puglia, L. Cantore, A. Mercuri, M. D'Amico, and D. Bindi (2016), Spectral models for ground motion prediction in the L'Aquila region (central Italy): evidence for stress-drop dependence on magnitude and depth, *Geophysical Journal International*, *204*(2), 697–718, doi:10.1093/gji/ggv448.

Perfettini, H., J. Schmittbuhl, and A. Cochard (2003), Shear and normal load perturbations on a two-dimensional continuous fault: 1. Static triggering, *J. Geophys. Res.*, *108*(B9), 2408, doi:10.1029/2002JB001804.

Petersson, N. A., and B. Sjögreen (2012), Stable and efficient modeling of anelastic attenuation in seismic wave propagation, *Commun. Comput. Phys.*, *12*(1), 193–225, doi:10.4208/cicp.201010.090611a.

Peyrat, S., and K. B. Olsen (2004), Nonlinear dynamic rupture inversion of the 2000 Western Tottori, Japan, earthquake, *Geophys. Res. Lett.*, *31*(5), doi:10.1029/2003GL019058, l05604.

Piatanesi, A., A. Cirella, P. Spudich, and M. Cocco (2007), A global search inversion for earthquake kinematic rupture history: Application to the 2000 western Tottori, Japan earthquake, *J. Geophys. Res.*, *112*(B7), B07,314, doi:10.1029/2006JB004821.

Pitarka, A., P. Somerville, Y. Fukushima, T. Uetake, and K. Irikura (2000), Simulation of near-fault strong-ground motion using hybrid Green's functions, *Bull. Seis. Soc. Am.*, *90*, 566–586.

Podvin, P., and I. Lecomte (1991), Finite difference computation of traveltimes in very contrasted velocity models: a massively parallel approach and its associated tools, *Geophys. J. Int.*, *105*(1), 271–284, doi:10.1111/j.1365-246X.1991.tb03461.x.

Press, W. H., B. P. Flannery, S. A. Teukolsky, and W. T. Vetterling (1992), *Numerical Recipes in Fortran, The Art of Scientific Computing, 2nd ed.*, Cambridge University Press, New York.

Razafindrakoto, H., P. Mai, M. Genton, L. Zhang, and K. Thingbaijam (2015), Quantifying variability in earthquake rupture models using multidimensional scaling: application to the 2011 tohoku earthquake, *Geophys. J. Int.*, *202*, 17 – 40.

Razafindrakoto, H. N. T., and M. P. Mai (2014), Uncertainty in earthquake source imaging due to variations in source time function and Earth structure, *Bull. Seismol. Soc. Am.*, *104*(2), 855–874, doi:10.1785/0120130195.

Ripperger, J., J.-P. Ampuero, M. P. Mai, and D. Giardini (2007), Earthquake source characteristics from dynamic rupture with constrained stochastic fault stress, *J. Geophys. Res.*, *112*(B4), 1–17, doi:10.1029/2006JB004515.

Ruiz, J. A., D. Baumont, P. Bernard, and C. Berge-Thierry (2007), New approach in the kinematic k^{-2} source model for generating physical slip velocity functions, *Geophys. J. Int.*, *171*(2), 739–754, doi:10.1111/j.1365-246X.2007.03503.x.

Ruiz, J. A., D. Baumont, P. Bernard, and C. Berge-Thierry (2011), Modelling directivity of strong ground motion with a fractal, k^{-2}, kinematic source model, *Geophys. J. Int.*, *186*(1), 226–244, doi:10.1111/j.1365-246X.2011.05000.x.

Ruiz, J. A., D. Baumont, P. Bernard, and C. Berge-Thierry (2013), Combining a kinematic fractal source model with hybrid Green's functions to model broadband strong ground motion, *Bull. Seismol. Soc. Am.*, *103*(6), 3115–3130, doi:10.1785/0120110135.

Satriano, C., L. Elia, C. Martino, M. Lancieri, A. Zollo, and G. Iannaccone (2011), Presto, the earthquake early warning system for southern italy: Concepts, capabilities and future perspectives, *Soil Dyn. Earthq. Eng.*, *31*(2), 137 – 153, doi:http://dx.doi.org/10.1016/j.soildyn.2010.06.008.

Schmedes, J., R. J. Archuleta, and D. Lavallée (2010), Correlation of earthquake source parameters inferred from dynamic rupture simulations, *J. Geophys. Res.*, *115*(B3), B03,304, doi:10.1029/2009JB006689.

Schmedes, J., R. J. Archuleta, and D. Lavallee (2012), A kinematic rupture model generator incorporating spatial interdependency of earthquake source parameters, *Geophys. J. Int.*, *192*(3), 1116–1131, doi:10.1093/gji/ggs021.

Sekiguchi, H., K. Irikura, and T. Iwata (2000), Fault geometry at the rupture termination of the 1995 Hyogo-ken Nanbu earthquake, *Bull. Seismol. Soc. Am.*, (February), 117–133.

Serpetsidaki, A., et al. (2014), New constraints from seismology and geodesy on the mw = 6.4 2008 movri (greece) earthquake: evidence for a growing strike-slip fault system, *Geophys. J. Int.*, *198*(3), 1373–1386, doi:10.1093/gji/ggu212.

Shao, G., and C. Ji (2012), What the exercise of the SPICE source inversion validation BlindTest 1 did not tell you, *Geophys. J. Int.*, *189*(1), 569–590, doi:10.1111/j.1365-246X.2012.05359.x.

Sokos, E., and J. Zahradník (2013), Evaluating centroid-moment-tensor uncertainty in the new version of ISOLA software, *Seismol. Res. Lett.*, *84*(4), 656–665, doi:10.1785/0220130002.

Sokos, E. N., and J. Zahradník (2008), Isola a Fortran code and a Matlab gui to perform multiple-point source inversion of seismic data, *Computers & Geosciences*, *34*(8), 967 – 977, doi:10.1016/j.cageo.2007.07.005.

Somerville, P., N. F. Smith, R. W. Graves, and N. Abrahamson (1997), Modification of empirical strong ground motion attenuation relations to include the amplitude and duration effects of rupture directivity, *Seismol. Res. Lett.*, *68*(1), 199–222, doi:10.1785/gssrl.68.1.199.

Somerville, P., et al. (1999), Characterizing crustal earthquake slip models for the prediction of strong ground motion, *Seismol. Res. Lett.*, *70*(1), 59–80.

Song, S. G. (2016), Developing a generalized pseudo-dynamic source model of mw 6.5–7.0 to simulate strong ground motions, *Geophys. J. Int.*, *204*(2), 1254–1265, doi:10.1093/gji/ggv521.

Spudich, P., and R. J. Archuleta (1987), Earthquake ground-motion calculation with applications to source parametrization of finite faults, in *Seismic Strong Motion Synthetics*, edited by B. A. Bolt, pp. 205–265, Academic Press, Orlando, Florida.

Steacy, S., J. Gomberg, and M. Cocco (2005), Introduction to special section: Stress transfer, earthquake triggering, and time-dependent seismic hazard, *J. Geophys. Res.*, *110*, B05S01.

Stein, R. (1999), The role of stress transfer in earthquake occurrence, *Nature*, *402*, 605–609.

Stein, R., A. Barka, and J. Dieterich (1997), Progressive failure on the North Anatolian fault since 1939 by earthquake stress triggering, *Geophys. J. Int.*, *128*, 594–604.

Stidham, C., M. Antolik, D. Dreger, S. Larsen, and B. Romanowicz (1999), Three-dimensional structure influences on the strong-motion wavefield of the 1989 Loma Prieta earthquake, *Bull. Seismol. Soc. Am.*, *89*(5), 1184–1202.

Tan, Y., and D. Helmberger (2010), Rupture directivity characteristics of the 2003 big bear sequence, *Bull. Seismol. Soc. Am.*, *100*(3), 1089–1106, doi:10.1785/0120090074.

Tinti, E., L. Scognamiglio, A. Cirella, and M. Cocco (2014), Up-dip directivity in near-source during the 2009 L'Aquila main shock, *Geophys. J. Int.*, *198*(3), 1618–1631, doi:10.1093/gji/ggu227.

Titarev, V. A., and E. F. Toro (2002), ADER: Arbitrary high order Godunov approach., *J. Sci. Comput.*, *17*, 609–618.

Twardzik, C., R. Madariaga, S. Das, and S. Custódio (2012), Robust features of the source process for the 2004 Parkfield, California, earthquake from strong-motion seismograms, *Geophysical Journal International*, *191*(3), 1245–1254, doi:10.1111/j.1365-246X.2012.05653.x.

Vackář, J., J. Burjánek, and J. Zahradník (2015), Automated detection of long-period disturbances in seismic records; MouseTrap code, *Seismol. Res. Lett.*, doi:10.1785/0220140168.

Valkaniotis, S., A. Ganas, G. Papathanassiou, and M. Papanikolaou (2014), Field observations of geological effects triggered by the January-February 2014 Cephalonia (Ionian Sea, Greece) earthquakes, *Tectonophysics*, *630*, 150 – 157, doi:10.1016/j.tecto.2014.05.012.

Vallée, M., and C. Satriano (2014), Ten year recurrence time between two major earthquakes affecting the same fault segment, *Geophys. Res. Lett.*, *41*(7), 2312–2318, doi:10.1002/2014GL059465.

Vallée, M., and M. Bouchon (2004), Imaging coseismic rupture in far field by slip patches, *Geophys. J. Int.*, *156*(3), 615–630, doi:10.1111/j.1365-246X.2004.02158.x.

Warren, L. M., E. C. Baluyut, T. Osburg, K. Lisac, and S. Kokkinen (2015), Fault plane orientations of intermediate-depth and deep-focus earthquakes in the japan-kuril-kamchatka subduction zone, *J. Geophys. Res. - Solid Earth*, doi:10.1002/2015JB012463.

Wei, S., S. Barbot, R. Graves, J. J. Lienkaemper, T. Wang, K. Hudnut, Y. Fu, and D. Helmberger (2015), The 2014 Mw 6.1 South Napa earthquake: A unilateral rupture with shallow asperity and rapid afterslip, *Seismol. Res. Lett.*, *86*(2A), 344–354, doi:10.1785/0220140249.

Yagi, Y., and Y. Fukahata (2011), Introduction of uncertainty of Green's function into waveform inversion for seismic source processes, *Geophys. J. Int.*, *186*(2), 711–720, doi:10.1111/j.1365-246X.2011.05043.x.

Zahradník, J., and S. Custódio (2012), Moment tensor resolvability: Application to southwest Iberia, *Bull. Seismol. Soc. Am.*, *102*(3), 1235–1254, doi:10.1785/0120110216.

Zahradník, J., and A. Plešinger (2010), Toward understanding subtle instrumentation effects associated with weak seismic events in the near field, *Bull. Seismol. Soc. Am.*, *100*(1), 59–73, doi:10.1785/0120090087.

Zeng, Y., and J. G. Anderson (1995), Subevent rake and random scattering effects in realistic strong ground motion simulation, *Geophys. Res. Lett.*, *22*(1), 17, doi:10.1029/94GL02798.

Zeng, Y., J. G. Anderson, and G. Yu (1994), A composite source model for computing realistic synthetic strong ground motions, *Geophys. Res. Lett.*, *21*(8), 725–728.

Zhang, L., P. M. Mai, K. K. Thingbaijam, H. N. Razafindrakoto, and M. G. Genton (2015), Analysing earthquake slip models with the spatial prediction comparison test, *Geophys. J. Int.*, *200*(1), 185–198, doi:10.1093/gji/ggu383.

Zhang, W., T. Iwata, K. Irikura, H. Sekiguchi, and M. Bouchon (2003), Heterogeneous distribution of the dynamic source parameters of the 1999 Chi-Chi, Taiwan, earthquake, *J. Geophys. Res. Solid Earth*, *108*(B5), doi:10.1029/2002JB001889, 2232.

Chapter 5

Appendix: Collection of publications

5.1 Statement of the author's contribution to the publications

All publications of this Thesis are my exclusive work or work I have significantly contributed to. I have contributed to discussions in all of the papers. If not stated otherwise, all my calculations were performed using my own codes.

I performed the broadband kinematic source simulations and contributed to discussions of the results in [P1, 5, 6, 10]. I contributed to [P3] by evaluating and discussing the possibility of the fault geometry identification by means of stress calculations. I led the collaborative effort in [P2, 8], providing non-planar fault geometries, source models and discussing the results. In [P4] I performed solely the quasi-dynamic earthquake cycle modeling (using also own code). I have introduced slip inversions method, coded them and performed all their applications in [P7, 9, 11, 12, 14, 15, 16]. In [P13, 14] the strong ground motion simulations that were carried out by G. Ameri under my supervision using my code. In [P17] I performed all the evaluations of the rupture models from the SIV experiment. Papers [P19, 18] represent my sole work including slip inversions and strong ground motion modeling.

5.2 List of appended publications

[P1] Gallovič, F., Burjánek, J. (2007). High-frequency Directivity in Strong Ground Motion Modeling Methods, *Annals of Geophysics, 50(2)*, 203-211, .

[P2] Käser, M., Gallovič, F. (2008). Effects of Complicated 3D Rupture Geometries on Earthquake Ground Motion and Their Implications: A Numerical Study, *Geophys. J. Int., 172*, 276-292, doi: 10.1111/j.1365-246X.2007.03627.x.

[P3] Zahradník, J., Gallovič, F., Sokos, E., Serpetsidaki, A., Tselentis, A. (2008). Quick Fault-Plane Identification by a Geometrical Method: Application to the Mw 6.2 Leonidio Earthquake, 6 January 2008, Greece, *Seism. Res. Lett., 79*, 653-662, doi: 10.1785/gssrl.79.5.653.

[P4] Gallovič, F. (2008). Heterogeneous Coulomb stress perturbation during earthquake cycles in a 3D rate-and-state fault model, *Geophys. Res. Lett., 35*, L21306, doi: 10.1029/2008GL035614.

[P5] Zollo, A., Iannaccone, G., Lancieri, M., Cantore, L., Convertito, V., Emolo, A., Festa, G., Gallovič, F., Vassallo, M., Martino, C., Satriano, C., Gasparini, P. (2009). The Earthquake Early Warning System in Southern Italy: Methodologies and Performance Evaluation, *Geophys. Res. Lett., 36*, special issue on New Methods and Applications of Earthquake Early Warning, L00B07, doi: 10.1029/2008GL036689.

[P6] Ameri, G., Gallovič, F., Pacor, F., Emolo, A. (2009). Uncertainties in strong ground-motion prediction with finite-fault synthetic seismograms: an application to the 1984 M 5.7 Gubbio, central Italy, earthquake, *Bull. Seism. Soc. Am., 99*, 647-663, doi: 10.1785/0120080240.

[P7] Gallovič, F., Zahradník, J., Křížová, D., Plicka, V., Sokos, E., Serpetsidaki, A., Tselentis, G-A.(2009). From Earthquake Centroid to Spatial-Temporal Rupture Evolution: Mw 6.3 Movri Mountain Earthquake, June 8, 2008, Greece, *Geophys. Res. Lett., 36*, L21310, doi: 10.1029/2009GL040283.

[P8] Gallovič, F., Käser, M., Burjánek, J., Papaioannou, Ch. (2010). Three-dimensional modeling of near-fault ground motions with nonplanar rupture models and topography: Case of the 2004 Parkfield earthquake, *J. Geophys. Res., 115*, B03308, doi: 10.1029/2008JB006171.

[P9] Zahradník, J., Gallovič, F. (2010). Toward understanding slip-inversion uncertainty and artifacts, *J. Geophys. Res., 115*, B09310, doi: 10.1029/2010JB007414.

[P10] Ameri, G., Emolo, A., Pacor, F., Gallovič, F. (2011). Ground Motion Simulations for the M 6.9 Irpinia 1980 Earthquake (Southern Italy) and Scenario Events, *Bull. Seism. Soc. Am., 101*, 1136-1151, doi: 10.1785/0120100231.

[P11] Gallovič, F., Zahradník, J. (2011). Toward understanding slip-inversion uncertainty and artifacts: 2. Singular value analysis, J. Geophys. Res., 116, B02309, doi: 10.1029/2010JB007814.

[P12] Gallovič, F., Zahradník, J. (2012). Complexity of the Mw 6.3 2009 L'Aquila (Central Italy) earthquake: 1. Multiple finite-extent source inversion, J. Geophys. Res., 117, B04307, doi: 10.1029/2011JB008709.

[P13] Ameri, G., Gallovič, F., Pacor, F. (2012). Complexity of the Mw 6.3 2009 L'Aquila (Central Italy) earthquake: 2. Broadband strong-motion modeling, *J. Geophys. Res., 117*, B04308, doi: 10.1029/2011JB008729.

[P14] Gallovič, F., Ameri, G., Zahradník, J., Janský, J., Plicka, V., Sokos, E., Askan, A., Pakzad, M. (2013). Fault process and broadband ground-motion simulations of the 23 October 2011 Van (Eastern Turkey) earthquake, *Bull. Seism. Soc. Am., 103*, 3164-3178, doi: 10.1785/0120130044.

[P15] Gallovič, F., Imperatori, W., Mai, P. M. (2015). Effects of three-dimensional crustal structure and smoothing constraint on earthquake slip inversions: case study of the Mw 6.3 2009 L'Aquila earthquake, *J. Geophys. Res. 120*, 428-449, doi: 10.1002/2014JB011650.

[P16] Sokos, E., Kiratzi, A., Gallovič, F., Zahradník, J., Serpetsidaki, A., Plicka, V., Janský, J., Kostelecký, J., Tselentis, G-A. (2015). Rupture process of the 2014 Cephalonia, Greece, earthquake doublet (Mw 6) as inferred from regional and local seismic data, Tectonophysics, *Tectonophysics, 656*, 131-141, doi: 10.1016/j.tecto.2015.06.013.

[P17] Gallovič, F., Ampuero, J.-P. (2015). A new strategy to compare inverted rupture models exploiting the eigen-structure of the inverse problem, *Seism. Res. Lett., 86*, 1679-1689, doi: 10.1785/0220150096.

[P18] Gallovič, F. (2016). Modeling velocity recordings of the Mw 6.0 South Napa, California, earthquake: unilateral event with weak high-frequency directivity, *Seism. Res. Lett., 87*, 2-14, doi: 10.1785/0220150042.

[P19] Gallovič, F. (2015). Scenario modeling of the 2014 Mw 6.0 South Napa, California, earthquake using an advanced broadband kinematic source model, *Extended abstract, Conference "Best Practices in Physics-based Fault Rupture Models for Seismic Hazard Assessment of Nuclear Installations"*, Vienna, Austria, November 18-20.

[P1]

High-frequency directivity in strong ground motion modeling methods

Frantisek Gallovic and Jan Burjanek
Department of Geophysics, Faculty of Mathematics and Physics, Charles University, Prague 8, Czech Republic

Abstract
We are investigating two distinct strong ground motion simulation techniques as regards their high-frequency directivity: i) the composite model with a fractal subevent size distribution, based on the method of summation of empirical Green's functions, and ii) the integral model with the *k*-squared slip model with *k*-dependent rise time, based on the representation theorem. We test the simulations in a 1D layered crustal model against empirical PGA attenuation relations, particularly with regard to their uncertainty, described by the standard deviation (σ). We assume that any synthetic model for a particular earthquake should not provide a PGA scatter larger than the observed scatter for a large set of earthquakes. The 1999 Athens earthquake ($M_w = 5.9$) is studied as a test example. In the composite method, the synthetic data display a scatter of less than $\pm 2\sigma$ around the empirical mean. The *k*-squared method displays a larger scatter, demonstrating strong high-frequency directivity. It is shown that the latter can be reduced by introducing a formal spectral modification.

Key words *strong motion modeling – earthquake source models – heterogeneous slip distribution – composite model – source directivity*

1. Introduction

Low-frequency directivity effects are well known. For example, there is a number of seismic recordings of recent earthquakes (*e.g.*, 1992 Landers, 1994 Northridge, 1995 Kobe, 1999 Chi-Chi), which show long-period velocity pulses caused by rupture propagation towards a station. This effect can be successfully explained by the apparent source time function varying with azimuth (Haskell, 1964).

However, high-frequency directivity is different. Somerville *et al.* (1997) showed on empirical data that the effect of directivity vanishes for short-period ground motions. Boatwright and Boore (1982) suggested that the total variation of PGA should not exceed a factor of 10.

Hartzell *et al.* (1999) compared several strong ground motion modeling techniques applied to the 1994 Northridge earthquake. However, they did not discuss the directivity effect inherent to the compared source models although it can drastically change the overall synthetic results (*e.g.*, PGA maps). In their study, the techniques under comparison were based on two kinds of earthquake source descriptions – composite and integral models. The composite model is understood to be a discrete sequence of independently rupturing subevents. The integral model utilizes the representation theorem with prescribed spatial-temporal distribution of the dislocation over the fault. In this paper we adopt two representative approaches of the composite and integral methods with the same fundamental features as those in the paper by Hartzell *et al.* (1999), see further.

We compare the high-frequency directivity of these two source models in a given crustal model. The main assumption is that any syn-

Mailing address: Dr. Frantisek Gallovic, Department of Geophysics, Faculty of Mathematics and Physics, Charles University, V Holesovickach 2, Prague 8, 180 00 Czech Republic; e-mail: gallovic@karel.troja.mff.cuni.cz

thetic (source + crustal) model for one particular earthquake should not provide an uncertainty of strong-motion characteristics larger than the uncertainty observed for a general set of earthquakes. Note that this assumption has to be understood as an empirical constraint on the physical parameters of the simulation model and/or on the simulation method itself.

In particular, we choose PGA as the studied characteristic since it is sensitive to high frequency directivity. We expect at least 95% of the simulated PGAs to fall within the $\pm 2\sigma$ range around the mean empirical attenuation curve. Such comparison could disprove the modeling techniques that break the $\pm 2\sigma$ bounds systematically (not only for one worst case scenario) if the attenuation relations are obtained from a sufficiently large data set. However, it cannot be used for technique validation unless we take into account all possible phenomena that boost the scatter of the simulation (*e.g.*, 3D structural effects, site effects, etc.). Note that PGA is just one special choice and that a similar comparison can be carried out for any other characteristics *e.g.,* duration, spectral levels at given frequencies, Arias intensity, etc.

2. Simulation techniques

Composite models are based on the assumption that the modeled event can be seen as a discrete sequence of independently rupturing subevents. We implement the composite model with Fractal Subevent Size Distribution (hereinafter only FSSD) described by Hartzell *et al.* (1999). The number of subevents with a characteristic dimension greater than R is proportionalto R^{-2}.The subevents do not overlap, and the sum of their areas equals the area of the target event. The subevents are distributed randomly over the fault, creating a typical fractal pattern. Both the final slip and duration of each subevent are related to its characteristic dimension, using constant stress-drop scaling. The subevents' source time functions are modeled using a simple point-source approximation (Brune, 1970) with corner frequency

$$f_c = c v_r / R \qquad (2.1)$$

where v_r is the rupture velocity. The constant of proportionality c characterizes the efficiency of the subevent high-frequency radiation given by subevent heterogeneity (*e.g.*, in its spatial stress drop distribution). We consider it to be a free parameter of the model. A detailed description can be found in Burjanek (2002).

In the integral models one prescribes the spatial-temporal evolution of the slip over the fault. Bernard and Herrero (1994) proposed a stochastic model with a k^{-2} slip distribution, k being the wave number. This means that the decay of the slip wave number amplitude spectrum is proportional to k^{-2} for large wave numbers, and its phase is random. This model, however, does not include asperities, which are a common feature of slip inversion results (Somerville *et al.*, 1999). To include asperities in the slip model, we adopt the so-called hybrid slip, which is a combination of the long-wavelength deterministic part (asperities) and short-wavelength stochastic part (random phase in spatial slip spectrum), preserving the k^{-2} spectral decay of the slip amplitude spectrum (see Gallovic and Brokesova, 2004a). In this model, hereinafter referred to as the k-squared model, the rupture propagates with constant velocity v_r in the form of a slip pulse of width L_0. Small-scale slip in homogeneities rupture within a time proportional to their spatial wavelength (Bernard *et al.*, 1996). This results in a non-uniform shape of the slip rate functions over the fault.

Note that both models, the FSSD and k-squared, display an omega-squared falloff in displacement source spectra, *i.e.* a high-frequency plateau in the acceleration source spectra.

3. Benchmark – 1999 Athens earthquake

We use two source models to simulate strong ground motions due to the 1999 Athens earthquake (Tselentis and Zahradnik, 2000). We consider 112 virtual receivers distributed radially around the epicenter along 16 profiles at epicentral distances of 4 to 28 km (shown later in fig. 3a). This station geometry has been chosen to compare the simulation results with the latest PGA attenuation relations for Greece by Skarlatoudis *et al.* (2003) defined with respect to the

epicentral distance. The relations were obtained from a data set of 225 earthquakes, mainly normal and strike-slip events with magnitudes of $4.5 \leq M \leq 7.0$. More specifically, we choose their attenuation curve for rock sites (class B, NEHRP, 1994), normal faulting and magnitude of the Athens earthquake ($M_w = 5.9$). All calculations are carried out up to 10 Hz as spectral amplitudes at higher frequencies were found to diminish due to near-surface attenuation (see also Margaris and Boore, 1998).

Note that the Athens earthquake is a representative of predominantly unilateral earthquakes, in which case we expect a significant directivity effect. The unilaterality of the rupture propagation does not seem to be an extreme scenario since, *e.g.*, McGuire *et al.* (2002) showed that unilateral earthquakes predominate in the global earthquake catalog.

3.1. *Source and propagation models*

We adopt the seismic moment 7.8×10^{17} Nm, epicentral location (38.08°N, 23.58°E), depth 12 km, focal mechanism (strike 123°, dip 55°, rake −84°) and the fault orientation from previous studies (for review see Zahradnik, 2002). The remaining parameters, *i.e.* length 11 km and width 8 km of the fault and asperity slip contrast 2 (necessary for the *k*-squared model with asperity only), are taken from the empirical relations of Somerville *et al.* (1999). The asperity slip contrast is defined as the ratio between the mean slip on asperity and mean slip on the whole fault. Somerville *et al.* (1999) also suggested one or two asperities covering 1/4 of the whole fault. For simplicity, we consider just one asperity. According to Plicka and Zahradnik (2002) we assume that the nucleation point (corresponding to the hypocenter) is located in the bottom-left corner of the asperity. The rupture is assumed to propagate radially at a constant rupture velocity $v_r = 2.8$ km/s.

The remaining free parameters (c for FSSD and L_0 for the *k*-squared models) are difficult to determine from empirical relations. We thus set them by trial-and-error ($c = 0.9$, $L_0 = 2.4$ km) to obtain the highest synthetic PGAs just below the mean $+ 2\sigma$ bound of empirical PGA attenua-

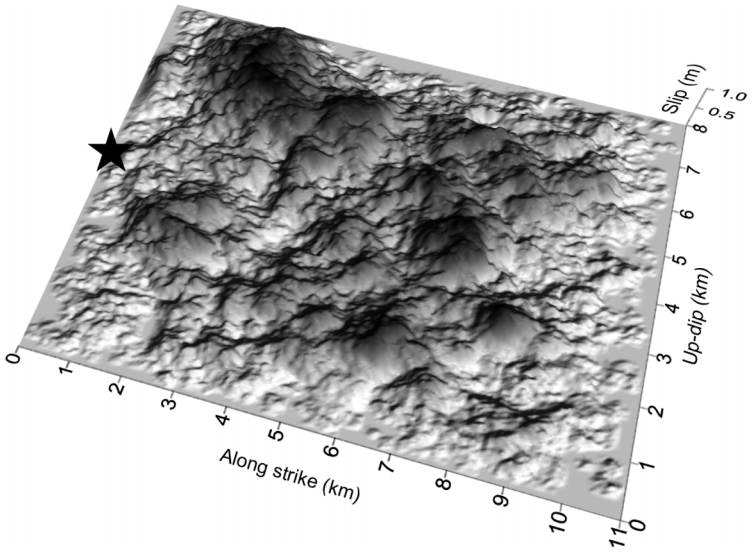

Fig. 1. An example of one random realization of the slip distribution employed in the *k*-squared method. The star denotes the nucleation point.

tion. We have found that parameter c in the FSSD model affects only the absolute level of the PGA values, not their scatter. Concerning the k-squared model, Brune's pulse is used as the slip velocity function. Parameter L_0 affects only the PGAs at the receivers in the direction of rupture propagation, leading to slight changes (up to 10%) in the PGA scatter. The k-squared model with the same parameters has also been tested by Gallovic and Brokesova (2004b) against macroseismic data. Figure 1 shows an example of the slip distribution used in the k-squared method.

Green's Functions (GF) are computed for a 1D isotropic crustal model with homogeneous layers (Tselentis and Zahradnik, 2000). In case of the FSSD model, we apply the discrete wave number method (Bouchon, 1981) to get full wave field GFs for all subevent station pairs. However, in the k-squared model, dense discretization of the fault is required, so that a large number of GFs is needed. Since we are interested in PGAs at relatively short epicentral distances, we use the ray theory and consider the direct S-wave only. Figure 2 shows a comparison of the full wavefield and direct S-wave accelerograms (using the k-squared model) for one selected station marked in fig. 3a. The station was chosen because of its position with respect to the fault where we expect the largest difference. It lies in the backward directivity zone, in the direction of the S-wave minimum and at the largest considered epicentral distance, where interference and/or reflected/refracted waves could be significant. Although the peaks do not coincide, the PGA values are in good agreement. An even better agreement was obtained for a few other neighboring stations of the same epicentral distance (not presented here), so that we believe that such an approximation of GF is acceptable for the given crustal model.

3.2. *Results*

We have computed the acceleration time histories at the 112 receivers using both methods. The computation is repeated for 10 realizations of the source random component (spatial distribution of subevents in the FSSD and slip phase in k-squared).

Mean PGA maps are shown in fig. 3a. Both maps exhibit strong azimuthal variations. The maxima are located at about the same positions

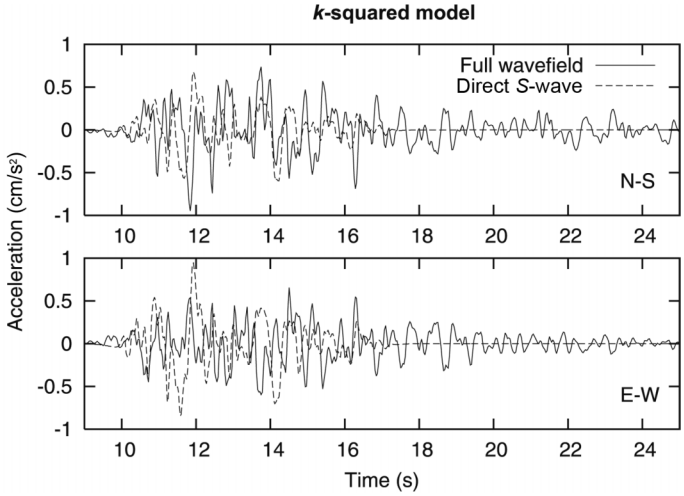

Fig. 2. A comparison of full wave field and direct S-wave accelerograms (k-squared model) for one selected station marked in fig. 3b.

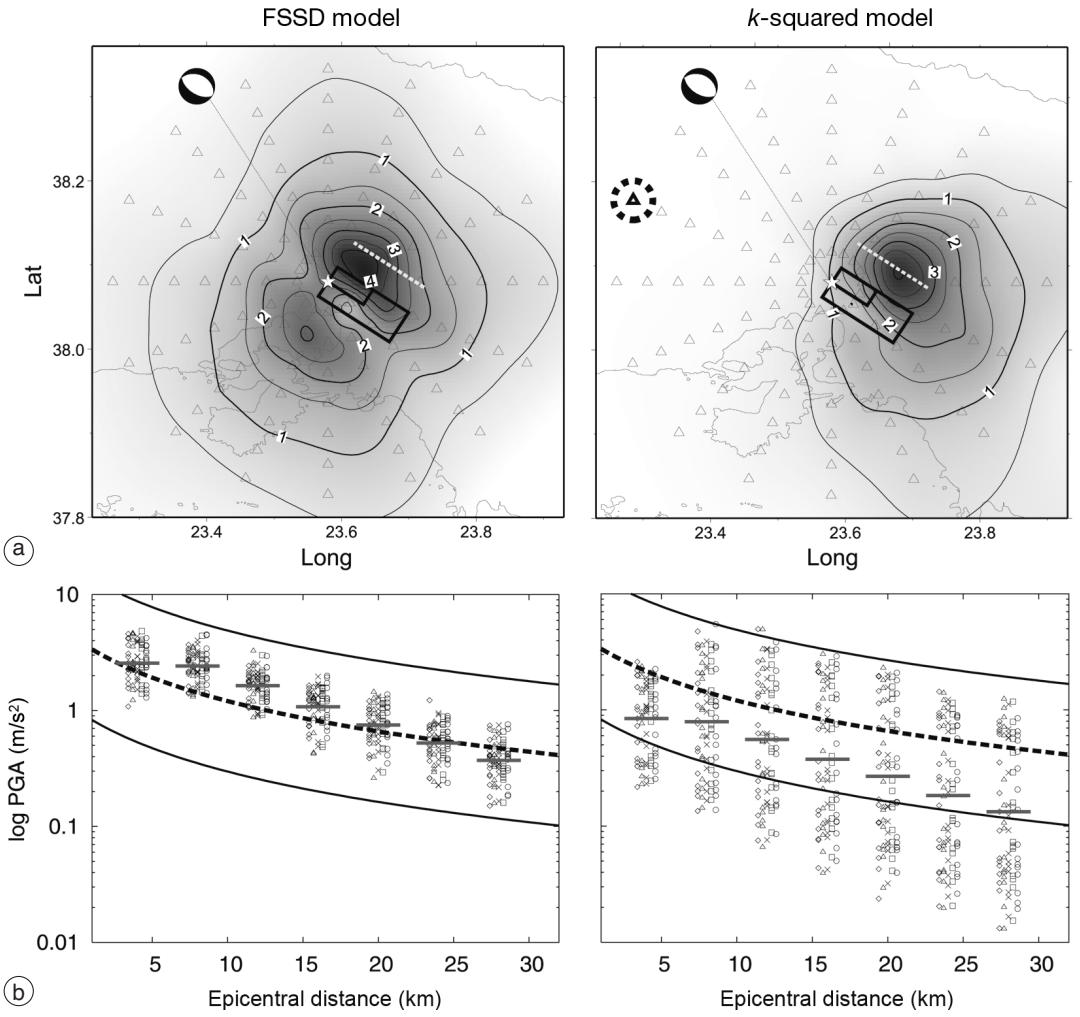

Fig. 3a,b. a) Maps of PGA (in m/s^2) averaged over 10 realizations of stochastic source models. Receivers are shown as triangles. The rectangles represent the fault and asperity surface projections. The stars in the middle of the maps correspond to the epicenter. The gray dashed lines represent fault traces on the surface. The highlighted receiver in the right panel relates to fig. 2. b) All simulated PGAs (symbols) plotted *versus* epicentral distance obtained for the first 5 realizations. The PGAs corresponding to different realizations are plotted with different symbols and are slightly shifted in the *x*-direction for better viewing in order to highlight the scatter of each realization. The strips of symbols appear due to the circular layout of the stations. The gray strokes denote PGA means at given epicentral distances of all 10 realizations. The mean empirical PGA attenuation curve and corresponding $\pm 2\sigma$ (Skarlatoudis *et al.*, 2003) are depicted by dashed and solid lines, respectively.

and reach similar values of about 4 m/s^2. The FSSD model provides two lobes of high PGAs next to the epicenter, in which one recognizes the combined effect of the directivity and *S*-wave radiation pattern. At larger epicentral distances, the PGA decays more or less regularly in all directions. On the contrary, the map provided by the *k*-squared model is dominated by a

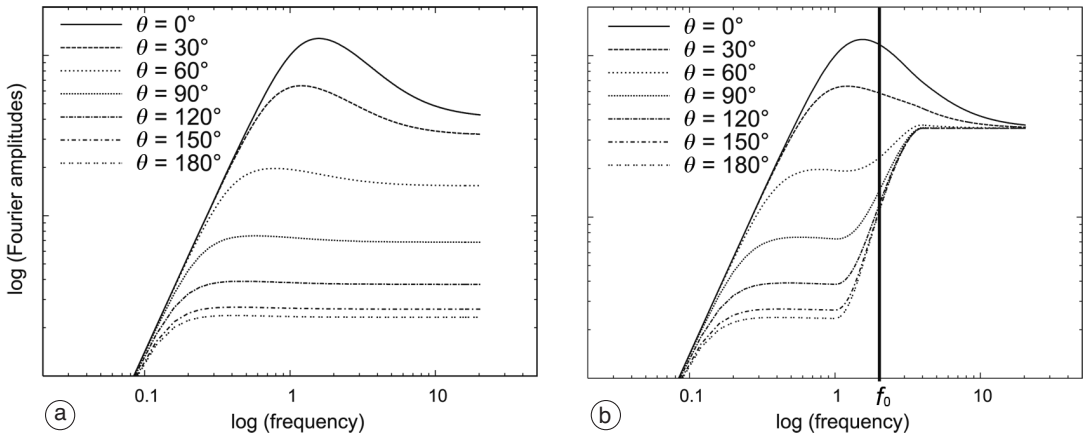

Fig. 4a,b. a) Theoretical acceleration source spectra of the *k*-squared model with *k*-dependent rise time for a line fault in the Fraunhofer approximation for various angles θ from the direction of rupture propagation (after Gallovic and Brokesova, 2004a). b) Same as a), but with formal spectral modification applied in this paper. Note that this figure is only schematic and we do not expect such sharp changes in the observed spectra. The transition could be smoother and/or would be masked by the oscillatory character of the Fourier spectra.

single high-PGA spot. From this spot, the PGA values decay much more steeply to the west than to the south-east (*i.e.* the direction of rupture propagation). This particular shape is caused mostly by the directivity effect.

Figure 3b shows all the simulated PGAs plotted with respect to the epicentral distance. The mean PGAs for given epicentral bins (gray strokes) roughly follow the overall decreasing trend of the mean attenuation curve. The mean PGAs at 4 and 8 km deviate from the trend. We ascribe this to the problem of epicentral distance adopted in the empirical attenuation relations. It is well known that this problem can be solved by different parametrization of the distance (distance from the fault, its surface projection, etc.). The trend of the mean PGAs also slightly differs from the empirical mean curve. This can be explained by the fact that depth and focal mechanism dependencies were not considered in the attenuation relations. Another problem could be an inappropriate crustal model adopted in the present study. The improvement of the fit with the empirical mean curve is beyond the scope of our paper.

We can see that in the FSSD method all the synthetic PGAs fall within the $\pm 2\sigma$ bounds around the empirical mean. The *k*-squared method yields a larger PGA scatter: all the PGAs fall under the $+2\sigma$ bound, however the lower bound -2σ is exceeded. We find that these low values come from stations located backwards to the direction of rupture propagation and are observed for each of all the stochastic realizations. Thus, the large scatter is caused by strong directivity in the *k*-squared method.

We explain the different PGA scatters of the two techniques by the different methodology used in high-frequency wave field modeling. In the FSSD model, the superposition of the subevents' time histories becomes incoherent for frequencies higher than the corner frequency of the smallest subevent. Thereby, constructive interference disappears and the resulting amplitude spectrum (plateau) is the RMS of the point-source subevent spectral plateaus (*e.g.*, Frankel, 1991), independently of the direction of rupture propagation. On the contrary, in the *k*-squared method, the resulting high-frequency plateau comes from coherent summation, *i.e.* constructive interference. The height of the plateau depends on the direction of the rupture propagation at all frequencies (see fig. 4a), which clearly explains the strong directivity of the *k*-squared model.

3.3. *Modification of the* k*-squared method*

Following Bernard and Herrero (1994), we can reduce the strong directivity by introducing a formal spectral modification. Its aim is to mimic the independence of the spectral plateau on the direction of rupture propagation as in the composite methods.

Gallovic and Brokesova (2004a) have shown, for line fault and Fraunhofer approximations, that the height of the high-frequency spectral plateau for the *k*-squared model is

$$A(\theta) \propto C_d(\theta)^2 X(aC_d(\theta)) \qquad (3.1)$$

where C_d is the coefficient of directivity (Joyner, 1991) depending on the angle θ between the station and the direction of rupture propagation, X corresponds to the Fourier spectrum of the slip velocity function, and a is a parameter affecting the wave-number dependence of the rise time (introduced by Bernard *et al.*, 1996).

Bernard and Herrero (1994) proposed an even more heterogeneous rupture process at small scales, particularly at scales smaller than the slip pulse width. This leads to more complicated slip velocity functions, stochastic at high frequencies. Those authors presume that the constructive interference disappears for frequencies higher than about $f_0 = v_r / L_0$ and the resulting height of amplitude spectral plateau becomes the same for all directions,

$$A_0 \propto RMS(A(\theta)) \,. \qquad (3.2)$$

Inserting (3.1) into (3.2) we obtain A_0 for the *k*-squared model with *k*-dependent rise time.

The spectral modification is illustrated in fig. 4b. At frequencies higher than $2f_0$, the spectral amplitude is multiplied by $A_0/A(\theta)$. At transition frequencies between $1/2\,f_0$ and $2f_0$, the spectrum is modified by a cosine function to avoid a sharp step in the spectrum.

We apply this simple modification to the synthetics. The resulting PGAs and mean PGA map are shown in fig. 5. As one can see, the PGA decay does not exhibit such strong azimuthal dependence as in the case of the *k*-squared model without correction (see fig. 3a,b). Moreover, all the PGAs now fall within the $\pm 2\sigma$ bounds around the empirical mean attenuation curve.

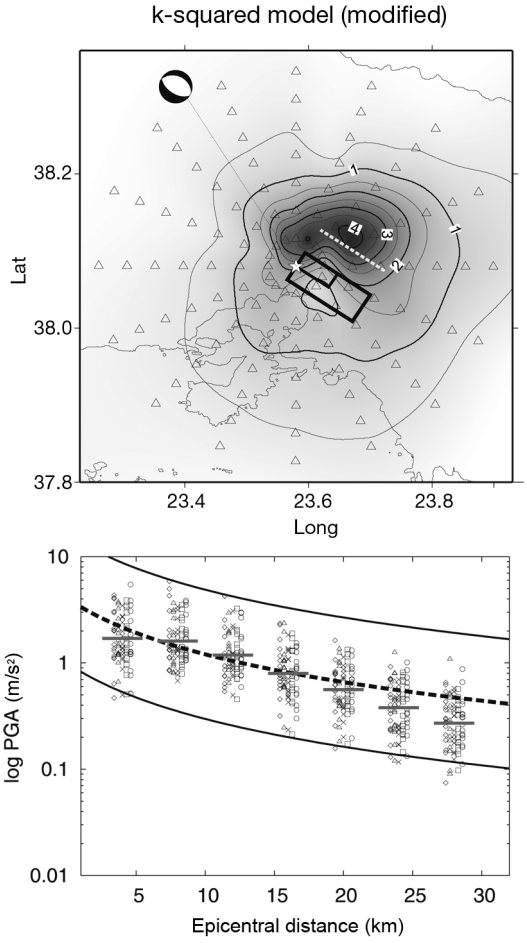

Fig. 5. Same as the right-hand plots in fig. 3a,b (*k*-squared model) after incorporating the formal spectral modification illustrated in fig. 4a,b.

4. Discussion and conclusions

In this paper we have compared two strong-motion modeling techniques with the empirical PGA attenuation relation, especially with the observed scatter. While the FSSD model provides a variation in PGA by a factor of less than

10, the *k*-squared model provides a factor of about 100.

We attribute the large scatter in the *k*-squared model to the strong high-frequency directivity effect, not present in the FSSD model. We performed a number of tests with the *k*-squared model, varying input source parameters (*e.g.*, v_r, L_0, shape of the slip velocity function) but we did not find that any of them reduced the scatter substantially. Note that the frequency-independent radiation pattern assumed in the *k*-squared model is not responsible for the very low PGA values in some directions (close to *S*-wave minima) because the same radiation pattern is present in the composite method as well. Moreover, we have tried to perform the computations with the *k*-squared model considering isotropic *S*-wave radiation with no significant change in the PGA scatter.

Many PGA attenuation relations provide an uncertainty by a factor of about 2 (Si and Midorikawa, 1999; Ambraseys *et al.*, 2005, etc.). Thus, assuming $\pm 2\sigma$ criteria, the maximum total variation corresponds to a factor of about 16. Hence, the large scatter provided by the *k*-squared model in a simple 1D layered medium seems to overestimate the observed scatter.

One can understand the uncertainty in attenuation relations as an indirect empirical constraint on the physical parameters of the source model. However, we have found no parameter of the *k*-squared model which could significantly decrease the large synthetic scatter (except for putting the nucleation point position close to the center of the fault). Therefore, we apply a formal high-frequency spectral modification (suggested by Bernard and Herrero, 1994) to the *k*-squared method that eliminates the directivity due to rupture propagation. The modification is formal and the physical reasons for small high-frequency directivity are unclear. A possible explanation is the incoherency at the source, as discussed above. However, the incoherency can also be caused by wave propagation in a 3D complex medium involving small-scale heterogeneities (*e.g.*, O'Connell, 1999). The details of these phenomena are beyond the scope of this paper.

The 2004 Parkfield earthquake represents a unique opportunity to compare the very well recorded data of a predominantly unilateral earthquake with recent attenuation relations as it has provided an unprecedentedly detailed view of the PGA distribution at close fault distances. The majority of the PGA data fits between the $\pm 2\sigma$ bounds of the recent attenuation curve (Bakun *et al.*, 2005) although the stations have not been classified according to their site conditions. Moreover, Shakal *et al.* (2006) report that there is no directivity dependence in the observed peak acceleration, which supports our results.

We believe that the standard deviation of the empirical attenuation relations represents robust information for calibration and possible rejection of strong-motion prediction methods. However, the data set has to be sufficiently large, including careful site classification and a large number of observations close (< 30 km) to the faults. The deployment of dense accelerometric networks in the last decade (in, *e.g.*, Japan, U.S.A., Taiwan) is very promising from this point of view. In this respect, our conclusion on the high-frequency directivity can be revised after more constrained (especially at fault distances smaller than 15 km) attenuation relations are available. Note that the comparison between the synthetic and observed scatter cannot be used for technique validations until one takes into account all possible phenomena that boost the scatter (*e.g.*, 3D structural effects, site effects, etc.).

Acknowledgements

The authors thank to Jiri Zahradnik, Johana Brokesova, Martin Mai, Antonio Emolo, Massimo Cocco, Giovanna Cultrera and an anonymous reviewer for their comments that helped to improve the manuscript. The work was supported by Marie Curie training network SPICE in the 6th Framework Program of the European Commission (MRTN-CT-2003-504267), Grant Agency of Charles University (279/2006/B-GEO/ MFF) and by Italian National Institute of Geophysics and Volcanology and of the Italian Civil Defence Department.

REFERENCES

AMBRASEYS, N., J. DOUGLAS, S. SARMA and P. SMIT (2005): Equations for the estimation of strong ground motions

from shallow crustal earthquakes using data from europe and the middle east: horizontal peak ground acceleration and spectral acceleration, *Bull. Earthquake Eng.*, **3**, 1-53.

BAKUN, W.H., B. AAGARD, B. DOST, W. ELLSWORTH, J. HARDEBECK, R. HARRIS, C. JI, M. JOHNSTON, J. LANGBEIN, J. LIENKAEMPER, A. MICHAEL, J. MURRAY, R. NADEAU, P. REASENBERG, M. REICHLE, E. ROELOFFS, A. SHAKAL, R. SIMPSON and F. WALDAUSER (2005): Implications for prediction and hazard assessment from the 2004 Parkfield earthquake, *Nature*, **437**, 969-974.

BERNARD, P. and A. HERRERO (1994): Slip heterogeneity, body-wave spectra, and directivity of earthquake ruptures, *Ann. Geofis.*, **XXXVII** (6), 1679-1690.

BERNARD, P., A. HERRERO and C. BERGE (1996): Modeling directivityof heterogeneous earthquake ruptures, *Bull. Seismol. Soc. Am.*, **86**, 1149-1160.

BOATWRIGHT, J. and D.M. BOORE (1982): Analysis of the ground accelerations radiated by the 1980 Livermore Valley earthquakes for directivity and dynamic source characteristics. *Bull. Seismol. Soc. Am.*, **72**, 1843-1865.

BOUCHON, M. (1981): A simple method to calculate Green's functions for elastic layered media, *Bull. Seismol. Soc. Am.*, **71**, 959-971.

BRUNE, J. (1970): Tectonic stress and the spectra of seismic shear waves from earthquakes, *J. Geophys. Res.*, **75**, 4997-5009 (correction, *J. Geophys. Res.*, **76**, 5002, 1971).

BURJANEK, J. (2002): A composite source model with fractal subevent size distribution, *Master Th.*, Charles University, Prague (available on line at http://geo.mff.cuni.cz/~burjanek/dipl.pdf).

FRANKEL, A. (1991): High-frequency spectral fall-off of earthquakes, fractal dimension ofcomplex rupture, *b*-value, and the scaling strength on faults, *J. Geophys. Res.*, **96**, 6291-6302.

GALLOVIC, F. and J. BROKESOVA (2004a): On strong ground motion synthesis with k^{-2} slip distributions, *J. Seismol.*, **8**, 211-224.

GALLOVIC, F. and J. BROKESOVA (2004b): The k^{-2} rupture model parametric study: example of the 1999 Athens earthquake, *Studia Geophys. Geod.*, **48**, 589-613.

HARTZELL, S., S. HARMSEN, A. FRANKEL and S. LARSEN (1999): Calculation of broadband time histories of ground motion: comparison of methods and validation using strong-ground motion from the 1994 Northridge earthquake, *Bull. Seismol. Soc. Am.*, **89**, 1484-1504.

HASKELL, N.A. (1964): Total energy and energy spectra density of elastic waves from propagating faults, *Bull. Seismol. Soc. Am.*, **54**, 1811-1841.

JOYNER, W. (1991): Directivity for non-uniform ruptures, *Bull. Seismol. Soc. Am.*, **81**, 1391-1395.

MARGARIS, B.N. and D.M. BOORE (1998): Determination of $\Delta\sigma$ and κ_0 from response spectra of large earthquakes in Greece, *Bull. Seismol. Soc. Am.*, **88**, 170-182.

MCGUIRE, J.J., L. ZHAO and T.H. JORDAN (2002): Predominance of unilateral rupture for a global catalog of large earthquakes, *Bull. Seismol. Soc. Am.*, **92**, 3309-3317.

NEHRP (1994): Recommended provisions for seismic regulations for new buildings and other structures, Part 1. Provisions, *FEMA 222A* (Building Seismic Safety-Council, Washington D.C.), pp. 290.

O'CONNELL, D.R.H. (1999): Replication of apparent nonlinear seismic response with linear wave propagation models, *Science*, **283**, 2045-2050.

PLICKA, V. and J. ZAHRADNIK (2002): Inversion of rupture nucleation from regional records by EGF method for unequal focal mechanisms of the mainshock and aftershock: the Athens 1999 earthquake, *Tectonophysics*, **359**, 81-95.

SHAKAL, A., H. HADDADI, V. GRAIZER, K. LIN and M. HUANG (2006): Some key features of the strong-motion data from the *M* 6.0 Parkfield, California, earthquake of 28 September 2004, *Bull. Seismol. Soc. Am.*, **96,** S90-S118.

SI, H. and S. MIDORIKAWA (1999): New attenuation relationships for peak ground acceleration and velocity considering effects of fault type and site condition, *J. Struct. Constr. Eng.*, **AIJ** (523), 63-70.

SKARLATOUDIS, A.A., C.B. PAPAZACHOS, B.N. MARGARIS, N. THEODULIDIS, CH. PAPAIOANNOU, I. KALOGERAS, E.M. SCORDILIS and V. KARAKOSTAS (2003): Empirical peak ground-motion predictive relations for shallow earthquakes in Greece, *Bull. Seismol. Soc. Am.*, **93**, 2591-2603.

SOMERVILLE, P.G., N.F. SMITH, R.W. GRAVES and N.A. ABRAHAMSON (1997): Modification of empirical strong ground-motion attenuation relations to include the amplitude and duration effects of rupture directivity, *Seismol. Res. Lett.*, **68**, 199-222.

SOMERVILLE, P., K. IRIKURA, R. GRAVES, S. SAWADA, D. WALD, N. ABRAHAMSON, Y. IWASAKI, T. KAGAWA, N. SMITH and A. KOWADA (1999): Characterizing crustal earthquake slip models for the prediction of strong ground motion, *Seismol. Res. Lett.*, **70**, 59-80.

TSELENTIS, G.A. and J. ZAHRADNIK (2000): The Athens earthquake of 7 September 1999, *Bull. Seismol. Soc. Am.*, **90**, 1143-1160.

ZAHRADNIK, J. (2002): Focal mechanism of the Athens 1999 earthquake by ASPO method, *Res. Rep.*, Department of Geophysics, Faculty of Mathematics and Physics, Charles University, Prague (available on line at http://seis30.karlov.mff.cuni.cz/papers/aspo/aspo.html).

(received June 5, 2006;
accepted December 6, 2006)

[P2]

Geophys. J. Int. (2008) **172,** 276–292 doi: 10.1111/j.1365-246X.2007.03627.x

Effects of complicated 3-D rupture geometries on earthquake ground motion and their implications: a numerical study

Martin Käser[1] and František Gallovič[2]

[1]*Department of Earth and Environmental Sciences, Geophysics Section, Ludwig-Maximilians-Universität, München, Germany. E-mail: martin.kaeser@geophysik.uni-muenchen.de*

[2]*Charles University, Faculty of Mathematics and Physics, Department of Geophysics, Prague, Czech Republic*

Accepted 2007 September 17. Received 2007 September 12; in original form 2007 April 26

SUMMARY

We present a numerical study of the effects of geometrically complicated 3-D ruptures on near-source ground motions. In most of the kinematic and dynamic rupture modelling studies or seismic moment tensor and slip inversions the strong assumption of a perfectly planar fault is made. However, it is known from geological field studies that real fault traces are not planar but characterized by relatively strong deflections, bends and other irregularities. In this paper we, investigate the effects of such non-planar earthquake ruptures on ground motion modelling in comparison to their equivalent planar ones. For this purpose we apply the highly accurate Discontinuous Galerkin method that is capable of incorporating the geometry of complicated non-planar rupture surfaces by a set of double couple point sources that do not have to coincide with the mesh vertices. We generate a set of kinematic rupture models characterized by random spatial deflections with various correlation lengths and root mean square values. These deflections then determine the associated spatial strike and dip variations. We find that the deflected rupture models have the same seismic moment tensor as the perfectly planar one, however, with a reduced scalar moment, which we correct for. After a sound validation of our modelling approach, we present the effects of the deflections on synthetic velocity seismograms computed in the vicinity of the rupture. We observe that these geometrical irregularities do not just lead to high frequency effects but can strongly affect the synthetics in the whole frequency band. Finally, we discuss our observations in detail and conclude that the correct incorporation of the geometrical properties such as local strike and dip variations of the rupture surface is an important issue. We also discuss possible implications for some seismological fields, such as strong-motion simulations or seismic moment tensor and slip inversions, where these results might have significant consequences.

Key words: Numerical solutions; Earthquake ground motions; Computational seismology; Wave propagation; Fractures and faults.

1 INTRODUCTION

In the dynamic and kinematic modelling of ground motions close to an earthquake rupture the source is often considered to be *perfectly planar* and characterized by constant strike and dip angles. However, field observations at the Earth's surface commonly show that geological faults are much more complicated at all scales (Bonilla 1979, http://earthquake.usgs.gov/regional/qfaults/). Studies of the deeper Earth's crust using techniques such as fault-zone guided waves (Li *et al.* 1994) and aftershock mechanism variations (Hardebeck 2000) suggest that the faults' geometrical complexities extend even to seismogenic depths. Just recently, researchers have started using geological information and advanced numerical methods to model rupture propagation on geometrically more complicated faults.

Dynamic rupture propagation is classically simulated on a planar fault. However, also in this field the attention was recently shifted to non-planar ruptures (Cruz-Atienza & Virieux 2004). Since the dynamic problem is difficult itself, the actual complicated fault geometry is usually approximated by a few planar segments, for example (Harris & Day 1999; Aochi & Madariaga 2003). These studies emphasize that geometrical discontinuities have an important effect on rupture propagation in terms of decreasing rupture speed, rupture arrest and generation of strong seismic wave radiation. Other studies, yet rather theoretical, concern dynamic rupture propagation on a piecewise planar rupture containing one or more kinks, that is, sharp changes of the rupture fault direction, (Bouchon & Streiff 1997; Aochi *et al.* 2000; Adda-Bedia & Madariaga 2006). In particular, Adda-Bedia & Madariaga (2006) found that the dynamic rupture propagation across the kink generates a special type

of circular *SH*-wave which is centred at the kink and related to the starting and stopping phases at this kink. However, such waves are induced by the very sudden change of the rupture geometry, which may not be realistic itself.

Although slip inversions of seismic ground motions has made considerable progress in recent years, still most of these inversions use planar source models. This is on one hand due to the lack of geometrical details of the faults, and on the other hand to simplify numerical computations. In the case of very large earthquakes again the rupture surface is approximated by a few planar segments of different orientations (Wald & Heaton 1994; Delouis *et al.* 2002; Zeng & Chen 2002) but with piecewise constant strike and dip angles on each segment. In some studies the rake (slip) angle is allowed to vary along the rupture plane during the inversion, showing significant rotations of the slip vector in the rupture plane (Delouis *et al.* 2002; Zeng & Chen 2002). Nevertheless, these studies do not try to retrieve the possible strike and dip variations related to the rupture's non-planar geometry.

Furthermore, in the forward modelling of strong ground motions mainly planar ruptures or at most a few planar segments (Pulido *et al.* 2004) are usually considered even though such an approximation may have significant consequences on the synthetic seismograms. For example, some authors report problems related to large amplitude differences at horizontal components in their synthetics, which are not observed in real data. To solve this problem Zeng *et al.* (1995) suggest to include rake variations in the synthetic ground motion calculation. They illustrated the effect on ground motions only for one station for the Uttarkashi thrust fault earthquake of 1991 October 19, showing that the synthetics then have comparable amplitudes at the horizontal components. Others, for example, Pitarka *et al.* (2000) or Satoh (2002), suggest to use a radiation pattern that vanishes with increasing frequency to get a better fit of synthetic and observed data. We hypothesize that such a need may be induced by neglecting geometrical complexities in terms of strike and dip variations of the rupture.

In summary, although it is well understood that the geometrical complexities of a rupture are able to significantly influence both the rupture dynamics and the generated ground motions, they are commonly neglected or, as in the case of geometrically very complicated ruptures, the planar fault approximation is extended by using a few planar rupture segments to capture the overall geometrical structure. Such studies however do not take into account the rupture topology that may be very complicated at all scales as it is observed in the field and, therefore, may bias important conclusions. To our knowledge, a thorough quantitative study of the implications of complicated 3-D ruptures is still missing. It is also not clear if strike and dip variations projected on a perfectly planar fault may serve as a satisfying representation of a truly 3-D non-planar rupture surface in terms of the radiated wavefield.

Therefore, we present in this paper a systematic analysis of the effects of different kinematic models of finite-extent rupture sources with complicated rupture geometries on synthetic velocity seismograms and the corresponding amplitude spectra. The rupture topology is assumed to be a continuous surface with random deflections without any sharp kinks, that is, with varying but continuous strike and dip angles. Since we are interested in the effects of the non-planarity itself, we define a set of kinematic earthquake models characterized by the same seismic moment and duration but with various correlation lengths and amplitudes of the deflections. This way, the models are similar regarding their kinematic properties, while we remark that their underlying dynamic models may be substantially different. On this set of earthquake rupture models, we apply the highly accurate Discontinuous Galerkin method (Dumbser & Käser 2006) to numerically simulate ground motions on a number of receivers surrounding the rupture. After validating our numerical approach, we show the influence of the ruptures' non-planarities on the resulting ground motions with respect to the radiation from the perfectly planar rupture. Finally, we discuss possible implications of the observed effects for some seismological applications, namely strong ground motion simulations or seismic moment tensor and slip inversions.

2 MODELLING SETUP

2.1 Source–receiver geometry and the crustal model

The setup of our model is similar to the well-defined 3-D test problem Layer Over Half-space (LOH.2) proposed in the final report of the *LIFELINES PROGRAM TASK 1A01* (Day 2001) of the Pacific Earthquake Engineering Research Center. This test case was part of a multi-institutional code validation project with reference and quasi-analytical solutions. Our computational domain has a lateral extent of 60 × 60 km and reaches 30 km depth as sketched in Fig. 1(a). Note, that for clarity we only show one quarter of the computational domain. The material parameters of the top 1 km (Medium 1) and the half-space beneath (Medium 2) are also given in Fig. 1(a).

The seismic wavefield is recorded up to a simulation time of 15s at 59 receivers on the free surface as indicated in Fig. 1(c). We remark, that the first 10 receiver locations are identical to the original setup of the LOH.2 test case (Day 2001), that is, $(x_i, y_i, z_i) = (i \cdot 600, i \cdot 800, 0)$ m, for $i = 1, \ldots, 10$. Receivers 11–20 are positioned equidistantly along the x-axis from $x = -1$ to -10 km, receivers 21–30 have the mirrored positions of the first 10 receivers with respect to the x-axis and receivers 31–59 are located equidistantly along the y-axis from $y = -10$ to 18 km, extending 10 km to the left-hand side and to the right-hand side of the rupture plane. This way, we sample different directions with respect to the rupture orientation and also cover various distances in the fault-normal and fault-parallel directions.

2.2 The ADER-DG method

The computational domain described in Section 2 is discretized by an unstructured, tetrahedral mesh of 336 049 elements. The discretization on the free surface is shown in Fig. 1(b). Furthermore, the mesh is generated in a problem-adapted manner, so that in the zone of interest, where the source and receivers are located, the seismic waves travel through a very fine tetrahedral mesh with an average edge length of 350 m. Towards the model boundaries the mesh is rapidly coarsened up to edge lengths of 3500 m to reduce the number of total elements and, therefore, computational cost. Even though absorbing boundaries are applied, waves grazing almost parallel along numerical model boundaries still can produce numerical artefacts that could pollute the seismograms. Such effects are avoided by the enlarged computational domain and the mesh coarsening towards the boundaries as weak artificial reflections disappear due to numerical diffusion (Käser *et al.* 2007). The refined zone reaches a depth of 7 km to include the entire rupture surface.

The numerical simulations are carried out by the highly accurate ADER-Discontinuous Galerkin scheme (ADER-DG) using Arbitrary high order DERivatives. The ADER-DG method has been recently introduced to the field of numerical seismology (Dumbser & Käser 2006; Käser & Dumbser 2006). It solves the heterogeneous elastic wave equations formulated as a linear hyperbolic system (velocity–stress formulation) with arbitrary high order of

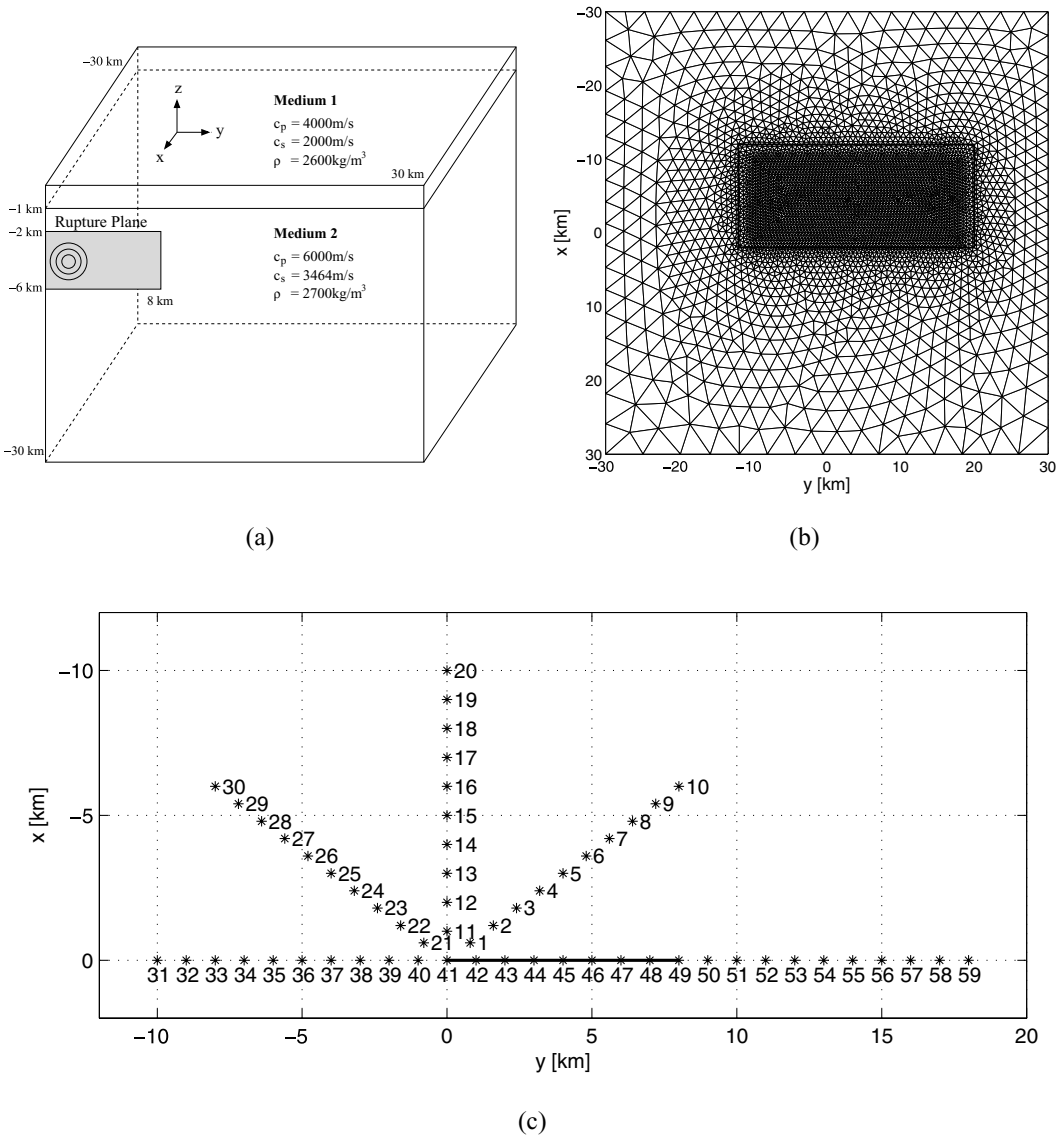

Figure 1. (a) Sketch of the model setup of the modified LOH.2 test case, corresponding to one quarter of the actual computational domain. (b) View of the gradually refined tetrahedral discretization of the computational domain from the top. We also indicate the zoomed section (thick rectangle) displayed in (c), where we show the map of the 59 receiver locations (stars) and the projection of the planar rupture on the surface (thick line).

accuracy in space and time on 3-D unstructured tetrahedral meshes. To this end, the numerical scheme combines the Discontinuous Galerkin Finite Element method with the ADER approach (Titarev & Toro 2002) using high order approximation polynomials and their derivatives for accurate time integration. In the DG framework the variables, that is, the velocities and stresses, are approximated by piecewise polynomials which allow for the introduction of discontinuities at element interfaces. Therefore, the well-established theory of numerical fluxes across element interfaces obtained by the solution of Riemann problems can be applied as in the finite volume framework (Toro 1999).

The main idea of the ADER approach is then a Taylor expansion in time in which all time derivatives are replaced by space derivatives using the so-called Cauchy–Kovalewski procedure which makes recursive use of the governing partial differential equation (Titarev & Toro 2002). The basis functions of the approximation polynomials are orthogonal in the tetrahedral reference element and, therefore, lead to diagonal mass matrices. Furthermore, increasing the polynomial approximation order exhibits spectral convergence on tetrahedral meshes (Dumbser & Käser 2006). The application of the ADER-DG method to a number of test cases (de la Puente *et al.* 2006; Dumbser & Käser 2006) and various comparisons to analytical and reference solutions obtained by other well-established methods confirm the performance of the ADER-DG method.

In particular, source terms and their heterogeneous properties in space and time as given by a kinematic rupture model of finite extent can be accurately included into the tetrahedral mesh due to the high resolution of the polynomial approximation inside each element. Hereby, the rupture surface is represented very generally by a set of point sources distributed arbitrarily in the computational domain and the space–time integration of the source contribution is accurately computed at each time step (Käser *et al.* 2007).

Let us emphasize that for the application of the ADER-DG method neither the source location nor the receiver locations have to

coincide with nodes of the tetrahedral mesh. This greatly simplifies the process of mesh generation when considering the non-planar rupture models as the mesh does not have to be aligned with the rupture surface. In fact, we are using the same tetrahedral mesh for all our non-planar rupture models.

2.3 Kinematic parameters of the finite source models

As stated above, for the ADER-DG method any kinematic rupture model is approximated by a grid of double couple (DC) point sources. Such an approximation for *perfectly planar* ruptures is a well-known problem in elastodynamics. It can be understood as approximative numerical solution of the representation theorem (Aki & Richards 2002). The theorem states that the ith component of displacement $\mathtt{u}$ measured at receiver location $\mathtt{r}$ can be obtained by an integral over the rupture surface S as

$$u_i(\mathtt{r}, t) = \int_S G_{ip,q}(\mathtt{r}, \mathtt{x}, t) * m_{pq}(\mathtt{x}, t)\, \mathrm{d}S, \quad \text{with } i, p, q \in [1, 2, 3] \tag{1}$$

where $m_{pq}(\mathtt{x}, t)$ is the moment tensor density depending on time t and position $\mathtt{x}$ on the rupture surface and $G_{ip}(\mathtt{r}, \mathtt{x}, t)$ represents the elastodynamic Green's tensor. The last subscript after the comma denotes the spatial derivative with respect to x_q (i.e. $G_{ip,q} = \partial G_{ip}/\partial x_q$). Note that classical tensor notation is used, which implies the summation over each index that appears twice. The symbol '$*$' means the time convolution. For simplicity, we will restrict ourselves to DC sources, so that we can consider the quantity $m_{pq}\,\mathrm{d}S$ in eq. (1) as an infinitesimally small DC source.

The integral over the whole rupture area S in eq. (1) can be divided into a sum over N usually equally sized rupture elements S_n, such that

$$u_i(\mathtt{r}, t) = \sum_{n=1}^{N} \int_{S_n} G_{ip,q}(\mathtt{r}, \mathtt{x}, t) * m_{pq}(\mathtt{x}, t)\, \mathrm{d}S. \tag{2}$$

Assuming that the rupture element is small enough that the Green's tensor spatial derivatives do not change much with respect to $\mathtt{x}$ within each rupture element S_n, $G_{ip,q}$ can be taken out of the integral in eq. (2), leading to

$$\begin{aligned} u_i(\mathtt{r}, t) &\approx \sum_{n=1}^{N} G_{ip,q}(\mathtt{r}, \mathtt{x}_n', t) * \int_{S_n} m_{pq}(\mathtt{x}, t)\, \mathrm{d}S \\ &= \sum_{n=1}^{N} G_{ip,q}(\mathtt{r}, \mathtt{x}_n', t) * M_{pq}^n(t), \end{aligned} \tag{3}$$

where $\mathtt{x}_n'$ denotes a particular location in the nth rupture element, usually its centre. When a planar fault is considered, the integral over the rupture element S_n in eq. (3) can simply be substituted by an equivalent DC moment tensor $M_{pq}^n(t)$ characterized by the corresponding total seismic moment, duration, etc. This way, the representation integral in eq. (1) over infinitesimally small DC sources is substituted by a sum over a finite number of elementary DC sources of finite size.

Let us explain the source geometry models adopted in our study. As stated in Section 1, we are dealing not with independent segments or sharp kinks, but with smooth, continuous rupture surfaces. We start with a *perfectly planar* vertical fault at $x = 0$ extending from $y = 0$ to 8 km and $z = -2$ to -6 km with the hypocentre located at $(x_h, y_h, z_h) = (0, 1, -4)$ km as shown in Figs 1(a) and (c). We discretize the rupture plane by a regular grid of 128×64 rupture elements in y- and z-direction, respectively, each consisting of a DC point source of size 62.5×62.5 m as discussed also in Section 2.4.2

Note that this spatial discretization is independent of the tetrahedral discretization of the computational domain. The rupture represents a right-lateral strike-slip earthquake with strike $\phi = 90^\circ$ and seismic moment $M_0 = 1.04 \times 10^{18}$ Nm. We associate the rupture (onset) time τ of each of the rupture elements proportional to the distance from the hypocentre assuming a constant rupture propagation speed of $v_r = 3\,\mathrm{km\,s^{-1}}$, that is,

$$\tau = v_r^{-1}\left[(y - y_h)^2 + (z - z_h)^2\right]^{1/2}. \tag{4}$$

Each rupture element has the same seismic moment $m_0 = M_0/(128 \times 64) = 1.27 \times 10^{14}$ Nm and the slip-rate function

$$s(t) = \frac{t - \tau}{T^2} \exp\left(-\frac{t - \tau}{T}\right) H(t - \tau), \tag{5}$$

where H is the Heaviside step function and $T = 0.1$ s is a parameter controlling the rise time.

Regarding the non-planar rupture models we use the same discretization as in the planar case. However, each of the rupture elements is now characterized by its local fault parameters and a so-called deflection, that is, the distance of the element's centre from the perfectly planar surface at $x = 0$ as shown in Fig. 2. These deflections are created using a random field generator following a similar approach as previously applied for heterogeneous slip distributions (Gallovič & Brokešová 2004). First, random numbers are prescribed to each of the rupture elements. Then this white noise is transformed to the spatial Fourier domain. Here the amplitude spectrum is modified by a k^{-3} function

$$P(k_y, k_z) = \left[1 + \sqrt{\left(\frac{k_y L}{K}\right)^2 + \left(\frac{k_z W}{K}\right)^2}\right]^{-3}, \tag{6}$$

where k_y and k_z are wavenumbers in the strike and dip directions, respectively. Parameter K controls the ratio between the correlation length of the random field and the rupture length $L = 8$ km and width $W = 4$ km. The modified spectrum is then high-cut filtered just below the Nyquist wavenumber and Fourier transformed back to the spatial domain. Finally, the random field root mean square (rms) responsible for the strength of the deflection in x-direction is adjusted afterwards according to the desired value. As we are considering approximations of a smooth rupture, the spatial variations of strike and dip due to the source geometry are computed for each rupture element by the spatial derivative of the deflection field in the strike and dip directions, respectively. As there are no discontinuities in the rupture geometry, the strike and dip variations are also continuous, characterized by k^{-2} decay in the strike and dip direction, respectively.

Concerning the remaining kinematic properties of the rupture elements of all non-planar rupture models (i.e. rupture time, seismic moments, slip velocity function), we keep them as in the case of the perfectly planar rupture. Let us remark that depending on the non-planarity of the rupture surface, the rupture propagation speed, in fact, varies slightly between different elements. This way, however, all source models have clearly the same total duration.

Let us discuss the final scalar seismic moment of the non-planar rupture models. We find that they are not the same as for the perfectly planar rupture. To analyse this, we sum up all the seismic moment tensors $M_{pq}^n(t = 0)$, see eq. (3). In all cases the final moment tensor corresponds again to a pure right-lateral vertical strike-slip earthquake as for the planar rupture model, however with lower scalar seismic moment. Therefore, we define a so-called *moment correction factor* as the moment ratio between the given planar model and each non-planar one. Then, in order to analyse ground motions

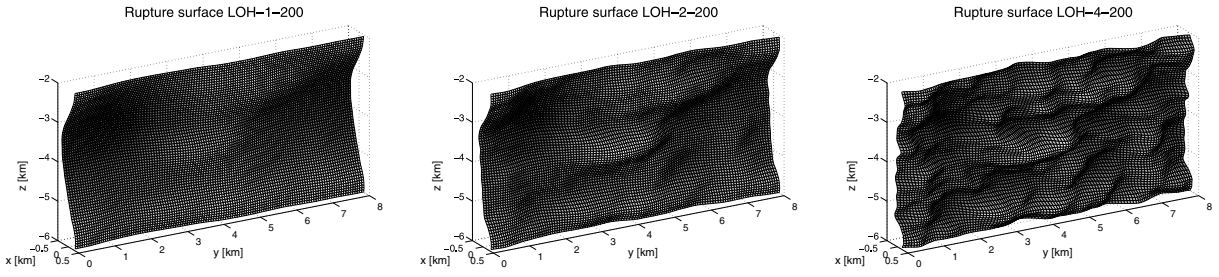

Figure 2. Rupture surfaces with different correlation lengths. Note that the rms value and the Fourier phase spectrum are the same for all three cases (a), (b) and (c). The top end of the rupture surface could be considered as a fault trace that would be visible on the surface if the rupture reached it.

Table 1. Spatial variations of the rupture model parameters with respect to the perfectly planar model adopted in this study.

		Deflections (m)		Strike (°)		Dip (°)		Rake (°)		Moment correction
Name	K	rms	Max	rms	Max	rms	Max	rms	Max	factor
LOH-0-000	0	0	0	0.0	0.0	0.0	0.0	0.0	0.0	1.00
LOH-1-200	1	200	513	7.4	20.5	17.0	37.4	0.0	0.0	1.09
LOH-2-200	2	200	640	12.9	38.4	23.9	56.0	0.0	0.0	1.20
LOH-4-050	4	50	164	6.6	23.5	11.8	35.8	0.0	0.0	1.05
LOH-4-100	4	100	327	12.8	41.0	21.6	55.3	0.0	0.0	1.19
LOH-4-200	4	200	654	23.3	60.1	35.3	70.9	0.0	0.0	1.72
LOH-4-200P	4	0	0	23.3	60.1	35.3	70.9	0.0	0.0	1.72
LOH-4-015R	4	0	0	0.0	0.0	0.0	0.0	15.0	46.0	1.03

caused by earthquake models characterized by the same seismic moment, we correct the seismograms by multiplying them by the corresponding moment correction factor.

Note that preserving the same rupture times, corrected seismic moments and slip functions for the rupture elements of the different rupture models ensures the representation of *equivalent* earthquake sources in terms of the total seismic moment and duration. Therefore, we can separately study the effects of different rupture geometries themselves.

In Table 1 we show the variations of the parameters of the different rupture models adopted in this study. The models differ in their correlation lengths given by parameter K of eq. (6) and rms of the deflections. The models are denoted as LOH-K–XXX, where XXX denotes the rms value in metres. The model LOH-0-000 represents the original perfectly planar rupture of the LOH.2 test case. Table 1 also gives the corresponding Moment correction factors discussed above. To have a consistent set of source models, we use the same initial random number distribution (see the random field generation above) for all the models. To illustrate the effect of the parameter K, Fig. 2 displays three different rupture surfaces characterized by the same rms value and various values of K. The reader can easily imagine how the rms value alters the deflections as it acts simply as a multiplicative factor on the deflections in x-direction.

Additionally, our study employs two other models given in Table 1. The model LOH-4-200P corresponds to the model LOH-4-200, where the local strike and dip variations are projected onto the perfectly planar rupture model, that is, the deflections are set to zero. The model LOH-4-015R is similar to the perfectly planar model LOH-0-000, however, instead of generating various deflections the random field is used to generate rake variations with $K = 4$ and an rms value of 15°.

2.4 Validation

2.4.1 ADER-DG versus discrete wavenumber

To confirm our statements about the accurate treatment of the geometrically complicated rupture models, we first validate the ADER-DG approach for the intended study as shown in the following section.

The ADER-DG method for tetrahedral meshes has been validated thoroughly by a number of model problems, for example, the original LOH test cases (Day 2001), in previous papers (de la Puente *et al.* 2006; Dumbser & Käser 2006; Käser *et al.* 2007). Nevertheless, to underline the accuracy and performance of the scheme, we also validate the method for this special case of kinematic non-planar rupture models presented here. Therefore, we compare the velocity seismograms obtained by the ADER-DG $\mathcal{O}4$ scheme, that is, fourth order of accuracy in space and time, for the LOH-4-200 model with the roughest rupture geometry with reference solutions computed by the Discrete Wavenumber (DWN) method (Bouchon 1981). We remark that the seismograms of both methods are filtered by the same low pass filter at 5 Hz. As an error norm we define the relative seismogram misfit energy

$$E = \sum_{j=1}^{n_t} \left(s_j^{\mathrm{ADER-DG}} - s_j^{\mathrm{DWN}}\right)^2 \Big/ \sum_{j=1}^{n_t} \left(s_j^{\mathrm{DWN}}\right)^2, \tag{7}$$

where $n_t = 1501$ is number of time samples in the seismograms, $s_j^{\mathrm{ADER-DG}}$ is the jth value of numerical ADER-DG $\mathcal{O}4$ seismogram and s_j^{DWN} is the corresponding reference value of the Discrete Wavenumber seismogram.

In Fig. 3, we show the results of E for the three velocity components obtained at all 59 receivers as indicated in Fig. 1(c). We

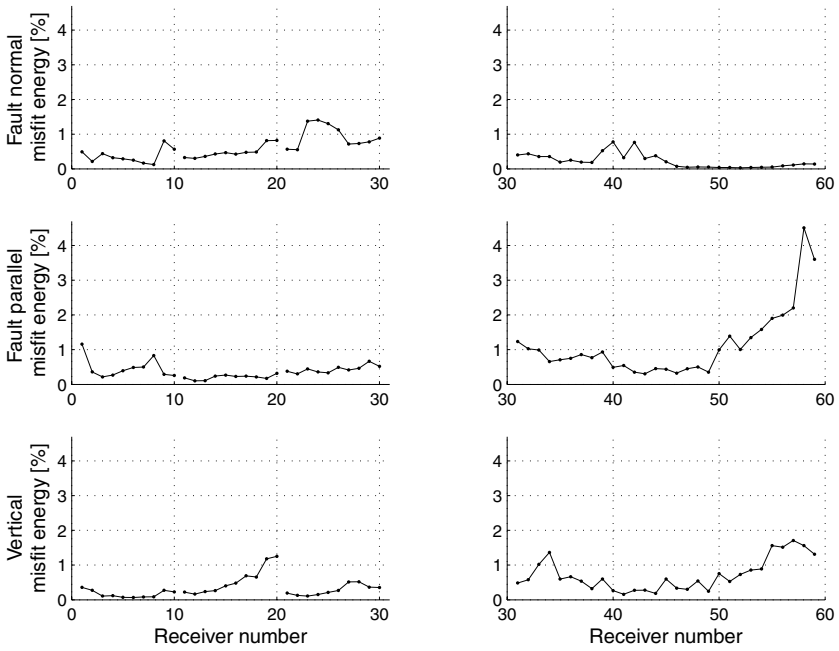

Figure 3. Seismogram misfit energy E between the Discrete Wavenumber method and the ADER-DG $\mathcal{O}4$ method for the rupture model LOH-4-200.

observe that E typically has values around 1 per cent, however, an increase of errors away from the rupture is visible especially from receiver 50 to 60. Based on these observations, we choose four receivers, namely no. 1, 20, 34 and 58, where relatively large misfits E appear and which cover different directions and distances with respect to the rupture position. For these receivers, Fig. 4 shows the comparison of the ADER-DG $\mathcal{O}4$ and the DWN seismograms indicated by the model notation LOH-4-200. As one can see, the fit is almost perfect, which is in agreement with the low values of E. To further support our statement that the ADER-DG $\mathcal{O}4$ method correctly takes into account the non-planar rupture, we compare these seismograms also with those obtained for the model LOH-4-200P where the strike and dip variations are the same, but the locations of the rupture elements are projected onto the perfectly planar surface (see Table 1). As shown in Fig. 4 the ADER-DG $\mathcal{O}4$ method correctly resolves the differences between the truly deflected LOH-4-200 model and the projected one LOH-4-200P although these differences are relatively small. We remark, that these differences will be further discussed later in the text.

We summarize that the above comparisons confirm that even in the discussed cases of relatively large misfits the ADER-DG $\mathcal{O}4$ results are very satisfying and, therefore, our results will reliable at least up to a frequency of 5 Hz. The validation demonstrates that the highly accurate ADER-DG $\mathcal{O}4$ method is well suited for this study as it correctly resolves important details in the synthetic seismograms.

2.4.2 Rupture geometry approximation

As stated above, we approximate the non-planar rupture geometry by a grid of elementary DC point sources. However, it is not straightforward how dense this grid spacing should be chosen to correctly account for the deflections effects on the recorded ground motion signals. In other words, we have to be sure that our approximation of the continuous, deflected rupture surface corresponds to the model we claim to study in terms of the radiated wavefield.

Concerning the error related to the approximation in eq. (3), Spudich & Archuleta (1987) have shown that the error is given mainly by neglecting the time variations of $G_{ip,q}$ within each rupture element. The associated error then depends, among others, on the temporal resolution (frequency) and the receiver location (source directivity). Given a maximum considered frequency, Spudich & Archuleta (1987) have shown that the fault has to be sufficiently sampled by the elementary DC sources at the shortest wavelength considered in the model, which is given by the the maximum frequency and the lowest velocity in the source area, that is, usually the rupture velocity. Additionally, they have shown that although the discretization error also depends on other factors such as the receiver position, the error generally decreases with decreasing frequency.

In our case of the *non-planar* rupture, the situation is even more complicated due to the fact that the elementary DC sources with an associated moment tensor $M^n_{pq}(t)$ should approximate non-planar elements of a deflected rupture surface as defined by eq. (3). As such, the non-planar elements do not radiate as single DC sources but in fact represent a superposition of infinitesimally small DC sources of slightly varying orientation, that is, of varying moment tensors. Therefore, their radiated wavefield corresponds rather to a point source characterized by a tensorial sum of the infinitesimal DC moment tensors. Therefore, the approximation using DC point sources could bias the resulting wavefield in the whole frequency band in addition to the frequency dependent error discussed above. On the other hand, since the representation theorem in eq. (1) is a linear function of $m_{pq}(\mathrm{x}, t)$, the approximate solution in eq. (3) will still converge with increasing refinement of the rupture discretization, that is, with increasing N.

Being aware of this issue, we validate the chosen approximation of the rupture geometry (128×64 rupture elements) by comparing the synthetic seismograms with those obtained for a refined discretization of the rupture model. Therefore, we refine the model with the roughest rupture geometry LOH-4-200 by Fourier interpolation on a 4×4 denser grid. Fig. 5 shows the seismogram misfit energy E between the resulting seismograms in a similar way as for

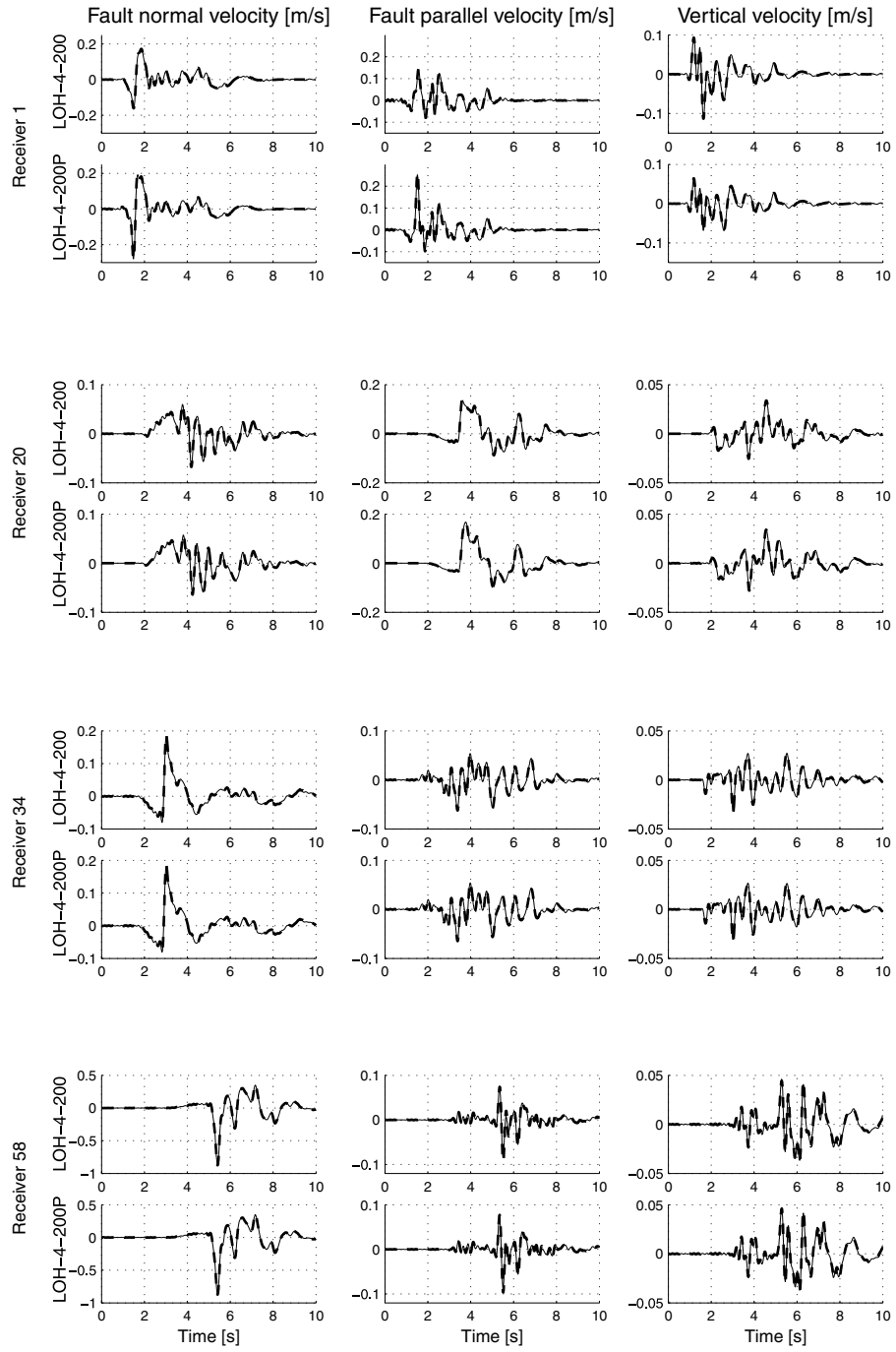

Figure 4. Validation of the numerical computations by comparing the ADER-DG $\mathcal{O}4$ (solid) and the Discrete Wavenumber (dashed) results for receivers 1, 20, 34 and 58 for the rupture surface models LOH-4-200 (non-planar) and LOH-4-200P (projected).

the case of ADER validation in Fig. 3. The plot exhibits a relatively strong dependence of E on the receiver position, which however does not follow a clear systematic trend. The maximum E reaches about 7 per cent with a typical value around 1–2 per cent, which is relatively small and comparable to the misfits between the ADER-DG $\mathcal{O}4$ and DWN method presented in Section 2.4.1

As an example, we present in Fig. 6 the comparison of velocity waveforms and their Fourier spectra for receiver 1, which is characterized by a large misfit value E at the fault parallel component as observed in Fig. 5. As one can see, the fit between the seismograms for our actual discretization of 128 $\times$ 64 rupture elements and the refined one is almost perfect at the fault normal and vertical component, while the first significant fault parallel velocity amplitude deviates clearly. This can be also seen in the corresponding Fourier spectra comparison shown in Fig. 6 bottom. The overall fit is, as in the time domain, almost perfect. However, let us emphasize the spectral difference for the fault parallel and especially for the vertical component in the low-frequency range. As discussed above, we attribute these effects to the error caused by the approximation of the non-planar rupture elements by pure DC sources. This effect

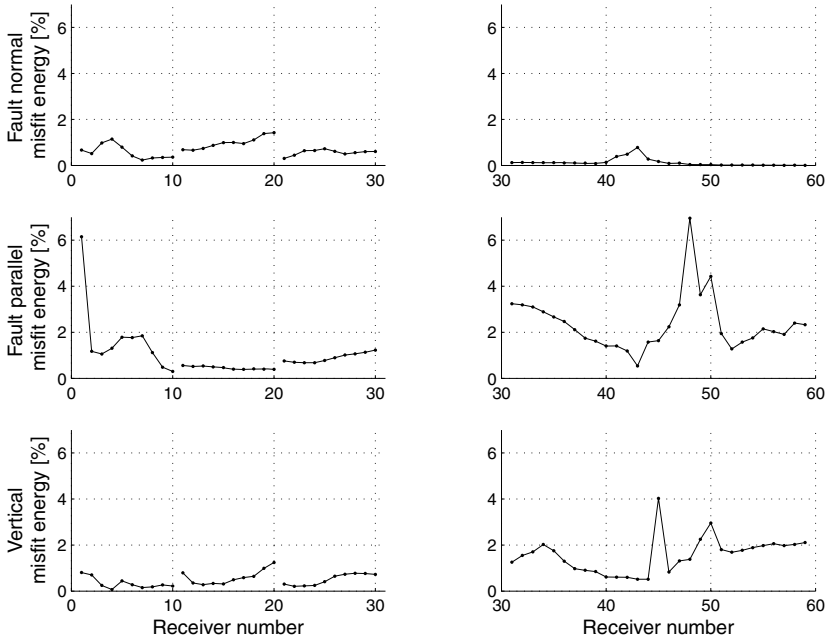

Figure 5. Seismogram misfit energy E between the used discretization of the rupture surface LOH-4-200 and it's 4×4 finer discretization.

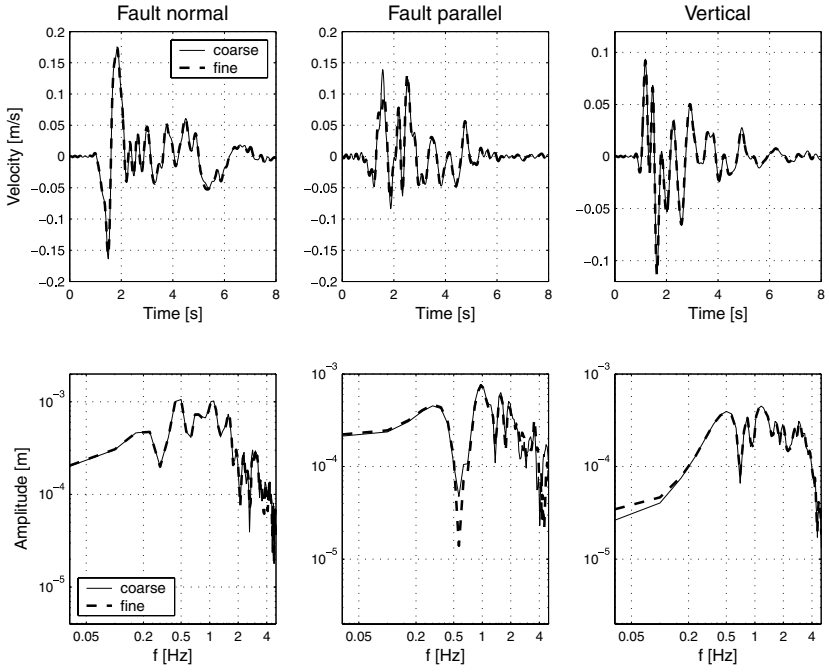

Figure 6. Comparison of seismograms (top) and spectra (bottom) of the used approximation for model LOH-4-200 and the 4×4 refined discretization of the rupture surface for receiver 1.

is also related to the sensitivity of the low-frequency motion to the rupture deflections and is discussed in more detail in the following section.

Despite the observed but small differences between the seismograms obtained with our actual discretization of the rupture model and the refined one, we consider the coarser discretization very satisfactory. Therefore, we will use the discretization into 128×64 rupture elements in all of the following simulations.

3 EFFECTS OF RUPTURE GEOMETRY VARIATION

After validating our numerical approach in the previous section, we present in the following our main results obtained by the ground motion simulations considering the different rupture models discussed above and summarized in Table 1. We choose the velocity seismograms and the corresponding amplitude spectra for receivers 1, 20,

36 and 54 to cover various distances and directions with respect to the rupture and to highlight the differences between off-fault and on-fault receivers. Note that the word on-fault is to be understood in a more general sense since by on-fault receivers we mean those located along strike direction as shown in Fig. 1(c). For convenience, in the following we will refer to the fault normal, fault parallel and vertical velocity components as FN, FP, and V components, respectively.

3.1 Effect of rms on the seismograms

In our first investigation, we keep the correlation length fixed at $K = 4$ and analyse the influence of the rms value of the deflections. The different components of the velocity seismograms presented in Fig. 7(a) show the changes in the waveforms when the rms value is gradually increased, that is, when the amplitude of the rupture model deflections is increased. Furthermore, for comparison we present the seismograms of the equivalent perfectly planar rupture model LOH-0-000 in Fig. 7(a). Note that for the on-fault receivers 36 and 54 the FP and V components for the LOH-0-000 case should theoretically be exactly zero, however, a very small signal can be observed, which is due to the irregularity of the tetrahedral mesh. However, the amplitude of these numerical artefacts is very small and does not affect the following investigations. Furthermore, we remark that all four seismograms inside each of the 12 panels are plotted on the same scale with zero referring to the onset of the LOH-0-000 seismogram. All other seismograms corresponding to increasing rms values are shifted by a constant to facilitate the visual comparison of the waveforms.

As we can see in Fig. 7(a), the introduction of the rupture non-planarity changes the seismograms significantly compared to the planar LOH-0-000 case for most of the receiver components. In particular, we observe that the waveforms of the FN and V components of the off-fault receivers 1 and 20 change gradually with increasing rms and show richer structure for enhanced geometrical complexity. An interesting observation in the FP and V components of receiver 1 is that the energy is released in a longer time window for the geometrically more complicated models. For the perfectly planar model LOH-0-000 we see a more pulse-like energy release on these components. As regards the on-fault receivers 36 and 54, the introduction of deflections, compared to the planar LOH-0-000 case, results in the generation of signals on their FP and V components. Their amplitudes increase with increasing rms values. On the other hand, at the same receivers the amplitudes and waveforms on the FN components remain almost unchanged.

3.2 Effect of correlation length on the seismograms

In Fig. 7(b) we show the results when keeping the rms values constant at 200 m and increasing the correlation length by decreasing K, that is, reducing the spatial wavelength of the geometrical variations as displayed in Fig. 2. In addition, we show again the synthetics obtained for the planar LOH-0-000 model. For better comparison the individual plots for a given receiver and component in Fig. 7(b) are scaled in the same way as in Fig. 7(a). We can see that introducing deflections of any correlation length has a significant effect on most of the seismograms as the waveforms change their characteristics compared to the perfectly planar model LOH-0-000. However, these effects appear to a different degree at different stations and components. A remarkable feature is that the behaviour of the FN components of all the receivers is very similar when changing K or rms values (compare Figs 7a and b). Their waveforms do not change rapidly when the non-planar fault is introduced regardless the actual value of K. The maximum amplitudes of the FN component seem to be only slightly affected by variations in K, but the waveforms show richer structure at the off-fault receivers 1 and 20, similar to Fig. 7(a). On the on-fault receivers 36 and 54 the amplitudes and waveforms of the FN component remain basically unchanged with increasing K. Similarly, the behaviour of the FP and V components of the most distant receiver 20 is almost the same when changing the K value (Fig. 7b) or the rms value (Fig. 7a). This suggests that the discussed components are sensitive to the actual correlation length almost in the same way as to the rms values. As regards the waveforms for other receivers and components, they change rapidly when the non-planar fault is introduced regardless of the actual value of K. For example, note the originally zero amplitudes of the FP and V components at the on-fault receivers show some signal when the non-planar fault is introduced regardless of the particular K value. Concerning the latter, the dependence of the waveforms on the K value is rather modest. Perhaps most interesting is the richer structure of the seismograms on the FP component of station 36 for increased K.

3.3 Effect of rms on the frequency spectra

Here, we are investigating the Fourier spectra of the seismograms discussed above. In Fig. 8(a) we display the amplitude spectra of the velocity seismograms shown in Fig. 7(a). Note, that the blue lines for the LOH-0-000 model at the FP and V components of the on-fault receivers 36 and 54 should theoretically again be zero. However, we leave them in the plots for completeness as they show the small numerical effects due to the irregular tetrahedral mesh. However, they will not be discussed in the following.

As in the previous plots of Fig. 7(a) we first keep the correlation length fixed ($K = 4$) and vary the rms value. The first and most important observation is that introducing deflections of the rupture surface can affect the whole frequency band at some receivers and not only the high-frequency range. In particular, at receiver 1 close to the rupture the amplitudes of the FN and V components in the high-frequency range approximately above 0.5 Hz are increasing with increasing deflections. The FP component shows the opposite trend in this frequency range. On receiver 20, much further away from the rupture, the low-frequency amplitudes of all components are not affected by the geometrical variations via the rms values, whereas the high-frequency amplitudes are systematically increased. For the on-fault receivers 36 and 54 the amplitude spectrum of the FN component remains basically unaffected by deflections. However, the spectra of the FP and V components show a very clear trend as the amplitudes in the whole frequency band strongly increase with higher rms values.

3.4 Effect of correlation length on the frequency spectra

In Fig. 8(b), we display the amplitude spectra of the velocity seismograms shown in Fig. 7(b) where we keep the rms value fixed and vary K. Again, the first and most important observation is that the geometrical complexity can affect the whole frequency band in some cases. In the high-frequency band above 0.5 Hz at the off-fault receivers 1 and 20 we observe increasing amplitudes for increasing K on the FN and V components. This trend is less clear at the FP component. In the low-frequency band especially the V component of receiver 1 is strongly affected where amplitudes decrease

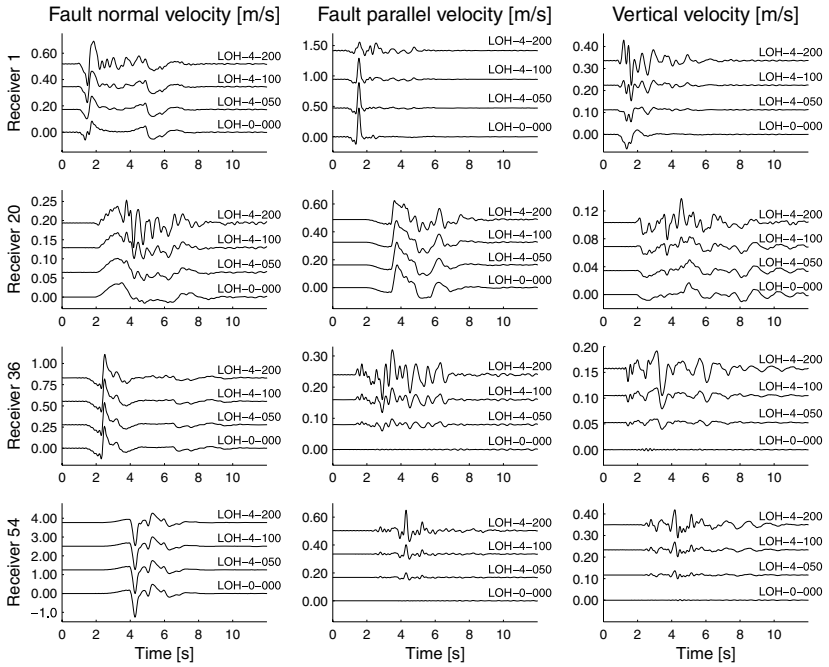

(a)

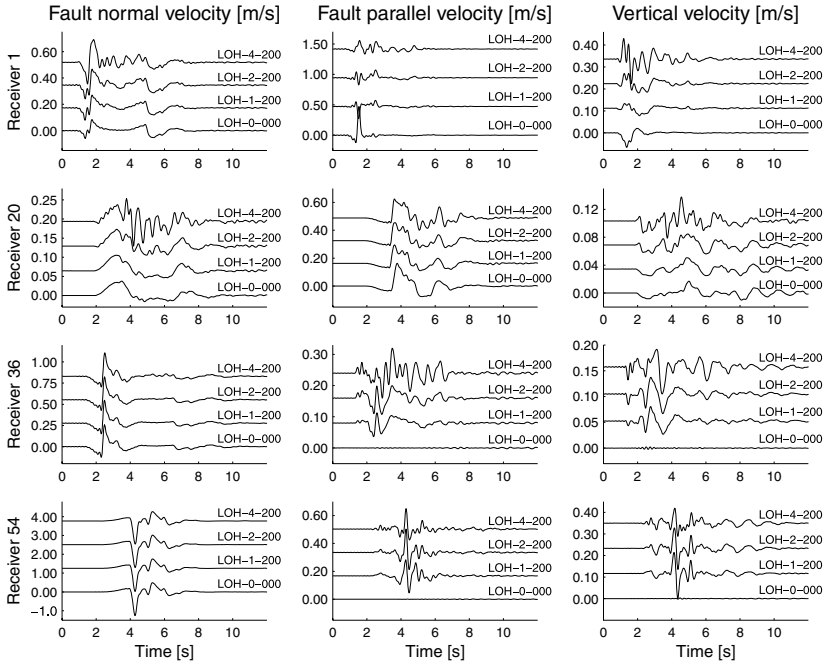

(b)

Figure 7. Synthetic velocity seismograms obtained for rupture surfaces of various geometrical parameters with (a) different rms value of the deflections and (b) different correlation lengths.

systematically with increasing K. However, we mention that this is not the case if different random numbers are used to generate the rupture model. At the distant receivers 20 the low-frequency band is again almost unaffected. The spectra of the FN component at the on-fault receivers 36 and 54 remain basically unchanged with varying K, similar to the rms variations. However, the situation is less clear at their FP and V components at these receivers as the increase of K does not show any clear systematic trend in the spectra in contrast to the previous case of fixed K and varied rms value in Fig. 8(a). Finally, let us emphasize that similar to the seismograms themselves (compare Figs 8a and b) also the spectra of the FN components at all receivers and the spectra of all components at the distant receiver

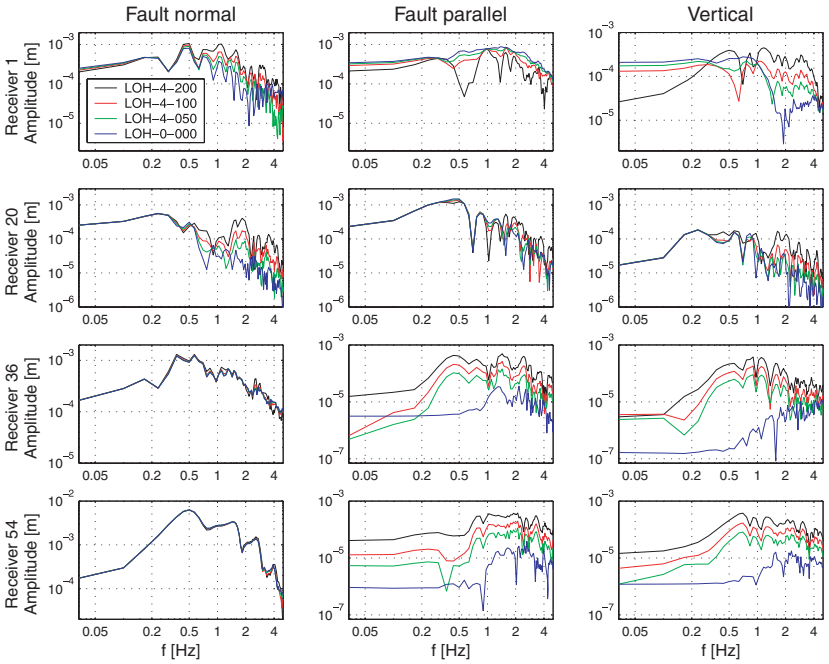

(a)

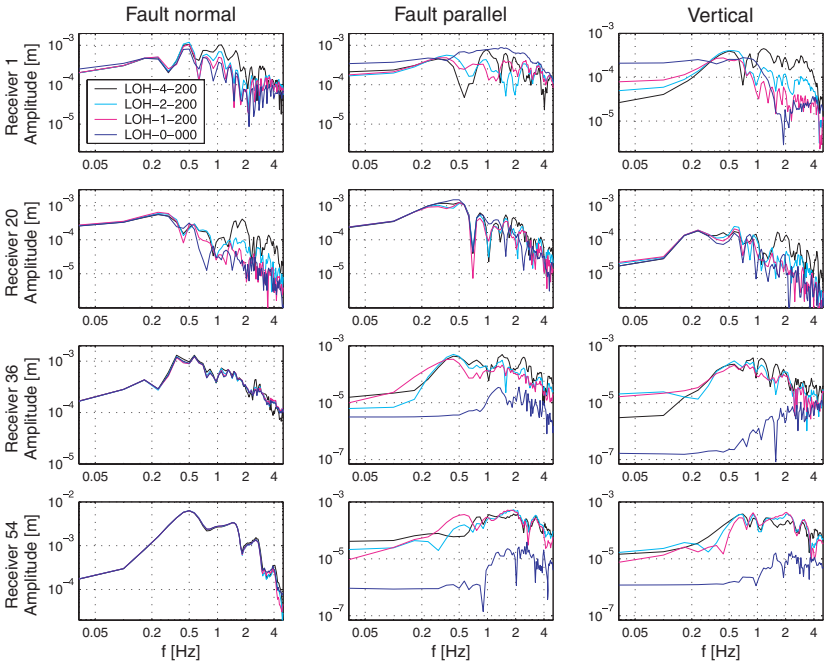

(b)

Figure 8. Comparison of the Fourier amplitude spectra of the synthetic velocity seismograms shown in Fig. 7, obtained for the rupture surfaces with a variation of the geometrical rupture parameters using (a) different rms value of the deflections and (b) different correlation lengths.

20 are remarkably insensitive to whether the rms or K values are changed as both variations seem to have very similar effects.

3.5 Effect of rms on the peak ground velocity

Furthermore, we examine the peak ground velocity (PGV) values of the three velocity components obtained at all 59 receivers. For the case of varying rms values, Fig. 9(a) shows that the PGV values of the 30 off-fault receivers in the left panels predominantly decrease with increasing distance from the hypocentre. Furthermore, increasing the geometrical complexity by means of increasing rms values leads to a better balance of FN and FP components at basically all receivers. In particular, at the off-fault receivers we can observe a gradual reduction of higher PGV values, for example, of

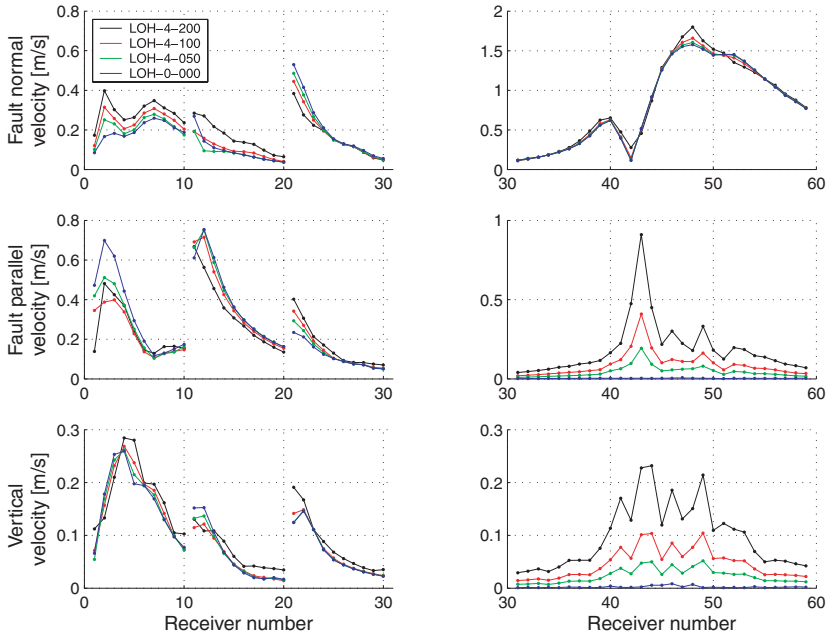

(a)

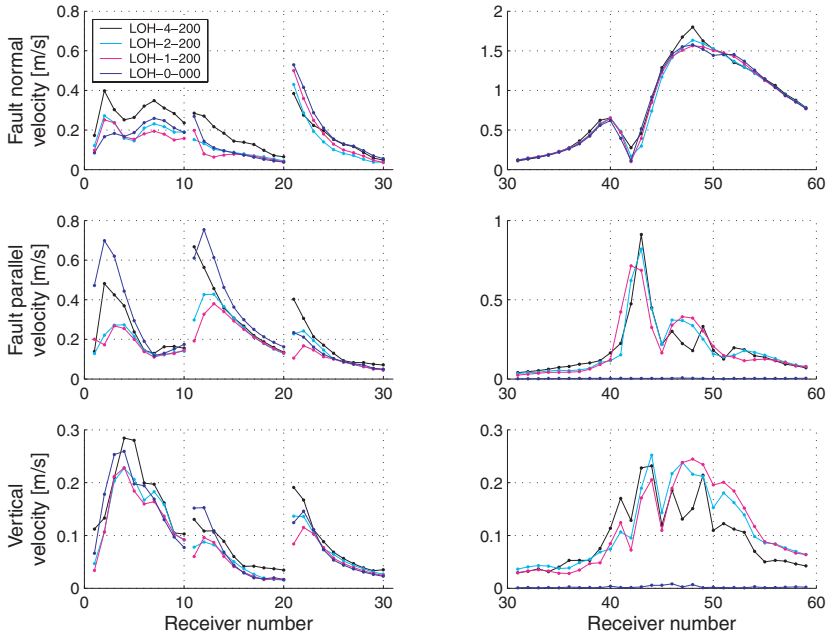

(b)

Figure 9. Comparison of the peak ground velocity of the synthetic seismograms, obtained for the rupture surfaces with a variation of the geometrical rupture parameters using (a) different rms value of the deflections and (b) different correlation lengths.

the FP components at receivers 1–20 and the FN components of receivers 21–30. In contrast, the smaller PGV values, for example, of the FN components at receivers 1–20 and the FP components of receivers 21–30 are gradually increased. However, the V component at off-fault receivers only shows a systematic trend at receivers 1–10. The on-fault receivers 31–59 originally have FP and V components of zero amplitudes for the perfectly planar model LOH-0-000, but adding deflections of increasing rms values increases the amplitudes in a very regular manner. These effects are more pronounced above the rupture from receiver 41 to 49 and rapidly decay with distance along the fault line, see also Fig. 1(c). The FN component, however, is less affected and shows slightly increased PGV values with increasing rms mainly above the right end of the rupture plane, that is, at receivers 47–49. Furthermore, the local minimum of the PGV values at receiver 42 nicely indicates the location of the hypocentre. Generally, Fig. 9(a) confirms our previous statement that the

increasing complexity of the geometrical model tends to balance the PGV differences in the three velocity components of all receivers.

3.6 Effect of correlation length on the peak ground velocity

Considering the results obtained for the rupture models with varying K in Fig. 9(b), the behaviour of the PGV values is less clear compared to the previous case in Fig. 9(a). However, the roughest model LOH-4-200 leads to larger PGV values of the FN component at the off-fault receivers 1–20 and the FP component at receivers 21–30. In contrast, the strongest reduction of PGV values of the FP component at receivers 1–20 and FN component at receivers 21–30 is observed for lower K values. Again no obvious trend can be observed for the V component. In strong contrast to the previous rms variations in Fig. 9(a) the K variations also do not show systematic changes at the on-fault receivers 31–59. Regarding the FN component the behaviour with increasing K is similar to the one of increasing rms values. However, the amplitudes of the FP and V components along the fault seem to jump from exactly zero for the LOH-0-000 case to some larger values when introducing rather smooth rupture complexity with $K = 1$, whereas a further increase of K has no systematic effect on the amplitudes. Finally, in analogy to Figs 7 and 8, the PGV values change less systematically with varying K than with varying rms values.

A quite surprising observation in both Figs 9(a) and (b) is also the behaviour of the PGV amplitudes of the FP components for the planar LOH-0-000 model. Moving just slightly away from the fault line (e.g. from 41 or 42 to receivers 1, 11 or 21), the PGV values basically *jump* from zero values on the fault to values that are even larger than those of the corresponding FN component. However, they quickly decay with increasing distance from the fault. This effect is less pronounced for geometrically more complicated rupture surfaces.

3.7 Real versus projected geometry variations

For completeness, our next test case concerns the question of whether the differences in the seismograms obtained for planar and non-planar ruptures are driven predominantly by the actual rupture geometry or by the strike and dip variations only. In other words, one can ask if a planar model including the actual geometrical complexities of the rupture only in terms of strike and dip variation will give the same results, or, if it is really necessary to correctly take into account the deflections in x-direction. This might be important for many numerical methods that have difficulties in following a deflected rupture surface with their discretization, for example, regular Cartesian Finite Difference grids. Therefore, we simplify our roughest rupture model LOH-4-200 in the way that we project the locations of all the elementary DC sources representing the rupture to a perfectly planar surface at $x = 0$, while keeping the strike and dip variation of the original LOH-4-200 model. This way, all spatial deflections are zero, however, each rupture element still carries the strike and dip variations of the LOH-4-200 model.

The results for the projected model are shown in Fig. 10 and are denoted as LOH-4-200P. We observe, that the differences between the projected LOH-4-200P and the deflected LOH-4-200 model are very small. However, coming back to Fig. 4 of the validation Section 2.4 and having a closer look at some seismograms, we observe some interesting details. The seismograms obtained for the LOH-4-200 and LOH-4-200P models at receivers 1 show quite clear amplitude differences. Furthermore, we observed that at receiver 20 the error is mainly due to small phase shifts of up to 0.05 s in the first half of the seismograms. The fit at receivers 36 and 54, however, is almost perfect.

To further investigate the errors associated with the projection approximation, we plot the relative seismogram misfit energy E of eq. (7) for all 59 receivers in Fig. 11 in a similar manner as for the validation in Section 2.4. We observe that the largest misfit is obtained for the off-fault stations 1–30. Looking closer on the

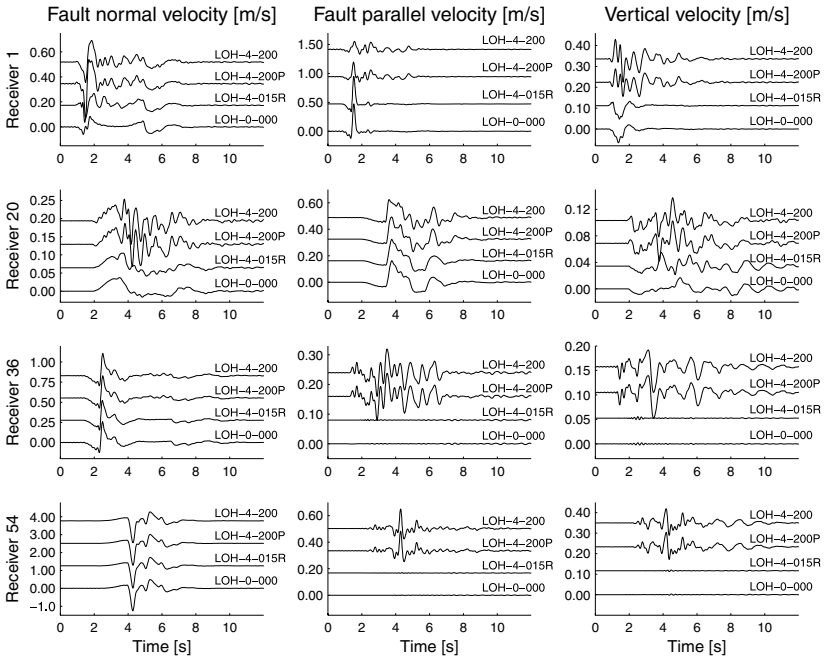

Figure 10. Comparison of the effect of rake variations and the projection of the strike and dip parameters to a planar rupture surface. Note that the seismograms for models LOH-4-200 and LOH-4-200P at receivers 1 and 20 are the same as in Fig. 4.

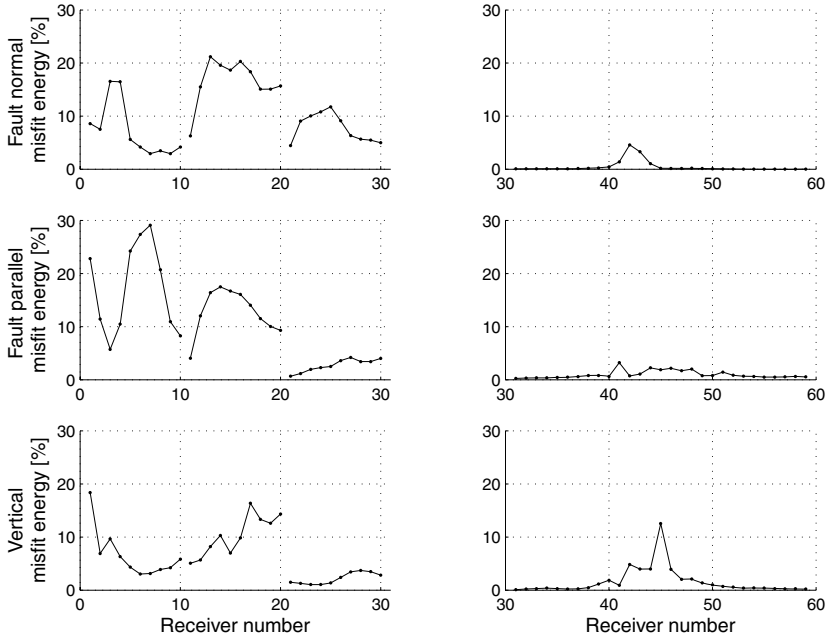

Figure 11. Seismogram misfit energy between the truly deflected rupture surface LOH-4-200 and the projected one LOH-4-200P.

differences of the corresponding waveforms, we observe that with increasing perpendicular distance from the rupture the misfit at some components is more and more dominated by small phase shifts of up to 0.05 s, for example, at receivers 7, 13 and 20 in approximately the first half of the seismogram. Contrary to that, the misfit E for the on-fault receivers is remarkably smaller. The seismograms at the on-fault receivers obviously show larger difference between the truly deflected LOH-4-200 and the projected, perfectly planar LOH-4-200P models only above the rupture location between receivers 41 and 49. We consider this as surprising since it means that the waveforms are less sensitive to the actual rupture geometry, in terms of the misfit energy E, right above the fault, while they become more sensitive with larger perpendicular fault distance. We have checked this result by the DWN method coming to the same conclusion. Nevertheless, despite the fact that we cannot easily explain this behaviour, we claim that the major properties of a geometrically complicated deflected rupture surface can be taken into account even with a simpler projected model. However, care has to be taken if very high accuracy is required or amplitudes and waveforms want to be analysed or interpreted in detail.

3.8 Effect of rake variations

For our final test case, we have computed a set of synthetic seismograms for the perfectly planar rupture, that is, no deflections in x-direction and constant strike and dip, where we apply the random field to generate rake variations with $K = 4$ and rms value of 15°. This model is indicated by LOH-4-015R as discussed in Section 2.3. The results are shown in Fig. 10 together with the seismograms obtained for the planar LOH-0-000 model for comparison. Note, that the scaling of the amplitude axes is identical to Fig. 7. In particular, only the FN component at receiver 1 and the FN and V components at receiver 20 show slightly richer structure, whereas the other components and receivers basically remain unchanged. Especially, the on-fault receivers do not show any signal on the FP and V components as the rupture is still perfectly planar like for the LOH-0-000 case. Therefore, it seems that pure rake variations do not affect the seismograms to the same extent as the introduction of deflections leading to non-planar rupture surfaces.

In summary, we have systematically examined a set of geometrically different rupture models (Table 1) by observing their effects on all three components of the velocity seismograms obtained at a number of receivers covering various distances and directions with respect to the source location. Furthermore, we have evaluated the influence of increasing geometrical complexity on the amplitude spectra and the PGV values. In the following we discuss our observations an draw conclusions regarding the possible implications for various fields of seismology.

4 DISCUSSION AND IMPLICATIONS OF THE RESULTS

We have presented a numerical study of the influence of possible geometrical complexities of rupture surfaces on the generated wavefield. To this end, we have created a set of rupture models characterized by different degrees of the geometrical complexity. We emphasize, that we also used different random numbers for the random field generator discussed in Section 2.3 to study the effects of different realizations of deflected fault models. As they qualitatively lead to the same results they confirm the results of our numerical study and our derived conclusions. Note that these deflected rupture models have the same seismic moment tensor as the perfectly planar one, however, with a reduced scalar moment, which we correct for. We remark, that of course the developed non-planar rupture models used in this study could still be far from reality. None of the parameters describing the random rupture deflections, namely the spectral decay, the correlation lengths or the rms values are precisely known. Moreover, these parameters can vary among different earthquakes and/or tectonic regions. Therefore, our models have to be understood as speculative test cases. As shown by the results above, it is not always possible to distinguish whether the variations in the seismic wavefield are caused by changes in the rms or K values, for

example, FN component in Fig. 9. Nevertheless, we believe that the determination of possible models characterizing typical geometrical properties of earthquake ruptures is of great importance.

Let us emphasize that here we are dealing only with kinematic and not dynamic models. This could be considered as a deficiency in our approach. However, the restriction to kinematic rupture modelling allows us to perform the study much more consistently. This means that all the rupture models, apart from their geometrical differences, are characterized by same kinematic properties, such as total seismic moment, rupture velocity, duration, slip velocity function, etc. Moreover, as we mention in Section 2.3, the different kinematic models considered may even have completely different underlying dynamic models. On the other hand, the dynamic models might theoretically constrain the range of the possible geometrical rupture models.

Our study shows that perhaps the most typical behaviour of velocity amplitudes of different components at a given receiver is their tendency to be more balanced as more geometrical complexity is introduced (see Fig. 9a). Moreover, the larger the differences between the components of the perfectly planar rupture are, the more sensitive are the amplitudes to the rupture deflections (see receiver 2, 12, 22 or 31–59 in Figs 9a and b.)

In the frequency domain in Figs 8(a) and (b) we observe that for increasing rms or correlation length, the whole spectrum can be affected, for example, for the FP and V components at receivers close to the rupture. This suggests that the energy between the components is distributed more equally in the whole frequency band when enhancing the geometrical irregularities of the rupture model. However, for the distant off-fault receiver 20 in Figs 8(a) and (b) the Fourier amplitudes at low frequencies typically are not affected by increasing rms or K values, while at high frequencies the amplitudes increase with geometrical complexity. This is due to the constraint seismic moment of all our rupture models that is governing the low-frequency motion. Moreover, we observe that the geometrical complexity introduces changes in the seismogram spectra starting almost always at the same frequency. In other words, we do not see any systematic dependence of this frequency on rms or K.

In the following we want to draw the readers attention to possible implications of the discussed observations for a number of different field in seismology affected by the effects of non-planar rupture geometries.

4.1 Implications to strong ground motion simulations

In strong ground motion simulations it is quite common that the synthetic seismograms exhibit large amplitude differences in the horizontal components, which are not observed in real data records. This experience is clearly supported by our study (see Fig. 9) and is a consequence of the strong effect of the radiation pattern. We show that gradually adding complexities to the rupture geometry balances these maximum values of the synthetics. Zeng *et al.* (1995) suggested to include rake variations in the simulations to overcome this problem of unrealistically large differences between the horizontal components in strong ground motion predictions. They illustrated the effect for one station for the Uttarkashi thrust fault earthquake showing that their synthetics then have comparable amplitudes at horizontal components. They also state that the strike and dip variations do not have such a strong effect. In our experience such a statement should depend on the position of the particular station with respect to the rupture (distance and azimuth). Moreover, we attribute this disagreement to the different principal source mechanisms assumed in the calculations. While Zeng *et al.* (1995) used a thrust fault, we only consider a strike slip fault, where, on the contrary, the rake variations in the LOH-4-015R model basically did not affect the amplitudes of the horizontal components.

Pitarka *et al.* (2000) or Satoh (2002), suggested the use of a radiation pattern that vanishes with increasing frequency to explain observed data. To our knowledge, this observation is not yet theoretically fully understood. Based on our numerical study we cannot fully explain this particular behaviour. In fact, our results show that the geometrical variations of the adopted source models can affect the seismograms in the whole frequency band depending on the receiver location and the analysed velocity component. Therefore, not all signals exhibit such a systematic frequency dependence, especially not those recorded at close fault distances (see Fig. 8). Another, rather high-frequency effect might have to be studied in order to explain this general behaviour observed in real data. Perhaps the most promising phenomenon that could exhibit such frequency-dependent effects is the scattering due to random medium properties. Since the ADER-DG method seems to be suitable for studying wave propagation in a random medium, this will be the subject of our further studies.

Generally speaking, we state that the small-scale geometrical variations of a 3-D non-planar rupture can be approximated by a mean planar fault, on which the rupture elements are projected, however, taking into account their actual strike and dip variations. Referring to Figs 4 and 11 this approximation will lead to satisfying results in terms of the radiated wavefield and misfits for many cases. From the practical point of view, this allows most numerical methods that are possibly not capable of incorporating the geometrical complexities of non-planar ruptures in their mesh to resolve most of the discussed effects. However, we emphasize that the small-scale variations in strike and dip should not be neglected even if projected onto a planar surface. This might be important for many numerical methods that have difficulties following a deflected rupture surface with their discretization, for example, regular Cartesian Finite Difference grids. Precisely speaking, this approach will lead to minor amplitude and phase discrepancies in comparison to a truly deflected rupture surface. Therefore, the modeller should be aware of the significance of the possibly introduced errors with respect to the desired accuracy of his synthetics. However, we remark that we only considered smooth geometrical variations of the rupture surface with respect to its mean, perfectly planar surface. Significant deviations from a mean, planar trend, such as bends, should definitely be approximated by separate rupture segments.

4.2 Implications to seismic moment tensor inversions

Zahradnik *et al.* (2007) show that two pure shear earthquakes of different orientations can introduce a non-DC component in the retrieved moment tensor if such a double event is considered as a single one in the inversion. Here, we represent our non-planar rupture surfaces by a grid of differently oriented elementary DC point sources. However, as mentioned above, the final moment tensor of the whole earthquake obtained as a sum of the moment tensors of all rupture elements has the same character as for the planar case, that is, the same strike, dip and rake angles with no non-DC component. However, as mentioned above the total scalar moment is lower and has to be corrected for.

We attribute the fact that our non-planar ruptures keep the character of a planar rupture in terms of the seismic moment to our particular generation of random distributions of strike and dip. They

vary randomly around a mean value always corresponding to the same planar rupture. Therefore, we state that for seismic moment tensor inversions, which are typically based on low-frequency data of stations of regional or teleseismic distances, the geometrical complexity as introduced in this paper does not seem to have an effect (see Fig. 8).

4.3 Implications to slip inversions

Our study shows that taking into account the non-planar character of a rupture surface could be of major importance, especially if the real rupture deflections were characterized by even larger rms values. Generally, the non-planar character of a rupture is neglected in slip inversions. Only if the rupture is clearly bent (e.g. Landers earthquake), the rupture is divided into several planar segments. In some cases, rake variations are also retrieved together with slip. However, strike and dip variations are still neglected. Considering our study, this can significantly bias the resulting slip image since the actual strike and dip variations have strong effects on the waveforms as shown in Fig. 7. Once again it has to be emphasized that the effects introduced by geometrical complex rupture surfaces can influence the whole frequency band depending on the receiver location with respect to the rupture distance and orientation, so that they cannot generally be avoided, for example, by simply low-pass filtering of the waveforms.

5 CONCLUSIONS

We have presented a numerical study of the effects of geometrically complicated 3-D ruptures on the radiated wavefield in the vicinity of the source. As currently most kinematic and dynamic rupture models are still based on the assumption of perfectly planar ruptures, we show how the variations of the geometrical rupture parameters at different scales can significantly influence the synthetic seismograms. The results show that the correct incorporation of the rupture complexity is important as the observed effects due to local variations of the rupture geometry parameters can strongly affect the waveforms and the corresponding Fourier spectra of the synthetics in the whole frequency band. We conclude that the observations of this study might have important implications for strong ground motion simulations or seismic moment tensor and slip inversions when realistic earthquake scenarios with very heterogeneous rupture kinematics are considered.

ACKNOWLEDGMENT

The authors thank the Deutsche Forschungsgemeinschaft (DFG), as the work was supported through the Emmy Noether-Program (KA 2281/2-1), the Marie Curie Research and Training Network Seismic Wave Propagation in Complex Media: a European (SPICE Network), part of the European Commission's Human Resources Mobility Programme, and research projects MSM 0021620800 of the Czech Ministry of Education and GACR 205/07/0502 of Grant Agency of the Czech Republic. We also thank the Leibniz-Rechenzentrum in Garching for their support to compute all numerical results presented in this work.

REFERENCES

Adda-Bedia, M. & Madariaga, R., 2007. Seismic radiation from a kink on an antiplane fault, *Bull. seism. Soc. Am.,* in press.

Aki, K. & Richards, P.G., 2002. *Quantitative Seismology,* University Science Books, Sausalito, California.

Aochi, H. & Madariaga, R., 2003. The 1999 Izmit, Turkey, earthquake: non-planar fault structure, dynamic rupture process, and strong ground motion, *Bull. seism. Soc. Am.,* 93,1249–1266.

Aochi, H., Fukuyama, E. & Matsu'ura, M., 2000. Spontaneous rupture propagation on a non-planar fault in 3-D elastic medium, *Pure appl. Geophys.,* 157,2003–2027.

Bonilla, M.G., 1979. Historic surface faulting—map patterns, relation to subsurface faulting, and relation to preexisting faults, *USGS Open-File Report 79-1239,* 36–65.

Bouchon, M., 1981. A simple method to calculate Green's functions for elastic layered media, *Bull. seism. Soc. Am.,* 71,959–971.

Bouchon, M. & Streiff, D., 1997. Propagation of a shear crack on a nonplanar fault: a method of calculation, *Bull. seism. Soc. Am.,* 87,61–66.

Cruz-Atienza, V.M. & Virieux, J., 2004. Dynamic rupture simulation of non-planar faults with a finite-difference approach, *Geophys. J. Int.,* 158, 939–954.

Day, S.M., 2001. Tests of 3D Elastodynamics Codes, LIFELINES PROGRAM TASK 1A01 *Final Report to Pacific Earthquake Engineering Research Center,* September 10, 2001. Coordinated by S.M. Day, San Diego State University.

de la Puente, J., Käser, M., Dumbser, M. & Igel, H., 2007. An arbitrary high order Discontinuous Galerkin method for elastic waves on unstructured meshes—IV. anisotropy. *Geophys. J. Int.,* 169, 1210–1228.

Delouis, B., Giardini, D., Lundgren, P. & Salichon, J., 2002. Joint inversion of InSAR, GPS, teleseismic, and Strong-Motion data for the spatial and temporal distribution of earthquake slip: application to the 1999 Izmit Mainshock, *Bull. seism. Soc. Am.,* 92,278–299.

Dumbser, M. & Käser, M., 2006. An arbitrary high order Discontinuous Galerkin method for elastic waves on unstructured meshes II: the three-dimensional isotropic case, *Geophys. J. Int.,* 167, 319–336.

Gallovič, F. & Brokešová, J., 2006. On strong ground motion synthesis with k^{-2} slip distributions, *J. Seismol.* 8,211–224.

Hardebeck, J.L., 2006. Homogeneity of small-scale earthquake faulting, stress, and fault strength, *Bull. seism. Soc. Am.,* 96,1675–1688.

Harris, R.A. & Day, S., 1999. Dynamic 3D simulations of earthquakes on an echelon faults, *Geophys. Res. Lett.,* 26,2089–2092.

Käser, M. & Dumbser, M., 2006. An arbitrary high order Discontinuous Galerkin method for elastic waves on unstructured meshes I: the two-dimensional isotropic case with external source terms, *Geophys. J. Int.,* 166,855–877.

Käser, M., Mai, M.P. & Dumbser, M., 2007. On the accurate treatment of finite source rupture models using ADER-DG on tetrahedral meshes, *Bull. Seism. Soc. Am.,* in press.

Li, Y.-G., Aki, K., Vidale, J.E., Lee, W.H.K. & Marone, Ch.J., 1994. Fine structure of the landers fault zone: segmentation and the rupture process, *Science,* 15,367–370.

Pitarka, A., Somerville, P., Fukushima, Y., Uetake, T. & Irikura, K., 2000. Simulation of near-fault strong-ground motion using hybrid Green's functions, *Bull. seism. Soc. Am.* 90,566–586.

Pulido, N., Ojeda, A., Atakan, K. & Kubo, T., 2004. Strong ground motion estimation in the Sea of Marmara region (Turkey) based on a scenario earthquake *Tectonophysics,* 391,357–374.

Satoh, T., 2002. Empirical frequency-dependent radiation pattern of the 1998 Miyagiken-Nanbu earthquake in Japan, *Bull. seism. Soc. Am.,* 92,1032–1039.

Spudich, P. & Archuleta, R.J., 1987. techniques for earthquake ground-motion calculation with applications to source parametrization of finite faults, in *Seismic Strong Motion Synthetics,* pp. 205–265, ed. Bolt, B.A., Academic Press, Orlando, Florida.

Titarev, V.A. & Toro, E.F., 2002. ADER: arbitrary high order Godunov approach, *J. Sci. Comput.,* 17,609–618.

Toro, E.F., 1999. *Riemann Solvers and Numerical Methods for Fluid Dynamics,* Springer, Berlin.

Wald, D.J. & Heaton, T.H., 1994. Spatial and temporal distribution of slip for the 1992 Landers, California, earthquake, *Bull. seism. Soc. Am.* 84, 668–691.

Zahradník, J., Sokos, E., Tselentis, G.-A. & Martakis, N., 2007. Non-double-couple mechanism of moderate earthquakes near Zakynthos, Greece, April 2006; explanation in terms of complexity. *Geophys. Prospect.,* in press.

Zeng, Y. & Chen, Ch.-H., 2002. Fault rupture process of the 20 September 1999 Chi-Chi, Taiwan, earthquake, *Bull. seism. Soc. Am.,* 91, 1088–1098.

Zeng, Y., Anderson, J.G. & Su, F., 1995. Subevent rake and random scattering effects in realistic strong ground motion simulation, *Geophys. Res. Lett.,* 22, 17–20.

[P3]

Quick Fault-Plane Identification by a Geometrical Method: Application to the M_w 6.2 Leonidio Earthquake, 6 January 2008, Greece

J. Zahradnik and F. Gallovic
Charles University

E. Sokos, A. Serpetsidaki, and A. Tselentis
University of Patras

Online material: The hcplot Matlab script, an aid for visualization of the *H-C* method of fault-plane identification.

INTRODUCTION

Focal mechanisms of earthquakes provide two nodal planes. A foolproof method of identifying which one is the fault plane is the "seismologist's dream." This is true because knowledge of causative faults is of key importance for seismotectonic studies. For example, intermediate-depth earthquakes, such as the one studied in this paper, rarely have known fault planes, but the correct interpretation of such a fault plane would help constrain regional geodynamic models of subducted plates and stress fields. It is equally important to identify active crustal blind faults, knowledge of which may improve earthquake hazard assessment.

The fault plane can sometimes be well "mapped" (constrained) by the spatial distribution of numerous early aftershocks. However, this technique has serious limitations. One of them is the fact that in sparsely instrumented regions, accurate location of weak aftershocks is impossible. Moreover, some events lack numerous aftershocks at the mainshock fault plane altogether (this is typical of intermediate-depth earthquakes). The apparently straightforward case, where an earthquake occurs at or close to a geologically well-known fault, also benefits from an independent check, because the "known" fault may have a complex tectonic structure at depth.

The most challenging task is the *quick* identification of the earthquake fault plane. If made in near real time, it might play a vital role in the fast simulation of strong ground motions (shake maps) for post-event emergency services. If "quick'" means a few hours or a few days after the event, the identification might still greatly contribute to assessing increased spatial probabilities of aftershocks based on the Coulomb stress-loading of neighboring faults due to the mainshock rupture (McCloskey *et al.* 2005).

Existing methods to identify the fault plane from seismograms are based mainly on finite-extent source models: distributed-slip models are generated for both nodal planes and the one that better fits the records is considered to be the fault plane. When near-fault records are available, this method can be applied even with very few stations (Delouis and Legrand 1999). However, using the nearest station records is highly vulnerable to location errors and complexities of the rupture process. Use of long-period regional or teleseismic records is also possible, often with relatively simple fault models. However, as a rule, the two nodal planes provide a waveform match that is just slightly different, so choosing one plane over the other often remains difficult (*e.g.,* Roumelioti *et al.* 2004). Conceptually similar are attempts to resolve the nodal-plane ambiguity by calculating the higher-order moment tensors for both planes and comparing the variance reduction; the advantage is that there is no need for a slip distribution model and applicability to weak events (McGuire 2004 and references therein). A new method to identify the fault by source scanning has recently been suggested by Kao and Shan (2007). In this method, the moment tensor solution is not needed, but other requirements are quite stringent, *e.g.*, the records must be close to the epicenter with well-separated *P* and *S* arrivals. Additional support of preferred slip directions on pre-existing zones of weakness can be also gained from the seismo-tectonic setting, in terms of regional stress fields and tractions acting on the nodal planes (Gephart 1985). In the case of well-expressed directivity effects, the macroseismic field may indicate the preferred nodal plane, even without any instrumental evidence. However, the macroseismic data are collected too late after the earthquake to provide a quick fault plane identification.

doi: 10.1785/gssrl.79.5.653

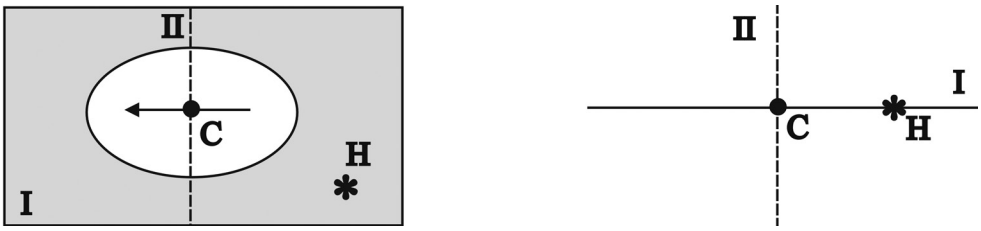

▲ **Figure 1.** Schematic explanation of the *H-C* method. Left: *H* (and star) = hypocenter, *C* = centroid, plane I and II are nodal planes, oval denotes a dominant slip region. Right: a different view of the same situation—a cross-section in which *H* identifies nodal plane I as the fault plane.

▲ **Figure 2.** Left: The typical situation, where *H* does not coincide exactly with any of the nodal planes. Right: Using several *H*s and *C*s, representing the uncertainty in their locations, can help to identify the fault plane.

THE *H-C* METHOD

This paper suggests a simple, innovative method, immediately applicable (under favorable conditions) when a reliable earthquake location and its centroid moment tensor solution (CMT) are available. Location, based on travel times, provides the hypocenter position (*H*), the place at which the rupture propagation initiated. The CMT solution from relatively long-period waveforms provides the centroid (*C*), which is the point-source approximation of the dominating slip region(s) on the fault. Further, the CMT solution also gives two planes passing through *C* (plane I and plane II) defined by the strike and dip angles of the moment-tensor solution.[1] Then, assuming a planar fault, the fault plane can be identified as that one among planes I and II that encompasses the hypocenter (Figure 1). In this paper this will be referred to as the *H-C* method. Although not yet broadly recognized as a useful tool for fault plane identification, its great potential is in simple linking of the independent pieces of short- and long-period seismic information.

What are the favorable conditions under which the *H-C* method works? A successful application needs: 1) a reasonably accurate determination of the *H* and *C* position; 2) a sufficient distance between *H* and *C*, larger than the individual errors of the *H* and *C* positions; and 3) earthquake geometry that is not very complex (explained in more detail below). The orientation of planes I and II also plays a role, but their strike and dip angles are often stable enough during the MT inversion (say within 10° each). In this sense, the usual uncertainty of the fault plane solution is less critical than the *H* and *C* positions. For example, for earthquakes where the uncertainty of *H* and *C* is of the order of 10 km, the method becomes usable when the *H-C* distance gets larger than 10 km, *i.e.*, starting at about **M** 6. Under special conditions, for example, in the presence of a dense local network providing better constrained *H* and *C* parameters, the method might be applicable at about **M** 5. These are only rough estimates based on empirical relations between the fault size and magnitude (Somerville *et al.* 1999). In practice, it is also important whether the data "see" the whole fault (at very long periods) or the individual largest asperities, and whether the rupture nucleates in, close to, or far from the asperity (Mai *et al.* 2005).

Due to inherent uncertainties of the *H* and *C* positions, it is not possible to combine just any individual location with an individual CMT solution; more likely the hypocenter does not fall in any of the planes I and II (the so-called *H-C* inconsistency is detected, Figure 2 left). The correct approach is based on the concept of *collective* solutions (Figure 2 right). We seek families of acceptable solutions (a set of the hypocenter locations and a set of planes I or II given by inherent uncertainty, use of different methods, structural models, etc.), and compare them collectively. We arrive at the *H-C consistency* more often when considering uncertainties in this way.

Routine agency data typically provide the individual (rather than collective) solutions; *H* and *C* are often calculated by different teams. Therefore, the *H-C* method rarely works with very preliminary agency data. Or, at least, solutions of several agencies should be employed. Revised solutions may perform better, particularly if *S* waves from near stations are included for a better depth estimate, but a specific *H-C* study by a single team is always preferable. It can be performed quickly enough, especially if applied to previously studied geographic regions and using seismic networks with performance that is well known.

1. For simplicity we may call them nodal planes, but, more often, this term is reserved for two planes passing through the hypocenter.

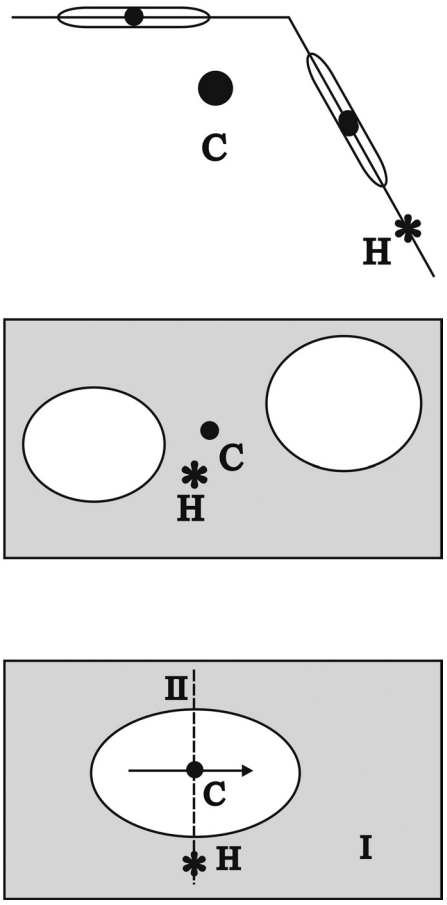

▲ **Figure 3.** Possible failures of the *H-C* method. Top: In this segmented fault, *C*, is out of both planar segments of the fault, including the segment encompassing *H*. Middle: In this almost symmetric bilateral rupture, although the fault is large, *C* appears too close to *H* when viewing the fault at very low frequencies. Bottom: the *H-C* line coincides with the intersection of plane I and II. *H* is in both nodal planes, so it cannot identify plane *I* as the fault plane.

Under such conditions, the operators are best aware of their alternative crustal models, the more and less reliable stations, noise levels, etc., so they can easily construct the families of the collective solutions, adequately reflecting typical model uncertainties due to varying data subsets.

A note regarding the *C* position: In practice, the MT inversion is often accompanied by a search of the source depth optimizing the waveform match, *i.e.*, assuming *C* under the epicenter. Although such an approximation may be good enough for retrieving the fault-plane solution, it is not sufficient for the *H-C* method. The *C* position should be searched in the 3D vicinity of the hypocenter and should extend sufficiently far, according to the magnitude of the studied earthquake (hence reflecting the expected fault length). We discuss this in more detail in the application section of this paper.

Last but not least, success of the *H-C* method is a matter of a suitable technique to *visualize* the geometrical configuration of the *H*, *C*, and planes I, II. We suggest a plotting tool allowing rotated (animated) 3D view (the hcplot script in Matlab, which accompanies this paper in the electronic supplement). Note that we don't need to know the precise extent of the rupture to visualize planes I and II.

The price we pay for the simplicity and speed of the *H-C* method is in its limitations (Figure 3). First of all, we have to keep in mind that the method is nothing but a quick guess of the likely fault plane. There is no chance to validate the result within the method itself. Only independent, detailed (and thus not "quick") posterior studies can prove or disprove the fault-plane identification. There are also situations in which the *H-C* method can fail due not to inaccuracy in *H* and *C*, but for a more fundamental reason. Imagine a segmented, piecewise planar fault (Figure 3 top). If the CMT solution is calculated from low-frequency data, "seeing" all segments as a single point source, then *C* is out of both segments and neither of the planes I and II passing through *C* encompasses the hypocenter. A large non-DC component can signal the source complexity in cases like this (Frohlich 1994). Obviously, increasing frequency, so as to "see" the two asperities separately, can help to recognize at least the segment encompassing *H*. Even more difficult would be the case analogous to Figure 3, top panel, in which the segment containing *H* releases much less seismic moment than the other segment, thus apparently putting *H* out of the fault plane. At the low-frequency range, problems may arise even on a single fault when an almost symmetrical bilateral fault is represented by the centroid position *C* very near to *H* (Figure 3 middle). In such a case, it may help to consider the centroid time. Finally, let us mention that the *H-C* method always fails where the line connecting *H* and *C* coincides with the intersection of the planes I and II (Figure 3 bottom).

Obviously, the *H-C* method is not equally suited for all events of the same magnitude. It depends on the geometry of planes I and II with respect to the hypocenter, because the hypocenter depth is always more problematic than the epicenter position (*E*). Therefore, a strike-slip event with two vertical planes I and II is the easiest case to resolve successfully (Figure 4 top). The fault identification can be performed by means of the epicenter only, because the problematic depth has no effect. The map-view analysis is sufficient, so no 3D visualization is needed in this special case. A vertical dip-slip event (or low-dip thrust) is also easy (Figure 4 middle): The vertical plane, as a fault-plane candidate, can be simply accepted or rejected by means of the epicenter position only. Of course, to confirm the horizontal (or subhorizontal) plane, we already have to care more about the hypocenter depth. Oblique normal and reverse events are the most difficult ones (Figure 4 bottom): in case of a highly uncertain location depth, *H* may fall in both planes I and II.

TEST EXAMPLES

To demonstrate both easy and difficult cases, the *H-C* method is applied in this section to three earthquakes with known fault planes (Figure 5). For simplicity, only agency solutions are used, although generally they cannot be conclusive due to limited *H*- and *C*-position accuracy, as discussed above.

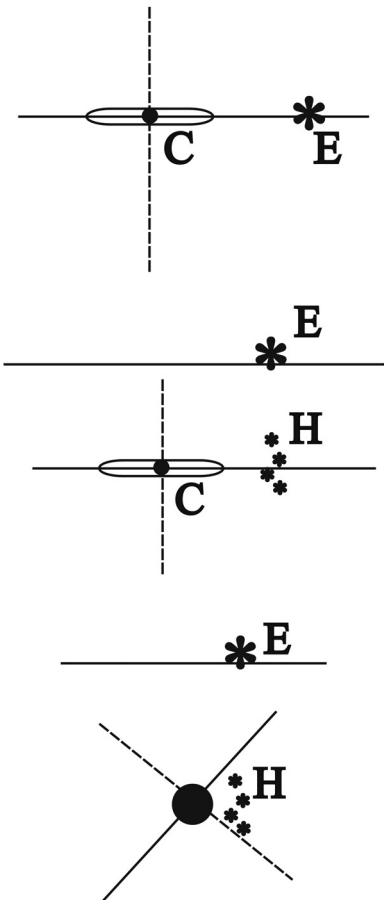

▲ **Figure 4.** A schematic illustration of the *H-C* method for different faulting mechanisms. Top: the simplest situation for a vertical strike slip when even a top view is helpful, without any 3D visualization, and epicenter *E* identifies the fault plane. Middle: a relatively easy fault plane identification for mechanisms when one of the nodal planes is vertical (or near vertical). Even *H* of inaccurate depth can successfully identify the fault plane. Bottom: The most difficult case of oblique fault planes. An *H* of inaccurate depth cannot solve this case, because it might appear equally close to both nodal planes.

Mw 6.0 Parkfield, Central California, 28 September 2004: The strike-slip case. Although based on the agency data (the Harvard CMT and the U.S. Geological Survey [USGS] location), the two individual solutions demonstrated that the hypocenter is closer to plane II, strike 321°, marked as green in Figure 5(A). This is the San Andreas fault segment, unambiguously mapped by the aftershock distribution (http://www.cisn.org/special/evt.04.09.28/Parkfield_DD/Park4.html; Thurber *et al.* 2006) and associated with the secondary surface rupture (Rymer *et al.* 2006).

Mw 7.1 Andreanof Islands, Aleutians, 19 December 2007: The low-angle thrust fault case. Even better than in the above example, the Harvard and USGS data are almost *H-C* consistent, and provide clear identification of the subhorizontal fault plane in Figure 5(B), typical of large subduction events in that region.

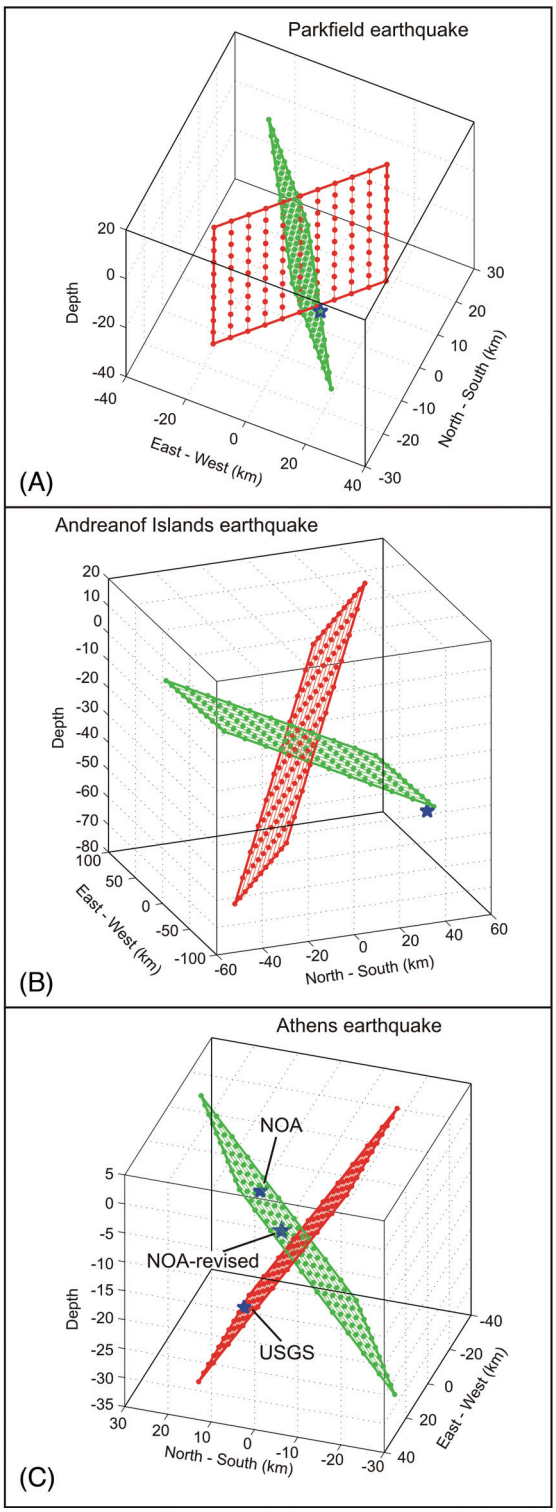

▲ **Figure 5.** Tests of the *H-C* method. (A) Parkfield, (B) Andreanof Islands, (C) Athens earthquake. Centroid is in the middle of the intersection of nodal planes I and II. Hypocenter is shown by the blue star. Only agency solutions are used: hypocenter of USGS and CMT of Harvard, except for the Athens earthquake. In the latter case two more hypocenter solutions are included (NOA preliminary and NOA revised). In all three tests the true fault plane is the green one, so the hypocenter should fall in that plane.

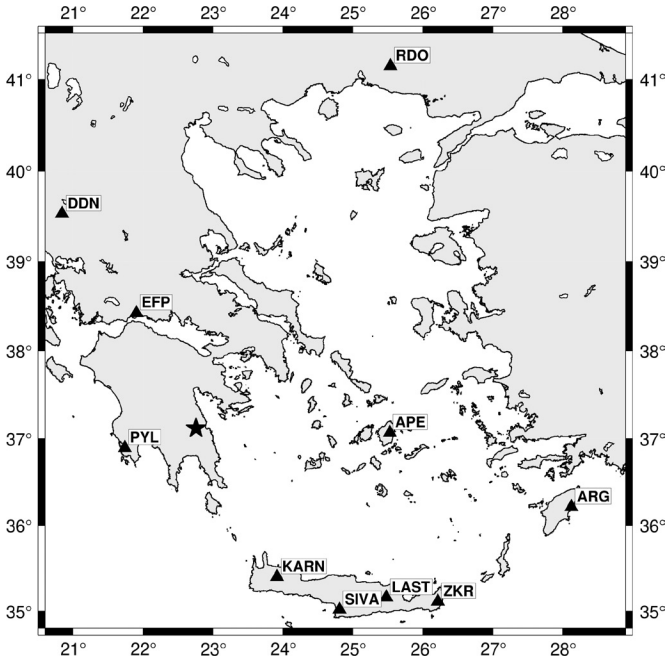

▲ **Figure 6.** Stations and networks (in brackets) used in the MT inversion: PYL, EFP, DDN [PSLNET, HP], ARG and RDO [GI-NOA, HL network], APE, LAST, ZKR, KARN, SIVA [GEOFON, GE].

Mw 6.0 Athens, Greece, 9 September 1999: The normal-fault case. This is an example of a difficult situation. As seen from Figure 5(C), the USGS location seems to prefer plane II (red, strike 284°) of the Harvard CMT solution, while the Greek Institute of Geodynamics, National Observatory of Athens (NOA) preliminary location identifies plane I (green, strike 116°). The NOA relocated hypocenter points to plane I again, which was indeed clearly mapped by the aftershock distribution as revealed by a temporary local network (Tselentis and Zahradnik 2000). In this case, using the individual agency solutions, the *H-C* method is not indicative enough. The reason is not only in the uncertainty of the solutions, but also in the less favorable geometry, as previously discussed (Figure 4 bottom).

The message of the test examples is simple: It is useful to try the *H-C* method even with preliminary agency data. If we get an *H-C* inconsistent case, it clearly shows that the *H* and *C* solutions need more accuracy. If we get an *H-C* consistent case, it still needs more verification. The next step is to add agency solutions, as they arrive after the earthquake, to obtain a more likely fault-plane candidate. Variability among the agency solutions also provides an uncertainty estimate, without which the *H-C* method cannot give reasonable results. Nevertheless, the most recommended procedure is a specifically focused application of the *H-C* concept, as illustrated in the next section.

Mw 6.2 LEONIDIO EARTHQUAKE

In this section, the *H-C* method introduced above is applied to the intermediate-depth earthquake of 6 January 2008 in southern Greece. The earthquake produced minor damage to the city of Leonidio and the surrounding region on the eastern coast of the Peloponnese, 120 km from Athens, but it was felt all over the country and in several places in southern Italy. Only a few aftershocks were located by regional networks: four $M_L \sim 3$ events and one **M** 4 event as late as 11 January; these definitely could not map the fault plane.

TABLE 1
Leonidio Earthquake; the Preferred Hypocenter Solution of this Paper. Crustal Model of Novotny *et al.* (2001), *Vp/Vs* = 1.75.

Origin (UTC)	Lat N (deg.)	Lon E (deg.)	Depth (km)
05:14:21	37.1055	22.7513	72

Hypocenter location. The HYPOINVERSE code was applied to invert the manual *P* and *S* picks from 15 stations; those used below for CMT (Figure 6), plus some extra stations (short period) from the Patras Seismological Laboratory network (PSLNET) and a few stations belonging to Aristotle University of Thessaloniki, up to 350 km away. The uncertainty was evaluated by repeated calculations with: a) various starting depths; b) various data subsets, *e.g.*, keeping only stations closer than 200 km; c) two V_p/V_s ratios; and d) two crustal models (Tselentis *et al.* 1996; Novotny *et al.* 2001). The latter provided the least root mean square (RMS) residuals, in particular for $V_p/V_s = 1.75$. The best-fitting location is shown in Table 1. The family of alternative hypocenter solutions is plotted in Figures 7 and 8.

CMT solution. Broadband records from the permanent seismological network PSLNET were studied, complemented with waveforms provided by other near-regional stations available through the ORFEUS data center and the GEOFON network. . Finally, three-component unclipped records from 10 stations were used in the MT inversion, providing fairly good azimuthal coverage of the event (Figure 6). Furthermore, the EW horizontal component (clipped) of the nearest station, PYL, was excluded. The epicentral distances range from 117 km to 490 km.

Various preliminary tests were carried out to find the appropriate crustal model and frequency band to achieve an acceptable waveform match. In particular, the crustal models proposed by Endrun *et al.* (2004) and Novotny *et al.* (2001) were tested at frequencies below 0.1 Hz. Finally, all the runs were performed in the model of Novotny *et al.* (2001), which provided a slightly better match,[2] using displacement waveforms from 0.02 to 0.07 Hz. The MT calculations were made with ISOLA software, available at http://seismo.geology.upatras.gr/isola (Sokos and Zahradnik 2008). Final runs included the centroid grid search in a 7 × 7 horizontal stencil (step 7 km) at three depths (step 5 km). The whole procedure was performed several times, with or without the *Z* and NS components of the PYL

2. In this paper, the model of Novotny *et al.* (2001) occasionally proved to be good for location as well as the MT inversion. However, in general, use of a single crustal model for both tasks is not necessary; the existing crustal models are rarely equally suitable in both the short- and long-period range.

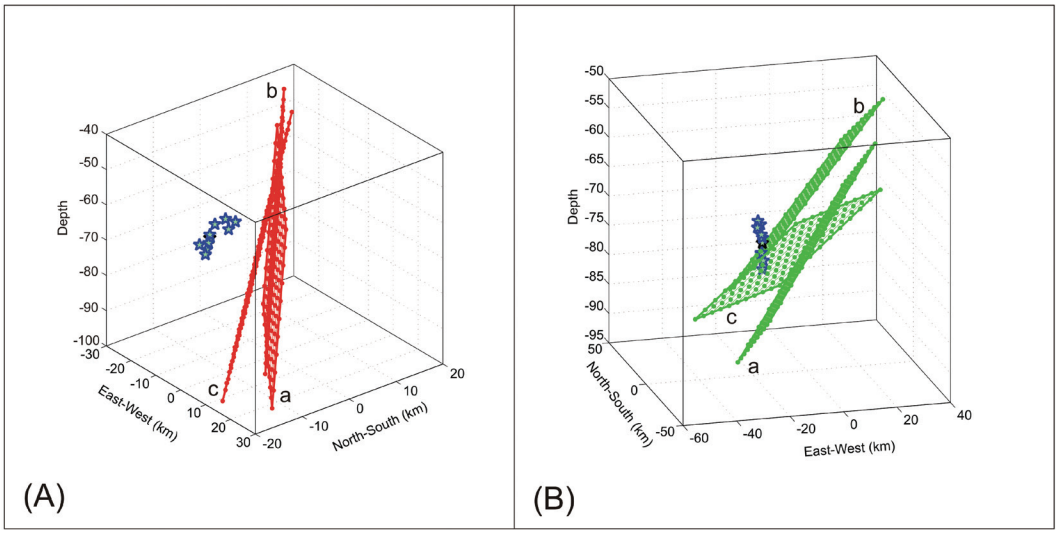

▲ **Figure 7.** Application of the *H-C* method to the Leonidio earthquake. (A) Three high-dip nodal planes illustrating uncertainty of the centroid determination. Centroid is in the middle of each plane. The blue stars show the family of hypocenter solutions of this paper. With such a distance between the hypocenters and the planes, it is unlikely that the high-dip nodal plane was the fault plane. (B) As in (A), but for the corresponding low-dip nodal planes. Proximity of the hypocenters (stars) to the planes indicates that the earthquake ruptured along such a low-dip fault. The three CMT solutions are as follows: (a) without station PYL, (b) with PYL-Z; (c) with PYL-Z and PYL-N.

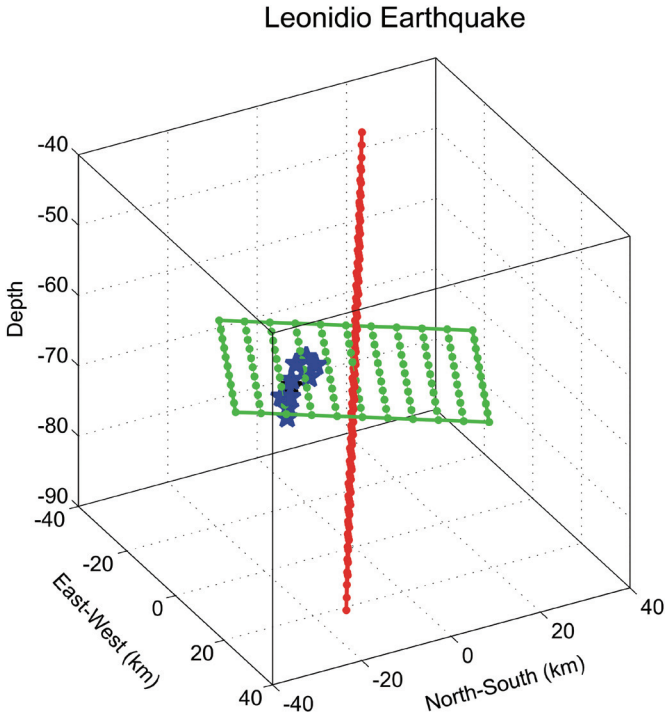

▲ **Figure 8.** The *H-C* plot of the preferred solution (Tables 1 and 2). Nodal planes I and II are shown in red and green, respectively. Centroid is in the middle of the intersection of the nodal planes. The alternative hypocenter solutions of the mainshock are shown in blue. The green plane encompasses the hypocenters, thus this low-dip nodal plane (strike 213°, dip 34°) is identified as the likely fault plane.

TABLE 2
Leonidio Earthquake; the Preferred CMT Solution of this Paper.

Centroid Time (UTC)	Lat N (deg.)	Lon E (deg.)	Depth (km)	Scalar moment (Nm)	M_w
05:14:25	37.1457	22.9502	65	1.5e+18	6.2
Strike I	**Dip I**	**Rake I**	**Strike II**	**Dip II**	**Rake II**
119°	87°	124°	213°	34°	5°
***P*-axis**	**Trend**	**Plunge**	***T*-axis**	**Trend**	**Plunge**
	181°	34°		59°	38°

station. Stability of the MT solution (the *C* position and the corresponding strike, dip, rake) was proved by jackknifing, *i.e.*, by repeatedly removing one station. The inversions indicate the NS position of *C* to be the most stable, the EW position plus/minus one 7-km grid step, and the *C* depth the least resolved, between 60 and 80 km. The preferred solution, considering the waveform match and the *H-C* consistency, is shown in Table 2 (the solution with the PYL-Z component). Three samples of the family of the alternative solutions are plotted in Figure 7.

The H-C analysis.[3] The nodal planes of the Leonidio earthquake differ considerably in their dip: plane I is almost vertical (strike of about 120°), and plane II has a low dip ~ 35° (strike of about 210°). Accordingly to our method section, this is a favorable situation. Figure 7 compares the position of the nodal planes

3. A quick preliminary result (Zahradnik *et al.* 2008a) was posted on the Web page of the European-Mediterranean Seismological Centre within one week of the earthquake.

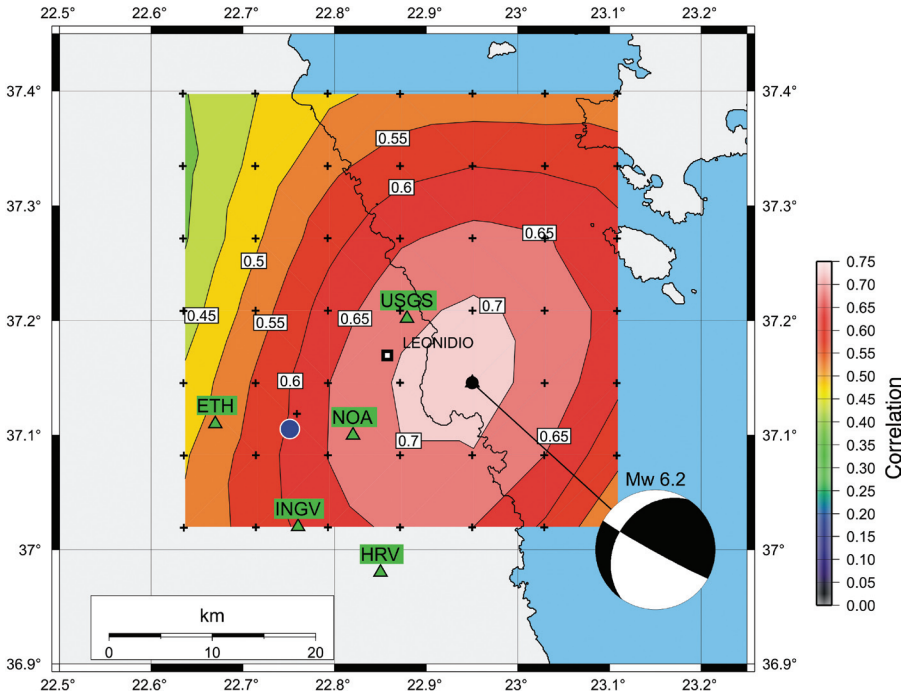

▲ **Figure 9.** Map view of correlation between the observed and synthetic waveforms at the depth of 65 km for the preferred solution. The preferred epicenter solution of this paper (Table 1) is shown by blue circle. Small black crosses mark the trial source positions at which the MT solution was performed, at various depths. The preferred centroid position (Table 3), the black dot, is connected with the corresponding "beach ball." The maximum correlation value 0.72 corresponds to the overall variance reduction of 0.51 at 10 stations. For comparison, the centroid positions of several agencies are shown by green triangles.

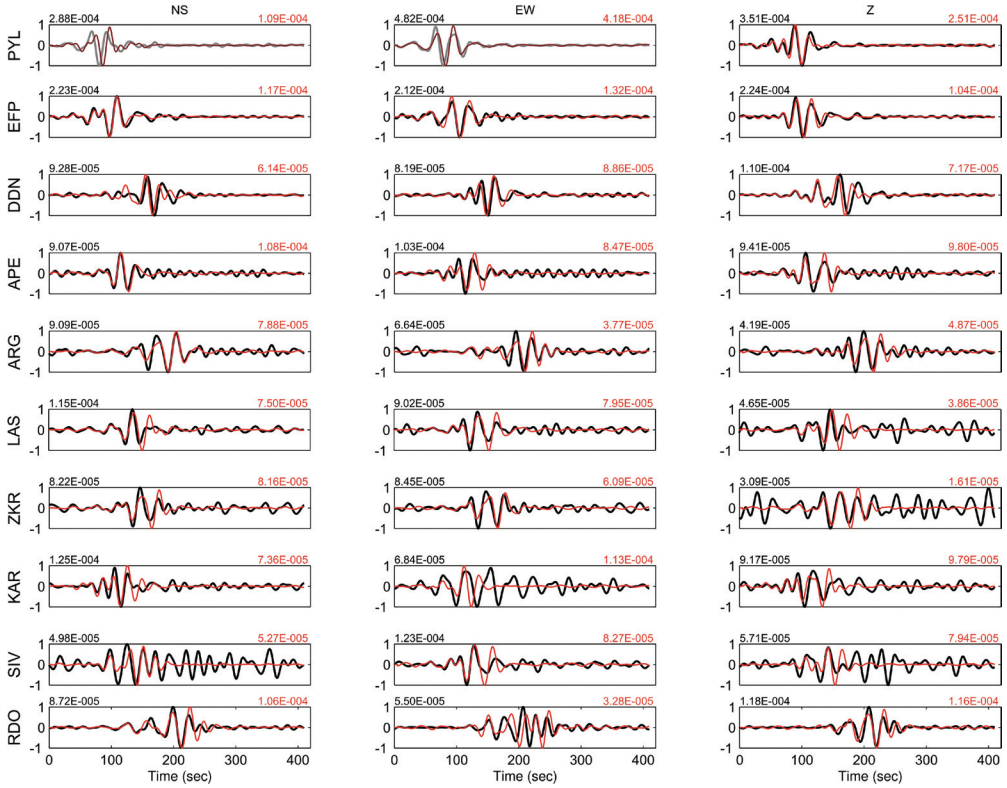

▲ **Figure 10.** Waveform match between the observed (black) and synthetic (red) waveforms for the preferred CMT solution. Maximum amplitudes are shown at the top of each panel in the same color. Gray waveforms weren't used in the inversion.

and the hypocenter solutions, separately for the high- and low-dip planes. Without a doubt, the hypocenter matches much better with the low-dip nodal plane. The preferred *H-C* solution is presented in Figure 8; the hypocenter of Table 2 is 2 km from the low-dip plane and 13 km from the high-dip one. (The animated 3D version of the plot [leonidio.avi] is in the electronic supplement.) Figure 9 gives the map view of the solution, together with the spatial correlation between the observed and synthetic waveforms. Finally, in Figure 10 a fairly reasonable waveform match between synthetic and observed waveforms is documented; the overall variance reduction is 0.51.

A few remarks to complement the analysis follow:

All tests provided an almost double-couple event, with a surprisingly stable and high DC percentage (around 90%). In contrast to complex events accompanied by low DC% (Zahradnik *et al.* 2008b), the Leonidio earthquake seems to represent a relatively simple rupture. The independent preliminary analysis shows that teleseismic data are in agreement with this observation (Kiratzi and Benetatos 2008).

Regarding the MT solutions of the other agencies, this paper is closer to the USGS CMT solution.

The significant difference between the centroid and origin time (of about 4 seconds), reported also by USGS, Harvard, and the Italian Istituto Nazionale di Geofisica e Vulcanologia (INGV) is another very stable feature of this event.

Tectonics and stress field. Finally we discuss the preferred solution in the frame of the seismotectonic environment. Since the Leonidio earthquake was not preceded by any earthquake that could be considered an obvious triggering event, it had to be invoked predominantly by the regional stress. The regional stress tensor in the studied region was investigated by Kiratzi and Papazachos (1995). The authors used five MT solutions of earthquakes $Ms > 5$ in the western part of the Hellenic arc (their region 1A). The strain-rate orientations associated with their stress tensor implied that the tectonic setting is characterized by a shortening of the subducting plate in a direction parallel to the trend of the Hellenic arc, basically in agreement with independent GPS data and geodynamic models. The regional stress is characterized by the dominant tension (azimuth 65°, plunge 55°), roughly perpendicular to the strike of the Hellenic arc in the studied region, and the subhorizontal pressure (azimuth 163°, plunge 6°) pointing along the arc (Figure 11). Furthermore, we found that the principal directions of this regional stress correspond to the smallest mean rotation angles (Kagan 1991) with respect to the *P* and *T* axes of the earthquake moment tensors involved in the stress inversion. Using the regional stress tensor (of unknown absolute value, thus normalized to unity), we evaluate the dimensionless traction for both nodal planes I and II of the Leonidio earthquake. We let TVN be the normal component of the traction vector with respect to the nodal plane and TVS the tangential component of the traction parallel to the slip vector, all calculated separately for both nodal planes (Figure 12 and Table 3). The normal components differ substantially for planes I and II. While the TVN is negative for plane I, it is positive for plane II. Therefore, the Coulomb failure

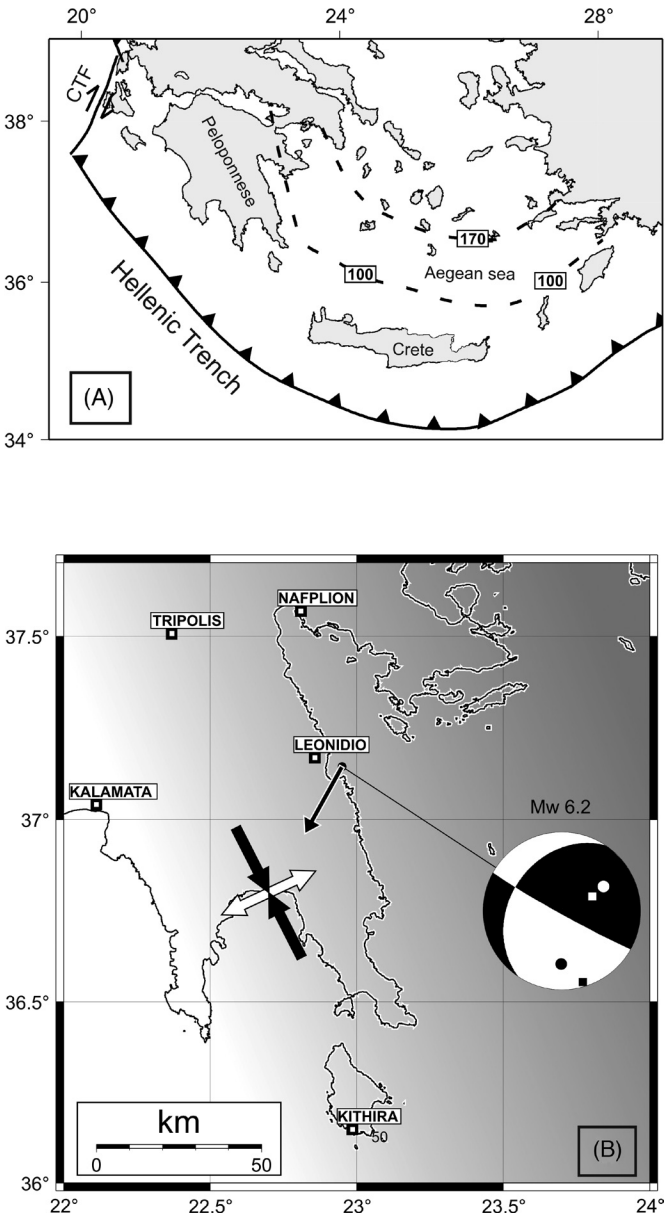

▲ **Figure 11.** Tectonics and stress field in the studied region. (A) Hellenic trench, Greece, where the African plate is subducting below the Aegean plate. CTF is the Cefallonia transform fault. Isolines in the Aegean Sea are mean depths of earthquakes (after Papazachos *et al.* 2000). (B) The increasing gray shade is a schematic illustration of the increasing depth of slab in the region (after Gudmundsson and Sambridge 1998). The *P* and *T* axes of the regional stress field (Kiratzi and Papazachos 1995), projected onto the horizontal plane, are shown by the arrows (the true *T/P* eigenvalue ratio is 1.25). The beach ball for the Leonidio earthquake, connected with the centroid, shows the *P* and *T* axes of the earthquake in circles, while those of the regional field are marked by squares. The main result of this paper, *i.e.*, the identification of the fault plane, is represented by the slip vector of the studied event (strike 209°, dip 3°). It shows the almost strike-slip motion of the top (hanging) block, as it moves along the low-dipping fault plane inferred in this paper.

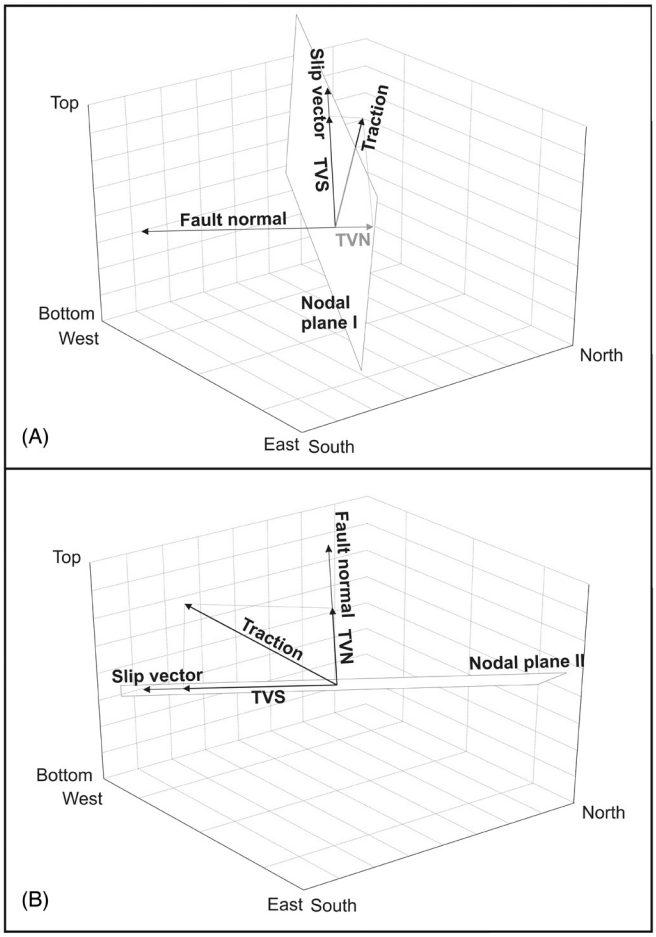

▲ **Figure 12.** Computed tractions corresponding to the regional stress field acting on the two nodal planes (I and II) of the Leonidio earthquake. TVS = the tangential component of the traction parallel to the slip vector, TVN = the normal component of the traction vector (Table 3). Note that the TVN value differs for planes I and II: while for plane II it is positive, for plane I it is negative. In this sense the Coulomb failure model supports the findings of the *H-C* method that the Leonidio earthquake ruptured the low-dip nodal plane II.

function CFF = TVS + μTVN also differs for the two slip vectors: CFF = 0.70 for the slip vector in the high-dip plane I, and CFF = 1.07 for the low-dip plane II. Here the effective friction coefficient μ = 0.5 is used. Generally, for deeper earthquakes, a higher value is also possible (Tibi *et al.* 2003), say μ = 0.8, thus further increasing the difference between planes I and II. If assuming a preexisting zone of weakness, the larger value of the stress criterion is an independent indication supporting plane II as the fault plane. Considering this together with the results of the *H-C* method discussed above, we conclude that the Leonidio earthquake ruptured along the low-dip plane II.

CONCLUSION

It is important to develop new methods for quick identification of an earthquake fault plane, without having to wait for the occurrence of aftershocks (if any, and if located satisfactorily). In particular, we need new methods that can be applied sooner than more complex and time-demanding studies, such as slip inversions, source-scanning algorithms, etc. The *H-C* method introduced in this paper allows identification of the fault plane by analyzing the geometrical configuration of the hypocenter (*H*), centroid (*C*), and the moment-tensor solution (nodal planes I and II). Note that such a successful though simple approach has not yet been recognized.

TABLE 3
Leonidio Earthquake and Its Interaction with the Regional (Unit) Stress Tensor: TVS = the Tangential Component of the Traction Parallel to the Slip Vector, TVN = the Normal Component of the Traction with Respect to the Nodal Plane, CFF = the Coulomb Failure Function; All Values Dimensionless.

Nodal plane	TVS	TVN	CFF
I	0.7941	–0.1962	0.6960
II	0.7906	0.5522	1.0667

We applied this method to the Leonidio earthquake of 6 January 2008. Taking into account uncertainties of the location and the waveform inversion, the near-regional waveform data from 117 km to 490 km, at frequencies 0.02 to 0.07 Hz, suggested that the *Mw* 6.2 Leonidio earthquake, along the eastern coast of the Peloponnese, represented *strike-slip motion along the low-dip fault plane* (strike 213°, dip 34°, rake 5°). Based on the regional stress field (Kiratzi and Papazachos 1995), characterized by shortening of the subducting plate in a direction parallel to the trend of the Hellenic arc, this preference for the low-dip plane was also supported by a quantitative estimate of the Coulomb failure function. As there were not enough Leonidio earthquake aftershocks to enable identification of the fault plane by the usual methods, the *H-C* method might be valuable for studies of the subduction process. In general, the *H-C* method may be useful in early warning systems and emergency operations after catastrophic events.

During the writing of this paper, the *H-C* method was applied to two more earthquakes in southern Greece, an **M** 6.9 on 14 February 2008 and an **M** 6.2, on 20 February 2008, and in each case preliminary identification of the fault plane was quickly (within one day) reported to the European-Mediterranean Seismological Centre (EMSC). These preliminary assessments can be found at http://www.emsc-csem.org/index.php?page=current&sub=recent.

To encourage a broader use of the *H-C* method, a visualization tool (the hcplot Matlab script) accompanies this paper in the form of an electronic supplement. The script quickly produces a 3D animated plot of the hypocenter, centroid, and nodal planes. The code is self-explanatory, intuitive, and easy-to-use. It is also possible to produce a movie for presentation purposes, independently of the Matlab environment. The electronic supplement includes a movie (leonidio.avi) related to the 6 January 2008 Leonidio earthquake.

ACKNOWLEDGMENTS

The authors acknowledge free access to waveforms of various European networks (MEDNET, GEOFON, GI-NOA) through ORFEUS and GEOFON data centers. The use of phase data from stations belonging to Aristotle University of Thessaloniki is also acknowledged. The work is a part of the following projects supported in the Czech Republic: GACR 205/07/0502, PostDoc GACR 205/08/P013, GAUK 279/2006/B-GEO/MFF, MSM 0021620860.

REFERENCES

Delouis, B., and D. Legrand (1999). Focal mechanism determination and identification of the fault plane of earthquakes using only one or two near-source seismic recordings. *Bulletin of the Seismological Society of America* **89**, 1,558–1,574.

Endrun, B., T. Meier, M. Bischoff, and H.-P. Harjes (2004). Lithospheric structure in the area of Crete constrained by receiver functions and dispersion analysis of Rayleigh phase velocities. *Geophysical Journal International* **158**, 592–608.

Frohlich, C. (1994). Earthquakes with non-double-couple mechanisms. *Science* **264**, 804–809.

Gephart, J. W. (1985). Principal stress directions and the ambiguity in fault plane identification from focal mechanisms. *Bulletin of the Seismological Society of America* **75**, 621–625.

Gudmundsson, O., and M. Sambridge (1998). A regionalized upper mantle (RUM) seismic model. *Journal of Geophysical Research* **B4**, 7,121–7,136.

Kagan, Y.Y. (1991). 3-D rotation of double-couple earthquake sources. *Geophysical Journal International* **106**, 709–716.

Kao, H., and S.–J. Shan (2007). Rapid identification of earthquake rupture plane using Source-Scanning Algorithm. *Geophysical Journal International* **168**, 1,011–1,020.

Kiratzi, A. A., and C. B. Papazachos (1995). Active seismic deformation in the southern Aegean Benioff zone. *Journal of Geodynamics* **19**, 65–78.

Kiratzi, A., and Ch. Benetatos (2008). The 6 January 2008 (*Mw* 6.2) Leonidio (southern Greece) intermediate depth earthquake: Teleseismic body wave modeling. Report to EMSC Web page, http://www.emsc-csem.org/index.php?page=current&sub=recent.

Mai, P. M., P. Spudich, and J. Boatwright (2005). Hypocenter locations in finite-source rupture models. *Bulletin of the Seismological Society of America* **95**, 965–980.

McCloskey, J., S. S. Nalbant, and S. Steacy (2005). Earthquake risk from co-seismic stress. *Nature* **434**, 291.

McGuire, J. J. (2004). Estimating finite source properties of small earthquake ruptures. *Bulletin of the Seismological Society of America* **94**, 377–393.

Novotny, O., J. Zahradnik, and G.-A. Tselentis (2001). Northwestern Turkey earthquakes and the crustal structure inferred from surface waves observed in the Corinth Gulf, Greece. *Bulletin of the Seismological Society of America* **91**, 875–879.

Papazachos, B. C., V. G. Karakostas, C. B. Papazachos, and E. M. Scordilis (2000). The geometry of the Wadati-Benioff zone and lithospheric kinematics in the Hellenic arc. *Tectonophysics* **319**, 275–300.

Roumelioti, Z., Ch. Benetatos, A. Kiratzi, G. Stavrakakis, and N. Melis (2004). A study of the 2 December 2002 (**M** 5.5) Vartholomio (western Peloponnese, Greece) earthquake and of its largest aftershocks. *Tectonophysics* **387**, 65–79.

Rymer, M. J., J. C. Tinsley III, J. A. Treiman, J. R. Arrowsmith, K. B Clahan, A. M. Rossinski, W. A. Bryant, H. A. Snyder, G. S. Fuis, N. A. Toke, and G. W. Bawden (2006). Surface fault slip associated with the 2004 Parkfield, California, earthquake. *Bulletin of the Seismological Society of America* **91**, 211–220.

Sokos, E., and J. Zahradnik (2008). ISOLA a Fortran code and a Matlab GUI to perform multiple-point source inversion of seismic data, *Computers & Geosciences* **34** (8), 967–977.

Somerville, P., K. Irikura, R. Graves, S. Sawada, D. Wald, N. Abrahamson, Y. Iwasaki, T. Kagawa, N. Smith, and A. Kowada (1999). Characterizing crustal earthquake slip models for the prediction of strong ground motion. *Seismological Research Letters* **70**, 59–80.

Thurber, C., H. Zhang, F. Waldhauser, J. Hardebeck, A. Michael, and D. Eberhart-Phillips (2006). Three-dimensional compressional wavespeed model, earthquake relocations, and focal mechanisms for the Parkfield, California, region. *Bulletin of the Seismological Society of America* **96**, S38–S49.

Tibi, R., D. A. Wiens, and H. Inoue (2003). Remote triggering of deep earthquakes in the 2002 Tonga sequences. *Nature* **424**, 921–925.

Tselentis, G.-A., N. S. Melis, E. Sokos, and K. Papatsimpa (1996). The Egion June 15, 1995 (6.2 ML) earthquake, western Greece. *Pure and Applied Geophysics* **147**, 83–98.

Tselentis, G.-A., and J. Zahradnik (2000). Aftershock monitoring of the Athens earthquake of September 7, 1999. *Seismological Research Letters* **71**, 330–337.

Zahradnik, J., E. Sokos, A. Serpetsidaki, and G.-A. Tselentis (2008a). The *Mw* 6.2 Leonidio, southern Greece earthquake of January 6, 2008: Preliminary identification of the fault plane. Report to EMSC Web page, http://www.emsc-csem.org/index.php?page=current&sub=recent.

Zahradnik, J., E. Sokos, G.-A. Tselentis, and N. Martakis (2008b). Non-double-couple mechanism of moderate earthquakes near Zakynthos, Greece, April 2006: Explanation in terms of complexity. *Geophysical Prospecting* **56**, 341–356.

University of Patras Geology Department
Seismological Laboratory
Rio 26504, Patras, Greece
esokos@upatras.gr
(E.S.)

[P4]

GEOPHYSICAL RESEARCH LETTERS, VOL. 35, L21306, doi:10.1029/2008GL035614, 2008

Heterogeneous Coulomb stress perturbation during earthquake cycles in a 3D rate-and-state fault model

F. Gallovič[1]

Received 8 August 2008; revised 7 October 2008; accepted 9 October 2008; published 11 November 2008.

[1] We perform a numerical experiment with quasi-dynamic continuous 3D fault model governed by a laboratory derived rate-and-state friction law. We test several cases in which the Coulomb stress (CS) increases either on the whole fault or only on its part. For the partial stressing we find that if the triggering is almost instantaneous (within 1–2 months), the nucleation takes place in the strike extent of the CS increase area. On the contrary, if the earthquake does not occur within these few months, it can nucleate anywhere on the fault, and even later than without the positive CS load. These features represent new findings which are unique for 3D model and cannot be explained by 1D spring-slider models. The finding might find applications in the aftershock (time-dependent) seismic hazard assessment. **Citation:** Gallovič, F. (2008), Heterogeneous Coulomb stress perturbation during earthquake cycles in a 3D rate-and-state fault model, *Geophys. Res. Lett.*, *35*, L21306, doi:10.1029/2008GL035614.

1. Introduction

[2] Earthquake triggering due to the Coulomb stress (CS) transfer is a well documented phenomenon in seismic active areas [see, e.g., *Steacy et al.*, 2005, and references therein]. The CS change ΔCS is a combination of change in normal stress $\Delta\sigma$ and traction $\Delta\tau$ in the slip direction,

$$\Delta CS = \Delta\tau - \mu\Delta\sigma, \tag{1}$$

where μ is a coefficient of friction. Generally, a positive CS change is considered to bring the fault closer to the failure, while a negative one to delay the earthquake occurrence. Recently, attempts have been made to study the CS triggering for various earthquake fault models [*Dieterich*, 1994; *Gomberg et al.*, 1998; *Roy and Marone*, 1996].

[3] In particular, *Perfettini et al.* [2003] performed a numerical study on CS triggering using 2D rate-and-state fault model explaining the clock advance of the earthquake occurrence due to positive CS change. For example, *Perfettini et al.* [2003] found oscillatory behavior of the clock advance as a function of CS load time around a mean value that is in agreement with simple Coulomb failure model. Note that the CS load was applied on the whole fault and no emphasis was put on the effect of CS on nucleation of the earthquake instability.

[4] In the present paper the study by *Perfettini et al.* [2003] is extended utilizing quasi-dynamic continuous 3D fault model governed by a laboratory derived rate-and-state friction law [*Dieterich*, 1979; *Rice*, 1993]. Besides applying the CS increase on the whole fault, we also apply it on parts of the fault only. Note that the latter cases do not have simple equivalents in the spring-slider models [*Roy and Marone*, 1996], and, therefore, have to be solved numerically. We pay attention to the spatial relation between the area of the CS increase on the fault and the nucleation point position. This is important for seismic hazard assessment, since ground motion estimates are highly sensitive to the nucleation point position.

2. Modeling Approach

[5] We assume a vertical strike-slip 3D fault discretized into $N_L \times N_W$ cells, constantly driven by a plate motion. At any time step t, frictional stress τ_i at fault cell i equals the product of normal stress $\sigma_i(t)$ and friction coefficient μ_i that itself depends on slip velocity $V_i(t)$ and state variable $\theta_i(t)$

$$\tau_i(V_i(t),\theta_i(t),\sigma_i(t)) = \sigma_i(t)\mu_i(V_i(t),\theta_i(t)). \tag{2}$$

[6] We utilize the laboratory-derived rate- and state-dependent coefficient of friction [*Dieterich*, 1979; *Ruina*, 1983], which successfully explains numerous earthquake phenomena [*Scholz*, 1998]. It reads

$$\mu_i(V_i(t),\theta_i(t)) = \mu^* + a_i \ln\left(V_i(t)/V^*\right) + b_i \ln\left(\theta_i(t)V^*/D_c\right), \tag{3}$$

where μ^* is the friction coefficient at reference velocity V^*, a_i and b_i are governing parameters and D_c is the characteristic friction distance. The state variable θ_i evolves as [*Linker and Dieterich*, 1992]

$$\frac{d\theta_i(t)}{dt} = 1 - \frac{V_i\theta_i}{D_c} - \frac{\alpha_i\theta_i}{b_i}\frac{\dot\sigma_i}{\sigma_i}, \tag{4}$$

where parameter α_i controls the state variable response to temporal change in normal stress σ_i.

[7] The frictional stress has to satisfy the shear stress condition on the fault

$$\tau_i(V_i(t),\theta_i(t),\sigma_i(t)) = \tau^0 - \frac{G}{2\beta}\left(V_i(t) - V^{pl}\right) + \sum_{j=1}^{N_L N_W} K_{ij}\left(d_j(t) - V^{pl}t\right) + \Delta\tau_i(t), \tag{5}$$

where τ^0 is the initial stress, V^{pl} represents the loading plate velocity, d_j denotes the slip at cell j and $\Delta\tau_i$ the stress change due to external source. Parameters G and β are shear

[1]Department of Geophysics, Faculty of Mathematics and Physics, Charles University in Prague, Prague, Czech Republic.

0094-8276/08/2008GL035614$05.00

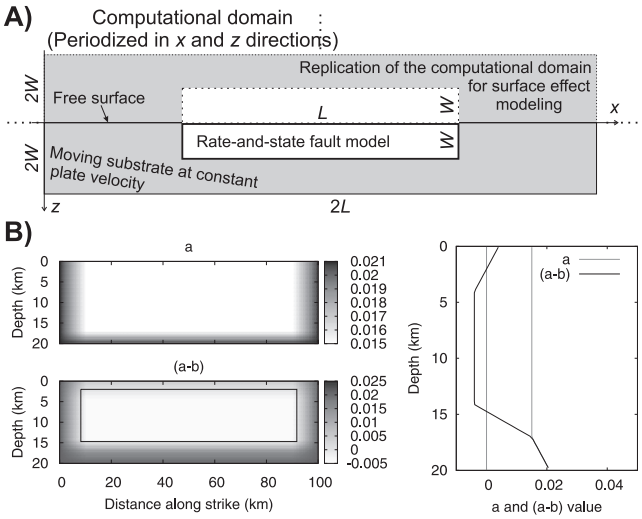

Figure 1. (a) Rate-and-state controlled vertical strike-slip fault (white bold rectangle) in 3D elastic halfspace. The computation domain extends twice the fault length and twice the fault width (solid gray rectangle). The computation is further replicated in the dip direction to account for the free surface effect (dashed rectangles). Due to the use of Fast Fourier Transform in evaluation of the stress distribution, the whole computational domain is in fact replicated in both along strike and along dip directions. Due to the zero-padding the replications do not influence the actual fault evolution. (b) Distribution of (left) a and (a-b) values on the fault and (right) their depth cross-section through the middle of the fault. The inner rectangle in Figure 1b (left) represents a boundary between the velocity weakening ($b > a$, inside the rectangle) and strengthening ($b < a$, outside the rectangle) fault area.

modulus and S-wave velocity, respectively. The second term on the right side imposes the radiation damping [*Rice*, 1993]. Kernel K_{ij} accounts for the static part of the dynamic elastic interactions among the cells (hence quasi-dynamic approach). *Perfettini et al.* [2003] derived this kernel for 2D antiplane fault. Here we use kernel that we have derived in analogous way but for 3D infinite homogeneous isotropic elastic medium (characterized by Lamé's parameters G and λ) utilizing the representation theorem [*Andrews*, 1974] and assuming that the slip remains in the horizontal (strike) direction during the whole earthquake cycle.

[8] Putting right sides of equations (2) and (5) into equation, differentiating it with respect to time, one arrives after simple algebra to a system of $N_L N_W$ ordinary differential equations

$$\frac{dV_i(t)}{dt} = \frac{\sum_{j=1}^{N_L N_W} K_{ij}\left(V_j - V^{pl}\right) - \sigma_i \dot{\theta}_i(\partial\mu_i/\partial\theta_i) - \mu_i\dot{\sigma}_i + \Delta\dot{\tau}_i}{\sigma_i(\partial\mu_i/\partial V_i) + G/(2\beta)}. \quad (6)$$

[9] Note that the last two terms of the numerator correspond to time derivative of the CS change equation (1) realizing that $\dot{\sigma}_i = \Delta\dot{\sigma}_i$. The system equation (6), after inserting equation (3), together with the other system of $N_L N_W$ (equation (4)), is to be integrated numerically to obtain the temporal evolution of slip velocities $V_i(t)$ and state variables $\theta_i(t)$ along the fault. We use Runge-Kutta algorithm with a fifth-order adaptive step-size control [*Press et al.*, 1992]. The sum in equation (6) can be written as a spatial convolution, and is evaluated by means of the 2D Fast Fourier Transform (FFT). Figure 1a shows the problem geometry together with zero-padding that allows to minimize the effect of artificial replications due to the use of FFT.

[10] All the parameters assumed in our study are listed in Table 1 or shown in Figure 1b. The normal stress σ is kept constant throughout the depth, which corresponds to high fluid overpressurization at depth as discussed by *Rice* [1993]. In our setting friction coefficient μ_i varies between 0.60–0.62. The discretization of the computational domain is dense enough to consider our fault model to be continuous [*Rice*, 1993].

3. Modeling Results

3.1. Regular Earthquake Cycle (No Coulomb Stress Load)

[11] At the beginning the fault is set to the steady state with slip velocities equal to the plate velocity ($V_i = V^{pl}$,$\theta_i = D_c/V^{pl}$). To artificially initiate the fault, we increase 10 times the slip velocity in the center of the fault at time $t = 0$ s. After this initiation, the fault evolves to a plate velocity driven regular cycle, which is characterized by periods of slow stable evolution of slip velocities and state variables, and occasional slip velocity instabilities (earthquakes). For the further discussion, we consider the earthquake to start when the slip velocity reaches a more or less arbitrarily chosen value of 1 mm/s anywhere on the fault. Utilizing this definition, the present fault model produces an earthquake instability regularly every 98 years (Figure 2a).

[12] The fault behaves periodically also in terms of distribution of slip velocities along the fault when approaching the instability (Figure 2b). Figure 2b also shows the position of the nucleation point defined as the point at which the slip velocity first reaches 1 mm/s. Note that in this case the nucleation point is doubled as the slip velocity reaches 1 mm/s simultaneously at two symmetrical points. The earthquake ruptures the whole fault.

[13] As an example, the slip accumulated during the period of 200–500 years is shown in Figure 2c. One can see the repetitive slow slip increase at the sides of the fault (governed by the velocity-strengthening border of the fault with $b < a$, see Figure 1b), and the sudden slip increase

Table 1. Parameters of the Model Under Study

Parameter	Description	Value
L	Fault length	100 km
W	Fault width	20 km
N_L	No. of samples along x-axis	1024
N_W	No. of samples along z-axis	256
G	Shear modulus	30 GPa
λ	Lamé's parameter	20 GPa
β	S-wave velocity	3 km/s
σ	Normal stress	75 MPa
V^{pl}	Plate velocity	3.5 cm/yr
D_c	Characteristic friction distance	2 cm
α_i	State variable parameter	0.2, $b_i > 0$ 0.0, $b_i = 0$
μ^*	Reference coefficient of friction	0.6
V^*	Reference slip velocity	1 μm/s

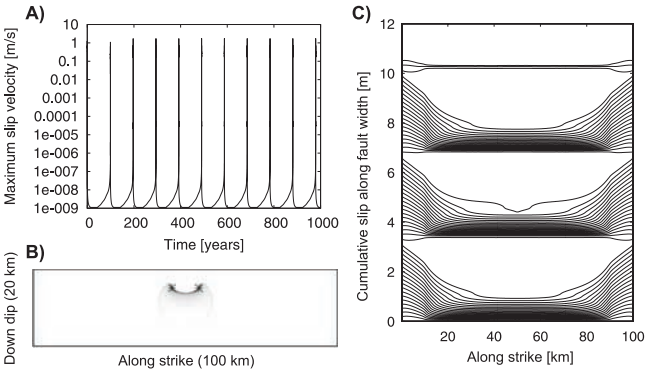

Figure 2. (a) Maximum slip velocity on the fault as a function of time t after the initiation at $t = 0$ yr. The regular earthquake cycle has period of 98 years. (b) Slip velocity snapshot at the time of the nucleation applicable for the third and all later earthquakes after the fault initiation. Stars denote two simultaneous nucleation points. (c) Cumulative slip integrated along the fault width plotted as a function of the along strike distance every 5 years (for the period of 200–500 years). Note the relatively slow creep at sides of the fault and the sudden slip during the earthquake instability.

during the earthquake instabilities in the velocity-weakening part of the fault ($b > a$, see Figure 1b) that balances the slip deficit.

3.2. Homogeneous and Heterogeneous Coulomb Stress Load

[14] Here we disturb the fault from its regular behavior by applying CS load after the earthquake which took place at 392 yr. We test cases in which the CS increases either on the whole fault (homogeneous load) or only on a fault patch (heterogeneous load). The stressed areas are shown in the top of Figure 3a.

[15] We apply the CS increase at various times after 392 yr to study also the influence of the actual stage of the earthquake cycle at which the CS is applied. Figure 3a shows the slip velocity snapshots at the time of the earthquake nucleation together with the nucleation points for various CS load times (rows) and various areas of the CS increase (columns). For simplicity, only increase of the tangential stress by 0.2 MPa or 1.2 MPa in case of homogeneous or patch loads, respectively, is assumed to represent the CS load (equation (1)).

[16] When the whole fault is subject to the CS increase (Figure 3a (left)), the slip velocities along the fault at the time of earthquake nucleation are different than during the regular cycle (Figure 2b) although they remain symmetrical. For some load times the earthquake even ''doubles'', nucleating simultaneously on the two opposite sides of the fault (e.g., for times 430 yr and 485–489 yr).

[17] In cases of the CS increase at parts of the fault (Figures 3a (middle) and 3a (right)), the fault evolution is not symmetrical any more. Early in the seismic cycle, for load times $\leq$470 yr, the earthquake nucleates at various places on the fault, being seemingly not related to the CS increase fault area. On the other hand, later in the earthquake cycle, for load times >470–480 yr, the nucleation point moves to the left part of the fault where the CS increase area is located. Nevertheless, the depth of the nucleation point is not well constrained by the depth of the CS area. Only, as our other test showed, when the CS patch is located exactly in the nucleation zone of the regular cycle, then the actual nucleation point lies in the CS patch for all CS times.

[18] Let us discuss the CS triggering with respect to the earthquake occurrence time. Without any disturbance, the next earthquake would occur at 490 yr during the regular cycle (see Figure 2a). Figure 3b shows the clock advance of the earthquake occurrence as a function of the CS load time. Note that the applied CS load is the same as above. As one can see in Figure 3b, the clock advance is an oscillating function, which is in agreement with the finding by *Perfettini et al.* [2003]. When the CS load is applied to

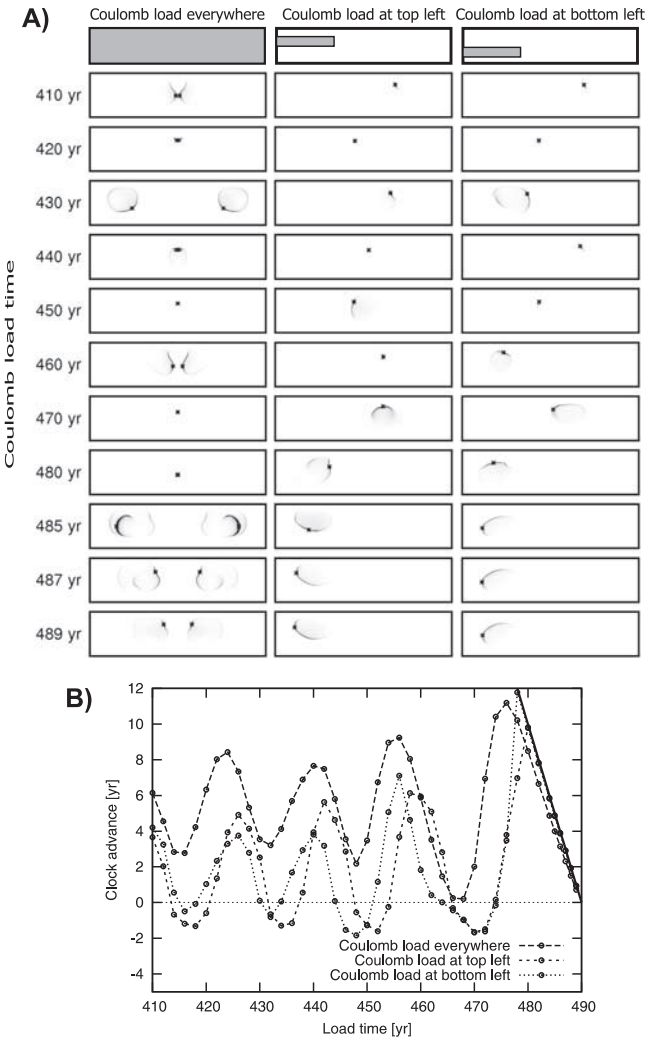

Figure 3. (a) Slip velocity snapshots at the time of earthquake nucleation for various times of the Coulomb load time (rows) and for various Coulomb increase areas on the fault (columns). Stars denote the nucleation points. (b) Clock advance dependence on the Coulomb load time (lines with circles) for the various areas of Coulomb stress increase (see legend). The solid line corresponds to maximum possible (instantaneous) clock advance. Coulomb stress loads are realized by tangential stress increase by 0.2 MPa or 1.2 MPa in case of homogeneous or patch loads, respectively.

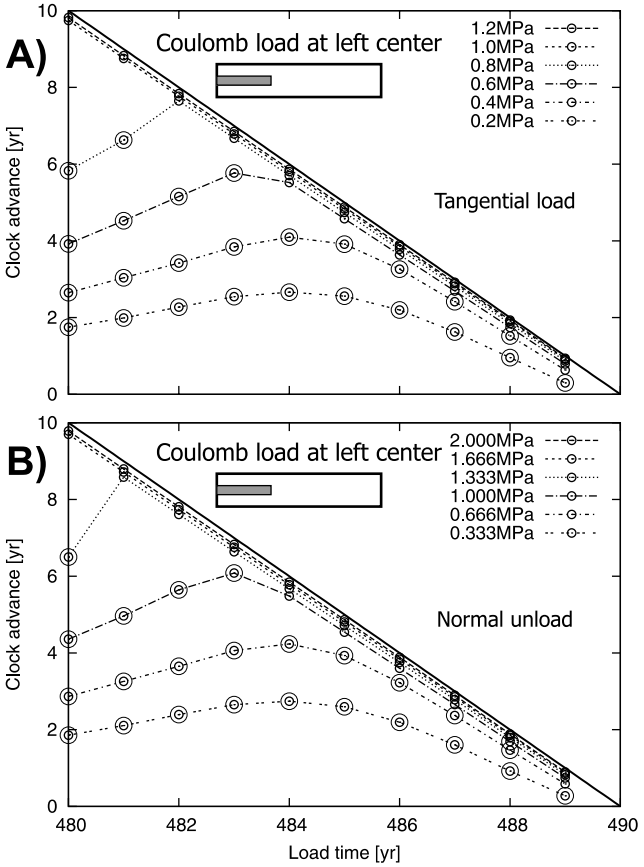

Figure 4. Clock advance as a function of the Coulomb stress load time for last 9 years before the regular earthquake occurrence (dashed lines with small circles). The Coulomb stress change is realized by (a) tangential load or (b) normal unload with various stress amplitudes (see legend). Note that the normal stress unloads, when multiplied by $\mu^* = 0.6$, correspond to the same Coulomb stress changes as realized by means of the tangential loads. The solid line corresponds to maximum possible (instantaneous) clock advance. The large circles are plotted if the nucleation point appear outside of the Coulomb stress change area.

the whole fault, the clock advance is always positive, which means that earthquake occurs always earlier with respect to the regular behavior. On the other hand, in case of stressing at fault patches, for some CS load times the clock advance is negative, meaning that the earthquake is delayed although the applied CS is positive.

[19] The detailed analysis of the modeling results allows a qualitative explanation of the fault response to the heterogeneous CS load. The CS load causes sudden increase of slip velocities in the stressed region. Early in the earthquake cycle when the increase is not strong enough to invoke the major earthquake instability yet, only a smaller event initiates, rupturing only a small part of the whole fault with the largest slip velocities being several orders of magnitude below the threshold in our earthquake definition (1 mm/s). The resulting stress drop increases stress in the surrounding, which then results in a very slow (of the order of km/yr) wave-like progression of the slip velocity-stress disturbance from the CS load area along the fault. As the fault is in the background driven by the plate velocity, at some point the fault may or may not get repetitively again to an almost unstable regime, during which the largest slip velocities do not exceed 1 mm/s, causing again the stress release and generation of the slow slip velocity-stress wave. These effects give rise to a complicated spatial-temporal pattern of rate-and-state behavior, which results not only in the positive clock advance for the major earthquake but also in the negative one, with the nucleation area being not confined in the CS load region.

[20] Let us further examine the CS loads later in the earthquake cycle when the CS load results in slip velocity increase sufficient enough to initiate directly the major earthquake in the CS load area. As the nucleation point is not much sensitive to the depth of the CS increase area (Figure 3a), we arbitrarily select area of the same size as before but located in the middle depth of the fault. Figure 4a shows clock advance as a function of load time (480–490 years) for various values of the tangential stress load. Figure 4b shows equivalent results obtained for normal stress unload. Note that tangential and normal stress values assumed (see legend in Figures 4a and 4b) correspond to the same CS change (equation (1)), regarding $\mu = 0.6$. As one can see, the resulting clock advances are almost the same in both cases, which supports the finding by *Perfettini et al.* [2003] that the results are independent on how the CS load is realized. Note that this holds even for earlier CS load times.

[21] Figure 4 shows that the clock advance approaches the instantaneous triggering (represented by the solid line in Figure 4) when increasing the CS load time. The way how it approaches depends on the CS value: The lower is the CS value, the later the CS load has to be applied to trigger the earthquake almost instantaneously (within 1–2 months after the stress load). Figure 4 also shows, by larger circles, cases when the nucleation point lies outside of the CS change area. As one can see, for the cases of almost instantaneous triggering the nucleation point lies in the Coulomb change area (see also Figures 3a (middle) and 3a (right)).

4. Conclusions, Implications, and Limitations

[22] We have studied Coulomb stress (CS) triggering for a 3D quasi-dynamic rate-and-state continuous fault model. We have applied positive CS loading at various stages of the seismic cycle not only on the whole fault as done by *Perfettini et al.* [2003] (in 2D), but also on only parts of the fault. Note that the latter cases do not have simple equivalents in the spring-slider models, and, therefore, have to be solved numerically. We have discussed the resulting clock advance and the mutual position of the nucleation point and the CS load area.

[23] This issue is of interest for seismic hazard assessment due to triggered earthquakes (aftershocks). It is because the nucleation point position on the fault strongly affects the spatial distribution of strong ground motions. Without any knowledge of the nucleation point the hazard maps are symmetrical around the anticipated fault [*Gallovič and Brokešová*, 2008]. The present paper shows that the rate-and-state fault model can help in constraining the hazard calculations. Let us assume that a strong earthquake has occurred and increased Coulomb stress on some part of a nearby active fault. One may expect that within the next

two months (the period of an almost instantaneous triggering, see above) the nucleation point will be located in the strike extent of the CS increase area, independently on the CS load amplitude. Such constraint might significantly modify the (time-dependent) hazard maps due to, e.g., highly pronouncing directivity effect. After this 'favorable' period of the two months the anticipated fault may still be triggered (not almost instantaneously), but in this case it can nucleate anywhere, and, moreover, even later than without the positive CS load.

[24] The studied model is highly idealized. Among others, no other interaction effects (such as viscoelastic stress transfer, pore pressure changes, etc.) than the static elastic stress redistribution are assumed. The other simplifications are perfectly planar vertical strike-slip fault, almost homogeneous distribution of the friction parameters (a, b, α), constant normal stress, and homogeneous medium embedding the fault, etc. We also select only few particular cases of the CS load areas (in terms of position and size). Nevertheless, we have found some new features of the rate-and-state fault response to the heterogeneous Coulomb stress load. Our results have to be considered as exploratory and suggestive to seek evidences in real triggering sequences. This, however, goes beyond the extent of this paper, and is left for further studies.

[25] **Acknowledgments.** Jiří Zahradník and an anonymous reviewer helped to improve the manuscript. The work is a part of the following projects supported in the Czech Republic: GACR 205/07/0502, PostDoc GACR 205/08/P013, GAUK 279/2006/B-GEO/MFF, and MSM 0021620860.

References

Andrews, D. J. (1974), Evaluation of static stress on a fault plane from a green's function, *Bull. Seismol. Soc. Am.*, *64*, 1629–1633.

Dieterich, J. H. (1979), Modeling of rock friction: 1. Experimental results and constitutive equations, *J. Geophys. Res.*, *84*, 2161–2168.

Dieterich, J. H. (1994), A constitutive law for rate of earthquake production and its application to earthquake clustering, *J. Geophys. Res.*, *99*, 2601–2618.

Gallovič, F., and J. Brokešová (2008), Probabilistic aftershock hazard assessment II: Application of strong ground motion modeling, *J. Seismol.*, *12, 65–78.*

Gomberg, J., N. M. Beeler, M. L. Blanpied, and P. Bodin (1998), Earthquake triggering by transient and static deformations, *J. Geophys. Res.*, *103*, 24,411–24,426.

Linker, M. F., and J. H. Dieterich (1992), Effects of variable normal stress on rock friction: Observations and constitutive equations, *J. Geophys. Res.*, *97*, 4923–4940.

Perfettini, H., J. Schmittbuhl, and A. Cochard (2003), Shear and normal load perturbations on a two-dimensional continuous fault: 1. Static triggering, *J. Geophys. Res.*, *108*(B9), 2408, doi:10.1029/2002JB001804.

Press, W. H., B. P. Flannery, S. A. Teukolsky, and W. T. Vetterling (1992), *Numerical Recipes in Fortran: The Art of Scientific Computing*, 2nd ed., Cambridge Univ. Press, New York.

Rice, J. R. (1993), Spatio-temporal complexity of slip on a fault, *J. Geophys. Res.*, *98*, 9885–9907.

Roy, M., and C. Marone (1996), Earthquake nucleation on model faults with rate- and state-dependent friction: Effects of inertia, *J. Geophys. Res.*, *101*, 13,919–13,932.

Ruina, A. L. (1983), Slip instability and state variable fricton laws, *J. Geophys. Res.*, *88*, 10,359–10,370.

Scholz, C. H. (1998), Earthquakes and friction laws, *Science*, *391*, 37–42.

Steacy, S., J. Gomberg, and M. Cocco (2005), Introduction to special section: Stress transfer, earthquake triggering, and time-dependent seismic hazard, *J. Geophys. Res.*, *110*, B05S01, doi:10.1029/2005JB003692.

F. Gallovič, Department of Geophysics, Faculty of Mathematics and Physics, Charles University in Prague, V Holešovičkách 2, Praha 8, 180 00 Czech Republic. (gallovic@karel.troja.mff.cuni.cz)

[P5]

Earthquake early warning system in southern Italy: Methodologies and performance evaluation

A. Zollo,[1] G. Iannaccone,[2] M. Lancieri,[2] L. Cantore,[1,3] V. Convertito,[2] A. Emolo,[1] G. Festa,[1] F. Gallovič,[1,4] M. Vassallo,[1,3] C. Martino,[1,3] C. Satriano,[1,3] and P. Gasparini[1,3]

Received 17 November 2008; revised 13 January 2009; accepted 15 January 2009; published 27 February 2009.

[1] We investigate the effect of extended faulting processes and heterogeneous wave propagation on the early warning system capability to predict the peak ground velocity (PGV) from moderate to large earthquakes occurring in the southern Apennines (Italy). Simulated time histories at the early warning network have been used to retrieve early estimates of source parameters and to predict the PGV, following an evolutionary, probabilistic approach. The system performance is measured through the Effective Lead-Time (ELT), i.e., the time interval between the arrival of the first S-wave and the time at which the probability to observe the true PGV value within one standard deviation becomes stationary, and the Probability of Prediction Error (PPE), which provides a measure of PGV prediction error. The regional maps of ELT and PPE show a significant variability around the fault up to large distances, thus indicating that the system's capability to accurately predict the observed peak ground motion strongly depends on distance and azimuth from the fault. **Citation:** Zollo, A., et al. (2009), Earthquake early warning system in southern Italy: Methodologies and performance evaluation, *Geophys. Res. Lett.*, *36*, L00B07, doi:10.1029/2008GL036689.

1. Introduction

[2] Earthquake Early Warning Systems (EEWS) are real-time information systems that are able to provide an alert on the potential damaging effects of an impending earthquake through the rapid telemetry and processing of data from dense instrument arrays deployed in the source region (regional systems) or in the site where the target to be protected is located (on-site systems) [*Kanamori*, 2005]. Following different technological and methodological approaches, prototypes or validated EEWS are currently operating in Japan, California (USA), Taiwan, Mexico, Turkey and Romania.

[3] In 2005, the development and implementation of a *regional* EEWS was started in southern Italy, based on a dense, wide dynamic seismic network deployed along the Apenninic belt region [*Weber et al.*, 2007], equipped with both acceleration and velocity sensors (see auxiliary material).[1] This is the region where large, destructive earthquakes in Italy have occurred during last centuries and there exist a significant probability for a $M > 5.5$ earthquake occurrence in the next decade [*Cinti et al.*, 2004].

[4] Methodologies for earthquake early warning assume a point-source model of the earthquake source and isotropic wave amplitude attenuation. These assumptions may be inadequate to describe the earthquake source and wave amplitude attenuation effects and they can introduce significant biases in the real-time estimation of earthquake location and magnitude. This issue is critically related to the EEWS performances in terms of expected lead-time (i.e., the time available for earthquake mitigation actions before the arrival of damaging waves) and of uncertainties in predicting the peak ground motion at the site of interest.

[5] The best practice would be to use the recordings of past strong earthquakes acquired at the network stations and, by means of an off-line analysis, to investigate the system capabilities to rapidly estimating the source parameters. This is not possible in the southern Apennines due to the relatively low seismicity rate in the magnitude range $M > 6$ and to the young age of the implemented EEWS. Therefore we adopted a different strategy, where the efficiency of early warning methodologies are investigated by the simulation of a large number of M6.9 and M6.0 earthquake scenarios, including the use of a standard 1-D Ground Motion Predictive Equation (GMPE) to predict the peak motion at distant sites.

2. Synthetic Waveforms and Earthquake Ground Motion Scenarios

[6] A massive synthetic waveform data-base has been produced for testing the performance of the southern Italy EEWS, using waveform play-back procedures which run off-line on simulated, synchronized earthquake records.

[7] The synthetic waveforms have been computed using the hybrid k-squared source model [*Gallovič and Brokesova*, 2007], which combines the integral approach based on the evaluation of the representation theorem for the low frequencies (<1 Hz) and the composite approach for the high frequencies (1–20 Hz). Both approaches are based on a common set of sub-sources providing "k-squared" slip distribution [*Herrero and Bernard*, 1994]. The source model is coupled with full-wavefield bedrock Green's functions for a 1D layered crustal model determined by the discrete wave-number method [*Bouchon*, 1981].

[1] Dipartimento di Scienze Fisiche, Università di Napoli "Federico II," Naples, Italy.
[2] Osservatorio Vesuviano, Istituto Nazionale di Geofisica e Vulcanologia, Naples, Italy.
[3] AMRA Scarl, Naples, Italy.
[4] Department of Geophysics, Charles University, Prague, Czech Republic.

0094-8276/09/2008GL036689$05.00

[1] Auxiliary materials are available in the HTML. doi:10.1029/2008GL036689.

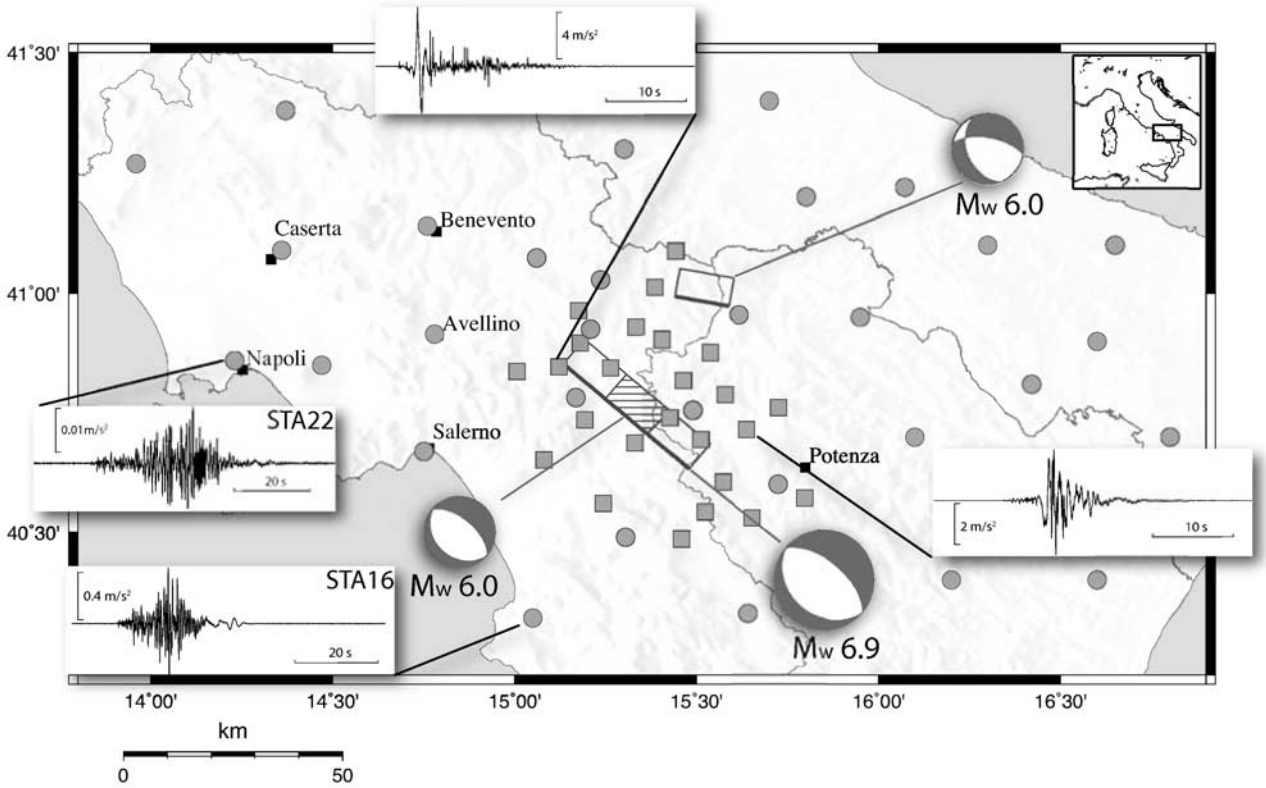

Figure 1. Acquisition layout of the numerical experiment for the evaluation of the EEW system performances and examples of synthetic accelerograms. Synthetic seismograms are computed at the early warning network (squares) and at a set of virtual stations (circles) in order to obtain a better coverage at regional scale. The locations of STA22 and STA16, whose PE plots are shown in Figure 2, are also indicated. The location, fault extent, focal mechanisms and moment magnitude of the simulated earthquakes are also shown.

[8] In this study we have simulated possible rupture scenarios for one M6.9 and two M6 earthquakes (Figure 1). The faults characteristics used for simulations are from the Italian active fault catalogue [*Basili et al.*, 2008]. The fault responsible for the main sub-event of the 1980 Irpinia earthquake is assumed as the source of the M6.9 earthquake. This fault is a NE dipping normal fault, striking along the Apennines direction (Figure 1). In the middle of the fault we assume a M6 event. The third M6 source is related to the causative fault of the 1930 earthquake that is a predominantly normal fault NE dipping located close to the north-eastern edge of the seismic network.

[9] The synthetic accelerograms corresponding to each earthquake scenario have been computed at the irregular grid of receivers shown in Figure 1. Only the ISNet stations are used for the real-time location and magnitude determination. For the Green's functions calculations, the 1D velocity model of *Improta et al.* [2003] is assumed.

[10] In total, 2 × 90 and 300 scenarios for the two M6 and the M6.9 earthquake, respectively, have been computed by considering variable nucleation points in the lower half of the fault, slip, and rupture velocity. The scenarios provide relatively large variability of the synthetics as illustrated in Figures 1 and 2. In order to make synthetic waveforms realistic in terms of ambient noise and site response, the records have been modified by adding synthetic noise as inferred from the observed power spectral density curves and by convolution with site transfer functions generated using the *Kennett*'s [1983] reflection matrix approach and P-, S-velocity and density profiles obtained from the Italian strong motion database (Working Group ITACA, 2008, http://itaca.mi.ingv.it).

3. Data Processing and Results

[11] We implemented a real-time, probabilistic evolutionary algorithm for early warning, whose main components are the automatic first-P picking, event location, magnitude estimation and prediction of ground motion intensity measure at a given target site.

[12] The automatic picks of P-arrival times on synthetic traces have been preliminarily carried out using a standard STA/LTA algorithm. The synthetic records have been filtered using a two poles, zero-phase shift Butterworth filter, in the frequency band 0.075–3 Hz following the processing scheme detailed by *Zollo et al.* [2006, 2007]. The three-component accelerograms have been double-integrated to obtain displacement and to evaluate the peak amplitude modulus in a time window Δt, as $PD = \max_{t \in Dt}\left(\sqrt{NS(t)^2+EW(t)^2+UD(t)^2}\right)$.

[13] At each second after the first automatically detected P-pick, the real-time location procedure proposed by *Satriano et al.* [2008] (RTLoc) is used to provide the hypocentral location, as soon as the first P–measurement is made available. Magnitudes are estimated from PD values in windows of 2 and 4 seconds for the P phase, and 2 seconds for the S phase following a Bayesian approach [*Lancieri*

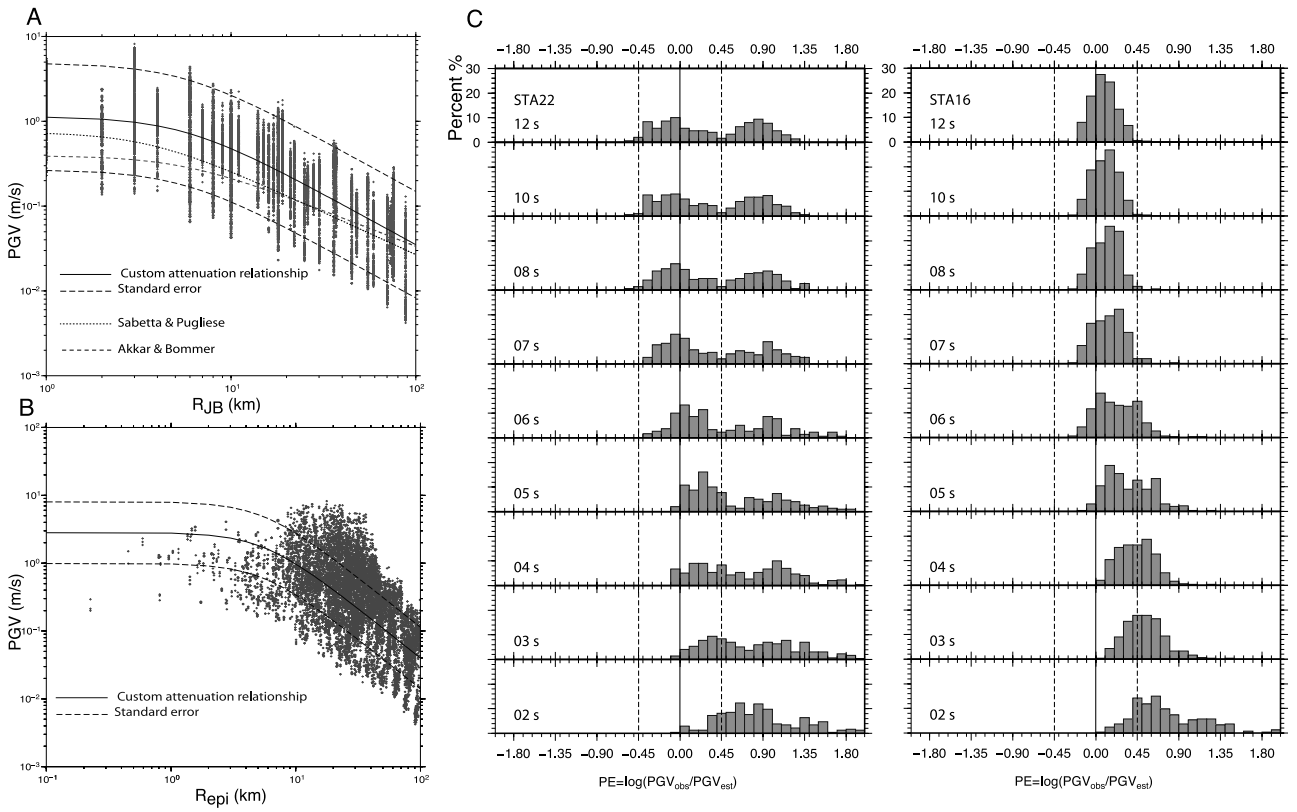

Figure 2. Comparison of synthetic PGV vs distance for various attenuation relationships assuming the M6.9 earthquake. (a) Synthetic database for PGV as function of the fault distance for the M 6.9 simulated earthquake. The GMPE for PGV (black line) has been obtained by measuring the peak (maximum between the two horizontal components) on synthetics and correlating to magnitude M and distance D, where D is defined as the minimum distance from the fault (Figure 2a) or the epicentral distance (Figure 2b). The dotted and dashed lines refer to the GMPEs proposed by *Sabetta and Pugliese* [1996] and *Akkar and Bommer* [2007], respectively. (b) Synthetic database for PGV as function of the epicentral distance for the M6.9 simulated earthquake. Black continuous line refers to the regression analysis performed in the present study, along with the estimated 1-sigma uncertainty bounds. The standard error value σ_E has been used in the definition of the Probability of Prediction Error (PPE) (see text). (c) Examples of PE distribution (see text for definition) vs time from the first P-arrival detected at the EW network at stations STA22 and STA16 (see Figure 1). The histograms are built based on synthetic accelerograms computed for 300 earthquake scenarios relative to an M 6.9 earthquake occurring inside the network. Ordinates are expressed in percent of the total number of scenarios. Dashed lines indicate the 1-sigma interval of the used GMPE.

and Zollo, 2008] (RTMag). PD values have been corrected for the distance attenuation and normalized at a reference distance of 10 km, based on a regression relationship between PD and magnitude and hypocentral distance obtained from synthetic waveforms.

[14] The earthquake location and magnitude parameters are used to predict the PGV at regional scale using the synthetic GMPE (Figure 2 and auxiliary material). Both representations in terms of the distance from the closest point of the fault and from the epicenter are shown in Figures 2a and 2b, the latter being used in the early warning methodology.

[15] At each second after the event origin and for each analyzed scenario, the earthquake location and magnitude predicted by the early warning procedures allows the estimation of i) the Maximum Lead-Time (MLT) (i.e., the delay of the S-phase arrival at the target with the time of first location and magnitude estimations), and ii) the Prediction Error on log(PGV), defined as PE = log (PGV^{obs}/PGV^{pred}), where PGV^{obs} is the PGV measured on the synthetic waveforms and PGV^{pred} is the value predicted by the EEWS using the synthetic GMPE model and the estimated earthquake location and magnitude.

[16] Furthermore, given the whole number of earthquake scenarios for a single earthquake, one can compute the distribution of parameter PE at each time step. Figure 2c displays examples of the evolutionary distribution of PE computed at two different sites for the M6.9 earthquake. The shape of the PE distribution depends on errors and failures on event identification and picking, on the complexity of the rupture process, on the number of stations used for early estimation of location and magnitude, and on the accuracy of the GMPE. The ideal distribution of the PE would be the one centered at 0 and having standard deviation smaller or comparable with that of the adopted GMPE model.

[17] Examples in Figure 2 indicate a time after the event origin, beyond which the distribution becomes stable, i.e., the addition of new observations does not change signifi-

cantly the distribution of PE, although its shape may differ from site to site.

[18] In general, the distributions in sites located along a direction orthogonal to the fault strike appear unimodal, while those for sites located along the strike direction are bimodal and show a larger dispersion. This can be attributed to persistent directivity effects contained in the simulated waveforms which, for some sites, cause data to be distributed symmetrically with respect to the GMPE that represents the median value.

[19] Following the example in Figure 2c, the Effective Lead-Time (ELT) at a given site can be defined as the time interval between the arrival of first S-wave and the time at which the distribution of parameter PE does not change with time. Denoting σ_E the standard deviation of the adopted GMPE model for PGV, we define the following stability criterion for PE distribution: given the range $[-\sigma_E; +\sigma_E]$ for the parameter PE, its distribution is stationary when the probability $P(PE \in [-\sigma_E; +\sigma_E])$ does not change significantly with time, i.e., less than 2%. We denote this probability as the Probability of Prediction Error (PPE), which is used, jointly with ELT, as an indicator of EEWS system performance, in terms of system capability to predict the strong motion parameter PGV, e.g., high values of PPE indicate acceptable system performances. Figure 3 shows the final results of EEWS performance analysis for a characteristic earthquake of M6.9 occurring inside the area covered by the seismic network. Results from simulations of M6 earthquakes occurring inside and at the border of the network are provided as auxiliary material. Concerning the event at the border of the network, we observe that the area with low values of PPE is larger while the ELT are generally smaller.

[20] The map of MLT and related variability are displayed in Figure 3a. A larger variability of parameter MLT is expected along the fault strike direction, because of the variability of rupture nucleation points along the fault. The MLT map should be directly compared with that of ELT (Figure 3b). The latter presents a shadow zone around the fault, having a radius of about 30 km, where we expect negative ELTs. It implies that for most scenarios the prediction of the PGV can be still improved as the magnitude value is updating: effectiveness of prediction inside the network may therefore depend on the specific source characteristics. As compared to the isotropic distribution of MLTs, the ELTs are on average 5s to 7s smaller, indicating that a value of magnitude for which the prediction becomes stable requires the P information from almost half of ISNet stations, with few of them already providing the 2s-S peak displacement. When comparing the ELT isolines to an isotropic distribution, we note a more pronounced elongation of ELT along the NW–SE, fault strike direction. Such a behavior can be related to the source radiation pattern and directivity, which are dominant along the fault strike direction with respect to other possible source complexities. Along the fault-strike direction the observed PGV is systematically higher than the predicted one and the probability to capture the true PGV (within one standard deviation) becomes quickly insensitive to improvements in the magnitude estimate.

[21] As concerns the distribution of parameter PPE (Figure 3c), smaller values are still concentrated in the fault strike direction and they can be ascribed to the dominant directivity effect as well as to wrong interpretation of the distance in the used attenuation law. The different station coverage, which are densely distributed in the Southern part of the fault, is the cause for higher values of PPE in the SE sector relative to NW. Finally PPE is high in the fault orthogonal direction, where large values indicate that the variability induced by finite fault effects is smoothed along this direction.

4. Discussion and Conclusions

[22] We have investigated the performance of the southern Italy EEWS in case of extended faulting processes occurring inside and at the border of the network. We have introduced the Effective Lead-Time, and the Probability of Prediction Error, the latter being an indicator of EEWS efficiency to predict the PGV. ELT shows a pronounced anisotropy along the fault-strike direction which is controlled by the focal mechanism and directivity. The map of PPE provides an image of the distribution of the prediction error related to different effects: network configuration, earthquake size and mechanism, attenuation relationship. In the analyzed case, it shows a larger variability around the fault, even at large distances, denoting the influence of rupture process complexity on EEWS capability to accurately predict the PGV at target sites.

[23] The map of PPE shows that systematic failures in PGV predictions may occur for sites located in or close to the fault strike direction, where observations are generally underestimated due to dominant directivity effects. As concerning the fault finiteness, the distance definition used for early warning needs to be revisited and the closest distance to the fault is likely to be the preferred distance in GMPE model. Improving the ground motion prediction of large earthquakes, at distances comparable with fault extension, requires the real time estimation of the fault geometry. The strike and slip can also be constrained 'a priori' by the tectonic context in which the earthquake occurs, while the fault extension can be related to the magnitude by empirical relationships [e.g., *Wells and Coppersmith*, 1994].

[24] The proposed methodology can be used to measure the performance of any operational EEWS, as well as a tool

Figure 3. Regional maps of Early Warning System performance indicators. The maps are computed for 300 earthquake scenarios for an M 6.9 occurring inside the network. See Figure 1 for earthquake location, fault extent and mechanism. (a) Distribution of average Maximum Lead-Time (MLT) in seconds (isolines) and the associated range of variation (grey shade). (b) Distribution of the Effective Lead-Time (ELT) in seconds. The shaded area inside the network indicates a zone with negative ELTs, where S-waves arrive before the distribution of PE becomes stable. (c) Distribution of PPE, the Probability of Prediction Error on parameter log (PGV) (see text for details). Shaded areas are obtained from a discrete representation of PPE, where lighter regions indicate a better efficiency of the EEWS to predict the PGV relative to darker regions.

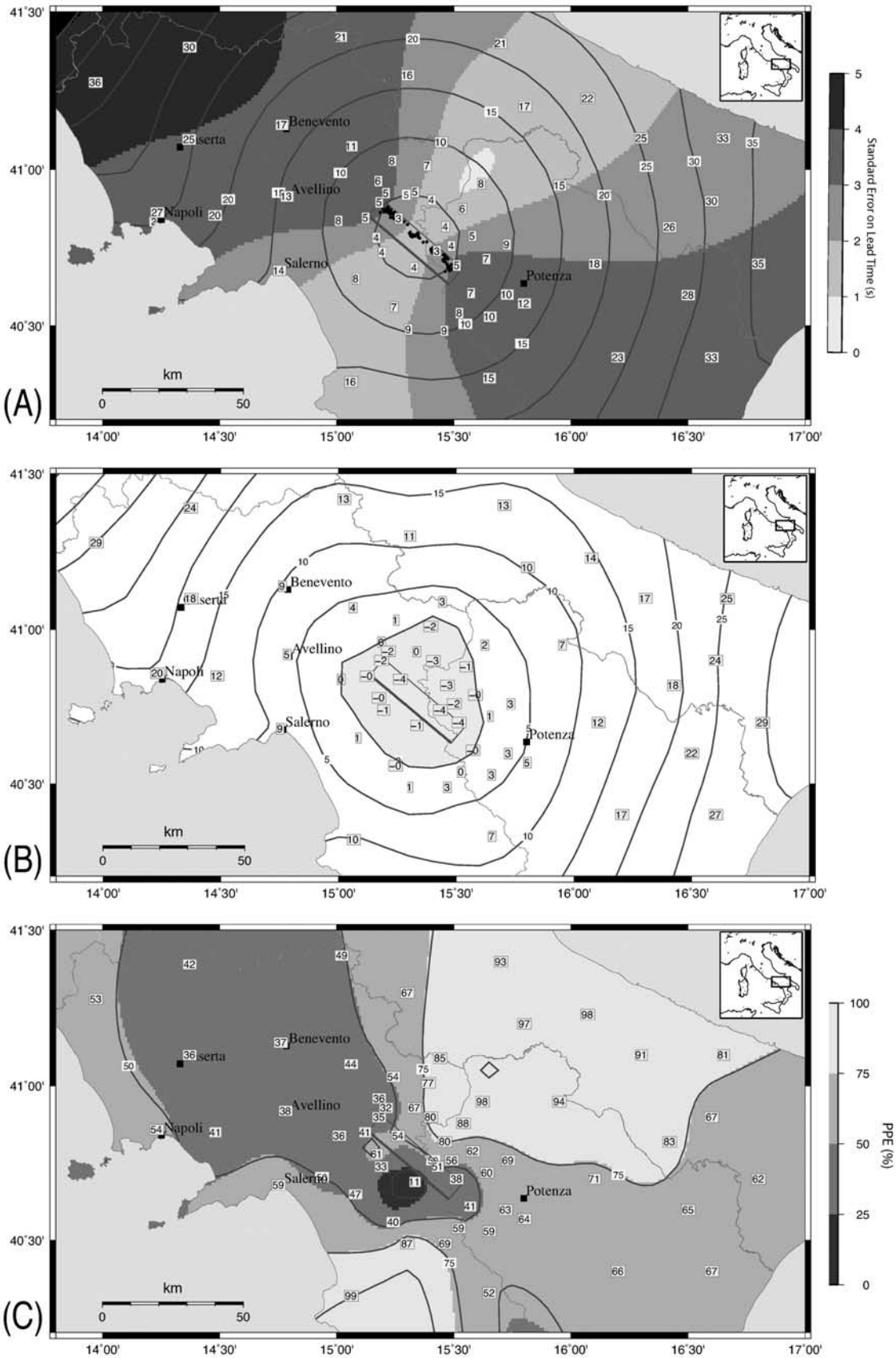
(A)
(B)
(C)
Benevento
Avellino
Napoli
Salerno
Potenza
km
0
50
14°00'
14°30'
15°00'
15°30'
16°00'
16°30'
17°00'
41°30'
41°00'
40°30'
Standard Error on Lead Time (s)
PPE (%)

Figure 3

for designing the optimal station distribution, according to faults existing in a given area. The joint computation of ELT and PPE maps can be used to identify the potential applications of an EEWS as a function of distance from the earthquake causative fault. Based on the inventory of possible automated and individual actions to be performed in few tens of seconds preceding the arrival of strong shaking [e.g., *Goltz*, 2002], the ELT and PPE maps can serve to identify which targets can be protected (schools, hospitals, high speed trains, ...) and to design the adequate mitigation action, given the available time and probability of prediction error.

[25] Concerning the southern Italy EEWS the effectiveness of prediction depends on the specific scenario, whose real-time characterization becomes crucial for issuing an alert. As an example, for the densely populated Naples urban area, ELT can range between 8*s* and 16*s*, and PPE between 50% and 60%, indicating that several mitigation actions could be effective before S-waves shake the town.

[26] We finally remark that a fully functional seismic network has been assumed, although failures in the technological components (sensors, data-loggers and transmission system) may occur during a large earthquake. A complete analysis would therefore require an intersection of the prediction with the probability of missing data from few stations.

[27] **Acknowledgments.** We wish to thank the two anonymous reviewers for their useful comments and suggestions. This work was partially funded by AMRA scarl through the EU-SAFER project (contract 036935).

References

Akkar, S., and J. J. Bommer (2007), Empirical prediction equations for peak ground velocity derived from strong-motion records from Europe and the Middle East, *Bull. Seismol. Soc. Am.*, *97*, 511–530, doi:10.1785/0120060141.

Basili, R., G. Valensise, P. Vannoli, P. Burrato, U. Fracassi, S. Mariano, M. M. Tiberti, and E. Boschi (2008), The database of individual seismogenic sources (DISS), version 3: Summarizing 20 years of research on Italy's earthquake geology, *Tectonophysics*, *453*, 20–43, doi:10.1016/j.tecto.2007.04.014.

Bouchon, M. (1981), A simple method to calculate Green's functions for elastic layered media, *Bull. Seismol. Soc. Am.*, *71*, 959–971.

Cinti, F. R., L. Faenza, W. Marzocchi, and P. Montone (2004), Probability map of the next M $\geq$ 5.5 earthquakes in Italy, *Geochem. Geophys. Geosyst.*, *5*, Q11003, doi:10.1029/2004GC000724.

Gallovič, F., and J. Brokesova (2007), Hybrid k-squared source model for strong ground motion simulations: Introduction, *Phys. Earth Planet. Inter.*, *160*, 34–50.

Goltz, J. D. (2002), Introducing earthquake early warning in California: A summary of social science and public policy issues, technical report, Governor's Off. of Emergency Serv., Pasadena, Calif.

Herrero, A., and P. Bernard (1994), A kinematic self-similar rupture process for earthquakes, *Bull. Seismol. Soc. Am.*, *84*, 1216–1228.

Kanamori, H. (2005), Real-time seismology and earthquake damage mitigation, *Annu. Rev. Earth Planet. Sci.*, *33*, 195–214.

Kennett, B. L. N. (1983), *Seismic Wave Propagation in Stratified Media*, 342 pp., Cambridge Univ. Press, Cambridge, U. K.

Improta, L., M. T. Bonagura, P. Capuano, and G. Iannaccone (2003), An integrated geophysical investigation of the upper crust in the epicentral area of the 1980, M_s = 6.9, Irpinia earthquake (southern Italy), *Tectonophysics*, *361*, 139–169.

Lancieri, M., and A. Zollo (2008), A Bayesian approach to the real-time estimation of magnitude from the early *P* and *S* wave displacement peaks, *J. Geophys. Res.*, *113*, B12302, doi:10.1029/2007JB005386.

Sabetta, F., and A. Pugliese (1996), Estimation of response spectra and simulation of nonstationary earthquake ground motion, *Bull. Seismol. Soc. Am.*, *86*, 337–352.

Satriano, C., A. Lomax, and A. Zollo (2008), Real-time evolutionary earthquake location for seismic early warning, *Bull. Seismol. Soc. Am.*, *98*, 1482–1494, doi:10.1785/0120060159.

Weber, E., et al. (2007), An advanced seismic network in the southern Apennines (Italy) for seismicity investigations and experimentation with earthquake early warning, *Seismol. Res. Lett.*, *78*, 622–634.

Wells, D. L., and K. J. Coppersmith (1994), New empirical relationships among magnitude, rupture length, rupture width, rupture area, and surface displacement, *Bull. Seismol. Soc. Am.*, *84*, 974–1002.

Zollo, A., M. Lancieri, and S. Nielsen (2006), Earthquake magnitude estimation from peak amplitudes of very early seismic signals on strong motion records, *Geophys. Res. Lett.*, *33*, L23312, doi:10.1029/2006GL027795.

Zollo, A., M. Lancieri, and S. Nielsen (2007), Reply to comment by P. Rydelek et al. on "Earthquake magnitude estimation from peak amplitudes of very early seismic signals on strong motion records", *Geophys. Res. Lett.*, *34*, L20303, doi:10.1029/2007GL030560.

L. Cantore, A. Emolo, G. Festa, F. Gallovič, P. Gasparini, C. Martino, C. Satriano, M. Vassallo, and A. Zollo, Dipartimento di Scienze Fisiche, Università di Napoli "Federico II," via Cintia, I-80126 Naples, Italy. (aldo.zollo@unina.it)

V. Convertito, G. Iannaccone, and M. Lancieri, Osservatorio Vesuviano, Istituto Nazionale di Geofisica e Vulcanologia, via Diocleziano 328, I-80124 Naples, Italy.

[P6]

Bulletin of the Seismological Society of America, Vol. 99, No. 2A, pp. 647–663, April 2009, doi: 10.1785/0120080240

Uncertainties in Strong Ground-Motion Prediction with Finite-Fault Synthetic Seismograms: An Application to the 1984 *M* 5.7 Gubbio, Central Italy, Earthquake

by Gabriele Ameri, František Gallovič, Francesca Pacor, and Antonio Emolo

Abstract This study investigates the engineering applicability of two conceptually different finite-fault simulation techniques. We focus our attention on two important aspects: first to quantify the capability of the methods to reproduce the observed ground-motion parameters (peaks and integral quantities); second to quantify the dependence of the strong-motion parameters on the variability in the large-scale kinematic definition of the source (i.e., position of the nucleation point, value of the rupture velocity, and distribution of the final slip on the fault).

We applied an approximated simulation technique, the deterministic-stochastic method and a broadband technique, the hybrid-integral-composite method, to model the 1984 M_w 5.7 Gubbio, central Italy, earthquake, at five accelerometric stations. We first optimize the position of the nucleation point and the value of the rupture velocity for three different final slip distributions on the fault by minimizing an error function in terms of acceleration response spectra in the frequency band from 1 to 9 Hz. We found that the best model is given by a rupture propagating at about 2.65 km/sec from a hypocenter located approximately at the center of the fault. In the second part of the article we calculate more than 2400 scenarios varying the kinematic source parameters. At the five sites we compute the residuals distributions for the various strong-motion parameters and show that their standard deviations depend on the source parameterization adopted by the two techniques. Furthermore, we show that Arias Intensity (AI) and significant duration are characterized by the largest and smallest standard deviation, respectively. Housner Intensity is better modeled and less affected by uncertainties in the source kinematic parameters than AI. The fact that the uncertainties in the kinematic model affects the variability of different ground-motion parameters in different ways has to be taken into account when performing hazard assessment and earthquake engineering studies for future events.

Introduction

Earthquake engineering analysis requires, as seismic input, a reliable and complete characterization of ground motion both in time and frequency domains. This information is needed especially with the increasing number of applications of nonlinear analysis techniques aimed at assessing the structural response and damage estimation from future seismic events. For time-series analysis, engineers often use a suite of natural accelerograms from past earthquakes that, based on certain selection criteria (magnitude, distance, site class, strong-motion parameter, tectonic environment, spectral matching, etc.), are suitable for the purpose (Stewart *et al.*, 2001; Bommer and Acevedo, 2004; Iervolino and Cornell, 2005). For other applications, such as hazard assessment or linear analysis for loss estimations in urban areas, the whole time series is not always necessary and an instantaneous measure of motion (e.g., peak ground acceleration [PGA]) could represent a satisfactory description. The level of ground motion for a particular site is generally assessed by means of ground motion prediction equations, where a ground-motion parameter (in general PGA, peak ground velocity [PGV], or spectral acceleration) is provided as a function of magnitude, distance, and site condition (Douglas, 2003 and references therein). In both cases the prediction of ground motion from future events can, thus, be estimated by using data recorded during past earthquakes.

It is accepted today that problems arise from the use of recorded data for prediction of future ground motions. Indeed, despite the huge growth of the recorded database dur-

ing the last years due to the increasing number of strong-motion networks installed in high-seismicity areas, the set of existing recordings always represents only a subset of possible earthquake scenarios. Consequently, the greater the number of parameters to be specified for the selection of natural accelerograms, the lower the number of them that will be extracted from the strong-motion database for the specific analysis. To keep this number reasonable (i.e., statistically significant), engineers are compelled to either reduce the number of searching criteria or expand the limits of the searching window (e.g., in terms of magnitude and distance). Moreover, the records should generally be scaled and/or modified to match (with some specified level of agreement) the elastic design spectrum prescribed by the adopted seismic code. This manipulation is, however, a thorny problem. For example, in case that the structure is located on a particular soil condition (e.g., basin), adjusting or scaling the spectral amplitude of a signal recorded on a rock site would never provide information on the long duration actually generated.

Several studies (e.g., Archuleta and Hartzell, 1981; Somerville *et al.*, 1997; Shakal *et al.*, 2006) have shown that, at distances comparable with few fault lengths and at frequencies of engineering interest, the finite-fault effects (directivity effects, fling step, hanging-wall/footwall effects, low-frequency pulses, radiation-pattern effects, etc.) are not negligible. The near-source ground motion from moderate-to-large events is strongly affected by the evolution of the rupture along the extended fault, causing complex spatial distribution of the observed values. The ground-motion variability close to the seismic source cannot be reproduced by empirical models accounting only for average characteristics of the motion.

An alternative to the use of records from past earthquakes comes from the advances in understanding the earthquake source and wave propagation processes. Numerical techniques, based on a kinematic source description, can be used to simulate realistic synthetic seismograms for engineering needs (Graves and Pitarka, 2004; Pacor *et al.*, 2005; Liu *et al.*, 2006; Gallovič and Brokešová, 2007; Ameri *et al.*, 2008; among many others). One advantage of such techniques is that once the amplification due to local geology is taken into account, the synthetic time series can be directly used; they result from a given earthquake scenario with selected magnitude, distance, propagation model, site conditions, and so on and do not need to be scaled or modified for any further applications.

However, these models require the definition of a large number of input physical parameters whose values rarely can be fixed *a priori*, leading to a limit on their use for studies related to prediction of ground motion. Indeed, even if we are usually able to identify a causative fault and to retrieve information on the propagation medium, we are not able to determine, for example, the rupture velocity, the space-time distribution of slip over the fault plane, or the position of the rupture starting point. To handle this principle lack of knowledge we are compelled either to make a strong assumption on the value of each kinematic parameter or to generate a large number of shaking scenarios (all equally probable) trying to constrain the input values to plausible ranges. While in the first case we generate a single earthquake scenario that is, anyway, only one of the possible realization without any statistical significance, in the latter we generate a number of ground-motion parameters for each site that, although complicated to manage for specific engineering purposes, can be statistically analyzed to infer some insights on the probability distributions of ground-motion values and related statistical estimators (mean, median, mode, standard deviation, etc.).

In this article we investigate the engineering applicability of two conceptually different kinematic simulation techniques. We focus our attention on two issues: first to quantify the capability of each method to reproduce the earthquake ground-motion parameters usually required for engineering analysis (e.g., PGA, PGV, spectral acceleration, Arias Intensity [AI], Housner Intensity [HI], and significant duration [T90]); second to quantify how the predicted values depend on the variability in the large-scale kinematic description of the source (i.e., position of the nucleation point, value of the rupture velocity, and distribution of the final slip on the fault).

The sensitivity of ground motion to the source parameters has been studied by several authors (Pavic *et al.*, 2000; Gallovič and Brokešová, 2004; Hartzell *et al.*, 2005; Sørensen *et al.*, 2007; Ripperger *et al.*, 2008; Wang *et al.*, 2008). However, only few studies evaluate how the uncertainties in the source parameterization propagates to ground-motion estimates also using different modeling approaches, and even fewer attempt to assess how the different ground-motion parameters are affected by these uncertainties.

The selected case study is the 1984 (M_w 5.7) Gubbio earthquake (central Italy), for which five near-source strong-motion records are available. This earthquake represents a typical moderate magnitude event, occurring in central Italy, where the scarcity of records and the important role of site amplification at the recording stations make the studies related to the earthquake rupture process and to ground-motion modeling particularly complicated. The analyses have been performed within the project titled S3—Shaking and damage scenarios in area of strategic and/or priority interest, developed in the frame of the 2004–2006 agreement between the Istituto Nazionale di Geofisica e Vulcanologia (INGV, National Institute of Geophysics and Volcanology) and the Dipartimento della Protezione Civile (Italian Department of Civil Protection) where the modeling of the reference earthquakes was aimed at computing shaking scenarios for the Gubbio town and the nearby basin (S3 Project, 2007, Deliverable D20).

Here, we present the modeling of the 1984 Gubbio earthquake at the five accelerometric stations, applying two different finite-fault simulation methods, namely the deterministic-stochastic method (DSM, Pacor *et al.*, 2005) and the hybrid-integral-composite method (HIC, Gallovič and Brokešová, 2007). We first optimize the model source

parameters in order to infer the best scenario fitting the observed data and to evaluate the capability of each technique to reproduce strong-motion parameters of engineering interest (peaks and integral values). In the second part of the article we analyze the strong-motion parameters distributions retrieved at each site from the computation of more than 2400 scenarios varying the source kinematic parameters. The obtained variability is then discussed both in terms of the simulation techniques and of the specific strong-motion parameter.

Source Model, Strong-Motion Data, and Site Effects

The Gubbio area (northern Umbria region, central Italy) is characterized by moderate magnitude earthquakes. The 29 April 1984 (5:03 UTC) earthquake struck the Gubbio and surrounding municipalities with moment magnitude M_w 5.7 and, to date, it is the strongest event recorded in the area.

The source of this event is related to the rupture of a segment of the Gubbio fault, considered to be an active fault (Mirabella *et al.*, 2004). The Gubbio fault is part of the seismogenic Umbrian fault system, which consists of a set of aligned north-northwest–south-southeast trending, southwest dipping normal faults. Based on the integration of geologic, geomorphic, and seismological data, Pucci *et al.* (2003) suggested that the low-angle Gubbio fault is formed by two individual segments capable of generating M 5.3–5.9 earthquakes (Fig. 1). The southern segment ruptured during the 1984 earthquake while the northern segment did not rupture recently nor historically. These two segments are also cataloged in the Database of Individual Seismogenic Sources (DISS v. 3.0.4) for Italy and some surrounding countries (see the Data and Resources section).

The source model adopted in this study corresponds to the rupture of the southern segment of the Gubbio fault (identified as ITGG037 in the DISS v. 3.0.4 database); however, we use a modified fault (hereinafter ITGG037mod) because in 1984 the earthquake apparently did not rupture the whole ITGG037 fault. The source dimensions were assigned following the scaling relations of Wells and Coppersmith (1994) while the seismic moment was calculated basing on the Hanks and Kanamori (1979) relations. The source characteristics of the ITGG037 and ITGG037mod faults are listed in Table 1.

The 1D propagation model for the Gubbio area (Table 2) has been extracted from a 3D-tomography study based on the inversion of P and S minus P arrival times from seismic records of the INGV network (M. Moretti and P. De Gori, personal comm., 2006; S3 Project 2007, Deliverable D20). The anelastic attenuation is implemented differently in each simulation method. We use a frequency-dependent Q_S function in DSM modeling and standard Q_P and Q_S values for each crustal layer in HIC modeling. Various studies on the attenuation properties are available for the area (Malagnini and Herrmann, 2000; Bindi *et al.*, 2004; Castro *et al.*, 2004). They are mainly based on the data set of seismic recordings collected during the 1997–1998 Umbria-Marche seismic sequence (M_{max} 6.0). We adopt the results from Castro *et al.* (2004)

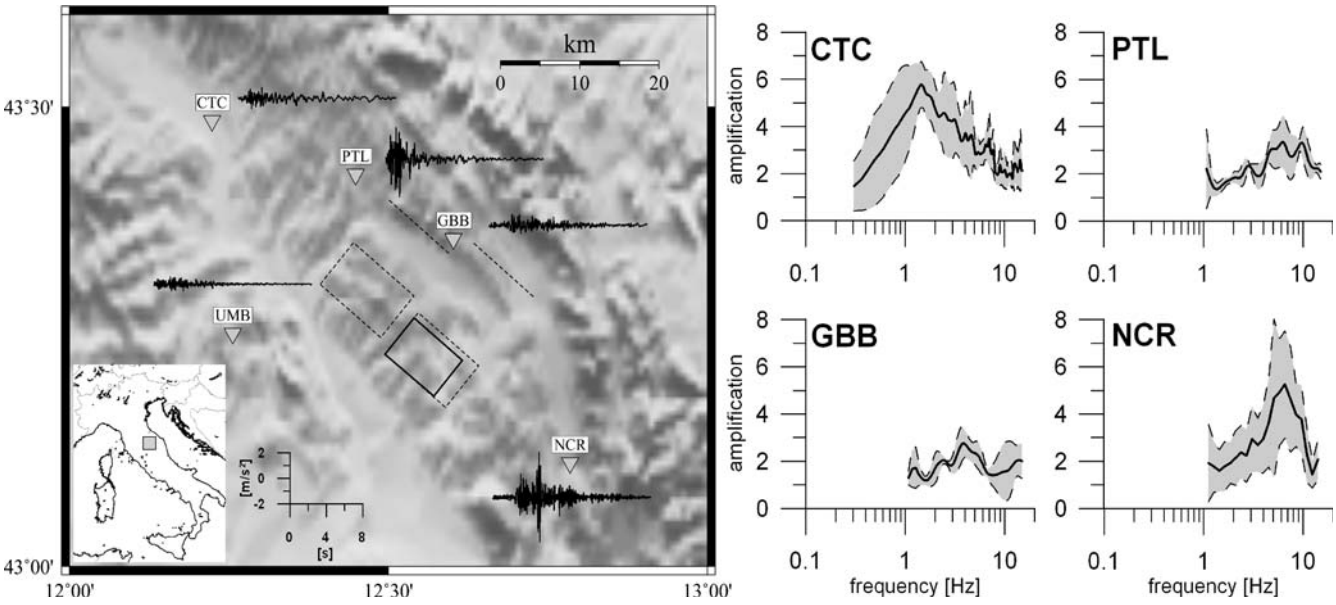

Figure 1. Accelerometric stations (gray triangles) triggered by the 1984 Gubbio earthquake and the Gubbio fault geometry; the dashed rectangles represent the surface projection of the fault plane. Dashed lines represent the hypothetical surface fault trace. The portion of the Gubbio fault used to simulate the 1984 earthquake is shown as a thick rectangle. For each station the north–south component of the recorded seismogram is presented. The four plots in the right-hand panel of the figure represent the HVSRs (mean ± 1standard deviation) determined for the accelerometric stations. The HVSRs computed at PTL, NCR, and GBB are considered reliable in the frequency range 1–15 Hz. Note that no HVSR is presented for the UMB station due to the lack of records.

Table 1
Fault Parameters Assumed for the 1984 Earthquake

Characteristics	ITGG037	ITGG037mod*
Length (km)	10.0	8.0
Width (km)	7.0	6.0
Strike (°)	130	130
Dip (°)	20	20
Rake (°)	−90	−90
Top depth (km)	4.0	4.3
Bottom depth (km)	6.4	6.4
Seismic moment (N m)	1.05×10^{18}	4.32×10^{17}
Moment magnitude	6.0	5.7
Mean slip (m)	0.5	0.3

See the Data and Resources section for information on the database for these events.

*Fault modified to fit the 1984 earthquake magnitude.

who performed a parametric inversion on the *S*-wave windows of the entire Umbria-Marche strong-motion data set that also includes accelerometric stations installed in the Gubbio area (i.e., GBB and GBP, located inside and nearby the basin). Castro *et al.* (2004) obtained a quality factor Q, representative of the *S*-wave train, approximated by the relation $Q_S = 31.2f^{1.2}$ up to $f = 9.0$ Hz. At higher frequencies the Q_S takes a nearly constant value of about 438 (see Table 2), which can adequately model the high-frequency attenuation near the site (κ parameter) as suggested by the authors themselves.

Five accelerometric stations belonging to the Italian strong motion network (RAN, Rete Accelerometrica Nazionale) were triggered by the 1984 Gubbio earthquake. Figure 1 shows a map of the study area together with the position of the stations and of the ITGG037mod fault. For each station, the north–south components of the recorded acceleration time series is also shown.

All stations were equipped with analog instruments. The data were corrected for the instrumental response and filtered with a cosine band-pass filter. The high-pass frequency was selected by visual inspection of the uncorrected Fourier spectrum. For all data it was set around 0.25 Hz, with the exception of the Umbertide (UMB) station waveforms that were filtered at 1 Hz because of high noise level. For the comparison with synthetic data, a low-pass filter at 10 Hz was applied, and time windows that start 1 sec before the first *S*-wave arrival and contain 85% of the energy of the records were used. These time windows were chosen with the aim of eliminating phases different from *S* waves as, for instance, the locally generated surface waves at the Città di Castello (CTC) station (see Fig. 1), which we are unable to model with the present crustal model. Strong-motion parameters computed from the processed data are reported in Table 3. The maximum acceleration (1.85 m/sec^2) was recorded at Nocera Umbra station (NCR), located about 20 km southeast from the fault, while the minimum one (0.20 m/sec^2) was observed at UMB, located about 25 km in the opposite direction. These differences in amplitudes can be ascribed in principle both to source and site effects.

Table 2
1D Propagation Model Adopted in Simulations*

Depth (km)	V_P (km/sec)	V_S (km/sec)	rho (kg/m^3)	Q_P	Q_S
0.00	4.05	2.17	2400	200	100
1.00	4.62	2.47	2400	200	100
2.00	5.19	2.76	2400	300	150
3.00	5.86	3.10	2750	600	300
5.00	6.20	3.33	2750	600	300
6.00	6.40	3.50	2750	600	300
12.00	6.50	3.53	2750	1000	500
24.00	6.60	3.59	2750	1000	500

The $Q_S(f)$ values from Castro *et al.* (2004) are used in the DSM simulations while frequency independent Q_P and Q_S values are used in the HIC simulations. $Q_S(f) = 31.2f^{1.2}$ for $f < 9.0$ Hz and $Q_S(f) = 438$ for $f > 9.0$ Hz.

*M. Moretti and P. De Gori, personal comm., 2006; S3 Project 2007, Deliverable D20

In the Umbria-Marche area, the site effects play an important role. Various authors (Bindi *et al.*, 2004; Castro *et al.*, 2004; Luzi *et al.*, 2005) exploited strong-motion data recorded mainly during the Umbria-Marche seismic sequence (1997–1998) to investigate site response in the area, providing both empirical and theoretical transfer functions for some of the accelerometric stations. Unfortunately, complete information on site amplification was not available for all the five stations used in this study. Detailed investigations are available for NCR (Marra *et al.*, 2000; Rovelli *et al.*, 2002; Cultrera *et al.*, 2003) and for GBB (Luzi *et al.*, 2005). Although both stations are located on shallow alluvial covers with $V_S < 360$ m/sec (Cattaneo and Marcellini, 2000; Luzi *et al.*, 2005), NCR is characterized by a very complex response site with strong amplification at frequencies higher than 5 Hz due to the presence of a buried wedge of weathered rock underlying the station (Rovelli *et al.*, 2002; Cultrera *et al.*, 2003).

In order to take into account site amplification at each site, we estimated average spectral ratios between horizontal and vertical components of ground motion (horizontal-vertical spectral ratio (HVSR) method; Lermo and Chávez-García, 1993; Field and Jacob, 1995) using the available accelerometric recordings from the database of the Italian strong-motion data (see the Data and Resources section; Fig. 1, right-hand panel). We are aware that the HVSRs do not provide the actual site transfer function but we decided to use them as the best information currently available to take into account site amplification at all stations used in this study. Furthermore, for NCR and GBB the fundamental frequencies and amplification factor detected with the HVSR method are in agreement with those estimated by other empirical techniques based on reference sites (i.e., generalized spectral inversion technique) as shown by Castro *et al.* (2004) and Luzi *et al.* (2005).

For NCR and GBB stations the HVSRs are well constrained (with five or more events recorded at the station) while at Pietralunga (PTL) the spectral ratio is computed

Table 3

Ground-Motion Parameters Computed for the *S*-Wave Time Window are Shown for Each Station and for Both Horizontal Components

Station Name	Horizontal Component	R_{hypo} (km)	PGA (m/sec^2)	PGV (m/sec)	AI (m/sec)	HI (m)	T90 (sec)
CTC	North–South	38.6	0.34	0.018	0.0080	0.056	3.2
	East–West		0.39	0.027	0.013	0.1	3
GBB	North–South	17.8	0.48	0.035	0.021	0.1	6.2
	East–West		0.72	0.034	0.035	0.12	4.9
NCR	North–South	21.5	1.8	0.048	0.12	0.076	3.5
	East–West		1.5	0.058	0.093	0.094	5.2
PTL	North–South	26.8	1.3	0.055	0.1	0.17	2.5
	East–West		1.4	0.080	0.11	0.2	3.3
UMB	North–South	26.5	0.21	0.0090	0.0040	0.023	3.8
	East–West		0.2	0.010	0.0040	0.023	4

Definitions of the column headings are as follows: hypocentral distance, R_{hypo}; peak ground acceleration, PGA; peak ground velocity, PGV; Arias Intensity, AI; Housner Intensity, HI; significant duration, T90. Waveforms are band-pass filtered as described in the text.

using only 3 recordings and has to be considered poorly constrained. For the UMB station the HVSR calculated with the only available record reports an amplification peak at about 15 Hz and lower amplifications (about a factor of 2) for frequencies below 10 Hz. Because only one record is used, the HVSR method cannot provide a statistically significant site amplification function and, therefore, we decided not to use it. In any case, this site is reported to be stiff soil or rock (Luzi *et al.*, 2005; Bindi *et al.*, 2006) and no large amplifications are expected. The CTC station is located on a very deep basin (Bordoni *et al.*, 2003), and it may not be appropriate to estimate the response site with the HVSRs as the vertical component of motion could be affected by amplification violating the fundamental assumption on which this technique is based (Castro *et al.*, 2004; Pacor *et al.*, 2007). In this case we used the empirical transfer function obtained by averaging standard spectral ratios for an array of stations located around the accelerometric station (Bordoni *et al.*, 2003; L. Luzi, personal comm., 2007).

As shown in the right-hand panel of Figure 1, the NCR station is strongly influenced by site effects with an amplification up to 8 (mean plus one standard deviation) at about 6 Hz. The CTC station is characterized by high-amplification values at low frequencies (around 1 Hz) related to the generation of low-frequency phases within the Città di Castello basin (Bordoni *et al.*, 2003). PTL and GBB sites are characterized by modest amplification values at 5–6 Hz.

Methods

The two kinematic modeling techniques applied in this study are briefly described in order to better understand the results presented in the article and to highlight differences in their modeling philosophy. For further explanation we refer to Pacor *et al.* (2005) for DSM, and Gallovič and Brokešová (2007) for HIC.

Deterministic-Stochastic Method (DSM)

The DSM method is based on the well-known stochastic model of Boore (1983, 2003) but introduces two important modifications in order to consider the rupture propagation over a finite fault. First it uses a so-called deterministic envelope computed solving a simplified formulation of the representation theorem (Aki and Richards, 1980). The envelope is used for windowing the white Gaussian noise in the time domain. It is obtained by summing the contribution by each subfault in the order prescribed by isochrones (loci of points on the fault characterized by the same arrival time at the site). Through the isochrone calculation (Spudich and Frazier, 1984), the envelope depends on the rupture time over the fault and on the travel time through the crustal structure. This modification leads to a different ground-motion envelope at each site, instead of a predefined functional form as in the classical Boore's method. The second modification involves the definition of the reference omega-squared source spectrum that scales the windowed noise Fourier spectrum. In the DSM method the spectrum parameters are derived deterministically. The seismic moment of the target earthquake sets the low-frequency level of the spectrum while, for each site, the standard corner frequency is replaced by the apparent corner frequency defined as the inverse of the rupture duration as perceived at the site.

The definition of a deterministic envelope based on the isochrones theory and the use of an apparent corner frequency make the modeled synthetics particularly sensitive to the direction of rupture propagation over the fault with respect to the site position and, therefore, to the location of the rupture starting point. Indeed, sites in the forward rupture direction receive the energy from a larger portion of the fault in shorter time duration than the sites in the backward direction.

Despite these modifications, DSM still preserves the very simple nature of the stochastic model where only few

parameters need to be specified in the ground-motion calculation. However, it also presents some important limitations: its stochastic basis does not allow the modeling of near-fault long-period ground motion (especially for moderate and large earthquakes) where a pure deterministic calculation is more adequate; it accounts only for direct *S*-wave propagation, so that subsequent arrivals cannot be simulated; however, this is a reasonable assumption in the near-fault distance range where the direct-*S* wave field is generally dominant in amplitude with respect to *P* waves and secondary phases.

Hybrid-Integral-Composite Method (HIC)

For this more advanced kinematic technique, the rupture process is decomposed into slipping on individual overlapping subsources of various sizes, distributed randomly on the fault plane, treated differently in low- and high-frequency ranges. A database of the subsources is first created consisting of each subsource's dimension, position on the fault, mean slip (and consequently seismic moment), and corner frequency. The subsource number-size distribution obeys a power law with fractal dimension $D = 2$, and their mean slips are proportional to their dimensions (so-called constant stress-drop scaling, Zeng *et al.*, 1994). Note that this scaling implies that the subsources compose a *k*-squared slip distribution (Andrews, 1980). The same database of subsources is used for both the frequency ranges: in the low-frequency range (up to 2 Hz), the representation theorem is employed. The static slip at any point is given by the sum of the static slips of all the subsources containing the point (assuming a *k*-squared slip distribution at each individual subsource). The rupture time is computed considering the distance of the point from the nucleation point and constant rupture velocity V_r. The slip velocity function is assumed to be a Brune's pulse with constant rise time (1 sec). In this frequency range the directivity is well modeled. Concerning the high-frequency range (above 0.5 Hz), the subsources from the database are treated as individual point sources with Brune's source time function characterized by seismic moments and corner frequencies from the database. The rupture times are given by the time the rupture needs to reach the subsource's center (assuming the same constant rupture velocity V_r). The synthetics computed in the low- and high-frequency parts are crossover combined between 0.5 and 2 Hz in the Fourier domain by weighted averaging of the real and imaginary parts of the spectrum. The source modeling method is combined with the discrete-wavenumber method (Bouchon, 1981), yielding full-wave field Green's functions.

In our particular application to the Gubbio earthquake the strong-motion synthesis is mostly controlled by the composite (high frequency) approach as the minimum frequency considered is 0.25 Hz or 1 Hz (depending on the station, as previously described). Because of the random subsource positions, the wave-field contributions sum incoherently in the composite model, and the directivity effect is very weakly reproduced in the synthetics. It can be shown that the high-frequency plateau *A* of the acceleration spectrum (characterizing the strength of high-frequency radiation) is inversely proportional to the duration of the earthquake squared ($A \propto V_r^2/(LW)$; Aki, 1967). However, the constant of proportionality is unknown, being tightly related to the actual small-scale physical evolution of the rupture and has to be, therefore, considered as a free parameter. However, in principle, we are unable to distinguish in the high-frequency range the value of the rupture velocity V_r and the constant of proportionality. As suggested in Gallovič and Brokešová (2007), we initially compared synthetic PGAs with a regional ground-motion prediction equation (Bindi *et al.*, 2006) valid for the studied area. We set the constant of proportionality to 1, and we will understand the value of V_r in a more general sense as the combination of the rupture velocity and the constant of proportionality.

Simulation of the 1984 Gubbio Earthquake

Model Parameters Optimization

In this section we determine the scenario that produces minimum-misfit values for acceleration response spectra (5% damping) in order to infer information on the rupture kinematics of the event from the forward modeling of high-frequency strong-motion data. Considering that no previous studies (as waveform inversion analysis) are available to *a priori* constrain the position of the rupture starting point (N_p) and the value of the rupture velocity (V_r), we simulate several possible scenarios, varying the value of these two kinematic parameters within plausible ranges, in order to define the best source model that reproduces the 1984 earthquake records. We also used three different k^{-2} slip distributions on the fault (Herrero and Bernard, 1994; Gallovič and Brokešová, 2004) with the same average slip value (Table 1). The slip models are generated assuming a single asperity and varying its position over the fault plane (Fig. 2): in the slip model 1 the main asperity is located in the middle of the lower half of the fault, in slip model 2 the asperity has been moved toward the southeastern end of the fault, while in slip model 3 it is located close to the northwestern edge.

We looked for the best model only in terms of two kinematic parameters (N_p, V_r) and, therefore, we preferred to apply a simple grid-search method rather than any more complicated searching algorithm suitable for optimization in multidimensional parameter space. The grid search is performed by simulating 810 scenarios for each slip model combining different hypocenter positions and rupture velocity values over the fault. The search was performed using synthetics generated by both DSM and HIC techniques. We investigate 90 nucleation points (equally spaced by 0.5 km, see Fig. 2) and 9 rupture velocities (ranging from $0.6V_S$ to $1V_S$; $V_S = 3.3$ km/sec). The choice of considering only nucleation points located in the lower half of the fault is in accordance with the findings in Mai *et al.* (2005), in which

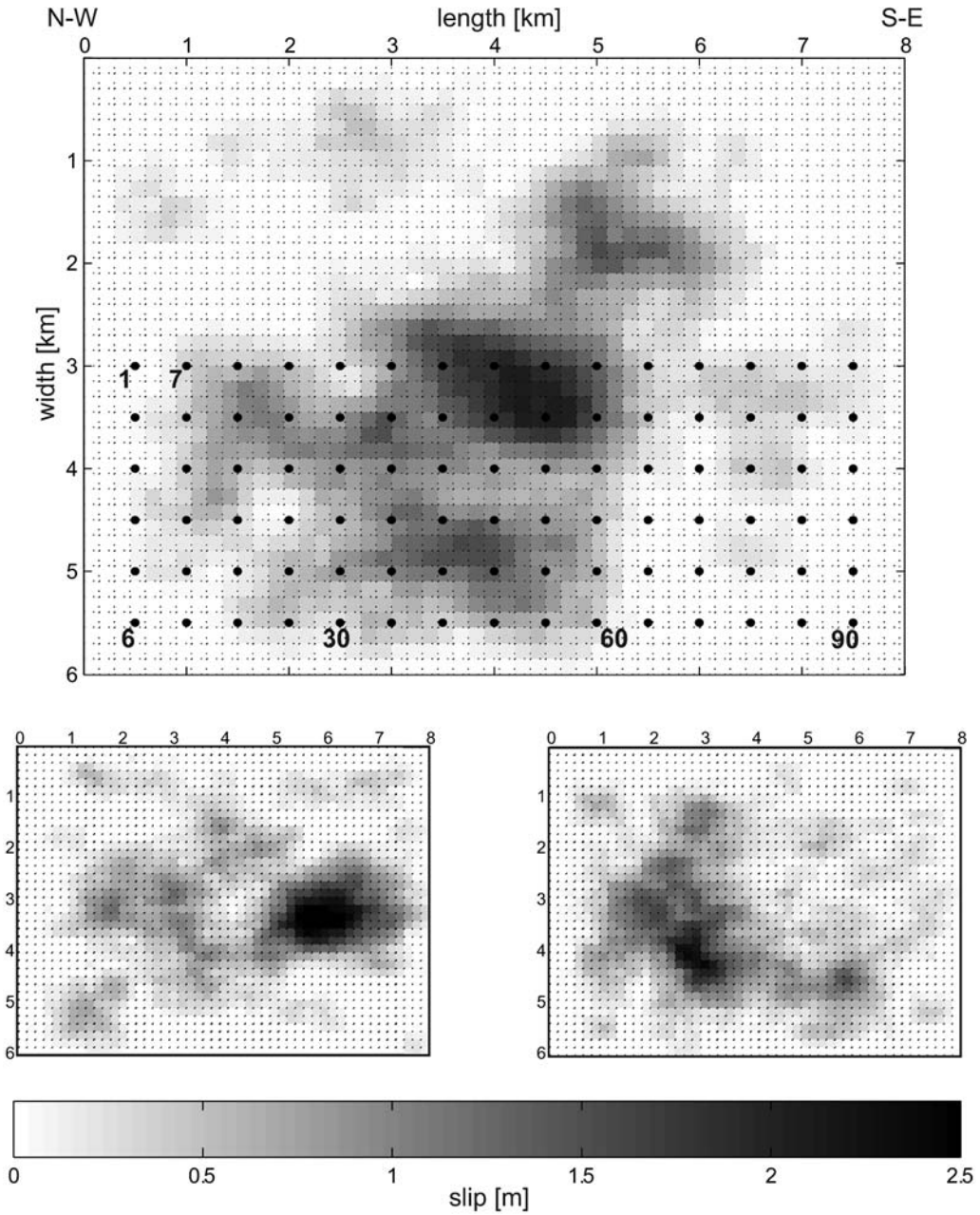

Figure 2. Fault geometry and the three k^{-2} final slip distributions adopted in the simulations. Black dots and labels show the position and number of nucleation points used in the grid search.

statistical analysis on a database of rupture models showed that rupture, in crustal earthquakes, tends to nucleate in the deeper sections of the fault.

To quantify the goodness of fit between synthetic and observed data, we define in the frequency domain an error function for each scenario as:

$$\varepsilon(N_p, V_r) = \frac{1}{m}\sum_{j=1}^{m} E_{\mathrm{rms}}(f_j), \tag{1}$$

where m is the number of the considered frequencies, N_p and V_r are the nucleation point and the rupture velocity of the considered scenario, respectively, and

$$E_{\mathrm{rms}}(f_j) = \left\{\frac{1}{n}\sum_{i=1}^{n}\left[\log\left(\frac{SA(f_j)_{\mathrm{obs}}}{SA(f_j)_{\mathrm{sim}}}\right)_i\right]^2\right\}^{1/2}, \tag{2}$$

with n as the number of stations and $SA(f)$ as the acceleration response spectra, 5% damped, computed at 34 selected frequencies in the band 1–9 Hz and for the mean between the horizontal components. Similar formulations have already been used in several studies (Graves and Pitarka, 2004; Castro and Ruíz-Cruz, 2005; Assatourians and Atkinson, 2007).

In order to account for the site amplification at the accelerometric stations, we multiply the Fourier amplitude

spectra of the synthetic time series computed at bedrock by the amplification function given by the HVSRs presented in the Source Model, Strong-Motion Data, and Site Effects section, obtaining ground-motion parameters at surface level.

The results of grid search for slip distribution 1 are shown in Figure 3. The upper panels show the values of ε for both modeling techniques. The best models (the absolute minimum of ε is about 0.17 and it is shown as a white star in Fig. 3) prefer rupture velocities around $0.9V_S$ (HIC best model) and $0.75V_S$ (DSM best model) with the nucleation point located close to the center of the fault for both methods ($N_p = 31$ and $N_p = 38$ for HIC and DSM best models, respectively). The pattern of the ε values shows that the HIC technique is more sensitive to the choice of rupture velocity. Scenarios with $\varepsilon < 0.20$ are obtained for $V_r > 0.8V_S$ but with a large number of hypocenter locations spanning almost all over the fault plane. The lower left-hand plot of Figure 3 shows the locations of nucleation points on the fault giving $\varepsilon < 0.2$ with a fixed $V_r = 0.9V_S$.

On the contrary, the right-hand panels of Figure 3 show that, adopting the DSM technique, scenarios with $\varepsilon < 0.2$ are obtained using a narrow range of V_r (from $0.7V_S$ to $0.8V_S$) and of nucleation point positions. Considering scenarios with $\varepsilon < 0.25$, the range of preferred V_r values increases (including almost all the considered values, depending on the hypocenter location) while the nucleation points remain constrained within an area around the center of the fault. Therefore, the choice of the position of rupture starting point seems to be of primary importance in the DSM modeling while it is secondary with respect to the choice of rupture velocity in HIC modeling. This behavior is strictly related to the different approach in simulating the rupture propagation on the fault adopted by the two techniques. As highlighted in the previous Methods section, DSM defines a deterministic envelope based on the computation of isochrones, which makes the technique especially sensitive to the position of the nucleation point. The HIC technique is, on the contrary, less sensitive to the nucleation point position (directivity) due to the incoherent summation of the subsource's contributions to the wave field in the high-frequency range.

The results of the grid search considering slip distribution 2 and 3 are not presented in the article because they are similar to those shown in Figure 3. The minimum ε values and their distribution in the space of possible solutions are

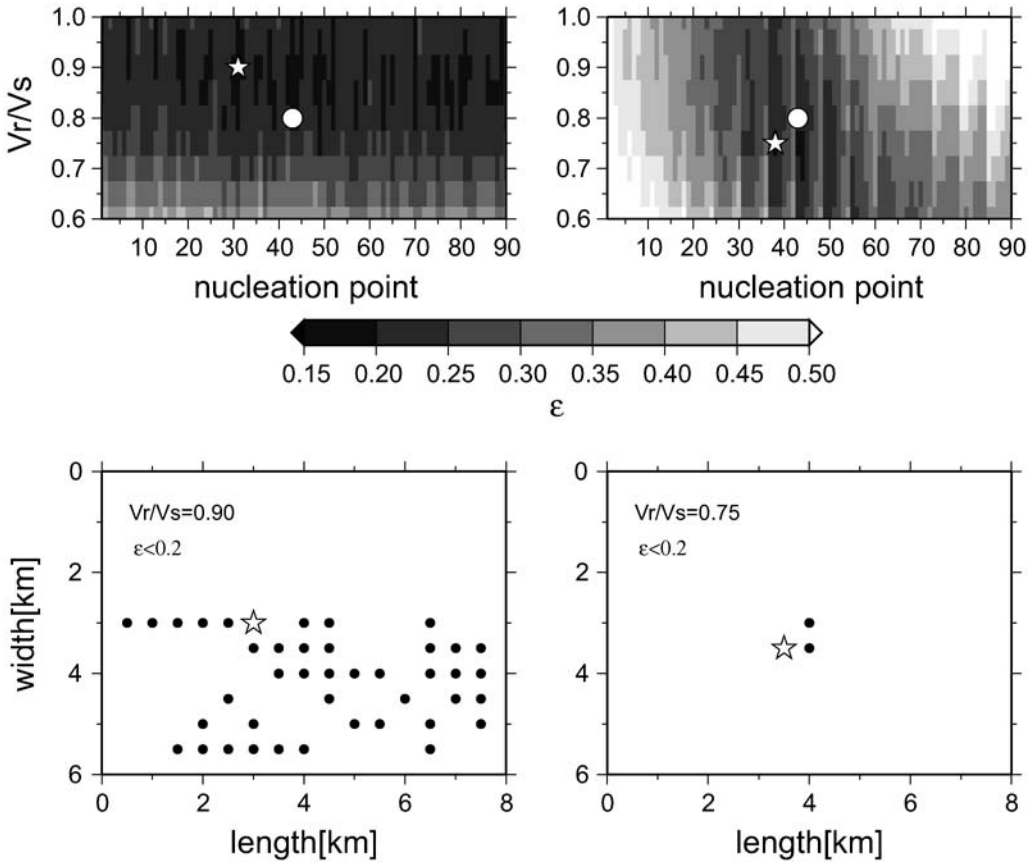

Figure 3. Grid-search results for HIC (left-hand plots) and DSM (right-hand plots) techniques. Upper panels: plots representing the value of ε as a function of the nucleation point (x axis) from 1 to 90 (see Fig. 2), and V_r/V_S values, that is, ratios of rupture velocity and shear-wave velocity (y axis), from 0.6 to 1.0. White stars correspond to the minimum values of ε, equal to 0.17 for both techniques, representing the best models. The unique best model is shown by the white dots. Lower panels: nucleation points (black dots) corresponding to a fixed V_r value (different for each technique and reported in the labels) for $\varepsilon < 0.20$ are represented on the fault plane.

consistent with those shown for slip model 1 (i.e., the rupture velocity is poorly constrained in DSM modeling while the hypocenter position is poorly constrained in HIC modeling). We conclude that, due to the moderate source dimension, the source–sites distances and the frequency band considered in the grid search, the goodness-of-fit estimator is sensitive predominantly to rupture velocity and nucleation point position and only loosely to the location of the main asperity of the slip model.

The grid search identifies two best models (one for each technique) presented in the lower panels of Figure 3. However, because a past earthquake corresponds to a single realization of all the possible rupture scenarios, we selected a unique best model that can reasonably represent the source kinematics of the 1984 Gubbio event. We searched for a single scenario that minimizes the ε function for both techniques, finding a hypocenter located at 4.0 km along strike and 3.0 km downdip ($N_p = 41$) and a rupture velocity equal to $0.8V_S$ (this unique model is represented in the top panels of Fig. 3 by a white dot). Slip distribution 1 is chosen, having no particular reason to prefer different dislocation models.

For each scenario, a model bias is obtained by averaging the residuals, that is, $\log_{10}(SA_{\text{obs}}/SA_{\text{sim}})$, among all stations at each frequency. Figure 4 presents the model bias for each technique considering the best models and the unique best model. A model bias of zero indicates that the simulation, on average, matches the observed ground-motion level. A negative model bias indicates overprediction of the observations and a positive model bias indicates underprediction of the observations. The best models have no significant bias over the frequency range from 1 to 9 Hz, with an average standard deviation of about 0.2, indicating that both simulation techniques are able to adequately capture the main characteristics of the ground-motion response. As expected, the unique best model gives worse results than the best models, leading to a slight underestimation for HIC simulations at frequencies higher than 4 Hz (Fig. 4a) and to overestimation for DSM synthetic at almost all frequencies (Fig. 4b).

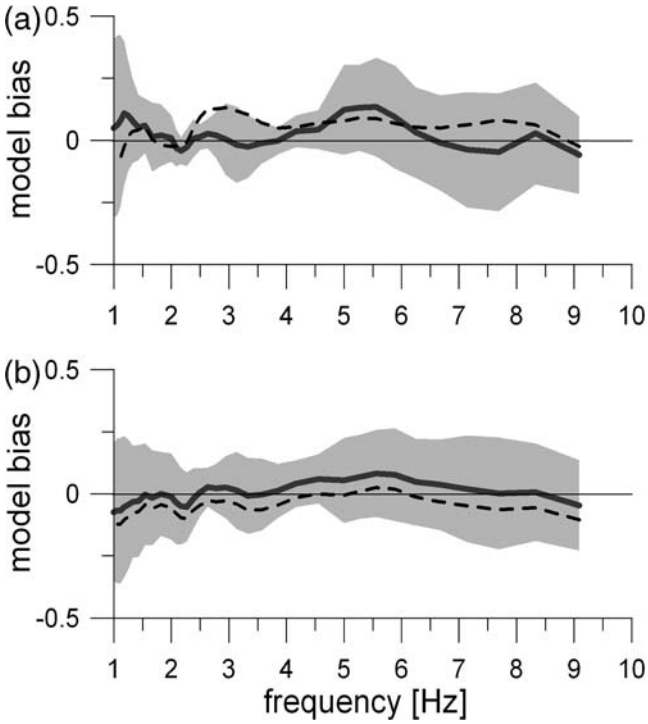

Figure 4. Spectral acceleration residuals ($\log_{10}(SA_{\text{obs}}/SA_{\text{sim}})$) as a function of frequency averaged over five sites and considering the best models for (a) HIC and (b) DSM techniques. The black curves and the light gray areas represent the median values and the standard deviations at each frequency, respectively. The median values considering the unique best model are also shown as a black dashed curve.

Comparison with Observed Data

As previously discussed, the adopted grid-search method is based on the comparison between observed and simulated acceleration response spectra in a restricted frequency range (1–9 Hz). In the following, we assess the reliability of the grid search results by more accurate comparisons between observed and synthetic ground motions for the selected source model.

Figure 5 shows the observed and simulated time series (both horizontal components) and acceleration response spectra (mean horizontal component) computed at the five stations, using the unique best model. The HIC method computes a time series very similar to the recorded ones, including *P* waves, *S* waves, and subsequent reverberations in the shallower crustal layers. NCR and CTC synthetic accelerograms match quite well with the recorded data, reproducing amplitudes and frequency content. The mismatch at PTL and UMB stations, mainly at frequencies higher than 4 Hz, could be ascribed both to radiation-pattern properties, because these sites are located close to the nodal planes for *S* waves, and to the approximated site amplification functions adopted in this study.

The waveforms obtained by the DSM method, accounting only for direct *S*-wave motion, appear to be much simpler than those observed and simulated by the HIC technique. However, the strong-motion phase is well reproduced, providing consistent results in terms of ground-motion parameters. The DSM response spectra match quite well with the data recorded at the NCR and UMB stations, while results similar to those obtained by the HIC method are found for data recorded at the PTL site, confirming the presence of peculiar site effects not accounted for in the HVSR function. An overestimation is visible at the CTC and GBB sites for frequencies greater than 6 Hz; however, the fits improve if a higher rupture velocity is adopted, as found from the grid-search analysis.

To quantify the comparison presented in Figure 5 we compute residuals for several ground-motion parameters usually required in engineering analysis (Fig. 6). We considered two instantaneous measures of motion (PGA and PGV) and three integral measures (HI, AI, and T90). T90 is defined

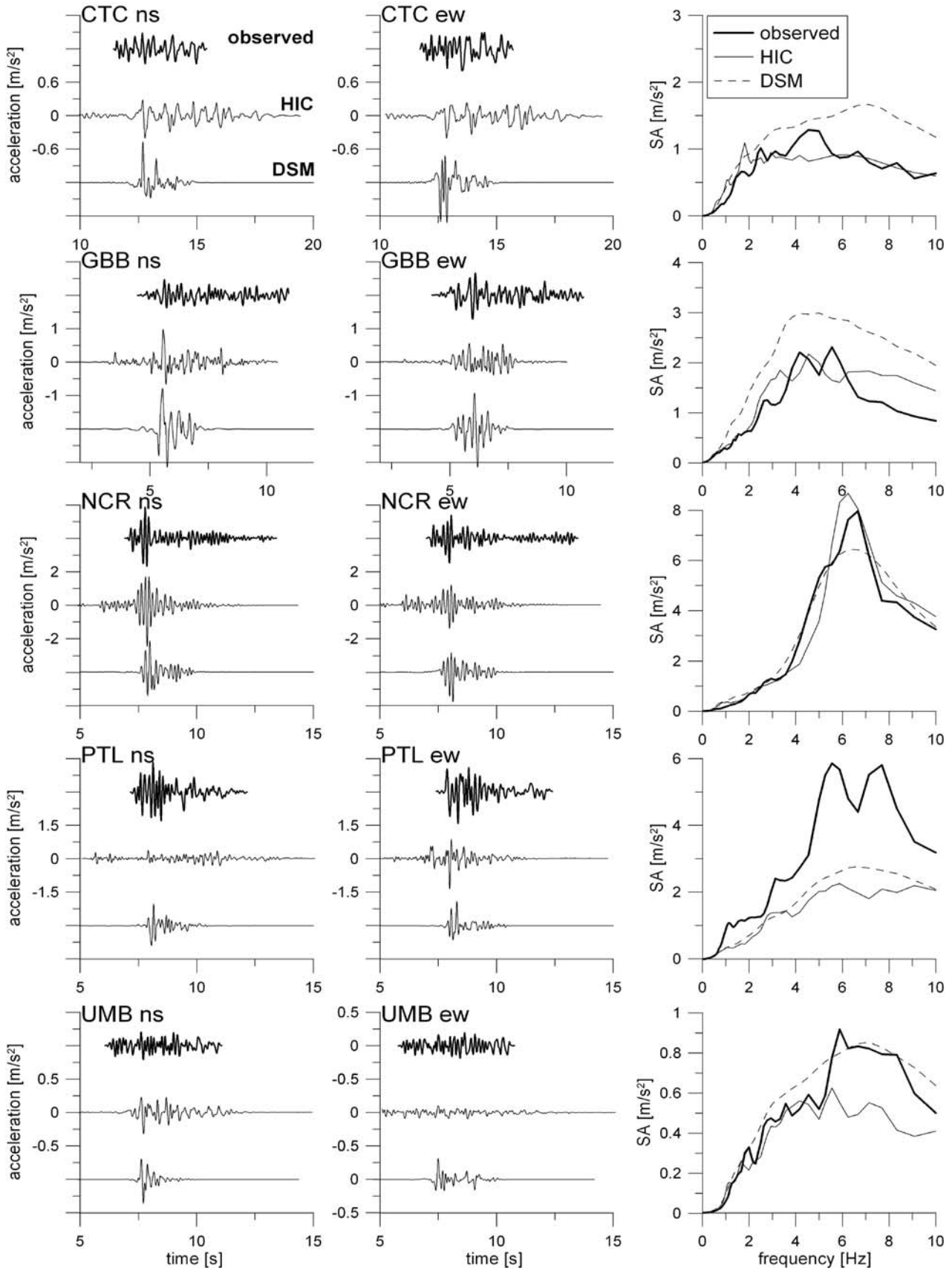

Figure 5. Comparison between observed (*S*-wave time window) and simulated time series (north–south and east–west component) and 5% damped acceleration response spectra (mean horizontal component) at the five stations and for both simulation techniques.

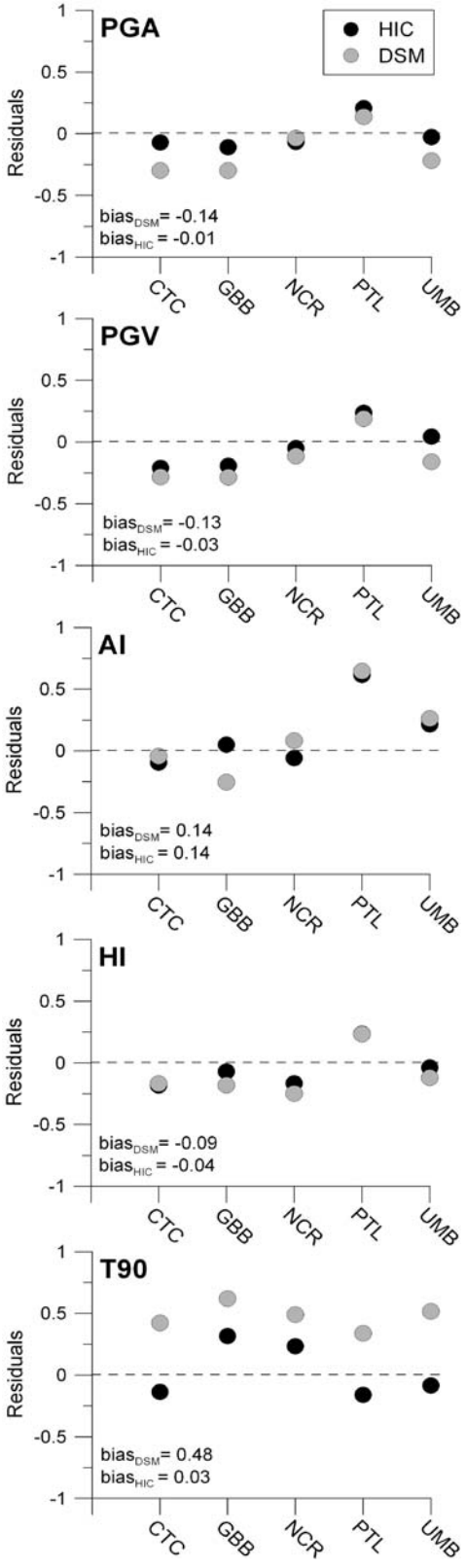

Figure 6. Residuals computed for different ground-motion parameters (mean horizontal component) at each station. Black and gray dots represent residuals computed using the HIC and DSM unique best model, respectively (see Fig. 3). For each parameter, the given model bias is computed by averaging the residuals over all the stations.

as the time interval between 5% and 95% of the cumulative square of the acceleration time history (Husid, 1969). All the parameters are computed from the time series filtered as described in the previous section. A model bias for each technique is also calculated averaging the residuals over the five stations. The synthetic peak values well reproduce the observed ones, and the residuals from both techniques are quite consistent. At CTC and GBB sites the overestimation of the high-frequency content of the observed spectra in the DSM synthetics produces larger PGA residuals (in any case not exceeding a factor of 2). Regarding AI and HI, both techniques provide comparable results and reproduce fairly well the observed parameters, particularly a lower bias is found for HI. At the PTL station, HIC and DSM underestimate the observed AI (by about a factor of 3), likely due to the aforementioned improper site response applied to the synthetics. DSM also overestimates the AI at the GBB site, related to the high-frequency content in the synthetic acceleration time series. DSM produces high-positive residuals for T90 with model bias equal to 0.48 indicating that the duration of observed strong motion cannot be captured by this technique. In fact DSM, simulating only the strong-motion phase of the seismogram, is able to reproduce the cumulative energy but it results in being contained in a too short and not realistic time duration.

Variability of Ground-Motion Parameters

Typically when computing ground-motion scenarios we are not able to compare results with observed data to calibrate, as discussed previously, the kinematic parameters of the model. The aleatory variability of these parameters can strongly affect the prediction of ground-motion values (Sørensen *et al.*, 2007). The choice of a particular rupture nucleation point could lead, for instance, to increasing PGA values with a consequent increasing hazard or loss estimate for a particular area (Ameri *et al.*, 2008, Ansal *et al.*, 2008). Furthermore, the variability of PGA values, associated with the specific choice of the kinematic parameters, could be different with respect to the variability of other parameters, such as AI, T90, or HI.

To investigate and quantify this variability as a function of the source kinematics, we compute the residuals for the different ground-motion parameters from the more than 2400 scenarios simulated, combining 6 rupture velocities, 90 nucleation points, and 3 slip distributions. The residuals at each station and for both techniques are presented in Figure 7 and in Table 4.

For both techniques and for all sites, the standard deviations of the residuals distributions for different ground-motion parameters are remarkably different. The AI residuals are characterized by the largest standard deviation (almost twice as large compared to the PGA and PGV ones). On the contrary, T90s have the lowest values of standard deviation, meaning a narrow range of predicted values: for instance, at the NCR site, about 68% of the T90 values from HIC syn-

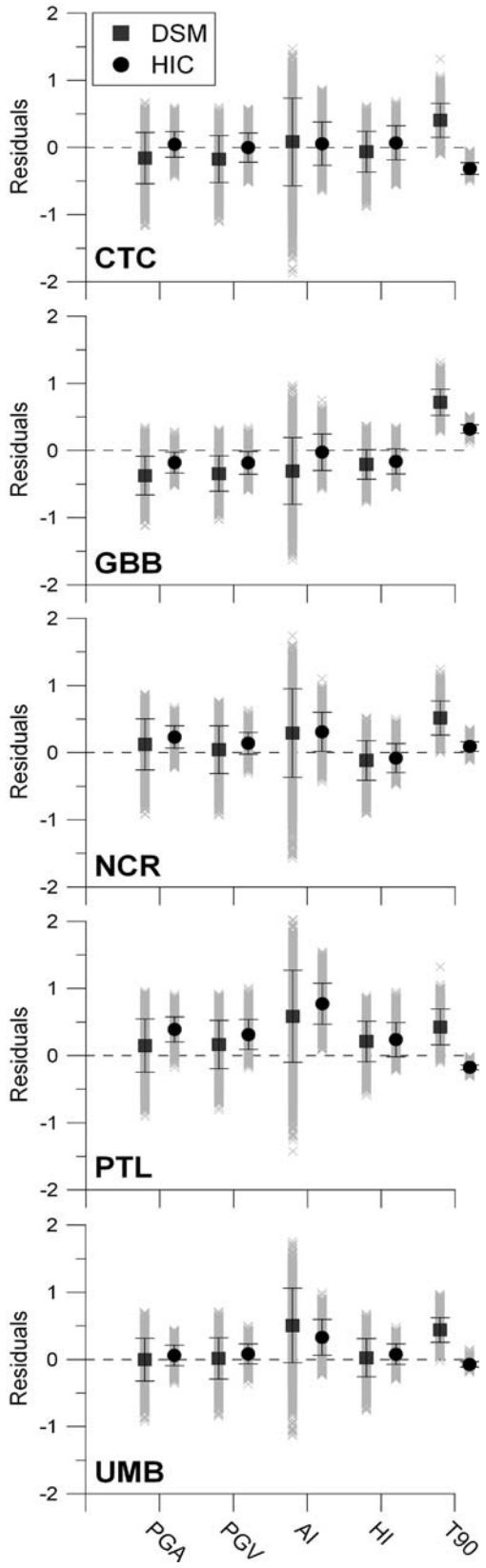

Figure 7. Residuals for all the 2430 scenarios, considering different ground-motion parameters at the five stations (gray crosses). The mean and standard deviation of the residuals distributions are shown for both modeling techniques (see also Table 4).

Table 4
Mean and Standard Deviation of the Residual Distributions at All Stations*

Station Name	DSM	HIC
	PGA	
CTC	−0.16 ± 0.38	0.05 ± 0.19
GBB	−0.37 ± 0.29	−0.18 ± 0.16
NCR	0.12 ± 0.38	0.23 ± 0.17
PTL	0.15 ± 0.40	0.39 ± 0.19
UMB	−0.01 ± 0.32	0.06 ± 0.15
	PGV	
CTC	0.09 ± 0.35	0.26 ± 0.22
GBB	−0.34 ± 0.26	−0.18 ± 0.17
NCR	0.04 ± 0.35	0.14 ± 0.16
PTL	0.17 ± 0.36	0.31 ± 0.22
UMB	0.02 ± 0.31	0.08 ± 0.15
	AI	
CTC	0.08 ± 0.65	0.06 ± 0.32
GBB	−0.30 ± 0.50	−0.03 ± 0.27
NCR	0.29 ± 0.66	0.31 ± 0.29
PTL	0.58 ± 0.68	0.77 ± 0.31
UMB	0.51 ± 0.55	0.33 ± 0.27
	HI	
CTC	−0.06 ± 0.30	0.07 ± 0.25
GBB	−0.21 ± 0.22	−0.16 ± 0.19
NCR	−0.12 ± 0.30	−0.08 ± 0.21
PTL	0.21 ± 0.30	0.24 ± 0.26
UMB	0.03 ± 0.28	0.08 ± 0.15
	T90	
CTC	0.40 ± 0.25	−0.31 ± 0.09
GBB	0.72 ± 0.19	0.32 ± 0.06
NCR	0.52 ± 0.25	0.09 ± 0.07
PTL	0.43 ± 0.27	−0.18 ± 0.04
UMB	0.44 ± 0.18	−0.07 ± 0.04

See Figure 7 also.
*Results are presented for each ground-motion parameter considering both simulation methods.

thetics are distributed in a range of 1 sec. PGA, PGV, and HI residuals present quite similar distributions with standard deviation included between the previous two. Other studies based both on recorded data (Abrahamson and Silva, 1996; Travasarou *et al.*, 2003; Massa *et al.*, 2008) and simulations from dynamic rupture models (Aochi and Douglas, 2006) have confirmed that the standard deviation associated with AI and T90 are larger and smaller, respectively, than that of most other ground-motion parameters. AI is proportional to the integral of the squared acceleration time series. As a consequence, this measure accounts for the effect of both the acceleration amplitude (squared) and the duration of motion. Therefore, it is expected to have a higher variability of AI with respect to the PGA although the variations of the model input parameters are the same. T90, in the absence of particular response site (e.g., basin effects) that could lead to large increase of signal's duration, depends primarily on the travel time through the crustal model (that is fixed for each station) and depends secondarily on the rupture duration. The latter is related to the fault-plane dimension (fixed) and to the

combination of nucleation point position and rupture velocity (variable). Thus, the variability of simulated T90 is mainly constrained by the small dimension of the considered causative fault.

Table 4 also shows that the value of standard deviation is station dependent. Although we considered only five sites, it is noteworthy that observers located approximately in the fault-parallel direction (CTC, NCR, and PTL) present larger dispersion (i.e., standard deviation) of the residuals with respect to sites located in fault-normal direction (GBB and UMB). This larger standard deviation is due to forward and backward directivity that increase the variability for certain sites.

The standard deviations of the residual distributions for HIC modeling are systematically smaller than those of DSM modeling. However, the mean values obtained by both techniques are consistent within the statistical error, except for the T90 (Fig. 7). The differences in the mean values of T90 distributions between the two simulation methods are consistent with the differences highlighted in Figure 6 for the best model.

As already discussed, the different variability between DSM and HIC results is related to the different numerical description of the extended source. Firstly, the HIC method is less sensitive to the choice of the location of nucleation points than DSM as found by the grid-search analysis; secondly, the HIC method is sensitive to the slip distribution because the low-frequency content of the ground motion is computed deterministically; however, the analyzed parameters are mainly controlled by the higher frequencies. Moreover, in the considered source–site distance range (from about 18 to 38 km) the effect of different slip distributions on the ground motion is not significant.

In summary, the differences in the residuals distributions related to the variability of the kinematic parameters are visible for both methods and at all sites and have important implications for prediction of ground motion from future events. For example, the standard deviation for the T90 residuals at the GBB station calculated with the HIC technique is 0.06; this means that, despite the large variability of the kinematic parameters, the variability in T90 is very small. On the contrary, AI residuals show the largest dispersion (especially with the DSM technique, $\sigma = 0.50$ at the GBB site), thus, in blind ground-motion prediction, we have to take into account that this parameter could be very sensitive to the variation of kinematic parameters.

Discussion and Conclusions

In the first part of the article we focused our attention on the modeling of the 1984 M_w 5.7 Gubbio earthquake at five accelerometric stations. After taking approximate corrections for site effects into account, we searched for optimal values of the free kinematic parameters considered in the study (i.e., the rupture velocity and the hypocenter position) by minimizing a misfit function expressed in terms of acceleration response spectra in order to infer the best scenario to fit the data.

We hypothesized 90 nucleation points located in the lower half of the fault and 9 rupture velocities (ranging from 0.6 to $1V_S$) and investigated all the possible combinations of these parameters. Moreover, we considered three different k^{-2} slip distributions over the fault moving the position of the main asperity.

We computed synthetic seismograms using two simulation techniques, the DSM (Pacor *et al.*, 2005) and the HIC (Gallovič and Brokešová, 2007), the former being able to reproduce high-frequency synthetic seismograms ($f >$ 0.5 Hz) accounting for the propagation of direct S waves and the latter being a more advanced technique able to produce full-wave-field broadband synthetics. The results provide some insight into the rupture process of the event based on high-frequency information in the observed data. In principle, the DSM method is capable of constraining both the nucleation point position and the rupture velocity as its synthetics are sensitive directly to these features. On the contrary, the HIC method provides synthetics only loosely sensitive to the directivity and generalized rupture velocity.

Based on joint results from both modeling methods, we found that the most probable nucleation point of the 1984 earthquake was located in an area around the center of the fault (see Fig. 3) resulting in a bilateral rupture propagating with a velocity close to 2.65 km/sec. Because of the moderate dimension of the source, the distances to the recording stations, and the frequency range considered in the grid search, the results are not substantially affected by the slip patch distribution. We want to point out that such results are not provided by inversion of recorded data but simply by minimizing the acceleration response spectra residuals from all the plausible scenarios simulated with both techniques. Although the few number of available stations represents a limit of the proposed approach, we are confident that their good azimuthal coverage (that constrain the hypocenter position on the fault) and their proximity to the source allow a reliable first estimation of the kinematics of Gubbio earthquake.

The modeling of the 1984 event allowed also to assess the capability of the adopted techniques to reproduce earthquake ground-motion parameters usually required in engineering analysis. Both modeling approaches have no significant spectral acceleration bias over the frequency range from 1 to 9 Hz, indicating that the simulation models adequately capture the main characteristics of the ground motion. Considering other commonly used strong-motion parameters we found that the peak values (acceleration and velocity), AI, and HI are well modeled by both simulation techniques. The HIC method appears to be the most complete technique providing lower model bias values and being able to reproduce, on average, also the duration of motion; on the contrary DSM failed in reproducing realistic time-series durations. Among the considered integral measures of ground

motion, HI turns out to be best reproduced by both simulation techniques, while AI seems to be the most difficult to model. It is particularly important, when performing scenario studies, to assess the capability of different simulation techniques to reproduce several ground-motion parameters, so we could be able to recognize *a priori* which simulation method is more suitable for a specific purpose. In this case DSM is able to adequately reproduce PGA, PGV, spectral acceleration, and HI with the advantage of requiring approximately half the computational time and a smaller number of input parameters than the HIC method. However, this latter technique is more appropriate when a correct evaluation of the duration of the ground shaking is required.

In the second part of the article we analyze all the scenarios produced for the 1984 earthquake fault to quantify how the variation of simulated strong-motion parameters is related to the variability (i.e., uncertainties) of the kinematic parameters of the model.

We study the residuals distribution of the five strong-motion parameters considered in this study, and we investigate two types of variability. The first variability depends on the modeling approach: the variances of the DSM synthetics distributions are systematically higher than the HIC ones. The second variability is related to the predicted strong-motion parameter: AI presents the widest distribution (highest standard deviation) while T90 presents the most narrow distribution (lowest standard deviation). PGA, PGV, and HI present similar distribution with standard deviation values between the two previously mentioned. These results are verified considering all the computed strong-motion parameters and at all the selected stations.

The standard deviations of residuals distributions also depend on the position of the site with respect to the extended fault. Stations located in the fault-parallel direction present larger standard deviations with respect to sites located in fault-normal direction. Although the reliability of this result is limited in the present study by the few number of available sites, it is consistent with the results of Ripperger *et al.* (2008) on the variability of PGV from dynamic rupture simulations performed assuming a heterogeneous initial stress field.

In order to better understand how uncertainties of different kinematic parameters for both simulation techniques contribute to variability of ground motion, Figure 8 shows the synthetic cumulative distribution functions (CDFs) computed at the GBB and NCR sites for PGV. In Figure 8a, the three CDFs are related to each slip model: we grouped the scenarios with a fixed slip model and variable nucleation point position and rupture velocity, obtaining a total number of 810 realizations. In Figure 8b the CDFs are calculated for three different rupture velocities ($0.6V_S$, $0.8V_S$, and $1V_S$) for a total number of 270 scenarios for each V_r (3 slip models, 1 rupture velocity, and 90 nucleation points). In Figure 8c the scenarios are grouped considering three nucleation areas containing 30 hypocenters each for a total of 810 scenarios (3 slip models, 9 rupture velocities, and 30 nucleations). We note that the choice of a particular slip distribution has a minimum influence in the ground-motion distribution (Fig. 8a). On the other hand, the variation of rupture velocity and nucleation point largely contributes to variability of ground motion. The CDFs in Figure 8b are shifted to larger PGV values as the selected V_r increases. The effect of the nucleation area (Fig. 8c) is more complicated being dependent on the position of the site; for instance, at the GBB site, nucleation areas 2 and 3 produce very similar PGV distributions. In general uncertainties in the hypocenter position produce a variability of ground motion of the same order or smaller than uncertainties in rupture velocity for the HIC method and of the same order or larger for DSM.

These results have important implications for ground-motion prediction. If we are interested in calculating, for instance, AI for a hypothetical earthquake scenario, we have to take into account that this parameter is very sensitive to the variability of kinematic parameters. Choosing a different value of rupture velocity or a different position of the nucleation point will affect the predicted AI more than the HI or PGA. Moreover, in the case of the considered earthquake and distance range, uncertainties in the slip model definition can be considered negligible while larger contribution to ground-motion variability is given by uncertainties in nucleation point location and rupture velocity. In other words, considering a single slip model (e.g., slip model 1) we would not significantly underestimate the variability of ground motion from a larger number of slip models.

Commonly, AIs and HIs are assumed to be closely related to the damage potential of an earthquake. The results of this study show that HI is the best modeled among the considered integral measures, the values provided by both simulation methods are highly consistent, and its variability is less affected by the lack of knowledge in the source kinematic properties (lower standard deviation). For these reasons HI should be preferred for evaluating, through the use of synthetic seismograms, the seismic response of structures subject to a hypothetical earthquake.

Finally, we highlight that, by computing several possible scenarios at each site, we produce synthetic probability distributions of engineering ground-motion parameters, which allow one to estimate every statistical quantity (e.g., median, maximum, percentiles, etc.) engineers would need for defining the seismic input in structural engineering or hazard studies.

Data and Resources

Seismograms recorded during the 1984 Gubbio earthquake used in this study can be obtained from the database of the Italian strong-motion data (Working Group Italian Accelerometric Archive [ITACA]) at http://itaca.mi.ingv.it (last accessed September 2008).

The causative fault of the 1984 earthquake is reported in the Database of Individual Seismogenic Sources (DISS), Version 3.0.4: A Compilation of Potential Sources for Earth-

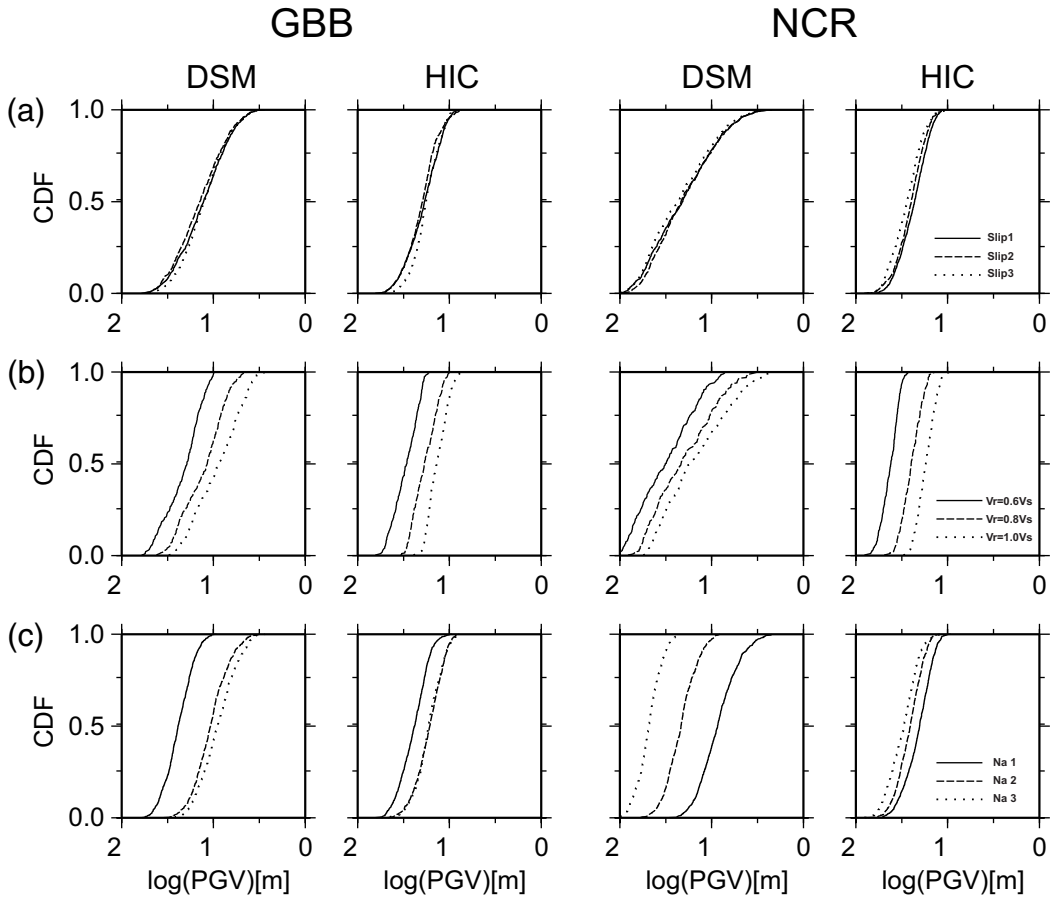

Figure 8. PGV synthetic CDFs computed at GBB and NCR stations for both techniques. (a) Each CDF is computed grouping scenarios that share the same slip model (810 scenarios for each slip model). (b) Each CDF is computed grouping scenarios that share the same rupture velocity (V_r) considering three selected values. (c) Each CDF is computed grouping scenarios that share the same rupture nucleation area (Na); for example, Na 1 contains nucleation points from 1 to 30 in Figure 2.

quakes Larger than M 5.5 in Italy and Surrounding Areas, available at http://www.ingv.it/DISS/, last accessed September 2008 (© INGV 2007; DISS Working Group, 2007; Basili *et al.*, 2007).

Some plots were made using the Generic Mapping Tools version 3.3.6 (Wessel and Smith, 1998; www.soest.hawaii.edu/gmt, last accessed September 2008).

Acknowledgments

This work was performed within the project titled S3–Shaking and damage scenarios in area of strategic and/or priority interest, supported by the Italian Civil Protection (DPC) and the Istituto Nazionale di Geofisica e Vulcanologia (INGV) for the time span of 2004–2007.

The manuscript has greatly benefited from careful review and comments of Karen Assatourians, Associate Editor Gail Atkinson, and an anonymous reviewer. We thank Sara Lovati and Lucia Luzi for providing information on site response in the area. Roberto Basili provided the fault parameters for the 1984 Gubbio earthquake. We particularly thank Paul Spudich and Dino Bindi for providing fruitful comments on an early version of the manuscript.

Gabriele Ameri carried out this work as a Ph.D. student of the Dipartimento per lo Studio del Territorio e delle sue Risorse, University of Genoa, Italy.

František Gallovič has been supported by the Grant Agency of the Czech Republic (Grant Number 205/08/P013) and Grant Number MSM0021620800 and by the Dipartimento di Scienze Fisiche, University "Federico II", Naples. Italy.

References

Abrahamson, N. A., and W. J. Silva (1996). Empirical ground motion models, report to Brookhaven National Laboratory.

Aki, K. (1967). Scaling law of seismic spectrum, *J. Geophys. Res.* **72,** 1217–1231.

Aki, K., and P. G. Richards (1980). *Quantitative Seismology: Theory and Methods*, Vol. **1** and **2,** W. H. Freeman, San Francisco, 932 pp.

Ameri, G., F. Pacor, G. Cultrera, and G. Franceschina (2008). Deterministic ground-motion scenarios for engineering applications: the case of Thessaloniki, Greece, *Bull. Seismol. Soc. Am.* **98,** no. 3, 1289–1303.

Andrews, D. J. (1980). A stochastic fault model, 1, static case, *J. Geophys. Res.* **85,** 3867–3877.

Ansal, A., A. Akinci, G. Cultrera, M. Erdik, V. Pessina, G. Tonuk, and G. Ameri (2008). Loss estimation in Istanbul based on deterministic earthquake scenarios of the Marmara Sea region (Turkey), *Soil Dyn. Earthq. Eng.* (in press).

Aochi, H., and J. Douglas (2006). Testing the validity of simulated strong ground motion from the dynamic rupture of a finite fault, by using empirical equations, *Bull. Earthq. Eng.* **4,** 211–229, doi 10.1007/s10518-006-0001-3.

Archuleta, R. J., and S. H. Hartzell (1981). Effects of fault finiteness on near-source ground motion, *Bull. Seismol. Soc. Am.* **71,** 939–957.

Assatourians, K., and G. M. Atkinson (2007). Modeling variable-stress distribution with the stochastic finite-fault technique, *Bull. Seismol. Soc. Am.* **97,** 1935–1949.

Basili, R., G. Valensise, P. Vannoli, P. Burrato, U. Fracassi, S. Mariano, M. M. Tiberti, and E. Boschi (2007). The database of individual seismogenic sources (DISS), version 3: summarizing 20 years of research on Italy's earthquake geology, *Tectonophysics* **453,** 20–43.

Bindi, D., R. R. Castro, G. Franceschina, L. Luzi, and F. Pacor (2004). The 1997–1998 Umbria-Marche sequence (central Italy): source, path, and site effects estimated from strong motion data recorded in the epicentral area, *J. Geophys. Res.* **109,** B04312, doi 10.1029/2003JB002857.

Bindi, D., L. Luzi, F. Pacor, G. Franceschina, and R. R. Castro (2006). Ground-motion predictions from empirical attenuation relationships versus recorded data: the case of the 1997–1998 Umbria-Marche, central Italy, strong-motion data set, *Bull. Seismol. Soc. Am.* **96,** no. 3, 984–1002.

Bommer, J. J., and A. B. Acevedo (2004). The use of real earthquake accelerograms as input to dynamic analysis, *J. Earthq. Eng.* **8,** no. S1, 43–92.

Boore, D. M. (1983). Stochastic simulation of high-frequency ground motion based on seismological models of the radiated spectra, *Bull. Seismol. Soc. Am.* **73,** 1865–1894.

Boore, D. M. (2003). Simulation of ground motion using the stochastic method, *Pure Appl. Geophys.* **160,** 635–676.

Bordoni, P., G. Cultrera., L. Margheriti, P. Augliera, G. Caielli, M. Cattaneo, R. De Franco, A. Michelini, and D. Spallarossa (2003). A microseismic study in a low seismicity area: the 2001 site-response experiment in the Città di Castello Basin (Italy), *Ann. Geophys.* **46,** no. 6, 1345–1360.

Bouchon, M. (1981). A simple method to calculate Green's functions for elastic layered media, *Bull. Seismol. Soc. Am.* **71,** 959–971.

Castro, R. R., and E. Ruíz-Cruz (2005). Stochastic modeling of the 30 September 1999 M_w 7.5 earthquake, Oaxaca, Mexico, *Bull. Seismol. Soc. Am.* **95,** no. 6, 2259–2271.

Castro, R. R., F. Pacor, D. Bindi, G. Franceschina, and L. Luzi (2004). Site response of strong motion stations in the Umbria, central Italy, region, *Bull. Seismol. Soc. Am.* **94,** no. 2, 576–590.

Cattaneo, M., and A. Marcellini. (2000). Terremoto dell'Umbria-Marche: analisi della sismicita' recente dell'appennino umbro-marchigiano—microzonazione sismica di Nocera Umbra e Sellano, (CNR-Gruppo Nazionale per la Difesa dai Terremoti, Roma).

Cultrera, G., A. Rovelli, G. Mele, R. Azzara, A. Caserta, and F. Marra (2003). Azimuth dependent amplification of weak and strong ground motions within a fault zone (Nocera Umbra, central Italy), *J. Geophys. Res.* **108,** no. B3, 2156, doi 10.1029/2002JB001929.

Douglas, J. (2003). Earthquake ground motion estimation using strong-motion records: a review of equations for the estimation of peak ground acceleration and response spectral ordinates, *Earth Sci. Rev.* **61,** no. 1–2, 43–104.

Field, E. H., and K. H. Jacob (1995). A comparison and test of various site-response estimation techniques, including three that are not reference-site dependent, *Bull. Seismol. Soc. Am.* **85,** 1127–1143.

Gallovič, F., and J. Brokešová (2004). The k^{-2} rupture model parametric study: example of the 1999 Athens earthquake, *Studia Geoph. Geod.* **48,** 589–613.

Gallovič, F., and J. Brokešová (2007). Hybrid *k*-squared source model for strong ground motion simulations: introduction, *Phys. Earth Planet. Interiors* **160,** 34–50.

Graves, R., and A. Pitarka (2004). Broadband time history simulation using a hybrid approach, *Proc. of 13th World Conf. on Earthquake Engineering*, Vancouver, British Columbia, 1–6 August 2004.

Hanks, T. C., and H. Kanamori (1979). A moment-magnitude scale, *J. Geophys. Res.* **84,** 2348–2350.

Hartzell, S., M. Guatteri, P. M. Mai, P. Liu, and M. Fisk (2005). Calculation of broadband time histories of ground motion, part II: kinematic and dynamic modeling using theoretical Green's functions and comparison with the 1994 Northridge earthquake, *Bull. Seismol. Soc. Am.* **95,** 614–645.

Herrero, A., and P. Bernard (1994). A kinematic self-similar rupture process for earthquakes, *Bull. Seismol. Soc. Am.* **84,** 1216–1228.

Husid, R. L. (1969). Analisis de terremotos: analisis general, *Revista del IDIEM* **8,** 21–42, Santiago, Chile.

Iervolino, I., and C. A. Cornell (2005). Record selection for nonlinear seismic analysis of structures, *Earthq. Spectra* **21,** no. 3, 685–713.

Lermo, J., and F. J. Chávez-García (1993). Site effect evaluation using spectral ratios with only one station, *Bull. Seismol. Soc. Am.* **83,** 1574–1594.

Liu, P., R. J. Archuleta, and S. H. Hartzell (2006). Prediction of broadband ground-motion time histories: hybrid low/high-frequency method with correlated random source parameters, *Bull. Seismol. Soc. Am.* **96,** no. 6, 2118–2130.

Luzi, L., D. Bindi, G. Franceschina, F. Pacor, and R. R. Castro (2005). Geotechnical site characterisation in the Umbria Marche area and evaluation of earthquake site-response, *Pure Appl. Geophys.* **162,** 2133–2161.

Mai, P. M., P. Spudich, and J. Boatwright (2005). Hypocenter locations in finite-source rupture models, *Bull. Seismol. Soc. Am.* **95,** no. 3, 965–980.

Malagnini, L., and R. B. Herrmann (2000). Ground-motion scaling in the region of the 1997 Umbria-Marche earthquake (Italy), *Bull. Seismol. Soc. Am.* **90,** 1041–1051.

Marra, F., R. Azzara, F. Bellucci, A. Caserta, G. Cultrera, G. Mele, B. Palombo, A. Rovelli, and E. Boschi (2000). Large amplification of ground motion at rock sites within a fault zone in Nocera Umbra (central Italy), *J. Seism.* **4,** 543–554.

Massa, M., P. Morasca, L. Moratto, S. Marzorati, G. Costa, and D. Spallarossa (2008). Empirical ground motion prediction equations for northern Italy using weak and strong motion amplitudes, frequency content and duration parameters, *Bull. Seismol. Soc. Am.* **98,** 1319–1342.

Mirabella, F., M. G. Ciaccio, M. R. Barchi, and S. Merlin (2004). The Gubbio Normal fault (central Italy): geometry, displacement distribution and tectonic evolution, *J. Struct. Geol.* **26,** 2233–2249.

Pacor, F., D. Bindi, L. Luzi, S. Parolai, S. Marzorati, and G. Monachesi (2007). Characteristics of strong ground motion data recorded in the Gubbio sedimentary basin (central Italy), *Bull. Earthq. Eng.* **5,** 27–43, doi 10.1007/s10518-006-9026-x.

Pacor, F., G. Cultrera, A. Mendez, and M. Cocco (2005). Finite fault modeling of strong ground motions using a hybrid deterministic–stochastic approach, *Bull. Seismol. Soc. Am.* **95,** no. 1, 225–240.

Pavic, R., M. G. Koller, P.-Y. Bard, and C. Lacave-Lachet (2000). Ground motion prediction with the empirical Green's function technique: an assessment of uncertainties and confidence level, *J. Seism.* **4,** 59–77.

Pucci, S., P. M. De Martini, D. Pantosti, and G. Valensise (2003). Geomorphology of the Gubbio Basin (central Italy): understanding the active tectonics and earthquake potential, *Ann. Geophys.* **46,** no. 5, 837–864.

Ripperger, J., P. M. Mai, and J.-P. Ampuero (2008). Variability of near-field ground motion from dynamic earthquake rupture simulations, *Bull. Seismol. Soc. Am.* **92,** 2217–2232.

Rovelli, A., A. Caserta, F. Marra, and V. Ruggiero (2002). Can seismic waves be trapped inside an inactive fault zone? The case study of Nocera Umbra, central Italy, *Bull. Seismol. Soc. Am.* **92,** 2217–2232.

S3 Project (2007). Scenari di scuotimento in aree di interesse prioritario e/o strategico. Deliverable D20: bedrock shaking scenarios: available at http://esse3.mi.ingv.it/deliverables/Deliverables_S3_D20.pdf.

Shakal, A., H. Haddadi, V. Graizer, K. Lin, and M. Huang (2006). Some key features of the strong-motion data from the **M** 6.0 Parkfield, California, earthquake of 28 September 2004, *Bull. Seismol. Soc. Am.* **96,** no. 4b, S90–S118.

Somerville, P. G., N. F. Smith, R. W. Graves, and N. A. Abrahamson (1997). Modification of empirical strong ground motion attenuation relations to include the amplitude and duration effects of rupture directivity, *Seism. Res. Lett.* **68,** 199–222.

Sørensen, M. B., N. Pulido, and K. Atakan (2007). Sensitivity of ground-motion simulations to earthquake source parameters: a case study for Istanbul, Turkey, *Bull. Seismol. Soc. Am.* **97,** no. 3, 881–900.

Spudich, P., and L. N. Frazer (1984). Use of ray theory to calculate high-frequency radiation from earthquake sources having spatially variable rupture velocity and stress drop, *Bull. Seismol. Soc. Am.* **74,** 2061–2082.

Stewart, J. P., S. J. Chiou, J. D. Bray, R. W. Graves, P. G. Somerville, and N. A. Abrahamson (2001). Ground motion evaluation procedures for performance-based design, Pacific Earthquake Engineering Research (PEER) Center Report 2001/09, University of California, Berkeley.

Travasarou, T., J. D. Bray, and N. A. Abrahamson (2003). Empirical attenuation relationship for Arias Intensity, *Earth. Eng. Struct. Dyn.* **32,** no. 7, 1133–1155.

Wang, H., H. Igel, F. Gallovič, A. Cochard, and M. Ewald (2008). Source-related variations of ground motions in 3-D media: application to the Newport-Inglewood fault, Los Angeles basin, *Geophys. J. Int.*, **174,** 202–214.

Wells, D. L., and K. J. Coppersmith (1994). New empirical relationships among magnitude, rupture length, rupture width, rupture area, and surface displacement, *Bull. Seismol. Soc. Am.* **84,** 974–1002.

Wessel, P., and W. H. F. Smith (1998). New, improved version of the Generic Mapping Tools Released, *EOS Trans. AGU* **79,** 579.

Zeng, Y., J. G. Anderson, and G. Yu (1994). A composite source model for computing realistic synthetic strong ground motions, *Geophys. Res. Lett.* **21,** 725–728.

Istituto Nazionale di Geofisica e Vulcanologia
via Bassini 15
20133 Milan, Italy
ameri@mi.ingv.it
(G.A., F.P.)

Department of Geophysics
Charles University
Prague, Czech Republic
(F.G.)

Dipartimento di Scienze Fisiche
Università degli Studi
"Federico II"
Naples, Italy
(A.E.)

Manuscript received 23 February 2008

[P7]

From earthquake centroid to spatial-temporal rupture evolution: Mw 6.3 Movri Mountain earthquake, June 8, 2008, Greece

F. Gallovič,[1,2] J. Zahradník,[1] D. Křížová,[1] V. Plicka,[1] E. Sokos,[3] A. Serpetsidaki,[3] and G-A. Tselentis[3]

Received 30 July 2009; revised 29 September 2009; accepted 13 October 2009; published 11 November 2009.

[1] We propose a new strategy to reveal the spatial-temporal evolution of the earthquake rupture process from near-regional data, without assuming a constant rupture velocity. The approach is based on a conjugate gradient method, for which we express analytically the required waveform-misfit derivative with respect to slip on the fault. The derivative is given by back-propagation of residual seismograms towards the source. A good initial source approximation is necessary, being obtained from hypocenter location and centroid-moment tensor solution. The iterative approach then gradually reveals major characteristics of the source process. As an application, we investigate a line source model of a damaging Mw6.3 earthquake in Greece, revealing predominantly unilateral rupture propagation and two or three main slip patches, one of which being significantly delayed, indicating a temporary rupture arrest. The region of largest slip coincides with the region of least abundant aftershocks between hypocenter and centroid. The method has application potential for shakemaps, emergency response, and/or aftershock hazard assessment.
Citation: Gallovič, F., J. Zahradník, D. Křížová, V. Plicka, E. Sokos, A. Serpetsidaki, and G-A. Tselentis (2009), From earthquake centroid to spatial-temporal rupture evolution: Mw 6.3 Movri Mountain earthquake, June 8, 2008, Greece, *Geophys. Res. Lett.*, *36*, L21310, doi:10.1029/2009GL040283.

1. Introduction

[2] Retrieval of earthquake source parameters is primarily needed for better insight into the physics of the faulting process. However, these parameters are useful also in practical real-time application, such as generating accurate shakemaps and planning emergency response [*Wald et al.*, 1999; *Convertito et al.*, 2009]. Many observational studies and numerical simulations [*Gallovič and Brokešová*, 2004; *Wang et al.*, 2008] further confirmed the importance of such parameters as the direction of the rupture propagation and position of main asperities since they dramatically affect the strong ground motions [see also *Mai*, 2009, and references therein]. Another application requiring accurate source parameters in near real-time is the aftershock hazard assessment [*Gerstenberger et al.*, 2005; *Gallovič and Brokešová*, 2008].

[3] Regional earthquake studies usually comprise hypocenter determination and calculation of the centroid-moment tensor (CMT), which represents a first-order approximation of the source process. Discriminating the fault plane out of the two nodal planes might follow, possibly complemented with a discrete representation of the earthquake by multiple point-sources. Further step is a gross estimation of the spatial-temporal rupture evolution in terms of, e.g., second-order moment tensors [*McGuire et al.*, 2002], slip patches [*Valle and Bouchon*, 2004] or continuous representation of the rupture evolution. For example, *Dreger and Kaverina* [2000] seek the best-fitting constant rupture velocity and rise time to reveal the continuous slip distribution on the fault. However, such parameterizations might bias the inverted slip model when the rupture evolution violates the simplifying presumptions.

[4] The present paper introduces a new non-parametric method to extend source models from their first-order approximation (CMT) to a more insightful image of the rupture evolution. *Larmat et al.* [2006] and *Ishii et al.* [2005] used seismic source time-reversal imaging, showing that back-propagated records refocus seismic waves at the right location and time of the earthquake. By a similar approach *Allmann and Shearer* [2007] localized a high-frequency asperity of the 2004 Parkfield earthquake. In our approach, starting from an initial source model based on the CMT solution, we back-propagate residual seismograms to obtain subsequent models by iteration, using a conjugate gradients technique. The new inversion strategy is applied to a damaging earthquake in Greece.

2. Method of Iterative Slip Inversion

[5] Based on recent adjoint tomographic methods [*Tromp et al.*, 2005], we address the earthquake rupture evolution from a similar viewpoint: the gradient of the waveform misfit with respect to the model parameters is analytically derived, which enables efficient minimization by routine methods of conjugate gradients. For simplicity, we assume a line fault of length L and formal width W, $L \gg W$. The j-th component of the synthetic seismogram $u_j(\boldsymbol{x}_i, t)$ at receiver $\boldsymbol{x}_i$ can be expressed by the representation theorem [*Aki and Richards*, 2002], i.e., by integration over the fault coordinate ξ of the slip velocity $s(\xi, t)$, varying with time t, convolved with the impulse response of the medium $H(\boldsymbol{x}_i; \xi, t)$ for a predetermined double-couple mechanism.

[6] We seek to estimate slip velocity $s(\xi, t)$ without any parameterizations of its spatial-temporal distribution (except its numerical discretization by piece-wise constant basis functions). Misfit is defined as an L2 norm between synthetic and observed seismograms, with an additional

[1]Faculty of Mathematics and Physics, Department of Geophysics, Charles University, Prague, Czech Republic.
[2]Department of Physics, Universita degli Studi "Federico II" di Napoli, Naples, Italy.
[3]Seismological Laboratory, Geology Department, University of Patras, Patras, Greece.

0094-8276/09/2009GL040283$05.00

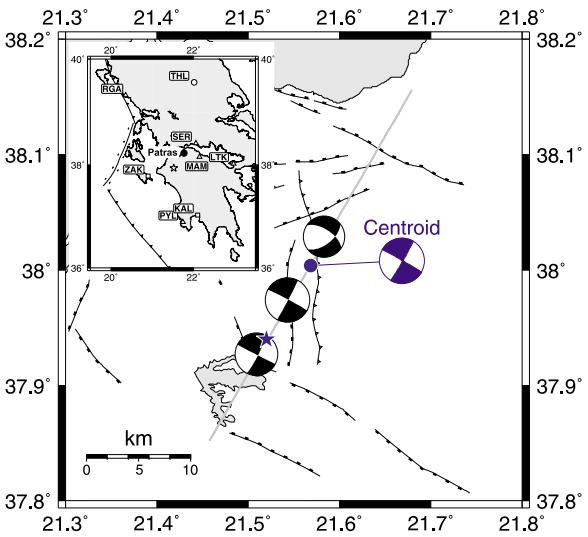

Figure 1. Two discrete representations of the 2008 Movri Mountain earthquake. A single point-source model (blue circle and beach ball scaled with respect to magnitude) and extended model composed of three point-sources. The blue star represents the epicenter. The grey line is the assumed fault, strike 30°, depth 17 km. The inset shows the stations used. Data from unclipped broadband velocigraphs (THL, RGA) and strong motion accelerographs (remaining stations) were used. Note that none of the local faults simply relates with this earthquake [*Koukouvelas et al.*, 2009].

stabilizing constraint on the scalar seismic moment, assumed to have a predetermined value M_{0fix} (from a previous CMT analysis),

$$\Lambda = \frac{1}{2L_u}\int_0^T \sum_{i,j}\left[u_j(\boldsymbol{x}_i,t) - u_j^{obs}(\boldsymbol{x}_i,t)\right]^2 dt - \frac{1}{2M_{0fix}^2}\left[M_0 - M_{0fix}\right]^2. \quad (1)$$

The normalizing factor L_u is the L2 data norm. The Fréchet differential of the misfit Λ can be expressed as

$$D\Lambda = \int_0^T \int_0^L \left(\frac{1}{L_u}\sum_{i,j} H(\boldsymbol{x}_i;\xi,-t) \star \left[u_j(\boldsymbol{x}_i,t) - u_j^{obs}(\boldsymbol{x}_i,t)\right] - \frac{1}{M_{0fix}^2}\left[M_0 - M_{0fix}\right]\mu W\right) Ds(\xi,t)\,d\xi\,dt \quad (2)$$

with rigidity denoted as μ. Equation (2) relates a small change of misfit $D\Lambda$ to small changes in the slip model $Ds(\xi, t)$ via the kernel in round brackets in which residual seismograms $u_j - u_j^{obs}$ are back-propagated in time towards the source. Furthermore, assuming the slip velocity function to be non-negative, we substitute $Ds(\xi, t) = s(\xi, t)D(\ln s(\xi, t))$; this is an implicit positivity constraint [*Tarantola*, 1987]. Equation (2) is the key ingredient for the minimization of Λ by the conjugate gradient method [*Press et al.*, 1992]. The inversion procedure is non-linear and iterative; it should start from a good first approximation, in our case represented by the CMT solution. For the complete derivation of equation (2) and the final discretized formula, see the auxiliary material.[1] Note also that generalization to 2D fault models is straightforward. The line-fault approximation was chosen due to a poor depth resolution in the present application.

3. Application to the 2008 Movri Mountain Earthquake

[7] On June 8, 2008 (12:25 UTC) an Mw6.3 strike-slip earthquake occurred in the north-western Peloponnese (Greece) without clear relation to mapped faults, but as close as ~30 km from Patras, the third major city of Greece [*Ganas et al.*, 2009]. Two victims were reported, along with hundreds of injuries and extensive damage, mainly in non-reinforced buildings. Although strong earthquakes are common in western Greece, this event took place in a region free of strong events throughout the historic observation period. The earthquake was followed by aftershock sequence with an irregular distribution, composed of at least two clusters.

[8] To investigate the Movri Mountain earthquake we proceeded in a *cascade* of the following procedures. First, the hypocenter was relocated at 37.94°N, 21.52°E, depth 19 km, 12:25:28.15 UTC. Then waveforms from eight near-regional stations (see Figure 1), band-pass filtered 0.01–0.2 Hz, were inverted for the deviatoric CMT using the ISOLA code [*Sokos and Zahradník*, 2008]: centroid position 38.00°N, 21.57°E, depth 17 km, 12:25:35.5 UTC, strike/dip/rake = 31°/84°/−179°, double-couple percentage 90%, scalar moment $3.4 \cdot 10^{18}$ Nm. The theoretical impulse responses were calculated in a layered crustal model [*Haslinger et al.*, 1999] using the discrete wavenumber method [*Bouchon*, 1981]. Second, following the H-C method [*Zahradník et al.*, 2008], the hypocenter and centroid were combined to identify the north-east south-west trending fault plane, without waiting for aftershocks; the rupture propagation direction was also indicated by the relative position of the hypocenter and centroid (Figure 1). Then, a multiple point-source solution, similar to *Zahradník et al.* [2005], was calculated again with the ISOLA code along a 40 km trial line passing through the centroid position. It revealed three significant contributions of a rather stable focal mechanism (Figure 1); the cumulative scalar moment was equivalent to the CMT solution.

[9] At this point, the new method described above is utilized. The centroid position, and time, along with its focal mechanism and scalar seismic moment from the previous steps are used as a first order approximation of the line source model (see Figure 2a, top left). We use the same frequency band and set of stations as for the initial three-point-source modeling. Progress of the slip-inversion iterations is shown in Figure 2a. During the first iteration steps the overall rupture-propagation direction emerges, while at later steps the slip becomes portioned, and the fit slightly increases. Starting from the 18th iteration, the slip model

[1] Auxiliary materials are available in the HTML. doi:10.1029/2009GL040283.

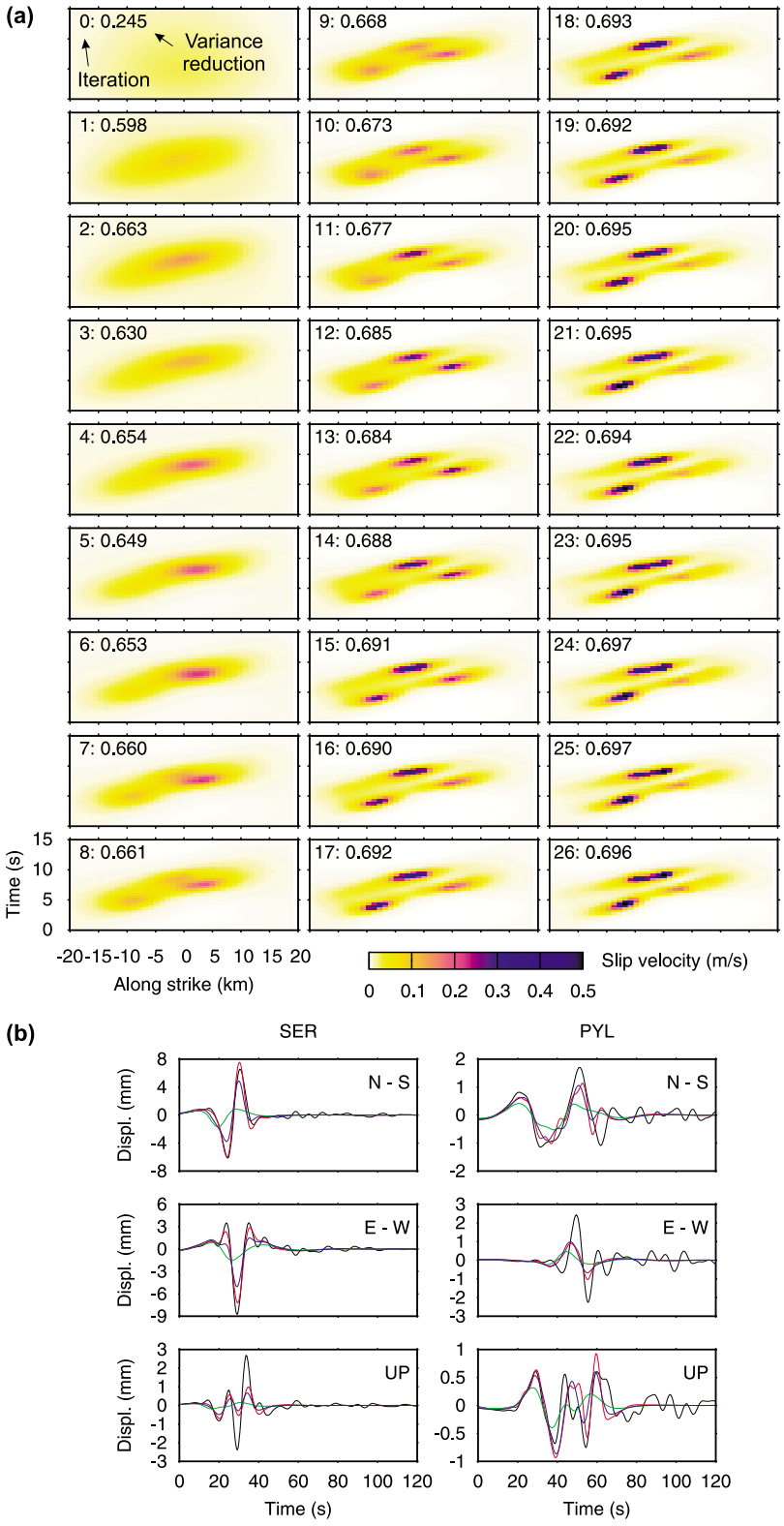

Figure 2. Continuous representation of the 2008 Movri Mountain earthquake based on the iterative method introduced in this paper. (a) Each frame visualizes one iteration of the temporal variation of the slip velocity along the line fault. Frame 0 is the starting model developed from the CMT model of Figure 1. In general, the iterations first show a single patch and reveal direction of the rupture propagation (from left to right), then decompose the slip into main asperities, and finally tend to focus each of them. (b) Matching data with synthetics. Near regional waveforms up to 0.2 Hz, corrected for instrument response, plotted in black for stations SER and PYL, are compared with synthetic seismograms for three selected iterations: 0 (green), 1 (blue) and 26 (red). Same comparison for other stations is presented in the auxiliary material (Figure A3 of Text S1).

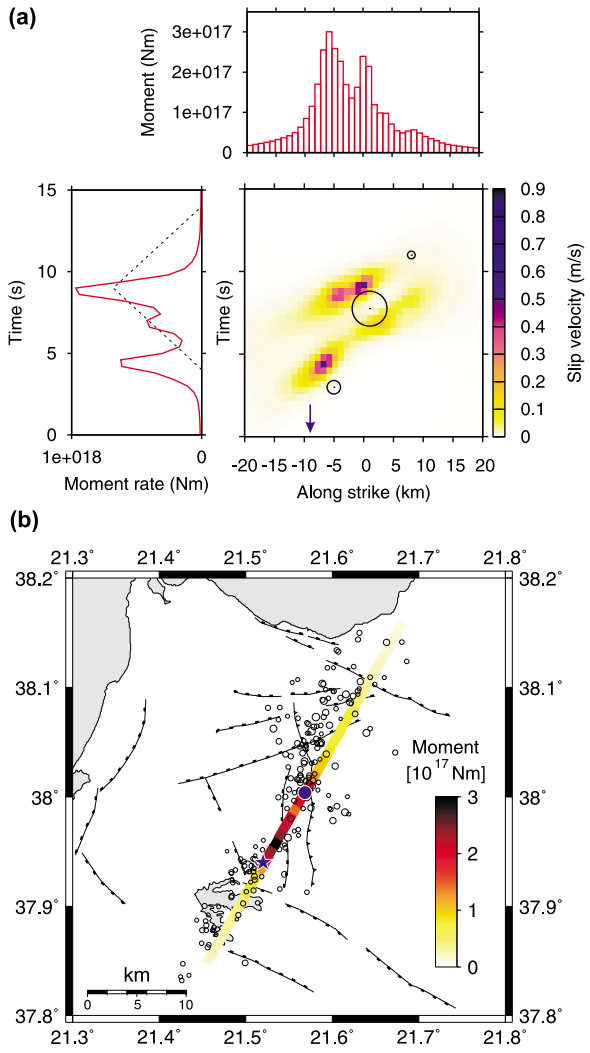

Figure 3. (a) Comparison of the continuous and discrete models. The distribution of the slip velocity along strike of the line fault (x-axis) and time (y-axis) for the 26th iteration (see Figure 2), in color, is superimposed with the three point-source subevents (black circles scaled with respect to scalar moment) from Figure 1. Blue arrow on the along-strike axis denotes epicenter (−8 km), while centroid is at 0 km. The red lines show the integrals of the color figure with respect to space and time, respectively. The dashed line represents the single point-source (centroid) solution. (b) Comparison between the continuous source model and the aftershocks relocated by double-difference method [*Waldhauser and Ellsworth*, 2000]. The moment distribution inverted in this study (from Figure 3a, top) is plotted onto the map projection of the steeply dipping fault plane. The aftershocks (small black circles) are least abundant in the maximum slip region located between the centroid (blue circle) and epicenter (blue star).

does not change much. Figure A1 of Text S1 of the auxiliary material shows a synthetic test resembling the inverted model. The iterative process is remarkably similar, also suggesting the asperity splitting in the later iteration steps.

[10] The waveform match of the final model has an overall variance reduction of 0.7. Figure 2b demonstrates details of the waveform fitting at two stations (PYL and SER); fit for other stations is presented in the auxiliary material (Figure A3 of Text S1). Figure A4 of Text S1 of the auxiliary material shows the waveform match for the 26th iteration of the new method and the CMT solution with main improvement in the duration of the dominant pulses of the records. Note that not all stations are equally sensitive to the rupture evolution. For example, the rupture propagation direction revealed in the first iterations are constrained by the stations lying along the fault line (SER, MAM, ZAK). Later, after this major contribution is removed from the data, coherent information from all stations suggests the splitting of the asperities.

[11] Figure 3a shows again the more or less arbitrarily chosen 26th iteration as the final model. Note that similar result was obtained when using a different crustal model and repeatedly removing each station (jack-knifing). The slip evolution exhibits predominantly unilateral rupture propagation (to the north-east) along a 20 km long segment of the fault, at a velocity of about 3 km/s starting close to the (independently determined) hypocenter. It is to emphasize that these features are data driven, and not constrained a priori. The slip velocity has at least two or three main episodes that roughly correlate with the previous three-point source model. Nevertheless, compared to the point sources, the patches found by the new method provide a considerably deeper insight into the spatial-temporal rupture evolution. An interesting finding is that one of the slip episodes features a significant time delay, most likely caused by a temporary rupture arrest. Note that such results could not be easily obtained with methods constraining the rupture velocity at a constant value.

4. Discussion and Conclusions

[12] In this study, a new iterative slip-inversion method based on back-propagation of residual seismograms is proposed. As an application, we investigate a recent damaging 2008 Mw6.3 earthquake in Greece, using near-regional data. The inversion method requires an initial approximation of the seismic source, which we obtain in cascade of operations: hypocenter relocation and determination of the centroid position and focal mechanism, complemented by identification of the fault plane. The iterative approach then gradually reveals major characteristics of the source process such as direction of the rupture propagation and dominant asperities.

[13] Figure 3b shows the final slip model from Figure 3a on a map in relation to the double-difference relocated aftershocks. The largest slip coincides with the region of the least abundant aftershocks (almost a gap), between hypocenter and centroid. Note that the north-east and south-west clusters of aftershocks differ in several aspects: The former group comprised events up to M 4.4, the latter contained only smaller magnitudes (M < 3.3). Moreover, first event of M ≥ 3 occurred in the south-western group as late as 13 hours after the mainshock, while, during the same period, there were more than 30 such events in the north-eastern group. We speculate that the north-eastern aftershocks might have been boosted by the predominantly unilateral rupture propagation, but a detailed study would require dynamic rupture modeling.

[14] The cascade methodology and the iterative slip inversion were primarily developed for obtaining gross features of the extended seismic source, extractable from near-regional waveforms at relatively low frequencies. Such data have recently been broadly available in near-real time. Finer details of the rupture evolution would require higher frequencies, local strong-motion stations, and significantly better constrained crustal models; as a rule, except a few densely instrumented regions of the world, such data are available only a considerable time after the event, thus preventing a near real-time analysis of the rupture process.

[15] The new methodology has two main advantages: (i) It provides a stable estimate of the rupture evolution (without splitting the slip pattern into ill-conditioned details). Robustness comes from the positivity constraint, fixed moment and a good initial approximation. (ii) It is quite fast, taking minutes on a PC. As such it has a strong application potential in shakemaps, emergency response, and/or in aftershock hazard assessment.

[16] **Acknowledgments.** Martin Mai and an anonymous reviewer helped to improve the manuscript. The authors acknowledge free Internet access of waveforms provided by NOA (THL) and ITSAK (stations ZAK, KAL); special thanks to Ch. Papaioannou. The remaining stations (RGA, MAM, SER, LTK, PYL) belong to the PSLNET network. Financial support: GAČR 205/07/0502, GAČR 205/08/P013, MSM0021620860, GAUK 14509. This research has benefited from funding provided by the Italian Presidenza del Consiglio dei Ministri - Dipartimento della Protezione Civile (DPC). Scientific papers funded by DPC do not represent its official opinion and policies.

References

Aki, K., and P. G. Richards (2002), *Quantitative Seismology*, Univ. Sci., Sausalito, Calif.

Allmann, B. P., and P. M. Shearer (2007), A high-frequency secondary event during the 2004 Parkfield earthquake, *Science*, *318*, 1279–1283.

Bouchon, M. (1981), A simple method to calculate Green's functions for elastic layered media, *Bull. Seismol. Soc. Am.*, *71*, 959–971.

Convertito, V., R. De Matteis, L. Cantore, A. Zollo, G. Iannaccone, and M. Caccavale (2009), Rapid estimation of ground-shaking maps for seismic emergency management in the Campania region of southern Italy, *Nat. Hazards*, in press.

Dreger, D., and A. Kaverina (2000), Seismic remote sensing for the earthquake source process and near-source strong shaking: A case study of the October 16, 1999 Hector Mine earthquake, *Geophys. Res. Lett.*, *27*, 1941–1944.

Gallovič, F., and J. Brokešová (2004), The k^{-2} rupture model parametric study: Example of the 1999 Athens earthquake, *Stud. Geophys. Geod.*, *48*, 589–613.

Gallovič, F., and J. Brokešová (2008), Probabilistic atershock hazard assessment II: Application of strong ground motion modeling, *J. Seismol.*, *12*, 65–78.

Ganas, A., E. Serpelloni, G. Drakatos, M. Kolligri, I. Adamis, C. Tsimi, and E. Batsi (2009), The Mw 6.4 SW-Achaia (western Greece) earthquake of 8 June 2008: Seismological, field, GPS observations and stress modeling, *J. Earthquake Eng.*, *13*, 1101–1124.

Gerstenberger, M. C., S. Wiemer, L. M. Jones, and P. A. Reasenberg (2005), Real-time forecasts of tomorrow's earthquakes in California, *Nature*, *435*, 328–331.

Haslinger, F., E. Kissling, J. Ansorge, D. Hatzfeld, E. Papadimitriou, V. Karakostas, K. Makropoulos, H.-G. Kahle, and Y. Peter (1999), 3D crustal structure from local earthquake tomography around the Gulf of Arta (Ionian region, NW Greece), *Tectonophysics*, *304*, 201–218.

Ishii, M., P. M. Shearer, H. Houston, and J. E. Vidale (2005), Extent, duration and speed of the 2004 Sumatra-Andaman earthquake imaged by the Hi-Net array, *Nature*, *435*, 933–936.

Koukouvelas, I. K., S. Kokkalas, and P. Xypolias (2009), Surface deformation during the Mw 6.4 (8 June 2008) Movri Mountain earthquake in the Peloponnese, and its implications for the seismotectonics of western Greece, *Int. Geol. Rev.*, in press.

Larmat, C., J.-P. Montagner, M. Fink, Y. Capdeville, A. Tourin, and E. Clévédé (2006), Time-reversal imaging of seismic sources and application to the great Sumatra earthquake, *Geophys. Res. Lett.*, *33*, L19312, doi:10.1029/2006GL026336.

Mai, M. (2009), Ground motion: Complexity and scaling in the near field of earthquake ruptures, in *Encyclopedia of Complexity and Systems Science*, edited by W. H. K. Lee and R. Meyers, pp. 4435–4474, Springer, New York.

McGuire, J. J., L. Zhao, and T. H. Jordan (2002), Predominance of unilateral rupture for a global catalog of large earthquakes, *Bull. Seismol. Soc. Am.*, *92*, 3309–3317.

Press, W. H., B. P. Flannery, S. A. Teukolsky, and W. T. Vetterling (1992), *Numerical Recipes in Fortran: The Art of Scientific Computing*, 2nd ed., Cambridge Univ. Press, New York.

Sokos, E., and J. Zahradník (2008), ISOLA A Fortran code and a Matlab GUI to perform multiple-point source inversion of seismic data, *Comput. Geosci.*, *34*, 967–977.

Tarantola, A. (1987), *Inverse Problem Theory: Methods for Data Fitting and Model Parameter Estimation*, Elsevier Sci., Amsterdam.

Tromp, J., C. Tape, and Q. Liu (2005), Seismic tomography, adjoint methods, time reversal and banana-doughnut kernels, *Geophys. J. Int.*, *160*, 195–216.

Valle, M., and M. Bouchon (2004), Imaging coseismic rupture in far field by slip patches, *Geophys. J. Int.*, *156*, 615–630.

Wald, D. J., V. Quitoriano, T. H. Heaton, H. Kanamori, C. W. Scrivner, and C. B. Worden (1999), TriNet shakemaps: Rapid generation of instrumental ground motion and intensity maps for earthquakes in southern California, *Earthquake Spectra*, *15*, 537–555.

Waldhauser, F., and W. L. Ellsworth (2000), A double-difference earthquake location algorithm: Method and application to the northern Hayward Fault, *Bull. Seismol. Soc. Am.*, *90*, 1353–1368.

Wang, H., H. Igel, F. Gallovič, A. Cochard, and M. Ewald (2008), Source-related variations of ground motions in 3-D media: Application to the Newport-Inglewood Fault, Los Angeles Basin, *Geophys. J. Int.*, *175*, 202–214.

Zahradník, J., A. Serpetsidaki, E. Sokos, and G-A. Tselentis (2005), Iterative deconvolution of regional waveforms and a double-event interpretation of the 2003 Lefkada earthquake, Greece, *Bull. Seismol. Soc. Am.*, *95*, 159–172.

Zahradník, J., F. Gallovič, E. Sokos, A. Serpetsidaki, and G-A. Tselentis (2008), Quick fault-plane identification by a geometrical method: application to the Mw6.2 Leonidio earthquake, January 6, 2008, Greece, *Seismol. Res. Lett.*, *79*, 653–662.

F. Gallovič, D. Křížová, V. Plicka, and J. Zahradník, Faculty of Mathematics and Physics, Department of Geophysics, Charles University, V Holešovičkách 2, 180 00 Praha 8, Czech Republic. (gallovic@karel.troja.mff.cuni.cz)

A. Serpetsidaki, E. Sokos, and G-A. Tselentis, Seismological Laboratory, Geology Department, University of Patras, GR-26504 Patras, Greece.

Appendix to the paper "From Earthquake Centroid to Spatial-Temporal Rupture Evolution: Mw 6.3 Movri Mountain Earthquake, June 8, 2008, Greece" by F. Gallovič, J. Zahradník, D. Křížová, V. Plicka, E. Sokos, A. Serpetsidaki, and G-A. Tselentis

Derivation of analytical formula for the misfit derivative

For simplicity we assume a line fault. The j-th component of synthetic seismogram $u_j(\boldsymbol{x}_i,t)$ at receiver $\boldsymbol{x}_i$ can be expressed using the representation theorem (Aki and Richards, 2002),

$$u_j(\boldsymbol{x}_i,t) = W\int_0^T\int_0^L H(\boldsymbol{x}_i;\xi,t-\tau)s(\xi,\tau)d\xi d\tau \tag{1}$$

where $s(\xi,t)$ describes the slip velocity evolution with time t and along the fault position ξ. The fault length and width are denoted L and W, respectively. $H(\boldsymbol{x}_i;\xi,t)$ is the impulse response due to a double couple source located at the fault in a generally inhomogeneous medium evaluated for the given receiver at $\boldsymbol{x}_i$. We seek slip velocity $s(\xi,t)$ without any parameterizations of its spatial-temporal distribution (e.g., by imposing a shape of the slip function, rise time, rupture time, etc.), thus the name "non-parametric inversion".

We define misfit as an L2 norm between synthetic, $u_j(\boldsymbol{x}_i,t)$, and observed seismograms $u_j^{obs}(\boldsymbol{x}_i,t)$, with an additional stabilizing constraint on the scalar seismic moment M_{0fix} fixed from the previous centroid analysis,

$$\Lambda = \frac{1}{2L_u}\int_0^T\sum_{i,j}\left[u_j(\boldsymbol{x}_i,t)-u_j^{obs}(\boldsymbol{x}_i,t)\right]^2 dt - \frac{1}{2M_{0fix}^2}\left[M_0-M_{0fix}\right]^2 \tag{2}$$

where the summations are over stations (i) and components (j), M_0 represents scalar seismic moment corresponding to $s(\xi,t)$ and L_u is the L2 norm of the observed data.

The best fitting model can be found by minimization of the misfit, which can be approached in many ways. Due to the large number of model parameters (in principle an infinite number because the slip is a continuous function of fault position and time), we adopt a technique analogous to time-reverse methods used typically in the adjoint seismic tomography studies (Tromp et al., 2005, Fichtner et al., 2006). In such methods, gradient of the misfit with respect to the model parameters is analytically derived and then used in minimization procedure based on, e.g., conjugate gradient techniques.

Realizing that the misfit (2) is a function of model parameters $s(\xi,t)$ via functionals $u_j(\boldsymbol{x}_i,t)$ and M_0, we can write the Fréchet differential of Λ (i.e. infinitesimal change of misfit due to infinitesimal changes of the slip model, $Ds(\xi,t)$),

$$D\Lambda = \frac{1}{L_u}\int_0^T\sum_{i,j}\left[u_j(\boldsymbol{x}_i,t)-u_j^{obs}(\boldsymbol{x}_i,t)\right]Du_j(\boldsymbol{x}_i,t)dt - \frac{1}{M_{0fix}^2}\left[M_0-M_{0fix}\right]DM_0 \tag{3}$$

$$Du_j(\boldsymbol{x}_i,t) = \int_0^T\int_0^L H(\boldsymbol{x}_i;\xi,t-\tau)Ds(\xi,\tau)d\xi d\tau \tag{4}$$

$$DM_0 = \int_0^T\int_0^L \mu W Ds(\xi,\tau)d\xi d\tau \tag{5}$$

Symbol μ represents the rigidity. Inserting (4) and (5) into (3) and realizing that the integration over t represents a convolution with time-reversed impulse response H, yields

$$\begin{aligned} D\Lambda &= \int_0^T \int_0^L \left(\frac{1}{L_u} \sum_{i,j} H(\boldsymbol{x}_i; \xi, -\tau) \star \left[u_j(\boldsymbol{x}_i, \tau) - u_j^{obs}(\boldsymbol{x}_i, \tau) \right] - \right. \\ & \left. \frac{1}{M_{0fix}^2} \left[M_0 - M_{0fix} \right] \mu W \right) Ds(\xi, \tau) d\xi d\tau. \end{aligned} \tag{6}$$

In equations (6) we can rename τ to t, obtaining equation (2) from the main article,

$$\begin{aligned} D\Lambda &= \int_0^T \int_0^L \left(\frac{1}{L_u} \sum_{i,j} H(\boldsymbol{x}_i; \xi, -t) \star \left[u_j(\boldsymbol{x}_i, t) - u_j^{obs}(\boldsymbol{x}_i, t) \right] - \right. \\ & \left. \frac{1}{M_{0fix}^2} \left[M_0 - M_{0fix} \right] \mu W \right) Ds(\xi, t) d\xi dt. \end{aligned} \tag{7}$$

Assuming the slip function is non-negative, we substitute $Ds(\xi, t) = s(\xi, t) D \ln s(\xi, t)$, where $D \ln s$ represents relative changes of the slip function. Equation (7) is then modified to

$$\begin{aligned} D\Lambda &= \int_0^T \int_0^L \left(\frac{1}{L_u} \sum_{i,j} H(\boldsymbol{x}_i; \xi, -t) \star \left[u_j(\boldsymbol{x}_i, t) - u_j^{obs}(\boldsymbol{x}_i, t) \right] - \right. \\ & \left. \frac{1}{M_{0fix}^2} \left[M_0 - M_{0fix} \right] \mu W \right) s(\xi, t) D \ln s(\xi, t) d\xi dt \end{aligned} \tag{8}$$

Note that the latter step introduces an implicit positivity constraint on the slip function.

The above mentioned formulation has been derived for a line fault model. Let us emphasize that generalization to a 2D fault model is straightforward. The line fault approximation was assumed in our particular application to the Movri Mountain earthquake as tests on both real data and synthetics showed almost no sensitivity to the source depth.

Numerical implementation

For numerical reasons $s(\xi, t)$ has to be expressed using some basis functions. Perhaps the simplest choice is to consider piece-wise constant functions with steps $\Delta\xi$ and Δt in space and time, respectively. This leads to discretization of the integrals in equation (8),

$$\begin{aligned} D\Lambda &= \sum_{k,l} K_{kl} D \ln s(\xi_k, t_l) \\ K_{kl} &= \left(\frac{1}{L_u} \sum_{i,j} H(\boldsymbol{x}_i; \xi_k, -t_l) \star \left[u_j(\boldsymbol{x}_i, t_l) - u_j^{obs}(\boldsymbol{x}_i, t_l) \right] - \right. \\ & \left. \frac{1}{M_{0fix}^2} \left[M_0 - M_{0fix} \right] \mu W \right) s(\xi_k, t_l) \Delta\xi \Delta t \end{aligned} \tag{9}$$

where summation over k and l is over spatial and time samples, respectively; $s(\xi_k, t_l)$ are the amplitudes of the discretized slip function and K_{kl} represents the corresponding gradient of the misfit function in the model parameter. With K_{kl} at hand one can utilize, e.g., the conjugate gradient method (Press et al, 1992) to minimize misfit (2) with the implicit positivity constraint.

Synthetic test

To test our slip inversion approach, we created a synthetic forward source model (see Figure A1a) that resembles the results obtained for the Movri Mountain earthquake. The delayed asperity is incorporated. The synthetic seismograms have been then inverted (assuming the same stations and frequency range).

The individual iterations are presented in Figure A1b. The inversion performs similarly as in the real case, see Figure 2a in the main text. The first iterations reveal the main direction of the rupture propagation. Starting with the 6th iteration the slip patch in the middle of the fault splits. The other iterations only slightly change the resulting model, which corresponds to only minor changes in the variance reduction. The slip models correctly reveal the three major slip segments, including the delayed asperity. The only less well reproduced feature is the partial rupture propagation to the south-west (left part of the figures). Furthermore, Figure A1c shows comparison between the input and the inverted source models in terms of the moment rate (left) and the distribution of moment release on the fault (right). The fit is relatively good, correctly tracing the main episodes in time and spatial domains.

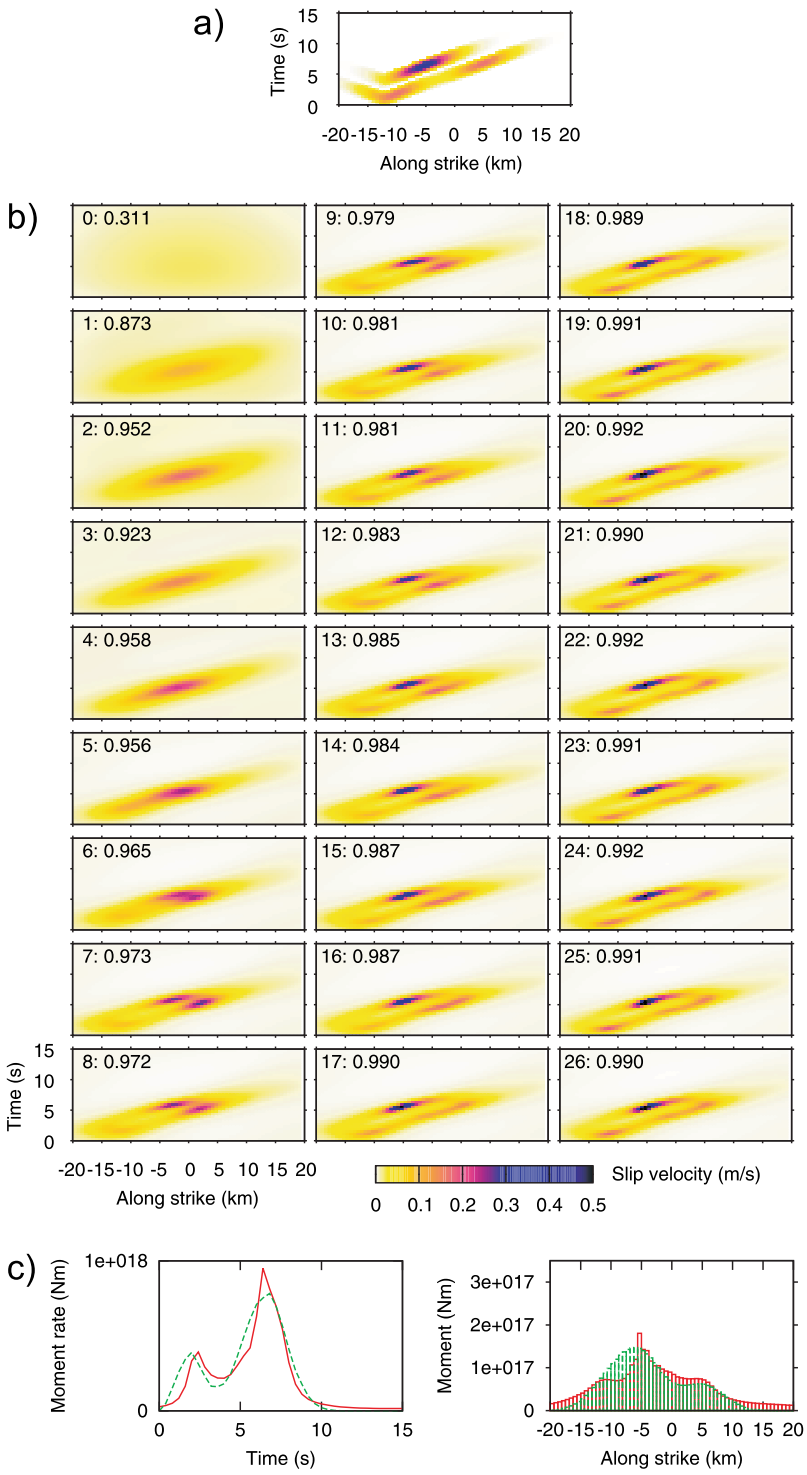

Figure A1. Synthetic test of the inversion method. a) Input source model to be inverted. b) Iterations of the slip inversion. The inscribed numbers represent the number of iteration and the corresponding variance reduction. c) Comparison between the input (green) and the inverted (red) rupture models in terms of the moment rate (left) and the distribution of moment release on the fault (right).

Additional figures

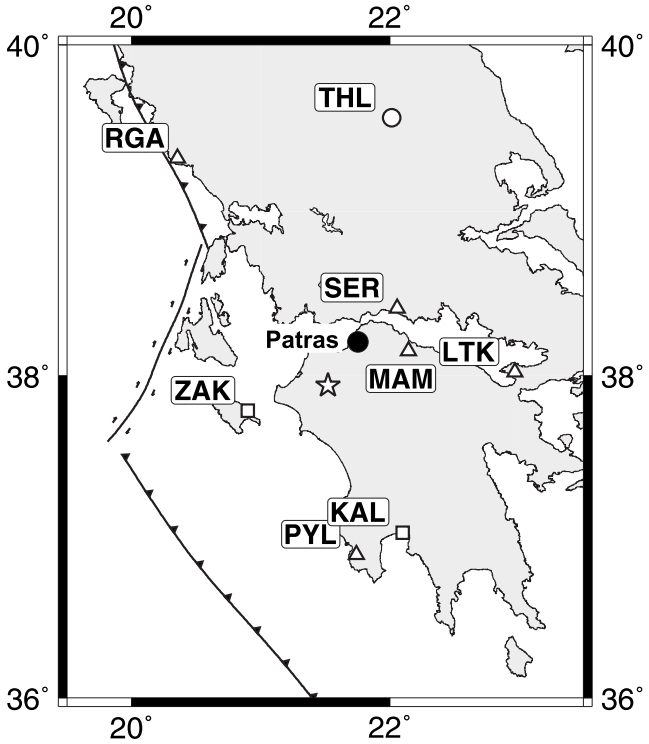

Figure A2. Distribution of stations used in the present study. Symbols refer to the station network: ITSAK (squares), NOA (circle), PSLNET (triangles). Main tectonic lines of the western Greece are displayed.

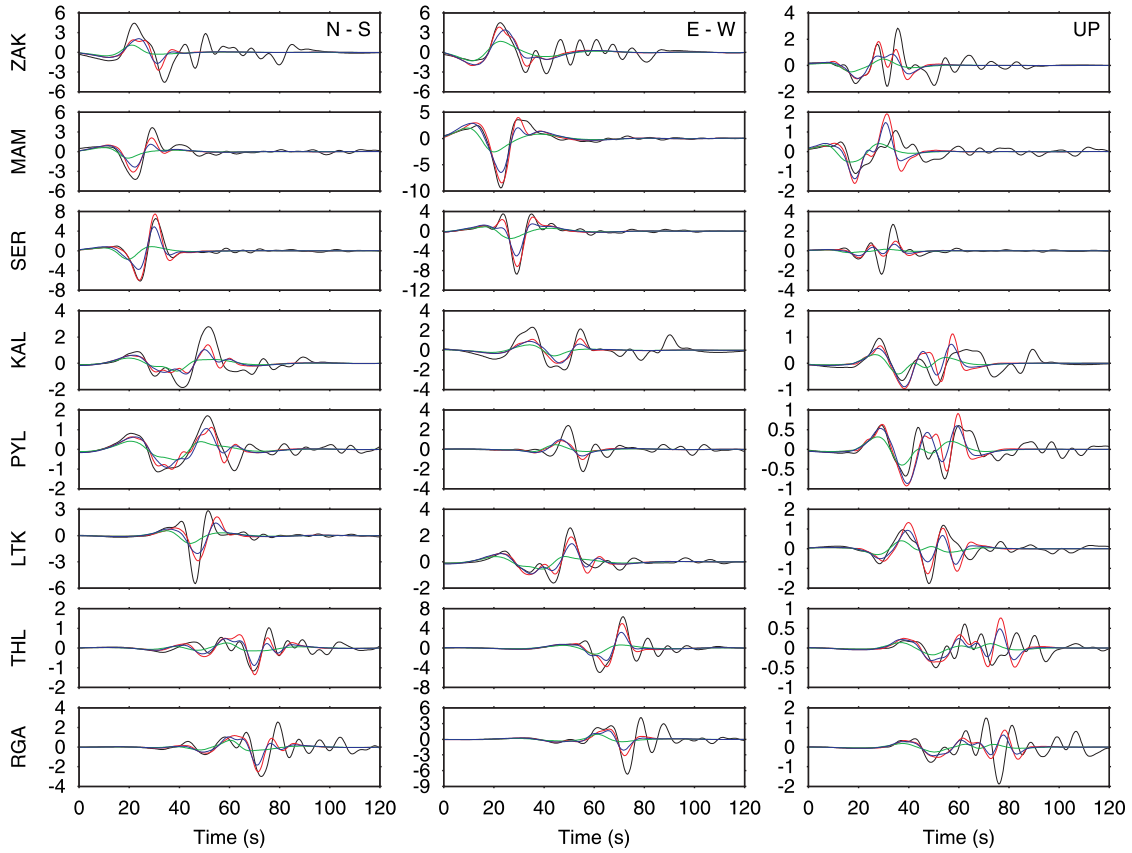

Figure A3. Matching data with synthetics. Near regional waveforms up to 0.2 Hz (displacement in millimeters), plotted in black, are compared with synthetic seismograms for three iterations, 0 (green), 1 (blue) and 26 (red). The station codes appear at left, see also Figure A2.

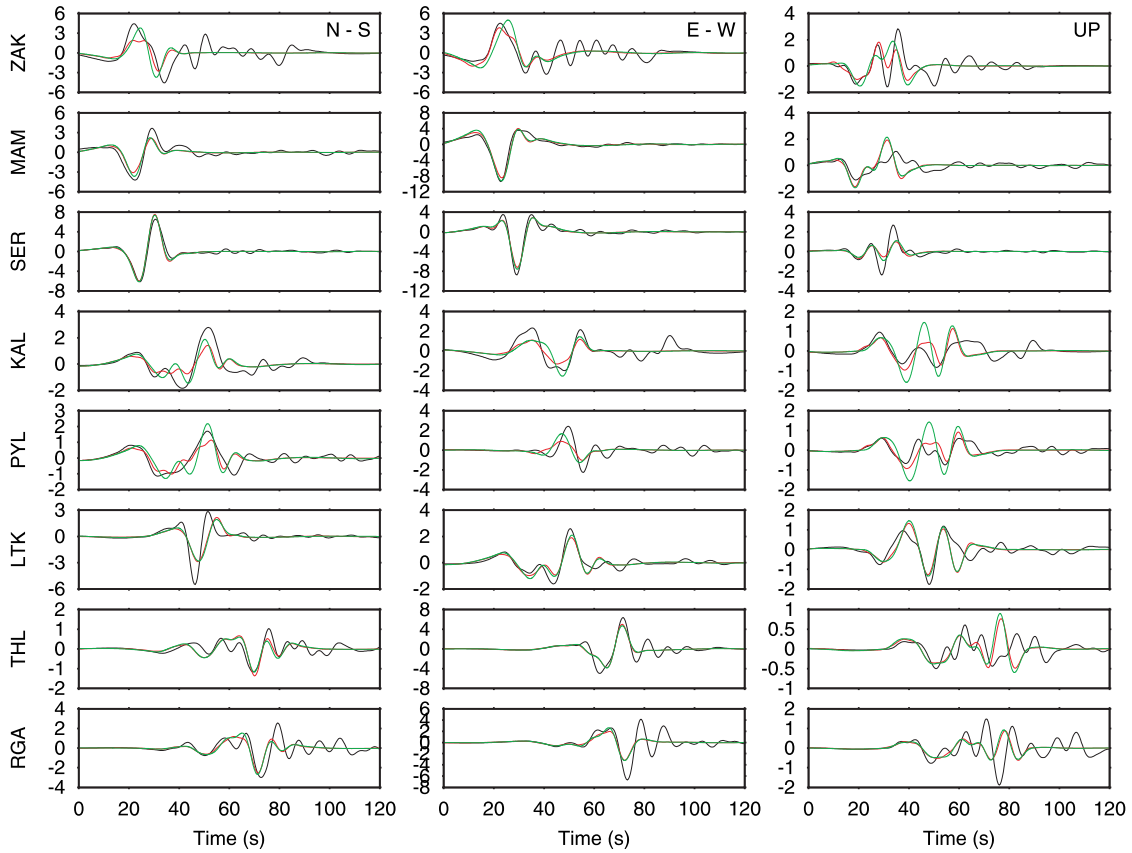

Figure A4. Same as Figure A3, only the observed waveforms (black) are compared with synthetic seismograms for the CMT solution (green) and the 26^{th} iteration of the slip inversion (red). Note especially the better fit of the duration of dominant pulses for the distributed slip model.

[P8]

JOURNAL OF GEOPHYSICAL RESEARCH, VOL. 115, B03308, doi:10.1029/2008JB006171, 2010

Three-dimensional modeling of near-fault ground motions with nonplanar rupture models and topography: Case of the 2004 Parkfield earthquake

F. Gallovič,[1] M. Käser,[2] J. Burjánek,[3] and C. Papaioannou[4]

Received 27 October 2008; revised 25 September 2009; accepted 15 October 2009; published 24 March 2010.

[1] We study the applicability of deterministic strong ground motion simulations at very near fault distances for a subvertical strike-slip fault model corresponding to the 2004 *M*6 Parkfield, California, earthquake in the frequency range up to 1 Hz. Theoretical modeling under the assumptions of a planar rupture and 1-D medium shows that as a consequence of the *S* wave radiation pattern, the particle motion for such close stations should be almost linear in the fault-normal (FN) direction, having fault-parallel (FP) and vertical (V) components of almost zero. However, as shown on the Parkfield earthquake recordings, observed particle motions are rather circular with peak velocities at FP and V components comparable to those at FN components. We investigate several realistic features that could explain this controversy, namely, nonplanar fault, realistic three-dimensional (3-D) medium, and the topography of the area. We test and quantify these hypotheses using discrete wave number and discontinuous Galerkin modeling methods applying 1-D and 3-D velocity structures, respectively, and two nonplanar rupture models. We compare the synthetic and observed particle motions and peak velocity ratios and conclude that deviations from a planar rupture geometry in reasonable bounds for the Parkfield fault and the influence of topography only partially explain the behavior of the observed seismograms. On the contrary, the heterogeneous 3-D velocity structure significantly reduces the synthetic peak ratios to values closer to 1 and provides rather circular particle motions. Therefore, the 3-D velocity model is crucial to obtain realistic estimates of ground motions at near-fault distances and is more important than the detailed fault geometry or topography in the Parkfield area.

Citation: Gallovič, F., M. Käser, J. Burjánek, and C. Papaioannou (2010), Three-dimensional modeling of near-fault ground motions with nonplanar rupture models and topography: Case of the 2004 Parkfield earthquake, *J. Geophys. Res.*, *115*, B03308, doi:10.1029/2008JB006171.

1. Introduction

[2] Studies concerned with the potential earthquake hazard and damage need realistic estimates of ground motion in a broad frequency band and in a broad range of distances at all three components. In particular, for the low-frequency band (<1−2 Hz) very close to the earthquake rupture, deterministic models [*Pitarka et al.*, 2000; *Mai and Beroza*, 2003; *Hartzell et al.*, 2005; *Gallovič and Brokešová*, 2007; *Wang et al.*, 2008] are preferable to stochastic methods [*Boore*, 1983] because they can capture near-fault effects. These models, being usually based on simple assumptions (planar fault, 1-D or relatively smoothly varying 3-D medium with no topography) are able to explain three component ground motions observed during real earthquakes at stations lying typically at distances larger than several kilometers from the fault. Nevertheless, as we demonstrate in this paper, problems may arise when simulating ground motions for stations lying very close to the earthquake fault. In particular, we take advantage of the well-studied 2004 *M*6 Parkfield, California, earthquake, which was recorded at stations lying basically above the fault rupture. On the basis of these recording, we show to what extent the deterministic methods are able to explain amplitudes at all the three ground motion components for such station locations in a low-frequency band. We discuss the ability of several modeling features to improve near-fault ground motion estimates.

[3] The earthquake of *M*6 struck the central coast of California at 1015:24 LT (Pacific Standard Time) (1715:24 UTC) on 28 September 2004. The hypocenter was 11 km southeast of Parkfield at a depth of approximately 8 km; the earthquake had a strike-slip mechanism on an almost vertical fault. The analysis of the aftershocks and the proposed rupture models indicate that the rupture occurred along the

[1]Department of Geophysics, Faculty of Mathematics and Physics, Charles University, Prague, Czech Republic.
[2]Department of Earth and Environmental Sciences, Ludwig Maximilians University, Munich, Germany.
[3]Swiss Seismological Service, Institute of Geophysics, ETH Zurich, Zurich, Switzerland.
[4]ITSAK, Thessaloniki, Greece.

0148-0227/10/2008JB006171

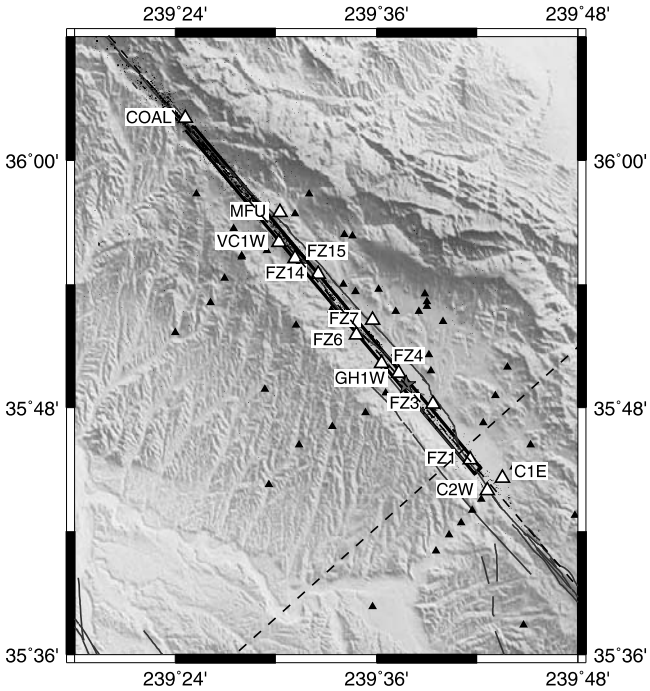

Figure 1. Map of the Parkfield area. Stations (small and large triangles), aftershocks (points), faults (thin lines), projection of the Parkfield rupture (bold line rectangle), projection of the cross sections of Figure 3 (dashed lines), and the main shock epicenter (star) are shown. In this paper we consider only stations displayed by large triangles together with their names. The elevation of the area under consideration ranges from 138 to 1335 m height.

same section of the San Andreas fault as those of the similar magnitude Parkfield earthquake series in 1881, 1901, 1922, 1934, and 1966 [*Nadeau et al.*, 1995; *Bakun and McEvilly*, 1979; *Toppozada et al.*, 2002]. The earthquake and its rupture propagation have been studied by many authors and even led to a special issue of the Bulletin of the Seismological Society of America [*Harris and Arrowsmith*, 2006], where most of the work was collected. A consensus was reached suggesting a rupture direction predominantly toward the northwest, opposite to the rupture propagation direction of the previous 1966 Parkfield earthquake. To date, the 2004 Parkfield earthquake has been a subject of a number of slip inversion studies using various kinds of data [*Hartzell et al.*, 2007; *Liu et al.*, 2006; *Dreger et al.*, 2005; *Kim and Dreger*, 2008].

[4] In particular, *Liu et al.* [2006] performed a slip inversion using strong motion data in the frequency band 0.16–1 Hz assuming a planar fault geometry and two different one-dimensional (1-D) velocity models separated by the fault plane to take into account different crustal properties northeast (NE) and southwest (SW) of the fault. This slip inversion suggested two main asperities located northwest (NW) and southeast (SE) of the epicenter. However, in their inversion, *Liu et al.* [2006] down-weighted vertical (V) components for all stations and deliberately omitted fault parallel (FP) components of three stations located almost above the earthquake fault plane or its prolongation in the strike direction. For these two components forward modeling produces synthetics with almost zero amplitudes, while the faut normal (FN) component show a strong signal, having linear particle motion perpendicular to the fault strike. This is due to the radiation pattern of a predominantly strike-slip rupture along a perfectly planar fault in a 1-D medium. On the contrary, the observed data are characterized by peak amplitudes of similar magnitude for all three components and rather circular particle motions. We claim that this inconsistency between modeled and observed particle motions (and FN/FP and FN/V peak velocity ratios) can be attributed to the simplifying assumptions usually made in the modeling process, namely, a fault model that is perfectly planar, a 1-D medium with no lateral variations of the material properties and the negligence of relevant free-surface topography.

[5] Note that the small peak velocity ratios represent a more general issue as they are observed in similar settings. For example, relatively large ratio was observed during the Kobe earthquake. *Irikura* [1996] shows that one of the near-fault stations was characterized by large ratio between FN and V components of 8.5, while the ratio between FN and FP components was lower, 2.5.

[6] There could be many explanations for the inconsistency described above, such as presence of the fault zone, anisotropy, nonlinear soil effect, etc. In our study, which is not intended to cover a complete set of possible physical models, we rather propose and quantitatively test only three hypotheses. In particular, the first one is based on nonplanar faults. *Käser and Gallovič* [2008] performed a numerical study on the radiation of seismic waves from kinematic nonplanar rupture models. They showed that an increasing geometrical complexity of a rupture surface can introduce relatively strong signals at FP and V components for stations lying above a vertical strike-slip fault, which would be of zero amplitude for a perfectly planar model. As mentioned above, this is mainly a consequence of the properties of the S wave radiation pattern. In the case of the nonplanar fault, both local strike and dip angles vary along the fault and thus the seismic radiation pattern is more distorted. Let us emphasize that the 2004 *M*6 Parkfield earthquake represents a unique opportunity to test such effects of nonplanar ruptures to explain the observed FP and V components because of a large amount of very near fault (<1–2 km) strong motion records (see Figure 1).

[7] The second hypothesis is that in the real Earth the seismic waves propagate in a complex 3-D medium that distorts the source radiation pattern. We do not attribute such effects to scattering due to stochastic properties of the medium since the study is performed in a relatively low frequency band up to 1 Hz in which the seismic waves are rather affected by deterministic larger-scale 3-D variations in the crustal structure. A number of 3-D tomographical crustal models exist for the Parkfield area [*Michelini and McEvilly*, 1991; *Eberhart-Phillips and Michael*, 1993; *Thurber et al.*, 2006], which further favors this region for this kind of study.

[8] As a third hypothesis the free surface topography in the Parkfield area could cause signals on the theoretically zero FP and V components. The influence of free surface topography has been studied by many authors, [e.g., *Bouchon*, 1973; *Zahradník and Urban*, 1984; *Geli et al.*, 1988; *Bouchon et al.*, 1996]. Typically, its effect has to be analyzed for each region separately and, moreover, usually depends strongly on

the frequency band of interest. Therefore, we will compare our results for the 3-D heterogeneous material including or omitting the free surface topography.

[9] To summarize, assuming frequency range up to 1 Hz we quantitatively study the effects of rupture nonplanarity, 3-D heterogeneous material and topography in terms of their ability to decrease synthetic FN/FP and FN/V peak amplitude ratios at stations lying above a vertical strike-slip fault closer to unity as observed in the Parkfield earthquake data. We start with the planar source model inverted by *Liu et al.* [2006]. Then, two speculative nonplanar rupture models are introduced. The slip distribution and rupture propagation of *Liu et al.* [2006] is transcribed on these nonplanar faults in order to have all rupture models consistent. The ground motions generated by these nonplanar earthquake source models are computed in both the 1-D medium adopted by *Liu et al.* [2006] and 3-D medium obtained by *Thurber et al.* [2006]. Finally, we show the influence of real surface topography.

[10] We compare the changes of the particle motions, synthetic seismograms, their Fourier spectra and peak velocity ratios with the real data observed during the 2004 Parkfield earthquake as a reference. We point out that we are not particularly interested in improving the fit with the observed waveforms. We rather study to what extent nonplanar fault geometries, the 3-D medium and the topography effects can distort the linear particle motions and improve FN/FP and FN/V amplitude ratios in terms of reducing them close to unity as observed in real data. In this respect, we discuss which of the model features are advisable to be taken into account in the slip inversions and strong ground motion simulations to provide realistic estimates for similar problems.

2. Stations and Recorded Data

[11] The 2004 *M*6 Parkfield earthquake was recorded by analog recorders operated by the California Geological Survey (CGS) network and digital recorders maintained by the U.S. Geological Survey (USGS) (Figure 1). In our study we consider only stations in a very close vicinity (<1.5 km) of the fault, which were also used in the slip inversion by *Liu et al.* [2006]. Thus the results are presented for 13 stations which exhibit typical features as described in the introduction and later in the text. *Liu et al.* [2006] used their recordings in the slip inversions after determining approximative correction to the site effects. The exceptions are stations MFU, FZ14 and COAL for which the site effect correction was not determined. Nevertheless, they were successfully used in the slip inversion. Note that some of the station components were not used in the inversion or not fitted. In particular, although FP and V components of COAL station were used in the inversion, the synthetic amplitudes are more than 20 times lower than the observed ones. FP components for stations C2W, GH1W, and FZ1 were completely omitted in the inversion for questionable polarities [*Liu et al.*, 2006]. We note that the fit is also poor due to the station position with respect to the rupture as explained in the introduction.

[12] Processed data (velocity records) were downloaded from the US National Center for Engineering Strong Motion Data (http://www.strongmotioncenter.org/). We applied a band-pass filter in the frequency band from 0.16 to 1 Hz following the work of *Liu et al.* [2006]. The lower and upper limits of the filter are dictated by inaccurate instrument performance below 0.16 Hz and the inability to model deterministically the Green's functions at high frequencies, respectively.

3. Crustal Models and Wave Propagation Codes

[13] The Parkfield area is geologically very complex. One of its most evident features is the substantial change of material properties across the San Andreas Fault (SAF) separating different geological units, namely, sedimentary Franciscan terrain in the NE and granitic Salinian block in the SW [*Brocher*, 2005]. This is not surprising as the SAF has undergone several hundreds of kilometers of cumulative slip, which brings together geological units originally developed far away from each other. The SAF has been subject to intensive research. For example, the studies of the fault zone head waves treated the fault as an abrupt material interface [*Ben-Zion and Malin*, 1991; *Ben-Zion*, 1990], while others considered the fault as a narrow (100–150 m) transition zone capable of producing fault zone trapped waves [*Li et al.*, 1990]. This damaged core layer (or fault zone) surrounding the fault is a low-velocity zone characterized by velocity reductions up to 40% and low Q values of ~30 [*Li et al.*, 2004]. Other investigations revealed that the structure at the SAF area is characterized by a wider (~1 km) damaged zone [*Unsworth et al.*, 1997] containing different fault branches that are visible on the surface. This zone spreads from the main fault trace in the northeast to the southwestern fracture zone.

[14] The crustal model of the Parkfield area has been subject to a number of 3-D tomographic studies [*Michelini and McEvilly*, 1991; *Eberhart-Phillips and Michael*, 1993]. In the present paper we use the most recent model by *Thurber et al.* [2006]. Starting from the model of *Eberhart-Phillips and Michael* [1993], *Thurber et al.* [2006] include a large number of earthquake events and active shots and present a new compressional wave speed (v_p) model with a locally increased resolution along the SAF (up to 1–2 km in the Parkfield area), particularly imaging the strong material contrast and its depth variation. As such, the model does not include the observed fault zone [*Li et al.*, 2004] as a distinct waveguide feature which is supposedly only 100–200 m wide. The 3-D velocity model by *Thurber et al.* [2006] only perhaps partly images the wider damaged zone as pointed out by *Lewis et al.* [2007]. Nevertheless, as the lowest S wave velocity in the damaged zone can by as low as 500 m s^{-1}, which corresponds to wavelengths of 500 m for our largest frequency of 1 Hz, such details are a few times below the resolution of *Thurber et al.*'s [2006] model (see section 3.2). With this respect, we emphasize that our study does not intend to cover an exhaustive set of all features possibly influencing the ground motions. Rather, it concentrates on distinct effects of nonplanar source models and 3-D velocity medium typically used in the ground motion modeling studies on the simulated three-component ground motions. Nevertheless, other features of the Parkfield area are presumably important and will be subject of our further study.

Table 1. Parameters of NE and SW Crustal Models Describing the Bimaterial Character of the Parkfield Area[a]

Depth (km)	v_p (km s^{-1})	v_s (km s^{-1})	ρ (g cm^{-3})	Q_P	Q_S
		NE Crustal Model			
0.0	2.0	1.1	2.0	70	35
0.7	3.8	2.2	2.3	300	180
1.4	4.3	2.4	2.3	340	190
2.0	4.8	2.7	2.3	450	250
3.6	5.3	3.1	2.5	500	300
7.6	5.8	3.3	2.7	550	300
14.3	6.2	3.8	2.8	600	350
20.5	6.8	3.8	2.8	650	350
24.6	7.0	4.0	2.8	700	400
		SW Crustal Model			
0.0	1.9	1.0	2.0	70	35
1.0	3.4	1.7	2.3	270	160
2.0	4.6	2.4	2.3	450	260
3.0	5.1	3.1	2.7	500	300
4.0	5.6	3.6	2.7	550	350
5.4	6.3	3.6	2.8	600	350
18.7	6.8	3.6	2.8	680	360

[a]After *Liu et al.* [2006].

[15] For comparison purposes, in accordance with *Liu et al.* [2006], we use also two 1-D velocity models approximating the bimaterial structure NE and SW of the fault separately. More details on the modeling are explained below.

3.1. One-Dimensional Crustal Models

[16] We adopt the two 1-D crustal models from *Liu et al.* [2006] shown in Table 1 to take into account the presence of different materials on the two sides of the fault. The models are derived from the 3-D models of *Eberhart-Phillips and Michael* [1993] and *Thurber et al.* [2006].

[17] The kinematic fault model is numerically approximated by 128 × 64 rectangular elements represented by double-couple point sources. For each source-receiver pair the Green's functions are calculated using the DWN method of *Bouchon* [1981]. The ground motion at a given station is then obtained by summing up contributions from all the point sources taking into account the prescribed slip history, which corresponds to the numerical evaluation of the fault surface integral in the representation theorem [*Aki and Richards*, 2002]. For details on the source model properties, see section 4. Note that we downsample the source model provided by *Liu et al.* [2006] in the electronic supplement with 260 × 95 samples. We have tested that our resolution is sufficient and results in decreased numerical expense due to a lower number of needed Green's functions.

[18] *Liu et al.* [2006] determined correction amplitude factors at the Parkfield array from the 1983 *M*6.5 Coalinga earthquake spectra in the frequency range of 0.16–1 Hz to approximate the site effects. Their corrected values are presented in the erratum. In order to validate our 1-D media simulations against their synthetic data we apply the same amplification factors.

3.2. Three-Dimensional Crustal Model

[19] For the simulations based on a 3-D velocity structure we use the model proposed by *Thurber et al.* [2006]. It is defined by values at nodes with spacing ranging from 2 to 5 km in the vicinity of the SAF. We interpolate this v_p model using cubic splines and derive the shear wave speeds (v_s) and densities (ρ) using the empirical relations of *Brocher* [2005] as suggested by *Thurber et al.* [2006]. Explicitly, we use

$$v_s = 0.7858 - 1.2344\,v_p + 0.7949\,v_p^2 - 0.1238\,v_p^3 + 0.0064\,v_p^4 \quad (1)$$

$$\rho = 1.6612\,v_p - 0.4721\,v_p^2 + 0.0671\,v_p^3 - 0.0043\,v_p^4 + 0.000106\,v_p^5, \quad (2)$$

where the unit of v_p, v_s and ρ are given in km s^{-1} and g cm^{-3}, respectively. We have near-surface minimum wave speeds of v_p = 1.224 km s^{-1} and v_s = 0.253 km s^{-1} at very localized parts of the model. Note that the rules given by *Brocher* [2005] have been derived only for $v_p > 1.5$ km s^{-1} so we simply extrapolate the rules to lower velocities obtaining a reasonable decrease of v_s velocities. Assuming our highest frequency of 1 Hz, the corresponding wavelength is of about 0.25 km. This is several times smaller than the resolution of the model by *Thurber et al.* [2006]. Nevertheless, we point out that this is a typical situation in the ground motion estimations. Assuming that we can at least partially approximate the site effects by using the interpolated 3-D model, we do not use the amplification factors determined by *Liu et al.* [2006]. Let us emphasize that the accurate knowledge of near-surface material properties is only crucial for the absolute amplitude values [*Olsen et al.*, 2003]. This means that this effect would influence all components rather equally, so it is not a critical point for the peak amplitude ratios we are mainly interested in.

[20] The simulation of the seismic wavefield in the 3-D crustal model was carried out by the ADER-DG method [*Käser and Dumbser*, 2006; *Dumbser and Käser*, 2006]. To this end, the computational domain of the Parkfield area was discretized by an unstructured tetrahedral mesh using roughly 1.5 million elements. The computational domain is bounded by absorbing boundaries along a prolate ellipsoid of length 100 km, width 60 km in the lateral extend and a depth of 28 km as shown in Figure 2.

[21] In the calculations when the topography is taken into account, the top of the mesh is bounded by the free surface given by the digital elevation model of the Parkfield area. The mesh spacing is variable and ranges from 300 m at the surface in the vicinity of the source projection to the surface and the receivers locations to 4000 m toward the remaining boundaries of the computational domain. The elastic parameters inside each element are determined by the velocity model described above. Cross sections through the 3-D heterogeneous v_p and v_s velocity model are shown in Figure 3. In particular, the cross sections in Figures 3a and 3c have the same along-strike location and fault-normal orientation as the one shown in Figure 3f of *Thurber et al.* [2006]. Similarly, the cross sections in Figures 3b and 3d have the same fault-normal location and along-strike orientation as the one shown in Figure 4b of *Thurber et al.* [2006]. This way, the body of high P wave velocity, as reported by *Eberhart-Phillips and Michael* [1993] and analyzed with respect to its importance for fault behavior by *Michael and Eberhart-Phillips* [1991], is nicely visible.

[22] The approximation order of the applied ADER-DG scheme is set to 5 in time and space providing sufficient

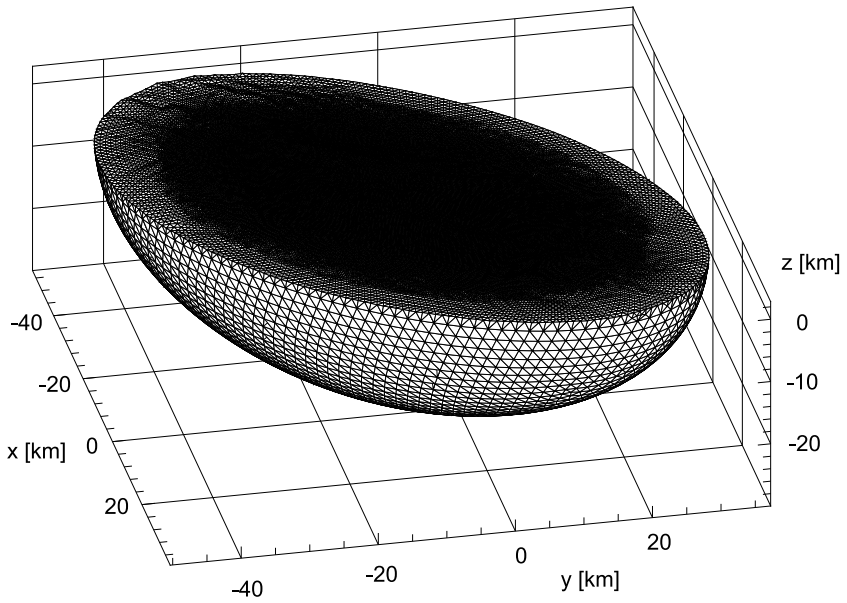

Figure 2. Discretization of the computational domain with an unstructured tetrahedral mesh with variable mesh spacing and smooth elliptic model boundaries to optimize the resolution of the simulation and avoid boundary effects.

accuracy of the numerical scheme as validated by the DWN method for a simplified, layered 1-D medium (not presented here [see, e.g., *Käser and Gallovič*, 2008]).

4. Source Models

[23] Here we introduce the geometrical fault models of the 2004 Parkfield earthquake considered in this paper. They are all based on the relocated aftershock distribution [*Thurber et al.*, 2006]. In a first-order approximation the aftershocks delineate a planar fault as used by *Liu et al.* [2006] that we denote as the *planar fault* (PF) model. However, when looking at the cross sections of the aftershock distribution in SW–NE direction apparent trends can be seen, such as the opposite dipping directions of the NW and SE part of the fault [see *Thurber et al.*, 2006, Figure 6b]. Moreover, an apparent variability of the aftershock distribution, especially in the upper part of the 2004 Parkfield rupture associated with the southwest fraction (SWF) zone [*Harris and Arrowsmith*, 2006; *Simpson et al.*, 2006], might suggest possibly even more complicated geometrical properties. Therefore, we introduce two nonplanar models, referred to as the *aftershock-constrained nonplanar fault* (ACNF) and the *aftershock-constrained nonplanar fault with stochastic component* (ACNFS), as shown in Figure 4. In order to emphasize the effects of rupture nonplanarity on the ground motion, especially the ACNFS model is considered as maybe an *extreme* case just allowed by the maximum lateral extent of the aftershock distribution. We keep all three models easily comparable by keeping their kinematic properties and scalar seismic moments the same as those for the inverted PF model (see further).

4.1. Planar Fault Model

[24] In accordance with the work of *Liu et al.* [2006], the geometry of the PF model is determined by fitting a plane through the Parkfield earthquake aftershocks [*Thurber et al.*, 2006], obtaining strike $\varphi = 140^\circ$ and dip $\delta = 87^\circ$. The hypocenter is located at 35.8185 N, 120.3706 W, and at a depth of 8.26 km. The fault has a length of $L = 40$ km and a width of $W = 15$ km and is buried 500 m below the surface as the surface breaks observed in the Parkfield area are considered to be secondary cracks, not direct coseismic surface rupture [*Rymer et al.*, 2006; *Simpson et al.*, 2006]. The RMS distance of the relocated aftershocks from this planar fault is 343 m.

[25] All the kinematic source parameters come from the inversion of strong motion records done for the same fault geometry by *Liu et al.* [2006], namely, the slip values, rake angles, rise times and rupture time distributions. Figure 4a shows the PF model geometry together with the distribution of scalar seismic moment. The scalar moment distribution is determined by the inverted slip values and a depth-dependent effective rigidity μ given by the formula for a source lying within a bimaterial interface [*Wu and Chen*, 2003]

$$\mu(z) = 2\mu^{NE}(z)\mu^{SW}(z)/\left(\mu^{NE}(z) + \mu^{SW}(z)\right), \qquad (3)$$

where $\mu^{NE}(z)$ and $\mu^{SW}(z)$ are the rigidities of the NE and SW crustal models at depth z, respectively (see Table 1). Note that the same scalar seismic moment distribution including the effective rigidity factors for the two separate 1-D models is used even when the 3-D model is considered. Consequently, all the models in our paper are characterized by the same scalar moment distribution. The total scalar seismic moment for the planar rupture model is 1.20×10^{18} N m as shown in Table 2. This table also shows source moment tensor parameters obtained by waveform inversions of teleseismic recordings carried out in Berkeley (0.98×10^{18} N m) and Harvard (1.13×10^{18} N m), which are in good agreement with the value used in this paper.

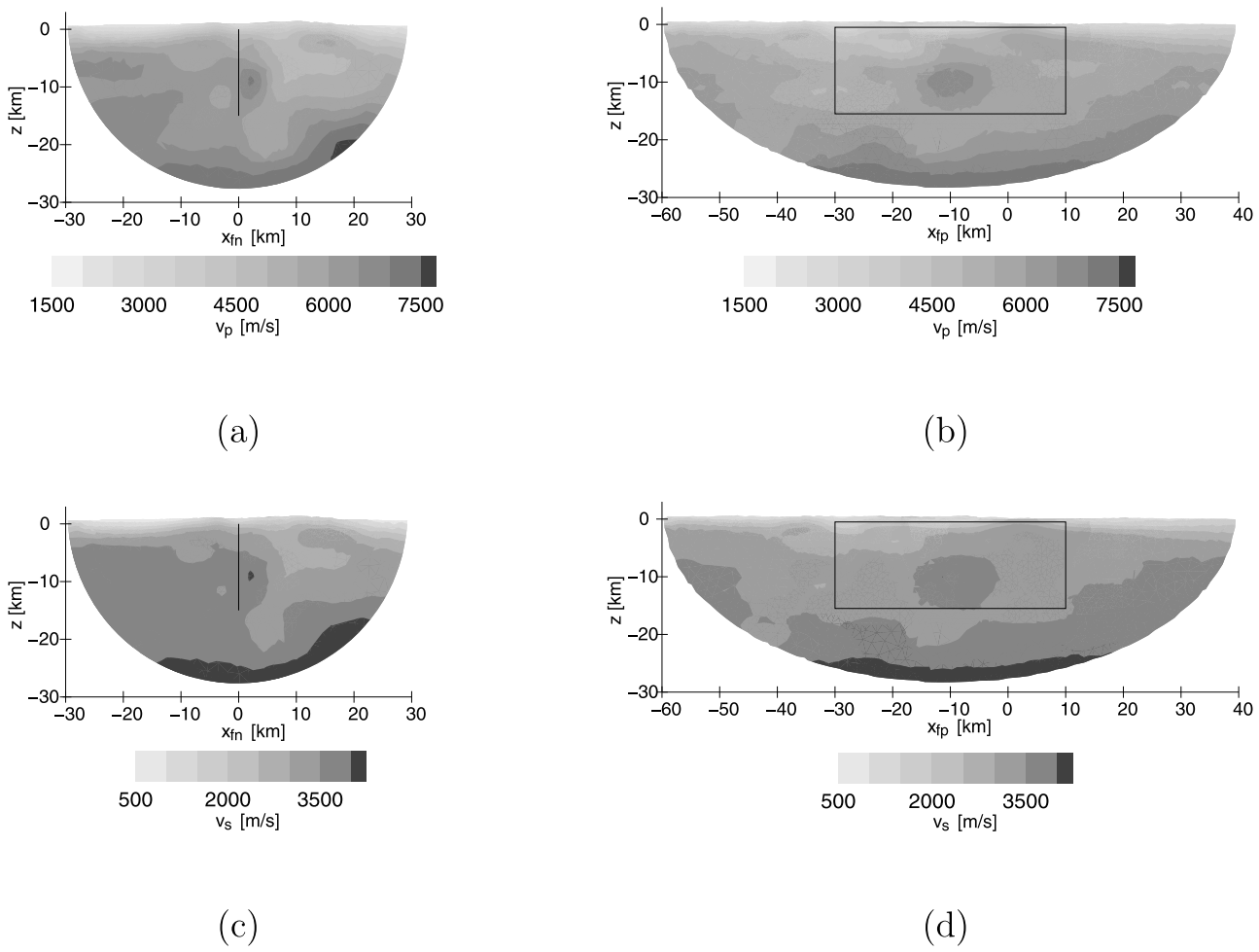

Figure 3. Cross sections of the 3-D velocity model. (a) and (c) Cuts through the v_p and v_s structure from SW to NE in the fault normal direction (x_{fn}) seen from the SE. (b) and (d) Cuts from NW to SE in the fault parallel direction (x_{fp}) seen from the SW. We also show the projection of the rupture surface dimension as a black line in Figures 3a and 3c or a rectangle in Figures 3b and 3d. Locations of the cross sections are shown in Figure 1.

4.2. Aftershock-Constrained Nonplanar Fault Model

[26] We group the aftershocks into 10 bins along the 40 km distance in the strike direction. Then we represent the local fault geometry by subplanes using a linear least squares approximation that leads to 10 subfaults of 4 km length and 15 km depth. We then connect the midpoints in strike direction of all subfaults at five equidistant depth levels together to a 10 × 5 grid. On the basis of this coarse mesh of the fault geometry, we construct a fine mesh of 128 × 64 point sources by cubic spline interpolation. The resulting fault model is shown in Figure 4b. The ACNF model accounts for the apparent trend in the aftershock locations; that is, the NW part seems to be characterized by an opposite dipping direction than the SE part. The RMS distance between the fault and the aftershocks is 282 m, which is lower with respect to the PF model. The strike and dip variations are determined by the fault geometry.

[27] The other kinematic parameters of the rupture process are kept the same as in the PF case. However, since the complex fault geometrical properties determine variations of strike and dip along the fault, the final seismic moment tensor of the whole ACNF model is not the same as that of the PF model. We analyze it in Table 2, showing that it is characterized by 1.4% of a compensated linear vector dipole (CLVD) component as described by *Frohlich* [1994]. Also we obtain a slightly lower seismic moment. In order to keep the scalar seismic moment of the planar and nonplanar model the same, we simply multiply the results obtained for the ACNF model by the ratio of scalar seismic moments for planar and ACNF models.

4.3. Aftershock-Constrained Nonplanar Fault With Stochastic Component Model

[28] As already mentioned above, the perhaps highly damaged shallow (<5 km depth) zone at the SAF area between the San Andreas Fault trace in the east and the southwest fracture zone is only poorly known [*Unsworth et al.*, 1997]. It presumably contains fault branches that extent to the surface, but the upper 5 km of the fault surface are very poorly constrained by aftershock distribution [see, e.g., *Thurber et al.*, 2006]. As the aim is to investigate whether variation of strike and dip angles is able to explain the observed peak velocity ratios, we introduce another speculative model that is even more nonplanar in its upper part

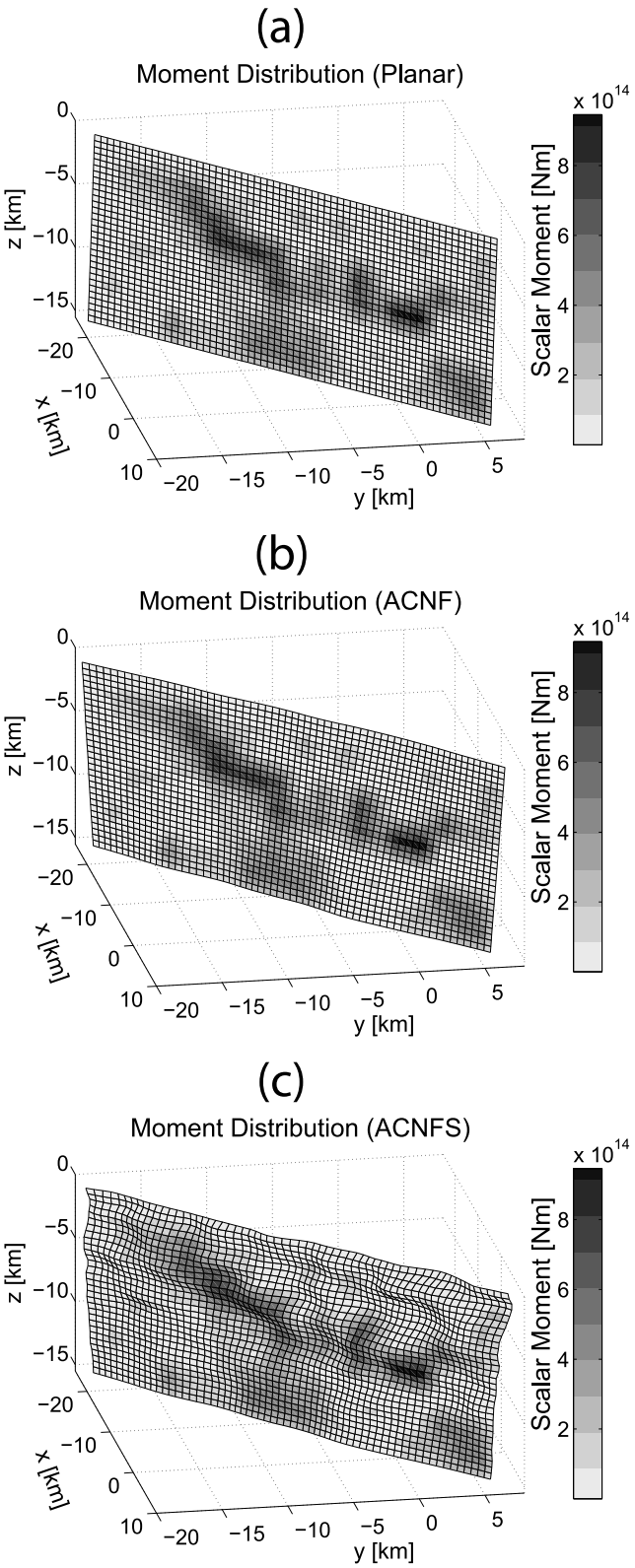

Figure 4. Scalar seismic moment distribution and geometries of the Parkfield source models considered in this work: (a) planar fault, (b) aftershock-constrained nonplanar fault (ACNF), and (c) aftershock-constrained nonplanar fault with stochastic component (ACNFS).

than the ACNF model. The ACNFS fault surface model has to be considered only as "exploratory and suggestive," representing the uncertainty at shallow depth where strike and dip of SAF are poorly constrained. Note that the larger the variations of strike and dip, the more pronounced effect on ground motions.

[29] Following the work by *Käser and Gallovič* [2008], we generate random geometrical deflections of the rupture surface from the ACNF model. The deflections, i.e., distances from the ACNF rupture surface, are created using a random field generator: First, random numbers are prescribed to each of the rupture elements. Then, this white noise is transformed to the spatial Fourier domain. Here the amplitude spectrum is modified by a k^{-3} function

$$P(k_x, k_z) = \left[1 + \left((k_x L_x)^2 + (k_z L_z)^2\right)^{3/2}\right]^{-1} \quad (4)$$

where k_x and k_z are wave numbers in the strike and dip directions, respectively, and L_x and L_z are correlation lengths in the corresponding directions. The modified spectrum is then high-cut filtered just below the Nyquist wave number and Fourier transformed back to the spatial domain. Finally, the random field root mean square (RMS) responsible for the strength of the deflections is imposed.

[30] We set L_x = 10 km and L_z = 3.5 km and the RMS values equal to 350 m. These stochastic deflections are modified by a linear function 1-z/W, where z goes from 0 (top of the fault) to W = 15 km (bottom of the fault). In this way, the variations are less severe in the lower part of the fault, where the aftershocks tend to delineate a smoother rupture surface. The spatial variations of strike and dip due to the source geometry are computed for each rupture element by the spatial derivative of the deflection field in the strike and dip directions, respectively.

[31] Figure 4c shows the generated ACNFS model used in our modeling. Its RMS deflections, i.e., RMS of distances of the ACNFS model from the PF model, is 382 m, which roughly corresponds to RMS distance between the PF model and the relocated aftershock distribution (343 m). This means that in a loose statistical sense the deflections of ACNFS model reflect the variability of aftershock locations with respect to a mean plane. As in the previous case of the ACNF model, we keep all the remaining kinematic parameters the same as for the PF case.

[32] Table 2 shows parameters of the moment tensor of this rupture model, being again different from those of the PF and ACNF models. The CLVD component represents about 2.9% of the seismic moment and the scalar seismic moment is again slightly lower than that for the PF model. We again multiply all the synthetics obtained by this source model by the moment correction factor given by the ratio between scalar moments of the ACNFS and the PF model in order to have all three fault models consistent.

5. Modeling Results

[33] We simulate ground velocities with both 1-D and 3-D subsurface velocity structures and all the fault surface models. Figure 5 shows observed and synthetic horizontal

Table 2. Observed and Modeled Moment Tensor Parameters of the 2004 Parkfield Earthquake[a]

Parameter	Moment Inversion		PF Model	ACNF Model	ACNFS Model
	Berkeley	Harvard			
Source composition					
Scalar moment (N m)	0.98×10^{18}	1.13×10^{18}	1.20×10^{18}	1.19×10^{18}	1.08×10^{18}
DC	98.8%	82.6%	100.0%	98.6%	97.1%
CLVD	1.2%	17.4%	0.0%	1.4%	2.9%
Iso	0.0%	0.0%	0.0%	0.0%	0.0%
Best DC parameters					
Strike	147.0°	321.0°	140.0°	139.7°	138.9°
Dip	83.0°	72.0°	87.0°	86.9°	87.4°
Rake	−175.0°	−177.9°	150.6°	150.6°	150.6°
Moment correction factors	–	–	1.00	1.01	1.11

[a]Note that in order to have all the models the same, we introduce the moment correction factor (ratio between the scalar moment of the planar and nonplanar rupture).

particle motions for all the models considered. Figures 6 and 7 show the synthetic seismograms in the time domain for the 1-D and 3-D models, respectively. Examples of corresponding Fourier amplitude spectra are shown in Figures 8 and 9. Note that the considered stations are ordered in Figures 8 and 9 according to their fault distance, the first and the last station lying at approximately 1.5 km to the NE and SW, respectively.

[34] We emphasize that our aim is not obtaining better fit with the observed data. The observed data, when compared to the inverted model (1-D medium, PF model), serves only for illustration of the best fit that can be obtained in the current setting. This "reference misfit" helps when evaluating the strong or weak influence of the individual model complexities (fault nonplanarity, 3-D medium, and topography), i.e., whether the change in particle motions, waveforms, and Fourier spectra when introducing, for example, a nonplanar fault is comparable to the misfit between the observed data and the synthetics for the best fitting model or not.

5.1. Effect of the Rupture Geometry in 1-D Media

[35] Figures 5 and 6 show the modeling results in the 1-D crustal models characterizing the bimaterial Parkfield area for all the three source models in terms of the horizontal particle motion and waveforms. Note that the results for the PF model, in fact, replicate the calculations of *Liu et al.* [2006] for their best fitting Parkfield model that we use in this study. Therefore, the fit to the observed data is the best achievable with our actual setup.

[36] The particle motions of the observed data (Figure 5) exhibit complex behavior at all distances, even very close to

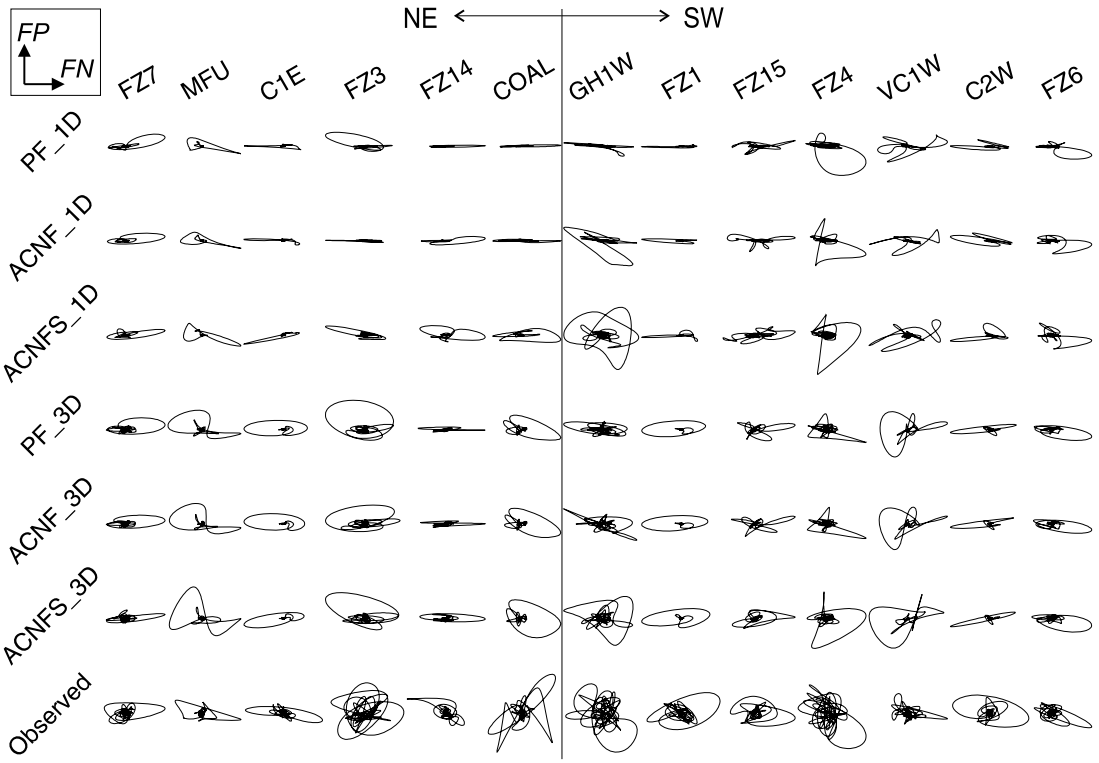

Figure 5. Horizontal particle motions for 13 stations closest to the rupture for all the models taken into account in this study and for the observed data. The vertical line illustrates the relative position of the fault.

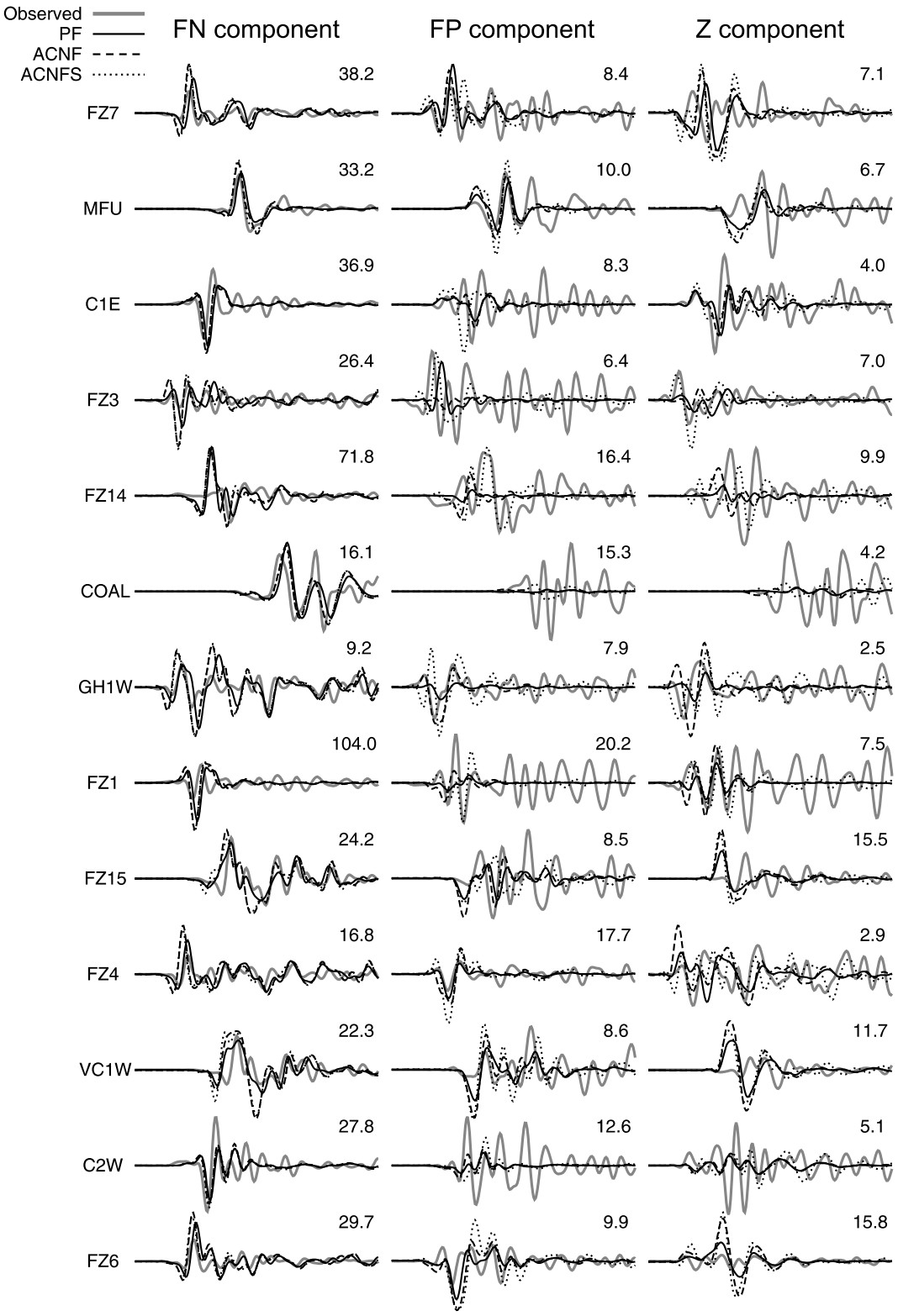

Figure 6. Synthetic velocity seismograms obtained for the three source models for the 1-D bimaterial medium. The values are the maxima from all the waveforms under comparison. The time axis corresponds to 18 s.

the earthquake rupture. On the contrary, the synthetic particle motions have strongly linear character (perpendicular to the fault strike) especially for the very close stations. Figure 5 further shows particle motions for both the nonplanar models ACNF and ACNFS. Generally, the most geometrically complex model ACNFS provides the most nonlinear polarization, for example, at stations FZ14, COAL, GH1W or FZ15. More distant stations do not

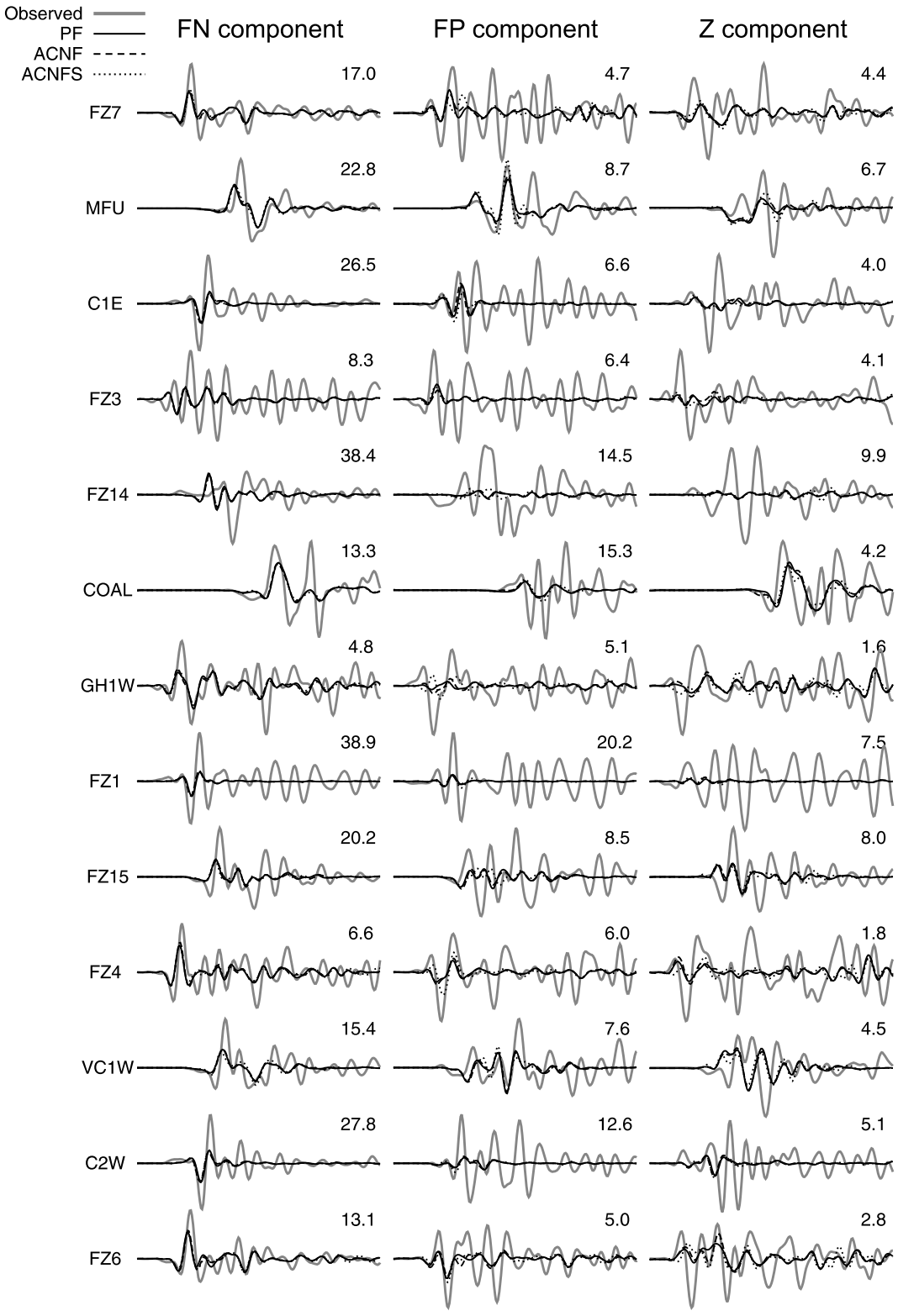

Figure 7. Synthetic velocity seismograms obtained for the three source models for the 3-D heterogeneous medium. The values are the maxima from all the waveforms under comparison. The time axis corresponds to 18 s.

change their particle motions much when adding the fault geometrical complexity. Interestingly, only for station FZ3 the ACNF model provides more linear particle motion than the PF model. Note that only in the case of the station GH1W the nonplanar rupture causes the particle motion to have similar complex shape as what is observed in real data.

[37] Regarding the waveform comparison for the PF model (Figure 6), the fit is better for the FN components

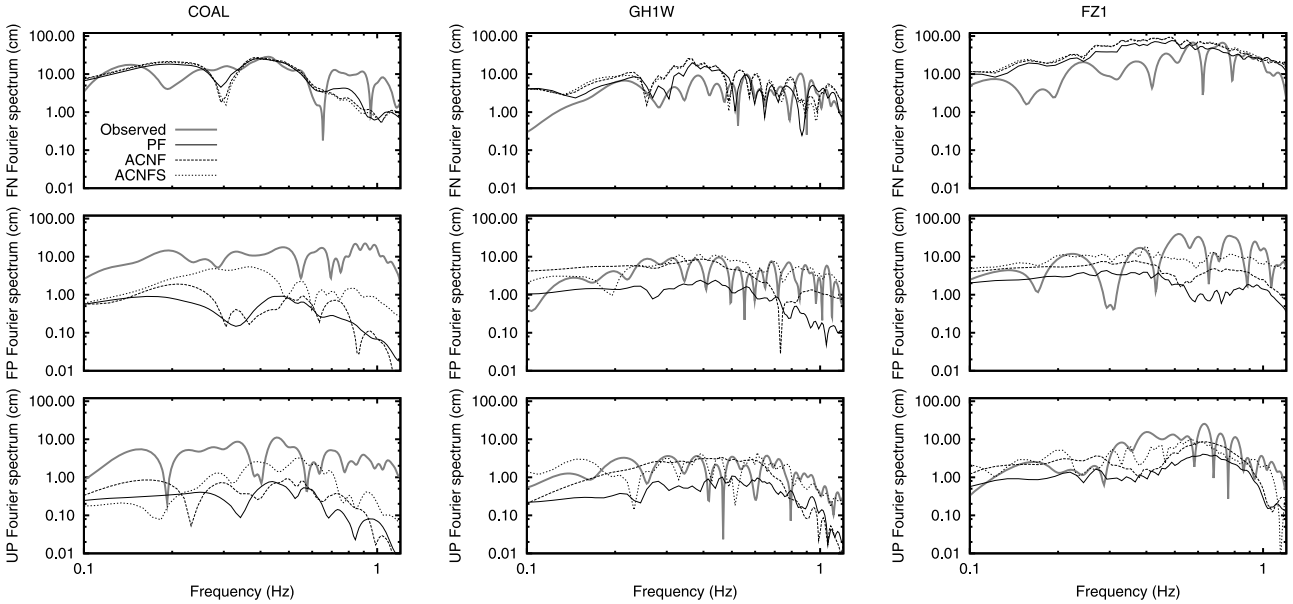

Figure 8. Fourier amplitude spectra of three selected seismograms shown in Figure 6 for the 1-D bimaterial medium.

than for the other two. In fact, some of the FP components of particular stations (FZ1, C2W and GH1W) were not used in the slip inversion by *Liu et al.* [2006]. The synthetics for the stations closest to the fault, e.g., FZ14, COAL, GH1W, and FZ1 are systematically characterized by very low amplitudes at FP and V components with respect to the FN components and, especially, to the observed data. The strong amplitude differences are related to the linear polarization explained above as a consequence of radiation pattern of a planar strike-slip rupture in a 1-D medium.

[38] Figure 6 also shows the synthetics for the nonplanar source models ACNF (dashed) and ACNFS (dotted). The FN components are almost insensitive to the variations of the fault geometry, which is in agreement with the results found by *Käser and Gallovič* [2008]. Note that this is due to the moment correction factor that scales the synthetics to the same scalar seismic moment. On the contrary, the FP and V components are generally more sensitive to the variations of the fault geometry, however, the variations need to be relatively strong as those associated with the ACNFS model. In general, the amplitudes of the FP and V components tend to increase with an increasing complexity of the fault geometry [*Käser and Gallovič*, 2008]. For example, while at COAL station the synthetics for the PF and the ACNF model are almost the same, those for the ACNFS model deviate much more. Only the stations FZ14, GH1W

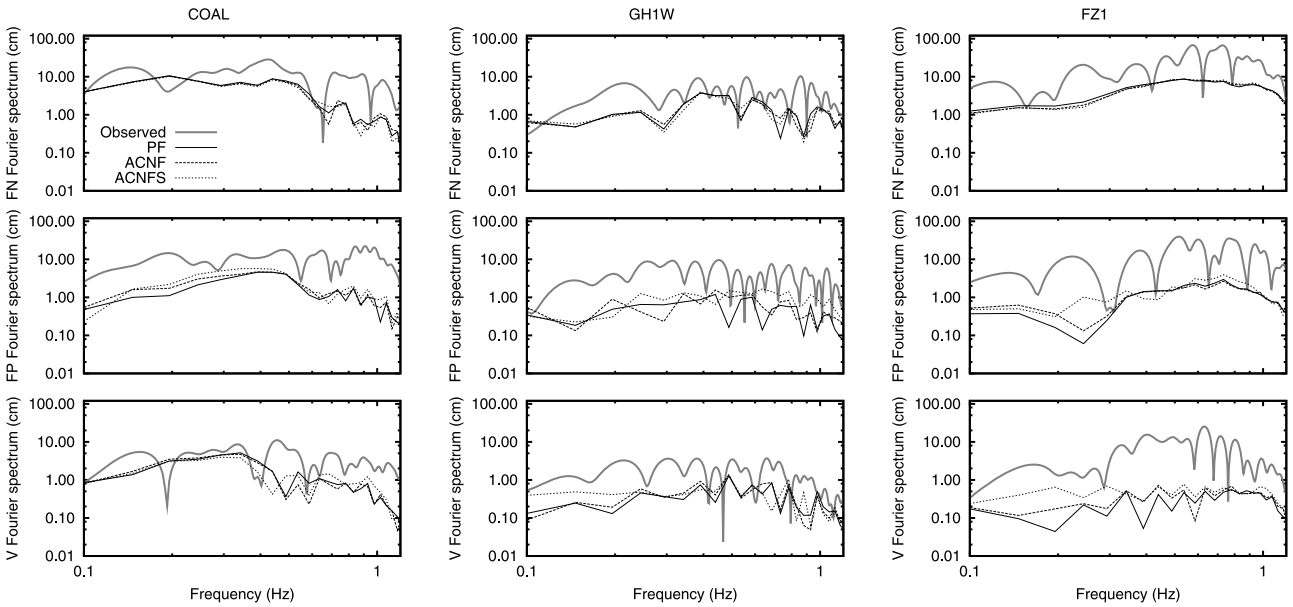

Figure 9. Fourier amplitude spectra of three selected seismograms shown in Figure 7 for the 3-D heterogeneous medium.

and FZ15 are characterized by a strong sensitivity even to the relatively small geometrical variations of the ACNF model. Nevertheless, the peak amplitude values still do not reach the observed ones.

[39] We point out that, generally, the nonplanar source models do not provide a better fit with the observed data on the FP and Z components. Station GH1W is the only exception, for which the nonplanar models, especially ACNF, lead to a better fit of the observed data at FP and V components. Nevertheless, the sensitivity of the stations to the geometrical variations of the fault is predominantly determined by the proximity of the station to strong local changes in the fault geometry. Let us emphasize that our aim was not to optimize the fault geometry to obtain a better fit of the observed waveforms. We rather recognize that at most of the stations the geometrical variations are not even strong enough to increase the synthesized amplitudes in such a way that their peaks would be more balanced among all station components as it is seen in observed data (see further). This is due to the fact that the particle motions are still too linear (see Figure 5).

[40] Figure 8 displays examples of the amplitude Fourier spectra for three closest stations for the 1-D velocity structure and the three source models. As before, the fit for the PF model (solid black) with observed data (solid gray) is the same as obtained by *Liu et al.* [2006]. The fit of the FN components is relatively good, while for the other components the synthetic amplitudes are much lower than the observed ones. Regarding the effect of fault nonplanarity on the spectra, we can see almost no difference at FN component with respect to the PF model, which is in agreement with our observation in the time domain. On the contrary, the other components are affected in the whole frequency range, which agrees with the finding by *Käser and Gallovič* [2008].

[41] Generally speaking, larger geometrical variations, i.e., the ACNFS (dotted line) with respect to the ACNF (dashed line) model, produce higher amplitudes in the Fourier domain. Nevertheless, the fault nonplanarity does not amplify the amplitudes sufficiently to fit the observed ones.

5.2. Effect of the Rupture Geometry in the 3-D Heterogeneous Medium

[42] Figure 5 shows the resulting particle motions for all the three source models computed assuming a heterogeneous 3-D velocity model. Only for stations FZ14 and C2W the PF model provides a linear particle motion. For the other stations (especially when compared with the results for the 1-D medium), the particle motions are relatively complex, being more similar to the observed ones. When adding the geometrical complexity by assuming source models ACNF and ACNFS, one can see that, contrarily to the modeling in the 1-D media, the basic character of the particle motions does not change much. Only at stations MFU, COAL, GH1W and FZ4 the particle motions become more elliptical.

[43] Figure 7 shows, similar to Figure 6, the synthetics for all the source models in the 3-D medium and the recorded data as a reference. As already observed for the particle motions, the synthetics are less sensitive to the variations of the fault geometry. Perhaps the only exception are the FP components at stations MFU, GH1W and FZ4. Therefore, in the following we will discuss mainly the results for the PF model since the statements also (or even more) hold for the nonplanar models ACNF and ACNFS.

[44] One can see that the fit between the simulated data and the observed data for the 3-D medium is generally worse than in Figure 6 for the 1-D media. Almost all the synthetics are characterized by smaller amplitudes and similar duration on the FN components. However, the amplitudes at the FP and V components are generally larger, which results in a better balance between the three components. The fact that the 3-D medium provides smaller amplitudes than the 1-D model can be surprising because typically including a 3-D crustal structure with low velocities under the surface results in amplified synthetic ground motion [e.g., *Frankel*, 1993; *Yomogida and Etgen*, 1993]. However, such crustal models contain basin-like structures, in which the ground motions are amplified by soft sediments and by constructive interference of waves trapped inside the basin. Our 3-D velocity model does not represent a basin-like structure but is characterized by strong velocity gradients in both vertical and horizontal directions. There are also near-surface low-velocity zones that can trap the energy and enhance the ground shaking. Our 3-D structural model also does not contain any discontinuities in wave velocities so that there are only weak refractions from the velocity gradients. Nevertheless, the 3-D structure seems to distribute the radiated energy more equally among the three components of motion, not preserving the linear polarization at the near-fault stations.

[45] Although the peak amplitudes at the FN components are smaller than those obtained for the 1-D medium, the waveforms themselves are similar to the observed ones. This amplitude difference cannot be simply explained by the small seismic moment of our source model (being linearly related to the synthetics), because it is already very close to that published by world agencies (see Table 2). The slip model would be quite different if the slip inversion was done assuming a more realistic 3-D velocity structure.

[46] As an example, Figure 9 shows for three stations the Fourier spectra corresponding to the time histories displayed in Figure 7. Generally, all the velocity components are not affected much by the fault nonplanarity. If we compare the overall shape of these spectra with respect to the spectra obtained for the 1-D media (Figure 8), they are characterized by very similar shapes especially for the FN component. However, the absolute level is smaller for the 3-D case.

5.3. Effect of Surface Topography

[47] Similar to the 3-D medium, the surface topography could produce the strong signals on the FP and V components which are not obtained by simplified models that do not incorporate the surface topography. Therefore, we compute synthetic ground motion taking into account the surface topography as given by a high-resolution digital elevation model [*Farr et al.*, 2007]. Because of the tetrahedral discretization of the computational domain, the mesh can be adapted to the topography using a surface triangulation with linear triangular element faces. We use again the velocity structure of *Thurber et al.* [2006]. However, as it is given only for a flat model surface we modify it in a way that the depth does not refer to an absolute depth but to a depth below the surface. Different approaches to combine

heterogeneous 3-D velocity models with real topography have been studied by *Ma et al.* [2007] or *Aagaard et al.* [2008].

[48] The results including the topography show only very small differences compared to the flat model, suggesting that the topography in the Parkfield area has little influence on the signals, at least in the frequency band 0.16–1 Hz used in our study. The most obvious effects are phase shifts due to the differences in station elevations when using the topographic model. However, the waveforms, amplitudes and spectra remain almost unchanged (not shown here). Therefore, in the following, we discuss only the influence of the topography on the peak amplitudes and its effects on the ratio between the FN, FP and V components.

5.4. Ratios of Peak Velocity Amplitudes

[49] As stated before, modeling in 1-D media with the PF model provides reasonable good fits at the FN components, while for some stations we are not able to explain the large amplitudes in the observed data at the FP and V components (C1E, FZ14, COAL, GH1W and FZ1).

[50] Peak velocity ratios of FN to FP and FN to V components are shown in Figure 10 for all the selected 13 stations. Note that these amplitude ratios correspond to the ratios between maximum heights and widths of the horizontal or vertical particle motions. Note that the observed data give typically ratios around 1–2 for the FN/FP ratio and about 4 for the FN/V ratio. Table 3 shows mean root-mean-square (RMS) errors between the observed and synthetic peak velocity ratios (computed from the logarithmic values) over all 13 selected stations for all the considered models.

[51] As already discussed above, there is a clearly visible large discrepancy between observed and synthetic ratios for the combination of the 1-D medium and the PF model (Figure 10, top). For example, at FZ14, COAL and FZ1 stations the FN/FP or FN/V ratio values are close to 30 or 40, respectively. For other stations this discrepancy is less but typically exceeds by far the observed ratios. The mean RMS error (from logarithmic values) is 1.54 and 1.29 for FN/FP and FN/V ratios, respectively (see Table 3).

[52] Figure 10 (top) further shows results for both the nonplanar faults in the 1-D medium. In general, introducing a larger degree of geometrical complexity of the source decreases the ratios and brings them closer to the observed values. This can be also seen from the decreased RMS values for the nonplanar models with respect to the PF model (Table 3). This general tendency is violated for station FZ3, for which the use of nonplanar models results in even larger ratio than the PF model. Although the ratios decrease for the nonplanar models, for stations such as COAL and FZ1 even the strongly deformed ACNFS model does not provide ratios as low as the observed ones.

[53] In the case of the 3-D medium (Figure 10, middle), synthetic ratios hold generally lower values than for the 1-D medium for all stations. This is manifested also by lower mean RMS values in Table 3, 0.88 and 0.82 for FN/FP and FN/V ratios, respectively. Nevertheless, stations FZ14 and FZ1 are still characterized by a strong discrepancy with the observed ratios.

[54] The increasing complexity of the fault geometry in the 3-D medium has only a minor influence on the peak ratios with respect to the PF model (see also velocity seismograms in Figure 7). Only for the above mentioned stations FZ14 and FZ1 the ratios considerably decrease when considering nonplanar faults. Thus the mean RMS decreases also even more with respect to the PF model for the 3-D medium.

[55] Let us recall that the results for the 3-D medium provide generally a worse fit with the observed data than that for the 1-D medium for which the source model with its particular slip distribution was originally determined. In particular, the FN component waveforms obtained for the 3-D medium are characterized by smaller absolute amplitudes with respect to those obtained for 1-D medium (compare Figures 6 and 7). On the other hand, the FP and V components are larger or at least similar, which causes that the FN/FP and FN/V ratios are reduced to values closer to the observed peak ratios, and the particle motions are more circular as observed for the real data (Figure 5).

[56] Finally, the introduction of the free surface topography and its effect on the peak velocity ratios is shown in Figure 10 (bottom). It leads to only little change of the FN/FP and FN/V ratios as can be seen also from the mean RMS values in Table 3. In particular, the topography effect slightly reduces ratios of the problematic stations FZ14 and FZ1. However, it is clear from Figure 10 (bottom) that the topography has a much weaker effect on the amplitudes than the variation of the fault surface geometry or especially the choice of velocity structure (see also Table 3).

6. Discussion

[57] Observed near-fault ground motions are characterized by features, which can hardly be explained by simplified models. Here, we study in particular the distribution of ground motions on horizontal and vertical components in a relatively low-frequency range (<1 Hz) for stations lying basically above the earthquake rupture. As we show on the example of the 2004 Parkfield earthquake recordings, the amplitudes observed at fault-normal (FN), fault-parallel (FP), and vertical (V) components are almost the same with complex (nonlinear) particle motions. On the other hand, simulations utilizing a planar source model (although with complex rupture evolution) and 1-D medium result in synthetics having typically a linear polarization perpendicular to the fault. Theoretically, this can be explained as a consequence of the properties of the radiation pattern. As simulations of near-fault ground motions are of interest for seismic engineers, we study certain model features that have to be considered in the modeling to provide more realistic ground motion estimates. In particular, we pay attention to the use of nonplanar rupture geometry, 3-D crustal model and free surface topography. Amongst others, as mentioned later, these three factors are capable of generating signals at the FP and V components but with different significance.

[58] We introduce three speculative fault models of increasing geometrical complexity, approximating the relocated aftershock distribution [*Thurber et al.*, 2006]: one is a perfectly planar fault (PF) as proposed by *Liu et al.* [2006], whereas the others are obtained by a piecewise interpolation of aftershock hypocenter locations; the aftershock-constrained nonplanar fault (ACNF) and the aftershock-constrained nonplanar fault with stochastic component (ACNFS). As

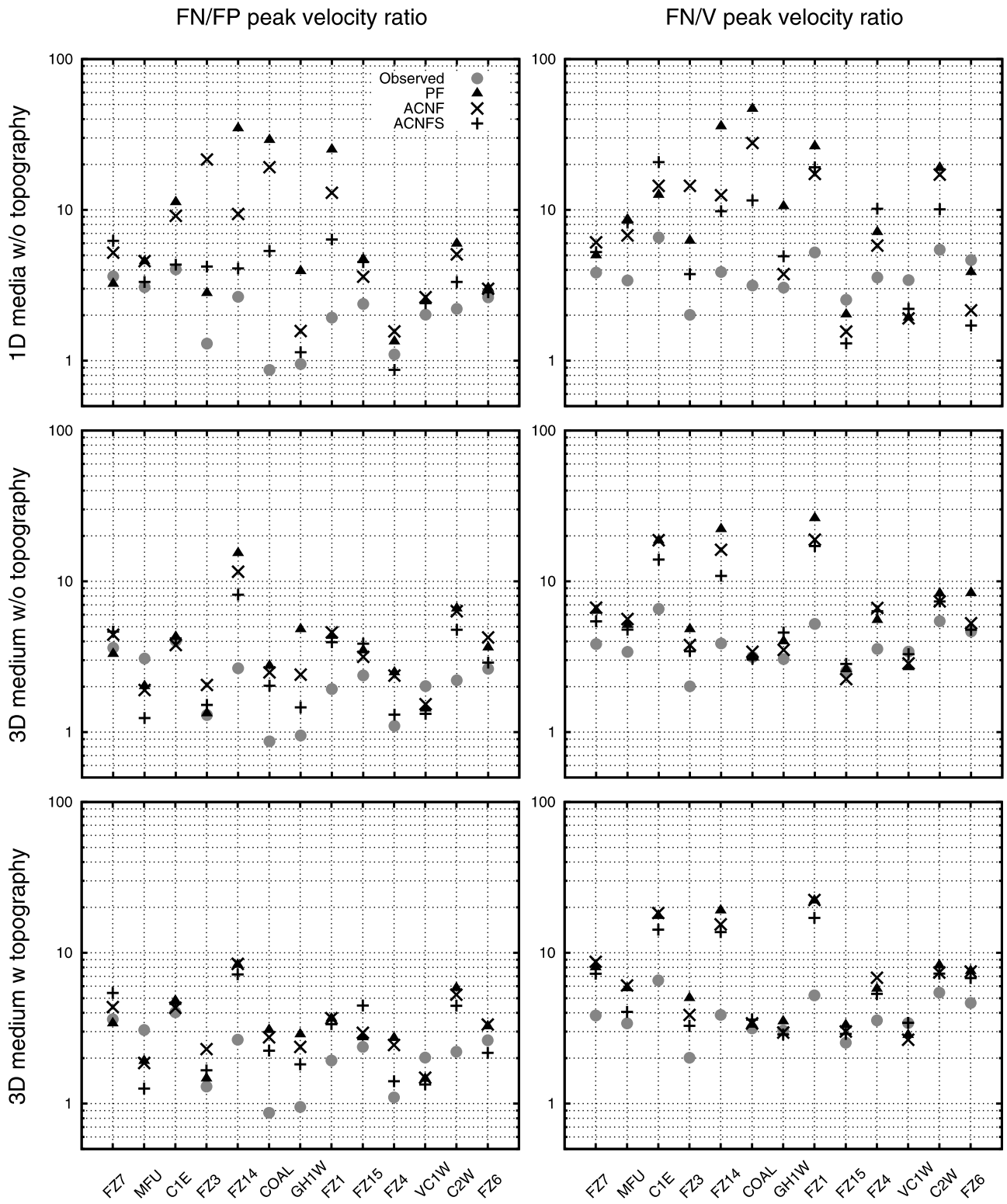

Figure 10. Results in terms of peak ground velocity (PGV) ratios for (top) the 1-D medium without topography, (middle) the 3-D medium excluding topography, and (bottom) the 3-D medium including topography.

regards the crustal model, we use both 1-D models and a 3-D velocity structure based on the model proposed by *Thurber et al.* [2006]. In both velocity structures we apply the different rupture models that all obey the same kinematic properties obtained from the slip inversion by *Liu et al.* [2006]. Finally, we incorporate the surface topography of the Parkfield region given by a digital elevation model.

[59] The effect of the kinematic nonplanar faults on the seismograms is rather small compared to the influence of the different velocity models. Interestingly, the effect of the

Table 3. RMS Errors of Peak Velocity Ratios for All the Models Considered in This Study

	FN/FP			FN/V		
Crustal model	PF	ACNF	ACNFS	PF	ACNF	ACNFS
1-D media without topography	1.54	1.39	0.75	1.29	1.09	0.88
3-D medium without topography	0.88	0.76	0.60	0.82	0.70	0.57
3-D medium with topography	0.72	0.69	0.61	0.79	0.75	0.60

rupture plane geometry is even smaller for the 3-D structure than for the 1-D one. The generally small effect of the rupture nonplanarity is due to the fact that the geometrical complexity of the fault models stays in reasonable limits given by the relatively small diffusion of the aftershocks that are assumed to delineate the rupture surface. The Parkfield area is a part of the San Andreas Fault, which, being seismically active for perhaps millions of years, has accommodated very long slip and is, therefore, relatively smooth especially in the strike direction. If a geometrically more complex rupture plane was taken into account, its sole geometry effect on the ground motion could be more severe [*Käser and Gallovič*, 2008]. However, in our opinion this would not be justifiable for the Parkfield fault.

[60] In general, mainly the fault parallel (FP) and vertical (V) components are affected by the nonplanarity of the fault. This supports the possibility to use only the FN components of stations lying almost above the fault in a slip inversion since they are less affected by the fault geometry.

[61] Figure 10 shows that for the 2004 Parkfield earthquake the 3-D velocity structure reduces the large amplitude differences obtained for a perfectly planar fault in a 1-D medium more than the increase of the fault nonplanarity. Therefore, we claim that highly accurate 3-D velocity structures are always crucial when modeling the ground motions close to the fault, especially on the FP and V components. In particular, local low-velocity structures near the surface and right below a station as well as local fault zone properties can strongly influence the wave amplitudes [see, e.g., *Jahnke et al.*, 2002; *Olsen et al.*, 2003; *Peng et al.*, 2000; *Li et al.*, 2004].

[62] Finally, we find that the effect of the free surface topography for the 2004 Parkfield earthquake is insignificant, regarding the stations of interest right above the fault and a frequency band of 0.16–1 Hz.

[63] Note that none of the models is successful in explaining the long duration of the observed records. This suggests that the *Thurber et al.*'s [2006] 3-D velocity model is missing a distinct fault zone that might generate resonant oscillation giving rise to the late arrivals [see, e.g., *Igel et al.*, 1997; *Hough et al.*, 1994; *Ben-Zion*, 1998]. However, the fault zones are usually associated with a very low Q factor that might suppress large amplitudes in coda of the synthetics. Another possible interpretation for the high amplitudes of late arrivals in some of the observed seismograms could be a strong back-scattering from other heterogeneities that are not resolved in Thurber et al.'s 3-D model. Therefore, we emphasize the importance of an additional study that will include a refined 3D model including the fault zone effects and/or the scatterers in detail to resolve this issue. Note also that such a model has to be very inhomogeneous since not all stations exhibit the strong late arrivals.

7. Conclusions

[64] In summary, our results show that a more realistic balance of the peak velocity amplitudes in the FN, FP and V components for near-fault stations are obtained when a 3-D heterogeneous velocity structure is taken into account although the 3-D model is still relatively smooth and does not include the fault zone. The effect of an increasing geometrical complexity of the rupture geometry is less important in our setting. However, its use can still lead to more realistic peak velocity ratios especially when considered together with a simple 1-D medium. The influence of the topography (in addition to a 3-D structural model) is of less significance, for the considered low-frequency band (up to 1 Hz).

[65] Our study suggests the FN components would be used in the slip inversion as they show stable features. Generally, amplitudes of our synthetic FN components in 3-D velocity structure are smaller than the other components, but their waveforms (in time and frequency domain) remain similar in the case of the 3-D or 1-D velocity model. The FP and V components seem to be more affected by the 3-D model, and, therefore, show a higher sensitivity to the quality of the 3-D model. Thus, features in the FP and V components are less robust when used in the inversion process where the velocity structure is uncertain. Furthermore, all components show a higher sensitivity to the velocity structure than to the fault geometry variations. Therefore, we support the suggestion by *Kim and Dreger* [2008] to exclude at least the FP and V components of the closest stations in the slip inversion due to their strong sensitivity to the quality of the Green's functions. To avoid the unrealistic linear polarization of the particle motions obtained from 1-D velocity models in combination with the planar fault, we strongly suggest using a well-constrained 3-D velocity model if available as it seems to be more important than the fault geometry.

[66] We emphasize that we used only a limited frequency range (up to 1 Hz). Some of the conclusions could also be true for high-frequency motion but they would have to be appropriately tested. Moreover, this is also not a complete study of all possible effects that could influence the ground motions. The existence of a fault zone structure is one of the most important effects to consider in further investigations. Furthermore, directional site effects [*Bonamassa and Vidale*, 1991], medium anisotropy [*Cochran et al.*, 2006], or nonlinear behavior [*Bataille and Calisto*, 2008; *Karabulut and Bouchon*, 2007; *Wu and Chen*, 2009] might also contribute to better explain the observed data.

[67] **Acknowledgments.** The work has been supported by EU project ITSAK-GR (MTKD-CT-2005-029627), the Grant Agency of Charles University (279/2006/B-GEO/MFF), MSM0021620800, Grant Agency of the Czech Republic (205/08/P013 and 205/07/0502), and Deutsche Forschungsgemeinschaft (Emmy Noether-Program KA 2281/2-1). We also thank the Leibniz Rechenzentrum in Garching for their support to compute the numerical results of the ADER-DG method presented in this work.

References

Aagaard, B. T., T. M. Brocher, D. Dolenc, D. Dreger, R. W. Graves, S. Harmsen, S. Hartzell, S. Larsen, and M. L. Zoback (2008), Ground motion modeling of the 1906 San Francisco earthquake I: Validation using the 1989 Loma Prieta earthquake, *Bull. Seismol. Soc. Am.*, *98*, 989–1011, doi:10.1785/0120060409.

Aki, K., and P. G. Richards (2002), *Quantitative Seismology*, Univ. Sci. Books, Sausalito, Calif.

Bakun, W. H., and T. V. McEvilly (1979), Earthquakes near Parkfield, California: Comparing the 1934 and 1966 sequences, *Science*, *205*, 1375–1377, doi:10.1126/science.205.4413.1375.

Bataille, K., and I. Calisto (2008), Seismic coda due to non-linear elasticity, *Geophys. J. Int.*, *172*(2), 572–580, doi:10.1111/j.1365-246X.2007.03639.x.

Ben-Zion, Y. (1990), The response of two half spaces to point dislocations at the material interface, *Geophys. J. Int.*, *101*, 507–528, doi:10.1111/j.1365-246X.1990.tb05567.x., (Corrigendum to "the response of two half spaces to point dislocations at the material interface," *Geophys. J. Int.*, *137*, 580–582, doi:10.1046/j.1365-246X.1999.1372001.x, 1999.).

Ben-Zion, Y. (1998), Properties of seismic fault zone waves and their utility for imaging low-velocity structures, *J. Geophys. Res.*, *103*(B6), 12,567–12,585, doi:10.1029/98JB00768.

Ben-Zion, Y., and P. Malin (1991), San Andreas Fault zone head waves near Parkfield, California, *Science*, *251*, 1592–1594, doi:10.1126/science.251.5001.1592.

Bonamassa, O., and J. E. Vidale (1991), Directional site resonances observed from aftershocks of the 18th October 1989 Loma Prieta earthquake, *Bull. Seismol. Soc. Am.*, *81*, 1945–1957.

Boore, D. M. (1983), Stochastic simulation of high-frequency ground motions based on seismological models of the radiated spectra, *Bull. Seismol. Soc. Am.*, *73*, 1865–1894.

Bouchon, M. (1973), Effect of topography on surface motions, *Bull. Seismol. Soc. Am.*, *63*(3), 615–632.

Bouchon, M. (1981), A simple method to calculate Green's functions for elastic layered media, *Bull. Seismol. Soc. Am.*, *71*, 959–971.

Bouchon, M., C. A. Schultz, and M. N. Toksoz (1996), Effect of 3D topography on seismic motion, *J. Geophys. Res.*, *101*(B3), 5835–5846, doi:10.1029/95JB02629.

Brocher, T. (2005), Empirical relations between elastic wavespeeds and density in the Earth's crust, *Bull. Seismol. Soc. Am.*, *95*, 2081–2092, doi:10.1785/0120050077.

Cochran, E. S., Y.-G. Li, and J. E. Vidale (2006), Anisotropy in the shallow crust observed around the San Andreas Fault before and after the 2004 *M* 6.0 Parkfield earthquake, *Bull. Seismol. Soc. Am.*, *96*(4b), S364–S375, doi:10.1785/0120050804.

Dreger, D. S., L. Gee, P. Lombard, M. H. Murray, and B. Romanowicz (2005), Rapid finite-source analysis and near-fault strong ground motions: Application to the 2003 M_w 6.5 San Simeon and 2004 M_w 6.0 Parkfield earthquakes, *Seismol. Res. Lett.*, *76*, 40–48, doi:10.1785/gssrl.76.1.40.

Dumbser, M., and M. Käser (2006), An arbitrary high order discontinuous Galerkin method for elastic waves on unstructured meshes II: The three-dimensional case, *Geophys. J. Int.*, *167*(1), 319–336, doi:10.1111/j.1365-246X.2006.03120.x.

Eberhart-Phillips, D., and A. J. Michael (1993), Three-dimensional velocity structure, seismicity, and fault structure in the Parkfield region, central California, *J. Geophys. Res.*, *98*(B9), 15,737–15,758, doi:10.1029/93JB01029.

Farr, T. G., et al. (2007), The Shuttle Radar Topography Mission, *Rev. Geophys.*, *45*, RG2004, doi:10.1029/2005RG000183.

Frankel, A. (1993), Three-dimensional simulations of ground motions in the San Benardino valley, California, for hypothetical earthquakes on the San Andreas Fault, *Bull. Seismol. Soc. Am.*, *83*, 1020–1041.

Frohlich, C. (1994), Earthquakes with non-double-couple mechanisms, *Science*, *264*, 804–809, doi:10.1126/science.264.5160.804.

Gallovic, F., and J. Brokešová (2007), Hybrid k-squared source model for strong ground motion simulations: Introduction, *Phys. Earth Planet. Inter.*, *160*, 34–50, doi:10.1016/j.pepi.2006.09.002.

Geli, L., P. Y. Bard, and B. Jullien (1988), The effect of topography on earthquake ground motion: A review and new results, *Bull. Seismol. Soc. Am.*, *78*(1), 42–63.

Harris, R. A., and J. R. Arrowsmith (2006), Introduction to the special issue on the 2004 Parkfield earthquake and the Parkfield earthquake prediction experiment, *Bull. Seismol. Soc. Am.*, *96*(4b), S1–S10, doi:10.1785/0120050831.

Hartzell, S., M. Guatteri, P. M. Mai, P. Liu, and M. Fisk (2005), Calculation of broadband time histories of ground motion, part II: Kinematic and dynamic modeling using theoretical Green's functions and comparison with the 1994 Northridge earthquake, *Bull. Seismol. Soc. Am.*, *95*(2), 614–645, doi:10.1785/0120040136.

Hartzell, S., P. Liu, C. Mendoza, C. Ji, and K. M. Larson (2007), Stability and uncertainty of finite-fault slip inversions: Applications to the 2004 Parkfield, California, earthquake, *Bull. Seismol. Soc. Am.*, *97*(6), 1911–1934, doi:10.1785/0120070080.

Hough, S. E., Y. Ben-Zion, and P. Leary (1994), Fault-zone waves observed at the southern Joshua Tree earthquake rupture zone, *Bull. Seismol. Soc. Am.*, *84*, 761–767.

Igel, H., Y. Ben-Zion, and P. C. Leary (1997), Simulation of SH- and P-SV-wave propagation in fault zones, *Geophys. J. Int.*, *128*(3), 533–546, doi:10.1111/j.1365-246X.1997.tb05316.x.

Irikura, K. (1996), Near-fault ground motions causing the great Hanshin Earthquake disaster (in Japanese), *Annu. Disas. Prev. Res. Inst. Kyoto Univ.*, *39*(A), 17–33.

Jahnke, G., H. Igel, and Y. Ben-Zion (2002), Three-dimensional calculations of fault-zone-guided waves in various irregular structures, *Geophys. J. Int.*, *151*(2), 416–426, doi:10.1046/j.1365-246X.2002.01784.x.

Karabulut, H., and M. Bouchon (2007), Spatial variability and non-linearity of strong ground motion near a fault, *Geophys. J. Int.*, *170*, 262–274, doi:10.1111/j.1365-246X.2007.03406.x.

Käser, M., and M. Dumbser (2006), An arbitrary high order discontinuous Galerkin method for elastic waves on unstructured meshes I: The two-dimensional isotropic case with external source terms, *Geophys. J. Int.*, *166*(2), 855–877, doi:10.1111/j.1365-246X.2006.03051.x.

Käser, M., and F. Gallovič (2008), Effects of complicated 3D rupture geometries on earthquake ground motion and their implications: A numerical study, *Geophys. J. Int.*, *172*(1), 276–292, doi:10.1111/j.1365-246X.2007.03627.x.

Kim, A., and D. S. Dreger (2008), Rupture process of the 2004 Parkfield earthquake from near-fault seismic waveform and geodetic records, *J. Geophys. Res.*, *113*, B07308, doi:10.1029/2007JB005115.

Lewis, M. A., Y. Ben-Zion, and J. J. McGuire (2007), Imaging the deep structure of the San Andreas Fault south of Hollister with joint analysis of fault zone head and direct P arrivals, *Geophys. J. Int.*, *169*, 1028–1042, doi:10.1111/j.1365-246X.2006.03319.x.

Li, Y.-G., P. Leary, K. Aki, and P. Malin (1990), Seismic trapped modes in the Oroville and San Andreas Fault zones, *Science*, *249*, 763–766, doi:10.1126/science.249.4970.763.

Li, Y.-G., J. H. Vidale, and E. S. Cochran (2004), Low-velocity damaged structure of the San Andreas Fault at Parkfield from fault zone trapped waves, *Geophys. Res. Lett.*, *31*, L12S06, doi:10.1029/2003GL019044.

Liu, P., S. Custodio, and R. J. Archuleta (2006), Kinematic inversion of the 2004 *M* 6.0 Parkfield earthquake including an approximation to site effects, *Bull. Seismol. Soc. Am.*, *96*(4b), S143–S158, doi:10.1785/0120050826, (Erratum to kinematic inversion of the 2004 M 6.0 Parkfield earthquake including an approximation to site effects, *Bull. Seismol. Soc. Am.*, *98*, 2101, doi:10.1785/0120080959, 2008.).

Ma, S., R. J. Archuleta, and M. T. Page (2007), Effects of large-scale surface topography on ground motions, as demonstrated by a study of the San Gabriel Mountains, Los Angeles, California, *Bull. Seismol. Soc. Am.*, *97*(6), 2066–2079, doi:10.1785/0120070040.

Mai, P. M., and G. C. Beroza (2003), A hybrid method for calculating near-source, broadband seismograms from an extended source, *Phys. Earth Planet. Inter.*, *137*, 183–199, doi:10.1016/S0031-9201(03)00014-1.

Michael, A. J., and D. Eberhart-Phillips (1991), Relations among fault behaviour, subsurface geology, and three-dimensional velocity models, *Science*, *253*, 651–654, doi:10.1126/science.253.5020.651.

Michelini, A., and T. V. McEvilly (1991), Seismological studies at Parkfield, part I: Simultaneous inversion for velocity structure and hypocenters using cubic B-splines parameterization, *Bull. Seismol. Soc. Am.*, *81*, 524–552.

Nadeau, R., W. Foxall, and T. V. McEvilly (1995), Clustering and periodic recurrence of microearthquakes on the San Andreas Fault at Parkfield, California, *Science*, *267*, 503–507, doi:10.1126/science.267.5197.503.

Olsen, K. B., S. M. Day, and C. R. Bradley (2003), Estimation of *Q* for long-period (>2 sec) waves in the Los Angeles basin, *Bull. Seismol. Soc. Am.*, *93*(2), 627–638, doi:10.1785/0120020135.

Peng, Z., Y. Ben-Zion, A. J. Michael, and L. Zhu (2003), Quantitative analysis of seismic fault zone waves in the rupture zone of the 1992 Landers, California, earthquake: Evidence for a shallow trapping structure, *Geophys. J. Int.*, *155*(3), 1021–1041, doi:10.1111/j.1365-246X.2003.02109.x.

Pitarka, A., P. Somerville, Y. Fukushima, T. Uetake, and K. Irikura (2000), Simulation of near-fault strong-ground motion using hybrid Green's functions, *Bull. Seismol. Soc. Am.*, *90*, 566–586, doi:10.1785/0119990108.

Rymer, M. J., et al. (2006), Surface fault slip associated with the 2004 Parkfield, California, earthquake, *Bull. Seismol. Soc. Am.*, *17*, 211–220.

Simpson, R. W., M. Barall, J. Langbein, J. R. Murray, and M. J. Rymer (2006), San Andreas Fault geometry in the Parkfield, California, region, *Bull. Seismol. Soc. Am.*, *96*(4b), S28–S37, doi:10.1785/0120050824.

Thurber, C., H. Zhang, F. Waldhauser, J. Hardebeck, A. Michael, and D. Eberhart-Phillips (2006), Three-dimensional compressional wavespeed model, earthquake relocations, and focal mechanisms for the Parkfield, California, region, *Bull. Seismol. Soc. Am.*, *96*(4b), S38–S49, doi:10.1785/0120050825.

Toppozada, T. R., D. M. Branum, M. S. Reichle, and C. L. Hallstrom (2002), San Andreas Fault zone, California; M $\geq$ 5.5 earthquake history, *Bull. Seismol. Soc. Am.*, *92*, 2555–2601, doi:10.1785/0120000614.

Unsworth, M. J., P. E. Malin, G. D. Egbert, and J. R. Booker (1997), Internal structure of the San Andreas Fault at Parkfield, *Calif. Geol.*, *25*(4), 359–362.

Wang, H., H. Igel, F. Gallovič, A. Cochard, and M. Ewald (2008), Source-related variations of ground motions in 3-D media: Application to the Newport-Inglewood fault, Los Angeles basin, *Geophys. J. Int.*, *175*, 202–214, doi:10.1111/j.1365-246X.2008.03878.x.

Wu, Z. L., and Y. T. Chen (2003), Definition of seismic moment at a discontinuity interface, *Bull. Seismol. Soc. Am.*, *93*, 1832–1834, doi:10.1785/0120020234.

Wu, Z. L., and Y. T. Chen (2009), Non-linearity and temporal changes of fault zone site response associated with strong ground motion, *Geophys. J. Int.*, *176*(1), 265–278, doi:10.1111/j.1365-246X.2008.04005.x.

Yomogida, K., and J. T. Etgen (1993), 3-D wave propagation in the Los Angeles basin for the Whittier-Narrows earthquake, *Bull. Seismol. Soc. Am.*, *83*, 1325–1344.

Zahradník, J., and L. Urban (1984), Effect of a simple mountain range on underground seismic motion, *Geophys. J. R. Astron. Soc.*, *79*, 167–183.

J. Burjánek, Swiss Seismological Service, Institute of Geophysics, ETH Zurich, No. 69.4, Soneggstrasse 5, CH-8092 Zürich, Switzerland.

F. Gallovič, Department of Geophysics, Faculty of Mathematics and Physics, Charles University, V Holešovičkách 2, Prague 8, 180 00, Czech Republic. (gallovic@karel.troja.mff.cuni.cz)

M. Käser, Department of Earth and Environmental Sciences, Ludwig Maximilians University, Theresienstrasse 41, D-80333 Munich, Germany.

C. Papaioannou, ITSAK, PO Box 53 Foinikas, Thessaloniki GR-55102, Greece.

[P9]

Toward understanding slip inversion uncertainty and artifacts

Jiří Zahradník[1] and František Gallovič[1,2]

Received 26 January 2010; revised 12 April 2010; accepted 29 April 2010; published 14 September 2010.

[1] The main concept of seismic source tomography, the projection lines along which the observed signals are back-projected to the fault, is extended to complete wavefields. The so-called "dynamic projection strips" (DPSs) are defined, and a method to construct the strips from individual waveforms is described. In this way, each individual station role in the inversion can be better understood. Synthetic models with two asperities (two unilateral and one bilateral rupture scenarios) are used as examples. They are analyzed using two independent slip inversion methods with similar results, bias of the rupture speed for all scenarios and a strong false asperity in the middle of the bilateral fault. Both artifacts can be explained by the DPS analysis as inherent nonuniqueness of the inverse problem due to the joint effect of the two true asperities. Removal of some slip artifacts by imposing various constraints is discussed, but most of the constraints are hardly applicable in practice. As such, it is recommended to look at least for possible indications of the most significant inversion artifacts. This seems to be feasible through combining DPSs derived from real data and synthetic models of various rupture scenarios for a given fault and stations. The ideas are applied to the Movri Mountain earthquake in Greece, Mw6.3, 8 June 2008. It appears that the earthquake was predominantly unilateral, however with a nonunique space-time slip pattern. Few equivalent nonsmooth models, all fitting the data equally well, are illustrated.

Citation: Zahradník, J., and F. Gallovič (2010), Toward understanding slip inversion uncertainty and artifacts, *J. Geophys. Res.*, *115*, B09310, doi:10.1029/2010JB007414.

1. Introduction

[2] Deciphering seismograms for the spatiotemporal evolution of a fault rupture (the slip inversion, in short) is essential for any progress in earthquake physics. It has been a challenging topic in seismology since the 1980s. Extensive reviews and comparisons of various methods, including techniques to assess the uncertainty of results, were recently presented by *Semmane et al.* [2005], *Piatanesi et al.* [2007], *Hartzell et al.* [2007], *Monelli and Mai* [2008], *Custódio et al.* [2009], etc. Databases of the slip inversion of large earthquakes have been created by M. Mai (http://www.seismo.ethz.ch/srcmod/) and D. Wald (http://pasadena.wr.usgs.gov/office/wald/slip_models.html), and empirical scaling laws have been derived [*Somerville et al.*, 1999; *Mai and Beroza*, 2000, 2002; *Lavallée and Archuleta*, 2003; *Lavallée et al.*, 2006]. Quick, almost real-time slip inversion has become a part of the activities after big events, for example, in relation to shake maps [*Wald et al.*, 1999; *Convertito et al.*, 2010], with direct application in postearthquake emergency measures. A better understanding of the earthquake source would also improve scenario studies for earthquake hazard assessment [*Pulido et al.*, 2004; *Ripperger et al.*, 2008; *Wang et al.*, 2008; *Ameri et al.*, 2009]. It has been clear from the very beginning that inversion is typically underdetermined and has a limited resolution; thus alternative models of significant earthquakes have always been discussed in an attempt to identify the most stable (robust) features of rupture evolution. Blind experiments on synthetic data [*Mai et al.*, 2007; *Gallovič et al.*, 2007] improved the physical insight into various methodologies. Nevertheless, systematic understanding of the inherent uncertainty of the slip inversions is still rather poor.

[3] To illustrate the problem, let us consider an example: Two working groups analyze an earthquake, one revealing asperities A and B and the other finding A and C. They claim "confirmation" of asperity A and broadly discuss whether B or C is more relevant. What we want to emphasize in the present paper is that sometimes even the robust feature A might be wrong. This is the case when the misfit function has a major deep local minimum that strongly attracts various misfit-minimization procedures, although this minimum is far from the true spatial-temporal slip pattern (with just a slightly lower misfit). Cases like that will be called spurious (or false) asperities.

[4] For example, *Page et al.* [2009] analyzed similar artifacts in the linear inversion of static GPS data using the resolution matrix [*Tarantola*, 1987]. Owing to the underdetermination of the problem, the data could not resolve tradeoffs among numerous model parameters. Thus false asperities appeared

[1]Department of Geophysics, Faculty of Mathematics and Physics, Charles University, Prague, Czech Republic.
[2]Department of Physics, Universita degli Studi Federico II di Napoli, Naples, Italy.

0148-0227/10/2010JB007414

in the poorly resolved areas, i.e., in places where the parameter uncertainty (due to the station network configuration) had its local maxima. However, *Page et al.* [2009] did not study the mechanism how artifacts are generated. The objective of the present paper is to study such a mechanism. We analyze the individual station contributions to the uncertainty of the slip imaging and how they sum up to produce the artifacts. Synthetic examples on errorless data demonstrate false asperities generated even when the stations best constraining the inversion are available, i.e., the directive and antidirective stations. The work was initiated and inspired by the practical inversion of a Mw6.3 earthquake [*Gallovič et al.*, 2009]. Synthetic experiments in the present followup paper use the same station distribution as for the real earthquake. The observed data are reanalyzed at the end.

[5] The method we adopt to understand the nonuniqueness of the slip inversion is most closely related to the tomographic source inversions [*Ruff*, 1984; *Menke*, 1985]. These authors studied wavefields in the far-field Fraunhofer approximation; the slip inversion was discussed in terms of the inverse Radon transform, and the concept of straight "integration lines" (or "projection lines") for P and S phases at the individual stations was developed. *Frankel and Wennerberg* [1989] relaxed the Fraunhofer approximation and discussed the curved projection lines; the P and S phases were modeled using the ray method. The authors stressed the limited resolution due to the (unavoidable) limited angular coverage of the projection lines; *Bindi and Caponetto* [2001] pointed out particular problems with bilateral faults. Our study extends the tomographic source inversion in two ways: (1) the concept of projection lines is extended to strips due to the finite size of the asperities, demonstrating how the strips may explain the inversion artifacts from the kinematic viewpoint, and (2) dynamic projection strips (DPS's), arising from complete low-frequency seismograms, are introduced, thus complementing the kinematic explanation of inversion artifacts. The waveform inversion is then performed by two recently developed methods, both treating full wavefields, including near-field effects and interference (surface) waves. The two methods have not yet been compared before. The "low-frequency" range, considered in this paper, is the range in which the finite source extent still plays a significant role, but, at the same time, Green's functions can be satisfactorily calculated for near-regional stations with structural models at hand.

2. Concept of Kinematic Projection Lines and Strips

[6] Assume a line fault composed of N point sources situated along the x-axis, $\boldsymbol{X}_j = \{x_j, 0, 0\}, j = 1, 2,\ldots, N$; the slip rate at each point is $s(t)$, e.g., a triangular signal. The far-field apparent source time function ASTF at station $\boldsymbol{Y} = \{x_{st}, y_{st}, z_{st}\}$ is then [*Aki and Richards*, 2002]

$$ASTF(\boldsymbol{Y}, t) = \sum_j A(x_j) s(t - \tau(\boldsymbol{Y}, x_j)), \tag{1}$$

$$\tau(\boldsymbol{Y}, x_j) = \tau_j = T^R(x_j) + T^P(\boldsymbol{Y}, x_j), \tag{2}$$

where $A_j = A(x_j)$ denotes the slip rate amplitude, $T_j^R = T^R(x_j)$ the rupture time and $T_j^P = T^P(\boldsymbol{Y}, x_j)$ is the travel time of a given phase, e.g., S wave, from the jth point source to station $\boldsymbol{Y}$. Given a set of ASTFs at several stations, the inverse problem is to determine x_j, A_j, T_j^R for $j = 1, 2,\ldots, N$. An essential concept is the "projection line" defined for station $\boldsymbol{Y}$ by

$$T_j^R + T_j^P = const = T^R(x) + T^P(\boldsymbol{Y}, x). \tag{3}$$

The projection line is a set of points in the $x - t$ plane (x and t corresponding to the along-strike position and time, respectively) such that each has the same signal arrival time τ_j at the station. The line represents the spatiotemporal uncertainty of the back-projection of the single-station signal. Thus the inversion, combining several stations, can be understood as the simultaneous location of the N events in space and time. Figure 1 shows examples of such lines drawn in the $x - t$ plot (see also below). Considering a wave traveling with constant speed V, the $T^R(x) = const - T^P(\boldsymbol{Y}, x)$ line is a hyperbola. It degenerates into inclined straight lines for stations situated along the x axis (along the fault strike). Such stations are characterized by the steepest angles with respect to the x axis among all possible station positions. If the Fraunhofer approximation is used, the projection line is a straight line for any station position. Note that the projection line should not be misinterpreted with an isochrone [*Spudich and Frazer*, 1984; *Bernard and Madariaga*, 1984; *Festa and Zollo*, 2006]. Our approach is more general without the necessity of prescribing the nucleation point and rupture velocity. The isochrone would be point(s) on the x axis corresponding to the intersection(s) of the projection line with the true slip segment(s).

[7] As an illustration (Figure 1a), assume a homogeneous medium, shear velocity $V_s = 3.4$ km/s, and a single asperity 10 km in length; the rupture starts at $\boldsymbol{X}_1 = \{0, 0, 0\}$ km at $t = 2$ s and propagates at speed $V_r = 2.5$ km/s. We consider two stations situated along the x axis, YF and YB in the forward ($x > 0$) and backward ($x < 0$) direction, respectively; their distance is unimportant. In the $x - t$ space we have two parallel projection lines for each station corresponding to the end points of the asperity, delineating the so-called "kinematic projection strips" (KPSs). As the widths of the strips equal the apparent source duration at the stations $L(1/V_s \pm 1/V_r)$, the strips are narrow and wide for YF and YB, respectively. If ASTF is known, it can be back-projected to the fault along the strip. The solution of the inverse problem is in the $x - t$ region in which the two KPSs intersect with one another. This intersection contains not only the correct solution (i.e., the true $x - t$ source segment), but also some vicinity that "blurs" the source image. Note that owing to the subhorizontal character of the KPSs for stations off the fault, adding more stations (YO in Figure 1a) would not eliminate the blurring even if the data were free of any error. Furthermore, if the forward directivity station is not present, the blurring would be extremely large (see the region delineated by the green and blue lines in Figure 1a). The blurring grows with decreasing V_r/V_s.

[8] Figure 1b shows even more dramatic artifacts arising from the overlapping of KPSs, related to multiple (in our

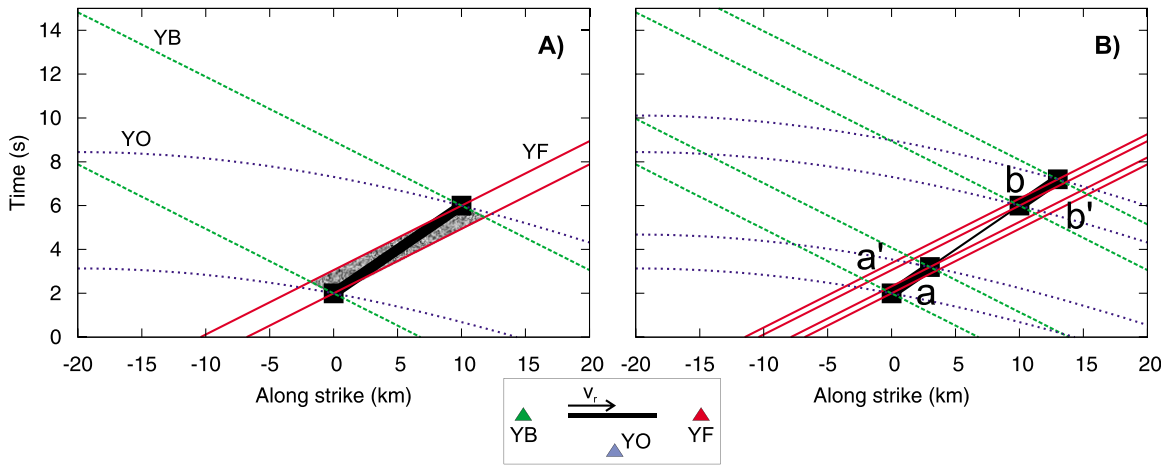

Figure 1. (a) Schematic $x - t$ plot for a single asperity rupturing from $x = 0$ to 10 km (bold line) with rupture velocity $V_r = 2.6$ km/s. The kinematic projection lines (assuming homogeneous medium with $V_s = 3.4$ km/s) are shown for the asperity end points (black squares), considering three stations (see inset for their respective positions with respect to the rupture propagation). Intersection of the three station strips (gray filled area) represents the uncertainty of the inverse problem ("blurring"). (b) Schematic $x - t$ plot for two asperities and three stations (in the same settings as for Figure 1a). The forward (YF) and backward station (YB) projection strips intersect not only at the spots including the asperities (a, b) but also at two other spots (a′, b′) where the slip inversion is expected to yield artifacts (wrong space-time positions of the asperities). Note that the third station (YO) does not help to constrain the inversion as it intersects all the four spots.

case two) asperities. Mathematically, the situation can be described as follows: Let a and b denote two asperities. The ith station seismogram can be symbolically expressed as $S_i = G(a \cup b)$, where G denotes the projection from model space (a and b) into data space (S_i). The contribution of ith station to the inversion is $G^{-1}(S_i) = a_i \cup b_i$, where a_i and b_i are the KPSs, representing the uncertainty with which asperities a and b are recognized by the ith station (color lines in Figure 1b). The multistation inversion can then be expressed as

$$G_1^{-1} \wedge G_2^{-1} \wedge \ldots \wedge G_N^{-1} = \bigcap_i (a_i \cup b_i), \tag{4}$$

which says that the solution matching simultaneously the data at all stations (the left-hand side of equation (4)) is inside the intersection of their kinematic strips (two strips a_i and b_i per ith station). For example, for $N = 3$ in Figure 1b, the solution of the inverse problem contains not only true asperities a and b but also the two false asperities a' and b'. This approach provides similar information to that from the resolution matrix of linear problems: we see how the true solution (a, b) is mapped to the inversion result (a, b, a', b'); see below for more details.

3. Concept of Dynamic Projection Strips

[9] To link the kinematics (projection lines and strips) with seismograms, we have to "look inside" the waveform inversion and show that each station actually contributes to the inversion through a "dynamic projection strip" (DPS) in the $x - t$ plane.

[10] The ith component of the ground-motion displacement for a line source can be expressed by means of the moment-tensor density m_{pq} and Green's tensor spatial derivatives $G_{ip,q}$:

$$u_i(\boldsymbol{Y}, t) = \int m_{pq}(x, t) * G_{ip,q}(\boldsymbol{Y}, x, t) dx. \tag{5}$$

Let $m_{pq}(x) = a_{pq} M(x) m(t - T^R(x))$, where a_{pq} (moment tensor density corresponding to unit slip) and $m(t)$ (unit moment time function) are independent of x, and $M(x)$ and $T^R(x)$ denote the x-dependent moment size and rupture time, respectively. Denoting $\tilde{s}_i(\boldsymbol{Y}, x, t) = m(t) * a_{pq} G_{ip,q}(\boldsymbol{Y}, x, t)$, discretizing (5) and omitting hereafter subscript i and symbol $\boldsymbol{Y}$ yields

$$u(t) = \sum_j M(x_j) \tilde{s}(x_j, t - T_j^R) = \sum_j W_j(t). \tag{6}$$

This is the sum of the complete point-source contributions $W_j(t) = M(x_j)\tilde{s}(x_j, t - T_j^R)$. In the far-field approximation each $W_j(t)$ can be summed up from the individual "phases" $k = 1, 2, \ldots, M$, say the P and S waves, multiples, surface waves, etc., with their appropriate travel times T_{jk}^P and the same source function $s(x, t)$:

$$u(t) = \sum_j \sum_k M(x_j) S_k(x_j) s(x_j, t - T_j^R - T_{jk}^P), \tag{7}$$

where $S_k(x_j)$ represents both the effect of the source station distance and of the focal mechanism. Obviously, equation (1) is a special case of (7) for a single phase, $k = 1$, with $M(x_j)S_1(x_j) = A_j$. Similarly to (1), using (7) we intend to describe the spatiotemporal uncertainty of the back-

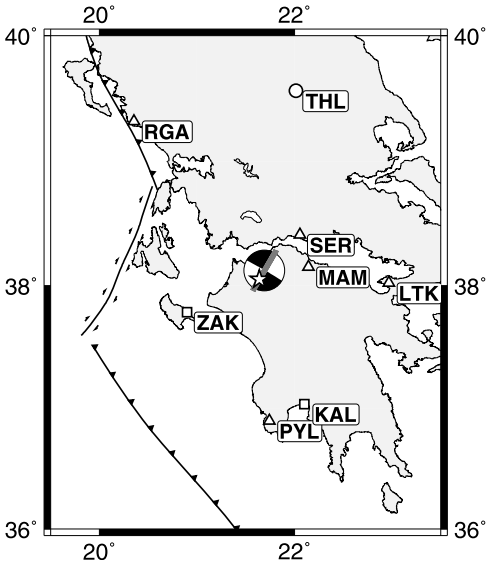

Figure 2. Movri Mountain Mw6.3 earthquake in Greece: the epicenter (asterisk), fault (gray bold line), focal mechanism, and eight near-regional stations. This setup is used in this paper for both synthetic and real-data modeling. Symbols refer to the station network: ITSAK (squares), NOA (circle), PSLNET (triangles). Main tectonic lines of western Greece are displayed.

projection of seismogram $u(t)$ into the $x - t$ plane on the fault. This means finding the point sources in the $x - t$ plane whose contribution at a given station is (approximately) the same as that of the individual W_j's. Similarly to equation (3), each term of (6) can be substituted by an arbitrary equivalent point source belonging to a set (DPS) characterized by

$$M(x_j)S_k(x_j)s(x_j, t - T_j^R - T_{jk}^P) \doteq \\ \doteq M(x)S(x)s(x, t - T^R(x) - T^P(x)). \tag{8}$$

This means that the set contains not only the true source points, but also the others whose position x, strength $M(x)S(x)$, and arrival time $T^R(x) + T^P(x)$, all together, fit approximately one of the W_j's. The "tricky point" of the DPS is that the real data do not provide the decomposition (6) into the individual W_j's. Therefore the DPS must be constructed by means of comparing the trial point source contributions in the $x - t$ plane with the complete record. The slip inversion is then responsible for partitioning the DPS into individual contributions W_j in the complete record (6) by simultaneously fitting all stations considered (see below).

[11] The construction of DPS for a given station is a grid-search-based signal-detection procedure:

[12] 1. Take a single-station three-component waveform $u_i(t)$, i denoting the component. For each trial $x - t$ point calculate the synthetic waveform y'_i(t) in a given crustal model, using the unit scalar moment. The moment-rate function of the elementary point source is effectively a delta function (e.g., we use a triangle of 1-s duration in this study while the maximum considered frequency is 0.2 Hz). The focal mechanism (strike, dip, rake) is assumed known.

[13] 2. Scale $y'_i(t)$ by assigning a proper scalar moment m, so that $u_i(t)$ is approximated by $y_i(t) = my'_i(t)$ in the least-squares sense; this yields

$$m = \frac{\sum_i \int u_i(t) y_i'(t) dt}{\sum_i \int y_i'^2(t) dt}. \tag{9}$$

Waveform $y_i(t)$ represents a single-source contribution W_j in (6). As $y_i(t)$ is complete, containing all body and surface phases, the summation over the phases (the second sum in (7)) is included implicitly, and no far-field approximation is made.

[14] 3. If $m > 0$, evaluate the fit between $y_i(t)$ and the entire waveform $u(t)$ by means of the variance reduction

$$varred = 1 - \frac{\sum_i \int [u_i(t) - y_i(t)]^2 dt}{\sum_i \int u_i^2(t) dt}, \tag{10}$$

or, alternatively, by means of $varred = c^2$, where c denotes the correlation,

$$c = \frac{\sum_i \int u_i(t) y_i(t) dt}{\sqrt{\sum_i \int u_i^2(t) dt} \sqrt{\sum_i \int y_i^2(t) dt}}. \tag{11}$$

For $m \leq 0$ set $c = 0$.

[15] 4. Finally, plot c as a function of the $x - t$ position. The compact regions of the nonzero values of c represent the DPSs for the station under study.

3.1. Dynamic Strips From Synthetic Experiments

[16] The DPS concept is illustrated on synthetic experiments based on our previous study of the Movri Mountain Mw6.3 earthquake in Greece [*Gallovič et al.*, 2009, Figure 2]. The study determined the centroid moment tensor from regional data, and identified the fault plane by analyzing the relative positions of the hypocenter and centroid [*Zahradník et al.*, 2008a], later confirmed by the aftershock distribution.

[17] The slip inversion tests were set up with the intention to cover a broader range of source models than preliminarily indicated for the studied event (the strategy recommended for structural tomography by, e.g., *Běhounková et al.* [2007]). We solve the forward and inverse problem for a line source containing two asperities with the rupture propagating at a constant speed V_r = 3.0 km/s. Three scenarios are considered in Figures 3a–5a, unilateral rupture propagation to the right or left, i.e., along $x > 0$, $x < 0$, and bilateral propagation from x = 0 km. The strike, dip, and rake (30°, 87°, −178°, constant along the fault), scalar moment (3.4×10^{18} Nm), source-line azimuth (30°) and depth (17 km) are the same in the forward and inverse problem. This also holds for the complete wavefield Green's functions that are considered "unspoiled," being calculated by the discrete wave number method [*Bouchon*, 1981; *Coutant*, 1989] in a 1-D crustal model [*Haslinger et al.*, 1999] between 0.01 and 0.2 Hz. Eight stations are considered, as in the real case (see Figure 2).

[18] Dynamic strips derived from (synthetic) waveforms at three stations, SER, ZAK, and RGA, are shown in Figures 3b–3d, 4b–4d, and 5b–5d. The $x - t$ plots are supplemented by the corresponding kinematic projection lines forward simulated in a homogeneous model with the S wave

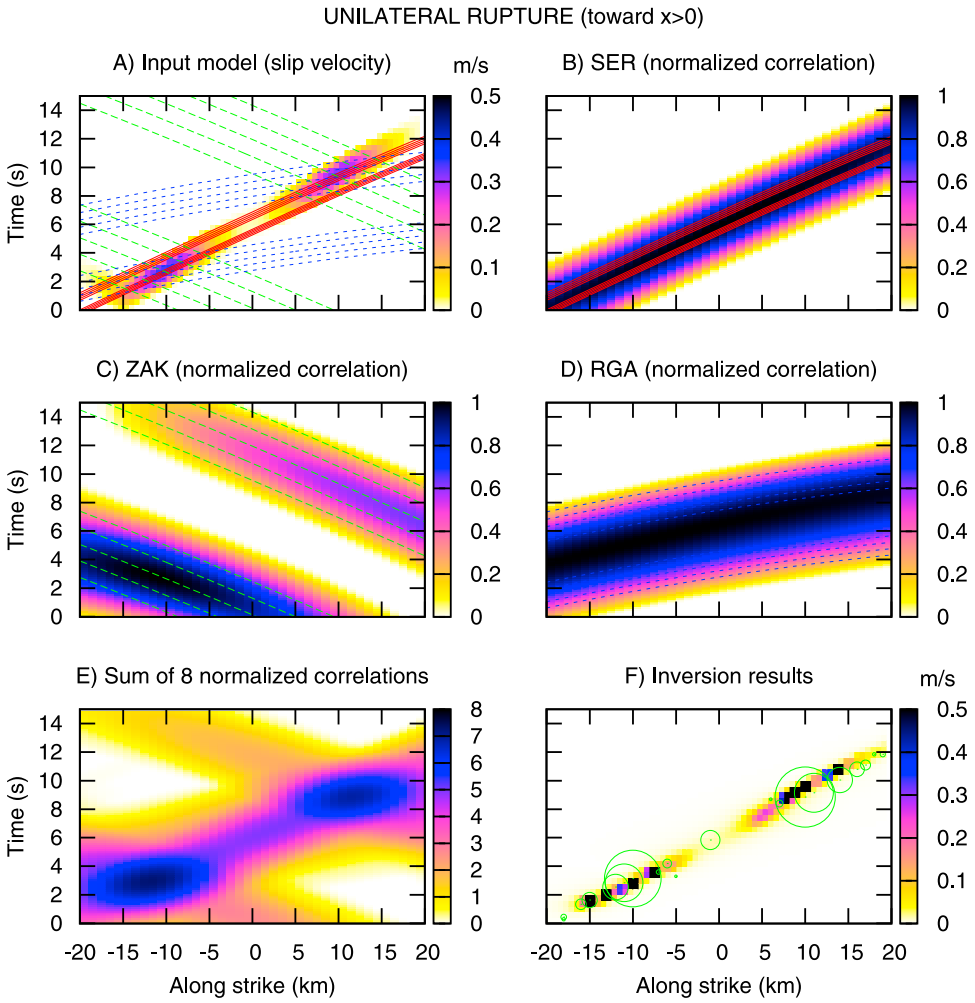

Figure 3. Synthetic model of a unilateral rupture propagation toward $x > 0$. (a) the assumed $x - t$ slip history (data) superimposed by the kinematic projection lines of SER (red), ZAK (green) and RGA (blue) stations (Figure 2). (b–d) Dynamic projection strips, (e) dark spots, i.e., the aggregate projection pattern constructed from all eight stations, (f) inverted $x - t$ plot calculated by two methods, iterative back-projection (method A, slip velocity shown by the color scale) and the modified ISOLA iterative deconvolution (method B, green circles proportional to scalar moment). The assumed frequency range is $f < 0.2$ Hz.

velocity at the source depth (V_s = 3.4 km/s); for simplicity, only five point sources per asperity are considered to form the KPSs. Note that the DPSs in Figures 3b–3d, 4b–4d, and 5b–5d follow approximately their kinematic counterparts, suggesting dominance of S and Lg waves.

[19] Another remarkable feature of the DPSs is that some of them are nonuniform, i.e., with correlation values varying along the strip. To explain this, consider the quality of the possible fit between the synthetic seismogram $y(t)$ due to a trial $x - t$ source point and the complete real waveform $u(t)$. In the optimum case, when the trial source belongs to the true finite-extent source, the synthetic $y(t)$ will fit one of the W_j's in (6) including all phases (P, S, Lg, etc.). If the trial source is out of the true source, it may still fit (approximately) some W_j when the arrival time and amplitude of a dominant phase satisfy (8); the correlation will be lower due to the bad fit of the other phases. Therefore the DPS has its geometry given implicitly by the travel times of such a dominant phase, and, in contrast to KPS, the DPS is nonuniform. The variations are also due to the fact that the $x - t$ points along the strip are characterized by different Green functions and different focal mechanism effects. However, some of these changes might be compensated by the tradeoff between S and M in (8).

[20] Looking again at Figures 3–5, the DPSs identify the directive and antidirective stations. Similarly to KPS, the DPS width is controlled by the directivity terms $T^R(x) + T^P(\boldsymbol{Y}, x)$, where T^P refers to the dominant phase. For example, in Figure 3 (assuming rupture propagation toward $x > 0$) station SER is in the forward direction; hence its strip is narrow. While the KPSs are controlled by the projection lines passing through the end points of the source, the waveforms processed with a finite frequency band provide "smeared" strips. Therefore DPS is not as narrow as its KPS

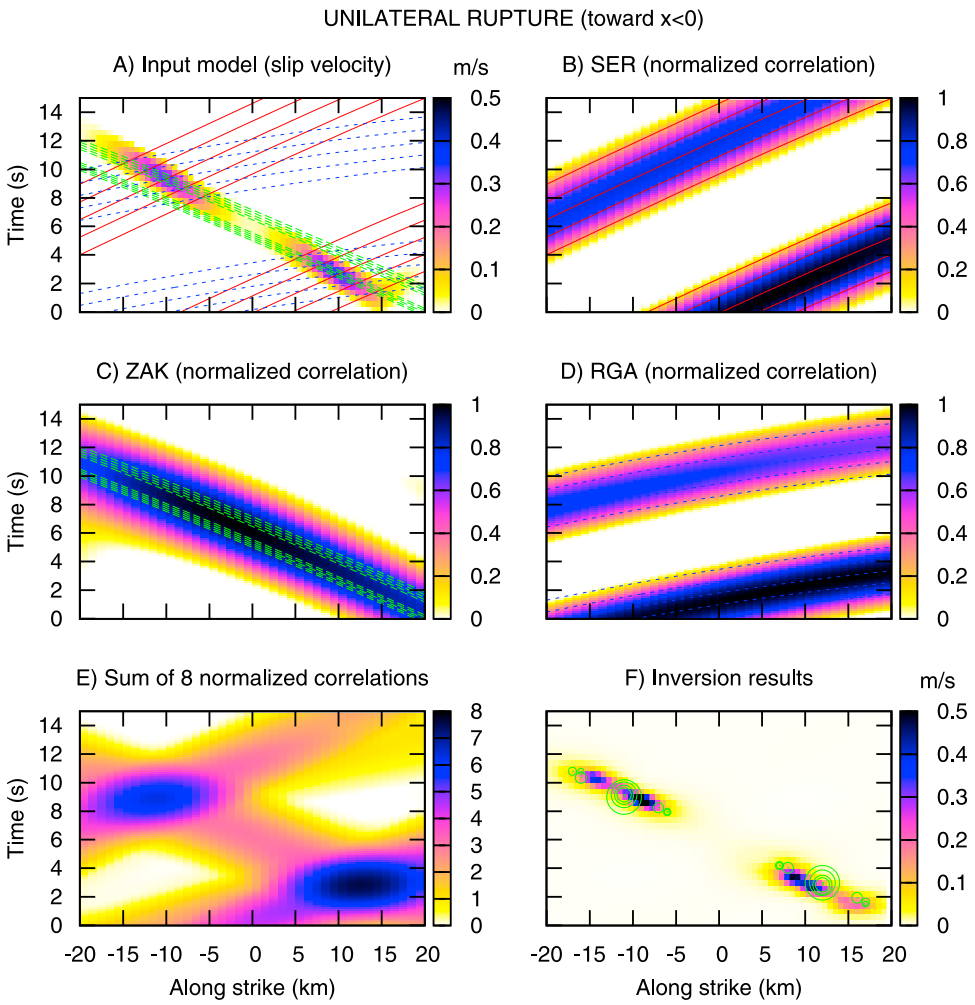

Figure 4. Same as Figure 3 but for the synthetic model of unilateral rupture propagation to the left (toward $x < 0$).

counterpart due to the limited frequency band. The minimum width of DPS is limited by the shortest considered period; as a rule, the strips of the directive stations are wider than the kinematic strips.

[21] The DPSs (similarly to KPSs) might also indicate multiple asperities. For example, the two strips of the antidirective station (ZAK) are well separated from one another, even in the limited frequency band under study. They clearly reflect the slip segmentation into two asperities. In contrast, station SER essentially "sees" only one asperity, since the two strips are close to each other and the limited frequency band further contributes to the merging effect. The off-fault station RGA has two broader strips that partially help to identify the two separate slip patches. Among all eight stations, ZAK is the most important one to recognize this segmentation. The lower intensity of one of the ZAK strips is also a notable effect. It corresponds to fitting a weaker wave contribution from the asperity that is more distant from ZAK; even if it matches the weak signal perfectly, the variance reduction is low due to the unfitted stronger signal from the closer asperity. This follows from the fact that the fit is measured between a single point source contribution and the entire seismogram. The dynamic strips in Figures 4b–4d and 5b–5d can be discussed in a similar way.

4. Dark Spots

[22] Normalized DPSs of all eight stations are summed up in Figures 3e–5e. The aggregate $x - t$ pattern is dominated by the local maxima of the correlation, for brevity called "dark spots," at which the DPSs of the individual stations overlap. The spots delineate the regions where asperities will be retrieved in the inversion, including artifacts (recall Figure 1b).

[23] Figure 3e shows the aggregate of the DPSs for the model of the rupture propagation toward $x > 0$, indicating two major dark spots. They represent a smeared image (due to the use of a limited frequency range) of the intersection of the KPSs shown in Figure 3a. The situation is similar to the schematic Figure 1b. The KPSs of stations SER and ZAK intersect one another in four regions, only two of them corresponding to the true source. The related DPSs are smeared so that the individual true and false crossings are not visible.

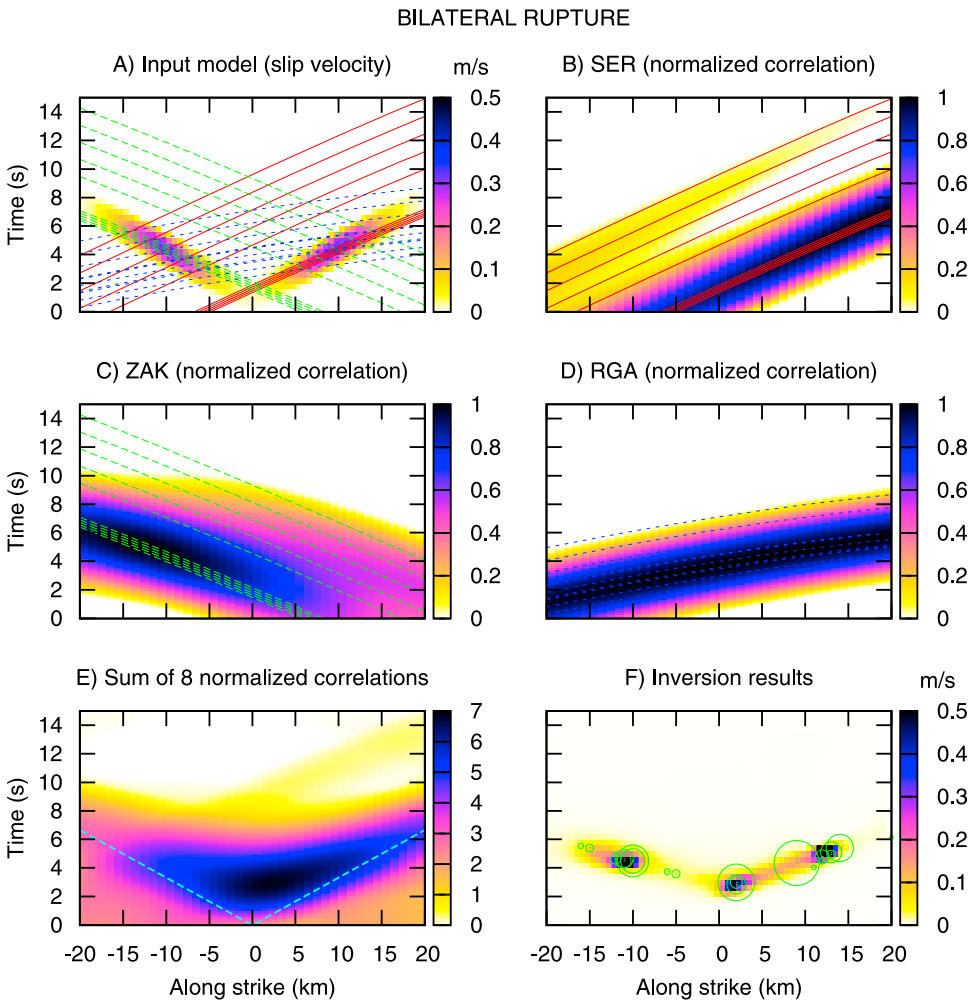

Figure 5. (a–f) Same as Figures 3 and 4 but for the synthetic model of bilateral rupture propagating from $x = 0$ km. This case is characterized by a strong artifact, the spurious asperity close to $x = 0$ km, independent of the inversion scheme used (compare Figures 5a and 5f), caused by the large value of the dark spot (Figure 5e) at $x = 0$ km. The cyan dashed line in Figure 5e represents the input bilateral rupture propagation with rupture speed $V_r = 3$ km/s.

Adding a third station (RGA), situated almost perpendicularly to the fault, or adding more stations, enhances the overlap of the strips around the true $x - t$ asperity, but also the spurious one due to the subhorizontal character of the DPS. The slip inversion might then have problems when inferring the $x - t$ asperity position (involving the rupture speed).

[24] An analogous experiment for the unilateral rupture propagation but in the opposite direction (toward $x < 0$), is displayed in Figure 4e. The same stations are used; SER and ZAK now play the roles of the antidirective and directive stations, respectively. The pattern of the dark spots can again be explained in terms of the KPS's based on the analogy with true (a, b) and false (a', b') asperities in the schematic Figure 1b. In Figures 3a and 4a, the KPSs intersections form analogous false and true asperities as in the schematic Figure 1b. One can see that the distance between the corresponding true and false asperities is larger in Figure 4a than in Figure 3a. In the low-frequency range, the more distant asperities a and a' produce more severe smearing. Therefore the inversion of the model with the rupture propagation toward $x < 0$ (Figure 4) is likely to meet greater difficulties when retrieving the asperity $x - t$ position than in the case of the model with the opposite rupture propagation (Figure 3). The difference is mostly due to the different angle between the fault and the respective directive station.

[25] In case of the bilateral rupture (Figure 5) two separate dark spots (such as in Figures 3 and 4) can no longer be seen, although the distance between the two asperities is still the same. This is because the fault and the station geometry yield no clear split of the DPSs. Instead, we get a single "V-shaped" dark spot. One can expect that the inversion might have problems in identifying the two separate asperities. In particular, note that the dark spot in Figure 5e is most intense even at a place of no real slip at all, close to $x = 0$ km. This is the place where the two directive strips of stations SER and ZAK cross each other. An additional station (e.g., RGA, see Figure 5d) does not essentially help, since the crossing

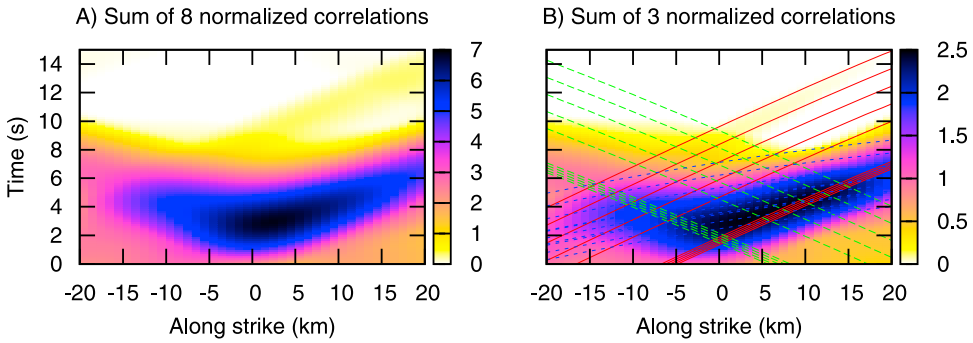

Figure 6. Comparison of the DPSs from eight and three stations for the synthetic bilateral scenario. (a) The aggregated projection pattern for eight stations (same as Figure 5e). (b) Similar pattern derived from three stations only. Their kinematic projection lines are displayed: SER (red), ZAK (green), and RGA (blue).

of the two narrow strips of SER and ZAK is strongly dominant. Moreover, the subhorizontal RGA strip itself passes close to $x = 0$ km, too. The other stations play a minor role in the identification of the two asperities and do not reduce the artifact close to $x = 0$ km, as demonstrated in Figure 6 where the dark spot from all stations is compared to that from the three stations only (namely SER, ZAK, RGA).

[26] To summarize, each DPS shows how the uncertainty of the model parameters (the $x - t$ tradeoff) is affected by an individual station for a given slip distribution. The DPS intersection, i.e., the dark spot, is then related to the uncertainty due to the whole station network. There is an analogy with the investigation of the parameter uncertainties by means of the resolution matrix of linear inversion problems [*Page et al.*, 2009]. Indeed, each row of the resolution matrix relates one input model parameter to its uncertainty in the inverse problem. Summing these rows with weights according to the finite-extent input source model would provide similar information as the dark spot. Note that while the resolution matrix itself is controlled only by the station distribution, the summed rows weighted by the true slip (or the dark spots) are already specific to the input model.

4.1. Role of DPSs and Dark Spots in the Slip Inversion: Comparison of Two Inversion Methods

[27] This section demonstrates that the inversion of the complete low-frequency waveforms is driven by the kinematic and dynamic strips. Waveforms are forward simulated at eight regional stations (Figure 2), assuming the three scenarios described in Figures 3a–5a. The inversion is performed by two methods called A and B. Both methods minimize the L2-norm misfit between the observed and synthetic waveforms, using the previously estimated scalar moment and focal mechanism, but not constraining the rupture velocity and/or the hypocenter location.

[28] In method A [*Gallovič et al.*, 2009], the misfit is expressed analytically as a function of the slip velocity, being itself a function of time and the along-strike position. The formulas are equivalent to the propagation of the residual wavefield back to the fault. The minimization is performed by the conjugate-gradient method [*Press et al.*, 1992]. The initial slip velocity model is a smooth 2-D function along the fault and of time. At each iteration, the slip velocity model is simultaneously updated along the whole fault, gradually revealing the major characteristics of the source process such as the direction of rupture propagation and dominant asperities. The constraints of the fixed seismic moment and positivity of the slip velocity are applied. No smoothing or damping is employed.

[29] Method B is a modification of the ISOLA software [*Sokos and Zahradník*, 2008] to build up a finite-extent source by consecutive retrieval of point-source subevents using iterative deconvolution. The subevents are grid searched in the $x - t$ space; the synthetics of each subevent match the residual wavefield (i.e. the difference between the data and cumulative contribution of the preceding subevents). The standard iterative deconvolution by *Kikuchi and Kanamori* [1991] tends to represent the whole wavefield by a few large point sources. To allow for a more realistic moment distribution in time and space, we introduce a simple modification: if the method requests a subevent with best-fitting moment m_{sub}, we allow only $m_{sub}\,fract$, where $0 < fract < 1$. Of course, using smaller *fract*, one needs more subevents to get the same total scalar moment; in this paper we use $fract = 0.25$ and need about 15–20 subevents to get the same moment. Using, for example, $fract = 0.10$ and 30–40 subevents we get different source details, but the overall pattern of the moment distribution remains unchanged. The modified iterative deconvolution is presented in this paper for the first time.

[30] The inversion results for the three scenarios, two unilateral and one bilateral, are shown in Figures 3f–5f. Methods A and B provide similar (although not identical) results. The general features such as hypocenter location and the overall direction of rupture propagation are resolved in all cases. In the unilateral models, the two asperities are also well retrieved in accordance with the presence of the two dark spots in the aggregated DPS (Figures 3e–5e). The retrieved asperities are isolated even in the bilateral model, although the "V-shaped" dark spot does not reveal a clear split (the inversion result represents a subset of the $x - t$ region covered by the spot). Nevertheless, the bilateral model has a significant drawback; the inversion (Figure 5f) yields not only the two true asperities but also an additional strong false asperity at the center of the fault. In method A the false asperity is almost independent of the starting model of the iterative inversion. In method B, the spurious asperity is already the second largest subevent required by the inver-

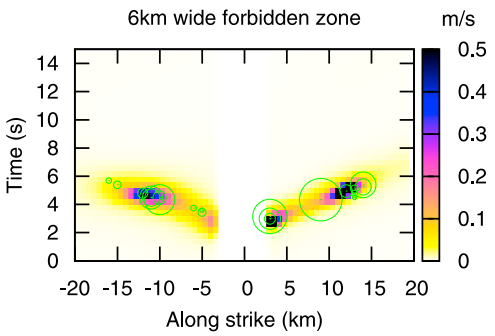

Figure 7. Same as Figure 5, i.e., synthetic model of a bilateral rupture propagation from $x = 0$ km but constraining the 6 km wide central region of the fault to experience no slip. Although the inversion artifact close to $x = 0$ km is avoided in both methods, the inverted slip is large at the border of the "forbidden" region. The example is a warning against misinterpreting the inversion result. If the solution tends toward the borders of the forbidden region, it does not imply that the forbidden region contains the true slip (compare with Figure 5).

sion. The waveform fit for the bilateral scenario is as good as for the other scenarios (the overall variance reduction larger than 0.9 in both methods).

[31] We try to artificially "forbid" the region around $x = 0$ km in the inversion (see Figure 7). The spurious asperity is avoided in both methods A and B. However, Figure 7 also shows that in such a case the inversions by both methods tend to put the slip as close to the forbidden zone as possible. This result is interesting from the viewpoint of possible misinterpretations of the inverse problem solutions: Assume a case in which we want to prove the existence of the asperity at $x = 0$ km. We formally forbid the corresponding zone and inspect the inversion progress. If the inverted slip tends to get close to the forbidden region (as happened in our case), the asperity at $x = 0$ km is understood to be a stable inversion feature. However, our example clearly shows that a stability like that does not ensure that the asperity is real.

[32] Although the hypocenter position and rupture direction are resolved by both methods, the rupture speed, evaluated by the least-squares fitting of the subsources (method B), differ from the true value of 3.0 km/s. For the unilateral propagation toward $x > 0$ and $x < 0$ the retrieved values equal 3.3 and 3.7 km/s, respectively. The distortion of velocity is a consequence of the effect shown schematically in Figure 1b where false asperities appeared although the false asperities themselves were not visible due to the blurring effect. The effect is present both for the three stations (as assumed in Figure 1b) or all eight. For the bilateral case, where the false asperity is a major effect, the retrieved speed is completely wrong (larger than 5 km/s in both directions).

[33] We emphasize that the described behavior of the waveform inversion is fully consistent with the DPS and KPS analysis presented in the preceding section (i.e., an artificial asperity for the bilateral model and greater problems in determining the rupture speed for $x < 0$ than for $x > 0$ unilateral models). Obviously, the station distribution is an important issue, but the azimuthal coverage is not poor. (In practice, at near-regional distances, it is rarely better.) We dispose of eight stations, five of which are in favorable positions, i.e., in the almost forward and backward directions (SER, MAM, THL, ZAK, PYL). Their combination plays a key role in constraining the inversion. Therefore the main problem is not only in the azimuthal coverage but also in the multiplicity of the true asperities that causes the nonuniqueness of the inverse problem.

[34] It is also important to emphasize that the dark spots determine the inverted slip pattern independently of the slip inversion approach used. The dark spots represent areas attracting the optimization procedures. The slip is always confined within the dark spots, but the details revealed inside the spots by different inversion methods are not necessarily the same. For example, in Figures 4f both methods yield a more focused ("peaked") $x - t$ pattern than in Figure 3f. On the other hand, the position of the "peaks" resolved by methods A and B in Figure 4f is not identical. And, importantly, the inferred pattern is also not exactly the same as the true asperity pattern.

[35] We emphasize that the concept of the dark spots attracting any inversion method holds even for the false asperities. Thus no method is better protected against the inversion artifacts than any other. It is possible that false intersections of directive strips at regions of no real slip might represent even the main common feature of different inversion schemes. Perhaps the only way to prevent the artifacts is to consider some prior constraints.

4.2. Constraints in the Slip Inversions

[36] As in any nonunique inverse problem, the result can be improved by imposing a constraint. Three possible constraints are considered here: (1) use of higher frequencies, (2) known rupture speed and hypocenter position, (3) independent prior knowledge of an asperity. They are applied to the most problematic bilateral scenario (Figure 5).

[37] 1. Figure 8 demonstrates the slip inversion of the bilateral model when the frequency band is extended up to 1 Hz. The full-wavefield Green's functions are again exactly the same in both forward and inverse modeling. The false asperity in the fault center is somewhat (but not completely) reduced in both methods A and B, see Figure 8f. This is so because the individual station DPS's in Figures 8b–8d are sharper when compared to those in Figures 5b–5d. The sharper DPS's result in a more constrained dark spot (compare Figures 5e and 8e) that drives the inversion better toward both asperities. The false crossing close to $x = 0$ km is less supported by station RGA. Nevertheless, the false intersection of the SER and ZAK directive strips is still present and attracts both methods to a spurious spot of no real slip at the fault center. However, this constraint is not only hardly applicable in practice because of the lack of sufficiently precise crustal models up to such a relatively high frequency, but its effectiveness to reduce false asperities is not optimal. More sophisticated methods based on spectral decomposition [*Ji et al.*, 2002] might better employ high-frequency data to improve pattern recognition.

[38] 2. Figure 9a, frequency range up to 0.2 Hz, compares the input slip velocity model for the bilateral scenario

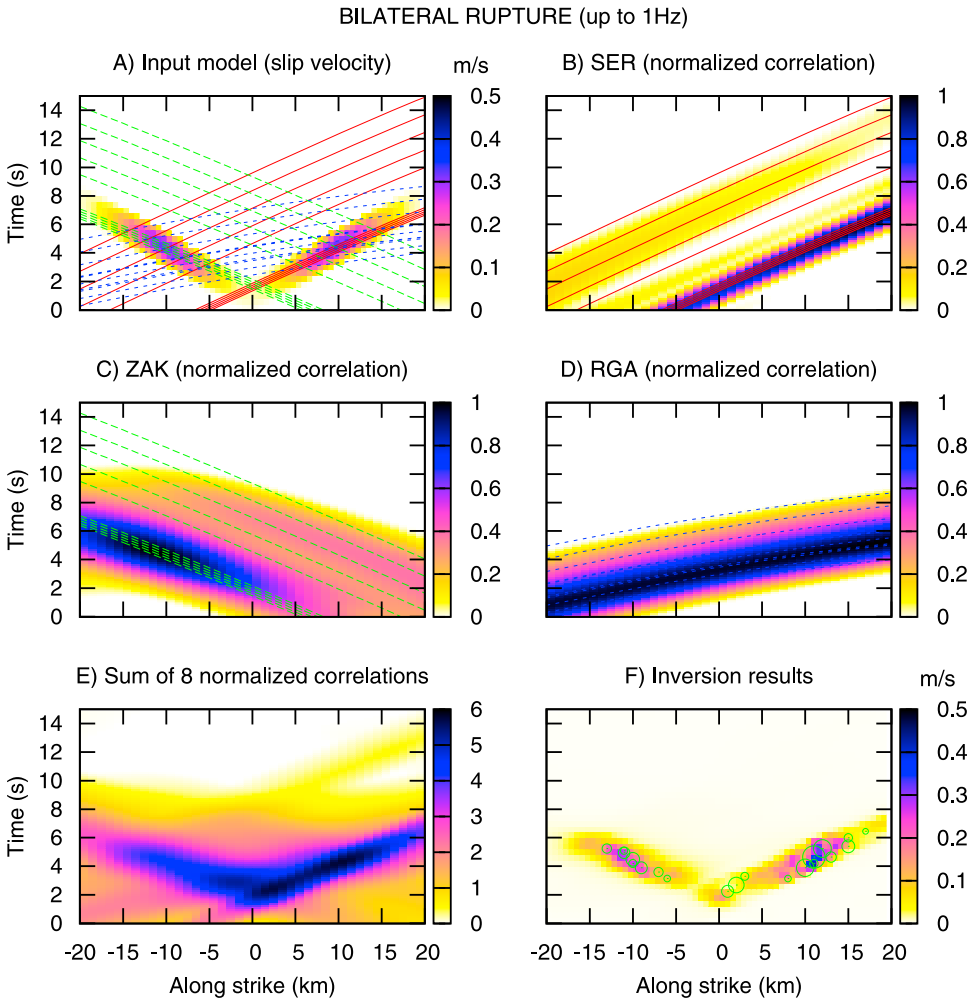

Figure 8. (a–f) Same as Figure 5, i.e., synthetic model of a bilateral rupture propagation from $x = 0$ km, but for the frequency band up to 1.0 Hz. The inversion artifact close to $x = 0$ km is partially reduced in both methods (see Figure 8f).

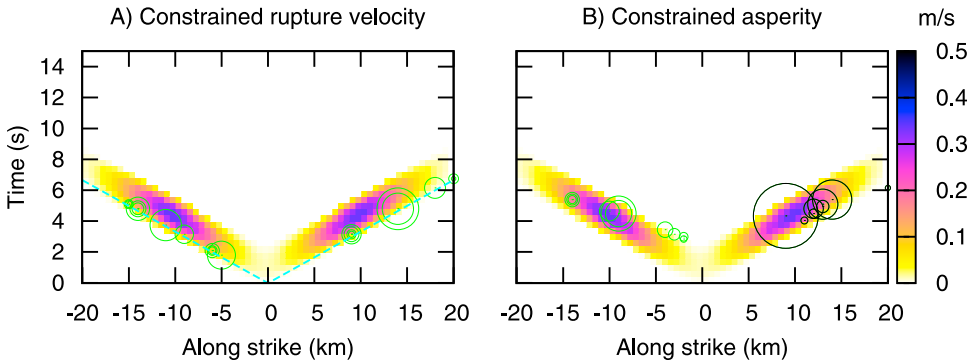

Figure 9. Slip inversion results by method B with constraints (symbols) compared with the input slip velocity model (color scale). The assumed frequency range is $f < 0.2$ Hz. (a) Same as Figure 5, i.e., synthetic model of a bilateral rupture propagation from $x = 0$ km, but inverted with a prior knowledge of the hypocenter position and the rupture speed (cyan line, also shown in Figures 5e). (b) Same as Figure 5 but with a prior constraint of the right-hand asperity (plotted in black). Note that the spurious asperity at $x = 0$ km was suppressed in both cases.

(plotted in the background by the color scale) with the inversion result by method B in which the rupture velocity and hypocenter were constrained. This means that only subevents whose $x - t$ positions follow the true hypocenter position and rupture speed, shown as the cyan line, were allowed. The true asperities are (approximately) inferred, while the false asperity is fully avoided. The explanation is simple. The inversion is driven by the intersection of the dark spot with the cyan line (representing the prescribed rupture propagation) shown in Figure 5e. This intersection is characterized by small correlation values at the hypocenter (x = 0 km); hence the artifact is missing and the true asperities are revealed. Note that if another hypocenter position or rupture velocity (within reasonable limits) are prescribed in the inversion, the slip model would be slightly different with approximately the same fit to the observed data (especially when imprecise Green's functions are used in real applications). This illustrates the mechanism behind the well-known tradeoff between rupture speed and slip that led to combined seismic and geodetic inversions [*Hernandez et al.*, 1999; *Custódio et al.*, 2009].

[39] 3. Since artifacts appear in the slip inversion due to the multiplicity of asperities, we try to constrain one asperity, hypothetically known from independent data in advance. The preliminary unconstrained inversion provided the point source subevents in the left, right and middle parts of the fault (Figure 5f). As an example, we suppose that independent data supported the existence of the right-hand asperity. We collect subevents from that part of the fault, and calculate the corresponding finite-extent synthetics for all stations; these synthetics are subtracted from original waveforms. (Remark: the definition of this initial finite source also includes the optimization of its scalar moment, analogous to equation (9).) The residual data, now already with one true asperity removed, are used as new input into the standard inversion by method B. Figure 9b compares the resulting subevent distribution with the input bilateral scenario (color scale). The constrained inversion reveals (approximately) the slip pattern in the left-hand part of the fault, but, most importantly, there is no spurious slip in the center of the fault. This is a direct consequence of equation (4); after prior removal of asperity a, the inversion is $G^{-1}(S_i) = b_i$, each station providing just a single strip (not shown here), and hence the solution provides asperity b only. This constraint seems to be the best, but prior knowledge of an asperity is obviously rare (except in combined inversions of seismic and geodetic data). Nevertheless, this constraint can be useful for variable initiation of the inversion when inspecting possible alternative solutions (see below).

[40] We emphasize that the above tests do not represent an exhaustive set of possible constraints. For example, we did not consider nonuniform gridding of the model parameters.

5. Real Data Example

[41] Here we demonstrate the applicability of the DPS concept on real data of the 2008 Movri Mountain Mw6.3 earthquake, Greece. It was the largest strike-slip earthquake that occurred in western Greece during the past 25 years [*Ganas et al.*, 2009] and its importance for seismic hazard assessment in Greece is thus obvious [*Tselentis et al.*, 2010]. A few years of anomalous seismicity pattern preceding the event was reported by *Chouliaras* [2009]. *Papadopoulos et al.* [2009] attributed the event to an unusual earthquake "storm" that struck Greece in 2008, in which four Mw > 6.2 earthquakes occurred during an unusually short time interval of 6 months. No surface ruptures related to the causative fault were observed. *Koukouvelas et al.* [2009] reported significant coseismic surface ruptures up to distances of 10 km from the epicenter. The source model was previously studied by *Konstantinou et al.* [2009] and *Gallovič et al.* [2009], both inferring a delayed asperity (see below). This section presents a critical review of that result.

[42] The fault and station geometry (Figure 2), crustal model, and also computational methods are the same as in the preceding synthetic tests. Figure 10a shows the retrieved dynamic strips in the frequency range 0.01–0.2 Hz. Time t = 0 s corresponds to the origin time of the earthquake. Stations SER and THL provide clear DPSs sloping toward $x > 0$ that are quite narrow, thus informing about predominant rupture propagation toward the northeast (compare with the synthetic test in Figure 3). On the contrary, stations ZAK, KAL, and PYL, situated southwest of the epicenter, feature wide DPSs with the opposite slope, further confirming the predominant northeast rupture propagation. The DPS at station ZAK may perhaps suggest splitting into two strips, indicating the presence of a second asperity. The DPS's provide no indication of bilateral rupture propagation.

[43] Figure 10b shows the dark spot for the Movri Mountain earthquake, i.e., summed DPSs from all eight stations. It confirms the northeast rupture propagation, existence of a strong asperity close to x = 0 km and a weaker slip at $x < 0$. No split of the $x - t$ slip pattern into several patches is indicated, perhaps due to the use of relatively low-frequency data.

[44] Figure 10c then compares the inversion results of methods A and B (method A having already been applied to the studied event by *Gallovič et al.* [2009], method B being newly added here). The inversion image is dominated by the rupture propagation along the positive x axis (toward northeast) with the strongest slip patch at x = 0 km, t = 10 s. Comparing this with the epicenter position at $x = -8$ km (arrow in Figure 10c), we conclude that the main patch (t = 10 s) had a significant time delay. The other important feature of the $x - t$ image is the patch close to the epicenter at t = 5 s, marking another delay with respect to the origin time. These two main features are common to methods A and B, while details are not the same. Similar differences between methods A and B (although smaller) were observed also in the synthetic tests (Figures 3f–5f). The waveform fit for both methods is almost the same (variance reduction 0.7), which suggests that both models obtained by methods A and B are equally acceptable.

5.1. Alternative Nonsmooth Models

[45] Two models equally well satisfying the observed data suggest the existence of other models which also fit the data. A simple tool for at least partly exploring the nonuniqueness of the source model is the prior constraint of a slip patch (see the previous section). We do not dispose of independent slip data, but we can (repeatedly) initialize the inversion with an arbitrary finite-extent source. As method B is technically

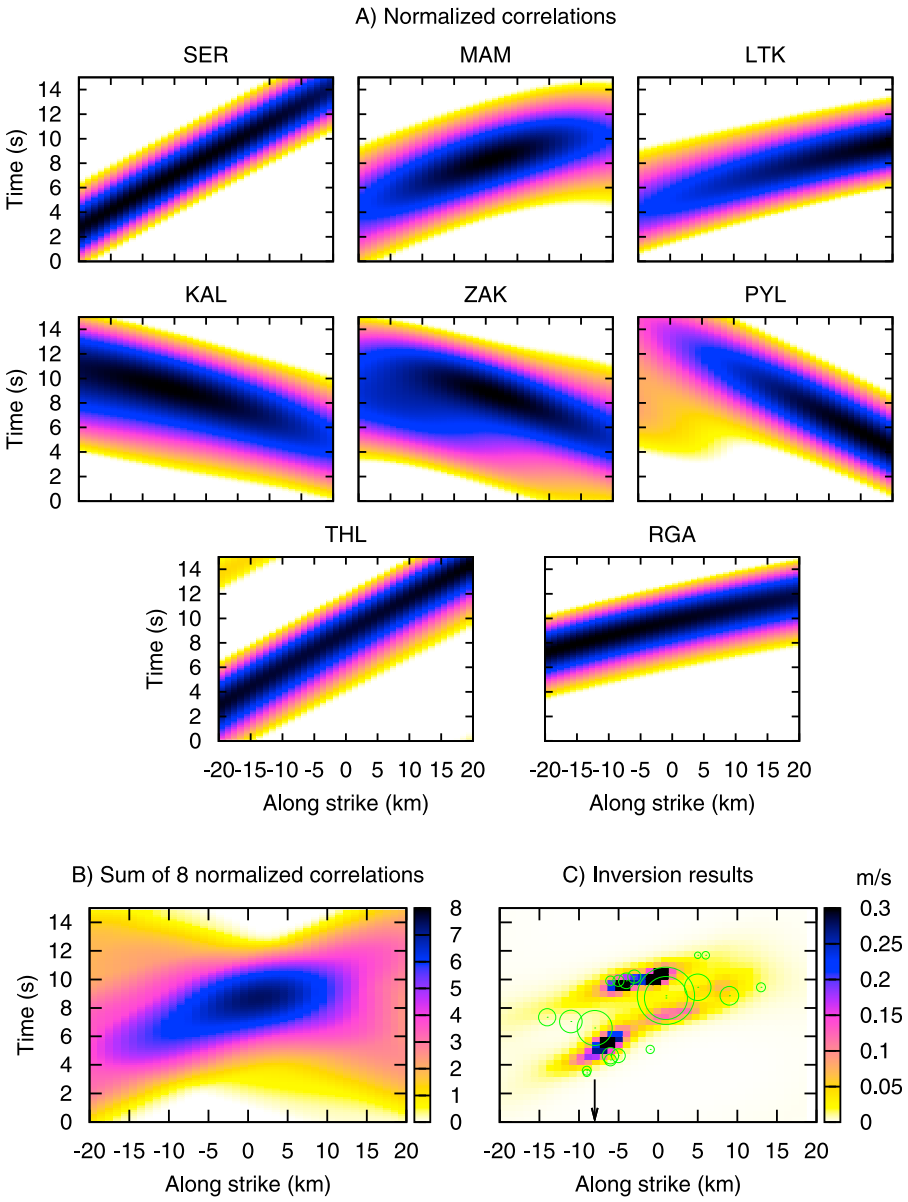

Figure 10. Inversion of real-data example (the Movri Mountain earthquake). (a) Dynamic projection strips for all eight stations (Figure 2). (b) dark spot, i.e., aggregate of all eight dynamic projection strips. (c) $x - t$ pattern inverted by two independent methods of this paper. Frequency band $f < 0.2$ Hz. The black arrow on the horizontal axis marks the epicenter position. The nonuniqueness of the source model (alternatives to Figure 10c) is demonstrated in Figure 11.

more suitable than method A for such a purpose, it is used further solely. Figure 11 shows the results of six tests of method B (circles) together with the previous result of method A (color scale). The latter is shown just for comparison; it represents merely one realization of the possible inversion results of method A.

[46] The first two tests (Figures 11a and 11b) use a part of the preliminary (unconstrained) $x - t$ plot, namely the groups of events at about $t = 5$ s ("early") and $t = 10$ s ("late"). When initiating the inversion with the late asperity, see Figure 11a, two patches are retrieved; one of them being the early asperity. Figure 11b shows the opposite case where, however, the final pattern consists of only two patches. Note also the variable size of the patches among the tests. Also note the close similarity between methods A and B in Figure 11b. The third test (Figure 11c) serves to enhance the latter effect by an artificial time shift of the initial early asperity (+1 s). The early asperity now being exactly the same as in method A, the second asperity is also common to both methods, and the whole image provided by method B simplifies considerably. Nevertheless, the coincidence of methods A and B cannot be interpreted as a preference for just that solution. Similarly to "pushing" method B to agree with method A, also method A can be initialized in different ways to agree with the unconstrained method B.

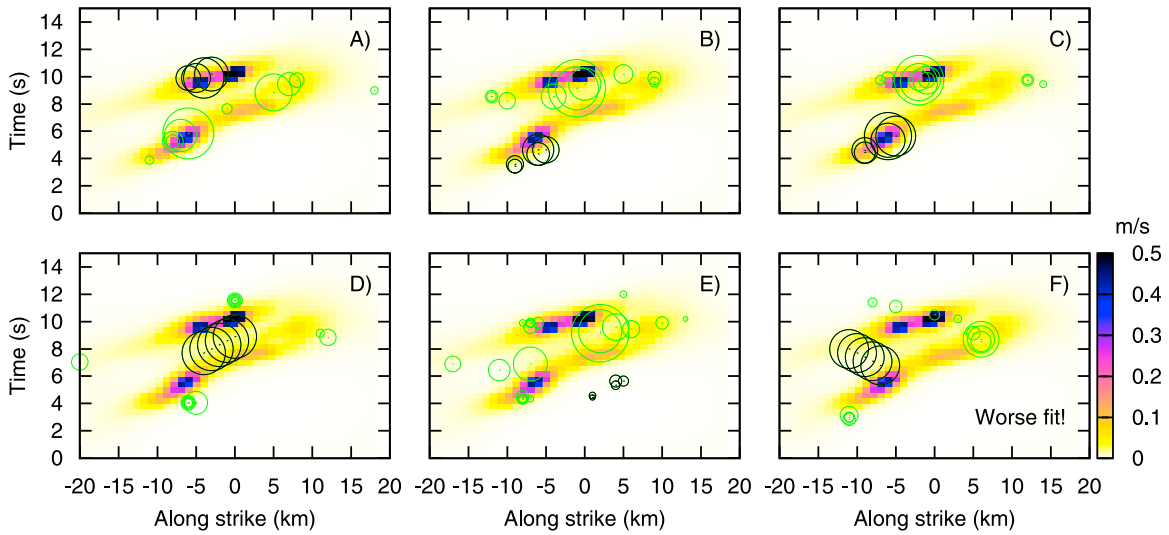

Figure 11. (a–f) Stability check of the real-data case from Figure 10. Shown are repeated solutions by method B, initializing each time the inversion with a different finite-extent source (plotted in black). Moment of the initial patch is optimized with respect to the real data. The colored background solution by method A, same as in Figure 10, is shown for comparison. All models satisfy the data equally well (*varred* = 0.7 and the same scalar moment), except for Figure 11f (*varred* = 0.66). The latter is an example of an inadequate solution, although the inversion was initiated inside the dark spot (Figure 10b). Note that the acceptable models include a few patches or a single homogenous patch (Figure 11d). Initiating the solution outside the dark spots is not harmful, see Figure 11e; it simply yields the same pattern as with the unconstrained asperities (Figure 10c) because the initiating subevents require almost no seismic moment. Not all the equivalent solutions found by method B (Figures 11a–11e) agree with the two main patches of method A, e.g., see Figure 11d. The agreement between the two methods is not indicative for model relevance.

[47] Figure 11d demonstrates the case where the two methods yield quite dissimilar results (again with the same fit, *varred* = 0.7). The inversion is initialized with a smooth homogeneous slip distribution in the region of no slip in the preceding tests, but still inside the dark spot. The data accept such a pattern "complementary" to that of Figures 11a–11c but practically do not need any slip in the two patches (t = 5 s and t = 10 s) shown in color. In Figure 11e we initiate the inversion with a slip assumed to occur well outside the dark spot, at about x = 5 km, t = 5 s. Such a patch requires almost no scalar moment, hence the resulting model (with *varred* = 0.7), is practically the same as in Figure 10c (unconstrained).

[48] Finally, to demonstrate that not every model within the dark spot is acceptable, Figure 11f shows the result for a prescribed homogeneous slip pattern with rupture propagation toward $x < 0$. In this case the data require an additional patch at x = 5 km, but the fit (for the same total moment as before) is worse, *varred* = 0.66.

[49] As all of the solutions in Figure 10c and Figures 11a–11e provide the same data fit (the overall variance reduction is 0.7) and the same total scalar moment, none of them can be considered as a preferable source model of the Movri Mountain earthquake. They merely partly illustrate the shape of the misfit function; it has several local minima of almost identical depth, allowing the data to be explained by a class of source models that are relatively far from each other (asperities located at different positions in space and time). Nevertheless, the investigated source models have two common features. (1) They never exceed the limits imposed by the correlation dark spot. (2) They tend to be rough, "peaked" at a few, two-three patches.

6. Discussion

[50] Our results for the Movri Mountain earthquake are basically similar to those obtained by *Konstantinou et al.* [2009], where, however, the fine details of the slip distribution on the 3 km scale were reported using the frequency range up to 0.1 Hz. Similarly to our study, they also found a large time delay of the main slip patch with respect to the origin time. Thus both studies seem to indicate that there was a temporary rupture arrest between the slip initiation and the main rupture episodes. The only difference is that *Konstantinou et al.* [2009], using regional data, also reported variations of the slip along the fault dip, for which (with similar station coverage) we found no resolution up to 0.2 Hz.

[51] It seems there is not much to improve for this earthquake with the available regional stations and crustal models. If we prefer a non-smooth source model, it is nonunique, represented by a suite of equivalent models. Alternatively, we can assume a smoothed model. For example, to declare that the inverted $x - t$ pattern is just the dark spot itself. Such a formal smoothing would negatively affect the applicability of the source model in strong motion simulations (it would underestimate the peak motions). Seeking correct assessments of the fault roughness is an important future goal [*Causse et al.*, 2010; *Burjánek and Zahradník*, 2007; *Gallovič*

and Brokešová, 2004], even if the nonsmooth model remains nonunique.

[52] Exploring the model space as much as possible and further evaluating statistical properties of equivalent source models would be a useful, though complicated task [*Piatanesi et al.*, 2007; *Liu et al.*, 2006]. The present paper indicates that the dark spots reduce the domain of the parameter space to be explored. *Monelli and Mai* [2008] suggested estimation of posterior marginal distributions of the model parameters based on exploration of the model space. Still, if the reduced model space is not sampled sufficiently, the true parameters may lie on the tails of the distributions (thus forming stable artifacts). Note that such persistent false features cannot be detected even by bootstrapping or jackknifing methods typically used in inverse problems, as showed by *Page et al.* [2009]. The failure of jackknifing (i.e., repeated exclusion of a station) can easily be understood thanks to the concept of dynamic strips. The exclusion of off-fault stations practically does not change the inversion result, simply because they do not contribute much to the inversion (see, e.g., Figure 6). On the other hand, by having only a few stations strongly constraining the solution (especially those close to the forward directivity azimuth), and excluding them, we loose the resolution, thus making the impression that the slip can be almost arbitrary. This effect can be easily understood also from Figure 1a if the projection strip of the forward directivity station (red) is omitted. The dark spot for the two remaining stations would then be extremely uncertain (see the area delimited by the green and blue lines in Figure 1a).

[53] The synthetic tests show that a few high-quality data with well constrained crustal models may provide an adequate solution. Of course, inverting many stations might also be useful since they complement each other as regards the relevance of the crustal model, instrumental behavior, noise, etc. Adding stations just to increase the azimuthal coverage is not always needed. Moreover, the formal use of too many station might implicitly overweight the data in certain azimuths as *Roumelioti et al.* [2009] warned. For example, distant stations (although perhaps reducing the azimuthal gap) may be harmful due to the more significant inaccuracy of Green's functions. Near stations should be used with caution as they might be corrupted by instrumental defects, often not obvious at first glance [*Zahradník and Plešinger*, 2005, 2010]. Such data at near stations tend to be fitted very well, thus biasing the inversion considerably [*Zahradník et al.*, 2008b].

7. Conclusions

[54] The objective of this paper was to investigate the uncertainties and possible artifacts of slip inversion due to the inherent non-uniqueness of the inverse problem. To exclusively study such uncertainties, we focused mainly on synthetic tests with noise-free data and exact crustal models. Two methods were applied and compared in this paper, (1) the iterative back-propagation method [*Gallovič et al.*, 2009] and (2) the modified iterative deconvolution with controlled moment release; the latter being presented for the first time here. The findings can be summarized as follows:

[55] 1. The slip inversion is similar to simultaneously locating multiple point sources without picking arrivals. Finite-size asperities can be retrieved at intersections of the arrival-time isolines forming so-called kinematic projection strips. The strips are narrow/broad for directive/antidirective stations, respectively. Each strip represents mapping from the model space to the single-station data space and back. Intersections of the station strips inform about mapping of the model space to the solution space. The intersections cover a larger domain than the true parameters, suggesting that the solution is nonunique.

[56] 2. We generalize the arrival time-based kinematic projection strips to complete wavefields, introducing the "dynamic projection strips" (DPSs) for individual stations. DPS is a set of points in the $x - t$ plane, such that each individual one fits a point-source contribution of the observed waveform. Not all the points of the strips are needed to fit the waveform. Most of them only represent the nonuniqueness of the station contribution. The waveform is fitted by a subset of points in the DPS. To find the true $x - t$ source segment, we need several stations. Intersections of their dynamic strips, the so-called dark spots, do include the true solution but also its vicinity (blurring). Moreover, strong artifacts occur in case of multiple (two or more) true asperities. Strong strips of the directive stations cross each other not only at true asperities but also at spurious dark spots, corresponding to regions of no real slip. The dark spots illustrate the mechanism which generates the nonuniqueness of the parameter values. It is similar to information provided by summed rows of the resolution matrix of linear problems, weighted according to the particular input slip model (thus being relevant not only to the station distribution, but also to the particular slip field).

[57] 3. This paper demonstrates that DPSs of individual stations may be constructed from both synthetic and real data. The strips (and their forward kinematic modeling for the synthetic tests) enable insight into the slip inversion, informing about the station contributions to the inversion. The shape of the DPS helps to identify the forward and backward stations. At backward stations the DPSs indicate possible multiple asperities. At forward stations, as a rule, the asperities are mutually merged. Multiple asperities with bilateral rupture propagation signalize possible false dark spots in the $x - t$ plots that might confuse the inversion.

[58] 4. The new concepts are used to interpret three synthetic models with two asperities (two unilateral rupture scenarios and one bilateral). The two unilateral scenarios provided somewhat different results, although using the same stations, since their geometry with respect to the rupture propagation direction was not the same. As the inversions are driven by the dark spots, the main problems were detected for the bilateral case providing a strong persistent false asperity in the middle of the fault (a spurious crossing of DPSs). Problems with spurious effects were common to both inversion methods investigated in this paper; they appear to be of a very general nature. Moreover, when the asperity location is "forbidden" in the inversion, the slip concentrates as close to the forbidden region as possible. Therefore such behavior of the inversion cannot be interpreted as proof that the asperity is true.

[59] 5. We discuss several ways of constraining the nonunique solution. Increasing the frequency might help to partially reduce some spurious asperities. However, in practical near-regional studies, this method is hampered by inaccuracies of the existing crustal models at higher frequencies

(above 0.2 Hz). Fixing the rupture speed from the hypocenter at its true value would be a good tool to prevent the artifacts, but the true speed and hypocenter position are not known precisely. Fixing the rupture speed at a constant value along the whole fault, together with fixing the hypocenter position, and searching for the best value of the rupture speed as a free parameter is a common strategy, but it might provide a biased rupture speed and slip model. The optimum constraint seems to be a prior knowledge of one true asperity. If the source contains only two asperities, such a constraint will make the inversion free of the spurious effect. However, prior constraint is not easy, except perhaps when using GPS data. In the absence of any prior information about the slip, initiating the inversion (repeatedly) with several finite-extent sources might be effective at least for partial exploration of the model space.

[60] 6. The line source model of the 2008 Movri Mountain Mw6.3 earthquake, previously studied by *Gallovič et al.* [2009], is compared with the independent results of the modified iterative deconvolution method. The DPSs of the individual stations were demonstrated for this earthquake. They supported the previous interpretation of the predominantly unilateral rupture propagation toward the northeast. No significant indication of bilateral propagation was found. The two independent methods provide reasonable agreement: the $x - t$ slip pattern features two-three asperities, characterized by a considerable time delay with respect to the origin time. On the other hand, as shown by the stability checks, the exact $x - t$ position of the asperities, as well as their exact size (exact "roughness" of the slip pattern) remain unresolved; the earthquake is to be represented by a few equivalent source models, all of which provide the same match with the observed waveforms.

[61] The inherent nonuniqueness of the slip inversion is well known. This paper tries to throw light on some of the "mechanisms" driving the inversion to different results equally well fitting the data. Blurring of the slip pattern and false asperities are presented as important and very general artifacts. They may have accompanied many of the published slip models, although not always explicitly recognized.

[62] Finally, note that all the conclusions were drawn for relatively low-frequency waveforms at near-regional distances. The line-fault approximation was chosen due to the poor depth resolution in the present application. The near-fault high-frequency studies might be less affected by the artifacts studied in this paper provided they utilize well-calibrated crustal models. Nevertheless, the DPS concept is applicable too, however, it would require truly extended (2-D) faults. Formal generalization of the DPS and KPS concept would be straightforward. Nevertheless, the along-dip resolution might differ from case to case and require further specific studies. The DPS and KPS concept can also be useful in experimental design when planning the best station positions for slip inversions.

[63] **Acknowledgments.** The authors thank M. Mai, C. Matyska, and an anonymous reviewer for useful comments. The authors greatly appreciate the free Internet access of waveforms provided by NOA (THL) and ITSAK (stations ZAK, KAL). The remaining stations (RGA, MAM, SER, LTK, PYL) belong to the PSLNET network, cooperated by the Charles University. Financial support: GAUK14509, GACR 205/08/P013, MSM0021620860. This research has benefited also from funding provided by the Italian Presidenza del Consiglio dei Ministri - Dipartimento della Protezione Civile (DPC). Scientific papers funded by DPC do not represent its official opinion and policies.

References

Aki, K., and P. G. Richards (2002), *Quantitative Seismology*, Univ. Sci. Books, Sausalito, Calif.

Ameri, G., F. Gallovič, F. Pacor, and A. Emolo (2009), Uncertainties in strong ground-motion prediction with finite-fault synthetic seismograms: An application to the 1984 M 5.7 Gubbio, central Italy, earthquake, *Bull. Seismol. Soc. Am.*, *99*, 647–663.

Běhounková, M., H. Čížková, C. Matyska, D. A. Yuen, and M. Wang (2007), Resolution tests of 3-D convection models by travel-time tomography: Effects of Rayleigh number and regular vs. irregular parameterization, *Geophys. J. Int.*, *170*, 401–416, doi:10.1111/j.1365-246X.2007.03458.x.

Bernard, P., and R. Madariaga (1984), A new asymptotic method for the modeling of near-field accelerograms, *Bull. Seismol. Soc. Am.*, *74*, 539–557.

Bindi, D., and A. Caponetto (2001), Tomographic imaging of the earthquake source: Numerical validation in two-dimensional approximation, *J. Geophys. Res.*, *106*(B4), 6643–6656.

Bouchon, M. (1981), A simple method to calculate Green's functions for elastic layered media, *Bull. Seismol. Soc. Am.*, *71*, 959–971.

Burjánek, J., and J. Zahradník (2007), Dynamic stress field of a kinematic earthquake source model with k-squared slip distribution, *Geophys. J. Int.*, *171*(3), 1082–1097.

Causse, M., F. Cotton, and P. M. Mai (2010), Constraining the roughness degree of slip heterogeneity, *J. Geophys. Res.*, *115*, B05304, doi:10.1029/2009JB006747.

Chouliaras, G. (2009), Seismicity anomalies prior to 8 June 2008, Mw = 6.4 earthquake in western Greece, *Nat. Hazards Earth Syst. Sci.*, *9*, 327–335.

Convertito, V., R. De Matteis, L. Cantore, A. Zollo, G. Iannaccone, and M. Caccavale (2010), Rapid estimation of ground-shaking maps for seismic emergency management in the Campania Region of southern Italy, *Nat. Hazards*, *52*, 97–115.

Coutant, O. (1989), Program of numerical simulation AXITRA, research report, LGIT, Grenoble.

Custódio, S., M. T. Page, and R. J. Archuleta (2009), Constraining earthquake source inversions with GPS data: 2. A two-step approach to combine seismic and geodetic data sets, *J. Geophys. Res.*, *114*, B01315, doi:10.1029/2008JB005746.

Festa, G., and A. Zollo (2006), Fault slip and rupture velocity inversion by isochrone backprojection, *Geophys. J. Int.*, *166*, 745–756.

Frankel, A., and L. Wennerberg (1989), Rupture process of the Ms 6.6 Superstition Hills, California, earthquake determined from strong-motion recordings: Application of tomographic source inversion, *Bull. Seismol. Soc. Am.*, *79*, 515–541.

Gallovič, F., and J. Brokešová (2004). On strong ground motion synthesis with k^{-2} slip distributions, *J. Seismol.*, *8*, 211–224.

Gallovič, F., R. Barsch, J. de la Puente, and H. Igel (2007), Digital library for computational seismology, *Eos Trans. AGU*, *88*, 559.

Gallovič, F., J. Zahradník, D. Křížová, V. Plicka, E. Sokos, A. Serpetsidaki, and G.-A. Tselentis (2009), From earthquake centroid to spatial-temporal rupture evolution: Mw6.3 Movri Mountain earthquake, June 8, 2008, Greece, *Geophys. Res. Lett.*, *36*, L21310, doi:10.1029/2009GL040283.

Ganas, A., E. Serpelloni, G. Drakatos, M. Kolligri, I. Adamis, Ch. Tsimi, and E. Batsi (2009), The Mw 6.4 SW-Achaia (western Greece) earthquake of 8 June 2008: Seismological, field, GPS observations and stress modeling, *J. Earthq. Eng.*, *13*, 1101–1124.

Hartzell, S., P. Liu, C. Mendoza, C. Ji, and K. M. Larson (2007), Stability and uncertainty of finite-fault slip inversions: Applications to the 2004 Parkfield, California, earthquake, *Bull. Seismol. Soc. Am.*, *97*(6), 1911–1934.

Haslinger, F., E. Kissling, J. Ansorge, D. Hatzfeld, E. Papadimitriou, V. Karakostas, K. Makropoulos, H.-G. Kahle, and Y. Peter (1999), 3D crustal structure from local earthquake tomography around the Gulf of Arta (Ionian region, NW Greece), *Tectonophysics*, *304*, 201–218.

Hernandez, B., F. Cotton, and M. Campillo (1999), Contribution of radar interferometry to a two-step inversion of the kinematic process of the 1992 Landers earthquake, *J. Geophys. Res.*, *104*(B6), 13,083–13,099.

Ji, C., D. J. Wald, and D. V. Helmberger (2002), Source description of the 1999 Hector Mine, California, earthquake, Part I: Wavelet domain inversion theory and resolution analysis, *Bull. Seismol. Soc. Am.*, *92*, 1192–1207.

Kikuchi, M., and H. Kanamori (1991), Inversion of complex body waves - III, *Bull. Seismol. Soc. Am.*, *81*, 2335–2350.

Konstantinou, K. I., N. S. Melis, S.-J. Lee, C. P. Evangelidis, and K. Boukouras (2009), Rupture process and aftershocks relocation of

the 8 June 2008 Mw 6.4 earthquake in northwest Peloponnese, Western Greece, *Bull. Seismol. Soc. Am.*, *99*, 3374–3389.

Koukouvelas, I. K., S. Kokkalas, and P. Xypolias (2009), Surface deformation during the Mw 6.4 (8 June 2008) Movri Mountain earthquake in the Peloponnese, and its implications for the seismotectonics of western Greece, *Int. Geol. Rev.*, *52*, 249–268.

Lavallée, D., and R. J. Archuleta (2003), Stochastic modeling of slip spatial complexities for the 1979 Imperial Valley, California, earthquake, *Geophys. Res. Lett.*, *30*(5), 1245, doi:10.1029/2002GL015839.

Lavallée, D., P. Liu, and R. J. Archuleta (2006), Stochastic model of heterogeneity in earthquake slip spatial distributions, *Geophys. J. Int.*, *165*, 622–640.

Liu, P., S. Custódio, and R. J. Archuleta (2006), Kinematic Inversion of the 2004 M 6.0 Parkfield earthquake including an approximation to site effects, *Bull. Seismol. Soc. Am.*, *96*, S143–S158.

Mai, M. (2009), Ground motion: Complexity and scaling in the near field of earthquake ruptures, in *Encyclopedia of Complexity and Systems Science*, edited by W. H. K. Lee and R. Meyers, pp. 4435–4474, Springer, New York.

Mai, P. M., and G. C. Beroza (2000), Source-scaling properties from finite-fault rupture models, *Bull. Seismol. Soc. Am.*, *90*, 604–615.

Mai, P. M., and G. C. Beroza (2002), A spatial random-field model to characterize complexity in earthquake slip, *J. Geophys. Res.*, *107*(B11), 2308, doi:10.1029/2001JB000588.

Mai, P., J. Burjánek, B. Delouis, G. Festa, C. Francois-Holden, D. Monelli, T. Uchide, and J. Zahradník (2007), Earthquake source inversion blindtest: Initial results and further developments, *Eos Trans. AGU*, *88*(52), Fall Meet. Suppl., Abstract S53C-08.

Monelli, D., and P. M. Mai (2008), Bayesian inference of kinematic earthquake rupture parameters through fitting of strong motion data, *Geophys. J. Int.*, *173*, 220–232.

Menke, W. (1985), Imaging fault slip using teleseismic waveforms: analysis of a typical incomplete tomography problem, *Geophys. J. R. Astron. Soc.*, *81*, 197–204.

Page, M. T., S. Custódio, R. J. Archuleta, and J. M. Carlson (2009), Constraining earthquake source inversions with GPS data: 1. Resolution-based removal of artifacts, *J. Geophys. Res.*, *114*, B01314, doi:10.1029/2007JB005449.

Papadopoulos, G. A., V. Karastathis, M. Charalambakis, and A. Fokaefs (2009), A storm of strong earthquakes in Greece during 2008, *Eos Trans. AGU*, *90*, 425–426.

Piatanesi, A., A. Cirella, P. Spudich, and M. Cocco (2007), A global search inversion for earthquake kinematic rupture history: application to the 2000 western Tottori, Japan earthquake, *J. Geophys. Res.*, *112*, B07314, doi:10.1029/2006JB004821.

Press, W. H., B. P. Flannery, S. A. Teukolsky, and W. T. Vetterling (1992), *Numerical Recipes in Fortran, The Art of Scientific Computing*, 2nd ed., Cambridge Univ. Press, New York.

Pulido, N., A. Ojeda, K. Atakan, and T. Kubo (2004), Strong ground motion estimation in the Sea of Marmara region (Turkey) based on a scenario earthquake, *Tectonophysics*, *391*, 357–374.

Ripperger, J., P. M. Mai, and J.-P. Ampuero (2008), Variability of near-field ground motion from dynamic earthquake rupture simulations, *Bull. Seismol. Soc. Am.*, *98*, 1207–1128.

Roumelioti, Z., C. Benetatos, and A. Kiratzi (2009), The 14 February 2008 earthquake (M6.7) sequence offshore south Peloponnese (Greece): Source models of the three strongest events, *Tectonophysics*, *471*, 272–284.

Ruff, L. J. (1984), Tomographic imaging of the earthquake rupture process, *Geophys. Res. Lett.*, *11*, 629–632.

Semmane, F., F. Cotton, and M. Campillo (2005), The 2000 Tottori earthquake: A shallow earthquake with no surface rupture and slip properties controlled by depth, *J. Geophys. Res.*, *110*, B03306, doi:10.1029/2004JB003194.

Sokos, E., and J. Zahradník (2008), ISOLA A Fortran code and a Matlab GUI to perform multiple-point source inversion of seismic data, *Comput. Geosci.*, *34*, 967–977.

Somerville, P., K. Irikura, R. Graves, S. Sawada, D. Wald, N. Abrahamson, Y. Iwasaki, T. Kagawa, N. Smith, and A. Kowada (1999), Characterizing crustal earthquake slip models for the prediction of strong ground motion, *Seismol. Res. Lett.*, *70*, 59–80.

Spudich, P., and L. N. Frazer (1984), Use of ray theory to calculate high frequency radiation from earthquake sources having spatially variable rupture velocity and stress drop, *Bull. Seismol. Soc. Am.*, *74*, 2061–2082.

Tarantola, A. (1987), *Inverse Problem Theory: Methods for Data Fitting and Model Parameter Estimation*, Elsevier Sci., New York.

Tselentis, G.-A., L. Danciu, and E. Sokos (2010), Probabilistic seismic hazard assessment in Greece. Part II: Acceleration response spectra and elastic input energy spectra, *Nat. Hazards Earth Syst. Sci.*, *10*, 41–49.

Wald, D. J., V. Quitoriano, T. H. Heaton, H. Kanamori, C. W. Scrivner, and C. B. Worden (1999), TriNet shakemaps: Rapid generation of instrumental ground motion and intensity maps for earthquakes in southern California, *Earthq. Spectra*, *15*, 537–555.

Wang, H., H. Igel, F. Gallovič, A. Cochard, and M. Ewald (2008), Source-related variations of ground motions in 3-D media: A pplication to the Newport-Inglewood fault, Los Angeles basin, *Geophys. J. Int.*, *175*, 202–214.

Zahradník, J., and A. Plešinger (2005), Long-period pulses in broadband records of near earthquakes, *Bull. Seismol. Soc. Am.*, *95*, 1928–1939.

Zahradník, J., and A. Plešinger (2010), Toward understanding subtle instrumentation effects associated with weak seismic events in the near field, *Bull. Seismol. Soc. Am.*, *100*.

Zahradník, J., F. Gallovič, E. Sokos, A. Serpetsidaki, and G.-A. Tselentis (2008a), Quick fault-plane identification by a geometrical method: application to the Mw6.2 Leonidio earthquake, January 6, 2008, Greece, *Seismol. Res. Lett.*, *79*, 653–662.

Zahradník, J., J. Janský, and V. Plicka (2008b), Detailed waveform inversion for moment tensors of M 4 events: Examples from the Corinth Gulf, Greece, *Bull. Seismol. Soc. Am.*, *98*, 2756–2771.

F. Gallovič and J. Zahradník, Department of Geophysics, Faculty of Mathematics and Physics, Charles University, V Holešovičkách 2, Prague 8, 180 00, Czech Republic. (jz@karel.troja.mff.cuni.cz)

[P10]

Bulletin of the Seismological Society of America, Vol. 101, No. 3, pp. 1136–1151, June 2011, doi: 10.1785/0120100231

Ground-Motion Simulations for the 1980 *M* 6.9 Irpinia Earthquake (Southern Italy) and Scenario Events

by Gabriele Ameri, Antonio Emolo, Francesca Pacor, and František Gallovič*

Abstract In this paper, we adopt three ground-motion simulation techniques (the stochastic finite-fault simulation code from Motazedian and Atkinson, 2005; the hybrid deterministic-stochastic approach with approximated Green's functions from Pacor *et al.*, 2005; and the broadband hybrid integral-composite technique with full-wavefield Green's functions from Gallovič and Brokešová, 2007), with the aim of investigating the different performances in near-fault strong-motion modeling and prediction from past and future events. The test case is the 1980 *M* 6.9 Irpinia earthquake, the strongest event recorded in Italy in the last 30 years. First, we simulate the recorded strong-motion data and validate the model parameters by computing spectral acceleration and peak amplitude residual distributions. The validated model is then used to investigate the influence of site effects and to compute synthetic ground motions around the fault. Afterward, we simulate the expected ground motions from scenario events on the Irpinia fault, varying the hypocenters, the rupture velocities, and the slip distributions. We compare the median ground motions and related standard deviations from all scenario events with empirical ground-motion prediction equations (GMPEs). The synthetic median values are included in the median $\pm$ 1 standard deviation of the considered GMPEs. Synthetic peak ground accelerations show median values smaller and with a faster decay with distance than the empirical ones. The synthetics total standard deviation is of the same order or smaller than the empirical one, and it shows considerable differences from one simulation technique to another. We decomposed the total standard deviation into its between-scenario and within-scenario components. The larger contribution to the total sigma comes from the latter, while the former is found to be smaller and in good agreement with empirical interevent variability.

Online Material: Comparison of observed and simulated waveforms and spectra.

Introduction

One of the key steps of a seismic hazard assessment study is the prediction of ground-motion parameters, assuming the occurrence of specific earthquakes. This goal may be easily pursued using ground-motion prediction equations (GMPEs) that provide the probability distribution of earthquake ground motion at a given site as a function of, for example, magnitude, distance, site condition, and fault mechanism (Ambraseys *et al.*, 2005; Boore and Atkinson 2008; Bindi *et al.*, 2009; Akkar and Bommer, 2010; among many others). Although they are retrieved through the analysis of recorded strong-motion data, the GMPEs account only for the average characteristics of the earthquake source and wave-propagation processes. In general, at distances comparable with the fault dimensions, the complexity and heterogeneity of the source rupture process may strongly influence the ground motion, especially in the case of moderate-to-large earthquakes (Archuleta and Hartzell, 1981; Heaton, 1990). This feature is crudely accounted for by GMPEs, due to the simplistic source parameterization adopted in the functional forms, and to the paucity of strong-motion data recorded at near-source distances for large magnitudes. This is the case in Italy, where only a few strong-motion data recorded in the proximity of the rupturing fault are available, even in the case of moderate-to-large instrumental earthquakes (Luzi *et al.*, 2008; also see the Data and Resources section for information about the Italian Accelerometric Archive).

An alternative approach to predict earthquake ground motions is represented by the simulation of synthetic accelerograms through either purely stochastic or hybrid

*Also at Dipartimento di Scienze Fisiche, Università degli Studi "Federico II", Napoli, Italy.

deterministic-stochastic methods. These methods are able to generate realistic seismograms in the frequency band of engineering concern, close to the causative fault (e.g., Zollo *et al.*, 1997; Mai and Beroza, 2003; Motazedian and Atkinson, 2005; Pacor *et al.*, 2005; Gallovič and Brokešová, 2007;) and can be used to perform earthquake scenarios studies (Aagaard *et al.*, 2008; Ameri *et al.*, 2008; Cultrera *et al.*, 2010). However, these methods are generally considered as advanced tools in hazard assessment framework, because compared with GMPEs, they require a larger number of seismological data about the earthquake source and the propagation medium, which are often uncertain.

The most widely used simulation techniques are based on a kinematic model of the extended source and require the specification of parameters describing the rupture evolution (slip function, rupture velocity, nucleation point position, etc.). These parameters have to be sought when one is interested in reproducing strong-motion records associated with an occurred earthquake (Mena *et al.*, 2006; Ameri *et al.*, 2009). On the contrary, when seismic hazard studies and earthquake scenarios are carried out, the parameters describing the rupture evolution need to be varied in order to produce a large number of scenario events. This approach is supported by the fact that it is not possible to predict which rupture scenario will occur on a seismogenic fault. In this way, various possible rupture processes, occurring on the same fault, are simulated and for each of them, synthetic seismograms are computed. The required strong-motion parameters at the site of interest are then expressed through a statistical analysis of the simulated seismograms (Convertito *et al.*, 2006; Emolo *et al.*, 2008; Cultrera *et al.*, 2010; Chiauzzi *et al.*, 2010), and the associated variability may be studied and quantified (Ripperger *et al.*, 2008).

The approximations introduced in the numerical representation of the rupture and wave-propagation processes entail, however, that the ground motion simulated at a given site by different techniques is generally different in some features (e.g., signal duration, peak values in specific frequency ranges, etc.). As a consequence, some techniques are not able to reproduce specific ground-motion characteristics as, for example, directivity pulses or polarization of ground motion.

Furthermore, synthetic seismograms should be validated in some way, in order to demonstrate the reliability of the ground-motion estimates. Some examples can be found in Convertito *et al.* (2006), Sørensen *et al.* (2007), Gallovič and Burjánek (2007), Gallovič and Brokešová (2007), Ansal *et al.* (2008), Ameri *et al.* (2008), Emolo *et al.* (2008), Cultrera *et al.* (2009), and Graves and Pitarka (2010).

In this paper, we apply three finite-fault simulation techniques to reproduce the ground motion during the 1980 *M* 6.9 Irpinia (southern Italy) earthquake and generate scenario events. The aim is to investigate the different performances of the simulation techniques in near-fault strong-motion modeling and prediction from past and future events. First, we synthesize accelerometric records at some of the near-fault sites that recorded the Irpinia earthquake and evaluate the capability of the simulation methods to reproduce the main features (amplitude and frequency content) of observed strong-motion data. Then we compute synthetic accelerograms at a dense grid of virtual observers, simulating a large number of possible scenario events. We produce, for each simulation technique, synthetic data sets that we treat statistically in order to evaluate the median ground motion and the associated variability. In particular, similar to what is done in the framework of the GMPEs (e.g., Atik *et al.*, 2010), we separate the total variability in the interscenario (between-scenario) and intrascenario (within-scenario) components. The interscenario component measures the variability among the average ground motions predicted by all scenario events, and the intrascenario variability measures the variability of the ground motion with respect to the average motion predicted for each earthquake scenario.

Simulation Methods

In this work we use three well-known simulation methods: the stochastic finite-fault simulation code (EXSIM, Motazedian and Atkinson, 2005; Boore, 2009), the hybrid deterministic-stochastic approach with approximated Green's functions (DSM, Pacor *et al.*, 2005), and the broadband hybrid integral-composite technique with full-wavefield Green's functions (HIC, Gallovič and Brokešová, 2007). Table 1 summarizes the main characteristics of each technique in terms of source and path parameters; Table 2 reports the input modeling parameters later described. Here, we recall some key elements about the source representation for each technique and refer, for further explanation, to the previously mentioned reference papers.

The EXSIM and DSM techniques are both an extension of the point-source stochastic method (Boore, 1983, 2003) to include the rupture propagation along an extended fault. The kinematic rupture model is simply described assigning the slip distribution, the rupture velocity, and the nucleation point on the fault. In EXSIM, the fault is divided into N subfaults; each of them is considered as a point source, emitting an ω-square spectrum. Ground motions produced by subfaults are summed in the time domain, with a proper time delay, to obtain the ground motion from the entire fault. The DSM generates acceleration envelopes using the isochrone theory (Bernard and Madariaga, 1984; Spudich and Frazer, 1984). For a given site, each instant of time of the envelope is constructed by summing the contributions to ground motion from the corresponding isochrone on the fault. The spectral content of the synthetic seismogram is then defined through a reference spectrum. This spectrum corresponds to an ω-square model, with fixed corner frequency (hereafter referred to as $\mathrm{DSM_{fix}}$) or with apparent corner frequency (hereafter referred to as $\mathrm{DSM_{app}}$), given by the inverse of the envelope duration, different from site to site. In this latter case the directivity-induced amplification effect on the ground motion related to the rupture

Table 1
Source and Wave-Propagation Processes as Modeled in the Considered Simulation Methods

Method	Source	Path
EXSIM (Motazedian and Atkinson, 2005; Boore, 2009)	The fault is divided into N subfaults; each of them is considered as a point source radiating an ω^2 spectrum. Ground motions produced by subfaults are summed in the time domain, with a proper time delay, depending on the rupture time distribution, to obtain the ground motion from the entire fault. The slip distribution and a constant rupture velocity can be specified.	Stochastic Green's functions: homogenous medium (V_S is specified at the source). Spectral attenuation is defined by geometrical spreading + quality factor + kappa. Frequency-dependent crustal amplification function, to account for wave amplification through the layered model. Distance-dependent duration of seismograms.
DSM (Pacor *et al.*, 2005; Ameri *et al.*, 2009)	An acceleration envelope is computed by the isochrone theory at any given site: the duration is defined by rupture propagation + crustal propagation. The envelope amplitude is modulated for the slip distributions on the fault. The deterministic envelope is then used to window a white noise time series and multiplied by an ω^2 reference spectrum. The finite-fault characteristics such as distance, radiation pattern and corner frequency (either apparent or fixed) are parameters of the spectrum.	Semistochastic Green's functions: Deterministic envelopes (duration and shape) defined through isochrones for a 1D layered medium. Spectral attenuation is defined by geometrical spreading + quality factor + kappa. Frequency-dependent crustal amplification function, to account for wave amplification through the layered model.
HIC (Gallovič and Brokešová, 2007)	The rupture process at the seismic source is described in terms of slipping of elementary subsources with fractal number-size distribution (fractal dimension 2), randomly placed on the fault plane. At low frequencies: based on the representation theorem assuming a final slip distribution composed from the subsources, which is characterized by a k-squared decay. At high frequency, instead, the ground-motion synthesis is obtained summing the contributions from each individual subsource treated as a point source. Low- and high-frequency synthetics are combined in the frequency domain.	Full-wavefield Green's functions by DWN technique. Spectral attenuation is defined by quality factor + kappa

Table 2
Parameters Used in the Simulation of the Irpinia 0 s and of the Scenario Events*

Parameter	Irpinia Earthquake (0 s event)	Method
Fault mechanism†	Strike: 315°, dip: 60°, rake: −90°	1,2,3
Fault dimensions	Length 35 km, width 15 km	1,2,3
Fault top depth	2.2 km	1,2,3
Focal depth	10.9 km	1,2,3
Seismic moment	2×10^{19} N m	1,2,3
Shear-wave velocity, V_S	3.2 km/s	1,2
Density, ρ	2.9 g/cm^3	1,2
Radiation pattern	0.55	1,2
Number of subfaults	Along strike 70; along dip 30	1,2,3
Slip distribution‡	#1	1,2,3
Nucleation point‡ (position from southeast edge)	Down-dip 10 km; along strike 5 km	1,2,3
Rupture velocity (V_r)‡	$0.8V_S$	1,2,3
Stress parameter ($\Delta\sigma$)‡	80 bars	1,2
k	0.03 s	1,2,3
Quality factor	100	1,2
Geometrical spreading	$1/R$	1,2
Distance-dependence duration§	$T_0 + 0.05R$ ($R > 10$ km)	1
Crossover frequency	0.5–2.0 Hz	3
Number of simulations	40	1,2

*The parameter required by each method is specified in the Method column (1, EXSIM; 2, DSM; 3, HIC).
†In the HIC method, random variations within ±30° from the adopted values are prescribed for the high-frequency subsources.
‡These parameters are changed in the scenario-events simulations; see the main text for details.
§Where T_0 is the subfault source duration defined as $1/f_{0sf}$ (f_{0sf} is the subfault corner frequency).

propagation along the extended fault is included in the ω-square spectrum by the apparent corner frequency.

The HIC technique simulates the rupture process in terms of slipping of elementary subsources with fractal number-size distribution (fractal dimension 2), randomly placed on the fault plane (Zeng *et al.*, 1994). At low frequencies, the source description is based on the representation theorem (integral approach, Aki and Richards, 2002), assuming a final slip distribution composed from the subsources, which is characterized by a k-squared decay (Herrero and Bernard, 1994; Gallovič and Brokešová, 2004). At high frequency, instead, the ground-motion synthesis is obtained summing the contributions from each individual subsource treated as a point source (composite approach). The Green's functions for both frequency bands are evaluated by the discrete wavenumber technique (Bouchon, 1981) in a layered 1D medium.

The 23 November 1980 *M* 6.9 Irpinia Earthquake

The Irpinia earthquake (southern Italy) is the largest event recorded by strong-motion instruments in Italy. The earthquake was widely studied and a complete review was published in a special issue of *Annals of Geophysics* (vol. 36, n. 1, 1993). It was a normal-faulting complex event that involved at least three distinct shocks starting in a time span of approximately 40 s (Fig. 1): the main event (further referred to as the 0 s event) was followed by two further rupture episodes delayed about 20 s and 40 s, respectively (Bernard and Zollo, 1989; Pantosti and Valensise, 1990). The characteristics of the 0 s event have been deeply investigated (Cocco and Pacor, 1993; Giardini, 1993; Pingue *et al.*, 1993); this shock was related to the rupture of a normal fault striking in the Apennine direction and dipping 60° toward the northeast (Table 2).

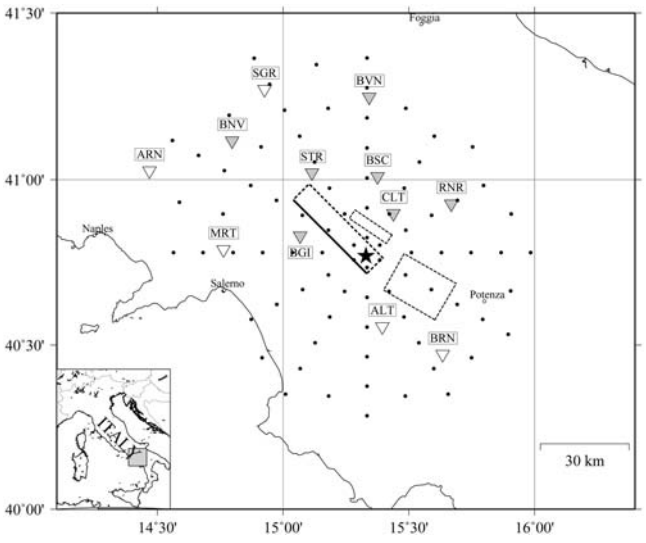

Figure 1. Geometry of the three fault segments whose rupture caused the 1980 Irpinia earthquake. The epicenter of the 0 s fault segment is shown by the black star; the fault top is shown by the thick black line. The 10 stations belonging to the Italian strong-motion network within 60 km of the epicenter are represented as triangles (see Table 1 for the station code). Filled triangles highlight the 7 stations that have been used in the strong-motion modeling performed in this study. Black dots indicate the 86 virtual receivers used in the scenario-events simulations. The virtual receivers are within 50 km of the fault surface projection.

The earthquake triggered 21 analog accelerometric stations, 10 of them at epicentral distances within 60 km (Fig. 1). The near-fault strong-motion records are characterized by a very long duration, about 80 s, and the three events can be clearly detected with the exception of the southernmost stations, BRN and ALT, which were likely triggered by the 20 s event. The recording stations in the epicentral area are classified mostly as rock and stiff sites. All information related to their geological and geotechnical characteristics are taken from the corresponding monographs recently published in the Italian strong-motion database (ITACA; see the Data and Resources section).

We selected seven near-fault stations that clearly recorded the 0 s event and are weakly affected by site effects (Table 3). The maximum peak ground acceleration (PGA) and peak ground velocity (PGV) values (3.01 m/s^2 and 0.70 m/s, respectively) were recorded at STR on the east–west component. These high peak ground motions may be ascribed to directivity effects related to the position of the site with respect to the direction of the rupture propagation on the 0 s fault (Cultrera *et al.*, 2010).

A rough estimation of the frequency content of the records may be inferred by the PGA/PGV ratio (Kwon and Elnashai, 2006), which is equal to $0.58 \pm 0.11\ g/\mathrm{ms}^{-1}$, considering the mean ratio for data in Table 3. Following the classification by Zhu *et al.* (1988) and Kwon and Elnashai (2006), the 1980 Irpinia near-fault ground motions can be classified as high velocity–low acceleration (HV–LA) records. Low PGA/PGV ratios signify earthquakes with low predominant frequencies, broader response spectra, and longer duration (Kwon and Elnashai, 2006). Other earthquakes in different tectonic environments (e.g., the M_w 7.4 1999 Chi-Chi earthquake) show similar HV–LA behavior.

Source and Propagation Models

In this work we used the fault geometry and 1D crustal model (Tables 2 and 4) as described by Cultrera *et al.* (2010), that simulated seismic scenarios from different rupture models of the 0 s fault, in order to study the source-related variability of low-frequency ground motions. The kinematic rupture model considered for the 0 s fault is based on the study of Cocco and Pacor (1993): the final slip distribution is characterized by two main asperities, the largest located close to the southern edge of the fault and the other located close to the northern edge, both at a depth between 6.5 and 11 km. Starting from the slip and rupture time distributions originally proposed by the authors, we calculated a k^{-2} slip model (Herrero and Bernard, 1994; Gallovič and Brokešová, 2004) shown in Figure 2a. The position of the nucleation

Table 3
Selected Accelerometric Stations and Relative Ground-Motion Parameters Recorded

Station	Code	R_{epi}* (km)	R_{JB}† (km)	$PGA_{max\,H}$ (m/s^2)	$PGV_{max\,H}$ (m/s)	PGA/PGV (g/ms^{-1})	EC8 class‡
Bagnoli	BGI	22	7	1.83	0.35	0.54	B
Benevento	BNV	58	28	0.58	0.09	0.64	B
Bisaccia	BSC	28	18	0.95	0.22	0.45	A
Bovino	BVN	54	35	0.47	0.06	0.75	B
Calitri	CLT	19	13	1.72	0.29	0.59	B
Rionero	RNR	36	29	0.97	0.15	0.66	B
Sturno	STR	33	4	3.10	0.70	0.45	B

*Calculated from the 1980 Irpinia earthquake epicenter (41.76° N, 15.31° E).

†The R_{JB} is the distance from the surface projection of the fault as introduced by Joyner and Boore (1981). The R_{JB} distance has been computed with respect to the 0 s fault.

‡The sites were classified according to the Eurocode 8 (CEN, Comité Européen de Normalisation, 2004) and the Italian Building Code (NTC08, Norme Tecniche per le Costruzioni, 2008), based on the shear-wave velocity averaged over the top 30 m of the soil profile (V_{S30}). The EC8 classes are the following: class A, $V_{S30} > 800$ m/s; class B, $V_{S30} = 360$–800 m/s; class C, $V_{S30} = 180$–360 m/s; class D, $V_{S30} < 180$ m/s; class E, 5 to 20 m of C- or D-type alluvium underlain by stiffer material with $V_S > 800$ m/s.

point (largest star in Fig. 2a) corresponds to the instrumental epicenter (40.76° N, 15.31° E); the rupture velocity was set at $0.8V_S$, where V_S is the shear-wave velocity (see Table 4).

The spectral attenuation was defined in terms of quality factor Q and high-frequency decay parameter κ (Anderson and Hough, 1984). The depth-dependent Q_p and Q_s values used for HIC simulations are reported in Table 4. In DSM and EXSIM, a $Q_S = 100$ was adopted in order to obtain results comparable with HIC simulations and as reported by Cultrera *et al.* (2010). We set $\kappa = 0.03$ s, according to literature estimates for rock and stiff sites (Margaris and Boore, 1998; Bindi *et al.*, 2004).

A crustal amplification function has been used in EXSIM and DSM simulation techniques to account for frequency-dependent amplification of seismic waves through the *S*-waves velocity profile of the crustal model (Boore and Joyner, 1997). For the Irpinia area, we adopted an amplification function for hard-rock sites (Siddiqqi and Atkinson, 2002; Atkinson and Boore, 2006), characterized by a shear-wave velocity near the surface of about 2000 m/s (class A according to the National Earthquake Hazards Reduction Program, 1994), which is comparable to the velocity we used (Table 4).

The value of the stress parameter $\Delta\sigma$ has been set to 80 bars on the basis of a trial-and-error analysis performed through the comparison of observed and synthetic high-frequency level of the Fourier amplitude spectra (S3 Project Deliverable D0, 2007).

The input parameters for the three techniques adopted to simulate the 0 s events are summarized in Table 2.

Modeling of the Strong-Motion Data

We calculated the synthetic seismograms at the selected stations using the three simulation techniques and adopting the source and propagation models described previously (Tables 2 and 4). The comparisons with the recorded data, in terms of acceleration and velocity waveforms (north–south and east–west components) and spectral acceleration (SA) in the frequency band 0.1–12 Hz, are reported in Ⓔ Figures S1 to S6 in the electronic supplement to this paper. Here, for example, we show the results for the HIC technique (Fig. 3). The HIC synthetics are the most suitable to discuss the goodness of the adopted rupture and propagation models because this approach adopts complete Green's functions and solves deterministically the representation theorem at low frequencies.

For most of the sites, the simulated time series are in good agreement with the recorded ones, both in time and frequency domains. The good fit for BGI station, located just a few kilometers from the fault, supports the reliability of the

Table 4
Velocity Model Used in This Simulation Study*

Depth (km)	V_P (km/s)	$V_S = v_P/1.81$ (km/s)	Density (g/cm^3)	Q_P	Q_S
0	3.5	1.93	2.3	200	100
2	4.5	2.49	2.5	300	150
4	5.7	3.15	2.6	500	200
10	6.5	3.59	2.7	750	250
25	7.5	4.14	2.9	900	300
35	8.1	4.48	3.2	1200	400

*This model is based on data from L. Improta (personal commun., 2007), and also loosely based on data from Amato and Selvaggi (1993) and Improta *et al.* (2003).

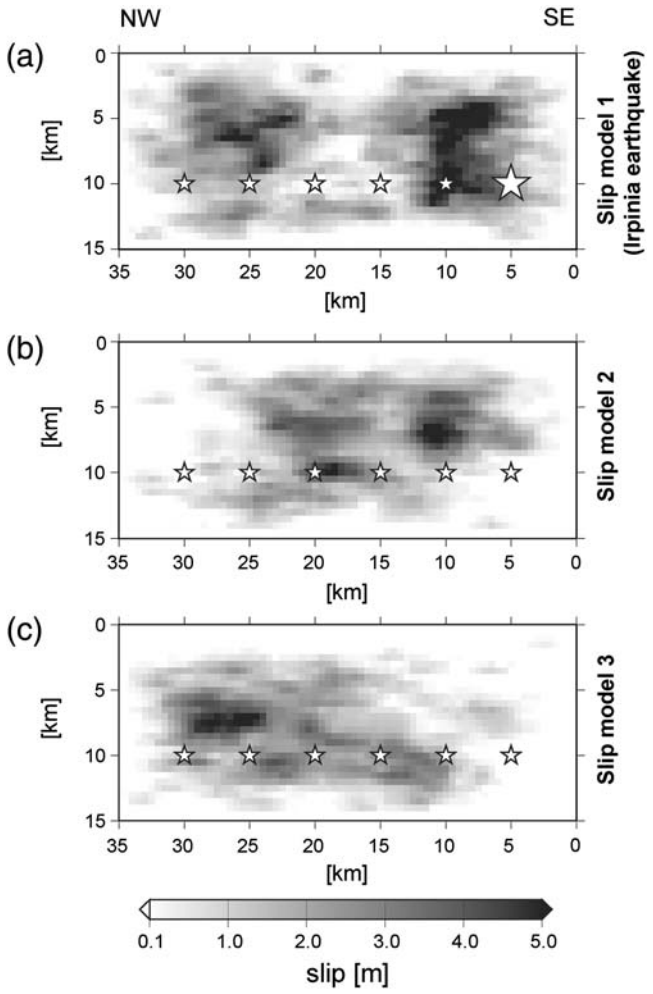

Figure 2. *K*-squared slip distributions and hypocenter locations (white stars) used in the simulations. Slip model in the top panel mimic the one inferred by Cocco and Pacor (1993), characterized by two main asperities, the largest located close to the southern edge of the fault and the other to the northern edge. This slip is used to model the Irpinia 1980 earthquake ground motions. The largest star represents instrumental hypocenter (40.76° N, 15.31° E). The fault plane is discretized into 70×30 subfaults.

adopted rupture model. Also the waveforms at the farthest stations, BVN and BNV, located about 30 km from the fault, are well simulated, indicating that the 1D propagation model accounts for the main observed phases. BSC synthetics spectra well reproduce the observed ones at frequencies larger than 1 Hz. The misfit at lower frequencies (around 0.5 Hz) is likely due to the velocity inversion in the soil profile below the station (Olivares and Silvestri, 2001; Cultrera *et al.*, 2010), not accounted for in the simulations.

A worse fit is obtained for CLT, RNR, and STR, where the observed ground motion is underestimated. Indeed, at CLT, the HIC synthetics are not able to simulate the large amplitude of the later arrivals, while at RNR the waveforms are deficient of high-frequency energy. Finally at STR, less than 5 km from the fault, we are only able to fit the first large phases of the north–south component. The lower ground-motion amplitude simulated in the east–west direction can be ascribed to the effect of the radiation pattern. This is not observed in the records, likely due to the small-scale variations of the source mechanism, not included in the model.

Regarding the other two simulation techniques (Ⓔ Figures S2, S3, S5 and S6, available as an electronic supplement to this paper), the use of simplified Green's functions does not allow us to reproduce correctly the phases of the observed seismograms. The spectral content and peak amplitudes are well reproduced at BGI and BSC and, similar to HIC, they are underestimated at RNR, CLT, and STR.

To summarize the modeling results and to assess the performance of the simulation techniques, we computed the SA, PGA, and PGV residuals ($\log_{10}$[observed/simulated]) at each station. Spectral acceleration residuals at each frequency are then averaged over the seven stations, yielding a measure of the model bias (Fig. 4). In general, the simulations provide small model biases, with a tendency to positive values (i.e., average underestimation) over the entire frequency range. This result is expected because the synthetics are simulated at bedrock, while the recording sites, although located on stiff soils, are characterized by variable local geology. Nevertheless, the models' biases do not exceed 0.25, which means an average underestimation of less than a factor of 2. HIC residuals are less scattered at low frequencies (< 1 Hz), while EXSIM and DSM have a similar σ_{bias} (i.e., similar scatter of the residuals), with a tendency to lower sigma in the intermediate frequency range ($\sigma_{\text{bias}} \approx 0.15$) and higher values at both low and high frequencies ($\sigma_{\text{bias}} \approx 0.25$). The positive and negative residuals outside the standard deviation are related to RNR, CLT, and STR sites, as already noted in Figure 3.

Possible site amplification at these stations are evaluated computing the horizontal-to-vertical spectral ratios (HVSR) (Lermo and Chávez-García, 1993), using all the strong-motion data available (Fig. 5). RNR, located on volcanic rocks, shows flat HVSR, while small broadband amplifications are obtained at CLT and STR, installed on silty clays and weathered sandstone, respectively. Note that the paucity of strong-motion data at RNR (three records), together with possible amplification on the vertical component, may lead to unreliable HVSR results.

The STR and CLT HVSR mean amplification curves are used to multiply the Fourier amplitude spectra of the synthetics computed at bedrock, maintaining the phases unchanged. The geometric mean acceleration response spectra of amplified synthetic time series are shown in Figure 6. In general, the fit improves, with the exception of HIC results at CLT. In this case an overestimation of the high-frequency content ($f > 2$ Hz) is observed; further investigations may be carried out to explain the role of the site response at this station.

In conclusion, due to the relatively small number of records considered, it is difficult to establish which method performs better in the modeling of the 1980 earthquake strong-motion data. We note a general consistency among the simulation results in terms of spectral accelerations and

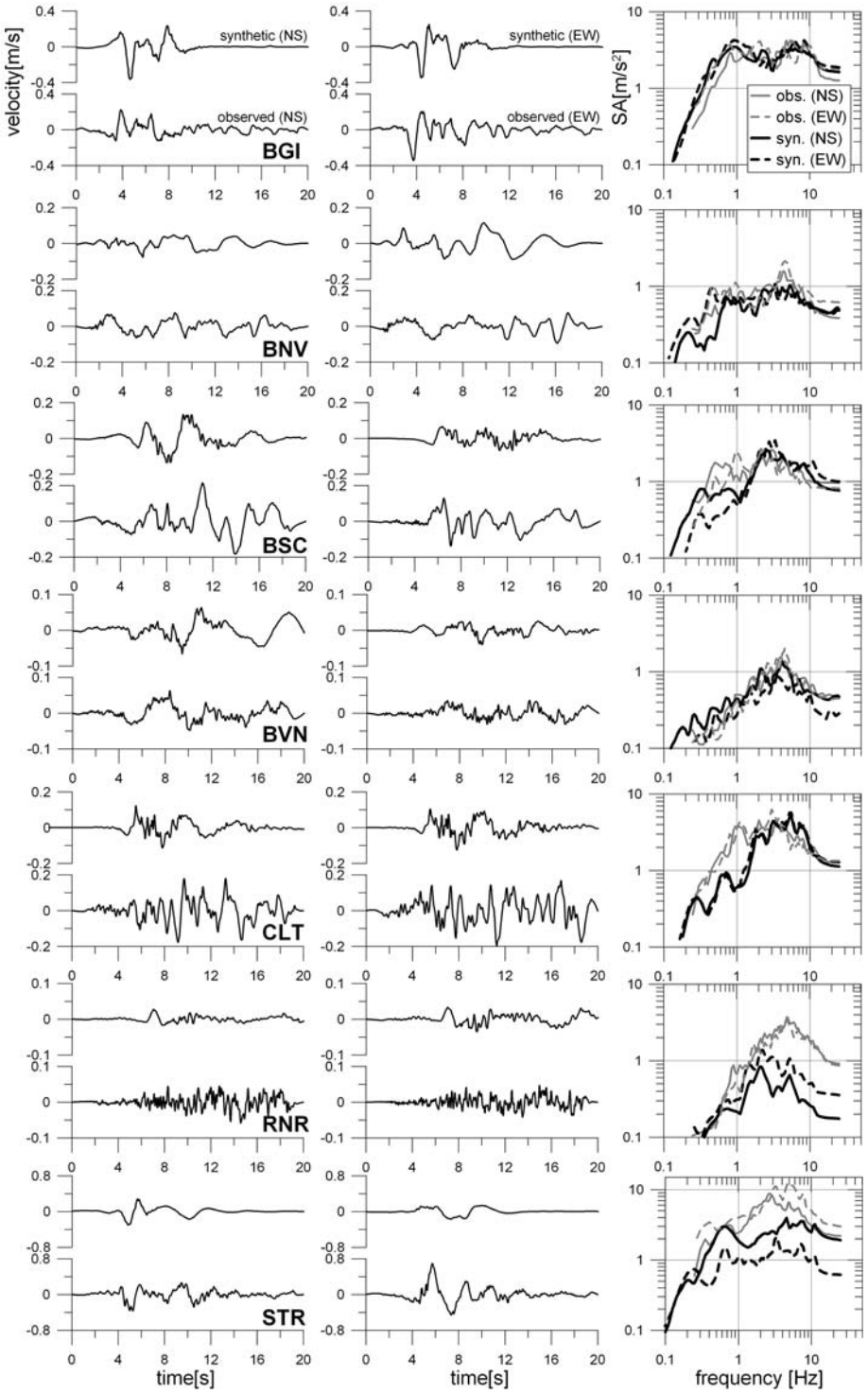

Figure 3. Comparison of north–south (NS) and east–west (EW) recorded and simulated velocity time series at the 7 selected stations (see Fig. 1) considering the HIC technique. The right panels show the comparison in terms of spectral accelerations (SA) at 5% damping. Time series have been filtered between 0.1 and 12 Hz, and the first 20 s of signal have been considered. Ⓔ See Figure S1 in the electronic supplement to this paper for a comparison of acceleration waveforms.

peak values, whereas the synthetic waveforms show notable differences in duration and phase. Moreover, the effect of local site amplification seems unimportant at the considered stations, except at RNR, where we are not able to explain the high-frequency content of the observed waveforms with the adopted source, propagation, and site parameters. Overall, the results presented in Figures 3 and 4 make us confident that the methods can be used to predict the bedrock ground motion associated to the 1980 and other scenario events for the study area.

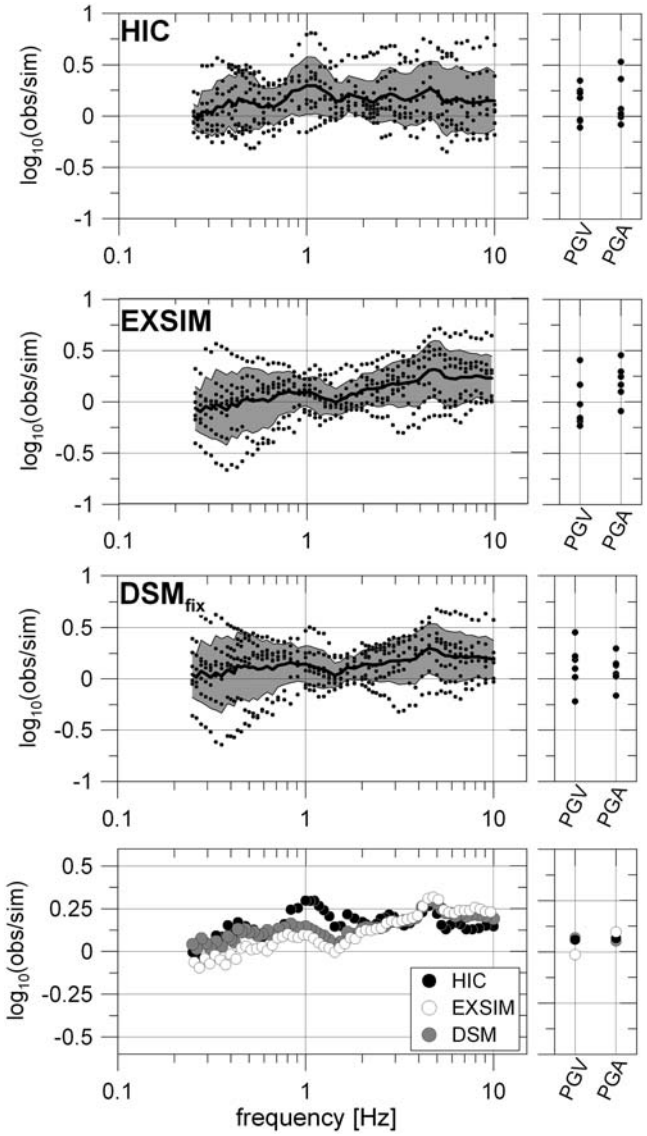

Figure 4. Spectral accelerations, PGV, and PGA residuals (black dots), defined as the $\log_{10}$(observed/simulated), considering the geometric mean of NS and EW components are shown for the three simulation techniques. Spectral acceleration residuals are computed for 17 frequencies ranging from 0.25 to 10 Hz. The model bias (black line), defined as the mean of the residuals at each frequency, and relative standard deviation (gray shaded area) are also shown. The bottom panel shows a comparison among the model biases computed with the three simulation techniques.

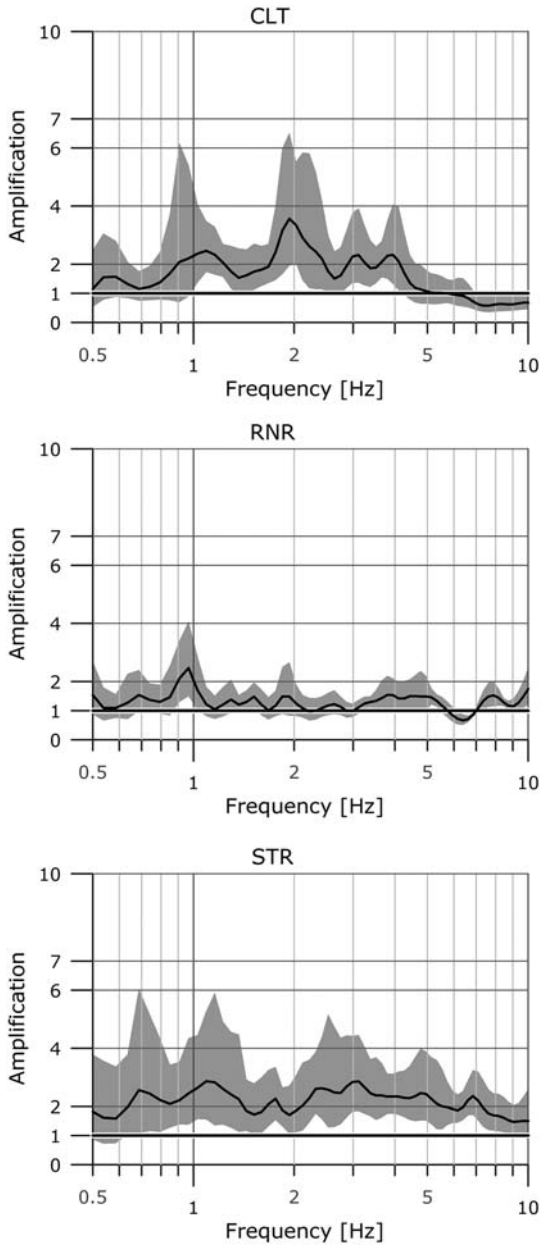

Figure 5. HVSR mean curves (black continuous lines) plus/minus one standard deviation (shaded area) computed for CLT, RNR, and STR stations using 6, 3, and 9 records, respectively. The analysis was performed on the *S*-wave windows selected starting about 1 s before the *S*-wave onset and ending when 90% of the total energy of the signal has been released, assuming that this interval corresponds to the strong-motion phase.

Ground-Motion Scenario

The validated model is used to simulate the ground motion for the 0 s event at a dense grid of 86 virtual receivers (their positions are shown in Fig. 1), in order to evaluate the spatial distribution of the ground motion predicted by the three methods. The PGA and PGV maps computed for bedrock sites are shown in Figure 7. For all the simulation techniques, the finite dimension of the fault produces contour lines slightly elongated in the fault-strike direction. Moreover, the ground motion decays more slowly in the northwestern direction, that is, in the direction toward which the rupture propagates rather than in the opposite direction.

The PGA maps simulated with DSM_{fix}, EXSIM, and HIC techniques show an almost isotropic distribution with respect to the fault projection, because similar approaches are implemented in modeling the high-frequency component of the radiation emitted by the extended source. For instance, in the HIC technique, the high-frequency content is simulated through an incoherent sum of the energy emitted by the

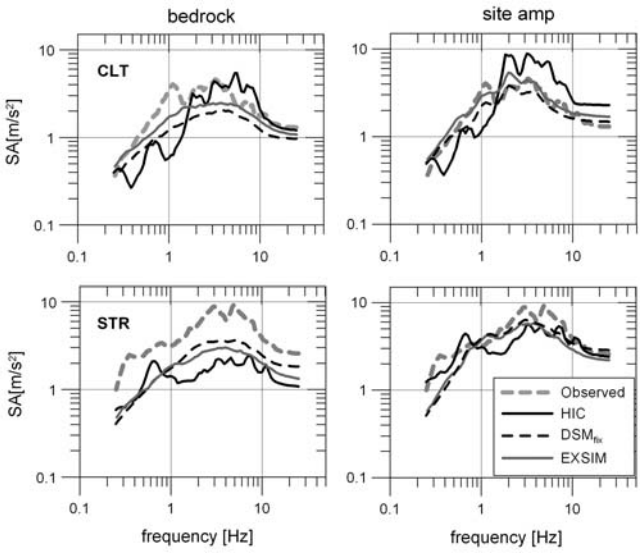

Figure 6. Comparison of simulated and observed spectral accelerations (SA, at 5% damping), geometric mean of north–south and east–west components, at CLT and STR stations. Left plots: simulations are performed at bedrock. Right plots: site amplification is accounted in the simulations by HVSR-based amplification functions (Fig. 5). DSM and EXSIM response spectra are geometric mean of the 40 realizations.

stochastic elementary subsources (composite approach), resulting rather independently from the source-to-receiver azimuth (see also Gallovič and Burjanek, 2007). On the other hand, the rupture directivity effects on the ground motion are evident in the HIC PGV map, where the area of maximum is shifted far from the epicenter and close to the BGI and STR stations. This is caused by the deterministic calculation of ground motion at low frequencies (mostly affecting the PGV), preserving the inherent directivity effect. In particular, the large PGV area in Figure 7a is due to the combined effect of the northwestern and up-dip rupture propagation, position of the second asperity (Fig. 2a), and radiation pattern.

We also showed in Figure 7d the maps generated with DSM_{app} in order to evaluate the influence of the apparent corner-frequency approach on the spatial distribution of ground motion. The peak ground motions strongly change with respect to DSM_{fix}, predicting large amplitudes close to the northwestern edge of the fault, thus modeling the effect of rupture directivity on both the simulated PGA and PGV. The difference between the DSM_{fix} and DSM_{app} predictions is due to the use of different corner frequencies in the source spectrum. In the first case, following the classical ω-square model, the corner frequency is defined as $f_c = 4.9\times 10^6 V_S(\Delta\sigma/M_0)^{1/3}$, assuming a fixed value for all sites. In the second case, the corner frequency is calculated as the inverse of the source duration as perceived at each site (i.e., the apparent corner frequency). For example, a corner frequency $f_c = 0.11$ Hz is obtained adopting $\Delta\sigma = 80$ bar. On the other hand, the apparent corner frequencies obtained at STR and CLT sites are $f_a = 0.16$ Hz and $f_a = 0.05$ Hz, respectively. Because the high-frequency plateau of the acceleration source spectrum in the ω-square model is proportional to $M_0 f_c^2$, it is clear that the two approaches can lead to very different simulated ground motions.

Although based on different approaches, DSM_{app} and HIC generate consistent PGV distributions. On the other hand, DSM_{app} generates high PGA values close to the STR station and small values at sites located in the opposite direction (e.g., RNR and CLT). Such large differences are, however, not observed in the records, suggesting that DSM_{app} might overemphasize the forward and backward directivity effects close to the fault.

To verify the reliability of the ground-motion scenario for the 0 s event, the synthetic PGA and PGV values are compared with predictions from Akkar and Bommer (2010, hereafter referred to as AkB10) GMPEs (Fig. 7, right panels).

For the three simulation techniques, the synthetic PGAs underestimate the empirical median prediction and show a stronger attenuation with distance, while the PGVs match the median values well over the considered distance range. Overall, the recorded peaks are better fitted by the synthetics both for acceleration and velocity.

The HIC PGV and DSM_{app} PGA and PGV values as a function of distance are largely scattered, and some values are outside of the AkB10 standard deviation. This scatter is caused by the concurrent presence, at similar R_{JB} distances, of receivers that experience both forward and backward directivity.

The ground-motion scenarios for the 0 s event show PGA that are, on average, smaller and decay faster with distance than the average predictions from the considered GMPE, confirming the HV–LA property observed from the Irpinia earthquake records. The average simulated PGA/PGV ratios are 0.71 ± 0.50 g/ms^{-1} for HIC, 0.49 ± 0.12 g/ms^{-1} for EXSIM, 0.60 ± 0.16 g/ms^{-1} for DSM_{fix}, and 0.57 ± 0.15 g/ms^{-1} for DSM_{app}.

Ground-Motion Prediction for M_w 6.9 Scenario Events

The next step of this study is the generation of ground-motion scenarios at bedrock, associated with a fault having the geometry, orientation, and seismic moment of the 0 s fault in order to characterize the potential variability in ground motions for future events of this size on the Irpinia fault. The variability related to the local site response is not included in this analysis.

A similar study was performed by Cultrera *et al.* (2010) using a discrete-wavenumber/finite-element technique with the aim of investigating the low-frequency parametric variability of the ground motion (up to 2 Hz) as a function of different source parameters (i.e., rupture velocity, slip distribution, nucleation point, and source time function). They showed how the distributions of spectral displacement at 2 s and of PGV depend on both azimuth and distance and how the simulated ground motion is influenced by the source parameters. In this study we extend the scenario-events

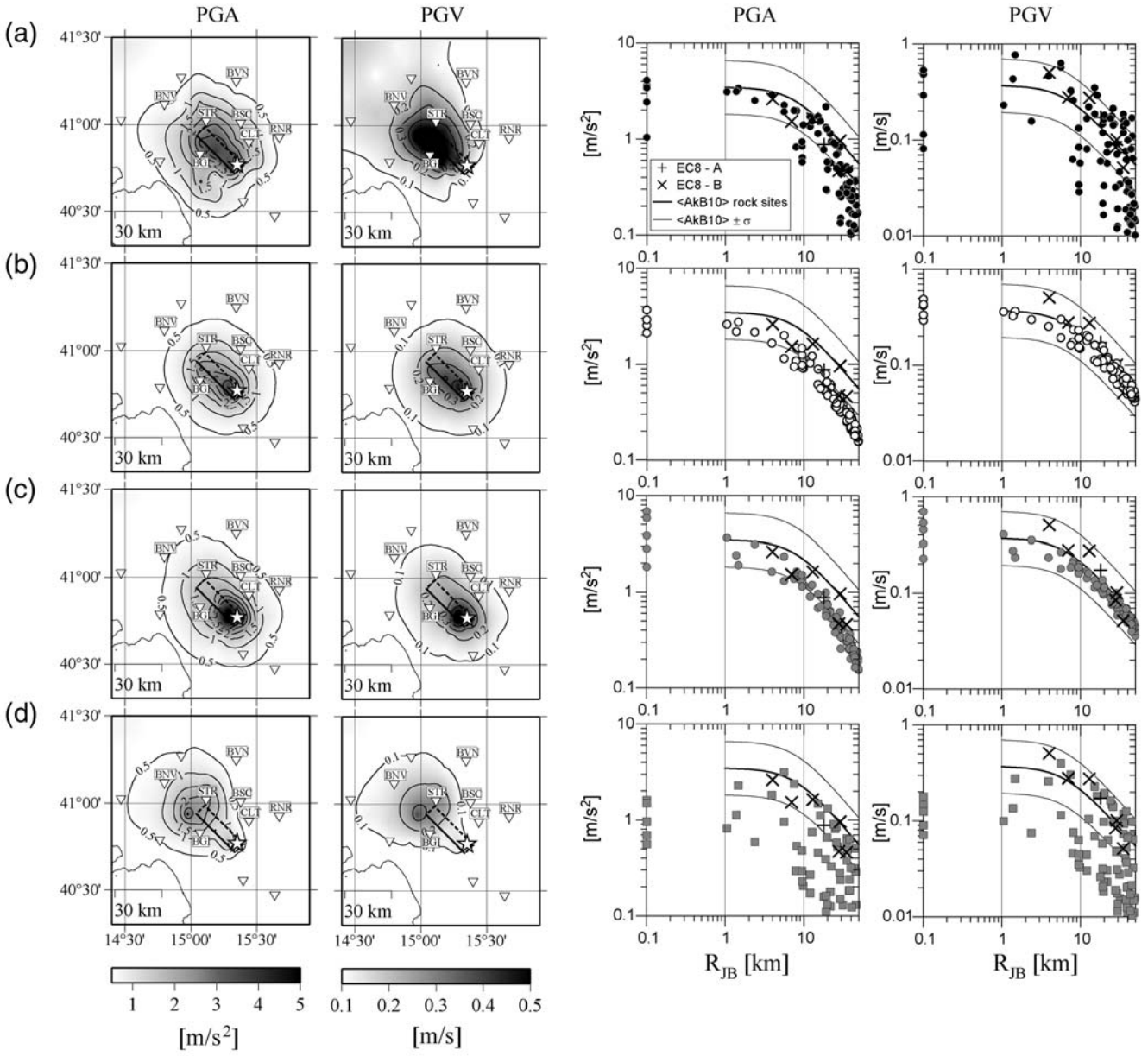

Figure 7. PGA and PGV values (geometric mean of north–south and east–west components) for the Irpinia earthquake rupture scenario simulated with HIC (a), EXSIM (b), DSM_{fix} (c), and DSM_{app} (d) techniques. Left columns show the map distribution of peak values and right columns their decay as a function of R_{JB}. The values are simulated at virtual grid points shown in Figure 1. Peak values recorded during the 1980 Irpinia earthquake (classified according to EC8 site classification) are also shown (right columns). The black curves in the right columns represent the median peak values ±1 sigma predicted by the Akkar and Bommer (2010), AkB10, model for rock sites class and M_w 6.9.

analysis to intermediate and high-frequency ranges and summarize the results estimating the median ground-motion values and the standard deviations associated with the parametric uncertainties of the model.

We constructed a large set of possible rupture models for various positions of the rupture nucleation point, final slip distributions on the fault, and rupture velocity values. The first set of scenario rupture models uses the same distribution of slip (Fig. 2a) and rupture velocity ($0.8V_S$) as for the simulation of the 1980 earthquake records; however, we considered six additional hypocenter locations spanning the length of the fault at a depth of about 11 km (Table 2). Further sets of rupture models were generated considering two alternative slip distributions with the same average slip value and different position of asperities (Fig. 2) and two alternative values of rupture velocities ($0.7V_S$ and $0.85V_S$). The two additional slip models are characterized by asperities located on the central portion and on the northwestern portion of the fault, respectively. Note that the same suite of hypocenters and rupture velocities is used for each slip distribution.

For each kinematic rupture model we simulated the time series considering the same receivers grid of Figure 1 and using HIC, EXSIM, and DSM_{app} techniques. Note that we did

not include the DSM_{fix} method as we have shown that it practically provides very similar results to EXSIM. In total, for each technique a data set composed of about 4500 accelerograms was produced, obtained by the combination of 54 rupture models and 84 virtual observers radially distributed within 50 km of the fault. The distribution of simulated PGA and PGV from all the considered rupture models, as a function of R_{JB}, is presented in Figure 8.

We compared simulated peak ground motions in terms of median estimates and related variability. We calibrated a simple functional form for the three synthetic data sets, using a similar approach as in empirical GMPEs. Here, no dependence on magnitude, anelastic attenuation term, and focal mechanism are introduced as magnitude and focal mechanism are fixed parameters in the simulations (M_w 6.9, normal fault), and the distance range is within 50 km.

A regression scheme based on the random effect model (Brillinger and Preisler 1985; Abrahamson and Youngs 1992) was adopted in order to decompose the total variability into its components (Strasser *et al.*, 2009; Atik *et al.*, 2010). To keep the terminology clear, we will refer to interscenario (i.e., between-scenario) and intrascenario (i.e., within-scenario) variability (instead of interevent and intraevent variability), because we are not dealing with different events, strictly speaking.

The regressions were performed for the geometric mean of the north–south and east–west components of peak ground motions. The assumed functional form is given by

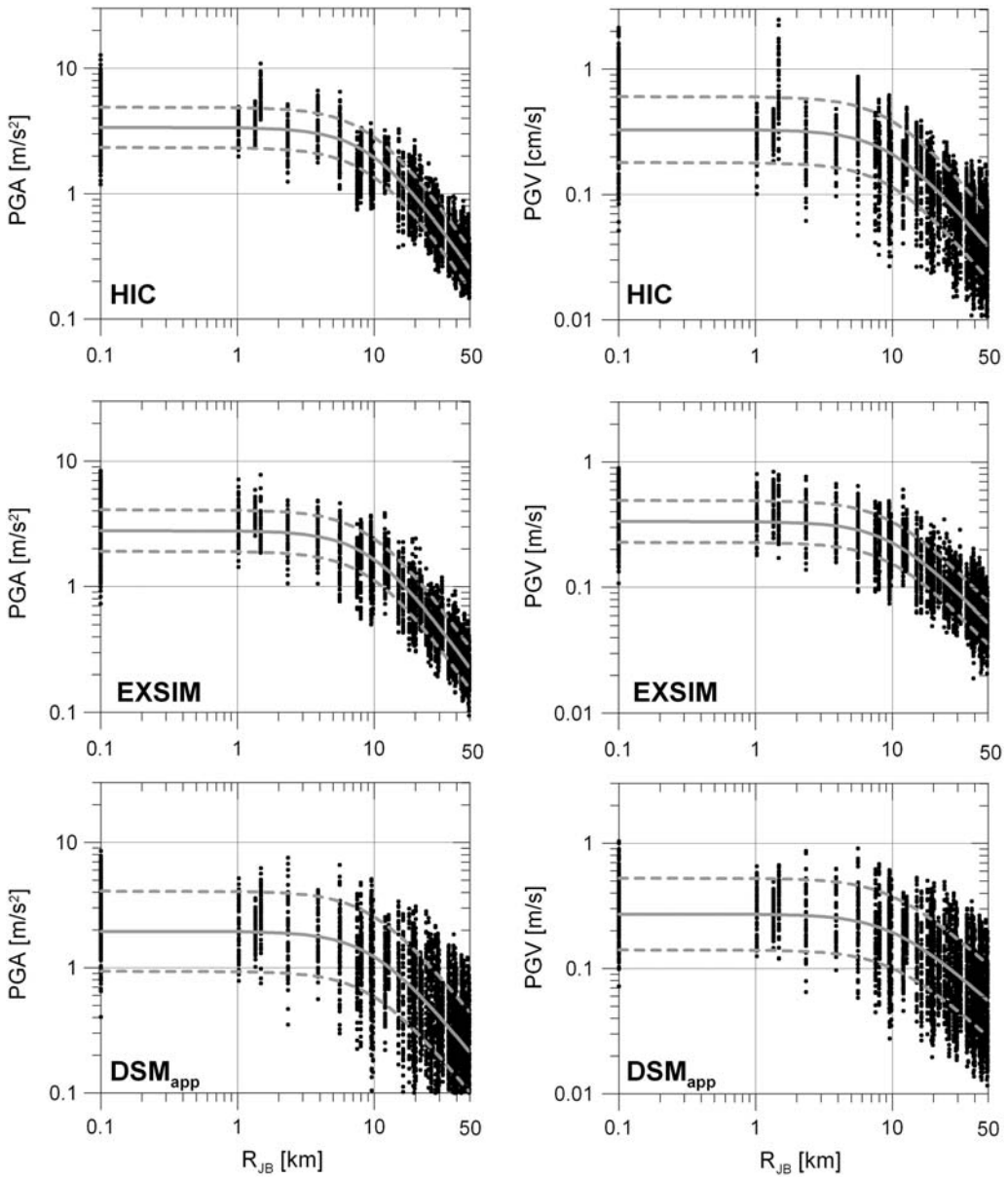

Figure 8. PGA and PGV (geometric mean of NS and EW components) from all earthquake scenarios (black symbols) versus R_{JB} distance. Median PGA and PGV $\pm\sigma_{TOT}$ estimated by equations (1) and (2) are shown by gray curves for HIC, EXSIM, and DSM_{app} simulations.

$$\log_{10} Y = a + c \log_{10} \sqrt{(R_{JB}^2 + h^2)} + \delta_{K,i} + \delta_{A,ij}, \quad (1)$$

where Y is the response variable (i.e., PGA or PGV); $h = 10.9$ km (the depth of the hypocenter in the source model), a and c are the coefficients of the regression, and $\delta_{K,i}$ and $\delta_{A,ij}$ represent the interscenario (depending on scenario event i only) and intrascenario (depending both on scenario event i and site j) residuals, assumed to be normally distributed with variances σ_K^2 and σ_A^2, respectively. The variability of median ground motions predicted for the various scenario events and the variability of ground motions with respect to the median motion predicted for each individual scenario event are represented by σ_K^2 and σ_A^2.

The total variance of model (1) is given by

$$\sigma_{TOT}^2 = \sigma_K^2 + \sigma_A^2. \quad (2)$$

Table 5 lists the regression coefficients and sigma values. Figure 8 shows the median curves $\pm\, \sigma_{TOT}$ estimated from equations (1) and (2), considering PGA and PGV calculated for the three data sets. The median ground-motion values of the three simulation methods are consistent, while the relative standard deviations show significant differences, also depending on the considered strong-motion parameter (see Table 5).

The observed difference in the total sigma values implies that DSM_{app} synthetics present the largest PGA variability, whereas only half of such variability is found for EXSIM and HIC peak accelerations. On the other hand, comparable PGV variabilities are found for HIC and DSM_{app}, while smaller variability is observed from the EXSIM simulations. The interscenario (σ_K) and intrascenario (σ_A) variabilities reveal that the larger contribution to the total sigma comes from the latter (i.e., spatial) variability. Moreover, it can be noticed that the interscenario standard deviations present the lowest values for EXSIM synthetics, whereas DSM_{app} and HIC peaks are characterized by similar σ_K, though HIC interscenario variability substantially increases for PGVs. These differences in σ_K values signify that the influence of the parametric uncertainties on ground-motion estimates is different for each technique. EXSIM method results loosely sensitive to variations in the kinematic rupture model. Conversely, in DSM_{app}, the calculation of isochrones and of the use of the apparent corner frequency, implies that the choice of the nucleation point position and of the value of rupture velocity has a large influence on the simulated ground motion. Finally, HIC synthetics, characterized by the largest interscenario variability, are calculated solving the representation theorem at low frequency. As PGV is sensitive to the intermediate frequency of the motion (where the deterministic and stochastic approaches are merged), we expect to observe a larger dependence on the source parameters (e.g., hypocenter location and slip distribution) than for stochastic methods.

Comparison with GMPEs

In Figure 9a the median PGA and PGV curves from simulated data sets are compared with the median $\pm 1\sigma$ of the AkB10 empirical GMPEs (AkB10 for $M_w = 6.9$) for the rock site class.

The synthetic PGA and PGV median curves are enclosed in the empirical standard deviation, but simulated PGAs exhibit a different decay with distance, attenuating faster for R_{JB} larger than 10 km. This feature, already observed in Figure 7, is common to the all examined rupture scenarios and cannot be considered a peculiarity of the 1980 Irpinia earthquake.

Regarding the synthetics variability (Table 5), the DSM and HIC total standard deviations for PGV are consistent with the AkB10 standard deviation. Conversely, the total synthetic sigma for PGA is similar to the empirical one only for DSM_{app}, while it is significantly smaller for the other two simulation techniques.

The median PGA and PGV $\pm$ interscenario (σ_k) and intrascenario (σ_A) for HIC are compared with the AkB10 predictions, considering the interevent and intraevent standard deviations separately (Fig. 9b,c). Synthetic interscenario and empirical interevent standard deviations have very similar values both for PGA and PGV, suggesting that the observed ground-motion variability associated with event-specific factors that we have not taken into account (e.g., stress drop, focal depth, etc.) is of the same order of magnitude as the variability caused by different rupture scenarios on the given fault.

Table 5
Regression Coefficients for Equations (1) and (2) for Each of the Adopted Simulation Techniques*

	PGA				PGV			
	DSM_{app}	EXSIM	HIC	AkB10†	DSM_{app}	EXSIM	HIC	AkB10†
a	3.657	3.987	4.121		2.407	2.666	2.831	
c	−1.366	−1.541	−1.592		−0.974	−1.141	−1.314	
σ_K	0.101	0.052	0.095	0.0994	0.091	0.053	0.131	0.1083
σ_A	0.303	0.157	0.129	0.2610	0.272	0.159	0.228	0.2562
σ_{TOT}	0.320	0.165	0.161	0.2790	0.287	0.167	0.263	0.2780

*Sigma values for the AkB10 model are also reported.
†For the AkB10 model the reported values for σ_K and σ_A refer to the interevent and intraevent standard deviations.

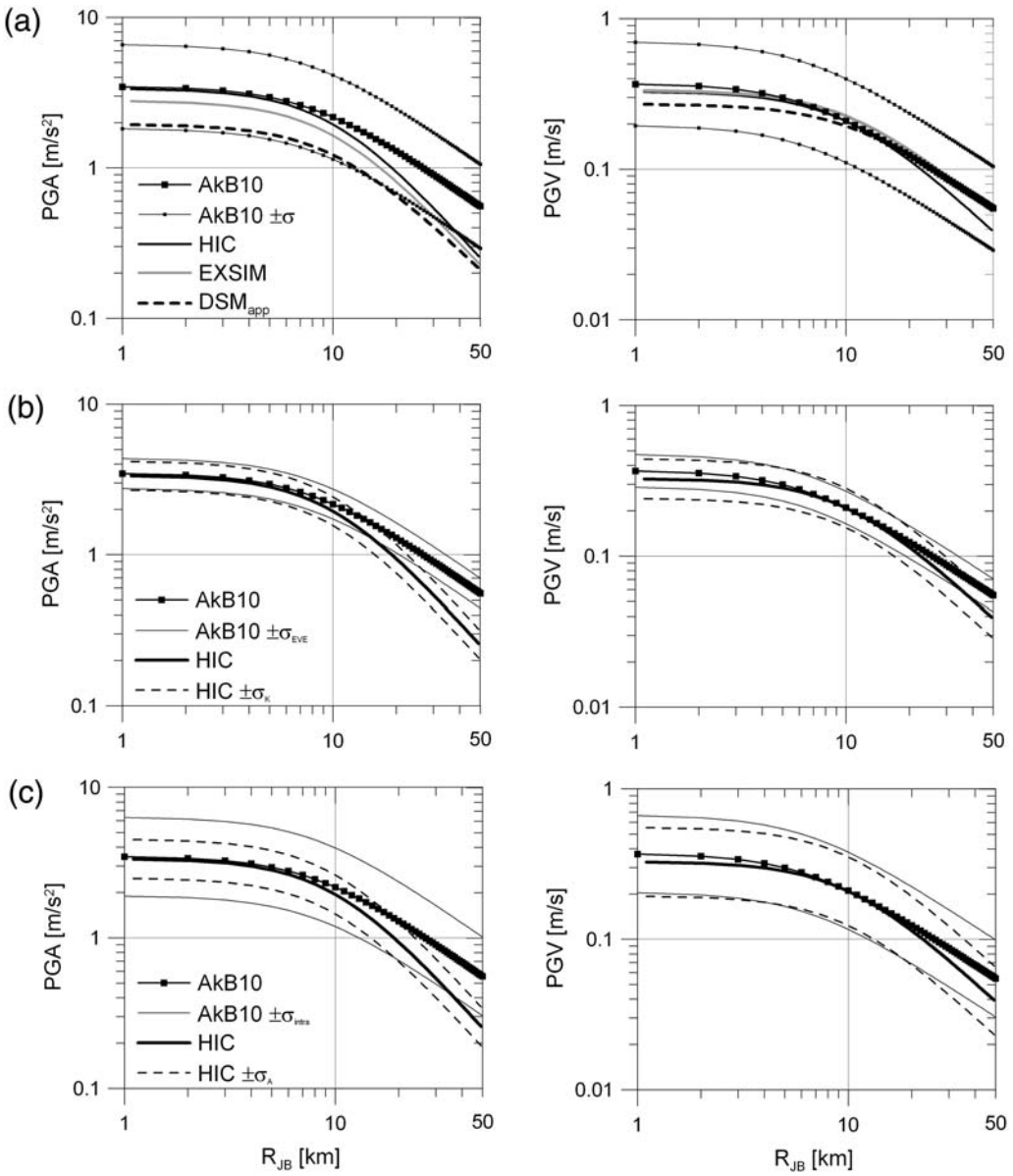

Figure 9. (a) Comparison of median PGA and PGV (equation 1) from simulations (DSM_{app}, EXSIM and HIC techniques) and Akkar and Bommer (2010), AkB10, GMPEs for rock site class and M_w 6.9. (b) Comparison of PGA and PGV median ± 1 interscenario sigma (σ_k) from simulations (HIC method only) and AkB10 median ± 1 interevent sigma. (c) Comparison of PGA and PGV median ± 1 intrascenario sigma (σ_A) from simulations (HIC method only) and AkB10 median ± 1 intraevent sigma.

In Figure 9c we observe that the synthetic intrascenario standard deviation is similar to the empirical one for PGV (right panel) and lower for PGA (left panel). This result means that, at low- to intermediate-frequencies (affecting the PGV), the observed ground-motion spatial variability, including effects depending on record-specific factors (e.g., directivity effects, different response for rock sites, etc.) is of the same order of magnitude as the synthetic one. The synthetic intrascenario variability account for directivity effects, radiation pattern, and source-sites geometry, but the site condition is equal for all sites. Thus, the larger values of PGA empirical intraevent standard deviation as compared with the synthetic one may be explained both by the lack of directivity effects at high frequencies in the synthetics and/or by the randomness in site response for rock sites that can make an important contribution in the observed high-frequency ground-motion variability.

Finally, we observe that DSM_{app} provides a PGA intrascenario variability larger than the AkB10 one (Table 5). This can be ascribed to the overestimation of the spatial variability related to directivity effects as shown in Figure 7.

Conclusions

In this paper we performed a simulation study for the 1980 M 6.9 Irpinia (southern Italy) earthquake. This seismic event is the largest recorded by strong-motion instruments in Italy, and it involved three distinct shocks. We focused our

attention on the 0 s event, which ruptured the largest fault segment.

The modeling of this event was performed with three finite-fault simulation methods, that is, the finite-fault stochastic method (EXSIM, Motazedian and Atkinson, 2005; Boore, 2009), the hybrid deterministic-stochastic method (DSM, Pacor *et al.*, 2005), and the broadband integral-composite approach (HIC, Gallovič and Brokešová, 2007), assuming the geometry and source kinematic models based on Bernard and Zollo (1989) and Cocco and Pacor (1993). To validate the model parameters, we first calculated synthetic seismograms at bedrock, in correspondence to seven strong-motion stations, classified as rock or stiff sites. We found a general consistency among the simulation results in terms of spectral accelerations and peak values, whereas the synthetic waveforms show remarkable differences in duration and phase. The goodness of fit of the modeling was then assessed by evaluating a model bias, based on acceleration response spectra residuals, that resulted within a value of ± 0.25 (in $\log_{10}$ units) around zero for all of the techniques. We verified that the local site response do not have a predominant effect on ground motion at the investigated stations, except at RNR, where we were not able to explain the high-frequency content of the observed waveforms with the adopted source, propagation, and site parameters.

The validated model was used to simulate the ground motion from the 0 s event at a regular grid of virtual receivers in order to study the ground-motion features at the regional scale. Because of the particular position of the hypocenter, we found peak distributions elongated approximately in the fault-strike direction. HIC and DSM_{app} techniques predicted larger PGV values toward the northwest as an effect of rupture directivity both along the strike and up-dip directions.

The second part of this study concerned the simulation of ground motions from scenario events associated with the 0 s seismogenic fault. We considered 54 different rupture models combining three slip distributions, three rupture velocities, and six positions of the hypocenter. We calculated the synthetic accelerograms, produced by each of the rupture processes, at a grid of 84 virtual receivers radially distributed within 50 km around the fault, with three simulation techniques. In this way, we constructed a data set of more than 4500 synthetic seismograms for each technique, suitable for statistical analyses. We used each synthetic data set to calibrate a simple functional form in order to describe the attenuation with distance of simulated motions from many rupture scenarios in terms of median PGA and PGV and related variability. From the regression analysis we found that the median curves of simulated ground motions are consistent, even if the simulation techniques describe in different ways the source and the wave-propagation processes. On the other hand, the total variability differs from one technique to another. This means that the effect of the parametric uncertainties of simulated ground motions depend on the simulation method.

We compared the synthetic predictions with the empirical GMPEs, and we found that the PGA synthetic median curves are smaller and exhibit a faster decay with distance than the GMPEs. Because the attenuation model used in the simulations have been validated with the data recorded during the 1980 Irpinia earthquake, we conclude that the considered empirical GMPEs for PGA may be too conservative in the case of occurrences of the assumed scenario events.

We also compare the empirical and synthetic standard deviations. Note that, formally, the two quantities describe different components of the total variability in ground-motion prediction: the modeling variability (for empirical GMPEs) and the parametric variability (for simulations) (see Toro *et al.*, 1997). When comparing ground motions variability from GMPEs and synthetics from scenario events, we have to consider that, on the one hand, the constructed scenarios account for the uncertainties of a few source parameters, while other sources of variability (e.g., differences in focal mechanism, site conditions, etc.) considered in GMPEs are fixed in the simulations. On the other hand, the synthetic motions are computed on a much denser distribution of sites around the fault with respect to what is observed in real earthquakes. In this respect, simulations account for a more complete characterization of the spatial distribution of near-fault ground motions. Moreover, it is possible to evaluate the ground-motion variability from different ruptures on the same fault, while, due to the actual lack of such episodes, this variability is missing in GMPEs.

The interscenario (σ_K) and intrascenario (σ_A) variabilities reveal that the larger contribution to the total sigma comes from the latter (i.e., spatial variability). The EXSIM synthetics are characterized by the smallest interscenario variability, while the HIC ones are characterized by the largest variability (especially for PGV) due to the deterministic calculations of the motion at low frequencies. The DSM_{app} synthetics present the largest intrascenario variability, which means that, on average, the simulations produce the largest spatial variability of ground motion. This is consistent with the large sensitivity of the DSM_{app} method to the position of the nucleation point that directly affects the rupture directivity (Ameri *et al.*, 2009), producing large spatial variation of ground motion around the fault. High-frequency directivity effects have been observed on strong-motion records from recent moderate-magnitude earthquakes: the 1997 M 5.6–6.0 Umbria–Marche events (Castro *et al.*, 2001; Castro *et al.*, 2008; Emolo *et al.*, 2008) and the 2009 M 6.3 L'Aquila earthquake (Akinci *et al.*, 2010). However, further studies should be carried out to understand if this phenomena could significantly affect the observed ground-motion variability even in this frequency range.

Data and Resources

Seismograms recorded during the 1980 Irpinia earthquake used in this study, the related ground-motion parameters and stations information can be downloaded from the

Italian Accelerometric Archive (ITACA) at http://itaca.mi.ingv.it (last accessed January 2011).

The EXSIM code has been downloaded from http://www.daveboore.com/software_online.htm (last accessed January 2011).

Some plots were made using the Generic Mapping Tools version 3.3.6 (Wessel and Smith, 1998; http://www.soest.hawaii.edu/gmt/; last accessed January 2008).

Acknowledgments

This research was funded by DPC–INGV agreement 2004–2007 within the project "S3—Shaking and damage scenarios in area of strategic and/or priority interest" and supported by Grant Agency of the Czech Republic (205/08/P013). We thank the associate editor Hiroshi Kawase, Giovanna Cultrera, and an anonymous reviewer for constructive comments and criticism that greatly improved the quality of the original paper. We thank Gail Atkinson, Dariush Motazedian, and David Boore for providing the EXSIM code. Dino Bindi and Lucia Luzi provided the code for the random effect model.

References

Aagaard, B. T., T. M. Brocher, D. Dolenc, D. Dreger, R. W. Graves, S. Harmsen, S. Hartzell, S. Larsen, K. McCandless, S. Nilsson, N. A. Petersson, A. Rodgers, B. Sjögreen, and M. L. Zoback (2008). Ground-motion modeling of the 1906 San Francisco earthquake, Part II: Ground-motion estimates for the 1906 earthquake and scenario events, *Bull. Seismol. Soc. Am.* **98,** 1012–1046.

Abrahamson, N. A., and R. R. Youngs (1992). A stable algorithm for regression analyses using the random effects model, *Bull. Seismol. Soc. Am.* **82,** 505–510.

Aki, K., and P. G. Richards (2002). *Quantitative Seismology*, Second Ed. University Science Books, Sausalito, California, 704 pp.

Akinci, A., L. Malagnini, and F. Sabetta (2010). Characteristics of the strong ground motions from the 6 April 2009 L'Aquila earthquake, Italy, *Soil Dyn. Earthquake Eng.* **30,** 320–335.

Akkar, S., and J. J. Bommer (2010). Empirical equations for the prediction of PGA, PGV and spectral accelerations in Europe, the Mediterranean region, and the Middle East, *Seismol. Res. Lett.* **81,** 195–206.

Amato, A., and G. Selvaggi (1993). Aftershock location and *P*-velocity structure in the epicentral region of the 1980 Irpinia earthquake, *Ann. Geophys.* **36,** 3–15.

Ambraseys, N. N., J. Douglas, S. K. Sarma, and P. M. Smit (2005). Equations for the estimation of strong ground motions from shallow crustal earthquakes using data from Europe and Middle East: Horizontal peak ground acceleration and spectral acceleration, *Bull. Earthquake Eng.* **3,** 1–53.

Ameri, G., F. Gallovič, F. Pacor, and A. Emolo (2009). Uncertainties in strong ground-motion prediction with finite-fault synthetic seismograms: An application to the 1984 *M* 5.7 Gubbio, central Italy, earthquake, *Bull. Seismol. Soc. Am.* **99,** 647–663.

Ameri, G., F. Pacor, G. Cultrera, and G. Franceschina (2008). Deterministic ground-motion scenarios for engineering applications: The case of Thessaloniki, Greece, *Bull. Seismol. Soc. Am.* **98,** 1289–1303.

Anderson, J. G., and S. E. Hough (1984). A model for the shape of the Fourier amplitude spectrum of acceleration at high frequencies, *Bull. Seismol. Soc. Am.* **74,** 1969–1993.

Ansal, A., A. Akinci, G. Cultrera, M. Erdik, V. Pessina, G. Tonuk, and G. Ameri (2008). Loss estimation in Istanbul based on deterministic earthquake scenarios of the Marmara Sea region (Turkey), *Soil Dyn. Earth. Eng.* **29,** 699–709.

Archuleta, R. J., and S. H. Hartzell (1981). Effects of fault finiteness on near-source ground motion, *Bull. Seismol. Soc. Am.* **71,** 939–957.

Atik, L. A., N. Abrahamson, J. J. Bommer, F. Scherbaum, F. Cotton, and N. Kuehn (2010). The variability of ground-motion prediction models and its components, *Seismol. Res. Lett.* **81,** no. 5, 794–801.

Atkinson, G. M., and D. M. Boore (2006). Earthquake ground-motion prediction equations for eastern North America, *Bull. Seismol. Soc. Am.* **96,** 2181–2205.

Bernard, P., and R. Madariaga (1984). A new asymptotic method for the modeling of near-field accelerograms, *Bull. Seismol. Soc. Am.* **74,** 539–558.

Bernard, P., and A. Zollo (1989). The Irpinia (Italy) 1980 earthquake: Detailed analysis of a complex normal faulting, *J. Geophys. Res.* **94,** 1631–1647.

Bindi, D., R. R. Castro, G. Franceschina, L. Luzi, and F. Pacor (2004). The 1997–1998 Umbria–Marche sequence (central Italy): Source, path and site effects estimated from strong motion data recorded in the epicentral area, *J. Geophys. Res.* **109,** B04312, doi 10.1029/2003JB002857.

Bindi, D., L. Luzi, M. Massa, and F. Pacor (2009). Horizontal and vertical ground motion prediction equations derived from the Italian Accelerometric Archive (ITACA), *Bull. Earthquake Eng.*, doi 10.1007/s10518-009-9130-9.

Boore, D. M. (1983). Stochastic simulation of high-frequency ground motion based on seismological models of the radiated spectra, *Bull. Seismol. Soc. Am.* **73,** 1865–1894.

Boore, D. M. (2003). Simulation of ground motion using the stochastic method, *Pure Appl. Geophys.* **160,** 635–676.

Boore, D. M. (2009). Comparing stochastic point-source and finite-source ground-motion simulations: SMSIM and EXSIM, *Bull. Seismol. Soc. Am.* **99,** 3202–3216.

Boore, D. M., and G. M. Atkinson (2008). Ground-motion prediction equations for the average horizontal component of PGA, PGV, and 5%-damped PSA at spectral periods between 0.01 s and 10.0 s, *Earthquake Spectra* **24,** 99–138.

Boore, D. M., and W. B. Joyner (1997). Site amplifications for generic rock sites, *Bull. Seismol. Soc. Am.* **87,** 327–341.

Bouchon, M. (1981). A simple method to calculate Green's functions for elastic layered media, *Bull. Seismol. Soc. Am.* **71,** 959–971.

Brillinger, D. R., and H. K. Preisler (1985). Further analysis of the Joyner–Boore attenuation data, *Bull. Seismol. Soc. Am.* **75,** 611–614.

Castro, R., R. F. Pacor, G. Franceschina, D. Bindi, C. Zonno, and L. Luzi (2008). Stochastic strong-motion simulation of the M_w 6 Umbria–Marche earthquake of September 1997: Comparison of different approaches, *Bull. of Seismol. Soc Am.* **98,** no. 2, 662–670, doi 10.1785/0120070092.

Castro, R. R., A. Rovelli, M. Cocco, M. Di Bona, and F. Pacor (2001). Stochastic simulation of strong-motion records from the 26 September 1997 (M_w 6), Umbria–Marche (Central Italy) earthquake, *Bull. Seismol. Soc. Am.* **91,** 27–39.

CEN, Comité Européen de Normalisation (2004). Eurocode 8: Design of Structures for Earthquake Resistance—Part 1: General Rules, *Seismic Actions and Rules for Buildings*, Brussels: Comité Européen de Normalisation.

Chiauzzi, L., A. Masi, M. Mucciarelli, M. Vona, F. Pacor, G. Cultrera, F. Gallovič, and A. Emolo (2010). Building damage scenarios based on exploitation of Housner intensity derived from finite faults ground motion simulation, submitted to *Bull. Earthquake Eng.*

Cocco, M., and F. Pacor (1993). The rupture process of the 1980 Irpinia, Italy, earthquake from the inversion of strong motion waveforms, *Tectonophysics* **218,** 157–177.

Convertito, V., A. Emolo, and A. Zollo (2006). Seismic-hazard assessment for a characteristic earthquake scenario: An integrated probabilistic-deterministic method, *Bull. Seismol. Soc. Am.* **96,** 377–391.

Cultrera, G., A. Cirella, E. Spagnuolo, A. Herrero, E. Tinti, and F. Pacor (2010). Variability of kinematic source parameters and its implication on the choice of the design scenario, *Bull. Seismol. Soc. Am.* **100,** 941–953.

Cultrera, G., F. Pacor, G. Franceschina, A. Emolo, and M. Cocco (2009). Directivity effects for moderate-magnitude earthquakes (M_w 5.6–6.0) during the 1997 Umbria–Marche sequence, central Italy, *Tectonophysics* **476,** 110–120.

Emolo, A., G. Cultrera, G. Franceschina, F. Pacor, V. Convertito, M. Cocco, and A. Zollo (2008). Ground motion scenarios for the 1997 Colfiorito, central Italy, earthquake, *Ann. Geophys.* **51,** 509–525.

Gallovič, F., and J. Brokešová (2004). The k^{-2} rupture model parametric study: Example of the 1999 Athens earthquake, *Studia geoph. et geod.* **48,** 589–613.

Gallovič, F., and J. Brokešová (2007). Hybrid *k*-squared source model for strong ground motion simulations: Introduction, *Phys. Earth Planet. In.* **160,** 34–50.

Gallovič, F., and J. Burjánek (2007). High-frequency directivity in strong ground motion modeling methods, *Ann. Geophys.* **50,** 203–211.

Giardini, D. (1993). Teleseismic observation of the November 23 1980, Irpinia earthquake, *Ann. Geophys.* **36,** 17–25.

Graves, R. W., and A. Pitarka (2010). Broadband ground-motion simulation uUsing a hybrid approach, *Bull. Seismol. Soc. Am.* **100,** 2095–2123.

Heaton, T. H. (1990). Evidence for and implications of self healing pulses of slip in earthquake rupture, *Phys. Earth Planet. In.* **64,** 1–20.

Herrero, A., and P. Bernard (1994). A kinematic self-similar rupture process for earthquakes, *Bull. Seismol. Soc. Am.* **84,** 1216–1228.

Improta, L., M. Bonagura, P. Capuano, and G. Iannaccone (2003). An integrated geophysical investigation of the upper crust in the epicentral area of the 1980, $M_s = 6.9$, Irpinia earthquake (Southern Italy), *Tectonophysics* **361,** no. 1–2, 139–169.

Joyner, W. B., and D. M. Boore (1981). Peak horizontal acceleration and velocity from strong-motion records including records from the 1979 Imperial Valley, California, earthquake, *Bull. Seismol. Soc. Am.* **71,** 2011–2038.

Kwon, O., and A. S. Elnashai (2006). The effect of material and ground motion uncertainty on the seismic vulnerability curves of a RC structure, *Engineering Structures* **28,** 289–303.

Lermo, J., and F. J. Chávez-García (1993). Site effect evaluation using spectral ratio with only one station, *Bull. Seismol. Soc. Am.* **83,** 1574–1594.

Luzi, L., S. Hailemikael, D. Bindi, F. Pacor, F. Mele, and F. Sabetta (2008). ITACA (ITalian ACcelerometric Archive): A web portal for the dissemination of Italian strong-motion data, *Seismol. Res. Lett.* **79,** 716–722.

Mai, P. M., and G. C. Beroza (2003). A hybrid method for calculating near-source, broadband seismograms: Application to strong motion prediction, *Phys. Earth Planet. Int.* **137,** 183–199.

Margaris, B. N., and D. M. Boore (1998). Determination of $\Delta\sigma$ and κ_0 from response spectra of large earthquakes in Greece, *Bull. Seismol. Soc. Am.* **88,** 170–182.

Mena, B., E. Durukal, and M. Erdik (2006). Effectiveness of hybrid Green's function method in the simulation of near field strong motion: An application to the 2004 Parkfield earthquake, *Bull. Seismol. Soc. Am.* **96,** S183–S205.

Motazedian, D., and G. M. Atkinson (2005). Stochastic finite-fault modelling based on a dynamic corner frequency, *Bull. Seismol. Soc. Am.* **95,** 995–1010.

National Earthquake Hazards Reduction Program (1994). FEMA report 222A/223A, Recommended provisions for seismic regulations for new buildings, Provision 1 and Commentary 2, Federal Emergency Management Agency, Washington, D.C.

NTC08, Norme Tecniche per le Costruzioni (2008). DM 140108, Ministero delle Infrastrutture, Roma, Gazzetta Ufficiale, http://www.cslp.it/cslp/index.php?option=com_content&task=view&id=66&Itemid=20 (in Italian). Last accessed January 2011.

Olivares, L., and F. Silvestri (2001). Analisi della risposta sismica e della subsidenza post-sismica del colle di Bisaccia a seguito del terremoto irpino-lucano del 1980, *Proc. X National Conference of ANIDIS* (in Italian).

Pacor, F., G. Cultrera, A. Mendez, and M. Cocco (2005). Finite fault modeling of strong ground motions uing a hybrid deterministic–stochastic approach, *Bull. Seismol. Soc. Am.* **95,** 225–240.

Pantosti, D., and G. Valensise (1990). Faulting mechanism and complexity of the 23 November 1980, Campania–Lucania earthquake, inferred from surface observations, *J. Geophys. Res.* **95,** 15319–15341.

Pingue, F., G. De Natale, and P. Briole (1993). Modeling of the 1980 Irpinia earthquake source : Constrains from geodetic data, *Ann. Geophys.* **36,** 27–40.

Ripperger, J., P. M. Mai, and J. P. Ampuero (2008). Variability of near-field ground motion from dynamic earthquake rupture simulations, *Bull. Seismol. Soc. Am.* **92,** 2217–2232.

S3 Project Deliverable D0 (2007). Scenari di scuotimento in aree di interesse prioritario e/o strategico, Deliverable D0: Tecniche di simulazione. http://esse3.mi.ingv.it/deliverables/Deliverables_D0_S3_last.pdf (in Italian). Last accessed January 2011.

Siddiqqi, J., and G. Atkinson (2002). Ground motion amplification at rock sites across Canada, as determined from the horizontal-to-vertical component ratio, *Bull. Seismol. Soc. Am.* **92,** 877–884.

Sørensen, M. B., N. Pulido, and K. Atakan (2007). Sensitivity of ground-motion simulations to earthquake source parameters: A case study for Istanbul, Turkey, *Bull. Seismol. Soc. Am.* **97,** 881–900.

Spudich, P., and L. N. Frazer (1984). Use of ray theory to calculate high-frequency radiation from earthquake sources having spatially variable rupture velocity and stress drop, *Bull. Seismol. Soc. Am.* **74,** 2061–2082.

Strasser, F. O., N. A. Abrahamson, and J. J. Bommer (2009). Sigma: Issues, insights, and challenges, *Seismol. Res. Lett.* **80,** 41–56.

Toro, G. R., N. A. Abrahamson, and J. F. Schneider (1997). Model of strong ground motions from earthquakes in Central and Eastern North America: Best estimates and uncertainties, *Seismol. Res. Lett.* **68,** no. 1, 41–57.

Wessel, P., and W. H. F. Smith (1998). New, improved version of the Generic Mapping Tools released, *Eos Trans. AGU* **79,** 579.

Zeng, Y., J. G. Anderson, and G. Y. Anderson (1994). A composite source model for computing realistic synthetic strong ground motions, *Geophys. Res. Lett.* **21,** 725–728.

Zhu, T. J., A. C. Heidebrecht, and W. K. Tso (1988). Effect of peak ground acceleration to velocity ratio on ductility demand of inelastic systems, *Earthq. Eng. Struct. Dyn.* **16,** 63–79.

Zollo, A., A. Bobbio, A. Emolo, A. Herrero, and G. De Natale (1997). Modelling of ground acceleration in the near source range: The case of 1976, Friuli earthquake ($M = 6.5$), northern Italy, *J. Seismol.* **1,** 305–319.

Istituto Nazionale di Geofisica e Vulcanologia
Sezione di Milano-Pavia, Via Bassini, 15
20133, Milano, Italy
ameri@mi.ingv.it
(G.A., F.P.)

Dipartimento di Scienze Fisiche
Università degli Studi "Federico II"
Napoli, Italy
(A.E.)

Charles UniversityFaculty of Mathematics and Physics, Dept. of Geophysics
V Holesovickach 2, Praha 8
180 00, Czech Republic
(F.G.)

Manuscript received 25 August 2010

[P11]

Toward understanding slip inversion uncertainty and artifacts: 2. Singular value analysis

František Gallovič[1] and Jiří Zahradník[1]

Received 28 June 2010; revised 5 November 2010; accepted 10 December 2010; published 18 February 2011.

[1] Seismic slip inversion is studied by means of singular value decomposition (SVD), with emphasis on the role of singular vectors and regularization of the solution. Because the stable part of the slip inversion result is given in terms of a linear combination of the leading singular vectors (representing directions in the model space most sensitive to data), the performance of the inversion depends simply on how well the real slip model can be expanded into these vectors. The analysis is demonstrated using a synthetic model of a symmetric bilateral rupture with two asperities. Inverting the data yields a persisting false asperity in the middle of the fault, regardless of the inversion scheme used, because such a model cannot be well represented by only the leading singular vectors. The parallel study of the singular vectors from the individual stations and the whole network is suggested in order to understand how to achieve balance between overregularized solutions (with possible slip inversion artifacts) and underregularized solutions (vulnerable to data errors). The ideas are applied to the Mw 6.3 Movri Mountain earthquake, 2008, Greece, showing a weak indication of an asymmetric bilateral rupture. We suggest that inversion methods, not working explicitly with singular vectors, may yield artifacts, the origin of which can be also often explained by the SVD technique. Therefore, practical earthquake studies should be broadly complemented by the analysis of the leading singular vectors, a simple tool to evaluate the efficiency and potential drawbacks of the slip inversion.

Citation: Gallovič, F., and J. Zahradník (2011), Toward understanding slip inversion uncertainty and artifacts: 2. Singular value analysis, *J. Geophys. Res.*, *116*, B02309, doi:10.1029/2010JB007814.

1. Introduction

[2] Seismic slip inversion treated as a linear inverse problem is, in the literature, understood to be extremely unstable. Thus, the problem is typically stabilized by supplementing with nonlinear constraints, such as the positivity of the slip (or the slip velocity) and/or spatial-temporal smoothing [*Das et al.*, 1996; *Olson and Apsel*, 1982; *Hartzell and Heaton*, 1983; *Sekiguchi et al.*, 2000]. While the effects of inaccurate crustal models and noisy data are studied quite often, less attention is being paid to the resolution of the ill-conditioned problem, where even accurate structural models and noise-free data may provide a solution far from the true one [*Monelli and Mai*, 2008; *Page et al.*, 2009].

[3] In particular, *Olson and Apsel* [1982] studied the slip inversion of real data by means of singular value decomposition (SVD) assuming several types of inversion regularizations. The authors divided the inversion solution into two parts: stable and unstable. The stable part is demanded by the data, while the unstable part is unrecoverable by the data alone. Thus the key question, not discussed yet, is whether the stable part reflects at least the major features of the true (input) model. If not, the inversion is said to contain artifacts. Recently, *Zahradník and Gallovič* [2010] (hereinafter referred to as paper 1) attempted to understand some of the slip inversion artifacts. References to papers related to slip inversion are given by paper 1.

[4] In paper 1, seismograms for several rupture scenarios were forward simulated in a near-regional network of stations, which is also employed in the present paper (Figure 1). The resulting waveforms were inverted by two independent methods (one based on the conjugate gradient technique using back propagation of the waveform residuals [*Gallovič et al.*, 2009] and the other based on iterative deconvolution of point source contributions [*Sokos and Zahradník*, 2008]). The inversions yielded biased rupture speeds and, most interestingly, a strong spurious slip in the central part of the bilateral rupture model where there was almost no slip in the forward model. As a motivation the latter problem can also be illustrated by inverting the bilateral input model (Figure 2a) by yet another method, namely, the nonnegative least squares approach using the NNLS routine of *Lawson and Hanson* [1974]. Smoothing in both space and time is used; details are explained in section 2 and

[1]Department of Geophysics, Faculty of Mathematics and Physics, Charles University, Prague, Czech Republic.

0148-0227/11/2010JB007814

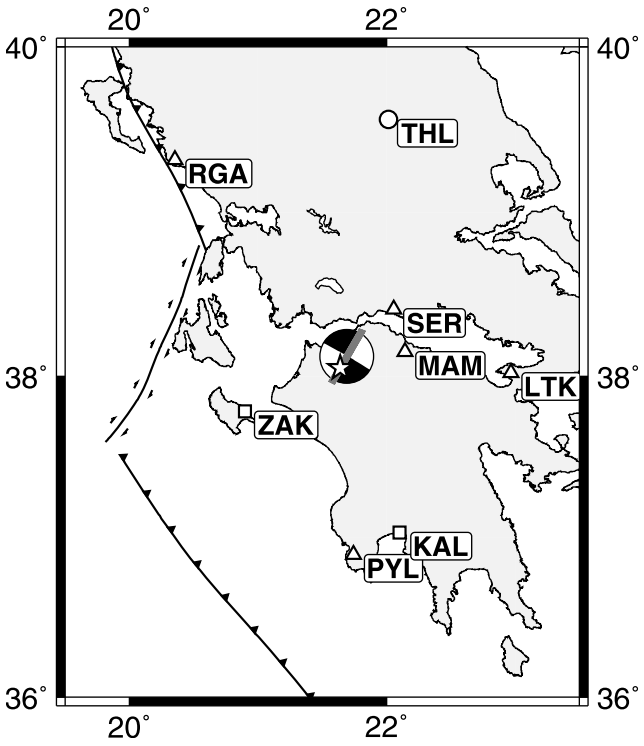

Figure 1. The Movri Mountain Mw 6.3 earthquake in Greece: the epicenter (asterisk), fault (gray bold line), focal mechanism (strike 30°, dip 87°, rake −178°) and eight near-regional stations are shown. This setup is used in this paper for inverting both synthetic and real data. The symbols refer to the station network: ITSAK (squares), NOA (circle), PSLNET (triangles). The main tectonic lines of western Greece are displayed.

in Text S1.[1] The result, presented in Figure 2b, also exhibits the persisting spurious asperity.

[5] In paper 1, the inversion behavior was analyzed by introducing so-called dynamic projection strips (DPSs). The DPSs were constructed by means of a "signal detector," a computation tool analyzing the correlation between complete observed waveforms and synthetics due to trial point sources. The strips were shown to be an extension of the projection line concept of seismic source tomography [*Ruff*, 1984; *Menke*, 1985]. They explain the role of the individual stations in the inversion, showing that the stations most constraining the inversion are those located along the fault direction. The DPS concept helped to explain the existence of the spurious asperity by combining the DPSs from all stations, giving rise to the so-called dark spot that also included the central part of the fault. As such, paper 1 represented an intuitive, physically based approach. The objective of the present paper is to complement it by a mathematically based approach.

[6] Since the forward problem under study is, in principle, linear, the inversion can be studied by the powerful technique of singular value decomposition, SVD [*Press et al.*, 1992; *Lawson and Hanson*, 1974]. Two factors restrict the applicability of the SVD technique in practice: (1) a large number of parameters, often technically prohibitive, (2) the need for nonlinear constraints, e.g., the slip positivity [*Olson and Apsel*, 1982; *Das et al.*, 1996], which are inapplicable in the SVD framework. Since the present paper aims at understanding the relations between mathematical and physical concepts, we can adopt simplifications to avoid these problems: a 1-D (line) source will keep the number of parameters low enough, and the main problems of slip inversions will be understandable even without the positivity constraint.

[7] The present paper shows how the above mentioned artifact (Figure 2b) can be explained by means of the SVD approach, which allows the separation of the stable and unstable parts of the solution. Furthermore, using SVD, we present a mathematical explanation of the DPSs and the dark spots and show how they control the inversion.

[8] The present paper has two parts. First, we explain the slip inversion procedure in terms of the well-known theoretical concepts of the SVD (linear algebra), such as singular vectors and regularization by means of truncation and smoothing. We also discuss the spatial-temporal complexity of the singular vectors to understand how to achieve balance between overregularized solutions (with possible artifacts), and underregularized solutions (vulnerable to data errors). Second, we apply the singular value analysis to the M6.3 earthquake, previously studied in paper 1. At the end we discuss that the features of the slip inversion procedure elucidated by the SVD are in the background of many slip inversion schemes, even those incorporating nonlinear

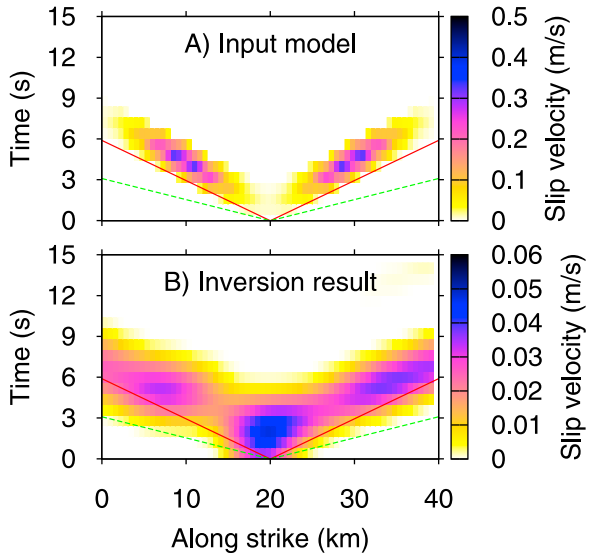

Figure 2. (a) Input slip velocity model for bilateral rupture propagation (prescribed source parameters). (b) Inversion result obtained by using the nonnegative least squares approach (NNLS). The solid red and dashed green lines correspond to S and P wave velocities at hypocentral depth, respectively. Note the disagreement of the major properties of the input and inverted source model, especially the spurious asperity in the center of the fault. A similar result is obtained even for other slip inversion methods (paper 1).

[1] Auxiliary materials are available in the HTML. doi:10.1029/2010JB007814.

constraints and those not explicitly working with singular vectors at all. We propose a procedure that should accompany detailed slip inversions to understand the role of the individual stations and to warn against potential drawbacks of the inversion.

2. Singular Value Analysis of Slip Inversion

2.1. Forward Problem

[9] The displacement wavefield u_j^s measured at station s, component j, is related to the earthquake slip velocity function $\Delta\dot{u}$ by means of the representation integral [*Aki and Richards*, 2002],

$$u_j^s(t) = \iint \Delta\dot{u}(x,\tau) H_j^s(x, t-\tau) dx d\tau, \tag{1}$$

where H_j^s are the displacement responses of the medium to excitation by a double-couple point source in space and step in time with unitary slip rate. After discretization of the spatial and temporal integrals, the representation theorem (1) can be expressed in matrix form:

$$\boldsymbol{u} = \mathbf{H}\boldsymbol{m}, \tag{2}$$

where vector $\boldsymbol{u}$ contains the displacement wavefields u_j^s of all stations and components considered, N elements in total; vector $\boldsymbol{m}$ encompasses M model parameters (samples of the slip velocity as a function of spatial coordinate and time). The two vectors are related to each other by matrix $\mathbf{H}$ [N rows × M columns], in which the jth column $\boldsymbol{H}(j)$ contains the impulse response due to the jth source position in space and time, $j = 1,\ldots, M$.

[10] We supplement (2) by a linear constraint on the scalar seismic moment M_0 that is assumed to be known in advance. It can simply be added to the matrix formulation (2),

$$\begin{pmatrix} L_u^{-1}\boldsymbol{u} \\ 1 \end{pmatrix} = \begin{pmatrix} L_u^{-1}\mathbf{H} \\ L_s^{-1}\boldsymbol{I} \end{pmatrix} \boldsymbol{m}, \tag{3}$$

or, in concise form,

$$\boldsymbol{d} = \mathbf{G}\boldsymbol{m}, \tag{4}$$

where $\boldsymbol{I}$ is a vector consisting of units, $L_u = \sqrt{\sum_{sij} u_{sij}^2}$ is the L2 norm of the data (i being the time index) and $L_s^{-1} = \mu\Delta S\Delta T/M_0$; μ is the rigidity of the medium, and ΔS and ΔT are the discretization elements of the fault area and the time interval, respectively. Note that the normalizing constants provide nondimensional data vector $\boldsymbol{d}$.

2.2. Inverse Problem

[11] If no additional constraints are added to the forward problem (4), it can be solved for $\boldsymbol{m}$ by the singular value decomposition (SVD) [e.g., *Press et al.*, 1992]. Matrix $\mathbf{G}$ can be uniquely decomposed into

$$\mathbf{G} = \mathbf{U}\Lambda\mathbf{V}^T, \tag{5}$$

where $\mathbf{U}$ [$N+1$, M] and $\mathbf{V}$ [M,M] are orthonormal matrixes ($\mathbf{U}^T\mathbf{U} = \mathbf{I}$, $\mathbf{V}^T\mathbf{V} = \mathbf{I}$) and Λ is a diagonal matrix consisting of singular values λ_i, $i = 1,\ldots, M$ (hereinafter assumed to be nonzero). Columns $\boldsymbol{V}_{(i)}$ of matrix $\mathbf{V}$ are so-called singular vectors. They are the eigenvectors of matrix $\mathbf{G}^T\mathbf{G}$ [M,M], forming an orthonormal basis system in the model parameter space. The $\mathbf{G}^T\mathbf{G}$ matrix contains the second derivatives of the L2 misfit with respect to the model parameters, the L2 misfit given by $1/2\|\boldsymbol{d} - \mathbf{G}\boldsymbol{m}\|^2$. The squares of singular values, λ_i^2, then represent the corresponding eigenvalues of matrix $\mathbf{G}^T\mathbf{G}$, expressing the sensitivity of the L2 misfit to changes of parameters $\boldsymbol{m}$ along the individual vectors $\boldsymbol{V}_{(i)}$. Columns $\boldsymbol{U}_{(i)}$ of matrix $\mathbf{U}$ are projections of basis vectors $\boldsymbol{V}_{(i)}$ into the data space (see equation (5)),

$$\boldsymbol{U}_{(i)} = \frac{\mathbf{G}\boldsymbol{V}_{(i)}}{\lambda_i}, \tag{6}$$

i.e., normalized seismograms related to the individual singular vectors. Being orthonormal in the data space, the $\boldsymbol{U}_{(i)}$ represent those eigenvectors of matrix $\mathbf{G}\mathbf{G}^T$[$N+1$,$N+1$] that correspond to its M nonzero eigenvalues.

[12] The Moore-Penrose pseudoinverse matrix of $\mathbf{G}$ can be expressed as

$$\tilde{\mathbf{G}} = \mathbf{V}\Lambda^{-1}\mathbf{U}^T. \tag{7}$$

The solution of the inverse problem, $\tilde{\boldsymbol{m}} = \tilde{\mathbf{G}}\boldsymbol{d}$, can thus be expressed as a linear combination of basis vectors $\boldsymbol{V}_{(i)}$,

$$\tilde{\boldsymbol{m}} = \sum_{i=1}^{M} \frac{\boldsymbol{U}_{(i)} \cdot \boldsymbol{d}}{\lambda_i} \boldsymbol{V}_{(i)}. \tag{8}$$

The $\boldsymbol{U}_{(i)}$ represent the vector basis in the M-dimensional data subspace that can be explained by the model parameters. The data vector in that subspace can be expressed as $\sum_{i=1}^{M}(\boldsymbol{U}_{(i)} \cdot \boldsymbol{d})\boldsymbol{U}_{(i)}$. The scalar product $\boldsymbol{U}_{(i)} \cdot \boldsymbol{d}$ can then be interpreted as a component of data vector $\boldsymbol{d}$ in the direction of basis vector $\boldsymbol{U}_{(i)}$. For the same reason, since $\boldsymbol{V}_{(i)}$ is the vector basis in the model space, ratio $(\boldsymbol{U}_{(i)} \cdot \boldsymbol{d})/\lambda_i$ represents the ith component of the parameter vector in the model space (see equation (8)). As such, equation (8) indicates that the data component = the parameter component times λ. Therefore, for a given change of a particular parameter component, a large or small λ yields a large or small change of the corresponding data component. Equally well, in case of inexact data (e.g., due to an inappropriate crustal model and/or additional noise), even a small error in a small data component can be amplified by the corresponding small λ to a large error in the respective parameter component. We further suppose that the singular vectors are sorted in descending order according to the size of their respective singular values λ.

[13] Putting (6) into (8), one obtains an alternative expression to that in (8),

$$\tilde{\boldsymbol{m}} = \sum_{i=1}^{M} \frac{\boldsymbol{V}_{(i)} \cdot \mathbf{G}^T\boldsymbol{d}}{\lambda_i^2} \boldsymbol{V}_{(i)} = \sum_{i=1}^{M} \frac{\boldsymbol{V}_{(i)} \cdot \tilde{\boldsymbol{c}}}{\lambda_i^2} \boldsymbol{V}_{(i)}, \tag{9}$$

where

$$\tilde{c}_i = \boldsymbol{G}_{(i)} \cdot \boldsymbol{d} = \frac{\boldsymbol{H}_{(i)} \cdot \mathrm{u}}{L_u^2} + \frac{1}{L_s}, \tag{10}$$

i.e., $\tilde{c}_i$ minus constant term $1/L_s$ is directly proportional to the scalar product of the impulse responses $\boldsymbol{H}(i)$ with data

vector $\boldsymbol{u}$. In this way, components of $\tilde{\boldsymbol{c}}$ are closely related to the correlations between the complete observed data $\boldsymbol{u}$ and "partial" synthetics $\boldsymbol{H}(i)$ corresponding to the individual point sources i with their respective location in time and space. Note the formal similarity between equations (8) and (9). While in the former equation the coefficients of the solution expansion are directly controlled by data vector $\boldsymbol{d}$, in the latter equation the data enter indirectly via $\mathbf{G}^T\boldsymbol{d} = \tilde{\boldsymbol{c}}$. Equation (9) suggests that the main role in the expansion to the first singular vectors is played by the similarity between them and $\tilde{\boldsymbol{c}}$. Any further features of the slip can only be obtained by employing singular vectors with smaller singular values. However, as already pointed out above, amplitudes of such singular vectors are more vulnerable to Green's function imperfections.

[14] Note that the interpretation of $\mathbf{G}^T$ d in terms of correlations (equation (10)) provides an alternative view of the least squares problem: fitting data $\boldsymbol{d}$ by parameters $\boldsymbol{m}$ ($\mathbf{G}\boldsymbol{m} = \boldsymbol{d}$, kernel $\mathbf{G}$) is substituted, via normal equations, by $\mathbf{G}^T\mathbf{G}\boldsymbol{m} = \mathbf{G}^T\boldsymbol{d} = \tilde{\boldsymbol{c}}$, i.e., by fitting correlations $\tilde{\boldsymbol{c}}$ by parameters $\boldsymbol{m}$, using kernel $\mathbf{G}^T\mathbf{G}$. Note that the definition of vector $\tilde{\boldsymbol{c}}$ is based on the same principle as the so-called "signal detector" of paper 1 (i.e., the correlations between the data and partial synthetics due to the individual point sources in the model space).

[15] As all singular values are sorted in descending order, the sum in equation (8) (or (9)) is typically not taken over the whole range M (total number of parameters) but only up to some $M' < M$, where λ (M') corresponds to the lowest singular value considered. The utilized singular vectors are termed the leading singular vectors. The idea is that (according to (8) or (9)) a given change in the parameter space in the direction $\boldsymbol{V}(i)$, associated with a small singular value $\lambda(i) < \lambda(M')$, yields a very small change in the data. Therefore, the effects of such small singular vectors can be suppressed. This is achieved by setting to zero all terms involving large values of $1/\lambda(i)$. Such an approach is practically useful since otherwise any small perturbation of $\boldsymbol{d}$ (e.g., due to noise, or due to imperfect knowledge of the propagating medium) yields a large change in $\boldsymbol{m}$, possibly driving the inversion to instabilities. Setting the coefficients of the solution expansion to zero for $\lambda(i) < \lambda(M')$ means that in the directions of the corresponding singular vectors $\boldsymbol{V}(i)$, the expansion coefficients are set to zero; this is one of the possible regularizations, and the resulting $\tilde{\boldsymbol{m}}$ is called the truncated solution. Other regularization approaches can be of course used. For example, regularization by adding linear smoothing constraints while keeping all singular vectors in the inversion. Similar and dissimilar effects of various regularizations are discussed further in the text and in Text S1.

2.3. Examples of Singular Vectors

[16] The singular vectors describe the slip inversion performance for a given fault position, distribution of stations and crustal structure. This information is independent of the specific parameters (the x-t rupture history) and data (seismograms) although, to be exact, matrix $\mathbf{G}$ is affected by the data through normalization constants L_u and L_s. However, they only serve to balance the weights of seismograms and the total seismic moment constraint. We show examples of singular vectors for a realistic configuration of a fault and near-regional stations, related to paper 1 (Figure 1). Matrix $\mathbf{G}$, containing the displacement impulse response of the medium (Green's functions and focal mechanism) is calculated by the discrete wave number method [*Bouchon*, 1981; *Coutant*, 1989] in a 1-D crustal model [*Haslinger et al.*, 1999] between 0.01 and 0.2 Hz. The source line depth is 17 km and the scalar seismic moment of the event is set to 3.4×10^{18} N m [*Gallovič et al.*, 2009]. We remind the reader that the shape of the singular vectors determines the final slip inversion solution (equation (8) or (9)) as these vectors form the basis system in the model space.

[17] Despite having eight stations in all at our disposal, in order to understand the individual role of the stations in the inversion, Figure 3 shows the singular vectors calculated assuming only single stations (namely, SER, ZAK, and RGA, see Figure 1 for their positions). The x and t components of the singular vectors are conveniently displayed in x-t diagrams. The vectors are sorted in descending order of their singular values. Although the singular vectors also include negative slip velocities (which is inevitable because the SVD approach cannot be combined with the positivity constraint), it does not preclude understanding the singular-vector properties. Indeed, for each of the three stations individually, the first singular vector (having the largest singular value λ_{max}) has basically all components of the same size (say, a "homogeneous" vector). The other singular vectors are "inhomogeneous," taking the shapes of the inclined strips with angles depending on the station azimuths. The steepest strips of the opposite orientation characterize the singular vectors of the SER and ZAK stations. Contrarily, the strips associated with the RGA station are closer to horizontal. The strips illustrate that in the inversion each station contributes to the information about the model parameters mostly in a particular x-t direction. Note that the strips and angles characterizing the station singular vectors can be understood in terms of source tomography [*Ruff*, 1984; *Menke*, 1985; *Zahradník and Gallovič*, 2010]. The steepest angles are associated with the stations located in the along-strike directions and are given by the wave velocity of the dominating phase (i.e., Lg wave in our case of near-regional distances).

[18] The very simple monotonic character of the singular vectors of the individual stations suggests that combined information from more stations (most importantly from SER and ZAK) can help the inversion to locate the real slip x-t position. Therefore, Figure 4 shows the singular vectors as in Figure 3, but when all the eight stations are considered together. The first singular vector, associated with λ_{max}, is again homogeneous. The next singular vectors up to $i = 5$ take the shape of elongated x-t patches because the inversion is dominated by the SER station (compare with the shape of the SER singular vectors in Figure 3). The dominance is due to the SER station's proximity to the fault, so that its amplitudes are significantly larger than those of the other stations. The next singular vectors are composed of still relatively large patches that have to be understood as combined information from all differently oriented strips found in the singular vectors of the individual stations (see Figure 3). These singular vectors will contribute to the inherent smoothness of the inverted truncated slip model (in terms of equation (8) or (9)) without any need of additional smoothing constraint (see also Text S1).

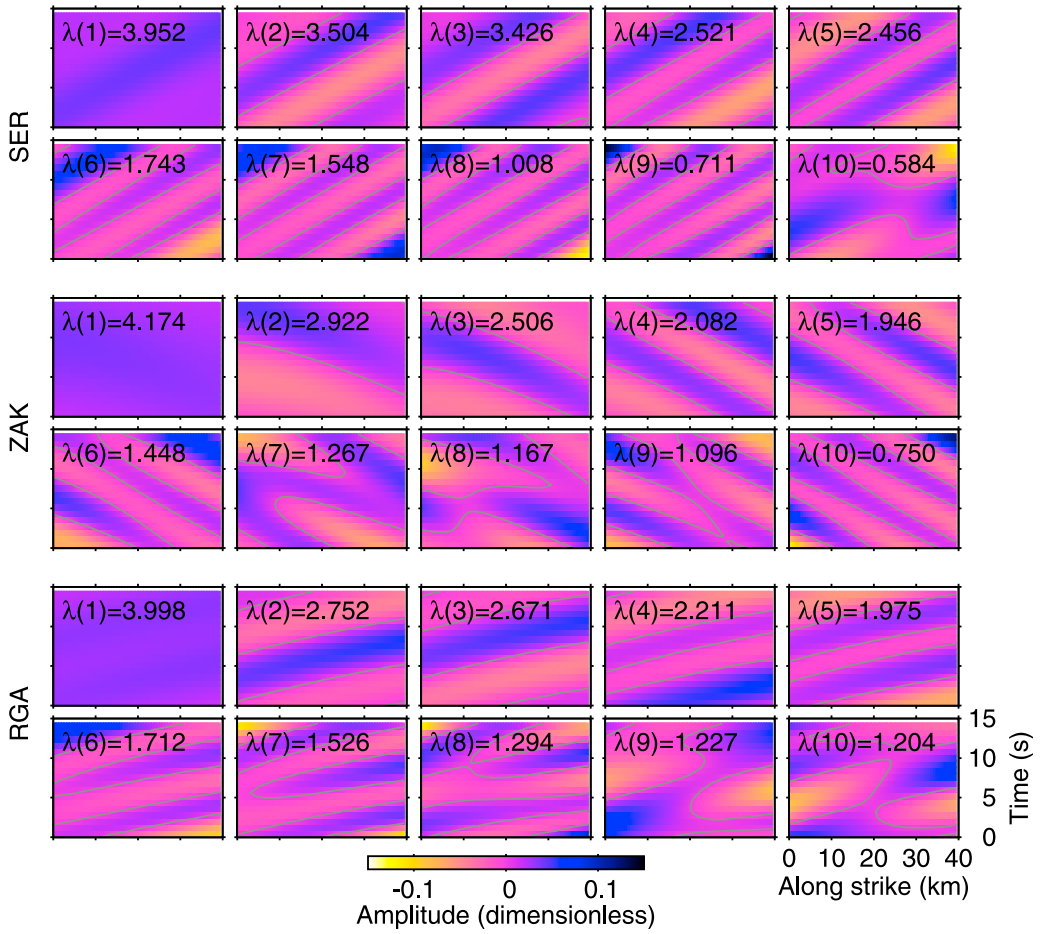

Figure 3. Leading singular vectors for a single-station linear problem of a line source in a 1-D crustal model. Each double row corresponds to one of the three selected stations (Figure 1). The spatial and temporal components of each singular vector are plotted against the horizontal and vertical axes, respectively; the size of the components is shown color coded. The values of the respective singular values λ are appended. Note the spatial-temporal complexity increasing with decreasing λ. The singular vectors depend on the assumed source and station positions and on the crustal structure.

[19] For larger i the singular vectors have more complex shapes, being increasingly more "oscillatory"; these are needed to reveal more detailed x-t structures in the slip model. However, as shown further, their proper combination might model not only small-scale, but also large-scale features of the slip pattern. For even smaller λ, the complexity of the singular vector increases up to "checkerboard" form.

[20] As stated above, the first singular vectors up to $i = 5$ in Figure 4 are dominated by the SER station. In Text S1 we show the singular vectors for the case when the station components are weighted according to the reciprocals of the seismogram L2 norms (thus weakening the role played by the SER station). Then, already the first singular vectors (up to $i = 5$) have the more complex shapes as for $i > 5$ in Figure 4. The explanation of how this can help in understanding the role of station weights in the inversion process is given in section 2.4.

2.4. Regularization (Synthetic Example)

[21] Now we use the singular vectors (examples are shown in Figures 3 and 4) to demonstrate how the slip inversion solution varies with different levels of truncation (zeroing contribution from singular vectors with small singular values). Figure 2a shows the synthetic input model considered. It corresponds to bilateral rupture propagation at constant speed, with two asperities located symmetrically on the fault to the northeast and southwest of the hypocenter (see the fault location in Figure 1). Note the almost zero slip in the center of the fault slip model.

[22] Figure 5 illustrates $\tilde{\boldsymbol{c}} = \mathbf{G}^T\boldsymbol{d}$ that is related to correlations between the data and impulse responses due to the individual sources at given x-t positions (see equation (10)). We remind the reader that $\tilde{\boldsymbol{c}}$ controls the contribution of the first leading singular vectors in the inversion solution expansion (see equation (9)). Figures 5a–5c assume only single stations used in the inversion (SER, ZAK, or RGA), while Figure 5d considers all eight stations together. Figures 5a–5c are dominated by strips of different angles. The strips show which of the point sources in the x-t space have their particular impulse responses correlated with the data vector. This closely relates the strips to the dynamic projection strips, introduced and discussed in paper 1. Figure 5d (employing all eight stations together) is related to the dark spot of paper 1. It is dominated by the northeastern

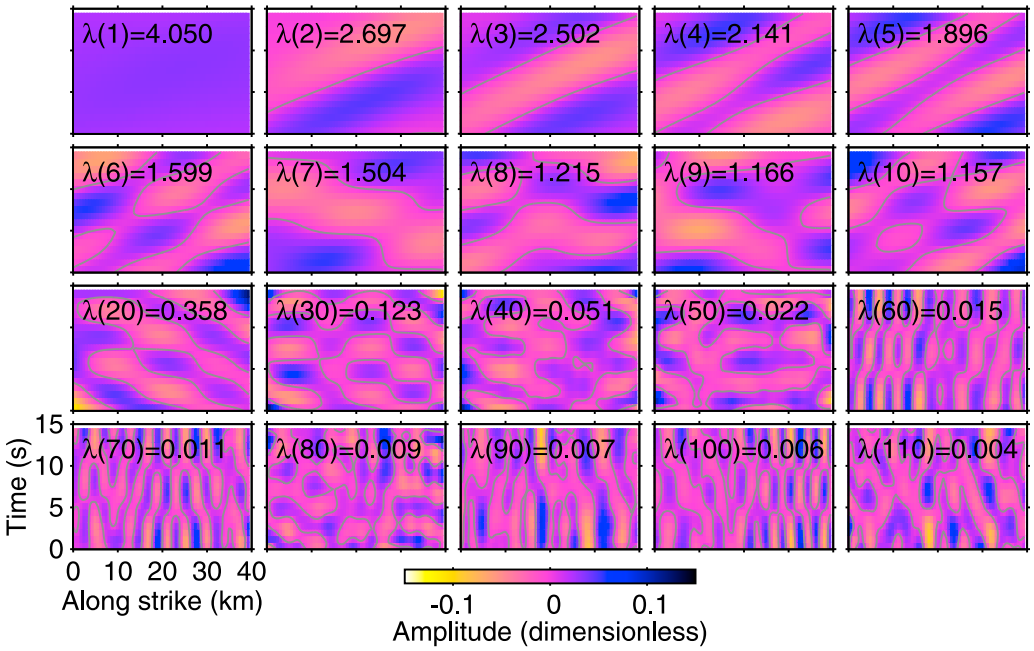

Figure 4. Singular vectors for the whole station network (Figure 1); the graphics are the same as in Figure 3. Comparison with the singular vectors of the single-station problems (Figure 3) shows that starting roughly at $\lambda(7)$, the singular vector pattern includes both "inclinations" typical of the individual stations. This property contributes to the resolution of the slip inversion. It is particularly important if the leading singular vectors already have this property (as in this case). Note that the shapes of the singular vectors (up to $i = 5$) are dominated by the SER station due to the proximity of this station to the source. In Text S1 we show the singular vectors for the case when the station components are weighted according to their L2 norm reciprocals. In such a case, the singular vectors take more complex shapes earlier. Note that the singular vectors with smaller singular values λ include a very complex pattern, theoretically being capable of providing details of the slip. However, their small λ reduces their practical use due to their high sensitivity to Green's function imperfections.

portion of the slip velocity, which is due to the proximity of the SER and MAM stations for which this part of the slip model is forward directive. Note that $\mathbf{G}^T\boldsymbol{d}$ has large amplitudes not only in the area of the existing slip (compare with Figure 2a) but also in the central part of the fault. In Text S1 we show this vector for the case when the station components are weighted according their respective L2 norm. In such a case, the SER and MAM stations are downweighted (due to their relative proximity to the fault) and the $\mathbf{G}^T\boldsymbol{d}$ plot is more symmetric, i.e., reflects the southwest asperity better, but still with a pronounced maximum in the central part of the fault.

[23] Now we evaluate the truncated solution (8) or, equivalently, (9) for the synthetic bilateral model. This can be done in two alternative ways:

[24] 1. The first way is to take the input model and multiply it by $\mathbf{G}$ to get synthetic data; these data can then be used in the inversion. Quantities $1/\lambda_i$ in (8) are set to zero beginning from a given $i = M'$ (as in the real data inversion).

[25] 2. Alternatively, start again from $\boldsymbol{m}$, now "skip" data $\boldsymbol{d}$ (not applicable in the real data inversion), and directly calculate the truncated solution as $\tilde{\boldsymbol{m}} = \mathbf{V}_p\mathbf{V}_p^T\boldsymbol{m} = \mathbf{R}\boldsymbol{m}$, where $\mathbf{V}_p$ is the matrix of singular vectors $\boldsymbol{V}(i)$ in columns with columns deleted beginning from $i = M'$. (The latter follows from substituting $\boldsymbol{d} = \mathbf{G}\boldsymbol{m}$ into the pseudoinverse problem $\tilde{\boldsymbol{m}} = \tilde{\boldsymbol{G}}\boldsymbol{d}$, obtaining $\tilde{\boldsymbol{m}} = \mathbf{V}\ \Lambda^{-1}\mathbf{U}^T\mathbf{U}\Lambda\mathbf{V}^T = \mathbf{V}_p\mathbf{V}_p^T\boldsymbol{m} = \mathbf{R}\boldsymbol{m}$.) Matrix $\mathbf{R}$ is called the resolution matrix. Comparing $\tilde{\boldsymbol{m}}$ with the given $\boldsymbol{m}$ provides important information about the inverse problem [*Lévêque et al.*, 1993].

[26] In some cases the resolution matrix itself can also be used to analyze trade-offs in the inverse problem. However, in our case it does not carry much useful information itself; it has almost constant diagonal elements (not shown here), suggesting the same trade-off for all points in the x-t plot.

[27] Figure 6 shows the inversion result for the synthetic example assuming various truncation levels and assuming either single stations in the inversion (SER, ZAK, RGA) or the complete set of eight stations. The regularization consists of removing (zeroing) singular vectors with singular values smaller than $\lambda_{\min}$, expressed as a fraction of $\lambda_{\max}$. Considering only the singular vectors with singular values larger than $\lambda_{\max}/5$ (Figure 6, first row), the resulting truncated slip image is relatively smooth, including also some negative values. When only one station is inverted, it retrieves the biased x-t slip pattern, controlled just by the corresponding singular vectors composed of the inclined strips (Figure 3). In particular, stations located approximately along the fault line (SER and ZAK) are able to recover only a part of the rupture that propagates in their directions because of the similarity between the singular vectors and the $\tilde{\boldsymbol{c}}$ plots (see equation (9)). The details of the rupture propagating away from the stations are hidden. All stations together yield a solution again similar to the $\tilde{\boldsymbol{c}}$ plot,

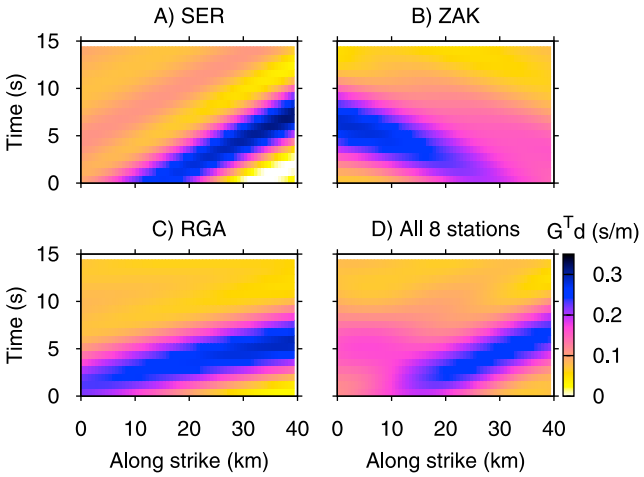

Figure 5. Analysis of the $\mathbf{G}^T\boldsymbol{d} = \tilde{\boldsymbol{c}}$ vector in the model space for the synthetic test (Figure 2a). The $\mathbf{G}^T\boldsymbol{d}$ components are proportional to the correlations between the complete seismograms (due to the finite extent source model) and the partial synthetics (due to single point sources at the individual x-t positions). (a-c) $\mathbf{G}^T\boldsymbol{d}$ for three single-station problems; (d) the whole network. The individual $\mathbf{G}^T\boldsymbol{d}$ vectors for each station are the mathematical counterpart of the dynamic projection strips of paper 1. They show what parts of the inversion solution are supported by each station for the specific input source model; see, for example, the narrow pattern of the $\mathbf{G}^T\boldsymbol{d}$ vector station SER due to the dominating forward directivity effect. Note that opposed to the singular vectors, the $\mathbf{G}^T\boldsymbol{d}$ vectors represent mixed information that is dependent not only on the stations but also on the slip model. However, since the information about the input model is transferred to the data, $\boldsymbol{d}$, the $\mathbf{G}^T\boldsymbol{d}$ vectors can be constructed also for the real data inversion, not only for synthetic tests. In Text S1 we show that in the case of station components weighted according to their respective L2 norm, the $\mathbf{G}^T\boldsymbol{d}$ vector for all stations has a more symmetric character, not being dominated by the proximity of station SER to the fault.

providing larger slip velocity values in the direction of the (closest) SER station.

[28] If more singular vectors are kept in the SVD solution ($\lambda_{min} = \lambda_{max}/10$ and $\lambda_{max}/100$, Figure 6, middle rows), the individual stations are able to recover gradually more details about the part of the rupture propagating away from them. The inversion employing all stations together also performs better; that is, it clearly shows the bilateral character of the rupture. However, the all-station inversion yields an asperity located in the center of the fault, where there is almost no slip in the input model (see Figure 2). We call this feature the "false asperity," or "artifact." Note that the (synthetic) data are fitted almost perfectly, with the variance reduction larger than 0.99. In paper 1 the same artifact was studied by two independent inversion methods, shown as an extremely stable persisting feature; this was explained in paper 1 by means of the dynamic projection strips. Here it is shown to have its equivalent mathematical explanation in terms of the truncated solution.

[29] Figure 6 (fourth row) shows the inversion result for an extreme case of the $\lambda_{min} = \lambda_{max}/1000$. In this case even the single-station inversion indicates the bilateral character of the input model. If we further add more singular vectors, we could, in principle, resolve the input model exactly (as none of the equations in the forward problem are linearly dependent). This is so thanks to the increased space-time complexity of the single-station singular vectors that are, however, associated with very small singular values. This makes their contribution to the solution vector very vulnerable to data errors and Green's function imperfections, thus inapplicable in real applications.

[30] This above explained study of the regularization by means of the solution truncation is supplemented by the case of the weighted synthetics in the inverse problem, presented in Figure S8 in Text S1. The regularization behaves analogously. The most regularized solutions ($\lambda_{min} = \lambda_{max}/5$) are similar to the $\mathbf{G}^T\boldsymbol{d}$ plots that due to the downweighted SER station, already indicate the bilateral character of the rupture (Figure S7a). However, the spurious central asperity is even stronger.

[31] In Text S1 we also present the results for another type of regularization based on space-time smoothing, utilizing both SVD and nonnegative least squares approaches (NNLS) to invert the synthetic waveforms (see also Figure 2b). Again, the spurious asperity is present. We interpret the existence of such an artifact common to different methods as follows. Despite the regularization used, the problem to be solved shares some common features with the nonregularized (original) inverse problem. Among the most important are combinations of model parameters that most affect the comparison of seismograms (i.e., singular vectors with large singular values), and an "extended" null space (i.e., unstable part of the solution composed of singular vectors with singular values close to zero). The aim of any inversion approach is to obtain as good fit with the data as possible, providing a stable solution. Clearly, the stable part of the solution is related to the singular vectors with the largest singular values. Various methods approach the search for the stable solution in different ways. The SVD truncation eliminates the extended null space singular vectors from the solution. The smoothing constraint preserves the already smooth singular vectors because they are able to fit the seismogram part of the data vector efficiently, while it modifies the other singular vectors to fit the smoothing equations. Iterative inverse solvers (iterative deconvolution and the conjugate gradient approaches from paper 1) follow the steepest descent of the misfit, which is again given by the first singular vectors. This interpretation suggests that many methods (even those not explicitly working with the singular vectors) might provide such a biased result.

3. Application to Real Data

[32] The application is shown for the Movri Mountain earthquake, analyzed in paper 1 [see also *Gallovič et al.*, 2009; *Konstantinou et al.*, 2009; *Cesca et al.*, 2010]. Here we reconsider the problem within the framework of the regularized SVD technique. The singular vectors, in which the inverse solution is expanded, are the same as before (Figures 3 and 4). Figures 7a–7c show $\tilde{\boldsymbol{c}}$ for stations SER, ZAK, RGA, similar to the synthetic case in Figures 5a–5c. The narrow strip at SER and the broad strip at ZAK suggest the predominance of a unilateral rupture, as explained in

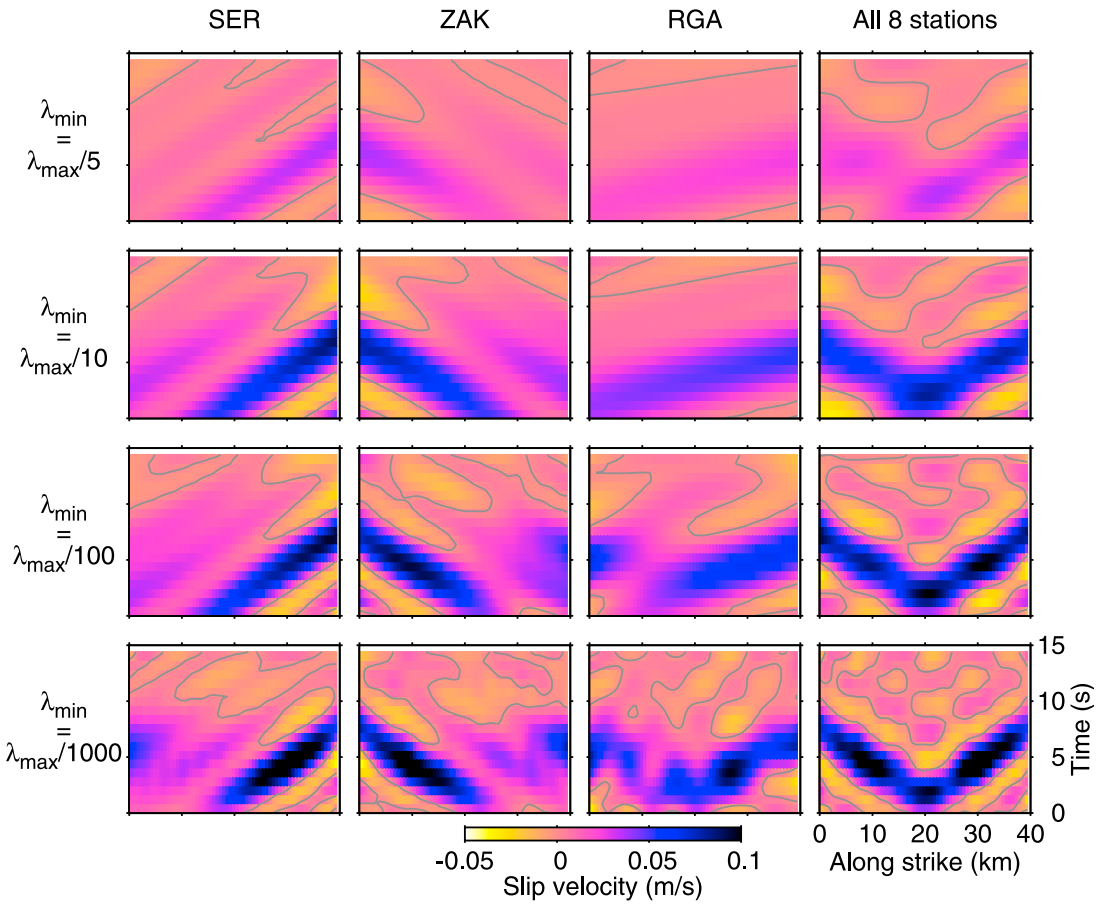

Figure 6. The truncated solutions of the slip inversion problem for the synthetic bilateral model (Figure 2a) assuming single stations (first to third columns) and the whole station network (fourth column). The x-t pattern of the inverted slip velocity model is color coded. The four rows correspond to various levels of the solution truncation, performed by zeroing singular vectors with λ smaller than given λ_{min} (see legend). The eight-station solutions in the first to third rows are characterized by an artifact, a spurious slip not existing in the input model. It is clearly demonstrated that the dominant combined effect of stations SER and ZAK, situated almost in the direction of the fault, yields the artifact. Only the weakly regularized solution (bottom right) is less affected by the artifact. Nevertheless, in practice, inevitable data errors and Green's functions imperfections prohibit the use of the weak stabilization. The artifacts cannot be easily detected since the data are fitted almost perfectly already for the first row, with a variance reduction of 0.997. Note the similarity between the strongly regularized solutions (first row) and the $\mathbf{G}^T\boldsymbol{d}$ vectors in Figure 5 (see explanation in text). Text S1 shows similar results when station weighting is considered.

paper 1. Figure 7d shows the $\tilde{\boldsymbol{c}}$ plot for the whole station network that further confirms the predominant rupture propagation. In Text S1, Figure S7b is an alternative for the case of weights applied to the station components. Figure S7b is less dominated by the unilateral trend as the closest station (SER) is downweighted with respect to the rest of the stations.

[33] Regarding the inversion, we use equation (8) (or, equivalently, equation (9)) directly employing the real data; the resolution matrix framework cannot be used as in the synthetic data case because the input model is not known. The sum in (8) or (9) is again calculated up to a given singular value λ_{min}, specified by a fraction of the maximum singular value λ_{max}. The truncated solutions for various λ_{min} employing either a single station or all stations are shown in Figure 8. In Text S1 we also present an analogous test for the case of the applied station component weights (Figure S9). Figure 8 (first and second rows) is for λ_{min} equal to $\lambda_{max}/3$ and $\lambda_{max}/5$. All the SVD solutions (both for the individual stations and all stations together) resemble the strips of $\mathbf{G}^T\boldsymbol{d}$ in Figure 7. This means that up to approximately $\lambda_{max}/5$ only the singular vectors having the highest correlation with $\tilde{\boldsymbol{c}}$ (see equation (9)) form the solution. In this way, one can already estimate from the $\mathbf{G}^T\boldsymbol{d}$ plot that the rupture predominantly propagated toward station SER. On the contrary, both $\mathbf{G}^T\boldsymbol{d}$ and the slip inversion for the ZAK station features a broader strip, separated into two substrips, suggesting two asperities. When all the stations are considered together, the unilateral rupture direction is further supported (even if the station weights are considered, see Figure S9 in Text S1).

[34] Assuming more singular vectors (up to $\lambda_{max}/9$) in the truncated solution, one can see that the coherent smooth

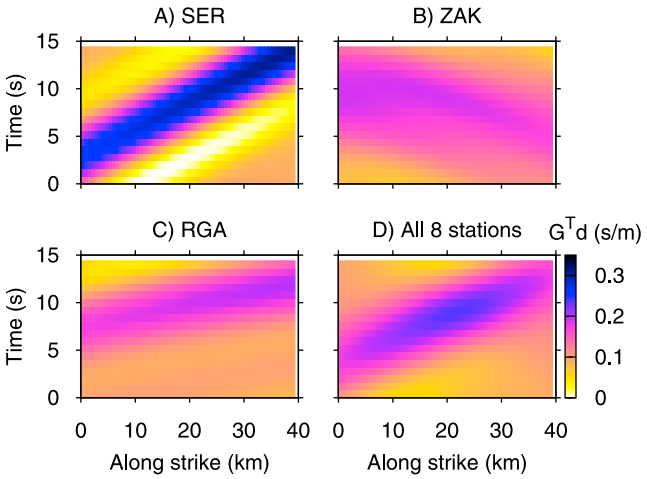

Figure 7. (a-c) The $\mathbf{G}^T\boldsymbol{d} = \tilde{\boldsymbol{c}}$ vectors as in Figure 5, but here for the real case of the Movri Mountain earthquake. (d) The mathematical counterpart of the dark spot in paper 1 is a bound within which the strongly regularized solutions will appear. The variability of the less regularized inversion results (Figure 8) will be determined by the complexity of the added singular vectors. The $\mathbf{G}^T\boldsymbol{d}$ vector for the weighted station components case is shown in Text S1; in that case the vector is less affected by station SER.

positive slip velocity areas split up (Figure 8), while the rest of the image starts being characterized by a larger amount of negative values. One can also see that the fit with the data in terms of variance reduction does not change much, from 0.679 for $\lambda_{min} = \lambda_{max}/3$ to 0.707 for $\lambda_{max}/9$. The slip velocity images for the minimum singular value smaller than $\lambda_{max}/20$ are already greatly distorted, having also large patches of negative values. This is so because the less constrained singular vectors, more vulnerable to imperfections in the synthetic Green's functions, already spoil the solution. Note that adding more singular vectors in the solution expansion cannot help as the associated errors would only be larger.

[35] To summarize, using only a few leading singular vectors, we arrive at a simple smooth model, moreover, controlled by $\mathbf{G}^T\boldsymbol{d}$. Further details are extremely vulnerable to data imperfections in terms of noise and/or improper crustal model, and thus depend on the minimization approach taken. A good example of such an uncertain detail is the indication of partial rupture propagation to the southwest (from 10 to 0 km, between 5 and 10 s). It is expressed by a larger slip velocity patch in Figure 8 (bottom right) (or, better, for the case of applied weights in Text S1 in Figure S9, $\lambda_{min} = 1/7 \ldots 1/20\lambda_{max}$). Note that the possibly asymmetric bilateral character of the rupture was suggested by other authors [*Konstantinou et al.*, 2009; *Cesca et al.*, 2010]. Our study seems to explain their finding but, at same time, warns that this might only be an artifact of the regularized solution. Similarly, the present study suggests that the split of the main asperity in space and time for the Movri Mountain earthquake obtained by the conjugate gradient technique [*Gallovič et al.*, 2009] and the equivalent solutions presented in Figure 11 of paper 1 have to be understood in the same way.

[36] Text S1 illustrates that the smoothing and/or using the NNLS approach does not help us to decide whether the Movri Mountain earthquake was an asymmetric bilateral rupture, or a predominantly unilateral rupture with a delayed central asperity. More details of the source model can be investigated only by supplementing the inversion by additional data (such as strong motion records, GPS) or additional constraints, such as hypocenter location, constant rupture velocity, etc. [*Dreger and Kaverina*, 2000]. However, as the data are insensitive to further details of the slip model, the (often uncertain) constraints would take over the inversion and the "refined" slip image would be determined by the constraints themselves. This limitation has not yet been broadly recognized in practical slip inversions.

4. Discussion and Conclusions

[37] The linear slip inversion is an unstable problem. Typically, it is stabilized by supplementing nonlinear constraints, such as positivity and/or spatial-temporal smoothing. This paper shows that many features of the slip inversion can already be understood in the linear formulation, i.e., where the singular value decomposition (SVD) is applicable. The SVD technique enables understanding issues such as instability, smoothing, trade-off and artifacts.

[38] The SVD creates a basis system in the model space in terms of the eigenvectors of matrix $\mathbf{G}^T\mathbf{G}$ (also called singular vectors). Each singular vector is supplemented by its singular value λ expressing the sensitivity of the data to changes along the corresponding singular vector in the model space. The inverse solution can be expressed as a sum of the singular vectors with weights proportional to the reciprocal of the singular values (equations (8) and (9)). We assume that the singular vectors are sorted according to their respective singular values in descending order. Starting with the analysis of singular vectors for individual stations, the first singular vectors are shown to have the character of smooth inclined strips with angles given by the station azimuths with respect to the fault strike. When the whole station network is considered, more complex shapes appear, being combination of the individual station strips. Such a "low-frequency" character of the singular vectors is an advantage because, typically, synthetic Green's functions perform better in the low-frequency band. The singular vectors with lower data sensitivity (small λ) have more complex ("high-frequency") shapes, being more vulnerable to Green's function imperfections and/or noise in the data.

[39] The slip inversion is first studied on a synthetic example of a symmetric bilateral rupture. It is shown that the slip model expansion into the first singular vectors is driven by $\tilde{\boldsymbol{c}} = \mathbf{G}^T\boldsymbol{d}$. This quantity is closely related to the so-called dynamic projection strips (DPSs) introduced in paper 1 as an extension of the projection line concept of seismic source tomography. DPSs were intended as a practical tool to identify the individual station contributions to the slip inversion, constructed by means of the "signal detector," i.e., a computational tool analyzing the correlation between complete observed waveforms and partial synthetics due to trial point sources. The present paper provides a mathematical explanation why the DPSs (i.e., $\tilde{\boldsymbol{c}} = \mathbf{G}^T\boldsymbol{d}$) control the inversion.

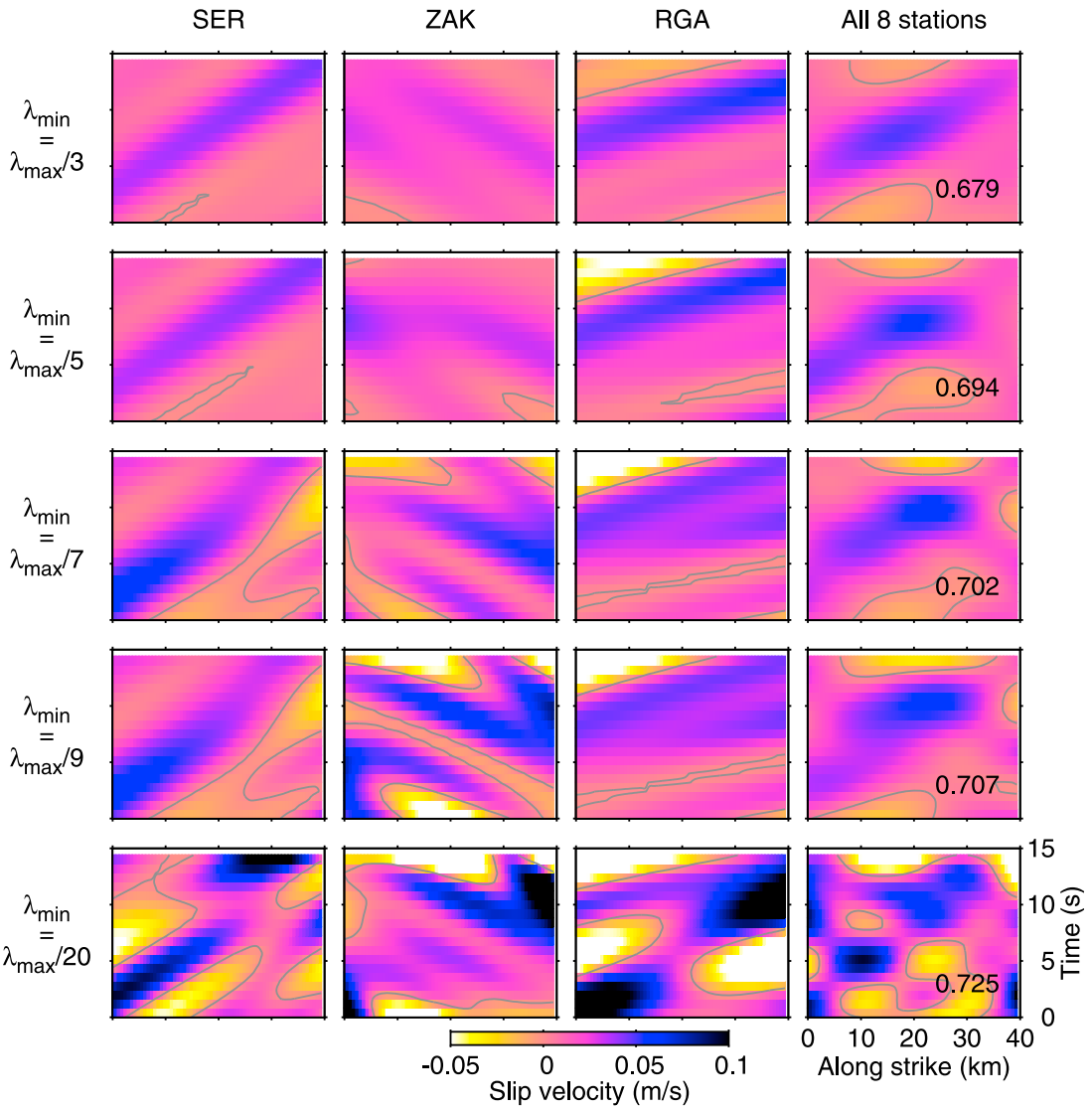

Figure 8. The truncated solutions (the slip velocity pattern) as in Figure 6 but here for the real case of the Movri Mountain earthquake. According to equation (9), the $\mathbf{G}^T\boldsymbol{d}$ vector of Figure 7, combined with progressively more complex singular vectors (i.e., with decreasing λ), increases the complexity of the slip model. Note that the slip velocity model in the fifth row (with the saturated color scale) is largely distorted. Adding more singular vectors would result in a completely "random" (unphysical) pattern due to the imperfections of the Green's functions employed. The numbers in the fourth column are the respective variance reductions. In Text S1 we show analogous results for the case of the weighting of the station components. That case (when the forward directive station SER is downweighted) weakly indicates a possibility of the rupture propagation also in the opposite direction (from 10 km at 5 s to 0 km at 8 s).

[40] When inverting waveforms for the slip velocity image, the sum over singular vectors is truncated, preserving only the so-called leading singular vectors. Keeping only a few leading singular vectors works seemingly as smoothing due to the smooth character of the singular vectors themselves. However, such regularizations (although providing a stable solution) may also have a negative effect on the inversion. For example, a symmetric bilateral rupture with a small amount of slip at the hypocenter is erroneously imaged as having a strong asperity at the hypocenter. Thus, the truncated solution not only limits the resolution, but in some problems even simple and stable structures in the parameter space may differ from the true ones. Note that this does not mean that the stable structures are incorrect. It is a correct part of the solution of the inverse problem, however, it is an incomplete representation (approximation) of the true solution.

[41] The spurious asperity artifact was previously described in paper 1, using two other inversion approaches including nonlinear constraints of positivity. In paper 1 the artifact was explained in terms of the DPSs. Here we interpret the effect as follows: The data fitting procedure implicitly starts by changing the parameters related to the largest singular values as they control the data fit most efficiently. This represents a stable part of the inverse problem. The inversion techniques then "move" along the

poorly constrained singular vectors. This is the unstable part, sensitive to inappropriate crustal models, noise in the data and the particular inversion approach, providing different (biased) details for different inversions. However, as shown in section 2.4, the dangerous artifacts may already arise in the most stable part, related to the largest singular values, when the singular vectors of small singular values are discarded from the solution.

[42] This is the reason why such artifacts are very persistent and difficult to recognize and/or remove. They are common to many inversion methods including those not explicitly working with the singular vectors at all. For example, Text S1 shows that for reasonable choices of the weight of the smoothing constraint in the inversion results in the same artifact as above even if the nonnegativity constraint is applied (see also Figure 2b). This is so because the first singular vectors are both smooth and also able to fit the seismogram part of the data, thus they are inverted as if without the smoothing constraint. The other singular vectors are modified and then used in the inversion to satisfy the smoothing equations only (having a small effect on the seismogram fit).

[43] Besides the slip artifact, the synthetic tests of paper 1 revealed a biased rupture velocity common to independent methods, mainly in the bilateral rupture model. The biased velocity can also be explained in terms of the solution truncation; the apparent rupture velocity is given predominantly by the inclined strips of the leading singular vectors controlled by the individual stations. That bias, common to different methods, is again nothing but the stable (although incomplete) part of the solution caused by the dominance of the leading singular vectors.

[44] By incrementally adding more singular vectors in the inversion of the synthetic example, the truncated solution is brought closer to the correct solution (i.e., removing the artifacts). In practice, however, as shown on the real near-regional data of the Movri Mountain earthquake, this is not practically feasible and regularization is unavoidable; the synthetic Green's functions deviate from the real ones, data contain noise; hence underregularized solutions are vulnerable to errors. In such a case the inversion would be unstable, clearly yielding unphysical source models. Therefore, the use of only a small number of singular vectors is inevitable. The opposite effect, i.e., the poor resolution of the overregularized solutions, is well known: the resulting slip pattern has no details; it is formed by a single patch or a few large patches. This paper paid attention to an additional (although related) issue that even the overregularized solution might contain artifacts and biases due to incomplete representation of the source model. This is an important practical warning against misinterpretation of stable features that look physically reasonable, but deviate from the true slip. Another lesson learned in this paper is a warning against checking resolution with a synthetic model similar to that one derived during the inversion of real data [see also *Lévêque et al.*, 1993]. Indeed, as the inverted model is already well represented by the leading singular vectors (even if the true slip is not), a synthetic test employing the same set of singular vectors will return the same model. Such result might be wrongly interpreted as a validation of the inverted image.

[45] In the presented example only the frequency range up to 0.2 Hz was considered. It is, therefore, important to discuss what happens when one uses a broader frequency range in the inversion (e.g., up to 1 Hz) and the same near-regional data. Again, as the singular values decrease, the singular vectors appear more and more similar to checkerboards. In the x-t plots, the size of the single cells can be related to a characteristic frequency and a characteristic wave number, which both generally increase as the singular values decrease. The leading singular vectors for the individual stations again have the strip character. However, in the case of considering the frequency range up to 1 Hz, the strips range from broad (such as those for $f < 0.2$ Hz) to very narrow ones. Furthermore, the associated singular values decay less quickly, thus with the same threshold $\lambda(M')$ we use a larger number of singular vectors, $M'' > M'$. Not surprisingly, when the associated singular vectors are employed in the inversion of synthetic data, the resulting slip image is sharper, reflecting the use of singular vectors with narrow strips. On the other hand, when the same singular vectors are used to invert real data, the resulting slip image does not change much (compared to $f < 0.2$ Hz). This can be explained by the effect of $\boldsymbol{U}(i) \cdot \boldsymbol{d}$ in the truncated solution sum (equation (8)). Indeed, the normalized seismograms $\boldsymbol{U}(i)$ (see equation (6)) corresponding to the singular vectors characterized by narrow strips are of a high-frequency character, and due to the crustal model imperfections, the scalar product of $\boldsymbol{U}(i)$ with the data vector d is very low, i.e., the contribution of such a singular vector in the inversion is "negligible." Note that this is not the case for the "high-frequency" singular vectors with low singular values ($>M''$) because although their $\boldsymbol{U}(i) \cdot \boldsymbol{d}$ are again low, the incorrect values of $\boldsymbol{U}(i) \cdot \boldsymbol{d}$ are amplified by the large reciprocal of their small singular values (see equation (8)), so these produce a kind of instable "high-frequency noise" in the inverted slip image. To conclude, the instabilities of the inversion take place, from the perspective of the linear SVD inversion, when taking into account singular vectors of small singular values with high-frequency $\boldsymbol{U}(i)$ being incorrect due to improper Green's functions, independently of the frequency range considered.

[46] Smooth model controlled only by the leading singular vectors (and by the $\tilde{\boldsymbol{c}}$ vector) can be inferred. Nevertheless, when properly understood, it already provides valuable information about the major features of the slip process. It bears an important piece of information about the predominant rupture direction, a possible delay of the major slip process with respect to origin time, etc. However, the proper understanding of the roles of the individual stations, possible biases, artifacts, and tradeoffs is required. This can be gained from parallel studies of the singular vectors of the inversion problem for a station network and for a suite of single-station problems. The highly regularized model can be understood as an important intermediate step between the centroid determination and a more advanced slip inversion. In the advanced slip inversion one can add additional data, e.g., strong motion records and/or GPS [*Page et al.*, 2009], which help correct biases in the slip model. If additional data are not available, physical constraints such as the hypocentral position and rupture velocity can be added, typically making the inversion nonlinear [*Dreger and Kaverina*, 2000]. However, one has to bear in mind that the resulting

finer details of the solution might then be forced by the constraints themselves, not always being sufficiently dictated by the data (i.e., being only allowed by them). Indeed, incorrect constraints (e.g., inaccurate hypocenter position) might bias the slip inversion, too.

[47] To give an example of how the singular vector analysis can be used to anticipate possible bias due to improper station coverage (e.g., the bias of the rupture speed and/or the presence of artifacts), let us discuss the role of station weights in the inversion. Nearby stations are typically characterized by larger amplitudes than the more distant stations. This causes the first leading singular vectors (for the whole station network) to be composed of those associated with the nearest station considered (SER in our case). This can be called implicit weighting. Thus, the inversion tends to first fit this station, which, however, leads to a bias of the inverted model (unilateral rupture propagation toward SER, see Figure 6, first row) because the problem is similar to a single-station inversion. Contrarily, weakening the SER station effect in the inversion (as in Text S1) leads to a less biased result (Figure S8) because now the leading singular vectors already contain information even from stations lying in the opposite direction from the fault. From a practical point of view, this only warns against implicit weighting in the inversion, which can bias the solution considerably. Therefore, at least some down-weighting of the closest station is always desirable. Of course, station weighting has to be done cautiously to avoid enhancing distant stations with less constrained Green's functions too much.

[48] Another example refers to the issue of improper azimuthal coverage. Figure 3 indicates that for example, if all stations had a similar azimuth, the singular vectors would all be elongated in the same direction. The patches would then not arise, x would strongly tradeoff with t, and the finite x-t structures could not be resolved. In simple words, the performance of the inversion depends on how well can the true slip distribution be expanded into the first eigenvectors of $\mathbf{G}^T\mathbf{G}$. Interpreters have to be aware of the spurious effects that might appear, as they are difficult to detect in the results. The bias caused can be learned from SVD and/or dynamic projection strip analysis of the synthetic inversion tests.

[49] Finally, let us emphasize again that all the ideas about singular vectors and their roles in the inversion are valid for many inversion schemes, i.e., even those that do not explicitly work with the singular vectors at all. We also point out that our discussion is not to be generalized to all types of artifacts. Here we have discussed only artifacts common to several inversion methods. Different regularization methods may yield additional different artifacts. However, as they differ across the methods, they are less dangerous, being easier to recognize.

[50] **Acknowledgments.** The authors greatly appreciate the free Internet access of waveforms provided by NOA (THL) and ITSAK (stations ZAK, KAL). The remaining stations (RGA, MAM, SER, LTK, PYL) belong to the PSLNET network, cooperated by the Charles University. We thank G. Festa and an anonymous reviewer for their valuable comments that significantly improved the manuscript. Financial support from GAUK14509, GACR 205/08/P013 and 210/11/0854, MSM0021620860.

References

Aki, K., and P. G. Richards (2002), *Quantitative Seismology*, Univ. Sci., Sausalito, Calif.

Bouchon, M. (1981), A simple method to calculate Green's functions for elastic layered media, *Bull. Seismol. Soc. Am.*, *71*, 959–971.

Cesca, S., S. Heimann, and T. Dahm (2010), Rapid directivity detection by azimuthal amplitude spectra inversion, *J. Seismol.*, *15*, 147–164, doi:10.1007/s10950-010-9217-4.

Coutant, O. (1989), Program of numerical simulation AXITRA, research report, Lab. de Geophys. Interne et Tectonophys., Grenoble, France.

Das, S., R. Suhadolc, and B. V. Kostrov (1996), Realistic inversions to obtain gross properties of the earthquake faulting process, *Tectonophysics*, *261*, 165–177.

Dreger, D., and A. Kaverina (2000), Seismic remote sensing for the earthquake source process and near-source strong shaking: A case study of the October 16, 1999 Hector Mine earthquake, *Geophys. Res. Lett.*, *27*, 1941–1944.

Gallovič, F., J. Zahradník, D. Křížová, V. Plicka, E. Sokos, A. Serpetsidaki, and G-A. Tselentis (2009), From earthquake centroid to spatial-temporal rupture evolution: Mw 6.3 Movri Mountain earthquake, June 8, 2008, Greece, *Geophys. Res. Lett.*, *36*, L21310, doi:10.1029/2009GL040283.

Hartzell, S. H., and T. H. Heaton (1983), Inversion of strong ground motion and teleseismic waveform data for the fault rupture history of the 1979 Imperial Valley, California earthquake, *Bull. Seismol. Soc. Am.*, *73*, 1553–1583.

Haslinger, F., E. Kissling, J. Ansorge, D. Hatzfeld, E. Papadimitriou, V. Karakostas, K. Makropoulos, H.-G. Kahle, and Y. Peter (1999), 3D crustal structure from local earthquake tomography around the Gulf of Arta (Ionian region, NW Greece), *Tectonophysics*, *304*, 201–218.

Konstantinou, K. I., N. S. Melis, S.-J. Lee, C. P. Evangelidis, and K. Boukouras (2009), Rupture process and aftershocks relocation of the 8 June 2008 Mw 6.4 earthquake in northwest Peloponnese, western Greece, *Bull. Seismol. Soc. Am.*, *99*, 3374–3389.

Lawson, C. L., and R. J. Hanson (1974), *Solving Least Square Problems*, 340 pp., Prentice-Hall, Englewood Cliffs, N. J.

Lévêque, J.-J., L. Rivera, and G. Wittlinger (1993), On the use of the checker-board test to assess the resolution of tomographic inversions, *Geophys. J. Int.*, *115*, 313–318.

Menke, W. (1985), Imaging fault slip using teleseismic waveforms: Analysis of a typical incomplete tomography problem, *Geophys. J. R. Astron. Soc.*, *81*, 197–204.

Monelli, D., and P. M. Mai (2008), Bayesian inference of kinematic earthquake rupture parameters through fitting of strong motion data, *Geophys. J. Int.*, *173*, 220–232.

Olson, A. H., and R. J. Apsel (1982), Finite faults and inverse theory with applications to the 1979 Imperial Valley earthquake, *Bull. Seismol. Soc. Am.*, *72*, 1969–2001.

Page, M. T., S. Custódio, R. J. Archuleta, and J. M. Carlson (2009), Constraining earthquake source inversions with GPS data: 1. Resolution-based removal of artifacts, *J. Geophys. Res.*, *114*, B01314, doi:10.1029/2007JB005449.

Press, W. H., B. P. Flannery, S. A. Teukolsky, and W. T. Vetterling (1992), *Numerical Recipes in Fortran, The Art of Scientific Computing*, 2nd ed., Cambridge Univ. Press, New York.

Ruff, L. J. (1984), Tomographic imaging of the earthquake rupture process, *Geophys. Res. Lett.*, *11*, 629–632.

Sekiguchi, H., K. Irikura, and T. Iwata (2000), Fault geometry at the rupture termination of the 1995 Hyogo-ken Nanbu earthquake, *Bull. Seismol. Soc. Am.*, *90*, 117–133.

Sokos, E., and J. Zahradník (2008), ISOLA A FORTRAN code and a Matlab GUI to perform multiple-point source inversion of seismic data, *Comput. Geosci.*, *34*, 967–977.

Zahradník, J., and F. Gallovič (2010), Toward understanding slip inversion uncertainty and artifacts, *J. Geophys. Res.*, *115*, B09310, doi:10.1029/2010JB007414.

F. Gallovič and J. Zahradník, Department of Geophysics, Faculty of Mathematics and Physics, Charles University, V Holešovičkách 2, Prague 8, 180 00, Czech Republic. (gallovic@karel.troja.mff.cuni.cz)

[P12]

Complexity of the Mw 6.3 2009 L'Aquila (central Italy) earthquake: 1. Multiple finite-extent source inversion

F. Gallovič[1] and J. Zahradník[1]

Received 28 July 2011; revised 20 February 2012; accepted 26 February 2012; published 19 April 2012.

[1] Strong ground motion recordings of the Mw 6.3 2009 L'Aquila earthquake are analyzed by a newly proposed slip inversion technique. The source model consists of Multiple Finite-Extent (MuFEx) subsources. The slip amplitude, rupture velocity, rake and risetime are assumed constant within each subsource. The size and location of the MuFEx subsources have to be inferred independently from other methods, preferably those free of strong constraints (such as constant rupture velocity over the whole fault, etc); here we use two published approaches satisfying such requirement: the truncated singular value decomposition and the iterative multiple-point source deconvolution. Each MuFEx subsource is characterized by an individual set of trial nucleation points, rupture velocities and nucleation times, which are grid-searched. For each combination of these parameters, the subsources' slip is determined by the least squares approach. This procedure thus provides not only the best fitting model, but also a whole range of acceptable models, allowing for the uncertainty analysis. The method is demonstrated on three synthetic tests. When applied to the L'Aquila data, both the best fitting model and the uncertainty analysis suggest that the event consisted of two major episodes, one with the rupture propagating immediately after the nucleation in the updip direction, the other being delayed by 3–4 s with dominant propagation toward the SE along the deeper part of the fault. The retrieved complexity of the rupture propagation warns against attempts to stabilize inversions by the use of a constant rupture velocity over the whole fault.

Citation: Gallovič, F., and J. Zahradník (2012), Complexity of the Mw 6.3 2009 L'Aquila (central Italy) earthquake: 1. Multiple finite-extent source inversion, *J. Geophys. Res.*, *117*, B04307, doi:10.1029/2011JB008709.

1. Introduction

[2] On 2009 April 6th at 01:32 UTC the town of L'Aquila in the Central Apennines (Italy) was hit by a Mw 6.3 earthquake (Figure 1). The earthquake occurred on a normal fault striking 140° along the Apennines dipping at 50°. The event caused nearly 300 casualties and heavy damage in L'Aquila town and several other villages *Ameri et al.* [2009]. The earthquake source process was a subject of many studies utilizing various data and approaches [*D'Amico et al.*, 2010; *Maercklin et al.*, 2011; *Walters et al.*, 2009; *Herrmann et al.*, 2011].

[3] In particular, to invert for the earthquake slip model *Cirella et al.* [2009] used the two-stage nonlinear technique by *Piatanesi et al.* [2007], utilizing both strong motion records and geodetic data. They observed anisotropic rupture propagation (faster in the updip direction and slower along the strike) and two major slip patches. Similarly, *D'Amico et al.* [2010], using back-projection, identified two slip patches, the one in the SE being delayed and of smaller amplitude than the one close to the hypocenter. In the inversion by *Scognamiglio et al.* [2010] a constant rupture velocity was assumed and two distinct best fitting models were found: for the faster velocity a few slip patches were found at shallow depths, while for the slower velocity the main slip patch was located further SE along the strike and at greater depths.

[4] These results suggest that the earthquake rupture propagation was complex. However, slip inversions are highly non-unique inverse problems, which depend strongly on the imposed constraints (such as constant rupture velocity and/or smoothing) [*Lay et al.*, 2010; *Zahradník and Gallovič*, 2010]. Different slip inversions of even the same event provide different models [*Clévédé et al.*, 2004], some of them being characterized by rupture evolution complexities, and some not. Therefore, there is a need to develop inversion techniques that provide not only the best fitting model, but also some uncertainty estimate. The uncertainty analysis of the slip inversion result is a challenging task, still being often neglected.

[5] Nevertheless, several methods of estimating the slip inversion uncertainties have been proposed [*Hartzell et al.*, 2007; *Piatanesi et al.*, 2007; *Emolo and Zollo*, 2005; *Cirella et al.*, 2008; *Monelli and Mai*, 2008]; for a brief

[1]Faculty of Mathematics and Physics, Department of Geophysics, Charles University, Prague, Czech Republic.

0148-0227/12/2011JB008709

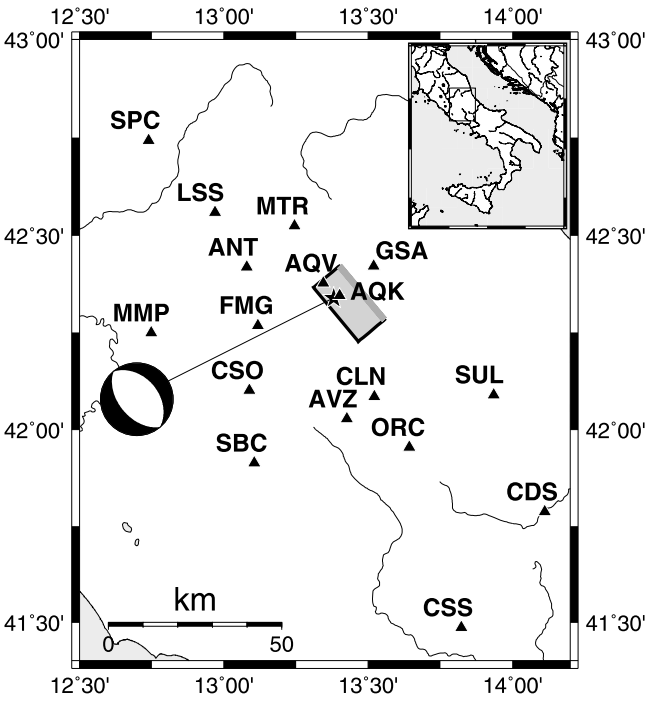

Figure 1. The fault geometry of the L'Aquila earthquake (gray box) with a dark gray line corresponding to the top edge of the fault. Selected strong motion stations operated by INGV and the Italian Civil Protection are shown as triangles. The asterisk indicates the epicenter. The inset shows the map of Italy with the region of interest (box).

review and criticism of the approaches, see the latter reference. In particular, *Monelli et al.* [2009], performed a full Bayesian analysis of the 2000 Western Tottori (Japan) earthquake, showing poor resolution power of the strong motion and GPS data, including strong spatial trade-offs among slip parameters. Although such an approach is perhaps the most complete, it is numerically very demanding (the authors report ~40 days of computational time). Also, the inferred trade-offs among parameters make it clear that the problem is rather over-parameterized when applied to real data. This is also in agreement with the finding by *Gallovič and Zahradník* [2011], who analyzed the slip inversion by means of singular value decomposition. Indeed, they showed that only a small fraction of the singular vectors can be utilized in a real data application, which leads to strong trade-off not only among spatial, but also temporal parameters. Thus decreasing the number of model parameters in a reasonable way is advisable.

[6] To have a smaller number of model parameters, it is necessary to parameterize the rupture evolution in a simpler way, while still being able to capture the major potential complexities of the earthquake ruptures. For example, *Vallée and Bouchon* [2004] introduced a patch model consisting of two adjacent ellipsoidal slip regions over which the rupture propagates at two generally different constant rupture velocities. The authors used a neighborhood algorithm to invert for the position and size of the ellipses and the respective rupture velocity values. The algorithm then provided not only the best fitting source model, but also some estimate of the model uncertainty. However, their parameterization prohibited such features as the rupture delay, rupture jumps, etc.

[7] To allow a more general rupture behavior, while still keeping the number of parameters low, we introduce a new inversion technique called the Multiple Finite-Extent (MuFEx) source model. The MuFEx model describes the earthquake rupture as a composition of slip on a few subsources (asperities/regions of slip). The slip amplitude, rupture velocity, rake and risetime are assumed constant within each subsource. The size and location of the subsources are a priori estimated (i.e., they are inferred independently by other methods). In particular, here we use the recently introduced approach based on the Truncated Singular Value Decomposition (TSVD) technique by *Gallovič and Zahradník* [2011] and the iterative deconvolution of multiple point sources (ISOLA package) by *Sokos and Zahradník* [2008]. Prescribing the dimensions and locations of the MuFEx subsources, the source parameters that the MuFEx inverts for are four at each subsource: the slip amplitude, nucleation point, rupture velocity, and nucleation time. Assuming an individual set of trial nucleation positions, rupture velocities and nucleation times for each subsource, we apply a grid-search procedure over all combinations of these parameters, while simultaneously solving a linear L2 inversion for the slip value. In this way, we obtain not only the best fitting model, but the whole family of plausible models that can be used for uncertainty analysis. Figure 2 demonstrates the approach by a flowchart.

[8] After explaining the MuFEx source model inversion, we apply the procedures to the real L'Aquila data following the MuFEx flowchart (Figure 2). We show that, although the earthquake was recorded with an excellent station distribution, the non-uniqueness of the inversion is expressed by relatively large uncertainties of the MuFEx source parameters. Nevertheless, some model features are shown to be robust, best demonstrated by comparison of the MuFEx results obtained for two alternative setups suggested by the preceding TSVD and ISOLA analysis. In the companion paper [*Ameri et al.*, 2012] we use the robust (major) characteristics of the retrieved model to constrain the modeling of strong ground motions in a broad frequency range (0.1–10 Hz), showing that these source characteristics are one of the most important pieces of information needed for strong ground motion modeling. The performance of the MuFEx source inversion is also demonstrated on three synthetic tests (assuming the fault and station geometry of the real L'Aquila earthquake), one of them being presented in Appendix A, the other two in the auxiliary material.[1]

2. Data and Green's Functions

[9] The L'Aquila earthquake provided the largest high-quality near-fault strong motion data set ever recorded in Italy for such a major event. Accelerograms recorded at 17 stations (Figure 1) are band-pass filtered between 0.06 and 0.3 Hz and double integrated to obtain ground displacement time histories. The high-pass filtering at 0.06 Hz is applied due to the long-period noise. Green's functions are

[1]Auxiliary materials are available in the HTML. doi:10.1029/2011JB008709.

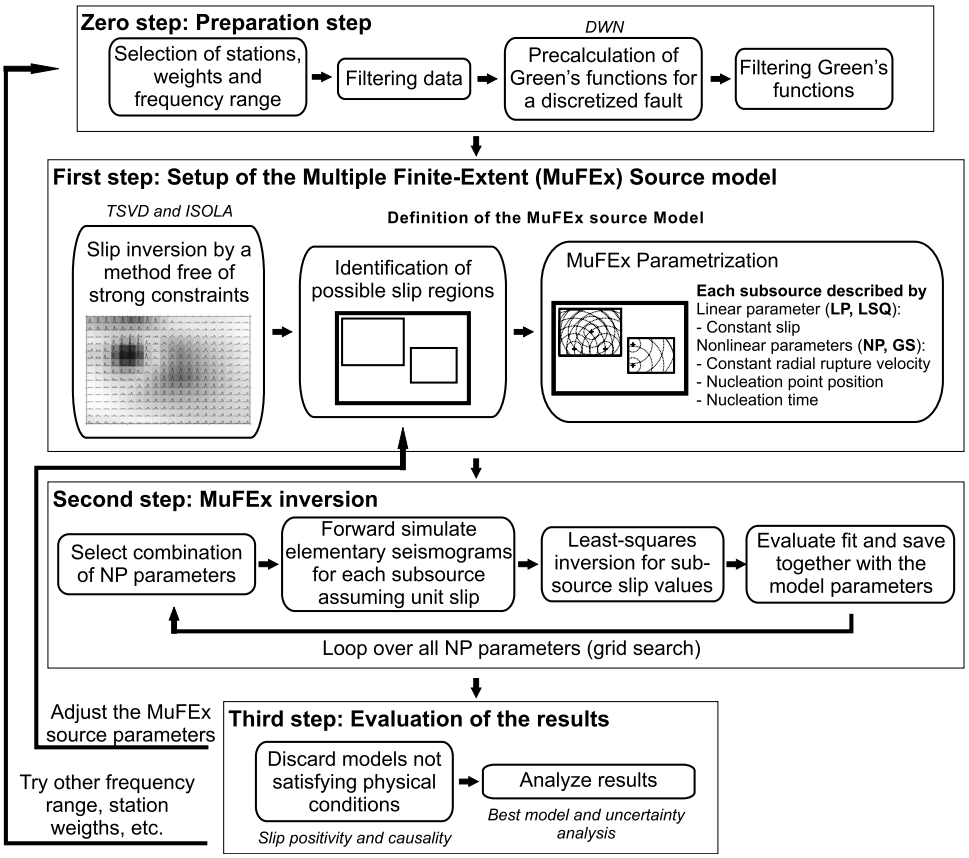

Figure 2. Flowchart of the proposed slip inversion approach. Notes in italics represent our particular choices. DWN denotes the Discrete Wave number approach. LSQ and GS denote whether the respective parameters are inverted by means of least squares approach or grid search, respectively.

calculated using the discrete wave number technique [*Bouchon*, 1981] in a 1D layered model (see the companion paper *Ameri et al.* [2012]). This technique provides full wavefield Green's functions including the near-field terms. They are also band-pass filtered between 0.06 and 0.3 Hz. The low-pass filtering at 0.3 Hz is applied due to the incompleteness of the crustal model leading to inability to correctly model Green's functions at higher frequencies. Moreover, in the frequency range considered, Green's functions are not very sensitive to the crustal model. No station weights according to epicentral distances and/or amplitudes were applied. For each waveform, we invert the complete wavefield of 100 s duration. Note that the same processing was applied in the synthetic tests.

3. Method

[10] The characterization of an earthquake rupture as a sequence of finite-extent subsources is not new. The Multiple Finite-Extent (MuFEx) source model results from the following reasoning. Generally, effects of the earthquake source finiteness are present in the wavefield at all distances and frequencies. However, under some conditions, these effects become negligible, allowing for simplification of the earthquake source description. At very low frequencies and distances much larger than the fault size, a finite-extent earthquake source can be approximated by a point source (centroid). Increasing the frequency range (and/or decreasing the source distance), finite-extent characteristics start to be apparent in the wavefield; thus, e.g., second-order seismic moments might be retrieved [*Backus*, 1977; *Adamová and Šílený*, 2010]. This means that the source can be approximated by a finite fault with constant slip and simple (radial) rupture propagation. Increasing the frequency range and decreasing the source distance even more (as in our case), we suppose that the earthquake can be further described by a few slip patches (finite-extent subsources). To capture possible complexities of the rupture propagation, we assume that these subsources can have their own independent nucleation points, rupture velocities and time delays. In this way, the number of estimated parameters can be held small enough so that the grid-search procedure (being best suitable for uniform exploration of a relatively small model space) can be used.

[11] The MuFEx source model has to be set up by a preliminary analysis (see the flowchart in Figure 2). In particular, the MuFEx inversion requires reasonable estimates of the number of subsources together with a reasonable estimate of their locations and dimensions. This part has to be attained by methods with no strong constraints (such as constant rupture velocity over the whole fault, etc). Here we use the Truncated Singular Value Decomposition (TSVD) and ISOLA techniques; alternatively other methods can be

used to setup the MuFEx model, e.g., based on imaging techniques [*Gallovič et al.*, 2009, and references therein].

4. Preliminary Setup of the MuFEx Subsources

[12] The Multiple Finite-Extent (MuFEx) source model requires a preliminary setup of the subsources, i.e., their number, position and dimensions. Here we show two (out of many) possible ways based on the Truncated Singular Value Decomposition (TSVD) approach and the multiple-point source deconvolution approach (ISOLA). Note that the two methods (when applied to the real L'Aquila records) result in somewhat different subsource setups. However, when using the two setups, the results remain similar, which indicates that the MuFEx inversions yield robust results (see further).

[13] ISOLA (from 'ISOLated Asperities') is a program package based on a multiple point-source iterative deconvolution of complete low-frequency waveforms. The moment tensor is solved by the least squares method, while the position and origin time of the point sources is grid searched [*Sokos and Zahradník*, 2008]. Besides routine application in the seismic service of the University of Patras, Greece, the method proved useful in a number of earthquake studies [e.g., *Zahradník et al.*, 2008, and references therein]. Finite-extent source applications of ISOLA work with no constraints on the rupture velocity and the nucleation point [*Zahradník and Gallovič*, 2010; *Gallovič et al.*, 2009]. In the application of this paper the multiple point-sources have a pure double-couple mechanism prescribed by the strike, dip and rake angles.

[14] The TSVD method needs a more detailed explanation here as it has been introduced very recently. *Gallovič and Zahradník* [2011] used this approach to study the performance of slip inversions, mostly to explain the non-uniqueness of the slip inversion and the nature of possible artifacts [see also *Zahradník and Gallovič*, 2010]. Equivalently, instead of "artifact" we use term "bias of the solution" against the true one. The approach was demonstrated for a line fault; however, its formal generalization to rectangular faults is straightforward.

[15] The TSVD inversion is based on a linear formulation utilizing the discretized version of the representation theorem [*Aki and Richards*, 2002]. We assume the slip velocity time history without any constraints, only that it has a finite duration (namely 10 s in the present applications). Thus, only the fault geometry and source duration are prescribed; the rupture propagation and shape of the slip velocity functions are not constrained. The slip can occur anywhere on the fault and anytime during the given source duration.

[16] The samples of the slip velocity time history (in time and space over the discretized fault) compose the model parameters vector $\boldsymbol{m}$. This vector is linearly related

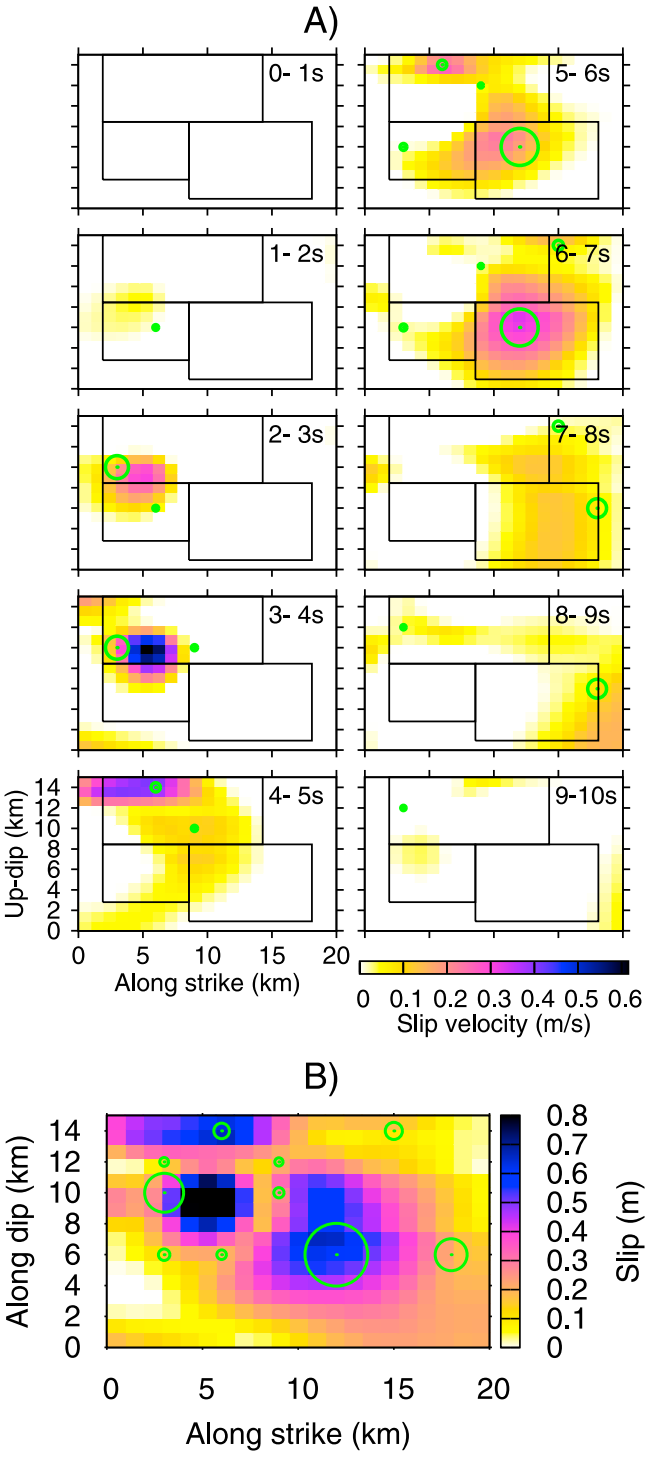

Figure 3. Setting up the MuFEx source model for the L'Aquila earthquake. (a) Rupture evolution snapshots obtained by the TSVD technique with truncation at 1/10 of the largest singular value. The fit with seismograms (variance reduction VR = 0.77) is shown in Figure 4. The areas with large slip velocities (see the color scale of the snapshots) are used for the preliminary setup of the MuFEx subsources (Figure 5a). Their final positions (rectangles) are constrained by trial-and-error to obtain reasonable fit with the observed data. The multiple point source (ISOLA) inversion is marked by green circles proportional to the moment (the largest circle corresponding to 6.6×10^{17} Nm, VR = 0.62). (b) Final slip model obtained by the TSVD inversion of the observed records of the L'Aquila earthquake. Note that the final slip is presumably highly biased (due to the TSVD truncation and the limited frequency range) as suggested by synthetic tests. Thus, the model has to be re-analyzed in terms of the MuFEx model.

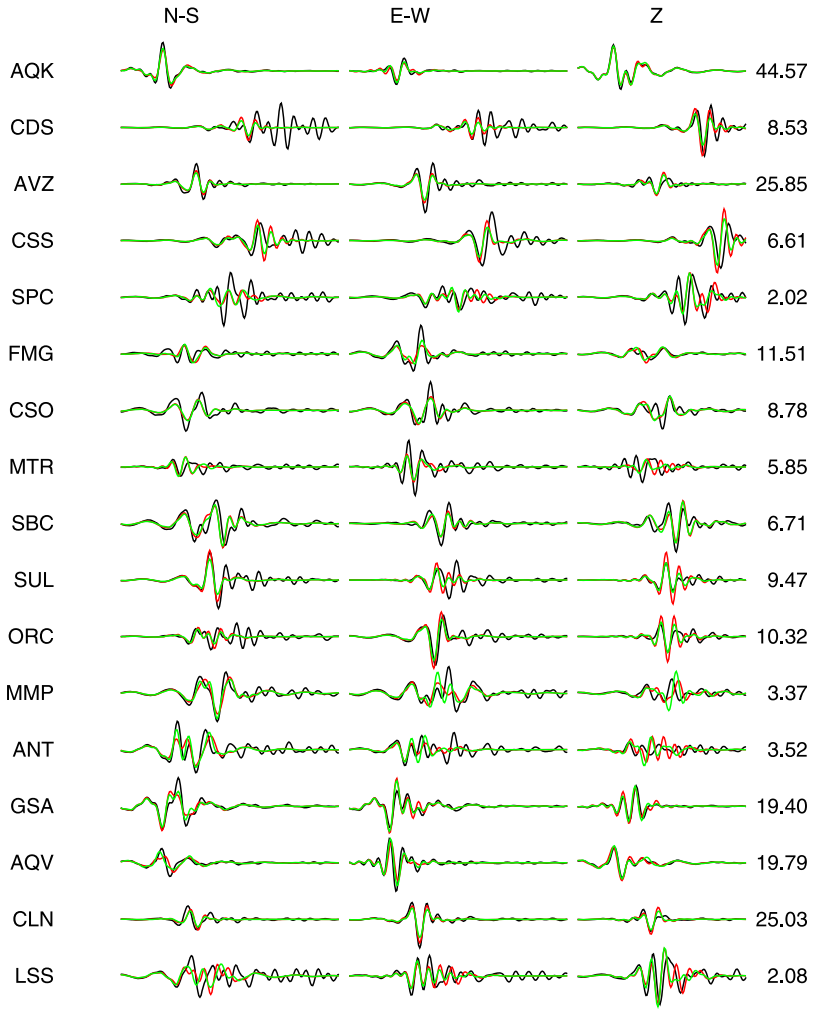

Figure 4. Comparison between observed (black) and synthetic displacements for the L'Aquila event (green for the TSVD approach, red for the best fitting MuFEx model shown in Figure 5a). The records are band-pass filtered in the range of 0.06–0.30 Hz and have a duration of 100 s. The maximum amplitudes of the observed records in mm are shown as numbers.

with the vector of seismogram samples $\boldsymbol{d}$ via matrix $\mathbf{G}$ containing the appropriate Green's functions [*Gallovič and Zahradník*, 2011]. Note that this formulation is equivalent to that of the commonly used multitime window method [*Sekiguchi et al.*, 2000] if the latter is used under relatively nonstandard conditions: number of time windows equal to one, duration of the time window equal to the entire duration of the event, and the time window at any point on the fault opens at the origin time of the earthquake. A similar approach, formulated in the frequency domain, was used for synthetic slip inversion tests by *Olson and Anderson* [1988]. In the present application of the TSVD method, the 20 × 15 km rectangular fault is discretized by 21 × 16 points. As data we use seismograms 102.4 s long, sampled at 0.4 s. The same sampling rate applies also to the slip velocity time windows (i.e., 10 s consists of 25 samples).

[17] The positivity constraint on the slip velocity is applied using the NNLS approach [*Lawson and Hanson*, 1974]. To regularize the solution, only the leading singular vectors are used which leads to the so-called truncated SVD solution. To be able to truncate while using NNLS, the augmented matrix approach is used [*Olson and Apsel*, 1982]. A new set of equations is thus added to the problem, zeroing the contribution from the truncated singular vectors in the solution.

[18] Similarly to *Gallovič and Zahradník* [2011] in the application to the 2008 Mw 6.3 Movri Mountain, Greece, earthquake, we found that the leading singular vectors (composing the final solution) are smooth functions of time and space, thus no additional smoothing is required. These vectors thus not only yield a stable solution, but they are also not very sensitive to the uncertainties in Green's functions in the investigated frequency range. Generally speaking, the success of the inversions depends on how well the true (unknown) slip model can be decomposed into the leading singular vectors. Thus it is important to have the singular vectors with a 'rich' space-time pattern; this happens, e.g., with a good station azimuthal coverage. *Gallovič and Zahradník* [2011] also showed that, if relatively strong truncation is applied (as in our case), the inversion result is close to the so-called dark spot introduced in the paper by

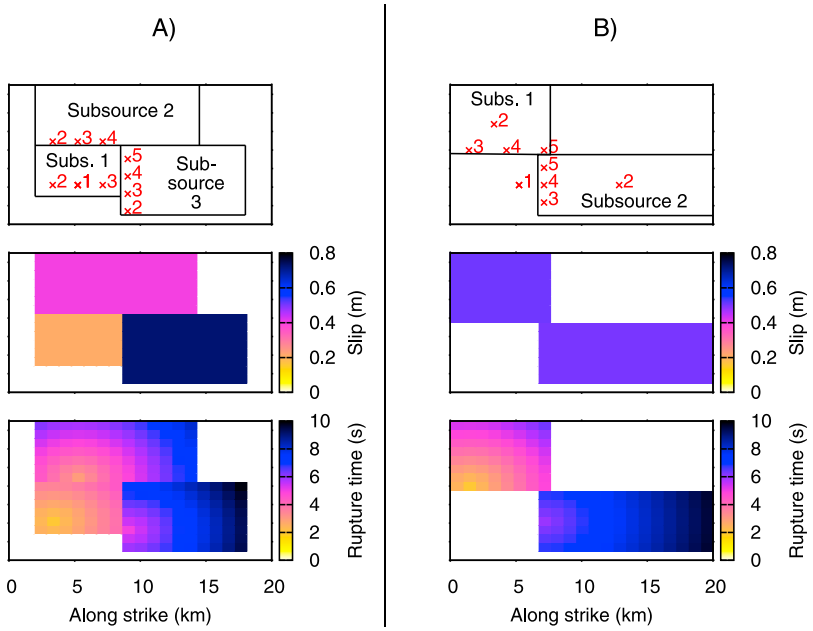

Figure 5. (a) Best fitting MuFEx model of the L'Aquila earthquake (VR = 0.72, see Figure 4). The top panel shows the subsources of the MuFEx model as obtained from the TSVD preliminary inversion (see Figure 3) and subsequent tuning by trial-and-error to obtain the best fit with the data. The numbered crosses represent trial nucleation points of the subsources. These are different for the different subsources, except for trial nucleation point #1 (corresponding to the published hypocenter location) common to all the subsources. The middle and bottom panels show the best fitting (grid-searched) MuFEx source model in terms of the final slip (assumed to be constant on the subsources) and rupture times (assuming a constant rupture velocity on each subsource), respectively. (b) Same as Figure 5a, but for an alternative setup of the MuFEx model (VR = 0.63), based on the ISOLA inversion (see green circles in Figure 3). Note the time delay of the bottom right subsource obtained independently of different MuFEx source setups. Furthermore, for both setups the seismic moment of the bottom asperity is close to 2e18Nm.

Zahradník and Gallovič [2010]. The dark spot shows areas in time and space (over the fault) whose 'partial' point source synthetics have a high correlation with the observed data (calculated simply as $\mathbf{G}^{\mathrm{T}}\boldsymbol{d}$). Thus, the dark spot, on the one hand, contains all the asperities of the true model, while, on the other hand, the intensity of the dark spot may not correspond well to the significance of the asperity. This also results in the artifacts analyzed in those studies.

[19] Figure 3a displays the resulting rupture snapshots from the TSVD inversion. The waveform fit is demonstrated in Figure 4. The truncation in TSVD is done at a singular value equal to 1/10 of the largest singular value. This provided what we subjectively judge to be the most complex rupture evolution without any major unphysical features such as "random" rupture occurrence on the fault. The truncation is required due to imprecise Green's functions in the real application. (Note that in the case of synthetic data, if we truncate at the machine double precision accuracy, the inversion result is almost perfect.) The truncation at 1/10 has a number of drawbacks, some of them being analyzed on three synthetic tests explained in Appendix A and the auxiliary material. A minor problem of the truncation is an analogy of the Gibbs effect, i.e., spurious oscillations ('ghosts') appear due to the use of a limited number of singular vectors. A major problem is related to strong artifacts, especially of the final slip model obtained by temporal integration of the slip velocity functions (Figure 3b). Indeed, *Gallovič and Zahradník* [2011] showed that the regularization can cause hardly detectable artifacts common to many inversion approaches. The problem is that the inversion result is not unique in principle, because only a limited number of singular vectors is used. Note that a similar conclusion was drawn by *Olson and Anderson* [1988]. Therefore, any single inversion result is insignificant. To determine the range of possible models in the TSVD method, one would have to explore all possible combinations of the unused singular vectors, which is obviously practically impossible. This leads us to introduce a more practical approach based on the MuFeX source model to alternatively obtain the uncertainty estimate.

5. MuFEx Source Inversion

[20] As there is no universal 'recipe' how to set up the MuFEx subsources, we present two alternatives in Figure 5. First let us concentrate on the setup shown in Figure 5a and Figure 3, dictated by the hypocenter position and the position of the large slip velocity values in the TSVD snapshots. Note that we prefer defining the subsources based on large slip velocity values instead of the final slip because the experience is that the latter is biased much more (see above). In the present setup, subsource 1 lies in the hypocentral area of the earthquake, subsource 2 at shallow depths, and the largest subsource 3 is located in the deeper part, further

along strike. Note that the TSVD final slip model (Figure 3b) suggests a relatively small slip for the subsource 3.

[21] The 'local' rupture on each of the MuFEx homogeneous subsources is assumed to propagate at constant velocity and radially from a nucleation point (several nucleation points are subject to the grid search). We assume several nucleation points to capture even cases in which the earthquake consisted of more than one event (e.g., a doublet). Another reason for allowing for more than a single nucleation point is that in real applications the major nucleation point (the hypocenter, obtained during kinematic location) is never free of errors. The slip velocity function at each fault point is assumed to have duration shorter than the reciprocal of the maximum frequency considered, 0.3 Hz, i.e., the risetime is arbitrary but smaller than 3.3 s. Thus the slip velocity time function is effectively a delta function in the investigated frequency range. Releasing this assumption might be a point for further studies.

[22] Eventually, each subsource is described by four parameters. Three of them – nucleation position, nucleation time, and the rupture velocity – are related nonlinearly to the wavefield. Their ranges (trial values) are selected according to the preliminary TSVD and ISOLA analysis and/or to be in reasonable physical limits. The three parameters are grid searched. The fourth parameter – slip of each subsource – is related linearly to the wavefield. Thus, for each combination (∼millions) of the subsource parameters, the slip is obtained by the least squares approach; we have checked that the least squares inversion is well-posed by inspecting the conditional number.

[23] In the present application, we tested rupture velocities between 1.5 and 3.5 km/s; the nucleation times vary between 0 and 7 s. The trial positions of the nucleation points can be seen in Figure 5a. They are different for the different subsources, except for trial nucleation point #1, corresponding to the published hypocenter location that is common to all the subsources.

[24] Grid-searching all the possible combinations of the input parameters (∼3 millions) results in an extensive database of models with quantitatively evaluated fit in terms of the variance reduction, $VR = \Sigma(obs\text{-}syn)^2/\Sigma(obs^2)$, where *obs* and *syn* denote the observed and synthetic waveforms, and the summation is over all stations, components and time samples. This database can be used to explore the uncertainty of the inverted model. To take into account only physically plausible models, grid-search results are filtered according to the following additional criteria: (1) all subsources must have positive slip, and (2) subsource 1 must originate at least 1 s before the other two subsources (if not nucleating from the common nucleation point #1).

[25] After the MuFEx model inversion is performed, the whole procedure can be repeated. Positions and/or dimensions of the subsources can be modified (including changes of the trial parameters) in order to obtain a possibly better fit with the data. Our experience is that modifications within +/−2 km do not change the results significantly in the present application.

[26] The best fitting model out of all (∼3 millions) grid-searched models is shown in Figure 5a. The rupture starts at nucleation point #2 in subsource 1. It is quickly followed by the onset of the shallow subsource 2. Later (∼5 s after the earthquake origin) subsource 3 is activated. In terms of the slip values, subsource 3 has the highest slip amplitude, which is in contradiction with the preceding TSVD analysis (see Figure 3b). This can be attributed to the different parameterizations of the TSVD and MuFEx inversions; MuFEx is much more constrained with fixed rectangular subsources, constant slip and radial rupture propagation. The fit of the TSVD and MuFEx synthetics with the observed records is shown in Figure 4. Note that the fit for the best fitting MuFEx source model is only slightly worse than for the TSVD model, although the former is much simpler than the latter. Moreover, for some station components the MuFEx source model provides an even better waveform fit than the TSVD model.

[27] Figure 6a shows the analysis of the plausible models. Each model is represented by a dot, represented by its parameter value and its VR value. This allows for studying uncertainties as a function of a threshold VR (the lowest acceptable VR). Note that only models with VR larger or equal to 95% of the best model (approximately 300 models) are shown for clarity. The plots allow the analysis of the uncertainty of the individual parameters separately. For example, regarding the rupture velocity at subsource 1, allowing only a small decrease of the fit with respect to the largest VR, almost all the tested velocity values are allowed. The uncertainty is slightly smaller for the rupture velocities at the other two subsources. The preferred values (in terms of VR) are 2 km/s, but for the deep asperity even larger values are allowed (especially for the smallest subsource 1).

[28] Thus, we can conclude that the inversion is very weakly sensitive to the actual rupture velocity inside the subsources, perhaps due to the relatively low frequency range and the source-station configuration in the present application. Note that the large uncertainty is the consequence of a strong trade-off among parameters; if a different rupture velocity is used, almost the same fit can be obtained when altering other parameters. Note that in alternative inversion approaches, working with a larger number of parameters, it would be much more difficult to investigate such a trade-off. In this sense, a reasonably limited number of the MuFEx parameters is advantageous.

[29] Studying the uncertainty plot in Figure 6a regarding the nucleation points, one can again observe the relatively small sensitivity of the data to the tested locations. Common nucleation point #1 is allowed for all subsources when decreasing the acceptable fit slightly (∼3%). On the contrary, the data are relatively sensitive to the nucleation times of the subsources. While the shallow subsource 2 prefers to rupture about 1 s after subsource 1, the deeper subsource 3 requires a longer time delay (4–6 s) despite approximately the same distance to the hypocenter on subsource 1. Although the subevent activation times are relatively well constrained, their interpretation in terms of average rupture velocities can be misleading. For example, the inferred time delay of the deep asperity might be equally well due to either slow-down of the rupture or partial rupture arrest.

[30] Figure 6a also shows the uncertainty of the slip on the individual subsources, as well as the total seismic moment. One can see that subsource 1 has the least amount of slip; allowing for a misfit as low as 95% of the largest value, the slip of subsource 1 can be even (close to) zero. Contrarily, subsources 2 and 3 require relatively large slip values ranging from 0.4 to 0.8 m. The retrieved total seismic

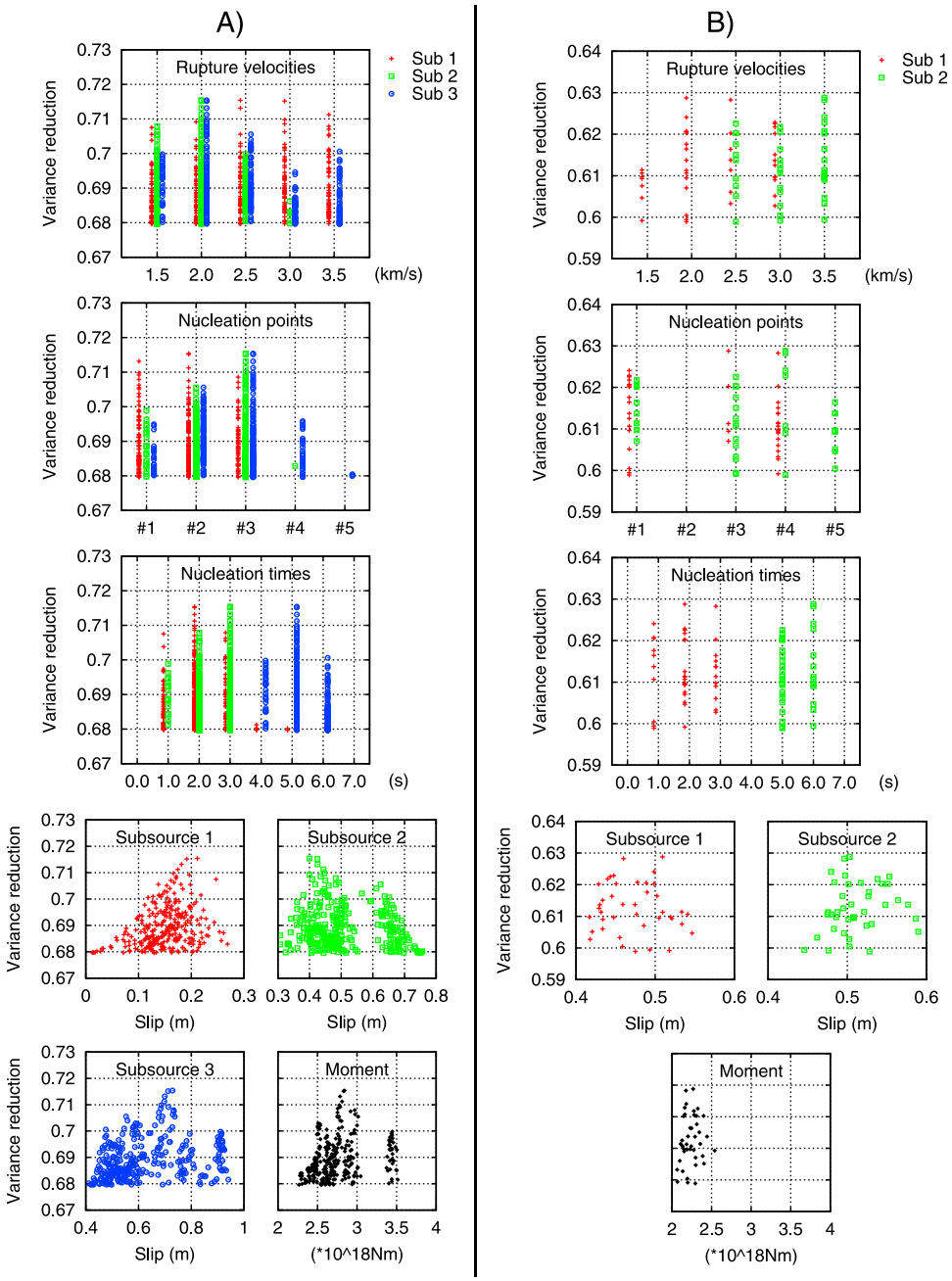

Figure 6. (a) Analysis of the grid-searched MuFEx source models with VR > 0.68 for the L'Aquila earthquake based on the TSVD preliminary inversion. The analyzed set consists of approximately 300 models out of 3 million trial ones. The first three plots from the top show the uncertainty of the MuFEx model parameters, namely the rupture velocities, nucleation points and nucleation times. For the location of the tested nucleation points see Figure 5. The remaining four plots analyze the slip distribution of the three subsources individually and the total seismic moment. Let us emphasize that all the analyzed models are characterized by the delayed start of subsource 3 (by 4–6 s), observable also in the best fitting model in Figure 5. (b) Same as Figure 6a, but for the MuFEx source models based on the ISOLA inversion (40 models with VR > 0.60 out of 40.000 trials). Note that the delayed bottom asperity is present again, and that the nucleation points located in the centers of the subsources (#2) are rejected by the inversion.

moment 2–3.5e18Nm covers a variety of results from published moment tensor solutions and other slip inversions.

[31] To verify the robustness of the inversion, we repeat the MuFEx analysis for an alternative setup based on the ISOLA inversion (see the green circles in Figure 3). We assume only two subsources, the centers of which are set to the locations of the maximum moment release. The dimensions of the subsources were estimated from the seismic

moments using the empirical relations of *Somerville et al.* [1999]. Figures 5b and 6b address this alternative setup. They again show the best fitting model and its uncertainty analysis, respectively. With this setup the fit to data is slightly lower. Nevertheless, the comparison with Figures 5a and 6a demonstrates that some results persist with both setups of the MuFEx source model: (1) a delay of the deep asperity is required, (2) the common nucleation from the earthquake hypocenter (point #1) is not prohibited, and (3) although the slip values for the deep asperity are different for the two setups, in both cases the corresponding seismic moment is close to 2e18Nm. However, some differences between the two setups can be observed. For example, the total seismic moment is lower for the ISOLA setup, which is related to neglecting a part of the fault with non-negligible slip. Also, higher rupture velocities (2.5–3.5 km/s) inside the deeper asperity are required for the ISOLA setup than for TSVD. In the ISOLA setup we have also tested an additional feature, namely the trial nucleation points located in the centers of the subsources (points #2); Figure 6b demonstrates that local bilateral rupture propagation on the subsources is rejected by the MuFEx uncertainty analysis.

6. Discussion and Conclusions

[32] The present paper deals with the inversion of the very well recorded Mw 6.3 2009 L'Aquila earthquake. This event had a complex rupture, with rapid changes of rupture velocity and/or rupture delay, so it had to be analyzed by a slip inversion technique free of strong constraints (such as constant rupture velocity over the fault). To this end, we used the Multiple Finite-Extent (MuFEx) source model with two or three homogeneous subsources to characterize the earthquake rupture; see the flowchart of the inversion in Figure 2. The preliminary inversions obtained with the Truncated Singular Value Decomposition (TSVD) method and the iterative deconvolution of multiple point sources (ISOLA) were used to initially constrain the positions and dimensions of the subsources. The use of several setups is important to assess the robustness of the MuFEx inversion. Note that in the present application we assume the subsources to be of rectangular shape just because of their simplicity (ellipses could also be used). The constant slip considered on the subsources and, hence, the stress singularities at the edges, do not harm the low-frequency slip inversion. Nevertheless, the MuFEx source model should not be used in 'high-frequency' (e.g., stress) analysis prior to proper tapering.

[33] An exhaustive automatic grid search of the free parameters of the MuFEx source model (namely individual nucleation points, rupture velocities and time delays of the subsources) allows robust identification of gross features of the rupture propagation complexity. Note that the approach is easily parallelizable; the present applications require ∼20 minutes on a standard 4-core PC.

[34] The inverse problem is characterized by a large uncertainty. Besides the analysis of the real data, the inversion uncertainty is analyzed also on three synthetic experiments (see Appendix A and auxiliary material). The input models for the synthetic tests are not only close to the real-data inversion result, but they also cover a range of different rupture propagation regimes and/or asperity positions. The tests show that the ISOLA technique and even more the over-parametrized TSVD inversion may provide highly biased results (see the discussion of the cause of the bias by *Zahradník and Gallovič* [2010] and *Gallovič and Zahradník* [2011]). However, they both serve as good indicators for the MuFEx setup source positions. The MuFEx source inversion shows large uncertainties for most of the parameters of the subsources, although we have pointed out above that the source-station geometry is excellent. This merely reflects the non-uniqueness of the inverse problem considering the present accuracy of Green's functions. Note that the retrieved uncertainties of the parameters can be analyzed also in terms of trade-offs among the analyzed parameters of the MuFEx source model. This is left for further studies.

[35] In spite of the considerable uncertainty of the finite-fault model, there is an important stable parameter: The MuFEx source inversion indicates that the L'Aquila event can be considered as a doublet. This is a robust feature, found for the two MuFEx source models obtained by the two preceding analyses by the TSVD and ISOLA approaches. (A similar unique stable feature was demonstrated for another event by *Monelli et al.* [2009]; this was the shallow asperity of the 2000 Western Tottori earthquake.) In the case of the L'Aquila earthquake, the first event, a shallow asperity located updip from the hypocenter, was reached by the rupture front relatively quickly after the earthquake origin. This might suggest a rupture jump ahead, meaning that the shallow asperity was triggered by P waves from the nucleation area. Or, perhaps more likely, the rupture propagated updip from the hypocenter at a relatively high rupture velocity due to the observed high S-wave velocity body in the source area, discovered by means of receiver functions [*Bianchi et al.*, 2010]. In the companion paper [*Ameri et al.*, 2012] it is shown that the shallow asperity is responsible for the low-frequency motion at the near-fault stations due to the updip directivity effect. The second event of the earthquake doublet is the SE slip asperity at larger depths characterized by a larger seismic moment and, most importantly, a considerable rupture delay of ∼3–4 s.

[36] *Cirella et al.* [2009] explained the observed L'Aquila data by a model with different rupture propagation velocities in the along-strike and updip directions, say by a smooth model. This is not in contradiction to our interpretation. Indeed, in the MuFEx model the detected delay might be only a manifestation of a fast slow-down of the rupture along a part of the fault SE of the hypocenter. The uncertainty of the MuFEx parameters demonstrates that the data resolution in the given frequency range is not capable of distinguishing whether the observed rupture propagation complexities were due to the highly varying rupture velocity or due to a temporal stopping of the rupture propagation.

[37] Note that the inferred complex rupture behavior is a distinct feature, suggesting that prescribing a constant rupture velocity over the whole fault in the slip inversions is not an adequate stabilizing constraint (as often used in practice). Indeed, in the inversion by *Scognamiglio et al.* [2010] a constant rupture velocity was assumed and two distinct best fitting models were found: for faster velocity few slip patches were observed at shallow depths, while for slower velocity the main slip patch was located further along the strike and at greater depths.

[38] Nevertheless, we found that constant velocities may be a good approximation for the individual subsources (the decrease of the variance reduction due to the simplification of the rupture model in the MuFEx approach was only a few percent compared to the TSVD technique). This suggests that the constant rupture velocities of the subsources are possible only due to the limited resolution of the data used. To increase the inversion resolution, one would need more precise (3D) Green's functions. It would allow the use of higher frequencies, thus involving more subsources in the MuFEx source model and/or allow the source properties to be characterized in even more detail.

[39] Note that a common approach in recent studies is to consider several so-called rupture segments [*Kaverina et al.*, 2002; *Sekiguchi et al.*, 2000]. As a rule, only a few alternative models with varying segments (and their parameters) are tested in such techniques. On the contrary, the MuFEx model is simpler because it has constant slip values over the individual subsources, but one can fully automatically explore all combinations of the rupture velocities, nucleation times and positions, thus assessing the inversion uncertainty. Despite the simplicity of the MuFEx model, it is still characterized by a relatively large uncertainty in most of the parameters. This suggests that the MuFEx parameterization is plausible. Over-parameterization in other methods might lead to incorrect interpretations and misleading conclusions, especially if a thorough uncertainty analysis is not performed.

[40] To conclude, the L'Aquila earthquake was characterized by a complex rupture process. Such complex ruptures have so far been reported mainly for large (mostly strike-slip) earthquakes. Indeed, strike-slip faults with significant surface ruptures are known to be composed of geometrically distinct segments with a complex style of rupture propagation (a partial rupture arrest on fault bends, a varying rupture velocity from sub-shear to super-shear, etc.), [*Beroza and Spudich*, 1988; *Kaverina et al.*, 2002; *Oglesby et al.*, 2004]. In other examples, such as the 1980 Mw 6.9 Irpinia earthquake, Italy, three distinct segments ruptured, being separated by 20 and 40 s from the first shock [*Bernard and Zollo*, 1989]. *Zahradník et al.* [2005] and *Benetatos et al.* [2007] reported a doublet character of the 2003 Mw 6.2 Lefkada, Greece, earthquake, where two segments were separated 40 km in space and 14 s in time. Here we inferred such robust behavior on a smaller and shorter scale (3 s time delay). It is important to identify the space-time complexities of earthquake ruptures as they might serve as constraints for dynamic models of earthquake ruptures. Accounting correctly for the rupture propagation complexities is also critical to strong ground motion simulations (see companion paper).

Appendix A

A1. Synthetic Test #1: Rupture Model Similar to the L'Aquila Earthquake

[41] Here we apply the MuFEx source inversion (see the flowchart in Figure 2) to synthetic data to test the performance of the inversion. The general characteristics of the source model (position and dimensions of the fault plane and focal mechanism) are the same as in the application to the real data of the 2009 L'Aquila earthquake.

[42] Figures A1a and A1b show the input slip model in terms of the slip-velocity snapshots and the final slip map, respectively. The model consists of two asperities located in the top left and bottom right portions of the fault. The rupture propagates radially at a constant rupture velocity of 3 km/s from a prescribed nucleation point. This synthetic model resembles the result from the inversion of the observed L'Aquila data (see the main text), excluding the inferred temporal delay. Additional tests with considerably different input models are presented in the auxiliary material.

[43] For the test slip model we calculate the 'observed' time series and then use them in the slip inversion as if they were real data. Green's functions are the same as in the real data application. To simulate the real-data application, the displacement seismograms are band-pass filtered between 0.06 and 0.3 Hz. No station weights according to epicentral distances and/or amplitudes have been applied. For each waveform we invert the complete wavefield of 100 s duration. The same processing is applied to the synthetic data in the inversion.

A2. Setup of the MuFEx Source Model

[44] Figure A1c shows the result of the TSVD and ISOLA inversions by means of snapshots of the rupture evolution. The fit of the TSVD synthetics with the 'observed' data is shown in Figure A2. The truncation in TSVD is done at a singular value equal to 1/10 of the largest singular value, i.e., at the same value as in the real data application. Note that the result again contains spurious oscillations ('ghosts') due to the use of a limited number of singular vectors. As the slip can occur anywhere at anytime along the fault within the prescribed 10s time windows, only gross features of the truncated SVD result have to be considered, e.g., the large slip velocity values and their positions in space and time. The fit with the observed data is almost perfect (Figure A2, green seismograms; VR > 0.99).

[45] The final slip model obtained by the TSVD method is displayed in Figure A1d. As can be seen by comparing Figures A1b and A1d, the resulting slip model is highly biased against the true solution. The reason is not imperfect Green's functions, because we use "perfect data" in the synthetic test. The bias is solely caused by the effect of the truncation (regularization). If we truncate at the machine's double precision accuracy, the inversion result is almost perfect. Additional tests indicate that, in the regularized solution, the NW top asperity is enhanced and the SE bottom asperity is weakened due to the proximity of the AQV and AQK stations. Note that the slip velocity snapshots as well as the final slip suggest a split of the shallow asperity. It is noteworthy that the independent analysis by ISOLA (see the green circles in Figures A1c and A1d, VR = 0.95) also splits the compact top-left asperity of the input model into two patches. This confirms that the observed artifacts may be common to different methods, even those not explicitly using any regularization. On the other hand, contrarily to the result of TSVD, ISOLA retrieved the bottom right asperity better in this case.

[46] Despite the bias of the final slip model, the major features of the TSVD snapshots can be used to build a preliminary MuFEx source model. We set the (three) MuFEx subsources to areas where large slip velocity values in the snapshots of Figure A1c occurred. We assumed two subsources covering

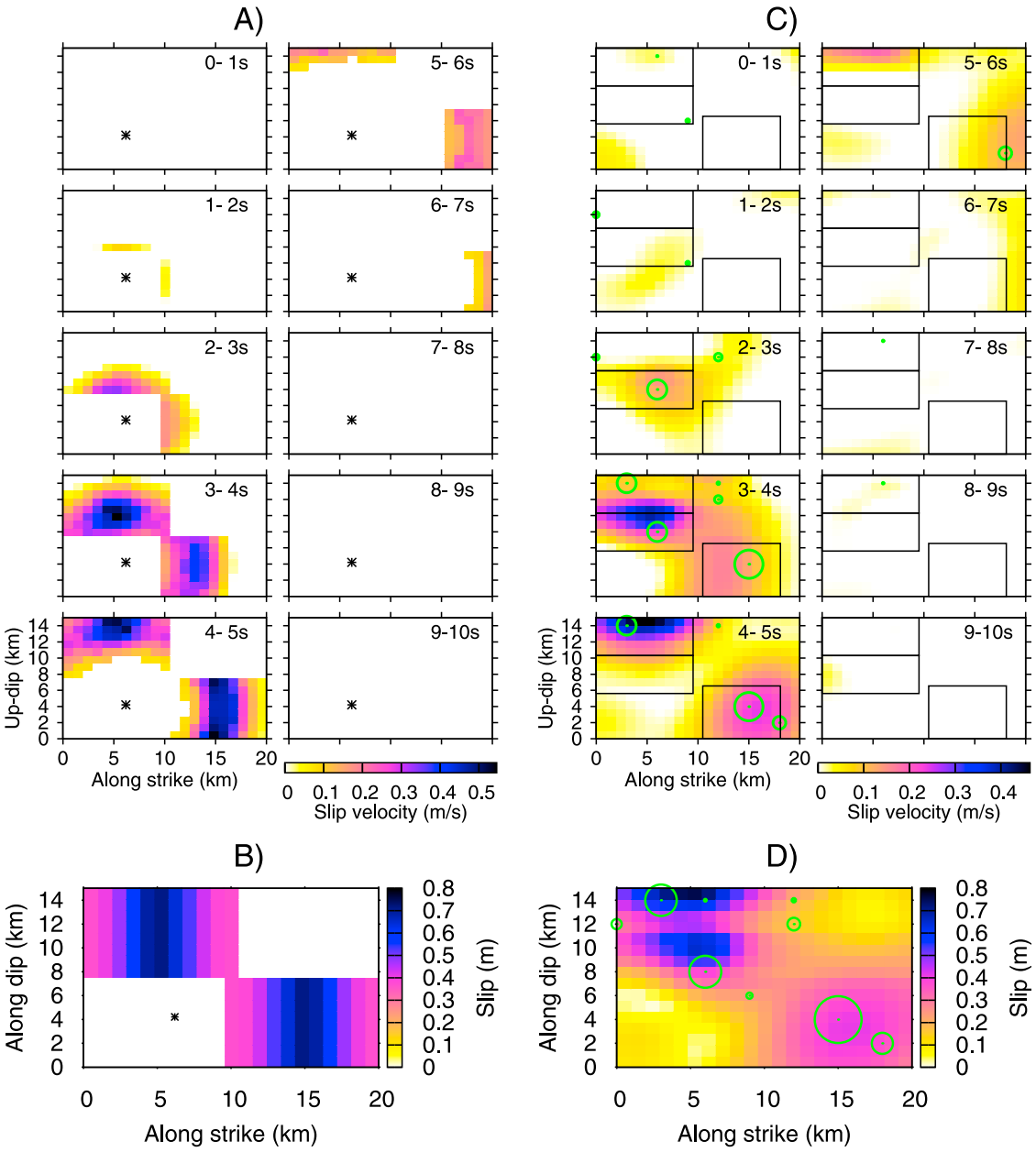

Figure A1. Setting up the MuFEx source model for synthetic test #1. (a) Slip velocity snapshots of the input model with radial rupture propagation at a velocity of 3 km/s from the hypocenter (star). (b) Final slip of the input model. (c) Snapshots of the model inverted by the TSVD approach with truncation at 1/10 of the largest singular value. The truncation level is the same as in the application of TSVD to the real data. The fit of the seismograms (VR = 0.99) is shown in Figure A2 (black and green). Green circles (VR = 0.95) correspond to the result of the ISOLA inversion; the largest circle corresponds to 6.5×10^{17} Nm. Here the ISOLA result is in good agreement with TSVD. Areas with large slip velocities (or location of the largest ISOLA point sources) are used for the first setup of the MuFEx subsources. The final MuFEx subsources are shown as rectangles. (d) Final slip of the inverted model. Note that the slip map is highly biased due to the effect of the truncation (regularization) during the inversion: compared to Figure A1b, the bottom right asperity is underestimated in TSVD and the top asperity is incorrectly split into two by both TSVD and ISOLA.

the area of the artificial split to simulate the real data application, in which we were not sure whether this was an artifact or a true slip feature. The dimensions of the subsources are given approximately by the spatial extents of the large slip velocity patches in Figure A1c.

A3. MuFEx Source Inversion

[47] The subsource positions together with the positions of the testing nucleation points are shown in Figures A3c and A3d. The nucleation points are different for the different

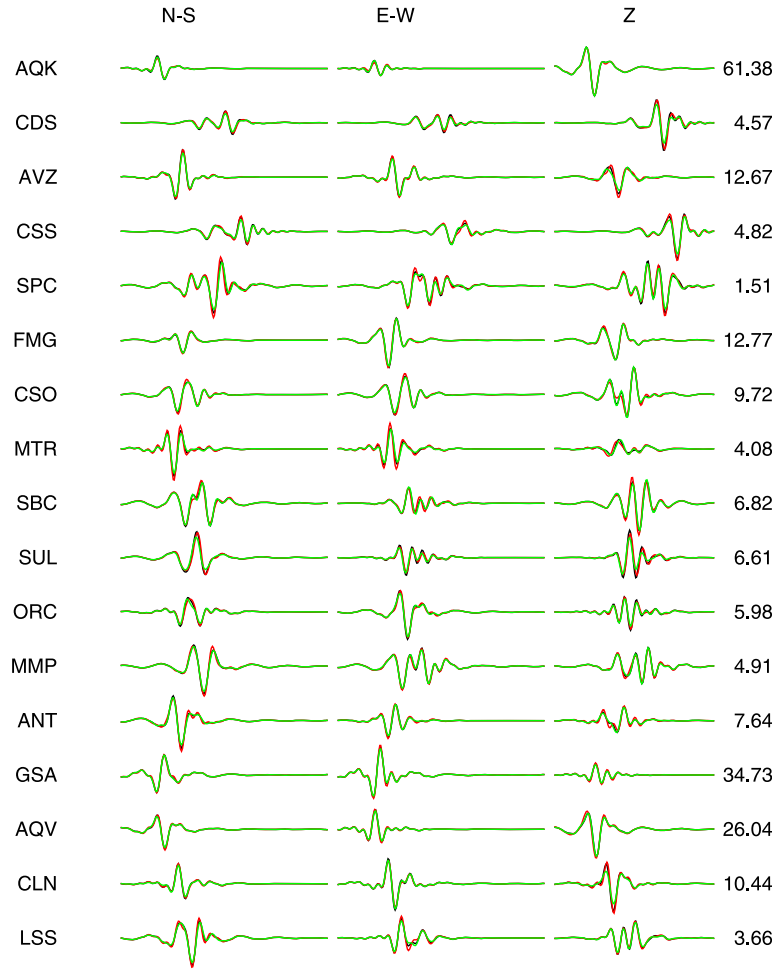

Figure A2. Comparison between 'observed' (black) and synthetic displacements for synthetic test #1 (green for the TSVD approach, red for the best fitting MuFEx model). All seismograms are band-pass filtered in the range of 0.06–0.30 Hz and have duration of 100 s as in the real data application. The maximum amplitudes of the observed records in mm are shown as numbers.

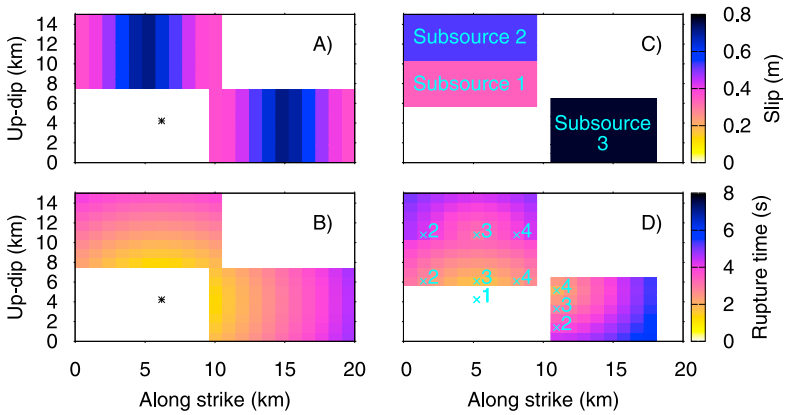

Figure A3. Synthetic test #1 of the inversion by the MuFEx source model. (a) Final slip (same as in Figure A1b), and (b) rupture times of the input test model. Asterisk denotes the hypocenter. (c, d) Best fitting (grid-searched) MuFEx model in terms of the final slip and rupture times, respectively. The numbered points represent trial nucleation points of the subsources; these are different for the different subsources, except for trial nucleation point #1, common to all the subsources. Figures A3c and A3d are to be compared with Figures A3a and A3b, respectively. The fit of the seismograms is shown in Figure A2 (black and red time histories); VR = 0.98. Note that total seismic moments of the two input asperities are well resolved by the MuFEx inversion.

subsources, except for trial nucleation point #1, corresponding to the hypocenter location of the input model, common to all the subsources. The tested rupture velocities and nucleation times cover the ranges of 1.5 to 3.5 km/s and 0 to 5 s, respectively.

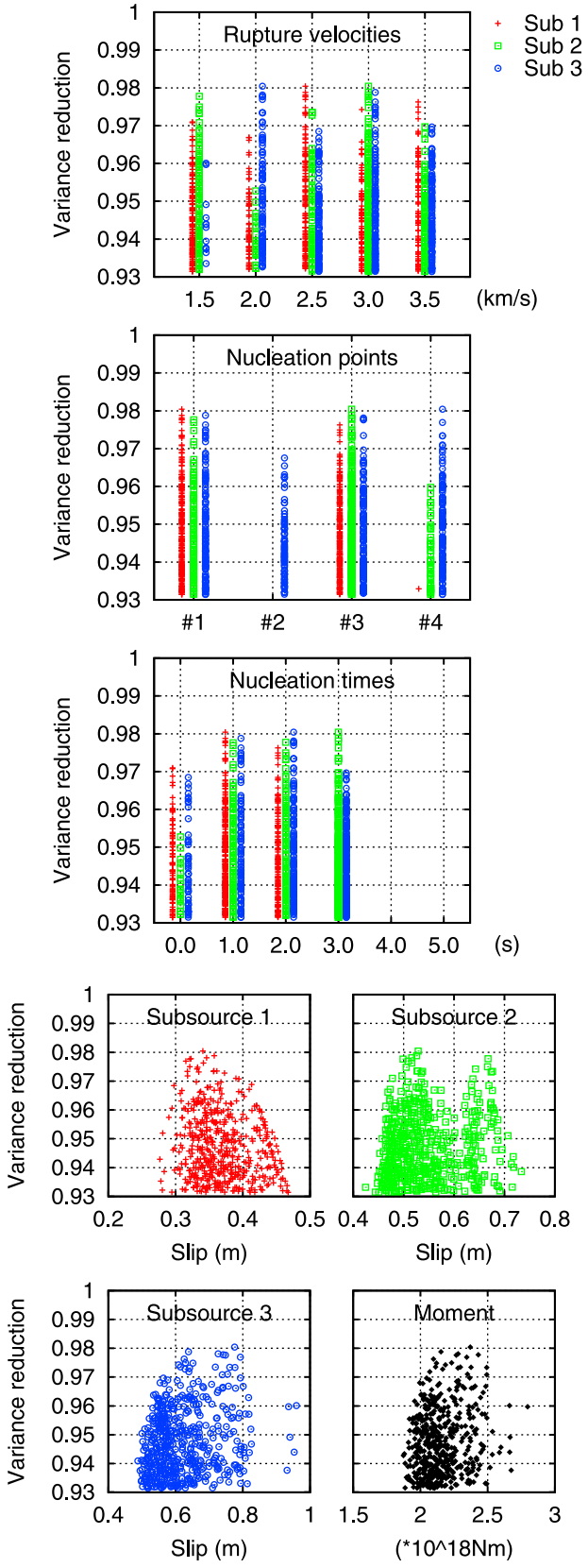

[48] Figures A3c and A3d show the best fitting MuFEx source model in terms of slip and rupture times, respectively, to be compared directly with the corresponding values of the input model in Figures A3a and A3b. Let us first emphasize that, in this synthetic test, the fit with the 'observed' data for such a simplified source model is almost as good as that for the TSVD inverted model (see Figure A2, red seismograms). At first sight, the agreement between the input and inverted source models is not perfect. However, perfect agreement cannot be anticipated because different parameterizations are used for the two models (namely a constant slip on localized subsources in the MuFEx model, opposed to a 'smoothly' varying slip along the fault in the input model). Furthermore, the subsources are not localized perfectly on the asperities of the input model. Therefore, subsource 1 and 2 have different slip values because they cover different parts of the fault area including those with no slip in the input model. Subsource 3 was setup smaller than in the input model and the slip is larger. Interestingly, summary moment of subsources 1 and 2 matches the moment of the top left input asperity (1e18Nm), and the moment of subsource 3 fits the moment of the bottom right asperity (1.4e18Nm). Thus the inversion has a tendency to constrain better the seismic moment of the subsources than their actual slip values. To conclude, considering the modelization errors, the general features of the rupture propagation is relatively well resolved.

[49] The uncertainty analysis of the MuFEx models is performed in the same way as in the main text with the real data. We only use models satisfying physical conditions as in the real data application. In Figure A4 we study the population of all grid-searched models (with VR down to 5% below the best model, for clarity). Regarding the rupture velocities, the plausible MuFEx source models include the true rupture velocity (3 km/s) but also almost all other tested velocity values with only a small drop of VR. One can see that the sensitivity to the rupture velocities is relatively poor (especially for subsource 1). Similarly in terms of the nucleation points, the correct common nucleation point #1 is included among the plausible models, however, more nucleation points are also allowed considering even only a slightly smaller VR. For subsources 1 and 2, the nucleation from the left part of the fault (point #2) is not allowed by the data. Regarding the nucleation times, the plausible values range from 0 to 3 s for all subsources, depending on the other parameters of the MuFEx source model. This suggests that, in agreement with the input model, no significant time delay is suggested (in contrast to what we found for the real data in the main text). Regarding the uncertainties of the subsources' slip and total seismic moment, the correct values (0.5 m for the slip values and 2.4e18Nm for the scalar

Figure A4. The uncertainty analysis of the whole population (500 models with VR > 0.93 out of ~2 million trial ones) of the grid-searched MuFEx source models for synthetic test #1. The description of the panels is the same as in Figure 6. For the location of the tested nucleation points see Figure A3. Note that the seismic moment of the input model (2.4e18Nm) corresponds to the best fitting model. The rupture velocity of 3 km/s of the input model is not well constrained.

moment) are covered. Moreover, the best fitting model has assigned the correct scalar moment. Note that the latter is not the case in all the synthetic tests we have performed, see the auxiliary material.

[50] **Acknowledgments.** The authors acknowledge free Internet access of waveforms provided by the Italian Strong Motion Network (ITACA, http://itaca.mi.ingv.it/). We thank to Martin Mai and three anonymous referees who helped to improve the manuscript. Financial support from GACR 210/11/0854, MSM0021620860, Charles University project UNCE12.

References

Adamová, P., and J. Šílený (2010), Non-double-couple earthquake mechanism as an artifact of the point-source approach applied to a finite-extent focus, *Bull. Seismol. Soc. Am.*, *100*, 447–457, doi:10.1785/0120090097.

Aki, K., and P. G. Richards (2002), *Quantitative Seismology*, Univ. Sci. Books, Sausalito, Calif.

Ameri, G., et al. (2009), The 6 April 2009 Mw 6.3 L'Aquila (central Italy) earthquake: Strong-motion observations, *Seismol. Res. Lett.*, *80*, 951–966, doi:10.1785/gssrl.80.6.951.

Ameri, G., F. Gallovič, and F. Pacor (2012), Complexity of the M6.3 2009 L'Aquila (central Italy) earthquake: 2. Broadband strong-motion modeling, *J. Geophys. Res.*, *117*, B04308, doi:10.1029/2011JB008729.

Backus, G. E. (1977), Interpreting seismic glut moments of total degree 2 or less, *Geophys. J. R. Astron. Soc.*, *51*, 1–25, doi:10.1111/j.1365-246X.1977.tb04187.x.

Benetatos, C., D. Dreger, and A. Kiratzi (2007), Complex and segmented rupture of the 14 August 2003(Mw 6.2) Lefkada (Ionian Islands) earthquake, *Bull. Seismol. Soc. Am.*, *97*, 35–51, doi:10.1785/0120060123.

Bernard, P., and A. Zollo (1989), The Irpinia (Italy) 1980 earthquake: Detailed analysis of a complex normal faulting, *J. Geophys. Res.*, *94*, 1631–1647, doi:10.1029/JB094iB02p01631.

Beroza, G. C., and P. Spudich (1988), Linearized inversion for fault rupture behavior: Application for the 1984 Morgan Hill, California, earthquake, *J. Geophys. Res.*, *93*, 6275–6296, doi:10.1029/JB093iB06p06275.

Bianchi, I., C. Chiarabba, and N. Piana Agostinetti (2010), Control of the 2009 L'Aquila earthquake, central Italy, by a high-velocity structure: A receiver function study, *J. Geophys. Res.*, *115*, B12326, doi:10.1029/2009JB007087.

Bouchon, M. (1981), A simple method to calculate Green's functions for elastic layered media, *Bull. Seismol. Soc. Am.*, *71*, 959–971.

Cirella, A., A. Piatanesi, E. Tinti, and M. Cocco (2008), Rupture process of the 2007 Niigata-ken Chuetsu-oki earthquake by non-linear joint inversion of strong motion and GPS data, *Geophys. Res. Lett.*, *35*, L16306, doi:10.1029/2008GL034756.

Cirella, A., A. Piatanesi, M. Cocco, E. Tinti, L. Scognamiglio, A. Michelini, A. Lomax, and E. Boschi (2009), Rupture history of the 2009 L'Aquila (Italy) earthquake from non-linear joint inversion of strong motion and GPS data, *Geophys. Res. Lett.*, *36*, L19304, doi:10.1029/2009GL039795.

Clévédé, E., M.-P. Bouin, B. Bukchin, A. Mostinskiy, and G. Patau (2004), New constraints on the rupture process of the 1999 August 17 Izmit earthquake deduced from estimates of stress glut rate moments, *Geophys. J. Int.*, *159*, 931–942, doi:10.1111/j.1365-246X.2004.02304.x.

D'Amico, S., K. D. Koper, R. B. Herrmann, A. Akinci, and L. Malagnin (2010), Imaging the rupture of the Mw 6.3 April 6, 2009 L'Aquila, Italy, earthquake using back-projection of teleseismic P-waves, *Geophys. Res. Lett.*, *37*, L03301, doi:10.1029/2009GL042156.

Emolo, A., and A. Zollo (2005), Kinematic source parameters for the 1989 Loma Prieta earthquake from the nonlinear inversion of accelerograms, *Bull. Seismol. Soc. Am.*, *95*, 981–994, doi:10.1785/0120030193.

Gallovič, F., and J. Zahradník (2011), Toward understanding slip inversion uncertainty and artifacts: 2. Singular value analysis, *J. Geophys. Res.*, *116*, B02309, doi:10.1029/2010JB007814.

Gallovič, F., J. Zahradník, D. Křížová, V. Plicka, E. Sokos, A. Serpetsidaki, and G.-A. Tselentis (2009), From earthquake centroid to spatial-temporal rupture evolution: Mw 6.3 Movri Mountain earthquake, June 8, 2008, Greece, *Geophys. Res. Lett.*, *36*, L21310, doi:10.1029/2009GL040283.

Hartzell, S., P. Liu, C. Mendoza, C. Ji, and K. M. Larson (2007), Stability and uncertainty of finite-fault slip inversions: Application to the 2004 Parkfield, California, earthquake, *Bull. Seismol. Soc. Am.*, *97*, 1911–1934, doi:10.1785/0120070080.

Herrmann, R., L. Malagnini, and I. Munafo (2011), Regional moment tensors of the 2009 L'Aquila earthquake sequence, *Bull. Seismol. Soc. Am.*, *101*, 975–993.

Kaverina, A., D. Dreger, and E. Price (2002), The combined inversion of seismic and geodetic data for the source process of the 16 October 1999 Mw 7.1 Hector Mine, California, earthquake, *Bull. Seismol. Soc. Am.*, *92*, 1266–1280, doi:10.1785/0120000907.

Lawson, C. L., and R. J. Hanson (1974), *Solving Least Square Problems*, 340 pp., Prentice-Hall, Upper Saddle River, N. J.

Lay, T., C. J. Ammon, A. R. Hutko, and H. Kanamori (2010), Effects of kinematic constraints on teleseismic finite-source rupture inversions: Great Peruvian earthquakes of 23 June 2001 and 15 August 2007, *Bull. Seismol. Soc. Am.*, *100*, 969–994, doi:10.1785/0120090274.

Maercklin, N., A. Zollo, A. Orefice, G. Festa, A. Emolo, R. De Matteis, B. Delouis, and A. Bobbio (2011), The effectiveness of a distant accelerometer array to compute seismic source parameters: The April 2009 L'Aquila earthquake case history, *Bull. Seismol. Soc. Am.*, *101*, 354–365, doi:10.1785/0120100124.

Monelli, D., and P. M. Mai (2008), Bayesian inference of kinematic earthquake rupture parameters through fitting of strong motion data, *Geophys. J. Int.*, *173*, 220–232, doi:10.1111/j.1365-246X.2008.03733.x.

Monelli, D., P. M. Mai, S. Jónsson, and D. Giardini (2009), Bayesian imaging of the 2000 Western Tottori (Japan) earthquake through fitting of strong motion and GPS data, *Geophys. J. Int.*, *176*, 135–150, doi:10.1111/j.1365-246X.2008.03943.x.

Oglesby, D. D., D. S. Dreger, R. A. Harris, N. Ratchkovski, and R. Hansen (2004), Inverse kinematic and forward dynamic models of the 2002 Denali Fault earthquake, Alaska, *Bull. Seismol. Soc. Am.*, *94*, S214–S233, doi:10.1785/0120040620.

Olson, A. H., and J. G. Anderson (1988), Implications of frequency-domain inversion of earthquake ground motions for resolving the space-time dependence of slip on an extended fault, *Geophys. J.*, *94*, 443–455, doi:10.1111/j.1365-246X.1988.tb02267.x.

Olson, A. H., and R. J. Apsel (1982), Finite faults and inverse theory with applications to the 1979 Imperial Valley earthquake, *Bull. Seismol. Soc. Am.*, *72*, 1969–2001.

Piatanesi, A., A. Cirella, P. Spudich, and M. Cocco (2007), A global search inversion for earthquake kinematic rupture history: Application to the 2000 western Tottori, Japan earthquake, *J. Geophys. Res.*, *112*, B07314, doi:10.1029/2006JB004821.

Scognamiglio, L., E. Tinti, A. Michelini, D. S. Dreger, A. Cirella, M. Cocco, S. Mazza, and A. Piatanesi (2010), Fast determination of moment tensors and rupture history: What has been learned from the 6 April 2009 L'Aquila earthquake sequence, *Seismol. Res. Lett.*, *81*, 892–906, doi:10.1785/gssrl.81.6.892.

Sekiguchi, H., K. Irikura, and T. Iwata (2000), Fault geometry at the rupture termination of the 1995 Hyogo-ken Nanbu earthquake, *Bull. Seismol. Soc. Am.*, *90*, 117–133, doi:10.1785/0119990027.

Sokos, E., and J. Zahradník (2008), ISOLA A Fortran code and a Matlab GUI to perform multiple-point source inversion of seismic data, *Comput. Geosci.*, *34*, 967–977, doi:10.1016/j.cageo.2007.07.005.

Somerville, P., K. Irikura, R. Graves, S. Sawada, D. Wald, N. Abrahamson, Y. Iwasaki, T. Kagawa, N. Smith, and A. Kowada (1999), Characterizing crustal earthquake slip models for the prediction of strong ground motion, *Seismol. Res. Lett.*, *70*, 59–80, doi:10.1785/gssrl.70.1.59.

Vallée, M., and M. Bouchon (2004), Imaging coseismic rupture in far field by slip patches, *Geophys. J. Int.*, *156*, 615–630, doi:10.1111/j.1365-246X.2004.02158.x.

Walters, R. J., J. R. Elliott, N. D'Agostino, P. C. England, I. Hunstad, J. A. Jackson, B. Parsons, R. J. Phillips, and G. Roberts (2009), The 2009 L'Aquila earthquake (central Italy): A source mechanism and implications for seismic hazard, *Geophys. Res. Lett.*, *36*, L17312, doi:10.1029/2009GL039337.

Zahradník, J., and F. Gallovič (2010), Toward understanding slip-inversion uncertainty and artifacts, *J. Geophys. Res.*, *115*, B09310, doi:10.1029/2010JB007414.

Zahradník, J., A. Serpetsidaki, E. Sokos, and G.-A. Tselentis (2005), Iterative deconvolution of regional waveforms and a double-event interpretation of the 2003 Lefkada earthquake, Greece, *Bull. Seismol. Soc. Am.*, *95*, 159–172, doi:10.1785/0120040035.

Zahradník, J., J. Janský, and V. Plicka (2008), Detailed waveform inversion for moment tensors of M ∼ 4 events: Examples from the Corinth Gulf, Greece, *Bull. Seismol. Soc. Am.*, *98*, 2756–2771, doi:10.1785/0120080124.

F. Gallovič and J. Zahradník, Faculty of Mathematics and Physics, Department of Geophysics, Charles University, V Holešovičkách 2, Praha 8, Prague 180 00, Czech Republic. (gallovic@karel.troja.mff.cuni.cz)

[P13]

Complexity of the Mw 6.3 2009 L'Aquila (central Italy) earthquake: 2. Broadband strong motion modeling

G. Ameri,[1] F. Gallovič,[2] and F. Pacor[1]

Received 28 July 2011; revised 16 February 2012; accepted 26 February 2012; published 21 April 2012.

[1] Near-fault strong-ground motions (0.1–10 Hz) recorded during the Mw 6.3 2009 L'Aquila earthquake exhibit great spatial variability. Modeling the observed seismograms allows linking distinct features of the observed wavefield to particular source and propagation effects and provides insights on strong motion complexity from this moderate magnitude event. We utilize a hybrid integral-composite approach based on a k-square kinematic rupture model, combining low-frequency coherent and high-frequency incoherent source radiation and providing omega-squared source spectral decay. Several source model features, proven to be stable by means of an uncertainty analysis in the preceding low-frequency (<0.2 Hz) multiple finite-extent source inversion (Paper 1), were constrained. Synthetic Green's functions are calculated in a 1D-layered crustal model including 1D soil profiles to account for site-specific response (where available). The results show that although the local site effects improve the modeling, the spatial broadband ground-motion variability is to large extent controlled by the rupture kinematics. The modeling thus confirms and further constraints the source model features, including the position and slip amount of the two main asperities, the largest asperity time delay and the rupture velocity distribution on the fault. Furthermore, we demonstrate that the crossover frequency dividing the coherent and incoherent wavefield, often considered independent on the station position, has to be variable in order to adequately reproduce both near and far station recordings. This suggests that the incoherency of the radiated wavefield is controlled by the wave-propagation phenomena and/or the initial updip rupture propagation was very smooth (coherent) up to relatively high frequencies (>2 Hz).

Citation: Ameri, G., F. Gallovič, and F. Pacor (2012), Complexity of the Mw 6.3 2009 L'Aquila (central Italy) earthquake: 2. Broadband strong motion modeling, *J. Geophys. Res.*, *117*, B04308, doi:10.1029/2011JB008729.

1. Introduction

[2] On April 6, 2009, at 1:32:40 UTC, a Mw 6.3 earthquake struck the L'Aquila city, one of the largest urban centers in the Abruzzo region (Central Italy), causing 308 casualties and large damage in the town and surrounding villages. The earthquake occurred along a NW-SE trending normal fault, 15–20 km long, dipping about 45° SW [*Chiarabba et al.*, 2009]. The hypocenter depth was estimated at about 9 km, located few kilometers southwest of the town center. This event represents the third largest earthquake recorded by strong motion instruments in Italy, after the 1980, Mw 6.9, Irpinia and the 1976, Mw 6.4, Friuli earthquakes.

[3] The earthquake has been recorded by several digital stations of the Italian Strong motion Network (*Rete Accelerometrica Nazionale*, RAN), operated by the Italian Department of Civil Protection (DPC). The collected records represent a unique data set in Italy in terms of number and quality of records, azimuthal coverage and presence of near-fault recordings [*Ameri et al.*, 2009a; *Zambonelli et al.*, 2011].

[4] About 14 strong motion stations were located within 50 km from the earthquake epicenter, 5 of them within the surface projection of the estimated rupture plane. Detailed geological and geophysical information are available for these stations and are collected into the station monographs accessible through the Italian strong motion database (ITACA, http://itaca.mi.ingv.it). In particular, the site response characterization of stations in the epicentral area largely benefited from several research activities carried out after the earthquake, described by *Gruppo di Lavoro M.S.-A.Q.* [2010] and *Cultrera et al.* [2011]. An overview on site responses of the accelerometric sites, based on the analysis of strong motion recordings, is found in the work of *Bindi et al.* [2009].

[5] Despite the moderate magnitude of the L'Aquila earthquake, the strong motion data in the vicinity of the fault depict a large variability of the observed shaking. Previous

[1]Istituto Nazionale di Geofisica e Vulcanologia, Milan, Italy.
[2]Faculty of Mathematics and Physics, Department of Geophysics, Charles University, Prague, Czech Republic.

0148-0227/12/2011JB008729

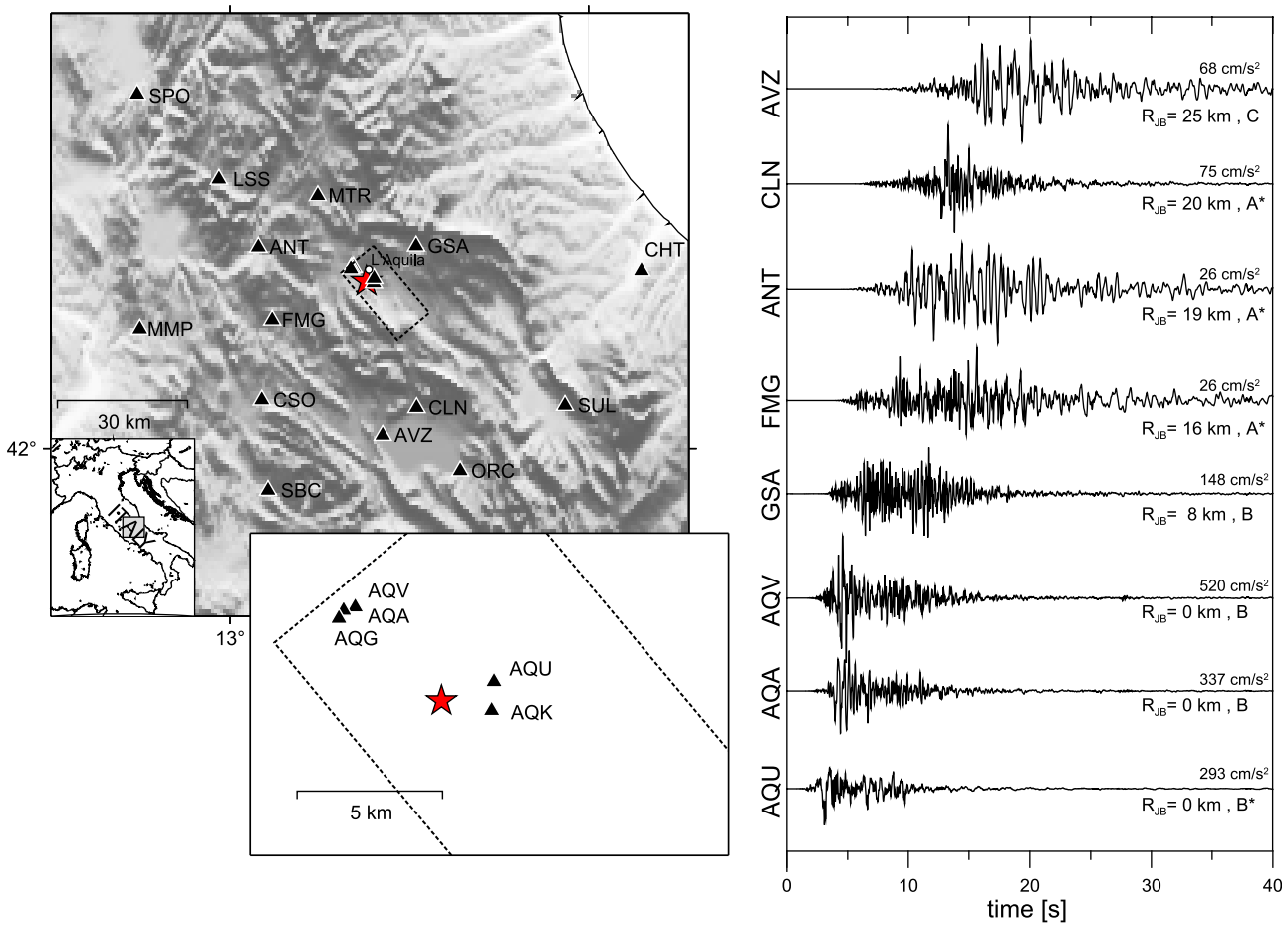

Figure 1. (left) Map showing the epicentral area of the 6 April 2009 L'Aquila earthquake. The strong motion stations are marked by triangles (see also Table 1). The inset shows a zoom on the near-fault (AQ_) stations. The earthquake epicenter and the surface projection of the rupture plane are indicated by the red star and the dashed rectangle, respectively. (right) Acceleration waveforms (North-South component), aligned on the earthquake origin time, recorded at selected sites around the fault. The peak ground acceleration values, the Joyner-Boore distance (R_{JB}) and the site classification according to EC8 are reported. Waveforms are band-pass filtered between 0.1 and 10 Hz.

studies have shown that, although local site effects and wave propagation influenced the ground motion characteristics, the rupture process substantially contributes to the spatial distribution of the observed ground motion [*Ameri et al.*, 2009a; *Akinci et al.*, 2010]. Source inversion studies performed for the L'Aquila earthquake using strong motion and geodetic data showed that the rupture followed a complex pattern with a slip distribution composed by at least two asperities and a variable rupture velocity over the fault plane [*Cirella et al.*, 2009; *D'Amico et al.*, 2010; *Scognamiglio et al.*, 2010]. Newly introduced multiple finite-extent inversion applied to the L'Aquila data, see the companion paper [*Gallovič and Zahradník*, 2011] (hereinafter referred to as Paper 1), confirmed the two major slip patches and suggested temporal delay (∼3 s) of the deeper one.

[6] Broadband ground motion simulation techniques based on kinematic rupture models can be used to study the effect of source complexity on strong ground-motion records. Most of such methods simulate the ground motion by combining the synthetics computed with deterministic and stochastic (or semi-stochastic) approaches for the low- and high-frequency parts, respectively [e.g., *Pitarka et al.*, 2000; *Mai and Beroza*, 2003; *Gallovič and Brokešová*, 2007; *Hisada*, 2008; *Ameri et al.*, 2008; *Mai et al.*, 2010; *Graves and Pitarka*, 2010]. These techniques are used to investigate past earthquakes [e.g., *Aagaard et al.*, 2008; *Ameri et al.*, 2009b] as well as to perform scenario-events studies [e.g., *Graves et al.*, 2011].

[7] One of the advantages of using forward modeling is that the effect of source input parameters on observed motions can be controlled and assessed individually. In this way, the most critical input parameter (if any) controlling the fit with the observed ground motion at a given station can be identified and insights on the source process can be retrieved by minimizing the difference between observed and simulated ground motions.

[8] In this study we investigate the ground-motion complexity observed during the 2009 L'Aquila earthquake performing broadband ground-motion simulations with a hybrid integral-composite technique based on a k^{-2} rupture model [*Gallovič and Brokešová*, 2007]. Starting from the

Table 1. Strong Motion Stations Considered in This Study

Code	Station Name	Longitude (°E)	Latitude (°N)	R_{epi} (km)	R_{JB} (km)	Site Class EC8[b]
AQG[a]	L'Aqulia-Colle Grilli	13.3370	42.3735	4.10	0.00	B
AQA[a]	L'Aquila-F. Aterno	13.3390	42.3760	4.20	0.00	B
AQV[a]	L'Aquila-Centro Valle	13.3439	42.3771	3.99	0.00	B
AQK	L'Aquila-Aquil Park	13.4010	42.3450	2.13	0.00	B
AQU	L'Aquila-Castello	13.4019	42.3539	2.18	0.00	B*
GSA[a]	Gran Sasso (Assergi)	13.5194	42.4207	14.15	8.59	B
MTR	Montereale	13.2448	42.5240	22.13	15.93	A*
FMG	Fiamignano	13.1172	42.2680	23.17	16.56	A*
ANT	Antrodoco	13.0787	42.4182	25.54	19.31	A*
CLN	Celano	13.5207	42.0852	31.79	19.95	A*
AVZ[a]	Avezzano	13.4259	42.0275	36.15	25.14	C
CSO	Carsoli	13.0881	42.1009	36.45	31.68	A*
LSS	Leonessa	12.9689	42.5583	40.62	35.63	A*
ORC	Ortucchio	13.6424	41.9536	49.19	37.34	A*
SUL	Sulmona	13.9343	42.0895	54.29	43.35	C*
MMP	Mompeo	12.7483	42.2492	52.86	45.87	A*
SBC	Subiaco	13.1055	41.9132	53.45	46.59	A*
CHT	Chieti	14.1478	42.3698	63.47	52.17	B
SPO	Spoleto	12.7406	42.7336	67.30	62.60	A*

[a]Station for which 1D site-specific soil profiles are used. See main text and Figure 3.
[b]EC8 classes with asterisks are attributed on the basis of geological/geophysical information (http://itaca.mi.ingv.it/ItacaNet/).

basic features of the multiple finite-extent inversion results, based on strong motion data at frequency below 0.2 Hz (see Paper 1), we "extend" the source model to higher frequencies, calculate broadband (0.1–10 Hz) synthetic seismograms and compare them with the recorded ground motions. We show that most of the observed complexity can be explained when properly combining site-specific and finite-fault effects. In particular, we test the effects of the rupture delay of the largest asperity, rupture velocity values, small-scale slip distribution and local site response. Finally, we investigate the relative contribution of coherent (i.e., deterministic) and stochastic processes in the ground-motion generation at different sites.

2. The April 6, 2009 L'Aquila Earthquake: Strong Motion Records

[9] The L'Aquila earthquake provided the most extensive set of high-quality near-fault strong motion records ever recorded in Italy for such a major event. It has been recorded by 14 stations within 50 km from the epicenter, 5 of them within the surface projection of the estimated rupture plane at distances less than 5 km from the epicenter (Figure 1 and Table 1). Three of these stations are part of an array deployed in the upper Aterno-river valley (AQG, AQA and AQV) whereas the other two (i.e., AQK and AQU) are in downtown L'Aquila. In the following we will refer to this group of near-fault stations simply as "AQ_."

[10] In Table 1, the sites are classified according to the Eurocode 8 [*Comité Européen de Normalisation*, 2004] and the Italian Building Code (http://www.cslp.it/cslp/index.php?option=com_docman&task=doc_download&gid=3255&Itemid=10) based on the shear wave velocity averaged over the top 30 m of the soil profile - $V_{s,30}$. The EC8 class each station has been attributed on the basis of direct measure of $V_{s,30}$ or on geological/geophysical information [*Di Capua*, 2009; *Di Capua et al.*, 2011].

[11] The acceleration waveforms at eight stations distributed around the fault are shown in Figure 1 (right), pointing out the remarkable azimuthal dependence of recorded ground motions in terms of peak values, frequency content, envelope, and durations. The closest stations, AQU, AQV and AQA, few kilometers apart, have similar durations although the peak values and frequency content vary. GSA and FMG accelerations, recorded at similar epicentral distance on the footwall and hanging wall sides of the fault, respectively, display remarkable differences in peak values (more than 5 times larger at GSA than at FMG), duration and frequency content. Moreover, at both stations, but to a larger extent at GSA, the waveforms show two distinct wave packets of similar amplitudes that are not equally well visible on the other records. Stations ANT, CLN and AVZ are approximately located at similar distances, in the strike direction (NW-SE), but on opposite sides of the fault. Again, the records show substantial differences. The peak acceleration reported at ANT is 3 times smaller than that at the other two stations while CLN record has smaller duration.

[12] The complexity observed in the accelerations time series, can be also found in the velocity waveforms. The AQ_ records are all characterized by pulses at the beginning of the signal that have been interpreted as near-source effects [*Ameri et al.*, 2009a; *Chioccarelli and Iervolino*, 2010].

3. Methodology

[13] For the strong ground-motion modeling we use hybrid integral-composite (HIC) approach introduced by *Gallovič and Brokešová* [2007]. This model is designed mostly for the earthquake ground-motion simulations, providing omega-squared source spectrum. It is based on techniques developed by *Andrews* [1980], *Herrero and Bernard* [1994], *Zeng et al.* [1994], *Gallovič and Brokešová* [2004], among others.

[14] The source model is divided into subsources with number-size distribution characterized by fractal dimension D = 2. For simplicity, the subsources are assumed rectangular with sizes given by integer fractions of the fault length L and width W, i.e., of sizes L/n × W/n, where level n = 2…N (in the present calculations we assume N = 8). Assuming constant stress drop scaling, the slip of the subsources is

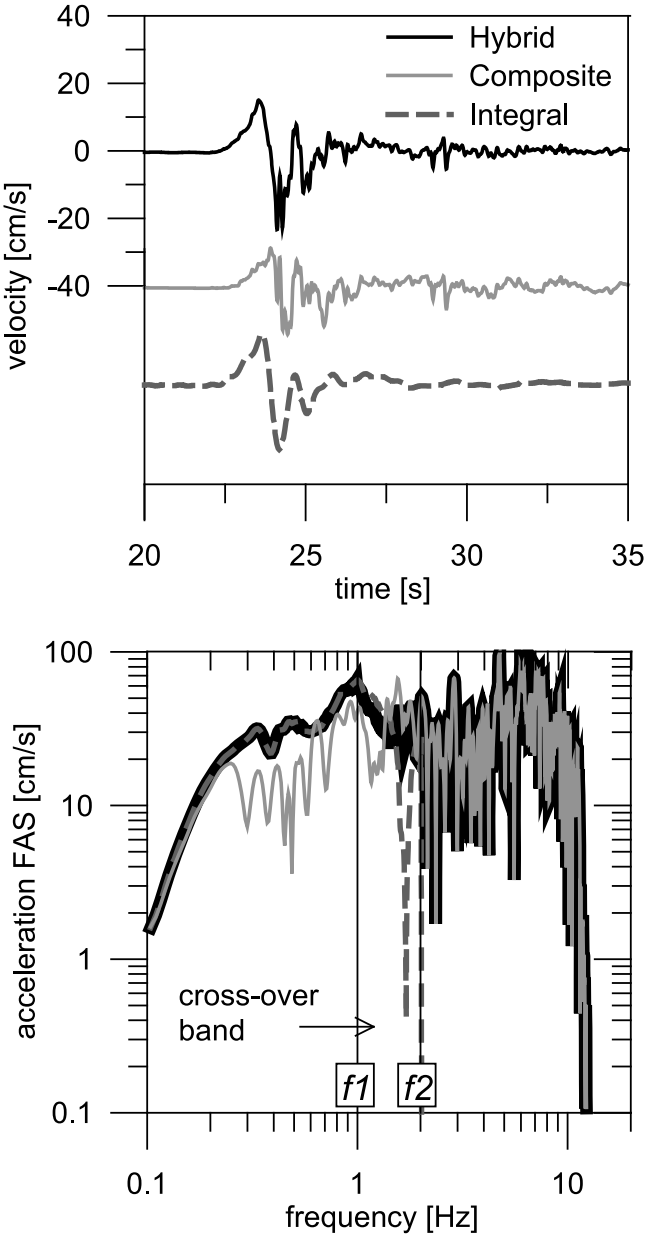

Figure 2. Example of calculation of hybrid broadband seismograms by combining integral and composite approaches. (top) Velocity seismograms and (bottom) Fourier amplitude spectra (FAS) from hybrid, composite and integral approaches. The combination of integral and composite seismograms is performed in the crossover frequency band (between bounding frequencies f1 and f2), where the synthetics spectra (both real and imaginary parts) are multiplied by weighting functions $\sin^2(x)$ and $\cos^2(x)$, with $x = (\pi/2)((f - f1)/(f2 - f1))$ and summed up (see *Gallovič and Brokešová*, 2007). The figure shows that the hybrid seismogram contain more complexity than the integral one, while enhancing (coherent) directivity effect with respect to the composite one.

reciprocally proportional to the level n. For the particular number-size distribution the number of subsources at level n equals to 2n-1. For n > 2 the subsources are distributed randomly over fault plane with possible overlap.

[15] Assuming that the subsources are characterized by statistically the same slip distribution (i.e., they are self-similar), the resulting slip distribution over the whole fault has k-squared decay at high wave numbers k [*Andrews*, 1980]. Thus, we prescribe k-squared slip distribution on each of the subsources to mimic that it is again composed of smaller subsources. To simulate the source radiation being coherent at small wave numbers and incoherent at large ones, we divide the calculations into two frequency bands. In the low-frequency band we use the representation theorem (integral approach). This utilizes the k-squared slip distribution composed by the subsources and delta function as the slip velocity function. In the high-frequency range, we assume that the subsources radiate Brune's source time functions with proper seismic moment and corner frequency given by the sizes of the subsources, measured from their centers (composite approach). Note that the same set of subsources is used in both the integral and composite parts of the simulations. This way, the directivity effect is modeled in the low frequency range, while it disappears at high frequencies due to the incoherent summation of the contributions of subsources [*Gallovič and Burjánek*, 2007]. Such model is thus in agreement with the engineering expectation of directivity derived from the regressions of recorded ground motions of moderate-to-large earthquakes [*Somerville et al.*, 1997; *Spudich and Chiou*, 2008] showing that directivity-induced amplification of ground motion can be recognized only in the low-frequency range (roughly below 1–1.5 Hz). However, whether these effects actually vanish at high frequencies due to rupture incoherencies and above which frequency they are no longer significant it is still a matter of debate [*Boatwright*, 2007; *Cultrera et al.*, 2009]. In order to also reduce the effect of the radiation pattern at high-frequencies we assume $\pm 30°$ random variations of the strike, dip and rake angles of the subsources in the composite part of the calculations.

[16] The integral and composite calculations are crossover combined in a given frequency band (see illustration in Figure 2). Note that this band implies up to which frequency the directivity effect is modeled. In the present paper we test several choices of the crossover band.

[17] The Green's functions for both calculations are computed by the discrete wave number technique, DWN [*Bouchon*, 1981], either in general 1D layered model or in specific 1D models for the individual stations that include low-velocity subsurface layers, where available. The DWN technique provides full wavefield Green's functions; no stochastic Green's functions are used.

4. Crustal Propagation Model and Site Effects

[18] In order to calculate the Green's functions in the study region we use the 1D velocity model proposed by *Bianchi et al.* [2010], based on receiver function analyses. We adopt the model derived at the FAGN station (belonging to the National Seismic Network (RSN, INGV-CNT) and localized close to the southeastern termination of the fault) because it is found in preliminary analysis to be more appropriate to

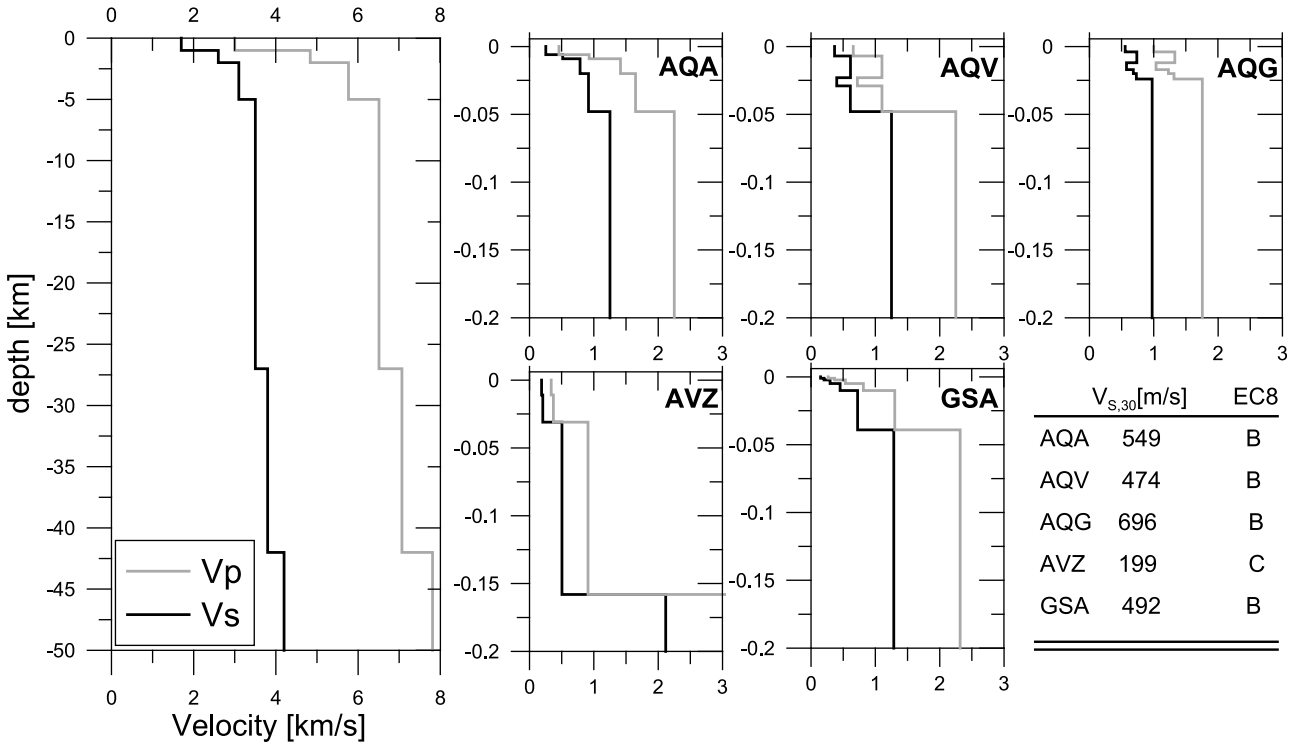

Figure 3. The 1D velocity models used in the simulations. (left) Velocity profile used for the L'Aquila region (see Table2). (right) Site-specific shallow soil profiles adopted at the respective stations (the profiles extends downward according to the regional model shown in Figure 3, left). The velocities have been measured through downhole and cross-hole tests at AQA, AQV and AQG and estimated with Multichannel Analysis of Surface Wave (MASW) at GSA and AVZ (http://itaca.mi.ingv.it/ItacaNet/). The $V_{s,30}$ values and the EC8 site classes for these stations are also indicated.

represent the general wave propagation over the whole study area (Figure 3, left and Table 2). The authors also provide another Vs profile for AQU station. The two models reveal strong differences for the shallow crust, whereas deeper features are similar. As reported by *Bianchi et al.* [2010], the very high Vs values (>4 km/s) found underneath AQU are a localized feature absent beneath the FAGN station where Vs values are within limits usually observed for carbonate rocks.

[19] Beside the regional wave propagation characteristics we need to account, in the simulated seismograms, for the effect of amplification (or de-amplification) of seismic waves occurring in the shallow-most soil layers (i.e., in the last tens of meters). Such effects are known to significantly modify the amplitude, frequency content and duration of the ground motion at the surface and should to be considered to model the observed ground motion.

[20] Despite all the available information, to decide how to include site effects in the modeling is not straightforward. The appropriate way would be to calculate the Green's functions for site-specific soil profile at each station. However, this approach conflicts with the fact that soil profiles are not available at most of the stations. Other commonly used approaches that do not require the knowledge of the soil profile utilize empirically derived amplification functions either based on reference site methods or on single-stations measurements. However, such functions generally describe the amplification of Fourier amplitude spectra only and do not provide information of phase modifications. Moreover, the reliability of the amplification curves depends on the number and quality of available records at the stations or on the adopted reference rock site.

[21] In this paper, we opt for incorporation of site response only by including site-specific 1D soil layers in the crustal model; for five of the closest stations to the epicenter (Figures 1 and 3, Table 1) such 1D profiles are available (http://itaca.mi.ingv.it/ItacaNet/). In particular, stations AQA and AQV are installed on the recent alluvial deposits of the Aterno river, made of gravels alternated to thin layers of finer deposits, that reach the seismic bedrock, defined by shear velocities larger 800 m/s, at depth of about 30 m and 50 m, respectively (see *Puglia et al.* [2011] and *Lanzo et al.* [2011] for details). Station AQG is installed on limestones

Table 2. Velocity Model Used for the L'Aquila Region[a]

Depth (km)	V_P (km/s)[b]	V_S (km/s)	ρ (g/cm^3)	Q_P	Q_S
0	3.16	1.70	2.50	200	100
1	4.83	2.60	2.84	400	200
2	5.76	3.10	2.94	400	200
5	6.51	3.50	3.15	400	200
27	7.00	3.80	3.26	600	300
42	7.80	4.20	3.50	800	400

[a]The model is based on the *Bianchi et al.* [2010] V_S profile for station FAGN. We simplified their V_S profile by removing the velocity inversion in the deep layer (between 13 and 19 km).
[b]Values are computed as $V_P = V_S$*1.86.

Table 3. Parameters Used in the Modeling

Parameter	Value	Input Parameter[a]
Fault mechanism	strike: 140°, dip: 50°, rake: −90°	IC
Fault dimensions	length 20 km, width 15 km	IC
Fault top depth	0.5 km	IC
Focal depth	9.0 km	IC
Seismic moment	2.5×10^{18} N m	IC
Stress drop	100 bars	C
Nucleation point (position from northwestern edge)	downdip: 11 km, along strike: 6 km	IC
Rupture velocity (Vr)	2 km/s (above 5 km depth)	IC
	3 km/s (below 5 km depth)	IC
Risetime	0.1 s	I
Number of subsource levels	8	IC
Total number of subsources	63	IC
Crossover frequency band	1.5–2.0 Hz (AQ_ stations)	IC
	0.3–0.6 Hz (other stations)	IC
Discretization of the fault plane	130 × 100 point sources	I

[a]I, C, and IC show whether the input parameter affects the Integral, Composite or both parts of the calculated wavefield.

and marly limestones and the seismic bedrock is reached at depth of 20–30 m. The GSA station is located on stiff soils (limestone and marls), the velocity profile shows some velocity increase in the first 10 m and a deeper layer with Vs of about 600 m/s down to 40 m. Below, a faster layer with a shear velocity of 1300 m/s is reported. Station AVZ is located on alluvial deposits and the Vs profile is characterized by a low velocity layer (about 200 m/s) for the first 35 m and a deeper layer with Vs of about 500 m/s that extends down to 160 m where the bedrock is found. For the remaining stations, the synthetics are computed using the 1D crustal model reported in Table 2 having a shear velocity at surface equal to 1700 m/s, without including site-specific effects.

[22] To properly describe the high-frequency spectral decay of synthetics, we adopt the κ operator, introduced by *Anderson and Hough* [1984]. We set κ = 0.03 s, that is a typical value for rock sites in central Italy [*Bindi et al.*, 2004].

5. Hybrid Source Model

[23] The source characteristics of the L'Aquila earthquake have been deeply investigated and a number of source models have been proposed based on analyses of strong motion, teleseismic, GPS, SAR and field data [*Anzidei et al.*, 2009; *Atzori et al.*, 2009; *Cirella et al.*, 2009; *Falcucci et al.*, 2009; *D'Amico et al.*, 2010; *Scognamiglio et al.*, 2010]. The rupture dimensions and location of the main slip patch are approximately shared by the various models.

[24] In this paper we use the same fault plane and mechanism as in Paper 1, i.e., a rectangular fault plane 20 km long and 15 km wide having a strike of 140° and dipping 50° toward southwest. The rake angle is −90° (pure normal-fault mechanism) and the hypocentral depth is 9 km (Table 3). Such fault geometry and focal mechanism essentially agree with all the previous studies. We constrain the basic features of the kinematic rupture model according to the low-frequency inversion performed in Paper 1: namely (1) the approximate location of the two main asperities, (2) the time delay of the southeastern asperity rupture, and (3) the decrease of rupture velocity in the shallow parts of the fault.

[25] The final HIC source model used to calculate synthetic seismograms up to 10 Hz is reported in Figure 4. The rupture time distribution is obtained assuming two rupture velocities (as marked also in Figure 4) and a nucleation point corresponding to the instrumental hypocenter. As suggested by the slip inversion, a rupture delay of the southern asperity by approximately 3 s is also included in the model. Although the low-frequency inversion suggests that the shallower subsource ruptured with a lower velocity than the deeper ones, the results show poor sensitivity to rupture velocity values. For this reason we test different values and set the final rupture velocity in the bottom and top part of the fault equal to Vr = 3 km/s and Vr = 2 km/s, respectively. Note that these values roughly corresponds to 85% of the average shear wave velocity at the relative depths.

[26] The final slip distribution is obtained constraining the positions of the three largest subsources (at level n = 2), that are characterized by the largest seismic moment, according

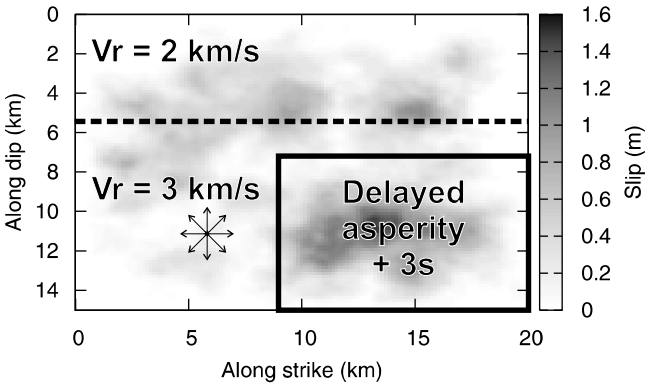

Figure 4. Kinematic rupture model used in the simulations. The final k-squared slip distribution composed of slip contributions from the fractal subsources is mapped by gray tones. The rupture velocity (V_r) values used in the top and bottom part of the fault as well as the location of the delayed asperity are illustrated. The outward vectors indicate the rupture nucleation point. The positions of the three largest subsources (at level n = 2) centers are: (8, 6), (12,11) and (15,11).

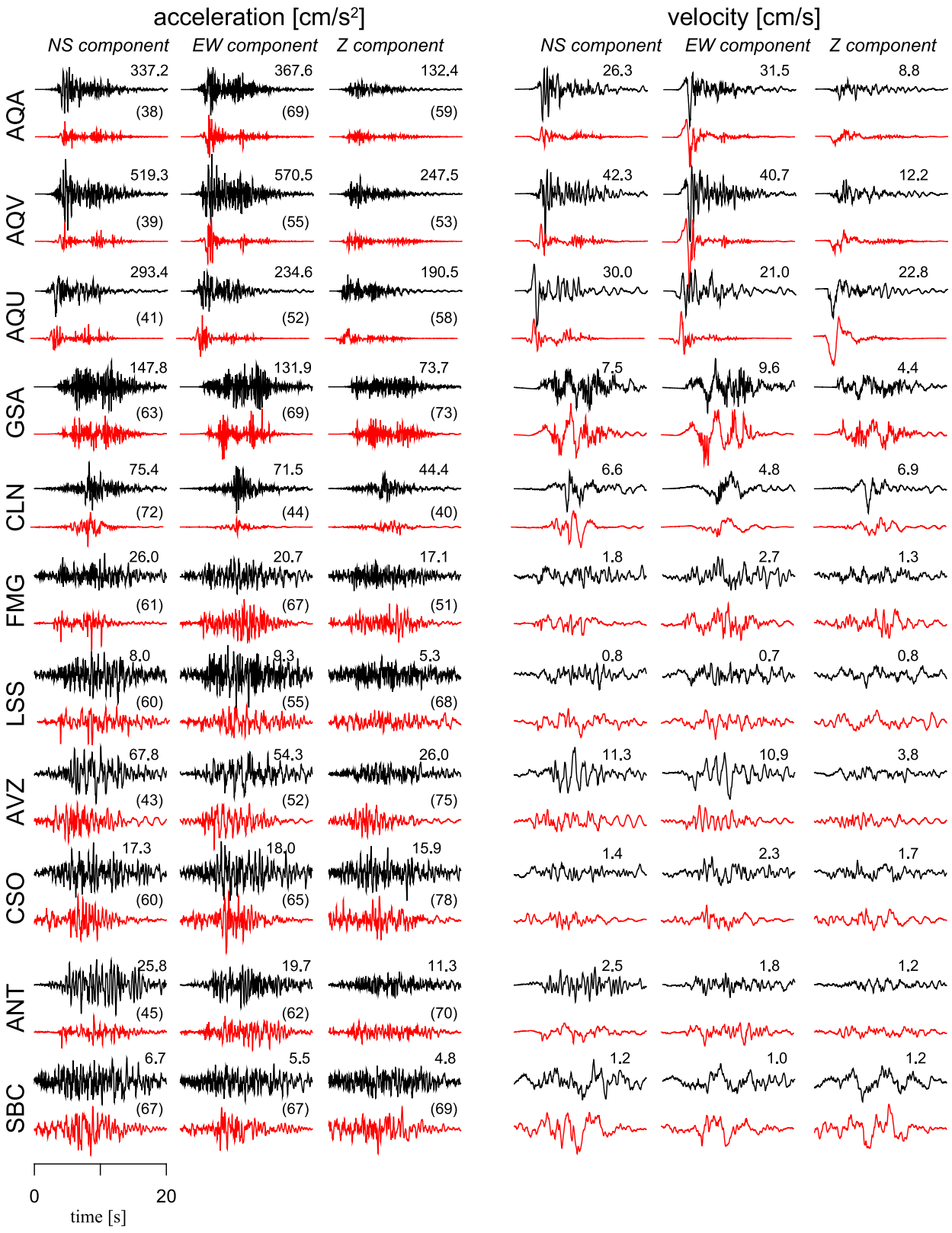

Figure 5. Comparison of recorded (black) and simulated (red) broadband three-component (left) ground-acceleration and (right) velocity waveforms at 11 selected sites (indicated in Figure 1) for the L'Aquila earthquake. North-South, East-West and vertical components are shown. The recorded and simulated motions for each station are scaled to the maximum value listed above each pair of waveforms. The numbers between brackets are the goodness-of-fit score. Waveforms are band-pass filtered between 0.1 and 10 Hz. Comparison for other stations is presented in the Supporting material.

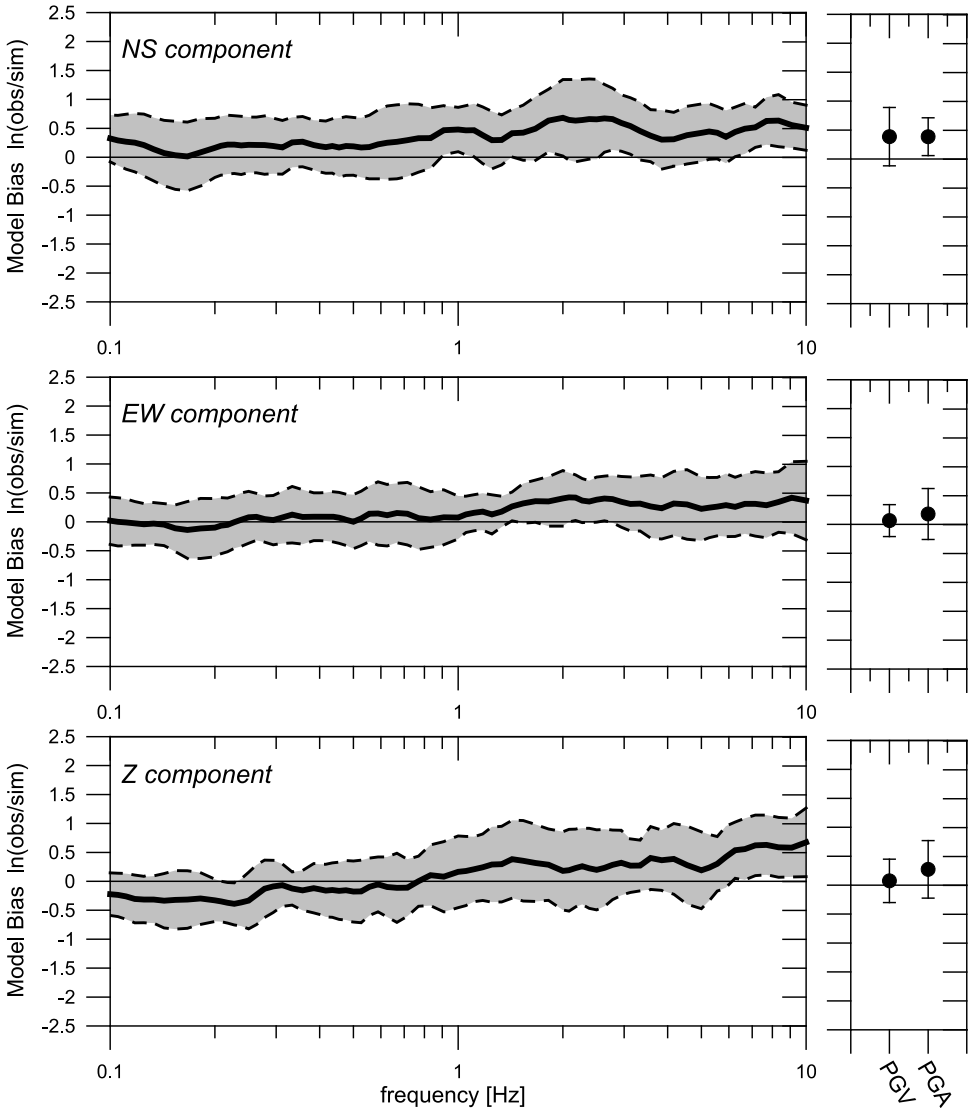

Figure 6. (left) Model bias (thick line) and standard deviation (shaded region) for 5% damped spectral acceleration using 15 sites for the L'Aquila earthquake. (right) Model bias and standard deviation for peak ground velocity (PGV) and peak ground acceleration (PGA) are also shown. (top) North-South component, (middle) East-West component, and (bottom) vertical component. Note that in the calculations we excluded 4 stations clearly problematic (i.e., MTR, SUL, ORC, CHT in the auxiliary material).

to Paper 1. In particular, one of them is placed "above" the hypocenter and the other two are set in the southern bottom part of the fault. At levels higher than 2, the remaining 60 subsources are randomly distributed over the fault plane following the defined number-size distribution, composing random high-wave numbers details of the slip distribution.

[27] Finally, the stress drop of the whole event is set to 100 bars based on estimates by *Bindi et al.* [2009] and on comparison between observed and synthetic high-frequency level of the Fourier amplitude spectra (see an example in the auxiliary material).[1]

[28] Note that, since the main features of this model are retrieved by the low-frequency inversion, the success of the broadband modeling depends on whether or not the observed high-frequency ground motions are affected/controlled by the low-frequency source features.

6. Results: Modeling of Strong Motion Records

[29] The HIC method allows for relatively fast ground-motion simulations, thus we performed a large number of trial calculations with the aim to obtain the "best fit" with recorded data. The sensitivity of the results to the local site response, rupture velocities, slip distribution at high wave numbers, rupture delay of second asperity and crossover frequency between the integral and composite approaches is investigated. Some of these results at specific sites will be discussed in the next paragraphs. Note that no artificial site-dependent time shifts were made because the recordings are accompanied by correct timings.

[1]Auxiliary materials are available in the HTML. doi:10.1029/2011JB008729.

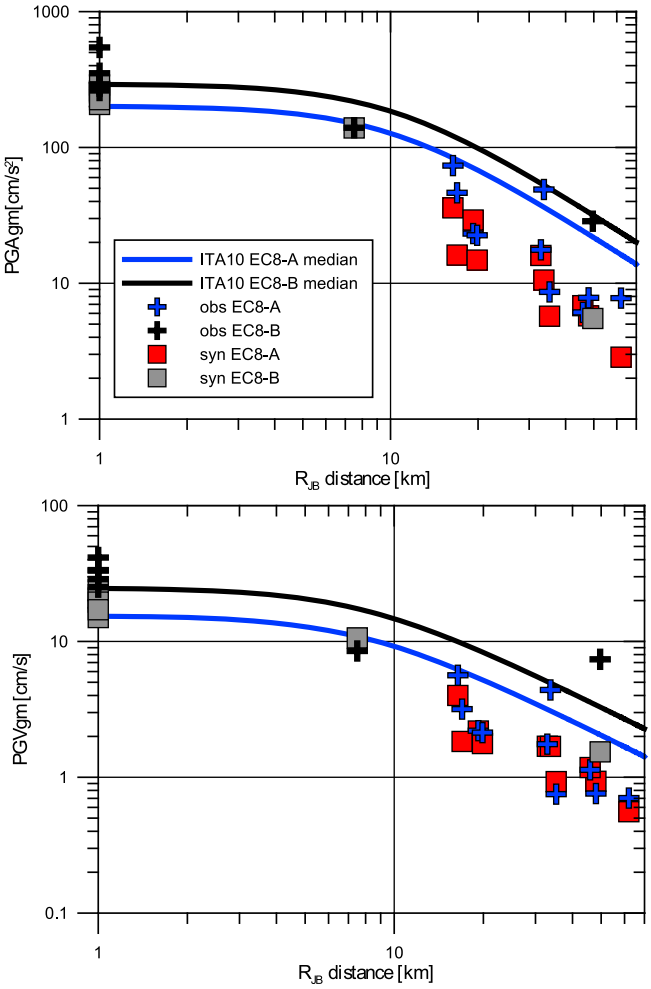

Figure 7. Observed (crosses) and simulated (squares) PGA and PGV (geometric mean of NS and EW components) as a function of Joyner-Boore distance (R_{JB}, minimum distance from the site and the surface projection of the rupture plane). Median estimates from *Bindi et al.* [2011] GMPEs (ITA10) are also shown. The symbols and lines colors represent the corresponding EC8 site class.

[30] The fit is judged according to the goodness-of-fit (GOF) criteria defined by *Olsen and Mayhew* [2010]. They proposed a GOF algorithm based on different metrics, among which we selected: Peak Ground Acceleration (PGA), velocity (PGV) and displacement (PGD), response spectral acceleration and smoothed Fourier spectrum averaged for periods between 0.1 and 10 s, energy duration 5–75% and cumulative kinetic energy. More details on the definition and selection of the different metrics can be found in the work of *Olsen and Mayhew* [2010]. The final GOF score is defined as GOF average (from 0 to 100) of the equally weighted abovementioned metrics.

[31] Based on these criteria, we define a so-called best model, whose main parameters are listed in Table 3. Figure 5 presents an overview of the modeling results for this model, showing comparison of synthetic and observed acceleration and velocity waveforms for 11 selected stations (Table 1 and Figure 1).The GOF score is reported for each station and each component. Both the observed and simulated waveforms are band-pass filtered between 0.1 and 10 Hz. The results for all the stations are reported in the auxiliary material (Figures S1–S9), also including the comparison of observed and simulated Fourier amplitude spectra (FAS).

[32] In general, the synthetics reproduce well the observed waveforms, despite the simplicity of the propagation models and the lack of site response for the most of the stations. The duration of the strong motion phase is well reproduced as well as the acceleration and velocity peak values. Concerning near fault sites (AQ_ stations), the synthetics show the characteristic velocity pulses with amplitude similar to the observed ones, at least on one component. However, an underestimation in the amplitudes and a lack of some high-frequency phases is noticed on the horizontal components (particularly on the North-South one), suggesting that more complex effects related to the presence of Aterno valley or details of source rupture model could affect the ground motion at these sites.

[33] A comparison between observed and simulated acceleration response spectra (5% damping) and acceleration and velocity peak values, PGA and PGV, is presented in Figure 6. For the best model, residuals are calculated as $\ln(Y_{obs}/Y_{sim})$, where Y is the ground-motion parameter (SA*(f)*, PGA, or PGV). The residuals are computed considering 15 out of the 19 stations presented in Table 1, excluding four stations (CHT, MTR, ORC and SUL) that are characterized by dominant site-specific phenomena, not explainable with the considered propagation model (see figures in the auxiliary material). The model bias is obtained by calculating the mean and standard deviation of the residuals over all stations for the considered ground-motion parameters. Figure 6 presents the model bias separately for horizontal and vertical components. A model bias of zero indicates that the simulation, on average, matches the observed ground-motion level. A negative model bias indicates overprediction of the observations and a positive model bias indicates underprediction of the observations.

[34] The comparisons shown in Figure 6 exhibit little systematic model bias across a wide frequency range. The standard deviation ranges from about 0.3 to 0.7 natural log units. There is a tendency to underestimate spectral ordinates above 1 Hz on all components that can be ascribed to the lack of site-specific amplifications at most of the stations. Only for the NS component the underestimation extends also to lower frequencies. As mentioned above, such underestimation is related to the AQ_ stations.

[35] Figure 7 compares the observed and simulated PGA and PGV (geometric mean of NS and EW components) as a function of distance. The distance-decay of the observed peak values is well described by the synthetic ones, although at few stations, where the site-specific effect is not considered, the underestimation is remarkable (examples are ORC and CHT stations, see the waveform comparisons in the auxiliary material). The peaks are also compared with estimates from empirical ground motion prediction equations (GMPEs) for the Italian territory [*Bindi et al.*, 2011]. Interestingly, the decay of the observed amplitudes for rock sites (EC8 class A) is better described by the simulated values than by the median estimates from the adopted GMPEs, at least over the distance range considered in our modeling. This result indicates that the ground motion in the epicentral

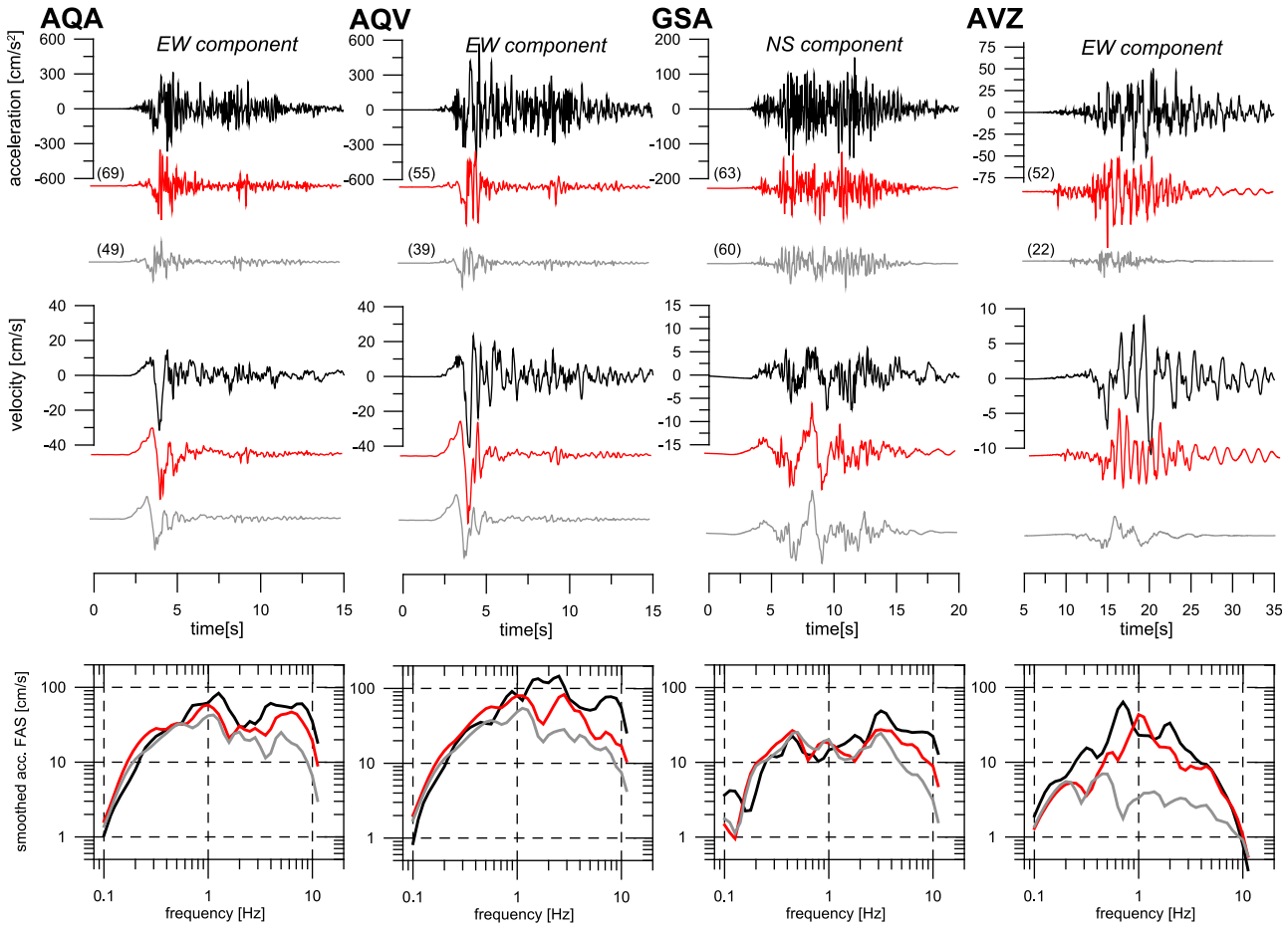

Figure 8. Effect of the subsurface site-specific soil profiles. (top, middle) Recorded (black), best model (red) and no-site-effects model (gray) ground-acceleration and velocity waveforms (one horizontal component) at four selected sites (indicated in Figure 1). The numbers between brackets are the goodness-of-fit score. (bottom) Corresponding smoothed acceleration Fourier amplitude spectra (FAS).

area of the L'Aquila earthquake attenuates faster than what prescribed by the GMPEs for similar magnitude earthquakes.

[36] In the following we discuss some interesting features of the modeling, illustrating the distinct sensitivity of individual station recordings to various properties of the source/propagation models. We mostly concentrate on near-fault stations, especially those with available 1D soil profile.

6.1. Effect of 1D Soil Profiles

[37] As explained in section 4, at five stations we simulate the ground motion including a 1D site-specific subsurface structure (see Figure 3). The introduction of the site-specific soil profile into calculation of the Green's function allows to better evaluate the site effects, taking implicitly into account the incoming wavefields with proper incident angles at the base of the profile.

[38] Figure 8 illustrates the importance of including such site-specific shallow layers to reproduce spectral amplitudes and waveform durations. Synthetic acceleration and velocity seismograms and acceleration FAS, calculated including or not the 1D soil profiles (red and gray color in Figure 8, respectively), are compared with observed ones at four sites. Indeed, the soil response effectively enhances the ground motions, especially above 1 Hz (see the comparisons of FAS in Figure 8, bottom).

[39] The most dramatic effect is observed at station AVZ where the FAS are increased 5–10 times over a broad frequency band. Accordingly, the velocity and acceleration wavefields are also enhanced, however, by a smaller factor. The large amplifications of the FAS is also due to the modeling of later phases generated by the wave propagation in the shallow layers, resulting in longer duration of the simulated records. The large amplification and duration lengthening at AVZ station are caused by the thick soft sediments of the Avezzano Plain over which the station is located. Site amplification effects at AVZ are also clearly recognized by empirical studies [*Bindi et al.*, 2009] that reported large amplifications (>5) for frequencies around 1 Hz.

[40] At the other stations the effect of the adopted 1D soil profile is lower. The durations are more or less preserved. The shape of velocity synthetics is only slightly modified (see, e.g., station GSA). In particular, at AQA and AQV, the large-amplitude waves between the wave packages coming from the two asperities remain unexplained. These differences are related to features not included in the adopted model, such

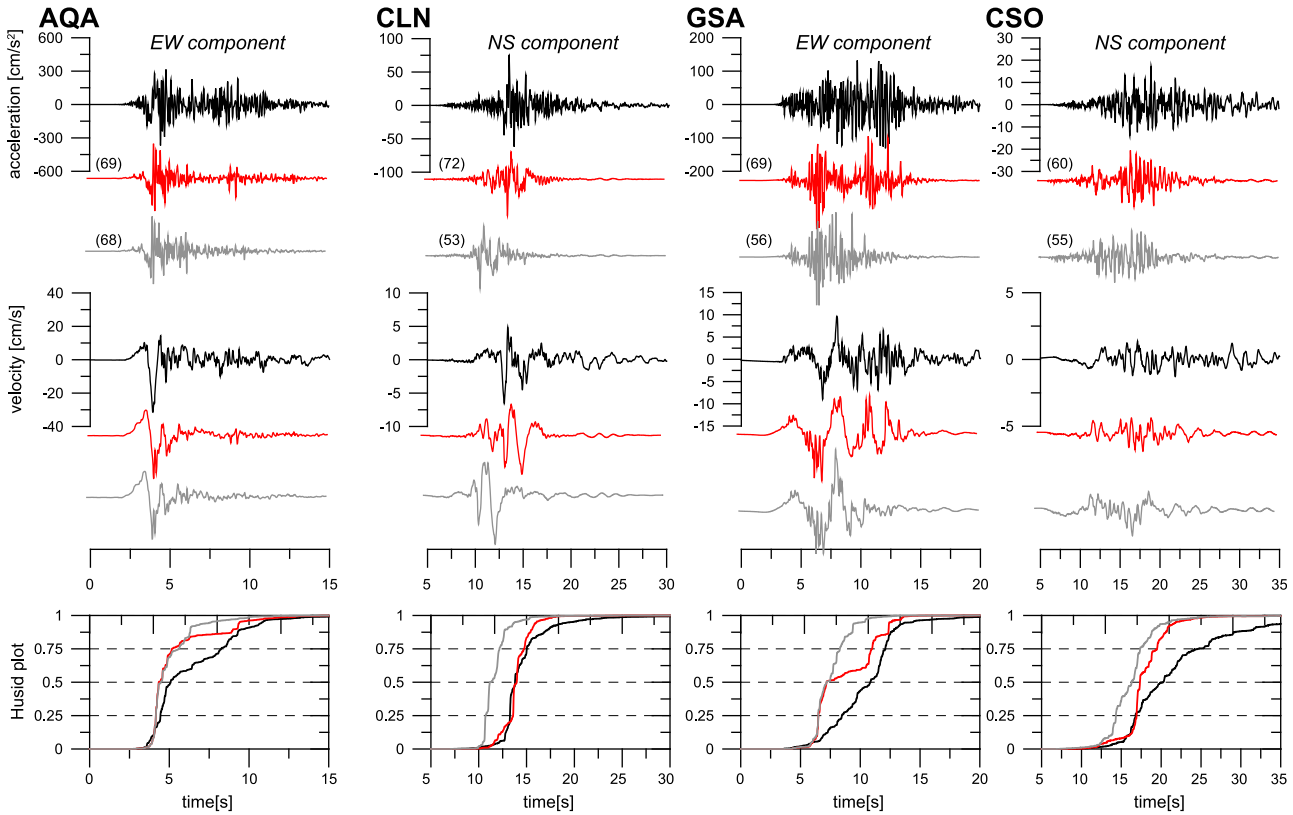

Figure 9. Effect of the asperity delay. (top, middle) Recorded (black), best model (red) and no-asperity-delay model (gray) ground-acceleration and velocity waveforms (one horizontal component) are compared at four selected sites (for their position see Figure 1). The numbers between brackets are the goodness-of-fit score. (bottom) Respective normalized Husid plots (cumulative squared acceleration).

as 3D crustal effects and/or additional complexities of the source model. The latter might be related to rupture propagation effects that we substitute in our model by the delay of the second asperity (see next section). Equally, there might be some slip complexities in the upper part of the rupture not resolved by the inversion. However, any such conclusions would have to rely on more precise Green's functions, taking into account, e.g., all possible reverberations of the complex 3D valley in the area.

6.2. Effect of the Delayed Asperity

[41] As already explained above, the slip inversion in Paper 1 suggests approximately 3 s rupture delay of the southeastern deep asperity (Figure 4). Figure 9 shows comparison with observed data in terms of acceleration and velocity time series and normalized Husid plots (cumulative squared acceleration) for the best model and a model neglecting the asperity delay. Four stations, having different distances and positions around the fault and being sensitive to this particular source feature, are shown.

[42] The best-model seismograms (red traces in Figure 9) well reproduce the major features of the observed time series, such as acceleration envelope, velocity pulses and the high-frequency content of the records. Acceleration records exhibit two wave groups at stations AQA and GSA. They are well explained by the delayed asperity, as can be seen when compared with the synthetics for the non-delayed model (gray traces in Figure 9). Interestingly, at the other two more distant stations (CLN and CSO) the two wave groups overlap. At these stations the non-delayed model results in early wave arrivals compared to what actually observed.

[43] In the velocity waveforms, the effect of the delayed asperity is best visible at CLN and partially at CSO and GSA stations. Indeed, at CLN, the model without the asperity delay exhibits a strong pulse at the beginning of the waveform, which is not present in the observed data. It is interesting to note that due to the position of CLN station with respect to the fault, the energy-time distribution is mainly controlled by the rupture time of the stronger SE asperity.

[44] The normalized Husid plots emphasize that the delayed-asperity results better capture the energy-time distribution of the observed data. Thus the broadband modeling confirms the significance of the rupture delay of the deeper asperity.

6.3. Effect of Rupture Velocity

[45] As explained in section 5, the best model is characterized by Vr = 3 km/s in the bottom part of the fault and Vr = 2 km/s in the upper part (see also Figure 4). Figure 10 shows the synthetic ground motions at AQA and GSA stations calculated for different rupture velocity values. As example, we show the acceleration and velocity seismograms obtained by removing the rupture velocity decrease in the shallow part of the fault and by extending the rupture velocity value in the shallow part to the whole fault. In the first

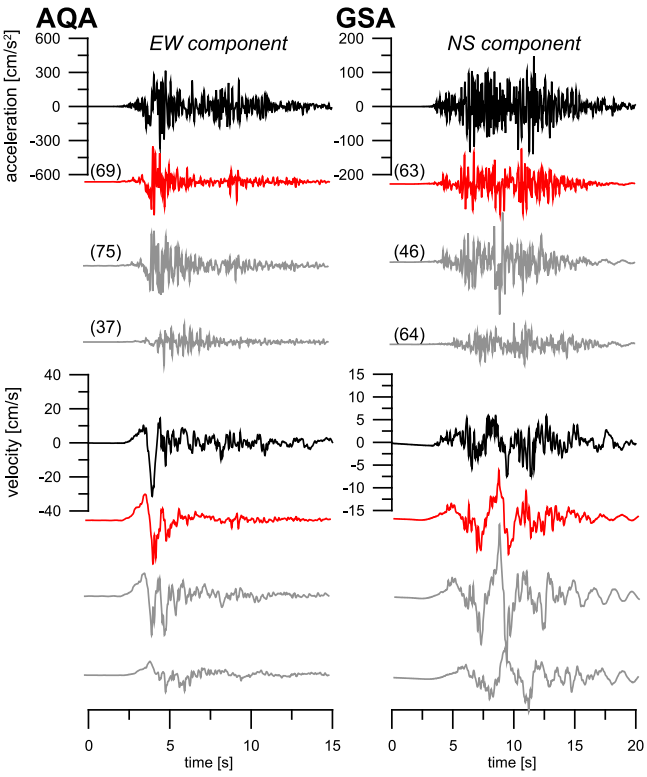

Figure 10. Effect of the rupture velocity. Recorded (black), best model (red), Vr = 3 km/s over the whole fault (gray, upper) and Vr = 2 km/s over the whole fault (gray, lower) ground-acceleration and velocity waveforms (one horizontal component) at two selected sites (indicated in Figure 1). The numbers between brackets are the goodness-of-fit score.

case (i.e., Vr = 3 km/s all over the fault) there is a clear enhancement of mid- and high-frequency amplitudes. The peak values are not substantially affected at AQA station and the major effect is the appearance of a second large velocity pulse whereas the first one remain unaffected. This second pulse is not observed in the recorded waveform suggesting that that the first pulse is related to the initial phase of the updip rupture propagation (i.e., between the hypocenter and 5 km depth). At GSA stations the observed velocity amplitudes are largely overestimated, demonstrating that the rupture velocity decrease in the shallow part of the fault is necessary to correctly model this updip station.

[46] In the second example (i.e., Vr = 2 km/s all over the fault) the waveforms at AQA show much smaller amplitudes and no strong velocity pulse is observed. For GSA, the small rupture velocity does not have a large effect at velocity waveforms, while the acceleration record is rather underestimated.

6.4. Effect of Slip Distribution at High Wave Numbers

[47] As explained in Section 5 we constrained the positions of the three largest subsources at level n = 2 of the HIC source model in order to reproduce the distribution of asperities retrieved in Paper 1. At levels larger than 2 the remaining 60 subsources are randomly distributed over the fault plane following the defined number-size distribution, composing random high wave numbers details of the slip distribution. The results presented so far are calculated using one single realization of the random distribution of these subsources (i.e., for one slip distribution). In Figure 11, we show the effect of 6 different realizations of the slip distributions, obtained by using different seeds in the random generator, on the ground acceleration and velocity simulated at AQA and GSA stations. As expected, the effect is stronger at AQA that is closer to the fault rupture, being sensitive to the details of the slip distribution. The ground motion amplitudes around 0.7–1 Hz are remarkably affected (mostly due to varying position of level 3 and 4 subsources) and, for some slip distributions, the velocity pulse amplitude decreases substantially. Examining the six models (labeled from 1 to 6 in Figure 11) we note that the larger low-frequency spectral content of models 1 and 5 with respect to the others is somehow related to the amount of slip "above" the hypocenter and toward the northwestern termination of the fault plane. At GSA station the six slip distributions produce less ground motion variations.

6.5. Effect of Crossover Frequency Band: From Integral to Composite Approach

[48] The crossover frequency range in the HIC model is a subject of choice. We remind the reader that this frequency divides the low-frequency (coherent/deterministic) and high-frequency (incoherent/stochastic) parts of the simulated wavefield. In other applications [*Gallovič and Brokešová*, 2007; *Gallovič and Burjánek*, 2007; *Ameri et al.*, 2009b; *Zollo et al.*, 2009; *Ameri et al.*, 2011], this range was set up around frequency of 1 Hz. The present application, dealing with stations located basically above the fault, deserves a more careful investigation of the crossover frequency value. Thus, Figure 12 shows comparison of observed velocities with synthetics for two crossover frequency ranges (1.5–2 Hz in red and 0.15–0.6 Hz in gray) at six selected stations around the fault located at increasing distance. The comparison is shown for velocity time series because (unlike the accelerations) the velocities are more sensitive to this low-to-intermediate frequency range. Note that when the crossover frequency range is set up to the smaller values, the HIC model becomes almost a purely composite model.

[49] At AQU and AQA stations, the arrival of the observed waveforms starts with a distinct onset and a strong directivity pulse. Both the onset and the pulse are better explained when the higher crossover frequency range is considered (i.e., 1.5–2 Hz). This means that the very close stations require the wavefield to arrive coherently up to the relatively high frequencies of 2 Hz. On the other hand, at GSA and CLN stations, located in the updip and along-strike rupture propagation directions, respectively, a better fit is obtained with the lower crossover frequency range (i.e., 0.15–0.6 Hz). At these stations, the integral part of the model produces too large low-frequency amplitudes due directivity effects that are not equally observed in the records. Slightly more distant stations, represented in Figure 12 by FMG and LSS (located in backward directivity directions) are less sensitive to this choice. Nevertheless, comparison of waveforms and FAS at these two and other stations indicate preference of lower crossover range.

[50] Figure 12 demonstrates that the use of higher crossover frequency range allows modeling the long-period pulses in velocity records observed at the closest stations by

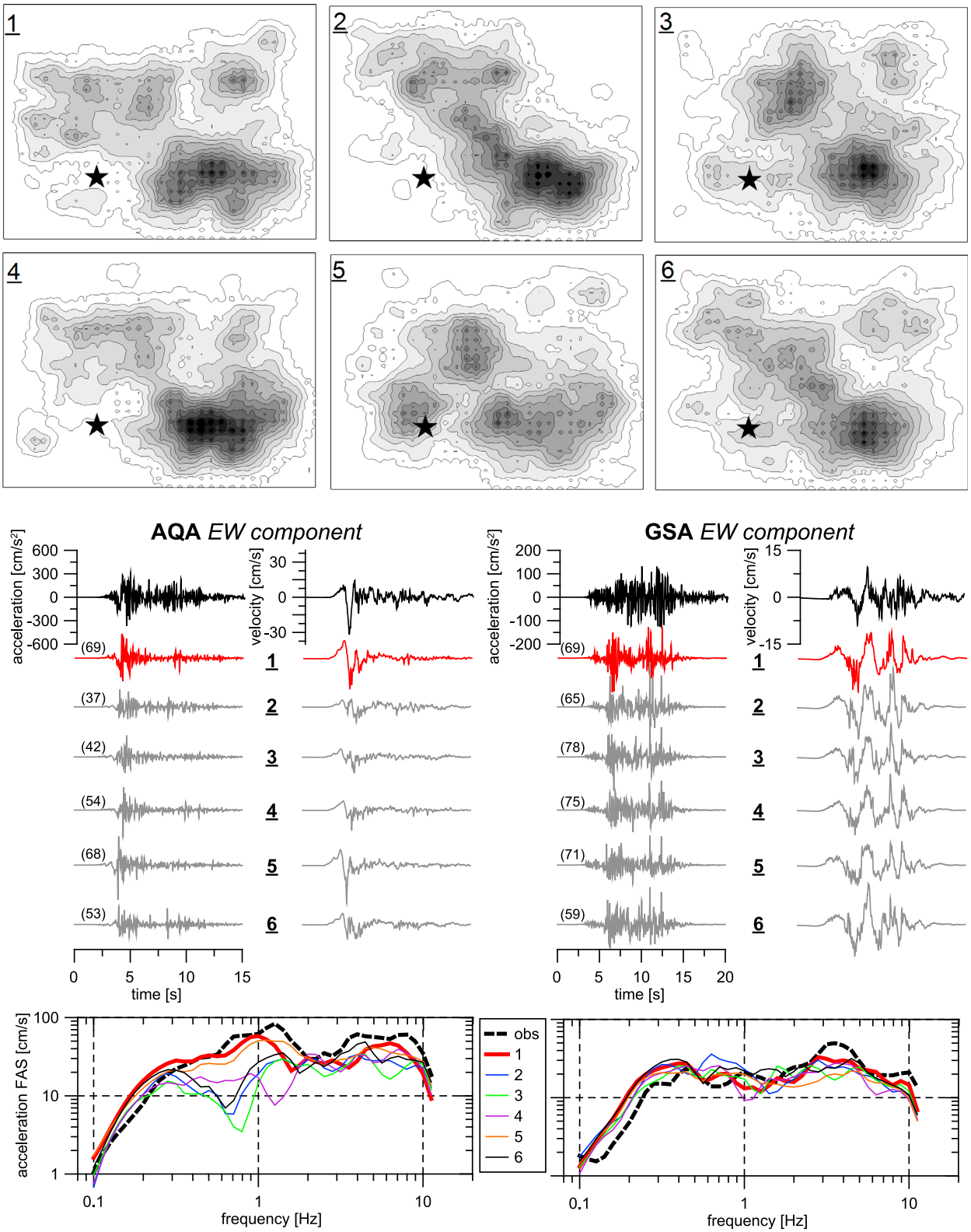

Figure 11. Effect of slip distribution at high wave numbers. (top) Six different slip models generated varying the random distribution of the small subsources (level > 2). The position of the largest subsources is kept constant. The black star represents the hypocenter. Model number 1 is the same reported in Figure 2. (middle) Recorded (black), best model (red) and different slip models (gray) ground-acceleration and velocity waveforms (one horizontal component) at two selected sites (indicated in Figure 1) are reported. The numbers between brackets are the goodness-of-fit score. (bottom) Corresponding smoothed acceleration Fourier amplitude spectra (FAS).

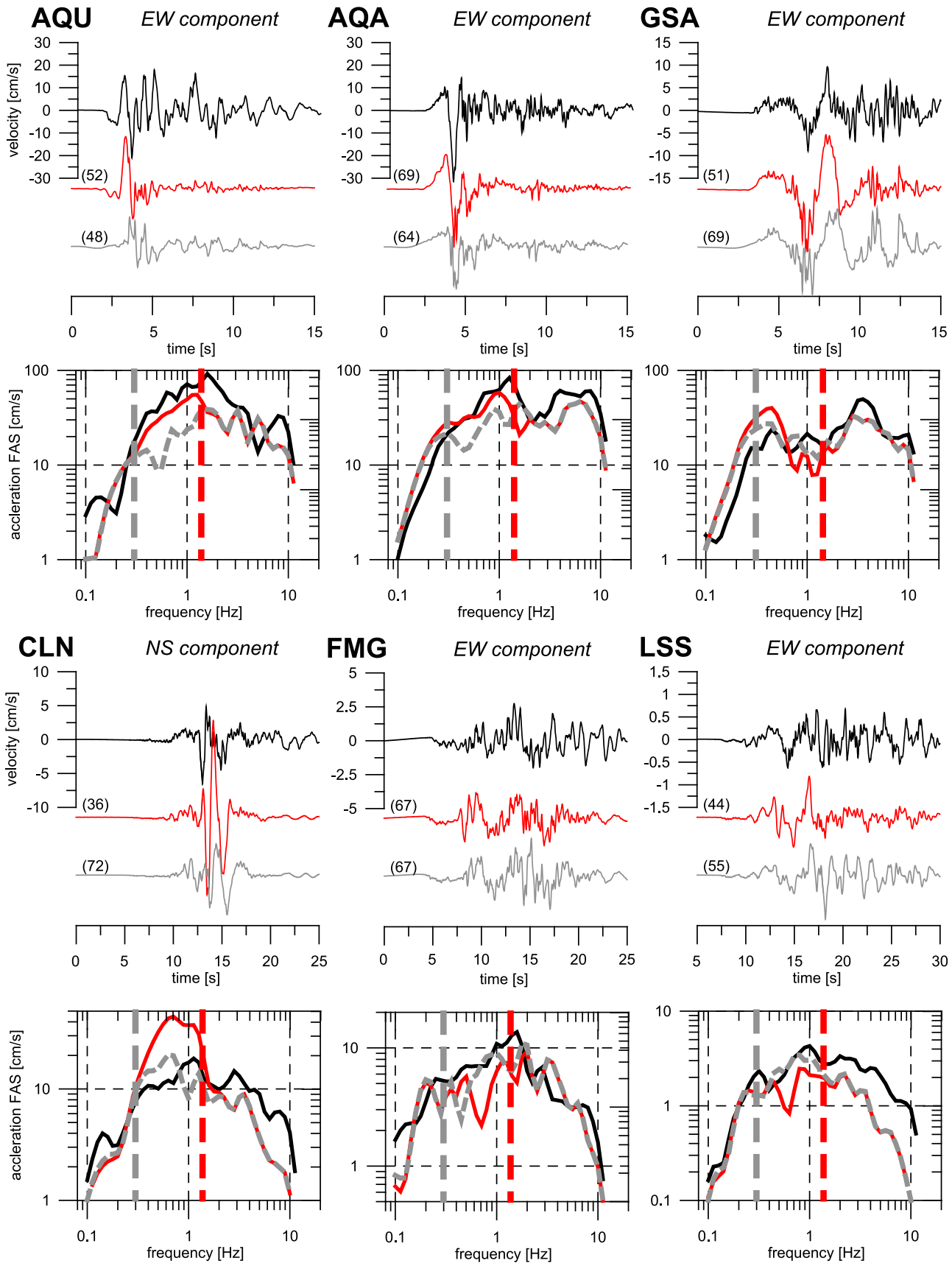
AQU
EW component
AQA
EW component
GSA
EW component
velocity [cm/s]
(52)
(48)
(69)
(64)
(51)
(69)
time [s]
acceleration FAS [cm/s]
frequency [Hz]
CLN
NS component
FMG
EW component
LSS
EW component
(36)
(72)
(67)
(67)
(44)
(55)

Figure 12

means of the integral approach. The lower frequency range for the further stations suggests that a purely deterministic modeling of rupture directivity is not suitable in this case, and that the stochastic (composite) approach is needed in almost the whole frequency band.

7. Discussion and Conclusions

[51] In the present paper we investigated the near-fault recordings of the Mw 6.3 2009 L'Aquila earthquake in a broad frequency range (up to 10 Hz) using a kinematic Hybrid Integral-Composite (HIC) earthquake source model. The recordings exhibited strong azimuthal and distance dependence. The main advantage of the HIC model was the consistent combination of low-frequency coherent and high-frequency incoherent ground motions, calculated by the use of the representation theorem and the composite approach, respectively. Several major parameters of the source model were constrained according to the preceding low-frequency (<0.2 Hz) inversion by means of the multiple finite-extent source model (see Paper 1). The considered stable major source parameters included position of the two main asperities (located, respectively, updip and southeast along-strike from the nucleation point), decrease of rupture velocity in the shallow part of the fault and time delay of the deeper asperity rupture. Other parameters of the HIC source model (namely, rupture velocity value, small scale slip distribution and stress drop) were investigated by comparison with observed records.

[52] The Green's functions were calculated in a 1D-layered crustal model including 1D soil profiles, where available, to account for site-specific response at the accelerometric stations. We demonstrated that the use of site-specific Green's functions improved the modeling results significantly in case of thick sediments layers (AVZ station). The variability observed at the considered near-fault sites was only partially related to local site amplification as it was also controlled by the rupture kinematics.

[53] Overall, the modeling results showed a remarkable fit with observed records despite the relative simplicity of the propagation models and the lack of site-specific amplification for most of the stations. Moreover, the decay of the observed PGA and PGV was better captured by synthetic values than by median estimates from regional GMPEs, suggesting that the predictions provided by such simple equations should be interpreted cautiously.

[54] We stress that in this study the broadband HIC source model, that was built on the basis of a low-frequency source inversion (see Paper1), prescribes a coherent rupture for low-frequency seismograms and incoherent (complex) rupture for the high-frequency ones. Implicitly, the 'high-frequency' (HF) sources, representing the complex rupture, are located in the centers of the 'low-frequency' (LF) asperities. Note that such approach does not always guarantee successful modeling of broadband ground motions. For instance, for huge (mostly) megathrust events there is an increasing evidence that the HF sources are adjacent to the LF asperities [*Meng et al.*, 2011a; *Meng et al.*, 2011b; *Simons et al.*, 2011; *Koper et al.*, 2011]. The small model bias across a wide frequency range supports the choice of the model parameters as well as the performance of the HIC approach to "extend" the low-frequency source model to higher frequencies, showing that, in the present case study, the HF radiation is co-located with the LF one. Nevertheless, a devoted study employing high-resolution back-projection techniques would have to be performed to eventually constrain the mutual location of the LF and HF sources.

[55] The main advantage of the modeling was that it allowed linking distinct features of the observed wavefield to particular source and propagation effects and provided insights on strong motion complexity from this moderate magnitude event. We showed that the source model complexities constrained from the kinematic inversion in the low-frequency range directly affected the strong-ground motion recordings also at higher frequencies. This was illustrated on example seismograms where the sensitivity to several source model features was shown.

[56] In particular, (1) the two slip asperities in the rupture model were necessary to explain the ground motion at the closest sites, where two distinct wave groups were clearly visible on recorded waveforms (e.g., AQ_, GSA stations). (2) The rupture delay of the southeastern asperity and the along-strike rupture propagation were essential to understand the CLN, GSA and CSO records. (3) The updip rupture propagation correctly explained the ground motion at GSA station. Tests regarding the effect of rupture velocity distribution on ground motion at this site showed that the decrease of rupture velocity in shallow part of fault was required to correctly fit the velocity waveforms, whereas larger rupture velocity values would have overestimated the observed amplitudes. (4) The near-fault AQ_ records were mainly controlled by the early phases of the rupture propagation that were responsible for the velocity pulses. The southeastern asperity, characterized by larger slip, generated the smaller later arrivals.

[57] The requirement of the rupture delay of the southeastern asperity to fit most of the near-fault records suggested that the earthquake might had experienced a first phase of rupture propagation in the updip direction and a second phase in the along-strike direction. It is not clear whether the two phases were separated by a rupture arrest or a slow-down of the rupture velocity. In any case, the earthquake can be regarded as a double event. Further studies should be performed to understand the dynamics of the L'Aquila earthquake in this respect.

[58] To obtain a better fit with the observed data we founded that the crossover frequency dividing the low-frequency coherent (integral) and high-frequency incoherent (composite) wavefields had to be variable, with larger values (>1.0 Hz) for the very close stations and smaller (<1 Hz)

Figure 12. Effect of the crossover frequency range. (top) Recorded (black) and simulated ground- velocity waveforms at six selected sites (indicated in Figure 1) are compared. The synthetics are calculated with two different crossover frequency ranges: 1.5–2 Hz (red waveforms) and 0.15–0.6 Hz (gray waveforms). The numbers between brackets are the goodness-of-fit score. (bottom) Smoothed acceleration Fourier amplitude spectra (FAS). Vertical lines mark the central frequencies of the lower (gray) and higher (red) frequency bands. Note that in this figure (unlike the others) the red seismograms does not represent the best model in all cases.

for more distant stations. Note that, typically, broadband simulation methods that combine the deterministic calculations at low frequency with stochastic approaches at high frequencies, use central crossover frequency constant at 1 Hz [e.g., *Kamae et al.*, 1998; *Hartzell et al.*, 1999; *Graves and Pitarka*, 2010]. This choice is based on the seismological observation that source radiation and wave-propagation effects tend to become random at frequencies above $f \approx 1$ Hz [e.g., *Pulido and Kubo*, 2004]. However, it sounds reasonable to expect that the frequency of transition between coherent and incoherent contributions varies also with magnitude and with distance [*Frankel*, 2009; *Mai et al.*, 2010]. *Frankel* [2009] investigated the magnitude dependence of the transition frequency by comparing simulated spectral accelerations from scenario events with empirical GMPEs. He used a transition frequency of 2.4 Hz for the Mw 6.5 ground motion simulations, which is close to our crossover frequency-band upper limit for the AQ_ stations. However, it is hard to compare his and our results because: (1) Frankel assumed the transition frequency based on comparison of strike-normal and strike-parallel Fourier spectra recorded at Rinaldi near-fault station during the Mw 6.7 Northridge earthquake; and (2) the distance dependence of the transition frequency was not investigated by the author. *Spudich and Chiou* [2006] compared the strike-normal to strike-parallel ratio of spectral acceleration for NGA strong motion data set (for Mw > 6) with that calculated from an approximation of theoretical double-couple S-wave radiation pattern in order to find an optimal water level preventing zero amplitudes in nodal directions. Indeed their results can be seen as an indication of the coherent/incoherent character of the records as a function of source-to-site distance and frequency. *Spudich and Chiou* [2006] indicated that the effect of theoretical radiation pattern, that we modeled in the integral part of the method, was seen in the data at very close distances (0–5 km from the rupture) even at relatively high frequencies (~2 Hz) whereas it decreased with increasing distances with a trend depending on the frequency.

[59] Our finding of the different preference of the crossover frequency (i.e., 1.5 Hz and 0.3 Hz central frequencies, Figure 5) by close and distant stations on one hand supports the distance dependence of the crossover frequency, ascribing propagation effects as the main cause of incoherency of ground motions. On the other hand, the updip propagation along the first asperity could have been very smooth (i.e., associated with negligible variations of the rupture parameters), without generating much incoherent high-frequency radiation. In this hypothesis we assume that the incoherency of the observed wavefield is mainly linked to heterogeneity of the source process. Combination of both features is most likely. This topic should be further investigated using near- and far-fault strong motion data from other earthquakes and dynamic modeling of heterogeneous ruptures.

[60] Concerning the near-fault AQ_ stations we have to admit that, although the main features of the waveforms were well reproduced, particularly for the east-west and vertical component, the simulations still pose some problems and we lacked energy after the large-amplitude arrivals. Critical aspects in this regard are: (1) the proximity of the stations to the point-sources, that may cause problem in the composite part (high-frequency) of the model; (2) the more complex radiation pattern for near-fault stations with respect to the simple double-couple radiation pattern adopted in HIC model at low-frequencies [*Pulido and Kubo*, 2004]. We tested that small variations of the fault strike in the low-frequency calculations did not eliminate the underestimation of the N-S component. This limitation likely lies in the use of a 1D crustal model whereas a fault embedded in a 3D medium would perhaps improve the modeling of radiation pattern even at low frequencies [e.g., *Gallovič et al.*, 2010]. (3) The slip distribution (at small scale) in the vicinity of the hypocenter. The variability of the ground motion for different high wave numbers slip distributions was noticeable in some case and we cannot exclude that some model could enhance the North-South amplitudes. Indeed, we stress that the high wave numbers details of the slip distribution that we used in this paper as "best model" should not be acknowledged as the best slip model for the earthquake. As such, it is only the best among the few tested random distributions in explaining the records, i.e., capturing the main broadband features of the near-fault records. However, some other high wave numbers random slip distribution could provide similar or better fit to the data, although determining such model cannot be the aim of this paper due to the other limitations of the modeling. (4) 3D site-effects due to wave propagation within the Aterno Valley basin might be important to explain the ground motions observed at AQ_ stations. Further studies should be performed in order to investigate the different causes.

[61] The presented results have strong conclusions not only to earthquake physics (see also Paper 1), but also to ground-motion simulations for hazard analyses and earthquake engineering applications. The set of scenario events should be enriched to include also models with characteristics found for the L'Aquila earthquake. The doublet character of the event has direct consequences on duration of the records, that is critical to assess the cyclic seismic response of structures. The variable crossover frequency, playing an important role especially at near-fault distances, should be also taken into account in scenario studies. Purely composite and/or stochastic models without the possibility of modeling the coherent low-frequency wavefield by the integral approach would meet difficulties when explaining the near-source directivity pulses observed at AQ_ stations. Correct modeling of pulse-type records is of great relevance to earthquake engineering because their seismic demand and spectral shape are different with respect to ordinary records and can generate much higher damage.

[62] **Acknowledgments.** The authors acknowledge free Internet access of waveforms provided by the Italian Strong Motion Database (ITACA, http://itaca.mi.ingv.it/). Financial support from Project RS1 (ReLUIS-DPC 2010–2013), NERA 262330, GACR 210/11/0854, MSM0021620860. We thank Kim Olsen for providing the GOF code and Rodolfo Puglia for providing the soil profiles used in the calculations. We particularly thank Jiří Zahradník for fruitful discussions. Finally, we acknowledge the constructive comments of the Associate Editor Martin Mai and of two anonymous reviewers that significantly improved the paper.

References

Aagaard, B. T., et al. (2008), Ground-motion modeling of the 1906 San Francisco earthquake, part II: Ground-motion estimates for the 1906 earthquake and scenario events, *Bull. Seismol. Soc. Am.*, *98*, 1012–1046, doi:10.1785/0120060410.

Akinci, A., L. Malagnini, and F. Sabetta (2010), Characteristics of the strong ground motions from the 6 April 2009 L'Aquila earthquake,

Italy, *Soil. Dyn. Earthquake Eng.*, *30*, 320–335, doi:10.1016/j.soildyn.2009.12.006.

Ameri, G., F. Pacor, G. Cultrera, and G. Franceschina (2008), Deterministic ground-motion scenarios for engineering applications: The case of Thessaloniki, Greece, *Bull. Seismol. Soc. Am.*, *98*(3), 1289–1303, doi:10.1785/0120070114.

Ameri, G., et al. (2009a), The 6 April 2009, M_w 6.3, L'Aquila (central Italy) earthquake: Strong-motion observations, *Seismol. Res. Lett.*, *80*, 951–966, doi:10.1785/gssrl.80.6.951.

Ameri, G., F. Gallovič, F. Pacor, and A. Emolo (2009b), Uncertainties in strong ground-motion prediction with finite-fault synthetic seismograms: An application to the 1984 M 5.7 Gubbio, central Italy, earthquake, *Bull. Seismol. Soc. Am.*, *99*, 647–663, doi:10.1785/0120080240.

Ameri, G., A. Emolo, F. Pacor, and F. Gallovič (2011), Ground-motion simulations for the M 6.9 Irpinia 1980 earthquake (southern Italy) and scenario events, *Bull. Seismol. Soc. Am.*, *101*(3), 1136–1151, doi:10.1785/0120100231.

Anderson, J. G., and S. E. Hough (1984), A model for the shape of the Fourier amplitude spectrum of acceleration at high frequencies, *Bull. Seismol. Soc. Am.*, *74*, 1969–1993.

Andrews, D. J. (1980), A stochastic fault model: 1. Static case, *J. Geophys. Res.*, *85*, 3867–3877, doi:10.1029/JB085iB07p03867.

Anzidei, M., et al. (2009), Coseismic deformation of the destructive April 6, 2009 L'Aquila earthquake (central Italy) from GPS data, *Geophys. Res. Lett.*, *36*, L17307, doi:10.1029/2009GL039145.

Atzori, S., I. Hunstad, M. Chini, S. Salvi, C. Tolomei, C. Bignami, S. Stramondo, E. Trasatti, A. Antonioli, and E. Boschi (2009), Finite fault inversion of DInSAR coseismic displacement of the 2009 L'Aquila earthquake (central Italy), *Geophys. Res. Lett.*, *36*, L15305, doi:10.1029/2009GL039293.

Bianchi, I., C. Chiarabba, and N. Piana Agostinetti (2010), Control of the 2009 L'Aquila earthquake, central Italy, by a high-velocity structure: A receiver function study, *J. Geophys. Res.*, *115*, B12326, doi:10.1029/2009JB007087.

Bindi, D., R. R. Castro, G. Franceschina, L. Luzi, and F. Pacor (2004), The 1997–1998 Umbria-Marche sequence (central Italy): Source, path, and site effects estimated from strong motion data recorded in the epicentral area, *J. Geophys. Res.*, *109*, B04312, doi:10.1029/2003JB002857.

Bindi, D., F. Pacor, L. Luzi, M. Massa, and G. Ameri (2009), The M_w 6.3, 2009 L'Aquila earthquake: Source, path and site effects from spectral analysis of strong motion data, *Geophys. J. Int.*, *179*, 1573–1579, doi:10.1111/j.1365-246X.2009.04392.x.

Bindi, D., F. Pacor, L. Luzi, R. Puglia, M. Massa, G. Ameri, and R. Paolucci (2011), Ground motion prediction equations derived from the Italian strong motion data base, *Bull. Earthquake Eng.*, *9*(6), 1899–1920, doi:10.1007/s10518-011-9313-z.

Boatwright, J. (2007), The persistence of directivity in small earthquakes, *Bull. Seismol. Soc. Am.*, *97*, 1850–1861, doi:10.1785/0120050228.

Bouchon, M. (1981), A simple method to calculate Green's functions for elastic layered media, *Bull. Seismol. Soc. Am.*, *71*, 959–971.

Comité Européen de Normalisation (2004), Eurocode 8: Design of structures for earthquake resistance—Part 1: General rules, seismic actions and rules for buildings, *Rep. EN 1998-1:2004*, Brussels.

Chiarabba, C., et al. (2009), The 2009 L'Aquila (central Italy) M_w6.3 earthquake: Main shock and aftershocks, *Geophys. Res. Lett.*, *36*, L18308, doi:10.1029/2009GL039627.

Chioccarelli, E., and I. Iervolino (2010), Near-source seismic demand and pulse-like records: A discussion for L'Aquila earthquake, *Earthquake Eng. Struct. Dyn.*, *39*, 1039–1062.

Cirella, A., A. Piatanesi, M. Cocco, E. Tinti, L. Scognamiglio, A. Michelini, A. Lomax, and E. Boschi (2009), Rupture history of the 2009 L'Aquila (Italy) earthquake from non-linear joint inversion of strong motion and GPS data, *Geophys. Res. Lett.*, *36*, L19304, doi:10.1029/2009GL039795.

Cultrera, G., F. Pacor, G. Franceschina, A. Emolo, and M. Cocco (2009), Directivity effects for moderate-magnitude earthquakes (Mw 5.6–6.0) during the 1997 Umbria–Marche sequence, central Italy, *Tectonophysics*, *476*, 110–120, doi:10.1016/j.tecto.2008.09.022.

Cultrera, G., M. Mucciarelli, and S. Parolai (2011), The L'Aquila earthquake—A view of site effects and building behavior from temporary networks, *Bull. Earthquake Eng.*, *9*(3), 691–695, doi:10.1007/s10518-011-9270-6.

D'Amico, S., K. D. Koper, R. B. Herrmann, A. Akinci, and L. Malagnin (2010), Imaging the rupture of the Mw 6.3 April 6, 2009 L'Aquila, Italy, earthquake using back-projection of teleseismic P-waves, *Geophys. Res. Lett.*, *37*, L03301, doi:10.1029/2009GL042156.

Di Capua, G. (2009), Progress report on the ongoing activity for constructing a catalogue of geological/geotechnical information at accelerometer stations, *Rep. INGV-DPC 2007-2009*, Ist. Naz. di Geofis. e Vulcanol., Rome. [Available at http://esse4.mi.ingv.it/images/stories/deliverable_d4.pdf.]

Di Capua, G., G. Lanzo, V. Pessina, S. Peppoloni, and G. Scasserra (2011), The recording stations of the Italian strong motion network: Geological information and site classification, *Bull. Earthquake Eng.*, *9*(6), 1779–1796, doi:10.1007/s10518-011-9326-7.

Falcucci, E., et al. (2009), The Paganica fault and surface coseismic ruptures caused by the 6 April 2009 earthquake (L'Aquila, central Italy), *Seismol. Res. Lett.*, *80*(6), 940–950, doi:10.1785/gssrl.80.6.940.

Frankel, A. (2009), A constant stress-drop model for producing broadband synthetic seismograms: Comparison with the next generation attenuation relations, *Bull. Seismol. Soc. Am.*, *99*, 664–680, doi:10.1785/0120080079.

Gallovič, F., and J. Brokešová (2004), On strong ground motion synthesis with k^{-2} slip distributions, *J. Seismol.*, *8*, 211–224, doi:10.1023/B:JOSE.0000021438.79877.58.

Gallovič, F., and J. Brokešová (2007), Hybrid k-squared source model for strong ground motion simulations: Introduction, *Phys. Earth Planet. Inter.*, *160*, 34–50, doi:10.1016/j.pepi.2006.09.002.

Gallovič, F., and J. Burjánek (2007), High-frequency directivity in strong ground motion modeling methods, *Ann. Geophys.*, *50*(2), 203–211.

Gallovič, F., and J. Zahradník (2011), Complexity of the M6.3 2009 L'Aquila (central Italy) earthquake: 1. Multiple finite-extent source inversion, *J. Geophys. Res.*, *117*, B04307, doi:10.1029/2011JB008709.

Gallovič, F., M. Kaser, J. Burjánek, and C. Papaioannou (2010), Three-dimensional modeling of near-fault ground motions with nonplanar rupture models and topography: Case of the 2004 Parkfield earthquake, *J. Geophys. Res.*, *115*, B03308, doi:10.1029/2008JB006171.

Graves, R. W., and A. Pitarka (2010), Broadband ground-motion simulation using a hybrid approach, *Bull. Seismol. Soc. Am.*, *100*, 2095–2123, doi:10.1785/0120100057.

Graves, R. W., B. T. Aagaard, and K. W. Hudnut (2011), The ShakeOut earthquake source and ground motion simulations, *Earthquake Spectra*, *27*, 273–291, doi:10.1193/1.3570677.

Gruppo di Lavoro, M. S.-A. Q. (2010), Microzonazione sismica per la ricostruzione dell'area aquilana (in Italian), report, 769 pp., Dip. della Protez. Civ., Regione Abruzzo, Italy. [Available at http://www.protezionecivile.gov.it/jcms/it/view_pub.wp?contentId=PUB25330.]

Hartzell, S., S. Harmsen, A. Frankel, and S. Larsen (1999), Calculation of broadband time histories of ground motion: Comparison of methods and validation using strong-ground motion from the 1994 Northridge earthquake, *Bull. Seismol. Soc. Am.*, *89*, 1484–1504.

Herrero, A., and P. Bernard (1994), A kinematic self-similar rupture process for earthquakes, *Bull. Seismol. Soc. Am.*, *84*, 1216–1228.

Hisada, Y. (2008), Broadband strong motion simulation in layered half-space using stochastic Green's function technique, *J. Seismol.*, *12*, 265–279, doi:10.1007/s10950-008-9090-6.

Kamae, K., K. Irikura, and A. Pitarka (1998), A technique for simulating strong ground motions using hybrid Green's functions, *Bull. Seismol. Soc. Am.*, *88*, 357–367.

Koper, K. D., A. R. Hutko, T. Lay, C. J. Ammon, and H. Kanamori (2011), Frequency-dependent rupture process of the 11 March 2011 Mw 9.0 Tohoku earthquake: Comparison of short-peroid P wave back-projection images and broadband seismic rupture models, *Earth Planets Space*, *58*, 1–4.

Lanzo, G., M. Tallini, G. Milana, G. Di Capua, F. Del Monaco, A. Pagliaroli, and S. Peppoloni (2011), The Aterno Valley strong-motion array: Seismic characterization and determination of subsoil model, *Bull. Earthquake Eng.*, *9*, 1855–1875.

Mai, P. M., and G. C. Beroza (2003), A hybrid method for calculating near-source, broadband seismograms: Application to strong motion prediction, *Phys. Earth Planet. Inter.*, *137*, 183–199, doi:10.1016/S0031-9201(03)00014-1.

Mai, P. M., W. Imperatori, and K. B. Olsen (2010), Hybrid broadband ground-motion simulations: Combining long-period deterministic synthetics with high-frequency multiple S-to-S backscattering, *Bull. Seismol. Soc. Am.*, *100*(5A), 2124–2142, doi:10.1785/0120080194.

Meng, L., A. Inbal, and J.-P. Ampuero (2011a), A window into the complexity of the dynamic rupture of the 2011 Mw 9 Tohoku-Oki earthquake, *Geophys. Res. Lett.*, *38*, L00G07, doi:10.1029/2011GL048118.

Meng L., J.-P. Ampuero, A. Sladen, and H. Rendon (2011b), High-resolution back-projection at regional distance: Application to the Haiti M7.0 earthquake and comparisons with finite source studies, *J. Geophys. Res.*, doi:10.1029/2011JB008702, in press.

Olsen, K. B., and J. E. Mayhew (2010), Goodness-of-fit criteria for broadband synthetic seismograms, with application to the 2008 Mw5.4 Chino Hills, CA, earthquake, *Seismol. Res. Lett.*, *81*, 715–723, doi:10.1785/gssrl.81.5.715.

Pitarka, A., P. Somerville, Y. Fukushima, T. Uetake, and K. Irikura (2000), Simulation of near-fault strong-ground motion using hybrid Green's function, *Bull. Seismol. Soc. Am.*, *90*(3), 566–586, doi:10.1785/0119990108.

Puglia, R., R. Ditommaso, F. Pacor, M. Mucciarelli, L. Luzi, and M. Bianca (2011), Frequency variation in site response as observed from strong motion data of the L'Aquila (2009) seismic sequence, *Bull. Earthquake Eng.*, *9*(3), 869–892, doi:10.1007/s10518-011-9266-2.

Pulido, N., and T. Kubo (2004), Near-fault strong-motion complexity of the 2000 Tottori earthquake (Japan) from a broadband asperity model, *Tectonophysics*, *390*, 177–192, doi:10.1016/j.tecto.2004.03.032.

Scognamiglio, L., E. Tinti, A. Michelini, D. S. Dreger, A. Cirella, M. Cocco, S. Mazza, and A. Piatanesi (2010), Fast determination of moment tensors and rupture history: What has been learned from the 6 April 2009 L'Aquila earthquake sequence, *Seismol. Res. Lett.*, *81*, 892–906, doi:10.1785/gssrl.81.6.892.

Simons, M., et al. (2011), The 2011 magnitude 9.0 Tohoku-Oki earthquake: Mosaicking the megathrust from seconds to centuries, *Science*, *332*, 1421–1425, doi:10.1126/science.1206731

Somerville, P. G., N. F. Smith, R. W. Graves, and N. A. Abrahamson (1997), Modification of empirical strong ground motion attenuation relations to include the amplitude and duration effects of rupture directivity, *Seismol. Res. Lett.*, *68*, 199–222, doi:10.1785/gssrl.68.1.199.

Spudich, P., and B. S.-J. Chiou (2006), Directivity in preliminary NGA residuals, Final Project Report for PEER Lifelines Program Task 1M01, *Rep. SA5146-15811*, 49 pp., Pac. Earthquake Eng. Res. Cent., Berkeley, Calif.

Spudich, P., and B. S. Chiou (2008), Directivity in NGA earthquake ground motions: Analysis using isochrone theory, *Earthquake Spectra*, *24*(1), 279–298, doi:10.1193/1.2928225.

Zambonelli, E., R. de Nardis, L. Filippi, M. Nicoletti, and M. Dolce (2011), Performance of the Italian strong motion network during the 2009, L'Aquila seismic sequence (central Italy), *Bull. Earthquake Eng.*, *9*, 39–65, doi:10.1007/s10518-010-9218-2.

Zeng, Y., J. G. Anderson, and G. Yu (1994), A composite source model for computing realistic synthetic strong ground motions, *Geophys. Res. Lett.*, *21*, 725–728, doi:10.1029/94GL00367.

Zollo, A., et al. (2009), The earthquake early warning system in southern Italy: Methodologies and performance evaluation, *Geophys. Res. Lett.*, *36*, L00B07, doi:10.1029/2008GL036689.

G. Ameri and F. Pacor, Istituto Nazionale di Geofisica e Vulcanologia, via Bassini 15, I-20133 Milan, Italy. (gabriele.ameri@mi.ingv.it)

F. Gallovič, Faculty of Mathematics and Physics, Department of Geophysics, Charles University, V Holesovickach 2, Praha 8, Prague 180 00, Czech Republic.

[P14]

Bulletin of the Seismological Society of America, Vol. 103, No. 6, pp. 3164–3178, December 2013, doi: 10.1785/0120130044

Fault Process and Broadband Ground-Motion Simulations of the 23 October 2011 Van (Eastern Turkey) Earthquake

by F. Gallovič, G. Ameri,* J. Zahradník, J. Janský, V. Plicka, E. Sokos, A. Askan, and M. Pakzad

Abstract On 23 October 2011 an M_w 7.1 earthquake occurred in eastern Turkey, close to the towns of Van and Erciş, causing more than 600 casualties and widespread structural damage. The earthquake ruptured a 60–70 km long northeast–southwest fault with a thrust mechanism, in agreement with regional tectonic stress regime. We studied the fault process of the event and the recorded ground motions using different sets of data. Regional records (0.005–0.010 Hz) are used to constrain the centroid moment tensor solution. Near-regional data, 100–200 km from the fault, are used for relocation of the hypocenter and, in the frequency range 0.05–0.15 Hz, for inversion of the rupture propagation by two methods: multiple point-source model (ISOLA) and multiple finite-extent (MuFEx) source model. MuFEx also provides an estimate of the model uncertainty, which is quite large due to unfavorable station distribution. We arrive at several plausible scenarios (equally well fitting the observed data including Global Positioning System coseismic displacements) with different styles of the rupture propagation. A few alternative source models are used for broadband (0.1–10 Hz) ground-motion simulations by means of the hybrid integral-composite source model. Only models comprising source complexities, such as a delayed rupture of shallow asperities, enable explanation of the acceleration record at the only available near-fault station, which exhibits a long duration and two prominent wave groups. These complex rupture models are used to simulate the ground motion in the near-fault area, specifically, at Van and Erciş, where records of the mainshock were missing, providing reasonable agreement with the observed spatial distribution of damage.

Introduction

The M_w 7.1 Van earthquake occurred on 23 October 2011 in eastern Turkey, close to the towns of Van and Erciş, causing more than 600 casualties and widespread damage. The earthquake ruptured a 60–70 km long northeast–southwest fault with a thrust mechanism, in agreement with tectonic stress regime of the region.

Basic parameters of the earthquake were reported soon after the earthquake occurrence on websites of the United States Geological Survey (USGS) and European–Mediterranean Seismological Centre (EMSC); see Tables 1 and 2. Later, the USGS web pages included also the teleseismic slip inversion. The EMSC pages published the source–time function calculated by the SCARDEC method (Vallée *et al.*, 2011) and a multiple point-source model (Zahradník and Sokos, 2011).

Several papers summarizing field evidences and damage observations were also published (Carydis *et al.*, 2012; Erdik *et al.*, 2012; Di Sarno *et al.*, 2013). To date, however, there are only a few journal papers dealing with the seismological aspects of the event. In particular, based on InSAR data Elliot (2013) found that the Van earthquake occurred on a pair of fault planes with common strike angle, but with dip and rake angles varying between 40°–55° and 64°–93°, respectively. Using teleseismic data Mendoza and Hartzell (2013) inferred a slip model similar to that presented on the USGS website (also derived using teleseismic data). All the models agree in locating the slip at rather large depths (> 10 km). However, in all cases the inferred slip models are rather simple, not explaining the later phases of the near-source recording of the Muradiye strong-motion station. Taskin *et al.* (2012) and Akansel *et al.* (2013) provided an overview of the available strong motion records, compared ground-motion amplitudes (e.g., peak ground acceleration [PGA], pseudospectral acceleration) with several empirical ground-motion prediction equations (GMPEs), and discussed the effects of the earthquake on man-made structures. Akinci and Antonioli (2013) adopted the finite-fault stochastic approach to model the high-frequency part of the observed data by using the finite-fault model proposed by the USGS. The authors calibrated some of the simulation input parameters by comparing recorded and synthetic

*Now at GEOTER International, 20 Zac du Pujol 2, Les Artauds Es, 13390 Auriol, France.

Table 1
Centroid Moment Tensor (CMT) Parameters Obtained by Global Agencies and Other Authors and in This Paper

CMT	Latitude (°N)	Longitude (°E)	Depth (km)	Origin Time	M_0 (10^{19} N·m)	Strike (°)	Dip (°)	Rake (°)
Global CMT	38.67	43.42	15.4	10:41:30.6	6.4	248	36	60
USGS CMT	39.451	43.354	16.0	10:41:44.5	9.9	272	19	101
USGS FF*	38.62	43.48	15	10:41:21.6	5.16	241	51	50–70
USGS *W* phase	38.852	43.840	13	10:41:21.6	5.6	241	51	58
SCARDEC	38.627	43.535	16–23	10:41:21	6.86	248	53	64
Elliott *et al.* (2013)†	38.592	43.386	14.1	-	4.4	258	45	83
This paper regional data‡	38.689	43.351	10	10:41:22.4	7.4	246	52	75
This paper near-regional data§	38.734	43.351	15	10:41:24.3	2.1	246	52	75

*Finite-fault inversion based on teleseismic data; location corresponds to the hypocenter, rake varies along the fault.
†Finite-fault inversion of a single-segment fault based on InSAR data.
‡Low-frequency inversion, single point-source approximation.
§Parameters correspond to major subevent only (which explains the low value of M_0). Depth is fixed; it is not shallower than 10 km but cannot be resolved in greater detail. Mechanism was fixed at the values of the previous row.

Table 2
Hypocenter Parameters Obtained by Global Agencies and in This Paper

Hypocenter	Latitude (°N)	Longitude (°E)	Depth (km)	Origin Time UTC
USGS	38.691	43.497	16	10:41:21
EMSC	38.78	43.40	10	10:41:23.4
AFAD	38.689	43.466	19	10:41:18.26
KOERI	38.76	43.36	5	10:41
This paper	38.716	43.405	8	10:41:21.2

ground motions, and then used the validated model to calculate PGA and peak ground velocity (PGV) maps in the epicentral area. Both Akansel *et al.* (2013) and Akinci and Antonioli (2013) provided a quantification of site effects on ground-motion amplitude at some of the recording stations by means of empirical and theoretical approaches.

Recent years have seen an increased interest not only in building plausible earthquake models, but also in assessing their uncertainty estimates (e.g., Emolo and Zollo, 2005; Hartzell *et al.*, 2007; Piatanesi *et al.*, 2007; Cirella *et al.*, 2008; Monelli and Mai, 2008; Monelli *et al.*, 2009; Page *et al.*, 2009; Duputel *et al.*, 2012; Twardzik *et al.*, 2012; Zahradník and Custódio, 2012, and references therein). For example, Clévédé *et al.* (2004) discuss the significant difference between finite-extent models of the Izmit earthquake retrieved by various authors.

Sometimes it is possible that based on the source models best fitting the relatively low-frequency seismic data we cannot explain the high-frequency data of engineering importance, and we need to seek explanation using other models than the best-fitting one, that is, using models in the parameter uncertainty limits. This is the case of the Van earthquake, as we explain in the present paper. Thus our objective is to build the source model of the Van earthquake, and, based on its uncertainty limits, to explain the observed high-frequency strong ground motions.

Our comprehensive paper of the 2011 M_w 7.1 Van earthquake starts with hypocenter relocation, centroid moment tensor (CMT) analysis by means of the full-waveform inversion using the ISOLA package (Sokos and Zahradník, 2008), and the multiple point-source (MPS) inversion. The latter is then extended to the inversion of the event considering multiple finite-extent (MuFEx) source model (Gallovič and Zahradník, 2012), grid searching for possible values of parameters of the subsources, namely nucleation times, nucleation point positions, and rupture velocities. Because of the unfavorable station locations (stations situated at large distances and almost exclusively in a single quadrant), the uncertainty of the source model is very large. We present three selected models to illustrate a broad variability in possible rupture propagation. Then we develop a broadband strong-motion model based on the inverted fault model and simulate strong ground motions using the hybrid integral-composite (HIC) source model. We show that the long duration of the closest Muradiye station, consisting of the 2–3 distinct wave packages in the observed accelerometric record, can be reproduced only when models with complex rupture propagation (such as a delayed rupture of shallow asperities) are considered.

Data

In this paper we use freely available data from several repositories. Regional broadband seismograms (see station map in Fig. 1) were acquired from Orfeus and from the International Institute of Earthquake Engineering and Seismology (IIEES) of Iran. In addition, the mainshock was recorded by several stations of the Turkish and Iranian strong-motion networks (Fig. 2) providing ~20 three-component recordings within ~200 km distance from the epicenter, including one near-fault Turkish station (Muradiye, 6503) at a distance of a few kilometers from the causative fault. Unfortunately, the latter is the only strong-motion station that was operative in the epicentral area (i.e., within 100 km from the earthquake fault) when the earthquake occurred. The station recorded strong motions of ~20 s long duration, consisting of 2–3 distinct wave packages with maximum peak acceleration reaching 2 m/s^2. Interestingly, the first wave package is less strong than the others. Explaining this waveform complexity in terms

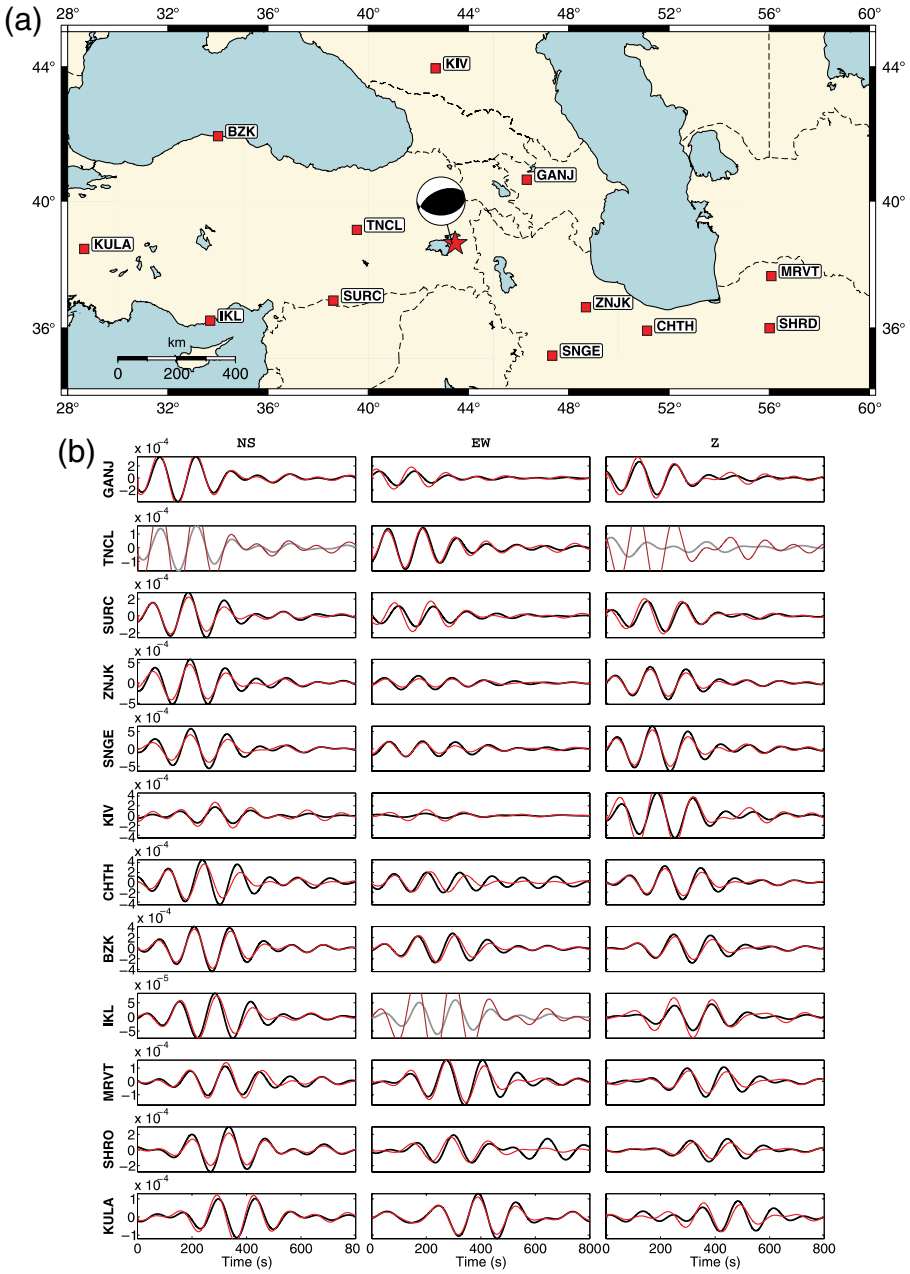

Figure 1. (a) Centroid Moment Tensor (CMT) solution (beachball) calculated by the ISOLA software for the Van earthquake using regional broadband seismograms in the frequency range 0.005–0.010 Hz. The used stations are shown by squares. (b) Waveform fit between observed (black) and synthetic data, amplitudes are in meters. The gray waveforms (namely station components TNCL-N, TNCL-Z, and IKL-E) were removed from inversion due to low-frequency data problems. The color version of this figure is available only in the electronic edition.

of a source effect is challenging and represents the main aim of the present paper.

Strong-motion records were available from the National Strong Motion Network of Turkey (TR-KYH), operated by the Turkish Earthquake Research Department (AFAD) and from the Iran Strong Motion Network (ISMN). Most of Turkish stations were equipped with Guralp CMG-5TD digital instruments and the ISMN stations were equipped with Kinemetrics SSA-2 digital accelerographs. Two of the Turkish stations (4902 and 6503) were equipped with a three-component GeoSig SMACH SM-2 sensor and a 12-bit digital converter that stores the digital record to solid-state memory. Nowadays these instruments are considered outdated due to the limited local storage, the low digitizer dynamic range, the lack of absolute time of the record, and the narrow sensor frequency response (with strong fall-off of the instrument response toward low frequency, starting already at $f \sim 0.3$ Hz). Moreover, this low-frequency response function is uncertain.

In addition to seismic stations, several permanent Global Positioning System (GPS) stations recorded surface displacement in the epicentral area. The coseismic displacements

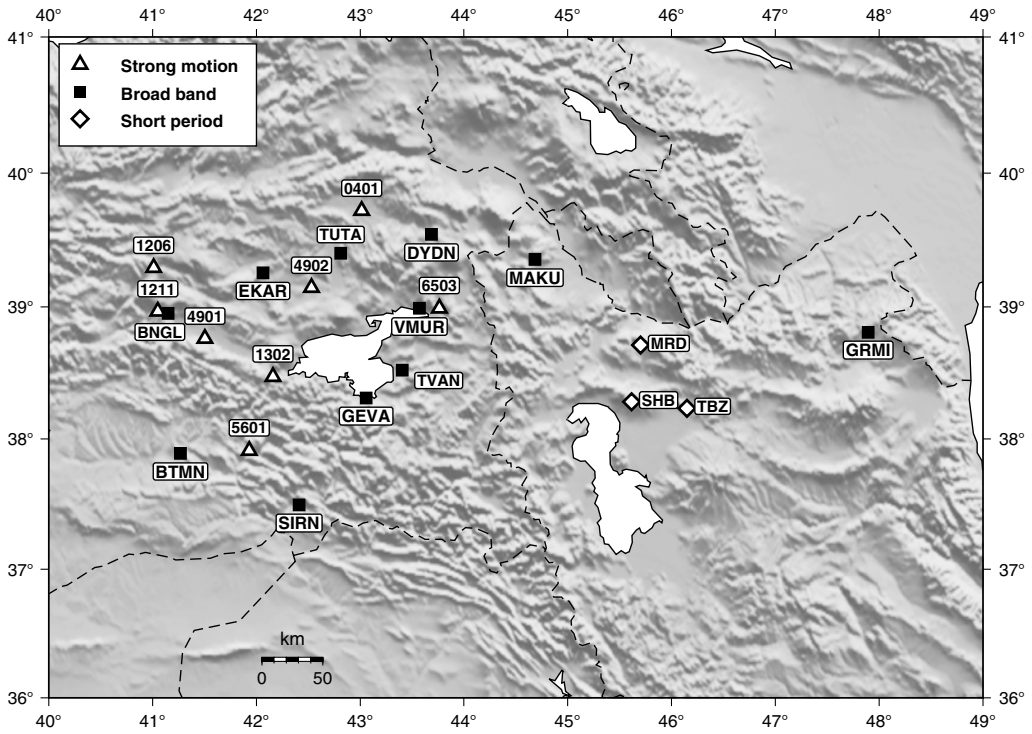

Figure 2. Location of near-regional strong-motion, broadband, and short-period stations (see legend) used in this paper.

(calculated by Rahsan Cakmak) are available at the Supersites web page. The largest horizontal offset of 5 cm was observed at GPS station MURA collocated with strong-motion station (Muradiye, 6503).

Crustal Model and Green's Functions

Wherever needed in this paper, full wavefield Green's functions are calculated by the discrete wavenumber method (Kennett and Kerry, 1979; Bouchon, 1981; Coutant, 1989). The 1D layered crustal model is based on Gök *et al.* (2011) and was received in tabular form from R. Gök (written commun., 2010). We considered the model corresponding to station CLDR; the only modifications are that we removed the low-velocity channel between the depths of 4 and 22 km and we reduced the velocity of the first kilometer to a more reasonable value. This latter modification is allowed because the original crustal profile had the topmost layer as thick as 2 km due to resolution limit. The adopted model is presented in Table 3.

Both data and Green's functions are always filtered in the same way. The high-pass filter is dictated by the low-frequency (instrumental) noise. The low-pass filter varies according to particular application. For source inversions the low-pass filtering is dictated by our ability to model deterministically Green's functions in layered 1D medium. Simply saying, the closer the recording stations are to the epicenter, the higher corner frequency of the low-pass filter can be used.

In case of the strong ground motion modeling of the Muradiye station, we approximate the local site effects by adding a site-specific soil profile on top of the crustal model. The soil profile is available through the Turkish Strong-Motion Database website and it is also reported by Akansel *et al.* (2013). The minimum V_S at the surface is 212 m/s and the maximum is 492 m/s at a depth of 32 m. The average V_S of the uppermost 30 m (V_{S30}) is 293 m/s.

Methods

The CMT solution and the MPS model are calculated by ISOLA (Sokos and Zahradník, 2008, 2013). It is a broadly used software package for inverting full waveforms at local-to-regional distances in low-frequency range. The moment

Table 3
Crustal Model Adopted in This Paper (Modified from Gök *et al.*, 2011)

Top Depth (km)	V_P (km/s)	V_S (km/s)	Rho (g/cm^3)	Q_P	Q_S
0.0	2.79	1.50	2.50	200	100
1.0	3.91	2.10	2.60	400	200
2.0	4.63	2.49	2.70	400	200
4.0	5.95	3.20	3.10	400	200
22.0	6.72	3.61	3.10	1000	500
37.0	7.07	3.80	3.15	1000	500
40.0	7.40	3.98	3.30	2000	1000
43.0	8.23	4.43	3.60	2000	1000

tensors are calculated by the least squares method, whereas the subevent position and time are grid searched.

MPS models are constructed using ISOLA by means of so-called iterative deconvolution (Kikuchi and Kanamori, 1991). ISOLA successively identifies and subtracts individual subevent contributions from complete waveforms. In the standard ISOLA approach, for the first subevent, the entire waveform is approximated by a single point-source contribution. This is obviously a strong approximation whose typical consequence is that the first subevent might be biased with respect to the true slip, both in space position and scalar moment. More specifically, the subevent moment is overestimated; we can say that the subevent consumes most of the total moment of the earthquake in a single point. Such a problem occurs mainly in case of an unfavorable station distribution which is just the case of the present paper. The same applies to all other subevents. To at least partly reduce this drawback we use the following modification: if the subevent requires moment m to fit the data, we assign to it only some fraction of m, for example, $m/4$ in the present paper. The total number of subevents is correspondingly increased (e.g., four times). The final result has the same total moment as in the standard approach, but the moment is less concentrated in the first few subevents. This modification has been proven useful by comparison with a slip inversion elsewhere (see section 4.1 of Zahradník and Gallovič, 2010).

For relocation standard methods HYPO (Lee and Valdés, 1989) and NonLinLoc (Lomax *et al.*, 2000) are used.

Slip inversion is performed by means of the Multiple Finite-Extent source inversion (Gallovič and Zahradník, 2012). The source is parameterized by finite-extent subsources, similarly as in the approach by Vallée and Bouchon (2004). In the present application we assume three rectangular subsources with constant slip and rupture velocity. Rise time is assumed smaller than the reciprocal of the maximum frequency considered (0.15 Hz), thus the delta function is considered. Each subsource has its individually ascribed set of trial nucleation positions, rupture velocities and nucleation times. We grid search all combinations of the subsource parameters, while simultaneously solving the least-squares problem for the subsource slip in each tested model. All models are eventually characterized by their fit with observed data (in terms of variance reduction, VR). Neglecting all models with negative slip values, and considering minimum acceptable VR, we arrive at a database of plausible rupture models.

For broadband modeling of strong ground motions we use the HIC approach (Gallovič and Brokešová, 2007; Ameri *et al.*, 2009; Zollo *et al.*, 2009; Ameri *et al.*, 2011; Chiauzzi *et al.*, 2011). In this approach, the rupture process is represented by overlapping subsources with fractal number-size distribution (the number of subsources decreases linearly with increasing subsource size). Note that here the term subsource does not have the same meaning as in the MuFEx modeling. Assuming the constant stress-drop scaling, the subsources compose a slip distribution with k^{-2} decay at high wavenumbers k (Andrews, 1980). In the low-frequency part of the modeling we use the representation theorem (hence integral approach). For high frequencies, each of the subsources is considered as a point source radiating from its center a Brune's pulse with corner frequency and seismic moment given by the size of the subsource (composite approach). This way, the nonrealistic directivity of the integral approach at high frequencies is diminished (Gallovič and Burjánek, 2007). Further, to reduce the effect of the radiation pattern, we assume ±30% variations of the subsource focal mechanism. The low- and high-frequency wavefields are crossover combined in the frequency domain between $f_1 = 0.3$ Hz and $f_2 = 1$ Hz by means of multiplication of both the real and imaginary parts of the spectrum by weighting functions $\sin^2(x)$ and $\cos^2(x)$, where $x = (\pi/2)[(f - f_1)/(f_2 - f_1)]$; see also Gallovič and Brokešová (2007). Note that no stochastic Green's functions are used.

Hierarchical Modeling

Step 1. Regional Data: Centroid Moment Tensor

Table 1 summarizes CMT solutions provided by international agencies, employing teleseismic data. The spread in the reported horizontal position of centroid is as large as ∼30 km (even up to ∼100 km when including the USGS CMT), and very large are also differences between the reported strike, dip (up to 30°), and rake angles (up to 50°). To better constrain the CMT solution we use broadband data from 12 regional stations (Fig. 1) and perform full waveform inversion in ISOLA software (Sokos and Zahradník, 2008). The epicentral distances range from ∼330 to 1290 km, and complete waveforms are inverted in the frequency range 0.005–0.010 Hz. Deviatoric solution provides a strongly dominant single point source, with a very high double-couple (DC) percentage, DC > 90%. Grid search over depth has almost no resolution. The horizontal grid search (10 × 10 km) provides the formally optimal source position at 38.689° N, 43.351° E, with the strike–dip–rake angles = 246°, 52°, 75°, respectively (Fig. 1). The waveform fit is shown in Figure 1b.

Step 2. Near-Regional Data: Hypocenter Relocation and Major Subevent

In the aftermath of the earthquake various institutions provided hypocenter locations (Table 2 reports the locations given by the main Turkish and International institutions) showing a significant variability for such a large magnitude event. We relocate the hypocenter using 20 *P*-wave and 7 *S*-wave readings obtained from the stations shown in Figure 2. Four alternative HYPO (Lee and Valdés, 1989) relocations considering different subsets of the data (e.g., *P* and *S*, only *P*, only near stations, or with a fixed depth) are shown by stars in Figure 3. The hypocenter depth varies from 8 to 15 km. Dots in Figure 3 are the relocation by the NonLinLoc method (Lomax *et al.*, 2000) (preferred depths were < 10 km). As a reference hypocenter solution for further study, we adopt

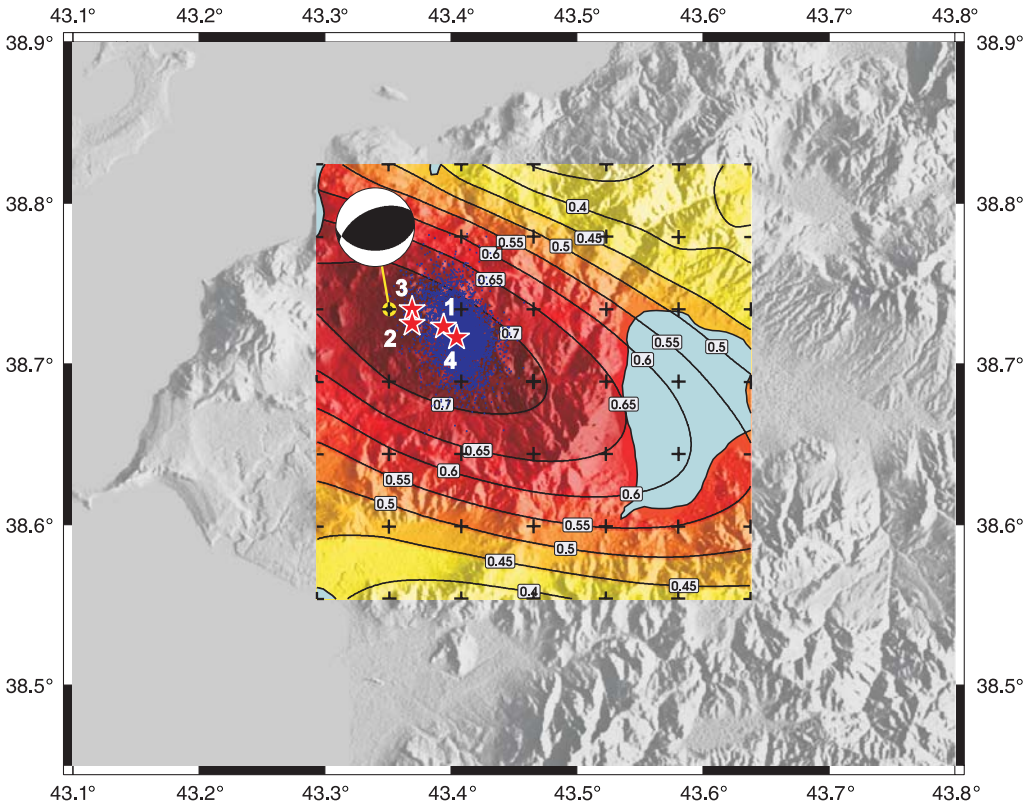

Figure 3. Four alternative hypocenter locations by HYPO (asterisks) and NonLinLoc location (dots) from all stations in Figure 2. The asterisks are identified with the individual HYPO solutions as follows: 1, using only *P* waves; 2, *P* and *S* waves (where available) using only near stations (< 120 km), fixing depth at 10 km; 3, same as 2 but with free depth; and 4, final solution of this paper, based on *P* and *S* waves from all stations, free depth. The beach ball corresponds to the major subevent inferred from near-regional strong-motion data (see Fig. 2), except stations 6503 and 4902, in frequency range 0.05–0.10 Hz by maximizing correlation (isolines) between the observed and synthetic waveforms. The color version of this figure is available only in the electronic edition.

the location from *P* and *S* waves (see Table 2 and asterisk 4 in Fig. 3). Note that the variability of the epicenter positions in Table 2 is much smaller (∼10 km) than among the centroid positions (Table 1). Nevertheless, the subsequent modeling (except the high-frequency HIC method) is fully independent of the hypocenter position.

Strong-motion (SM) data from six near-regional stations (triangles in Fig. 2) are used for the finite-extent source inversion. From the set of stations we had to exclude stations 6503 and 4902 because of strong fall-off of the instrument response toward low frequency, starting already at $f \sim 0.3$ Hz. Moreover, this low-frequency response function is uncertain (see Data section). The retained stations are in the distance range 120–220 km from the epicenter. In this step we increase (with respect to the CMT analysis) the frequency band to 0.05–0.10 Hz in order to obtain a better spatial resolution of the source.

In this band the wavefield at studied stations can no longer be explained with a single point source as the seismograms are affected by the finite extent of the source. Therefore, the waveform inversion (ISOLA) already requires a few subevents of a comparable size. At this step of the analysis we concentrate on the major subevent. For the same reason (due to finite-extent source effects), the deviatoric inversion cannot be used, because now it (artificially) produces a very large (> 50%) non-DC component. The DC focal mechanism is kept fixed from the broadband solution (step 1) with no preference between 10 and 20 km. The horizontal grid search (5×5 km) maximizes correlation between observed and synthetic waveforms for the major subevent at 38.734° N, 43.351° E (where the beachball is attached in Fig. 3). Elongation of the correlation isolines in the northwest–southeast direction is due to limited azimuthal coverage of the SM stations (worse than in the hypocenter location, where more stations were available).

Step 3. Near-Regional Data and GPS: Finite-Extent Source Inversion

At this stage we invert the near-regional SM data in the frequency range 0.05–0.15 Hz to get a deeper insight into the rupture process. First we use the MPS inversion. Then the MPS inversion is used to set up the MuFEx model.

We use a fault plane passing through the point defined by the coordinates of the major subevent assuming its strike and dip parameters (see step 2; Table 1), whereas the depth is fixed at 15 km. This plane encompasses the reference

hypocenter if we increase our hypocenter depth (Table 2) by just 2 km, thus satisfying the consistency of the hypocenter-centroid position (Zahradník *et al.*, 2008). The inferred fault plane is also in agreement with the InSAR data (Elliott *et al.*, 2013).

In the MPS inversion DC subevents (position, rupture time, and scalar moments) were searched in a grid along the fault plane. The strike, dip, and rake of the subevents are kept fixed according to the CMT solution of step 1. The moment rate of each subevent is a triangle duration of 10 s. The duration has been setup by means of simple preliminary tests, in which it was varied (e.g., 5–15 s). Varying the subevent duration (while keeping the finite-frequency range 0.05–0.15 Hz unchanged) affects the variance reduction and the total seismic moment. The used value of 10 s maximized the variance reduction while, simultaneously, it prevented the moment to grow above the agency reported solutions. Naturally, with absent frequencies below 0.05 Hz, our finite-fault solutions (computed by any method) tend to underestimate the scalar moment and the moment magnitude. Indeed, the MPS solution converged with total moment magnitude M_w 7.0 instead of Global CMT value of M_w 7.1. It would be possible to formally increase the moment by adding more subevents, but their position, timing, and size would be unstable.

Figure 4 shows the space–time distribution of the MPS model moment release, projected onto the horizontal plane. The waveforms are matched with variance reductions VR = 0.53. The MPS solution was repeated with altered parameters to find out its common (stable) features: (1) the moment distribution is relatively compact, (2) the largest subevents are close to epicenter (star in Fig. 4), (3) the smaller subevents are always delayed by ~3 s, and situated southwest from the main patch. Very late small subevents (> 12 s after the main subevent) also exist, but their position is unstable.

The MPS solution exhibits a more or less unilateral rupture propagation in the southwest direction. However, this might be merely an artifact due to the poor azimuthal station coverage. To overcome this issue, we setup a MuFEx source model that allows for a general rupture propagation including possible rupture propagation complexities (rupture jumps and delays) (Gallovič and Zahradník, 2012).

In the MuFEx inversion (see also Methods section) the source is parameterized by three rectangular subsources with size and position (Fig. 5) based on the MPS inversion. Trial and error adjustments to obtain the best waveforms match suggest uncertainty of at least 3–5 km in both size and position. Trial values of the subsource parameters (rupture velocities, nucleation points, and times) can be learned from Figure 5; the total number of trial model reaches three million. Neglecting all grid-searched models with negative slip values, and considering models whose variance reduction is at least 95% of the best VR value (0.45), we arrive at a database of 497 plausible models. Their parameters expressing the uncertainty of the MuFEx inversion are explored in Figure 5a. Note that the database of plausible MuFEx models

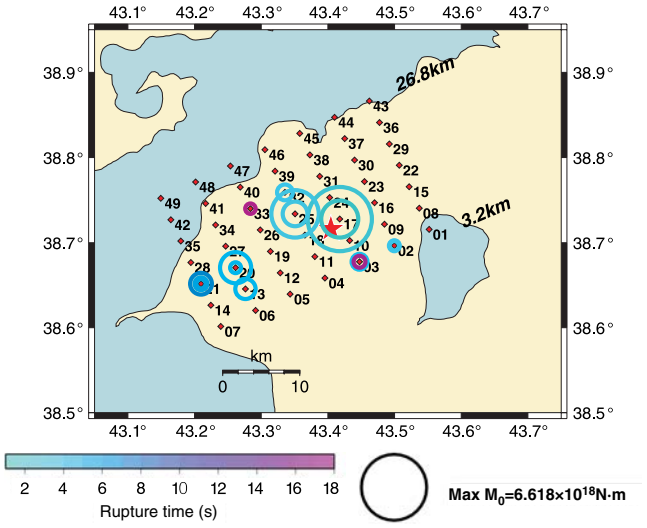

Figure 4. Multiple point-source inversion (frequency range 0.05–0.15 Hz; VR = 0.53) based on the data from near-regional strong-motion stations (see Fig. 2) except stations 6503 and 4902. Radii of the circles are proportional to moment of the subevents. The bottom right circle shows the moment scale. The epicenter of this paper is shown by asterisk. The numbers to the right of the fault plane indicate the depth of its top and bottom edges. The color version of this figure is available only in the electronic edition.

(representing uncertainty of the slip inversion) is relatively rich due to unfavorable station distribution. The uncertainty is especially pronounced in case of subsource 2, lying east of the hypocenter. To further limit the number of plausible slip models, we use a posterior check against the GPS data in terms of variance reduction between observed and synthetic coseismic displacements. The synthetic coseismic displacements are evaluated in a homogeneous half-space using the Okada (1992) closed-form solutions.

To show more clearly how different the individual MuFEx source models can be, we selected three scenarios with very different styles of the rupture propagation (Fig. 5b): model M1, rupture of subsource n.2 is delayed by ~10 s; M2, subsource n.1 ruptures first and then shallow subsources are activated; and M3, regular rupture propagation from a single nucleation point (no multiple nucleation points, no rupture delays). Rupture velocity (V_r) is 3 km/s for all models. The fit with observed data and the GPS vectors is shown in Figure 6. Note that despite the very different style of rupture propagation the fit with the observed waveforms is practically the same for all three models. The differences in fit of the GPS data are given mostly by the slip value of subsource n.2.

Step 4. Near-Fault Muradiye (6503) Station: Broadband Modeling

The alternative source models retrieved by the MuFEx analysis are used as a basis for broadband (0.1–10 Hz) ground-motion simulations by means of the HIC approach (Gallovič and Brokešová, 2007; see Methods section). We

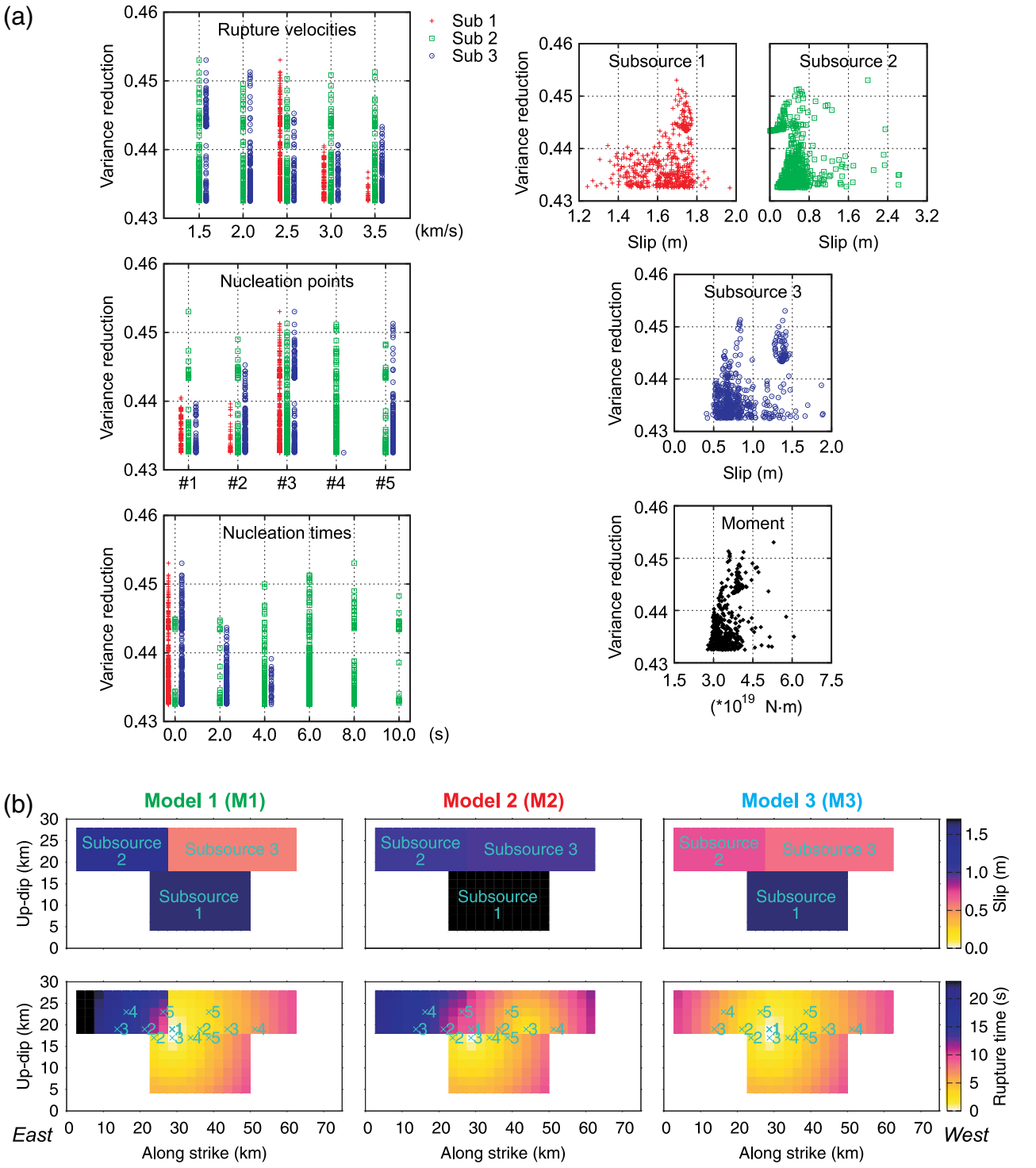

Figure 5. (a) Analysis of grid-searched MuFEx source models that almost equally well fit the data of near-regional strong motion stations (see Fig. 2) except for stations 6503 and 4902. The analyzed set consists of approximately 497 models out of the total number of three million trial models. Each model is shown in the graphs as a point with variance reduction (VR) on *y* axis and particular model parameter value on the *x* axis. The three plots on left show the uncertainty of the rupture velocities, nucleation points, and nucleation times of the MuFEx subsources. The tested nucleation points are shown in panel (b) as crosses with numbers; nucleation point 1 is the same for all subsources and corresponds to the reference hypocenter of this paper (see Table 2 and asterisk in Fig. 4). The plots on right analyze the uncertainty of slip of the three subsources individually and the total seismic moment. (b) Three examples of alternative MuFEx source models from the above discussed set of models, shown in terms of slip distribution (top panels) and rupture time (bottom panels) distributions. The models were selected in order to have a large variability in terms of rupture propagation and slip amplitudes. The comparison of displacement waveforms and static GPS vectors for these three models is presented in Figure 6. Total seismic moment of the models M1–3 is 3.8, 4.0, and 3.2×10^{19} N·m, respectively, that is, values corresponding to M_w 7.0. The color version of this figure is available only in the electronic edition.

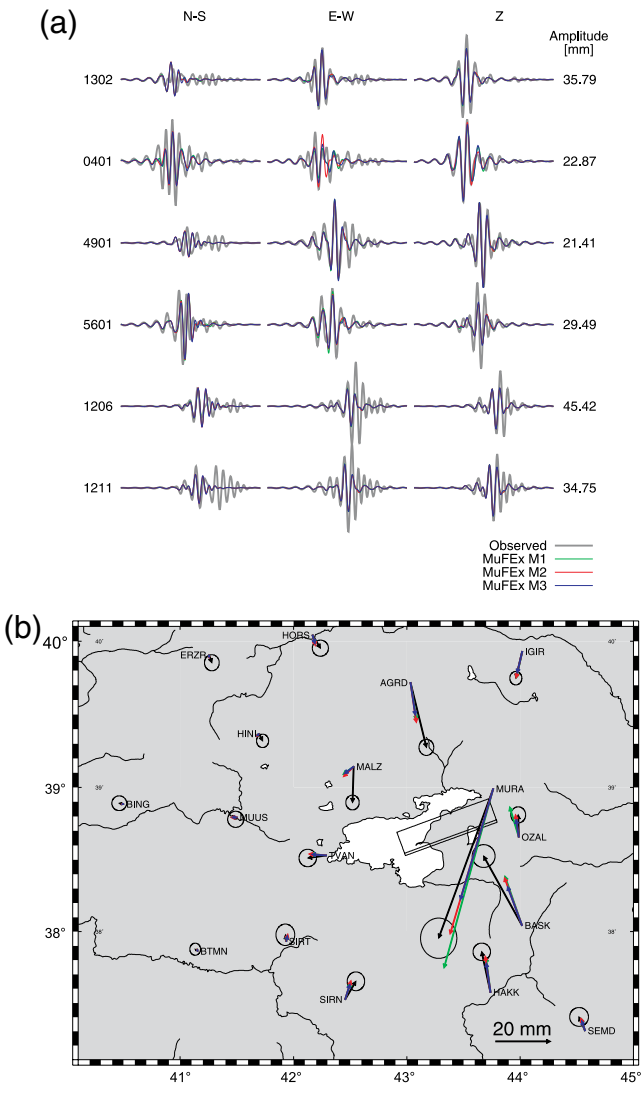

Figure 6. (a) Comparison of complete observed and synthetic displacement waveforms of near-regional strong motion stations (see Fig. 2, VR = 0.43–0.45, duration 100 s) used in the MuFEx source inversion. Note that the seismograms for the models M1–3 are almost the same although the rupture models differ significantly (see Fig. 5). Numbers refer to the peak displacements. (b) Comparison of observed GPS vectors with synthetic for models M1–3. The surface projection of the fault is displayed. The color version of this figure is available only in the electronic edition.

impose the position of the largest subsources of the HIC model at places roughly corresponding to the subsources considered in the MuFEx source analysis. The other (smaller) subsources are distributed randomly over the fault plane. We use a single random realization as an example, see Figure 7. The same slip-distribution model is complemented with three different examples of the rupture propagation. We consider the three cases of MuFEx models M1–3 (see previous and the lower panels of Fig. 5) with the rupture velocity of 3 km/s. In addition, in model M4 we consider the same uniform style of rupture propagation as for M3 (radial rupture propagation at

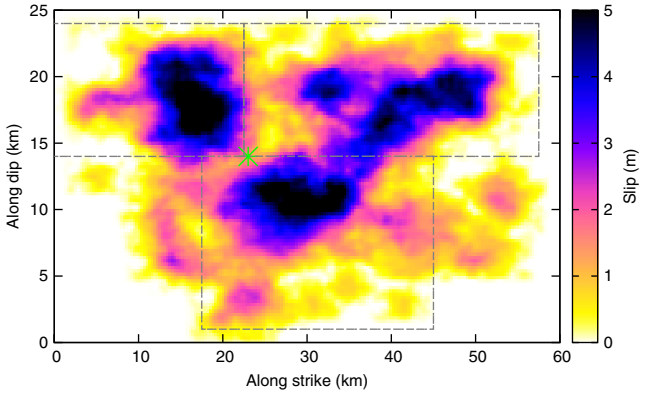

Figure 7. The adopted k-squared slip distribution and fault model for broadband (0.1–10 Hz) ground-motion simulations by means of the hybrid integral-composite approach (Gallovič and Brokešová, 2007). The dotted rectangles correspond to MuFEx subsources (Fig. 5) that served as a basis for the HIC model. See Figure 5 for temporal rupture evolution in terms of distribution of rupture times. The color version of this figure is available only in the electronic edition.

3 km/s) but with the rupture velocity of 2 km/s; this was done to test the effect of a slow rupture velocity on the results.

The results of the modeling of Muradiye records by including or not including the local site response (see Crustal model and Green's functions section for details) are presented in Figure 8 for source model M1. In the time domain, peak acceleration values are enhanced twice with almost no change in duration when the site-specific structure is included in the simulation. In Fourier domain the site effect increases spectral amplitudes in a broad frequency band, and mostly for $f > 0.5$ Hz, improving significantly the fit with observed spectra. We note that there are still some differences between the observed and simulated horizontal Fourier spectra around 1 Hz. Nevertheless, the use of the site-specific soil profile at Muradiye represents a clear improvement in the modeling.

Figure 9 compares the modeling results for the Muradiye station with observed data for the 4 selected rupture models. The comparison is presented in terms of acceleration and velocity waveforms and acceleration Fourier amplitude spectra. In particular, models M3 and M4 with simple rupture propagation are characterized by relatively short duration of waveforms when compared to the observed data (both in acceleration and velocity). Moreover, most of the energy is released in the first 10 s of the seismograms. On the other hand, the observed seismograms are characterized by longer duration, with their peak amplitudes (both in acceleration and velocity) located not at the beginning of the records but rather in the central part (around 15 s after the onset). Only models M1 and M2, including late rupture of the northeast asperity (n.2 in MuFEx analysis in Fig. 5) are able to explain those late wave packages observed in the recordings. Recall that these models were revealed only by grid searching all model parameter values in the MuFEx source inversion.

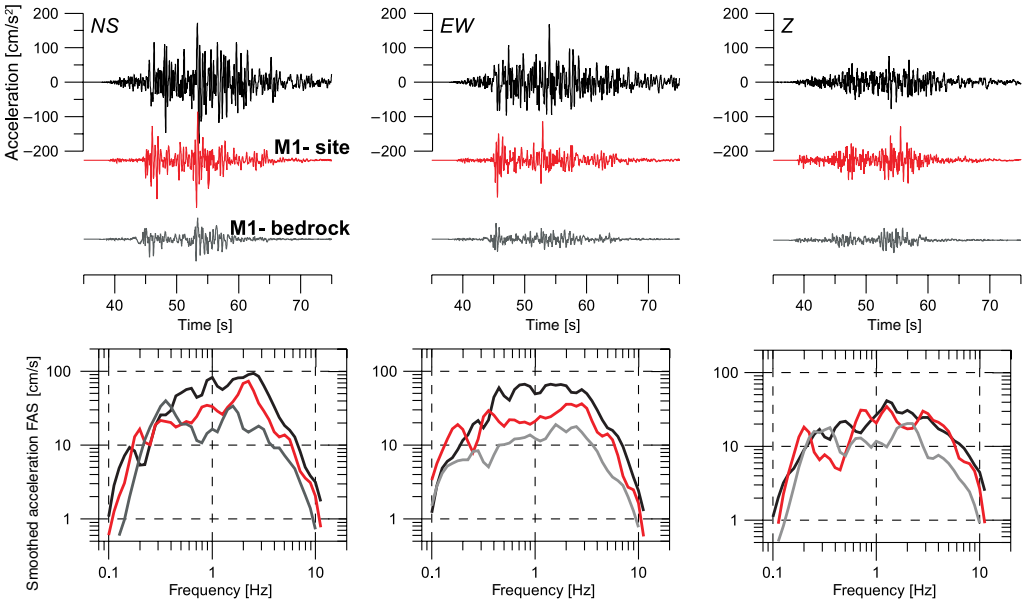

Figure 8. Modeling results at Muradiye (6503) station, including or not including the local soil profile in the calculations. Observed three-component acceleration time series and smoothed acceleration Fourier amplitude spectra are compared with simulated ones for soil and bedrock site conditions. The results are presented for source model M1. The color version of this figure is available only in the electronic edition.

In Fourier domain, models M1, M2, and M3 explain equally well the spectral amplitudes. Thus the overall frequency content of the waveforms at Muradiye station is not particularly affected by the style of the rupture propagation. Only model M4, characterized by the same circular rupture style of model M3 but with a much smaller rupture velocity, provides small amplitudes compared to the observed ones.

In terms of modeling of the Muradiye records the results clearly suggest that models M1 or M2 are successful, being able to adequately explain the amplitude levels and temporal characteristics (duration and number of wave packages) of the observed seismograms.

Step 5. Near-Fault Strong Ground Motion Simulations

Using the HIC modeling technique validated by means of the Muradiye records, we simulate bedrock ground motions at a dense grid of virtual receivers in the epicentral region, up to 50 km from the fault. We adopted three of the source models presented in the previous section, excluding model M4 that clearly provided the worse fit at Muradiye. The results are presented in terms of PGV and PGA maps in Figure 10. The maximum values on the maps reach approximately 1g in PGA and 1.2 m/s in PGV. All the maps are characterized by two distinct spots of high values above the fault that are related to the two subsurface asperities in the HIC model (see Fig. 7). The strength of the eastern spot, however, differs from one scenario to another, depending on the timing of the rupture evolution (i.e., details of the rupture propagation).

The spatial distribution of PGA from the models resembles the spatial extent of the distribution of damage in adobe masonry buildings obtained from a detailed site survey (Fig. 11) with two spots toward the northeast and southwest of the epicenter. It is known from previous studies (e.g., Erberik, 2008) that vulnerability of wall-bearing masonry structures correlates with PGA mostly due to their short fundamental periods.

Figure 12 compares the simulated PGA and PGV values for models M1 and M2 with estimates from empirical GMPEs. We select two empirical models suitable for the area: the model by Akkar and Bommer (2010) based on data from Europe and the Middle East and the model by Akkar and Cagnan (2010) based exclusively on data from Turkish earthquakes (Van earthquake excluded). The GMPEs are calculated for an M_w 7.1 up to 50 km from the fault and for site conditions representative of rock. The comparison shows: (1) a relatively close similarity between peak values from models M1 and M2 in terms of attenuation with distance, and (2) a good overall agreement of simulated values with empirical GMPEs (median $\pm$ one standard deviation) both in terms of amplitude level and distance decay, supporting the reliability of the proposed model to predict bedrock ground motions in the epicentral area of the Van earthquake.

Figure 13 shows the synthetic seismograms calculated using the four models M1–4 at Van and Erciş, Turkey, located at approximately the same epicentral distance (30 km). Note that the seismograms corresponding to the different source models do not differ much from each other, except for model M4 that is characterized by generally smaller amplitudes. This is so because at such distances the ground motion

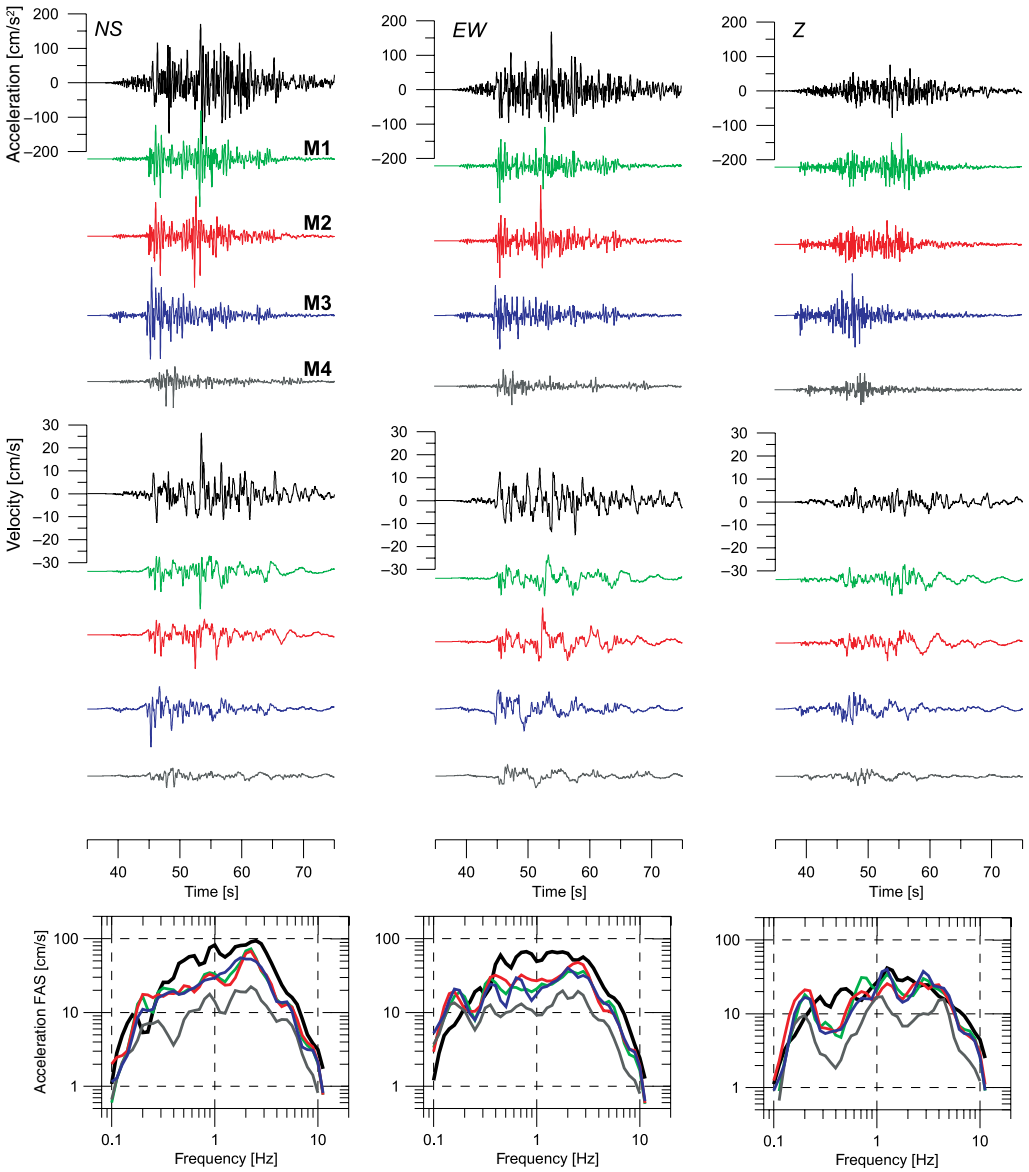

Figure 9. Modeling of Muradiye records using several rupture models. Observed three-component acceleration and velocity time series and smoothed acceleration Fourier amplitude spectra are compared with the ones simulated with four different rupture models. The models share the same slip distribution (Fig. 7) and differ in style of rupture propagation. The color version of this figure is available only in the electronic edition.

is already not very sensitive to the details of the rupture evolution. For both cities the peak values in models M1–3 range between 0.1*g* and 0.2*g* in PGA, and 0.1 and 0.2 m/s in PGV. Interestingly, Erciş was damaged to some extent more severely than Van (Akansel *et al.*, 2013). This observation could suggest local site amplifications in Erciş which are not included in the models presented here, and/or differences in the construction quality of the buildings in the two cities.

Discussion

Our analysis of the Van earthquake shows that the uncertainty of its slip model is rather large due to the unfavorable station distribution. Indeed, the only data being usable for (near-regional) slip inversion were recorded at rather large distances (~100 km) and almost exclusively in a single southwest quadrant. Based on singular value analysis and theoretical considerations from the earthquake source tomography (Ruff, 1984; Menke, 1985), Gallovič and Zahradník (2011) showed that the inverse problem may suffer from strong artifacts. In particular, when all stations are located predominantly in one direction (a single azimuthal quadrant) from the fault, the resulting model can overestimate the rupture propagation toward the stations. In other words, rupture propagation in the opposite direction and/or possible up-dip propagation is not well pronounced in the observed data, and thus it cannot be easily retrieved.

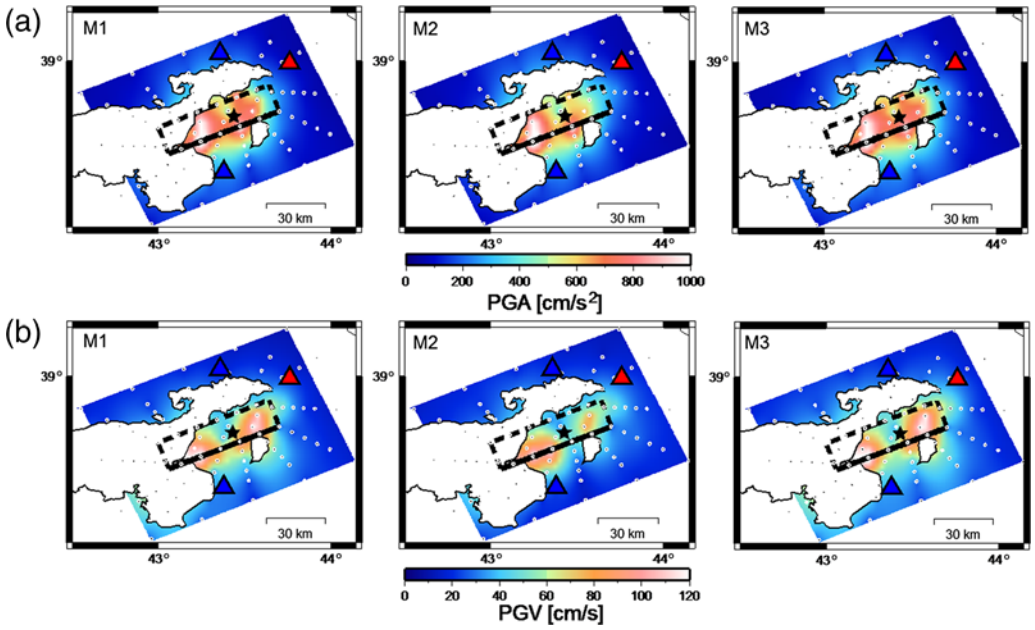

Figure 10. (a) PGA and (b) PGV maps calculated using models M1, M2, and M3 at a grid of virtual receivers (dots) on at the surface situated up to 50 km from the fault. The geometric mean of horizontal components is used. The epicenter (star), fault (rectangle), MURA station (eastern triangle), and Van and Erciş cities (southern and northern triangles, respectively) are shown. Site effects are not taken into account. The color version of this figure is available only in the electronic edition.

To overcome this, we adopt a simple but efficient parameterization of the source by the model of MuFEx subsources (Gallovič and Zahradník, 2012). The rupture propagation is described by a few (three in the present paper) finite-extent subsources. Each subsource is parameterized by its own set of trial rupture velocities, nucleation points, and onset times. We grid search all possible combinations of the parameters, while simultaneously solving for (constant) slip values by means of the least-squares inversion. This procedure ends with a database of plausible models that, in the present paper, vary significantly in terms of all aspects of the rupture propagation.

For strong ground motion modeling we use the HIC approach (Gallovič and Brokešová, 2007). We follow the approach of Ameri *et al.* (2012) who constrained basic features of the HIC model of the 2009 L'Aquila earthquake by the preceding MuFEx analysis by Gallovič and Zahradník (2012). In our case, we consider several MuFEx models to constrain (or initiate) the HIC model. The HIC source models are used to model the only available near-fault station in a broad frequency band (0.1–10 Hz). We show that the long duration of the closest Muradiye station, consisting of 2–3 distinct wave packages in the observed accelerometric record, can be reproduced only when models with complex rupture propagation (such as a delayed rupture of shallow asperities) is considered.

Using the same source models we also present bedrock ground motion estimates for the whole Van area, including seismograms simulated in Van and Erciş, where no instruments recorded the event. Despite that the predictions suggest

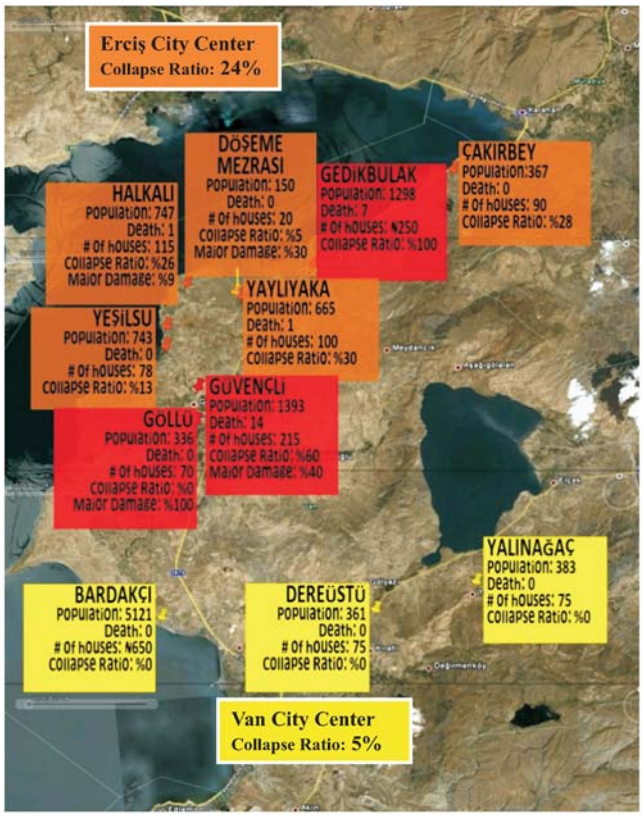

Figure 11. Spatial distribution of damage in villages located within the meizoseismal area (symbols). Erciş and Van city centers are also shown in the figure along with the collapse ratios of a sample of surveyed buildings in the field. The earthquake impact ranges from the high damage and collapse ratios to slight or no damage. (For further details, please see Akansel *et al.*, 2013). The color version of this figure is available only in the electronic edition.

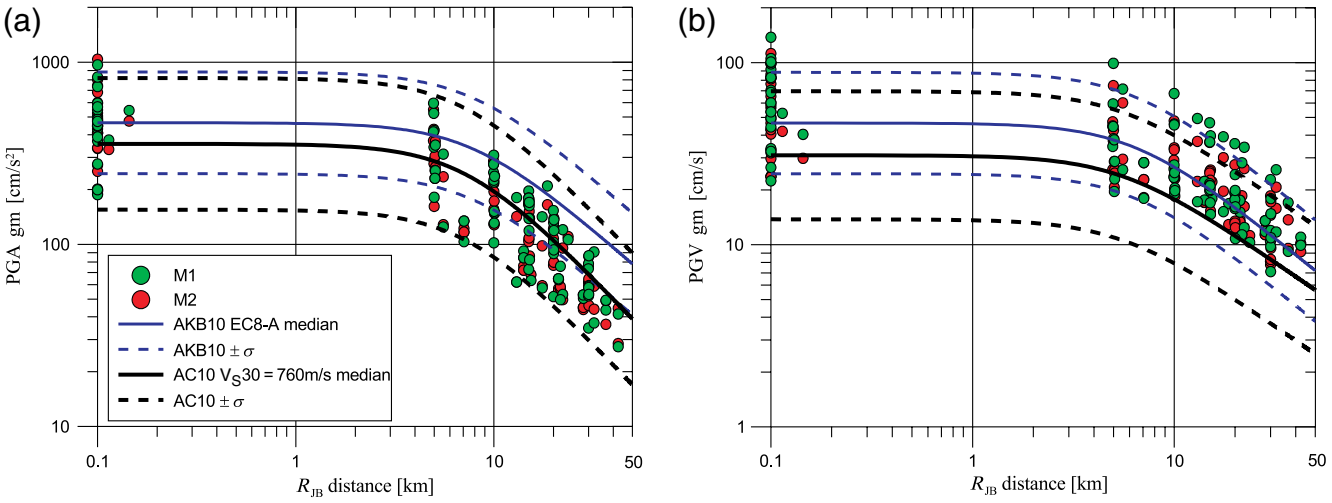

Figure 12. Comparison of (a) PGA and (b) PGV predicted from M1 and M2 models with empirical GMPEs (AKB10-Akkar and Bommer, 2010; AC10-Akkar and Cagnan, 2010) as a function of fault distance for the geometric mean of horizontal components. The GMPEs are calculated for M_w 7.1 and a reverse fault mechanism. The color version of this figure is available only in the electronic edition.

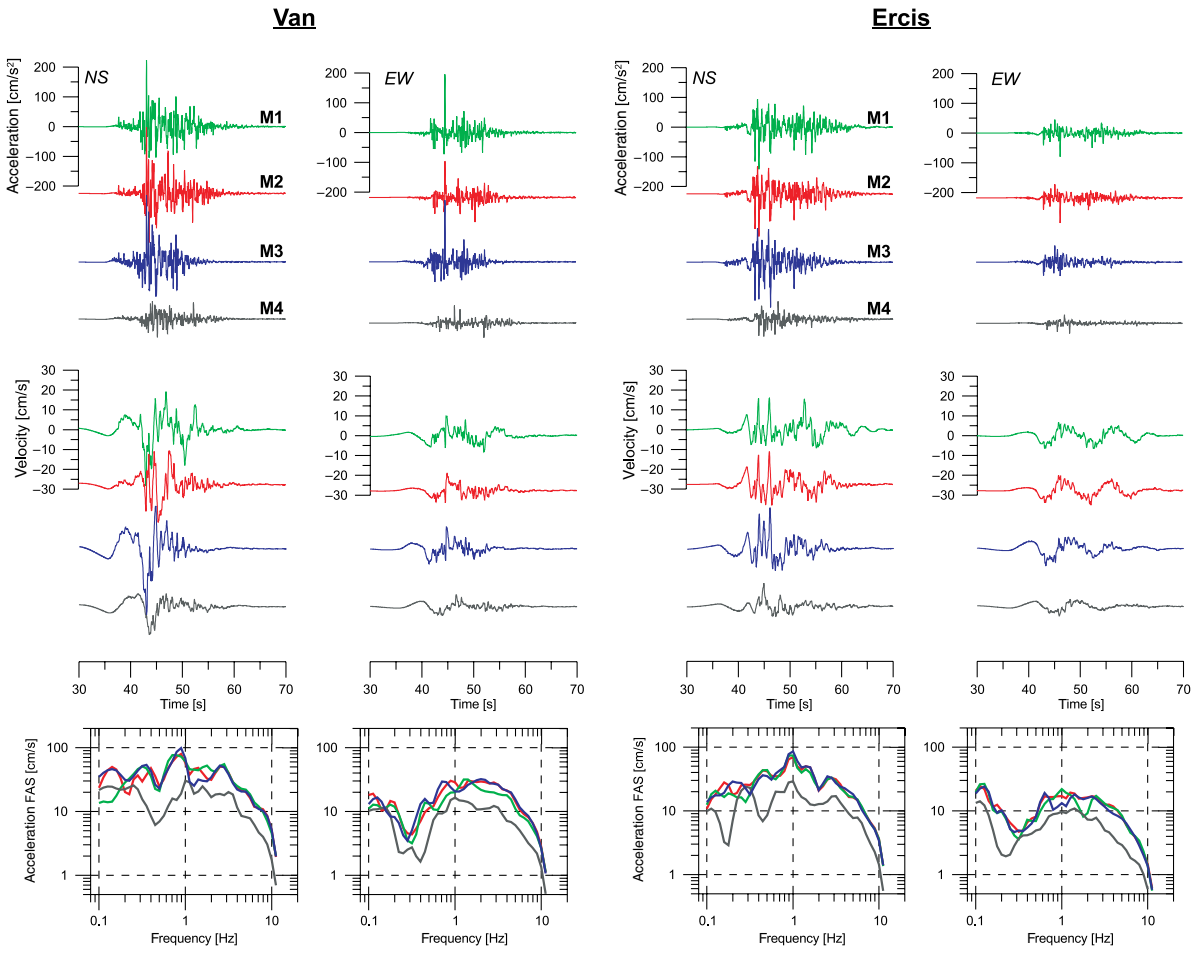

Figure 13. Strong ground motion simulation at cities of Van and Erciş (see Fig. 10 for their position). Horizontal components of acceleration and velocity time series and smoothed acceleration Fourier amplitude spectra are shown for the four different rupture models. The color version of this figure is available only in the electronic edition.

similar levels of ground motion, the observed structural damage in city of Erciş was larger than in Van. This difference could be attributed to different building properties in Van and Erciş or local site amplifications in Erciş.

Conclusions

Our comprehensive paper of the 2011 M_w 7.1 Van earthquake starts with hypocenter relocation, CMT analysis by means of the full-waveform inversion using the ISOLA package, and the MPS inversion. The latter is then extended to the inversion of the event considering MuFEx source model, grid searching for possible values of parameters of the subsources, namely nucleation times, nucleation point positions, and rupture velocities. Because of the unfavorable station coverage (stations situated at large distances and almost exclusively in a single quadrant), the uncertainty of the source model is very large. We present three selected models to illustrate a broad variability in possible rupture propagation. Then we develop a broadband strong-motion model based on the inverted fault model and simulate strong ground motions using the HIC source model. We show that the long duration of the closest Muradiye station, consisting of 2–3 distinct wave packages in the observed accelerometric record, can be reproduced only when models with complex rupture propagation (such as a delayed rupture of shallow asperities) is considered. The model is used to predict the ground motions in the epicentral area, including the cities of Van and Erciş, where recording stations were not deployed.

Data and Resources

TR-KYH (http://kyhdata.deprem.gov.tr) and ISMN provided free Internet access to accelerograms. Broadband data were obtained thanks to Orfeus (http://www.orfeus-eu.org/), Earthquake Research Department (AFAD) in Ankara, and the IIEES of Iran. GPS data (coseismic displacements) were acquired from Supersites repository (http://supersites.earthobservations.org/van.php). Many of the figures were prepared using the Generic Mapping Tools package (http://www.soest.hawaii.edu/gmt/). All electronic addresses referenced here were last accessed February 2013.

Acknowledgments

We are grateful to Karel Vachek for coseismic GPS modeling. Coseismic displacement was retrieved from raw GPS data by Rahsan Cakmak. Tuğbay Kılıç, Abdullah Sandikkaya, and Sinan Akkar provided information on the Turkish data used in this paper. We appreciate also suggestions provided by the Associate Editor Michel Bouchon and two anonymous reviewers that led to significant improvement of the presentation of the results. We acknowledge financial support from Project NERA 262330 and the Czech Republic Grants: GACR 210/11/0854, MSM 0021620860 and Charles University project UNCE 204020/2012.

References

Akansel, V., G. Ameri, A. Askan, A. Caner, B. Erdil, Ö. Kale, and D. Okuyucu (2013). The 23 October 2011 M_w 7.0 Van (Eastern Turkey) Earthquake: Interpretations of Recorded Strong Ground Motions and Post Earthquake Conditions of Nearby Structures, *Earthquake Spectra* (in press).

Akinci, A., and A. Antonioli (2013). Observations and stochastic modelling of strong ground motions for the 2011 October 23 M_w 7.1 Van, Turkey, earthquake, *Geophys. J. Int.* **192,** 1217–1239.

Akkar, S., and J. J. Bommer (2010). Empirical equations for the prediction of PGA, PGV, and spectral accelerations in Europe, the Mediterranean region, and the Middle East, *Seismol. Res. Lett.* **81,** 195–206.

Akkar, S., and Z. Cagnan (2010). A local ground-motion predictive model for Turkey and its comparison with other regional and global ground-motion models, *Bull. Seismol. Soc. Am.* **100,** 2978–2995.

Ameri, G., A. Emolo, F. Pacor, and F. Gallovič (2011). Ground-motion simulations for the M 6.9 Irpinia 1980 earthquake (Southern Italy) and scenario events, *Bull. Seismol. Soc. Am.* **101,** 1136–1151.

Ameri, G., F. Gallovič, and F. Pacor (2012). Complexity of the M_w 6.3 2009 L'Aquila (Central Italy) earthquake: 2. Broadband strong-motion modeling, *J. Geophys. Res.* **117,** no. B04308, doi: 10.1029/2011JB008729.

Ameri, G., F. Gallovič, F. Pacor, and A. Emolo (2009). Uncertainties in strong ground-motion prediction with finite-fault synthetic seismograms: An application to the 1984 M 5.7 Gubbio, central Italy, earthquake, *Bull. Seismol. Soc. Am.* **99,** 647–663.

Andrews, D. J. (1980). A stochastic fault model: 1. Static case, *J. Geophys. Res.* **85,** 3867–3877.

Bouchon, M. (1981). A simple method to calculate Green's functions for elastic layered media, *Bull. Seismol. Soc. Am.* **71,** 959–971.

Carydis, P., E. Lekkas, Ch. Papaioannou, A. Tsokos, and J. Delakouridis (2012). The October 23 ($M_w = 7.2$) and November 9 ($M_w = 5.7$), 2011 Van, Turkey earthquakes. A geoscientific and engineering report, *Ingenieria Sismica* **29,** 13–36.

Chiauzzi, L., A. Masi, M. Mucciarelli, M. Vona, F. Pacor, G. Cultrera, F. Gallovič, and A. Emolo (2011). Building damage scenarios based on exploitation of Housner intensity derived from finite faults ground motion simulations, *Bull. Earthq. Eng.* **10,** 517–545.

Cirella, A., A. Piatanesi, E. Tinti, and M. Cocco (2008). Rupture process of the 2007 Niigata-ken Chuetsu-oki earthquake by non-linear joint inversion of strong motion and GPS data, *Geophys. Res. Lett.* **35,** no. L16306, doi: 10.1029/2008GL034756.

Clévédé, E., M.-P. Bouin, B. Bukchin, A. Mostinskiy, and G. Patau (2004). New constraints on the rupture process of the 1999 August 17 Izmit earthquake deduced from estimates of stress glut rate moments, *Geophys. J. Int.* **159,** 931–942.

Coutant, O. (1989). *Program of Numerical Simulation AXITRA, Research Report*, Lab. de Geophys. Interne et Tectonophys., Grenoble, France.

Di Sarno, L., C. Yenidogan, and M. Erdik (2013). Field evidence and numerical investigation of the $M = 7.1$ October 23 Van, Tabanli and the M_w 5.7 November earthquakes of 2011, *Bull. Earthq. Eng.* **11,** 313–346.

Duputel, Z., L. Rivera, Y. Fukahata, and H. Kanamori (2012). Uncertainty estimations for seismic source inversions, *Geophys. J. Int.* **190,** 1243–1256.

Elliott, J. R., A. C. Copley, R. Holley, K. Scharer, and B. Parsons (2013). The 2011 M_w 7.1 Van (Eastern Turkey) earthquake, *J. Geophys. Res. Solid Earth* **118,** 1619–1637, doi: 10.1002/jgrb.50117.

Emolo, A., and A. Zollo (2005). Kinematic source parameters for the 1989 Loma Prieta earthquake from the nonlinear inversion of accelerograms, *Bull. Seismol. Soc. Am.* **95,** 981–994.

Erberik, M. A. (2008). Generation of fragility curves for Turkish masonry buildings considering in-plane failure modes, *Earthq. Eng. Struct. Dynam.* **37,** 387–405.

Erdik, M., Y. Kamer, M. B. Demircioglu, and K. Sesetyan (2012). 23 October 2011 Van (Turkey) earthquake, *Nat. Hazards* **64,** 651–665.

Gallovič, F., and J. Brokešová (2007). Hybrid k-squared source model for strong ground motion simulations: Introduction, *Phys. Earth Planet. In.* **160,** 34–50.

Gallovič, F., and J. Burjánek (2007). High-frequency directivity in strong ground motion modeling methods, *Ann. Geophys.* **50,** 203–211.

Gallovič, F., and J. Zahradník (2011). Toward understanding slip inversion uncertainty and artifacts: 2. Singular value analysis, *J. Geophys. Res.* **116,** no. B02309, doi: 10.1029/2010JB007814.

Gallovič, F., and J. Zahradník (2012). Complexity of the *M* 6.3 2009 L'Aquila (central Italy) earthquake: 1. Multiple finite-extent source inversion, *J. Geophys. Res.* **117,** no. B04307, doi: 10.1029/2011JB008709.

Gök, R., R. J. Mellors, E. Sandvol, M. Pasyanos, T. Hauk, R. Takedatsu, G. Yetirmishli, U. Teoman, N. Turkelli, T. Godoladze, and Z. Javakishvirli (2011). Lithospheric velocity structure of the Anatolian plateau-Caucasus-Caspian region, *J. Geophys. Res.* **116,** no. B05303, doi: 10.1029/2009JB000837.

Hartzell, S., P. Liu, C. Mendoza, C. Ji, and K. M. Larson (2007). Stability and uncertainty of finite-fault slip inversions: Application to the 2004 Parkfield, California, earthquake, *Bull. Seismol. Soc. Am.* **97,** 1911–1934.

Kennett, B. L. N., and N. J. Kerry (1979). Seismic waves in a stratified half space, *Geophys. J. Roy. Astron. Soc.* **57,** 557–583.

Kikuchi, M., and H. Kanamori (1991). Inversion of complex body waves—III, *Bull. seismol. Soc. Am.* **81,** 2335–2350.

Lee, W. H. K., and C. M. Valdé (1989). HYPO71PC. Toolbox for Seismic Data Acquisition, Processing, and Analysis, *IASPEI Seismological Software Library*, 1. IASPEI & SSA.

Lomax, A., J. Virieux, P. Volant, and C. Berge (2000). Probabilistic earthquake location in 3D and layered models: Introduction of a Metropolis-Gibbs method and comparison with linear locations, in *Advances in Seismic Event Location*, C. H. Thurber and N. Rabinowitz (Editors), Kluwer, Amsterdam, 101–134.

Mendoza, C., and S. Hartzell (2013). Finite-fault source inversion using teleseismic *P* waves: Simple parameterization and rapid analysis, *Bull. Seismol. Soc. Am.* **103,** 834–844.

Menke, W. (1985). Imaging fault slip using teleseismic waveforms: Analysis of a typical incomplete tomography problem, *Geophys. J. Roy. Astron. Soc.* **81,** 197–204.

Monelli, D., and P. M. Mai (2008). Bayesian inference of kinematic earthquake rupture parameters through fitting of strong motion data, *Geophys. J. Int.* **173,** 220–232.

Monelli, D., P. M. Mai, S. Jónsson, and D. Giardini (2009). Bayesian imaging of the 2000 Western Tottori (Japan) earthquake through fitting of strong motion and GPS data, *Geophys. J. Int.* **176,** 135–150.

Okada, Y. (1992). Internal deformation due to shear and tensile faults in a half-space, *Bull. Seismol. Soc. Am.* **82,** 1018–1040.

Page, M. T., S. Custódio, R. J. Archuleta, and J. M. Carlson (2009). Constraining earthquake source inversions with GPS data: 1. Resolution-based removal of artifacts, *J. Geophys. Res.* **114,** no. B01314, doi: 10.1029/2007JB005449.

Piatanesi, A., A. Cirella, P. Spudich, and M. Cocco (2007). A global search inversion for earthquake kinematic rupture history: Application to the 2000 western Tottori, Japan earthquake, *J. Geophys. Res.* **112,** no. B07314, doi: 10.1029/2006JB004821.

Ruff, L. J. (1984). Tomographic imaging of the earthquake rupture process, *Geophys. Res. Lett.* **11,** 629–632.

Sokos, E., and J. Zahradník (2008). ISOLA A Fortran code and a Matlab GUI to perform multiple-point source inversion of seismic data, *Comput. Geosci.* **34,** 967–977.

Sokos, E., and J. Zahradník (2013). Evaluating centroid-moment-tensor uncertainty in the new version of ISOLA software, *Seismol. Res. Lett.* **84,** 656–665.

Taskin, B., A. Sezen, U. M. Tugsal, and A. Erken (2012). The aftermath of 2011 Van earthquakes: Evaluation of strong motion, geotechnical and structural issues, *Bull. Earthq. Eng.* **11,** 285–312.

Twardzik, C., R. Madariaga, S. Das, and S. Custódio (2012). Robust features of the source process for the 2004 Parkfield, California, earthquake from strong-motion seismograms, *Geophys. J. Int.* **191,** 1245–1254.

Vallée, M., and M. Bouchon (2004). Imaging coseismic rupture in far field by slip patches, *Geophys. J. Int.* **156,** 615–630.

Vallée, M., J. Charléty, A. M. G. Ferreira, B. Delouis, and J. Vergoz (2011). SCARDEC: A new technique for the rapid determination of seismic moment magnitude, focal mechanism and source time functions for large earthquakes using body wave deconvolution, *Geophys. J. Int.* **184,** 338–358.

Zahradník, J., and S. Custódio (2012). Moment tensor resolvability: Application to Southwest Iberia, *Bull. Seismol. Soc. Am.* **102,** 1235–1254.

Zahradník, J., and F. Gallovič (2010). Toward understanding slip inversion uncertainty and artifacts, *J. Geophys. Res.* **115,** no. B09310, doi: 10.1029/2010JB007414.

Zahradník, J., and E. Sokos (2011). Multiple-point source solution of the M_w 7.2 Van earthquake, October 23, 2011, Eastern Turkey, http://www.emsc-csem.org/Files/event/239856/Van_ISOLA.pdf.

Zahradník, J., F. Gallovic, E. Sokos, A. Serpetsidaki, and G.-A. Tselentis (2008). Quick fault-plane identification by a geometrical method: Application to the M_w 6.2 Leonidio earthquake, January 6, 2008, Greece, *Seismol. Res. Lett.* **79,** 653–662.

Zollo, A., G. Iannaccone, M. Lancieri, L. Cantore, V. Convertito, A. Emolo, G. Festa, F. Gallovič, M. Vassallo, C. Martino, C. Satriano, and P. Gasparini (2009). The earthquake early warning system in southern Italy: Methodologies and performance evaluation, *Geophys. Res. Lett.* **36,** L00B07, doi: 10.1029/2008GL036689.

Charles University in Prague
Faculty of Mathematics and Physics
Department of Geophysics
Prague, V Holešovičkách 2
18000 Praha 8, Czech Republic
gallovic@karel.troja.mff.cuni.cz
jz@karel.troja.mff.cuni.cz
jansky@seis.karlov.mff.cuni.cz
vp@karel.troja.mff.cuni.cz
(F.G., J.Z., J.J., V.P.)

Istituto Nazionale di Geofisica e Vulcanologia
Milano, via Bassini 15
20133 Milan, Italy
gabriele.ameri@gmail.com
(G.A.)

University of Patras
Geology Department, Seismological Laboratory
Rio, 26504 Patras, Greece
esokos@geology.upatras.gr
(E.S.)

Middle East Technical University
Department of Civil Engineering and
Earthquake Engineering Research Center
Dumlupınar Bulvarı No: 1
06800 Çankaya Ankara, Turkey
aaskan@metu.edu.tr
(A.A.)

University of Tehran
Institute of Geophysics
P.O. 14155-6466
Tehran, Iran
mehrdadpakzad@gmail.com
(M.P.)

Manuscript received 16 February 2013;
Published Online 22 October 2013

[P15]

AGU PUBLICATIONS

JGR

Journal of Geophysical Research: Solid Earth

RESEARCH ARTICLE
10.1002/2014JB011650

Key Points:
- L'Aquila earthquake slip inversion using strong motion and HR-GPS waveforms
- Tests with 3-D and 1-D Green's functions identify (un)resolvable source features
- L'Aquila rupture was partially inhibited by a deep localized afterslip patch

Correspondence to:
F. Gallovič,
gallovic@karel.troja.mff.cuni.cz

Citation:
Gallovič, F., W. Imperatori, and P. M. Mai (2015), Effects of three-dimensional crustal structure and smoothing constraint on earthquake slip inversions: Case study of the *Mw*6.3 2009 L'Aquila earthquake, *J. Geophys. Res. Solid Earth*, *120*, 428–449, doi:10.1002/2014JB011650.

Received 30 SEP 2014
Accepted 2 DEC 2014
Accepted article online 9 DEC 2014
Published online 31 JAN 2015

Effects of three-dimensional crustal structure and smoothing constraint on earthquake slip inversions: Case study of the *Mw*6.3 2009 L'Aquila earthquake

František Gallovič[1], Walter Imperatori[2,3], and P. Martin Mai[2]

[1]Faculty of Mathematics and Physics, Department of Geophysics, Charles University in Prague, Prague, Czech Republic, [2]Division of Physical Science and Engineering, King Abdullah University of Science and Technology, Thuwal, Kingdom of Saudi Arabia, [3]Now at the Swiss Seismological Service, Swiss Federal Institute of Technology, ETH, Zurich, Switzerland

Abstract Earthquake slip inversions aiming to retrieve kinematic rupture characteristics typically assume 1-D velocity models and a flat Earth surface. However, heterogeneous nature of the crust and presence of rough topography lead to seismic scattering and other wave propagation phenomena, introducing complex 3-D effects on ground motions. Here we investigate how the use of imprecise Green's functions—achieved by including 3-D velocity perturbations and topography—affect slip-inversion results. We create sets of synthetic seismograms, including 3-D heterogeneous Earth structure and topography, and then invert these synthetics using Green's functions computed for a horizontally layered 1-D Earth model. We apply a linear inversion, regularized by smoothing and positivity constraint, and examine in detail how smoothing effects perturb the solution. Among others, our tests and resolution analyses demonstrate how imprecise Green's functions introduce artificial slip rate multiples especially at shallow depths and that the timing of the peak slip rate is hardly affected by the chosen smoothing. The investigation is extended to recordings of the 2009 *Mw*6.3 L'Aquila earthquake, considering both strong motion and high-rate GPS stations. We interpret the inversion results taking into account the lessons learned from the synthetic tests. The retrieved slip model resembles previously published solutions using geodetic data, showing a large-slip asperity southeast of the hypocenter. In agreement with other studies, we find evidence for fast but subshear rupture propagation in updip direction, followed by a delayed propagation along strike. We conjecture that rupture was partially inhibited by a deep localized velocity-strengthening patch that subsequently experienced afterslip.

1. Introduction

On 6 April 2009, the Abruzzo region in the central Apennines (Italy) was struck by an *Mw*6.3 earthquake, producing significant damage in the city of L'Aquila and its neighboring villages [*Ameri et al.*, 2009]. The event originated at 9 km depth and ruptured a NE-SW striking SE dipping fault that is well constrained by relocated aftershocks [*Valoroso et al.*, 2013]. The fault orientation and the normal-faulting mechanism are in agreement with the extensional trend of the central Apennines.

The L'Aquila earthquake has been studied extensively in terms of ground-shaking and earthquake source characterization, making use of the large amount of available high-quality data. Several studies have been devoted to slip inversions, using strong-motion stations [*Poiata et al.*, 2012], static geodetic GPS, and/or synthetic aperture radar (SAR) data [*Cheloni et al.*, 2010; *Trasatti et al.*, 2011; *D'Agostino et al.*, 2012; *Serpelloni et al.*, 2012; *Gualandi et al.*, 2014] including waveforms inferred from high-rate (HR)-GPS receivers [*Avallone et al.*, 2011], and various data combinations [*Cirella et al.*, 2009, 2012; *Zhang et al.*, 2012]. Most of the studies reveal a complicated rupture evolution in which the coseismic rupture initiated with fast updip (in-plane) rupture propagation [*Tinti et al.*, 2014], followed by along-strike (antiplane) delayed rupture propagation along a large-slip asperity. Based on geodetic data, significant afterslip has been inferred in areas of small coseismic slip [*Cheloni et al.*, 2010; *D'Agostino et al.*, 2012; *Yano et al.*, 2014]. *Gualandi et al.* [2014] suggest that the region of postseismic slip does not migrate along the fault and thus could be explained by stationary geologic conditions that lead to mildly velocity strengthening behavior.

Gallovič and Zahradník [2012] utilized near-source strong-motion data ($R < 50$ km) with maximum frequency of 0.2 Hz to invert for a low-resolution representation of the rupture process, fitting the data satisfactorily with three homogeneous slip patches. In the present study, we extend this earlier work by increasing the frequency range to 0.5 Hz, considering only the closest stations (up to 20 km fault distance), but without sacrificing the azimuthal coverage. In addition, we include HR-GPS displacement records to augment the data set. We apply a linear slip-inversion technique and study the effects of using imperfect Earth crust models for computing the Green's functions. In addition, we analyze potential biases and artifacts due to applied smoothing constraint. To this end, we perform a series of synthetic tests to understand the behavior of our inversion scheme, which enables us to more reliably interpret the estimated kinematic rupture evolution. The main question we address here is: Are we able to extract more information about the rupture process when limiting the inversion to data analyzed at short distances but higher frequencies, while using a more general source description?

Linear inversions with minimal a priori constraints, especially when using long time windows such as in the present paper, provide a general description of the source model. The result of the inversion is the estimation of the temporal evolution of slip rate as a function of fault position without any prescribed nucleation point, shape of the slip rate function, or rupture speed. Therefore, such a linear inversion has the potential to infer even very complex features of the rupture evolution, such as delays, slip reactivation (multiple rupturing), or rupture-propagation reversals. In principle, the formulation allows also to correctly reveal the supershear rupture propagation, together with the associated trailing Rayleigh pulse [*Dunham and Archuleta*, 2004; *Mello et al*., 2014].

Kinematic finite-fault earthquake source inversions constitute a nonunique inverse problem, which is often linearized by imposing strong a priori constraints (e.g., constant rupture velocity). In contrast, many studies using nonlinear inversion techniques, applied to synthetic test cases, document the strength of these methods to accurately estimate the rupture process [e.g., *Shao and Ji*, 2012; *Konca et al*., 2013; *Razafindrakoto and Mai*, 2014]. For example, *Shao and Ji* [2012] have demonstrated for the SPICE source inversion validation BlindTest 1 that the nonlinear inversion performs well. However, such "positive" tests are typically performed under idealistic conditions (frequency range 0–2 Hz, precise Green's functions and fault location, perfect station coverage, etc.) that are far from real-data applications. In some cases the authors "simulate" the real conditions, e.g., by introducing imperfections in the Green's functions [*Graves and Wald*, 2001; *Ji et al*., 2002; *Piatanesi et al*., 2007; *Konca et al*., 2013; *Razafindrakoto and Mai*, 2014] or by adding uncorrelated Gaussian noise to the "observed" data [*Cohee and Beroza*, 1994; *Sekiguchi et al*., 2000; *Shao and Ji*, 2012; *Bernauer et al*., 2014].

Interestingly, the apparent quality of the inverted slip models, derived for synthetic test cases, is in contradiction to the large variability found in rupture models for a single earthquake, obtained by different authors using various inversion methods and/or data sets (see the SRCMOD database [*Mai and Thingbaijam*, 2014] for numerous cases). For example, *Clévédé et al*. [2004] compare models of the Izmit earthquake inverted by various authors applying different inversion techniques, some of them being characterized by rupture complexities, and some not. To understand the inversion performance properly, one needs to perform synthetic tests under conditions that are as realistic as possible.

In this paper, prior to the real-data application, we perform a series of synthetic tests to understand the behavior of linear slip inversion when applying a long time window in which slip is allowed to occur on each point of the fault (i.e., the time window is chosen as long as the total rupture duration). The inversion is stabilized by enforcing slip rate positivity and applying smoothing using an a priori defined covariance matrix. We then discuss in detail the effect of smoothing and the use of imperfect Green's functions. All tests are performed under realistic conditions by considering (i) real station distribution, (ii) the same frequency range as used in the real-data case, (iii) the crustal model being based on 3-D tomography and including topography and realistic random velocity variations. In the inversion tests we consider a smooth target model as well as a spike dislocation model to analyze the inversion resolution in detail. Appendix A discusses results for an additional synthetic test based on Slip Inversion Validation 1 (SIV1) benchmark. We then invert real data recorded during the *Mw*6.3 2009 L'Aquila earthquake using Green's function calculated for a 3-D tomographic model. We emphasize that the inversion result have to be interpreted carefully and case dependent, taking into account the lessons learned from the synthetic tests, in order to be able to reliably conclude which of the model features are well resolved and which of them are questionable.

2. Inversion Method

We consider a rectangular fault with length L and width W. The displacement wavefield $\mathbf{u}(\mathbf{r}, t)$ measured at station $\mathbf{r}$ is related to slip rate $\Delta\dot{u}(\xi, t)$ distributed along fault $\Sigma(\xi)$ by means of representation theorem [*Aki and Richards*, 2002]. Assuming that the earthquake slip direction is independent of time, the representation theorem simplifies to

$$\mathbf{u}(\mathbf{r}, t) = \iint_{\Sigma} \Delta\dot{u}(\xi, \tau)\mathbf{G}(\mathbf{r}, \xi, t-\tau)\mathrm{d}\xi\mathrm{d}\tau, \tag{1}$$

where $\mathbf{G}(\mathbf{r}, \xi, t)$ is the displacement response of the medium at location $\mathbf{r}$ due to a point excitation by a double-couple source at position ξ with unit step function in time (in the following we call $\mathbf{G}$ as Green's functions despite the more general definition by *Aki and Richards* [2002]).

Depending on how the slip rate functions are parameterized, two general classes of methods can be distinguished. The first class, linear inversion techniques (also called multitime window) are based on a discretized version of the representation theorem (1). The slip rate functions are parameterized by elementary functions (overlapping narrow triangles, delta like, etc.), acting in several time windows. The windows span various time intervals ranging from relatively small fraction of source duration [e.g., *Hartzell and Heaton*, 1983; *Delouis et al*., 2002] up to the total rupture duration [e.g., *Olson and Anderson*, 1988; *Frankel and Wennerberg*, 1989; *Das and Kostrov*, 1994; *Gallovič et al*., 2009; *Gallovič and Zahradník*, 2011; *Fan et al*., 2014]. This formulation typically requires a large number of model parameters that are linearly related to the wavefield. The inversion is then performed considering regularization by applying smoothing and a positivity constraint. The second class of inversion methods, so-called nonlinear (or parametric) inversion, utilizes the representation theorem as well, but the shape of the slip rate function is prescribed a priori. In this case, the source model is parameterized in terms of physical quantities (such as rupture-onset time, risetime, and peak slip rate) that are, generally, nonlinearly related to the wavefield. Various nonlinear optimization techniques have been applied to obtain earthquake rupture models that fit the utilized data [e.g., *Hartzell and Lui*, 1995; *Hartzell et al*., 1996; *Piatanesi et al*., 2007; *Monelli and Mai*, 2008].

The major advantage of nonlinear inversions is that they work with a much lower number of parameters, thus allowing for an efficient uncertainty analysis [*Monelli et al*., 2009; *Cirella et al*., 2012; *Gallovič and Zahradník*, 2012; *Razafindrakoto and Mai*, 2014]. In contrast, although the linear inversion can now be performed fast and efficiently on common desktop computers, any practical uncertainty analysis is prohibited due to the overwhelming number (thousands) of model parameters. Thus, these methods can be tested only by synthetic tests, such as those performed in the present paper.

Our method is based on a linear approach, in which the spatial and temporal integrals in (1) are discretized with steps ΔL, ΔW, and Δt, respectively. The representation theorem (1) can then be expressed in matrix form as $\mathbf{d} = \mathbf{Gm}$, where vector $\mathbf{d}$ contains the displacement wavefield $\mathbf{u}$ of all stations and components considered and vector $\mathbf{m}$ encompasses model parameters in terms of spatial and temporal samples of the slip rate. Alternatively, one can think of the model parameterization as by means of a piecewise constant function in time and space, where model parameters $\mathbf{m}$ consist of its space-time amplitudes. Matrix $\mathbf{G}$ contains the responses to point-source excitations by the individual elementary spatial-temporal elementary subfaults of model vector $\mathbf{m}$.

Our inverse problem requires regularization. We assume that, statistically, the model parameters are close to prior model $\mathbf{m_A}$ with prior covariance matrix $\mathbf{C_M}$ (acting as a smoothing constraint). Furthermore, we apply a weighted constraint on the value of the slip model's seismic moment, assuming that it is equal to a previously determined value M_0. Thus, we aim at minimizing the L2-norm misfit function (here shown in nondimensional form),

$$M(\mathbf{m}) = \frac{1}{2}(\mathbf{d}-\mathbf{Gm})^T\mathbf{C_D}^{-1}(\mathbf{d}-\mathbf{Gm}) + \frac{1}{2}(\mathbf{m}-\mathbf{m_A})^T\mathbf{C_M}^{-1}(\mathbf{m}-\mathbf{m_A}) + \frac{1}{2\sigma_{Mo}^2}(\mathbf{E}\cdot\mathbf{m}-M_0)^2, \tag{2}$$

where $\mathbf{C_D}$ denotes the data covariance matrix, σ_{Mo} is the weight of the seismic moment constraint, and $\mathbf{E}$ is a vector of seismic moments of the elementary subfaults, $E_i = \mu_i\Delta L\Delta W\Delta t$. We assume $\sigma_{Mo} = M_o$, and $\mathbf{m_A} = 0$. We consider $\mathbf{C_M}$ to be composed of discretized covariance function $\sigma_M{}^2 c_M(\tau, x, y)$ with temporal lag τ, and with spatial lags x (along strike) a y (along dip), where σ_M is the marginal standard deviation of the model

parameters (c_M itself has unit variance). We assume further that the Fourier spectrum of c_M (i.e., slip rate power spectral density) is proportional to

$$c_M(f,k_x,k_y)\sim\left(\frac{1}{1+(k_xL)^2+(k_yW)^2}\right)^2. \tag{3}$$

This way, prior model parameters are statistically independent of time, and in the spatial domain they follow k^{-2} amplitude spectrum (with radial wave number $k=\sqrt{k_x^2+k_y^2}$). The particular choice of the spectral decay in (3) follows theoretical [*Andrews*, 1980; *Herrero and Bernard*, 1994] and observational [*Somerville et al*., 1999; *Mai and Beroza*, 2002] studies on spatial properties of earthquake slip distributions.

We apply the nonnegativity constraint on the slip rates by means of the Nonnegative Least Squares (NNLS) method [*Lawson and Hanson*, 1974]. In summary, we solve the following augmented system of equations corresponding to the problem (2),

$$\begin{pmatrix}\mathbf{U_D}^{-T}G\\ \mathbf{U_M}^{-T}\\ \frac{1}{\sigma_{Mo}}E\end{pmatrix}\boldsymbol{m}=\begin{pmatrix}\mathbf{U_D}^{-1}d\\ 0\\ \frac{1}{\sigma_{Mo}}M_0\end{pmatrix}. \tag{4}$$

In equation (4), matrices $\mathbf{U_D}$ and $\mathbf{U_M}$ are (upper)triangular matrices obtained by Cholesky decomposition ($\mathbf{C}=\mathbf{U}^T\mathbf{U}$) of $\mathbf{C_D}$ and $\mathbf{C_M}$, respectively. The augmented matrix and augmented data vector in (4) are inputs to the NNLS subroutine by *Luo and Duraiswami* [2011] that take advantage of the efficient multicore Intel Math Kernel Library. We note that *Fan et al*. [2014] formulated the linear inverse problem in frequency domain, which, however, prevented them from applying the positivity constraint.

For simplicity, we consider all data points statistically independent and identically distributed. For such a particular choice the data covariance matrix becomes $\mathbf{C_D}=\sigma_D{}^2\mathbf{I}$, where $\mathbf{I}$ and σ_D are the identity matrix and the data standard deviation, respectively, and $\mathbf{U}^{-1}=\mathbf{U}^{-T}=1/\sigma_D\mathbf{I}$ in equation (4).

In the following, we test effects of the chosen smoothing constraint, controlled by the ratio of data and prior model standard deviations, σ_D/σ_M. Therefore, without loss of generality we can fix, e.g., σ_M at a prescribed value (1 m/s in the present application). Then the smoothing strength is controlled formally just by the value of σ_D. Note that σ_D represents the data error (in meters). Thus, if the data error is considered large (by setting σ_D large), the smoothing constraint dominates the result, and vice versa.

3. Data

Strong-motion data of the L'Aquila earthquake were recorded by a dense network of near-field accelerometric stations. The closest recording sites lie above the causative fault: station AQG is a part of an array deployed in the upper Aterno River valley, and AQU is located in downtown L'Aquila. At epicentral distances up to ~20 km the earthquake was recorded by another five stations, namely, GSA (Gran Sasso), MTR (Montereale), FMG (Fiamignano), ANT (Antrodoco), and CLN (Celano). The AQU station belongs to the MedNet network (http://mednet.rm.ingv.it/data.php), while the remaining ones belong to the Italian strong-motion network (RAN) (http://www.protezionecivile.gov.it/jcms/it/ran.wp). In addition, the earthquake was recorded by two 10 Hz GPS receivers situated just above the causative fault (ROIO, Poggio di Roio, and CADO, Fossa), located at 2.3 km and 10.4 km epicentral distance, respectively. Figure 1 shows the location of these stations along with the surface projection of the assumed rupture plane.

The accelerometric records have been detrended and band-pass filtered using a causal (minimum-phase) fourth-order Butterworth filter (corner frequencies 0.05 Hz and 0.5 Hz). The lower frequency is given by the presence of instrumental noise in the data, while the upper corner has been found as the maximum frequency at which we can reliably compute the Green's functions. *Avallone et al*. [2011] processed the raw 10 Hz GPS data to obtain ground displacement records; resulting HR-GPS waveforms are low-pass filtered using a causal (minimum-phase) fourth-order Butterworth filter with corner frequency at 0.5 Hz. This processing removes effects of a ~1 Hz harmonic wave observed at CADO, which has been interpreted as a waveguide effect [*Avallone et al*., 2014]. For the synthetic experiments in this study we apply the same filter to both

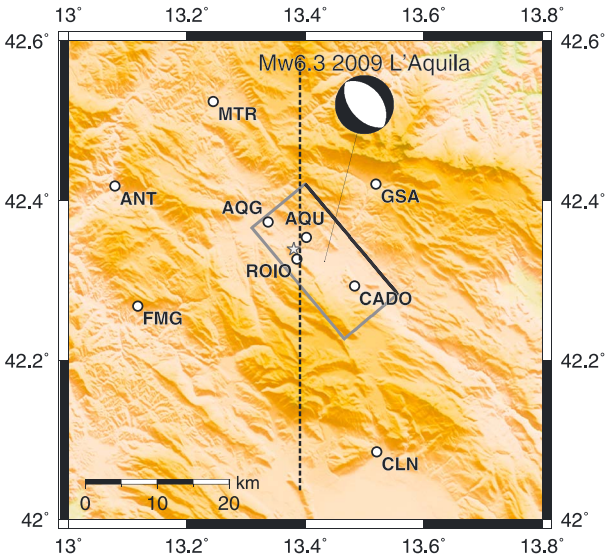

Figure 1. Map view of stations used in this study and fault plane solution of the L'Aquila main shock. CADO and ROIO are HR-GPS stations, while the others are accelerometric stations. The rectangle outlines the surface projection of the fault model considered (fault top side is in black); the star marks the epicenter. The dashed line indicates the location of the velocity cross sections shown in Figure 2.

computed and real accelerometric and HR-GPS data to provide a consistent picture of the inversion performance.

4. Fault Model and 3-D Green's Functions

We assume the same fault plane as used by *Gallovič and Zahradník* [2012] and *Ameri et al*. [2012]. The parameters are listed in Table 1. The fault plane measures 20 km along strike and 15 km downdip.

To examine how inaccurate Green's functions affect the source inversion, we consider three velocity models with different levels of complexity (Figure 2). The first model (C1) is a 1-D velocity model composed of homogeneous horizontal layers, as utilized by *Ameri et al*. [2012] and *Gallovič and Zahradník* [2012]. Such flat-layered crustal models are commonly assumed in source inversion studies. The second crustal model (C2) is the 3-D tomographic velocity model of *Di Stefano et al*. [2011], derived by inverting *P* and *S* wave travel times observed on a dense local network. Finally, we introduce a third model (C3) in which we add small-scale random velocity perturbations to the previous deterministic 3-D model C2 following the work of *Imperatori and Mai* [2012]. In particular, the random field is characterized by a Von Karman correlation function with correlation length of 5 km, Hurst exponent 0.3 and standard deviation 10%. Although there is ambiguity in the choice of the correlation function parameters, the values used in this study are commonly assumed for the upper crust [*Hartzell et al*., 2010, *Imperatori and Mai*, 2012; *Takemura and Furumura*, 2013]. In addition, we introduce the topography of the area into models C2 and C3. To maintain similar fault depths across all models, we align the average elevation above sea level (675 m) in models C2 and C3 with the surface of the flat model C1.

Table 1. Model and Computational Parameters Considered in Both the Synthetic Tests and the Inversion of the Real Recordings of the *Mw*6.3 2009 L'Aquila Earthquake

Parameters	Values
Fault mechanism	Strike: 140°, dip: 50°, rake: −90°
Fault dimension	Length: 20 km, width: 15 km
Focal depth	9.0 km
Nucleation point position (from NW fault edge)[a]	Updip: 4 km, along strike: 6 km
Nucleation point geographical coordinates[a]	42.339°N, 13.381°E
Scalar seismic moment	2.5×10^{18} Nm
Spatial fault discretization	1 × 1 km
Time sampling	0.4 s
Duration of slip rate functions	10 s
Waveform frequency range (displacements)	0.00–0.5 Hz (GPS stations); 0.05–0.5 Hz (accelerometers)
Station weights	1 (AQG, AQU) 1/3 (ROIO, CADO) 3 (others)

[a]The nucleation point position is considered only in the forward models in the synthetic tests. The inverse problem is formulated without the prescription of a nucleation point. The point serves also as a reference point to describe the geographic position of the fault plane.

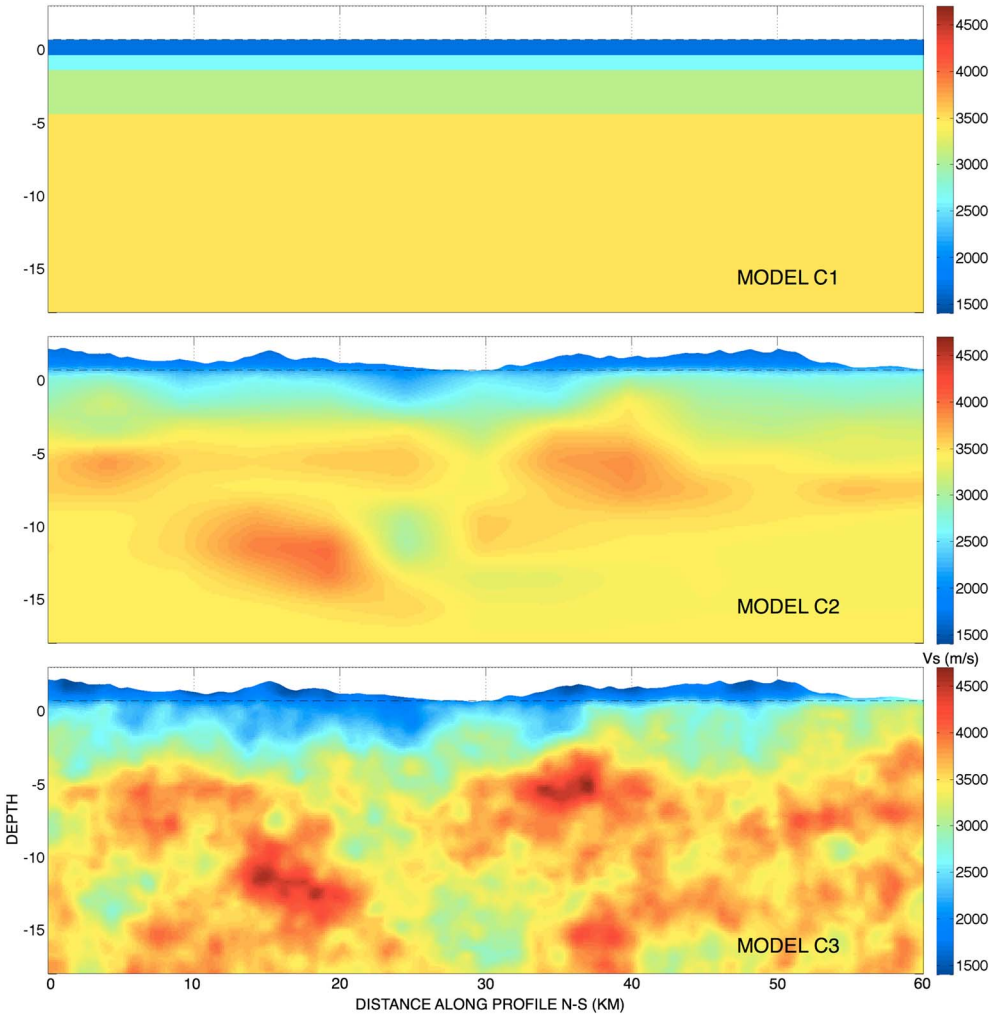

Figure 2. Cross section of the crustal models for the L'Aquila region considered in this study (see Figure 1). C1: 1-D regional velocity model [*Ameri et al*., 2012]. C2: 3-D tomographic model of *Di Stefano et al*. [2011]. C3: Model C2 with superposed random velocity perturbations. Velocity heterogeneities follow a Von Karman correlation function [*Imperatori and Mai*, 2012] with correlation length 5 km, Hurst exponent 0.3, and standard deviation 10%. Model C3 is used to generate input data for the synthetic tests, which are then inverted using the crustal models C1 and C3. Model C2 is used in the inversion of the real data recorded during the L'Aquila earthquake.

Velocity heterogeneity and topography are responsible for complex wave propagation phenomena such as scattering, multipathing, and mode conversion [e.g., *Lee et al*., 2009; *Imperatori and Mai*, 2012]. Recently, *Magnoni et al*. [2014] have shown that during the L'Aquila earthquake the topographic relief influenced ground motion already at low frequencies, especially the coda waves. Their study also pointed out that lateral heterogeneities were essential for reproducing many of the recorded waveform complexities.

In our study we use model C3 to compute synthetic seismograms that are then treated as input data for testing the inversion when assuming velocity models C1 or C3. Velocity model C2 is used later in the inversion of observed data of the L'Aquila event.

We recall that matrix **G** of the forward problem (see equation (4)) contains displacement waveforms at elementary subfaults distributed along the fault. We compute the corresponding seismograms for each subfault-receiver pair up to maximum frequency of 0.5 Hz. Each subfault has the same fault mechanism (Table 1), a unit scalar seismic moment, and effectively impulse slip rate function (i.e., risetime is shorter than the inverse of maximum frequency). In the remainder of this study, we refer to these waveforms as Green's functions.

Green's function calculations are carried out using the second-order finite-difference code WPP [*Nilsson et al.*, 2007]. The numerical method is based on summation-by-part stencils, featuring efficient absorbing boundaries, vertical mesh refinement, and viscoelastic attenuation [*Petersson and Sjögreen*, 2012]. In addition to heterogeneous Earth models, the code also handles complex topography by means of curvilinear grid meshing. To obtain 40 s long time series, the computational time required for each simulation reaches up to 25 min on 2048 cores of a BlueGene-P if topography is included.

5. Inversion Model Setup

The fault plane discretization described above must be chosen such that the representation integral (equation (1)) is correctly evaluated up to the highest frequency of interest. In particular, the subfault size must be a fraction of the minimum wavelength in the modeling, given by the ratio between the maximum frequency and the minimum velocity in the model. Note that underdiscretization of the fault (i.e., considering too large subfaults) leads to artificial ringing effect in the synthetics [e.g., *Spudich and Archuleta*, 1987; *Sekiguchi et al.*, 2002; *Beresnev*, 2003].

Considering a maximum frequency of 0.5 Hz, corresponding to a shortest resolved wavelength of ~6 km, we find that a 1 km discretization step, both along dip and along strike, is sufficient. The temporal sampling is set to 0.4 s. Since the corresponding Nyquist frequency (1.25 Hz) is well above the maximum frequency considered, each slip rate sample represents effectively a delta function (see section 2).

The inversions are performed using three-component displacement waveforms. We define station weights to balance the importance of stations in the inversion (Table 1). In particular, we assign low weights to the high-rate GPS stations since they have relatively long duration (due to the static displacement) and apply high weights to the far-distant stations to compensate for their smaller amplitudes due to geometrical spreading. We do not show effects of station coverage throughout the paper because, with the chosen station weights, the effect of removing a single station is small, although selected station weights may have an effect on the bias of the estimated slip model; this will be discussed later in the text.

6. Synthetic Tests

Let us first review some general properties of the linear slip inversion. Despite being not explicitly expressed in equation (4), the minimization of misfit function (2) is implicitly controlled by the condition number of matrix $\mathbf{G}^T\mathbf{G}$. We note that matrix $\mathbf{G}$ of the forward problem is composed of Green's functions (GFs), and thus, $\mathbf{G}^T\mathbf{G}$ contains cross correlations of the GFs along the fault. Therefore, the performance of linear slip inversion is determined by the variability of the GFs along the fault. Due to the necessity of fine fault sampling to accurately compute the representation integral, adjacent GFs are very similar and hence strongly correlated. This effectively lowers the rank of $\mathbf{G}^T\mathbf{G}$, and thus, this matrix is generally not invertible. To correct for this, regularization by smoothing or inclusion of a prior covariance matrix must be performed. In particular, in case of distant (near-regional) receivers, the difference between neighboring GFs is merely a time shift, leading to strong spatial-temporal trade-offs [*Zahradník and Gallovič*, 2010; *Gallovič and Zahradník*, 2011]. In the extreme case of using only direct *S* waves, modeled as rays in the Fraunhoffer approximation, the forward problem becomes equivalent to the Radon transform with a well-defined kernel in the space-time domain, implying that, in principle, some slip models cannot be inferred [e.g., *Menke*, 1985; *Bindi and Caponnetto*, 2001].

In the present applications, we deal with near-source data in a 1-D layered and 3-D complex structures. Therefore, the wavefield is inherently complex, even at relatively low frequencies ($<$ 0.5 Hz), comprising near-field and intermediate-field terms (consisting of both *P* and *S* waves) and free surface effects. Therefore, the GFs are much more variable along the fault plane with respect to the near-regional case, and thus, $\mathbf{G}^T\mathbf{G}$ is better conditioned, and the inversion should be better constrained. Nevertheless, we stress that it is important to first properly understand the effects of smoothing and utilization of imperfect GFs before application to the real data.

As an initial test (target) model we assume a simple Haskell-like slip distribution (Figure 3), resolved onto the fault plane of the L'Aquila earthquake. Slip is constant along dip, while in the along-strike direction, it is characterized by smoothly varying amplitude with two distant maxima. The rupture propagates radially from the hypocenter, chosen as the actual hypocenter of the L'Aquila earthquake (Table 1). The shape of the target

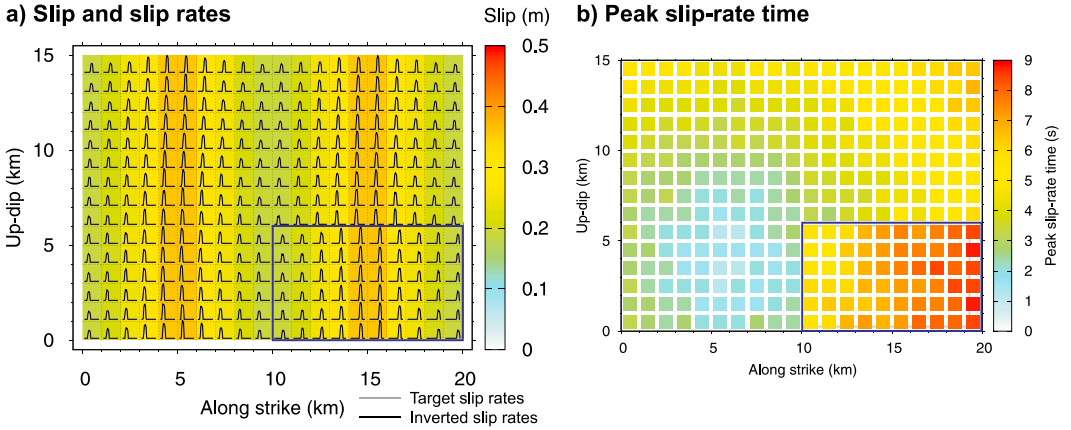

Figure 3. (a) Slip model for benchmarking the inversion approach, including slip rate functions of 10 s duration plotted on each of the 1 × 1 km subfault (black lines). All the slip rate functions start at the hypocentral time, thus covering the total rupture duration. (b) Rupture times at which the peak slip rate is achieved. Note the delayed rupture in the bottom right (blue rectangle). Figure 3a shows both the target and inverted slip rates (see legend). The inversion is carried out on displacement waveforms calculated using crustal model C3 (Figure 2), making no prior assumption on the rupture-propagation speed, applying very weak smoothing, and using the Green's functions (GFs) computed also for model C3. The use of exact GFs allows for a very weak regularization (slip rates in black and grey are indistinguishable), leading to an almost perfect source image, with predicted peak slip rate times within one time sample from the target ones.

slip rate functions and its risetime are constant along the fault. The rupture-front arrival in the bottom right of the fault is chosen to be delayed by 3 s to test the effect of such an abrupt change in rupture propagation on the inversion. We consider a smooth slip distribution to test possible occurrence of artificial slip heterogeneity. The synthetics are calculated using crustal model C3 (Figure 2).

6.1. Effect of Smoothing

In a first series of inversion tests we consider precise GFs (calculated in the 3-D structural model C3) to isolate effects of the chosen smoothing on the inversion. Apart from the target model, Figure 3 shows the inverted slip rates if minor smoothing is considered (σ_D = 1e−6 m). The differences between the inverted and the target slip rates are negligible; the precision of the estimated times of peak slip rate is within plus/minus one time sample. This shows that if the fault parameterization is exactly the same as considered for the target model and if exact GFs are used, only weak regularization is required and an almost perfect source image is obtained. Nevertheless, we emphasize that such smoothing levels are impossible in practice since such ideal conditions are never met. In practical applications the selection of the smoothing strength is to some extent ambiguous. Several ways on how to formally determine the suitable smoothing level have been introduced, such as the *L*-curve method or the Akaike's Bayesian Information Criterion, introduced by *Yoshida* [1989] in the slip-inversion studies.

Here we select three smoothing levels based on the experience from the tests with imprecise GFs and the real-data application to best illustrate the inversion behavior when changing σ_D. The same values of σ_D are used consistently throughout the whole paper. Figure 4 depicts the inversion testing results applying the selected smoothing strengths (larger σ_D means weaker smoothing). Note that we do not show the waveform fits because the seismograms are almost identical in all cases with variance reduction larger than 0.998.

In case of weak smoothing (σ_D = 0.01 m), slip rates are well resolved over almost the entire fault (see Figure 4). Problematic are artificial secondary slip rate pulses around the area of delayed rupture. This illustrates that spatial smoothing may generate time domain artifacts. Indeed, the smoothing constraint is applied to all time instances. Therefore, in the fault region of delayed rupture the slip rates are spatially smeared into neighboring cells at a given time, which introduces spurious peaks in the nondelayed fault area. Conversely, the nondelayed fault area introduces earlier artificial slip rate peak on the delayed asperity.

When smoothing is increased (Figures 4b and 4c), the above-described problem of artificial secondary slip rate pulses is extended to larger distances away from the border of the delayed asperity. Additionally, the deterioration of the inferred model becomes stronger, especially in the downdip direction and in the right

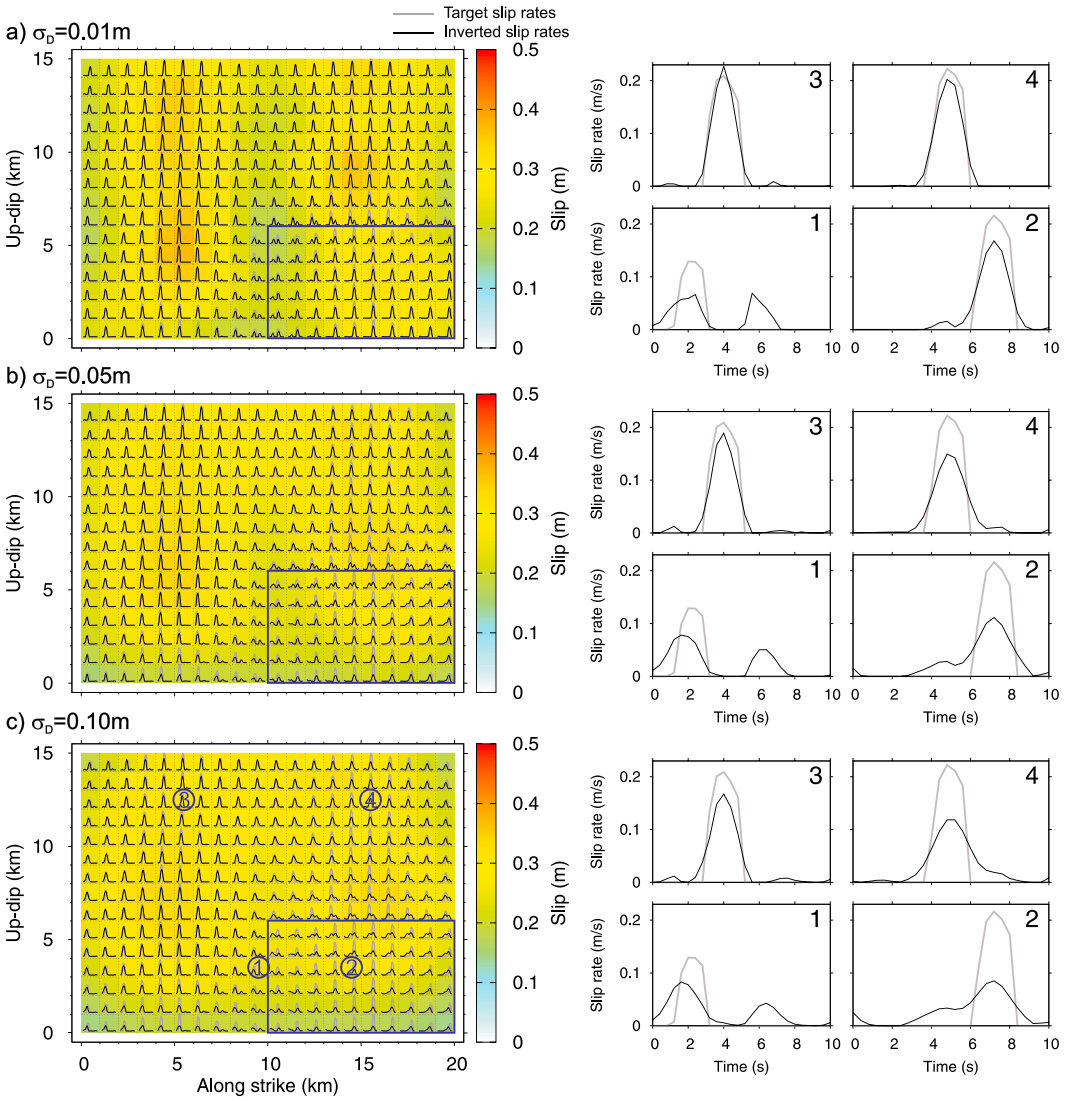

Figure 4. (a–c) Inversion of the synthetic data with precise 3-D Green's functions (crustal model C3 in Figure 2) for various smoothing strengths (the larger σ_D, the weaker the smoothing) to isolate the effect of smoothing. (left column) Blue rectangles indicate where rupture is delayed in the target model (see also Figure 3). (right column) Zoom into slip rates at selected points on the fault (see the Figure 4c (left) for their position). Target slip rates are depicted by grey lines; the inverted ones are shown in black.

part of the fault. Figure 4 also shows that with increasing smoothing level there is an apparently stronger temporal smoothing of the slip rates. It results in incorrectly resolved risetime and rupture time, while still approximately preserving the peak slip rate times.

The results also suggest that the quality of the inversion decreases with increasing hypocentral distance. Indeed, when increasing the smoothing strength the deterioration of slip rate is weaker closer to the hypocenter (see point no. 3 in Figure 4) than farther from the hypocenter (see point no. 4 in Figure 4). Similar effects can be observed in additional tests that we conducted, based on the SIV "inv1" benchmark (see Appendix A and Figure 3a), assuming almost perfect station coverage. A similar observation of decreasing quality of estimated rupture parameters with increasing hypocentral distance was made by *Razafindrakoto and Mai* [2014]. We interpret this behavior as an induced apparent temporal smoothing of slip rates due to the spatial averaging from slip rates on nearby cells. Early in the rupture process, the true slip rates are localized around the hypocenter, while later the slip rates are distributed over a larger portion of the fault. Therefore, the averaging effect is less pronounced in the beginning (near the hypocenter) than later during the rupture.

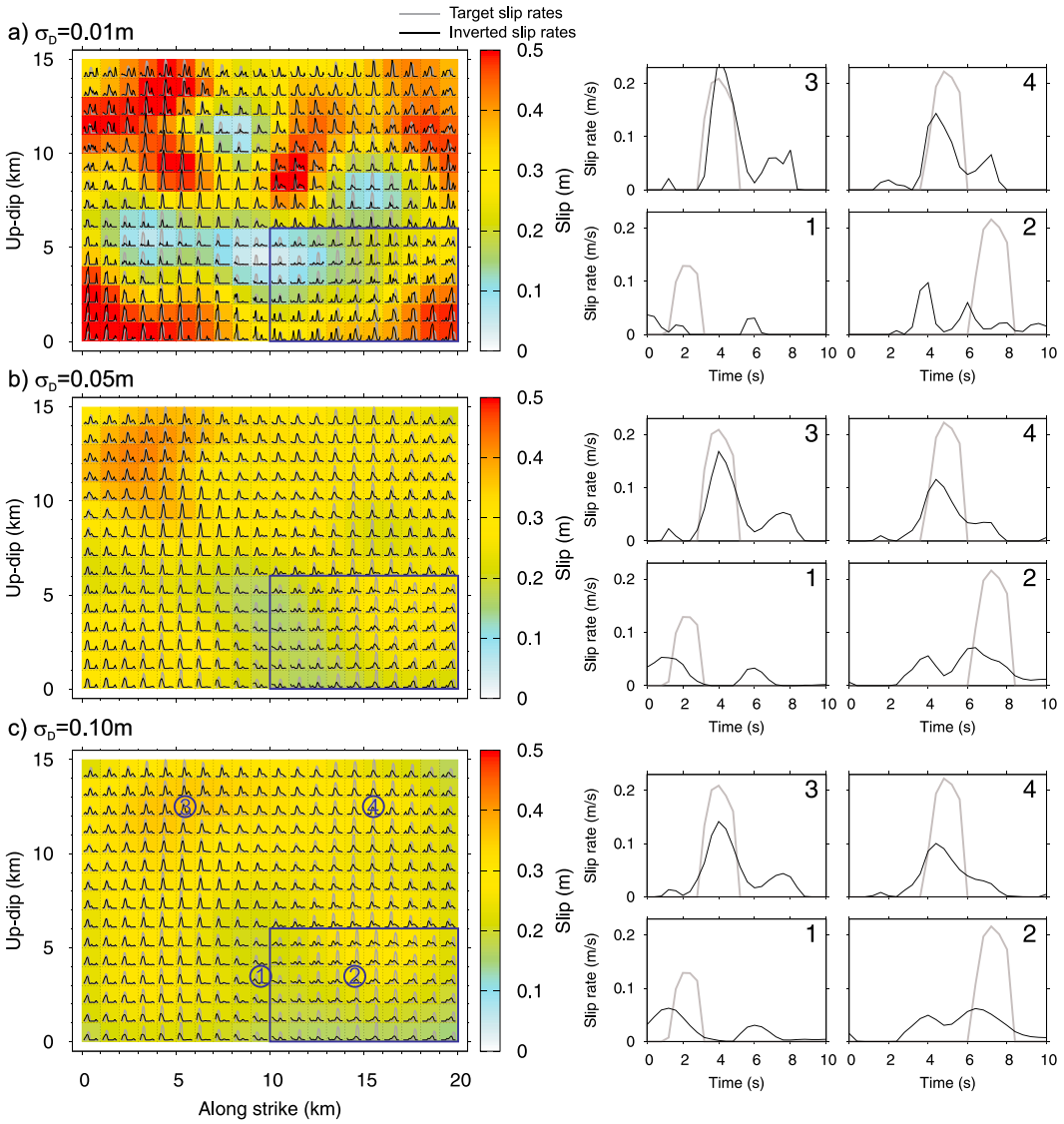

Figure 5. Same as Figure 4 but for the case when approximate (1-D) Green's functions (crustal model C1 in Figure 2) are used in the inversion.

6.2. Effect of Incorrect Green's Functions

Here we repeat the above tests, but considering GFs calculated in the approximate 1-D structural model (C1) to analyze the impact of using imperfect GFs in the inversion. Figure 5 shows the inversion of the synthetic data when applying identical smoothing as in Figure 4. In case of the smallest σ_D, the inferred model suffers from the presence of many strong artifacts both in the final slip (artificial asperities and low-slip areas) and in the shapes of slip rates (occurrence of artificial multiple peaks). Obviously, the inversion tends to map all the inconsistencies of the GFs into the inferred source model. We point out that if values of σ_D are even smaller than those considered in Figure 5, the slip image becomes much more "noisy" with clearly unphysical rupture propagation (rupture "jumping" from one side of the fault to the other).

Increasing the smoothing leads to suppression of the majority of artificial slip rate peaks. Thus, smoothing masks effects of using imperfect Green's functions, at the expense of revealing other negative effects of the smoothing. For example, the artificial two peaks of slip rates in the rupture-delay transition area coincide with those already observed in Figure 4 in case of perfect (3-D) GFs, i.e., those arising from the spatial smoothing. Similar interpretation applies to the apparent decrease of slip amplitudes in the bottom and the top right part

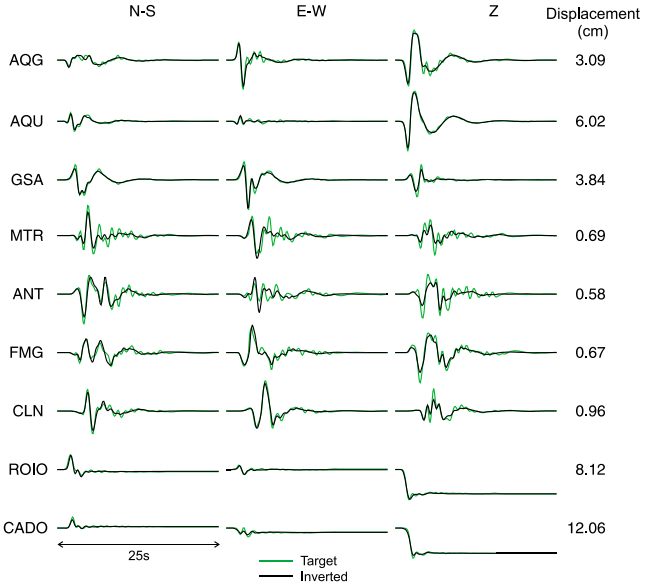

Figure 6. Comparison of target waveforms (green) calculated using the 3-D structural model C3 and predicted ones (black) corresponding to the inverted source model using 1-D Green's functions (model C1) and smoothing $\sigma_D = 0.1$ m. Variance reduction is 0.99.

of the fault (compare Figures 4 and 5). However, there are additional spurious slip rate multiples, e.g., in the top left and right part of the fault, which were not observed in the case of the perfect 3-D GFs. Thus, we associate them with strong disagreement between the 1-D and 3-D GFs.

Figure 6 shows a comparison of target waveforms with those corresponding to smoothing parameter $\sigma_D = 0.1$ m. Although the variance reduction is 0.99, we do observe significant differences between the waveforms, especially at larger distances (stations MTR, ANT, FMG, and CLN). We recall that if the same smoothing is applied when using perfect 3-D GFs, the waveform comparison is almost perfect. Thus, differences in target and inverted waveforms in Figure 6 are related to 3-D crustal structure complexity that is not captured by the 1-D GFs.

Similar to the case of smoothing with perfect 3-D GFs, we find that when using approximate 1-D GFs the smoothing effect generates an apparent broadening of the slip rates functions (Figure 5). Figure 7 compares inverted peak slip rate times for identical smoothing ($\sigma_D = 0.1$ m), documenting that the peak slip rate times are well resolved in both cases of precise and imprecise GFs almost everywhere along the fault. The only exceptions are located at the rupture-delay transition, especially where the artificial slip rate peaks exceed the true ones. Note that the other inversion example based on the SIV1 benchmark (see Appendix) with sharper slip rate onset shows more significant bias due to smoothing.

6.3. Spike-Resolution Analysis With Imprecise Green's Functions

Here we introduce another resolution test. The target source model consists of just a single slip rate spike located at a prescribed position on the fault. Inversion of such a source model serves to reveal the resolution power of the inversion, which is largely controlled by the effect of smoothing. Furthermore, to capture potential additional consequences when using imprecise GFs, we calculate the target synthetics using GFs from model C3, while we invert the resulting synthetics using the 1-D GFs from model C1.

Figure 8 shows examples of our spike-resolution analysis for smoothing $\sigma_D = 0.05$ m assuming three different positions of the spike on the fault. The inferred slip rates are generally spread in space, documenting the expected effect of smoothing. In fact, the spreading is present even if the same GFs are used for generating target waveforms and their inversion and is controlled by the value of σ_D. Using different GFs in the forward and inverse calculations introduces additional spurious slip rate pulses on the fault, whose occurrence and position depend on the position of the tested slip rate spike. For example, if the spike is located as shown in Figure 8 (middle), artificial slip at the shallow right part of the fault can be observed. On the contrary, if the spike is located just 3 km farther to the right, no slip is inferred at shallow depths but the slip amplitude is larger. We explain this effect by the proximity of the CADO station to the tested location of slip rate spike. This suggests that the resolution and reliability (e.g., as small artifacts as possible) of the inversion strongly depends on the relative location of the stations with respect to regions of high-moment release and the presence of significant crustal inhomogeneities.

The spike-resolution analysis also allows for testing effects of the station distribution and may help in defining the station weights prior to the real-data inversion. We have tested cases (not shown here) when a single station was given a much larger weight (i.e., a single station was used in the inversion). In this case, the

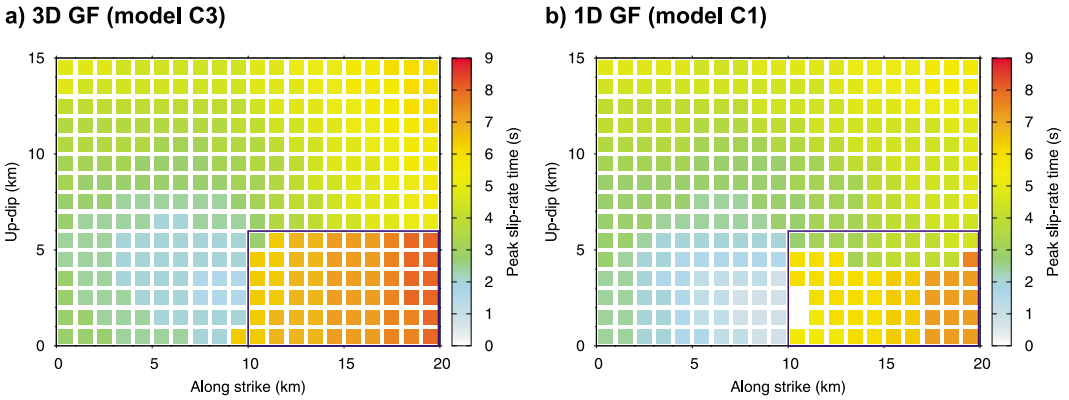

Figure 7. Stability of peak slip rate times (smoothing $\sigma_D = 0.05$ m). The delayed rupture area of the target model is marked by the blue rectangle.

inverted source model showed forced rupture propagating toward the station, as described first by *Olson and Anderson* [1988] [see also *Zahradník and Gallovič*, 2010; *Gallovič and Zahradník*, 2011]. Therefore, good azimuthal station coverage is crucial. If an azimuthal gap exists (which will be the case in almost all real applications), it should be compensated by proper weighting. Stations weights should therefore not be chosen merely according to the measured amplitudes but also according to spatial density and distribution of the stations. In contrast, increasing the weight of distant stations is advisable to compensate for the geometrical spreading of wave amplitudes, which implicitly decreases the amplitude-based weight of the station. However, the increased weighting of distant stations should be treated with caution due to the general deterioration of quality of (synthetic) GFs with increasing distance that hence may lead to amplification of artifacts due to the imperfection of the GFs.

7. Inversion of Real Data

In this section we apply the inversion method to the recorded data of the L'Aquila earthquake. Note that the inversion setup for this real-data case is the same as for the above synthetic tests (see description in section 5).

7.1. Inverted Slip Models

Figure 9 shows results of real-data inversion for various smoothing strengths (σ_D) using 3-D GFs for crustal model C2. Values of σ_D are identical to those chosen in the synthetic tests. Also, the apparent increase of source complexity with decreasing σ_D is similar to that observed in synthetic tests with imprecise Green's functions (see Figure 5). In particular, the source model obtained with $\sigma_D = 0.01$ m (Figure 9a) demonstrates how the inversion maps unaccounted wave propagation effects into the source model.

The other two models, considering $\sigma_D = 0.05$ m and 0.10 m (Figures 9b and 9c, respectively), are smoother than the previous one. The static slip distribution is dominated by a single slip patch located ~5 km above the hypocenter and ~5 km to the southeast. This solution resembles slip models inferred in previous studies employing geodetic data (GPS and SAR) [e.g., *Cheloni et al.*, 2010; *Trasatti et al.*, 2011; *Serpelloni et al.*, 2012; *D'Agostino et al.*, 2012; *Gualandi et al.*, 2014]. Solutions obtained when considering strong-motion data (using velocity seismograms) tend to have this large-slip asperity at greater depths (see comparison study performed by *Cirella et al.* [2012]). In addition, Figure 9 shows the distribution of the peak slip rate times. In all cases, the peak slip rate times suggest fast updip propagation, followed by a delayed along-strike propagation, which is also in agreement with other studies.

To gain more insight into the inversion result, Figure 10a shows the rupture evolution in terms of slip rate snapshots. For reference, we display the hypocenter location (which is not a priori constrained in our inversion scheme) and areas of significant afterslip [*Gualandi et al.*, 2014]. We find that the major slip starts ~2–3 s after the origin and ~2 km updip from the hypocenter. This point corresponds to the origin of the impulsive phase determined by *Di Stefano et al.* [2011] from the observed seismograms, marking the beginning of the large moment release. The rupture propagates first in the updip direction, reaching

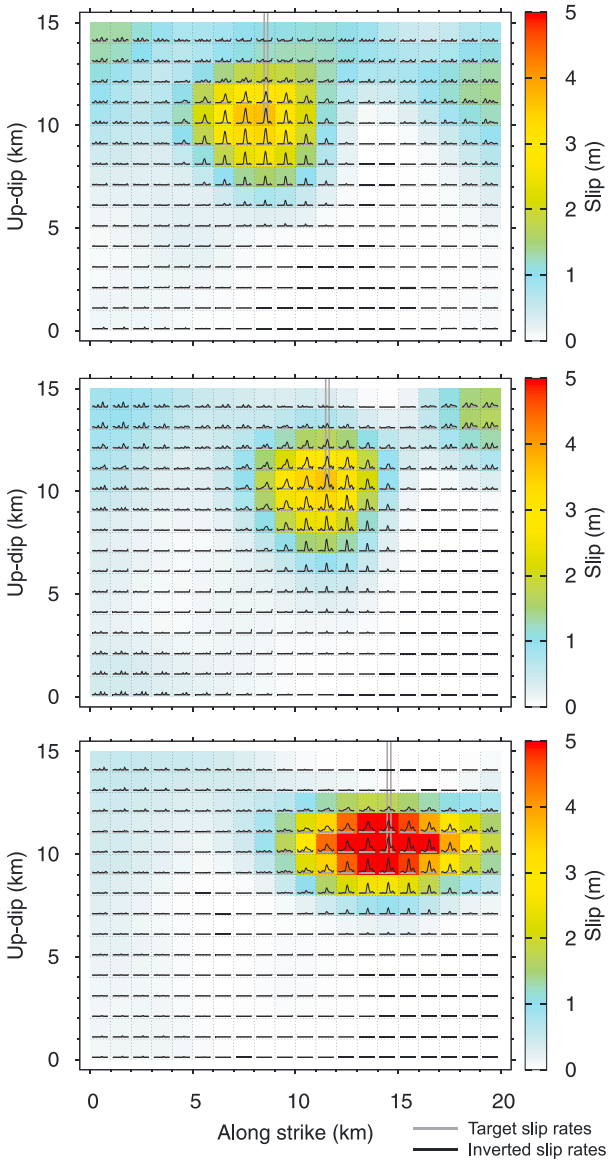

Figure 8. Tests showing inversion results (smoothing $\sigma_D = 0.05$ m) when the target model consists of a single slip rate spike at a selected point on the fault and when the synthetics are computed in the 3-D medium (grey), while the inversion is performed with 1-D Green's functions (black). The individual plots correspond to different choices of the position of the target slip rate spike.

the surface after 4–5 s, and then continuing into the region above the afterslip area. About 1–2 s later, the rupture appears to renucleate at the border of the afterslip area. After perhaps joining the rupture propagating from above, the deeper asperity then starts breaking, avoiding entering the afterslip area to the right.

Figure 10b shows the waveform fit for the model with smoothing parameter $\sigma_D = 0.05$ m, resulting in a total variance reduction of 0.95. Note that due to the chosen station weights (see section 5) the quality of the misfit decreases only slightly with increasing distance, although the amplitudes of the distant stations are up to an order of magnitude smaller than those of the near stations. Note that the waveform fit is somewhat worse than in the synthetic case where we used 1-D GFs to invert target seismograms computed with the most complex 3-D GFs. This suggests that the true Earth structure generates reverberations (mostly at later times) that are not modeled by the structural model by *Di Stefano et al.* [2011], resulting also in generally lower variance reduction. We speculate that a more accurate velocity model, including the L'Aquila basin, could improve the waveform fit.

7.2. Critical Appraisal of Details of the Inverted Model

The synthetic tests presented in section 6 and in Appendix A warn against taking the inversion result at face value. The inversion, due to the use of imperfect GFs and applying a smoothing constraint, suffers from various artifacts that may mislead the interpreter. Thus, we here critically discuss some detailed features of the source model based on the lessons learned from the synthetic tests and then present alternative source models whose predicted seismograms, if inverted, would lead to practically the same slip image. Some of our comments are graphically presented in the plot of peak slip rate times in Figure 9.

Figure 9 shows that the inverted slip rate functions are characterized by two apparent peaks at the hypocenter. Such a shape of the slip rate function is expected in case of supershear rupture, in which the first rupture pulse is followed by the trailing Rayleigh pulse [*Dunham and Archuleta*, 2004; *Mello et al.*, 2014]. This mechanism is particularly appealing since the rupture propagated updip in in-plane mode at high velocity. However, one has to recall the artifacts introduced by smoothing close to a delayed asperity, suggesting that this particular shape of the slip rate functions is an artifact rather than a real feature. *Cirella et al.* [2012] also concluded that there is no signature of supershear rupture at the initial stage of the rupture.

Our inferred model consists of relatively long duration rupture at the large-slip asperity (crack-like rupture behavior). This conflicts with the model by *Cirella et al.* [2012], who used a nonlinear approach and inferred

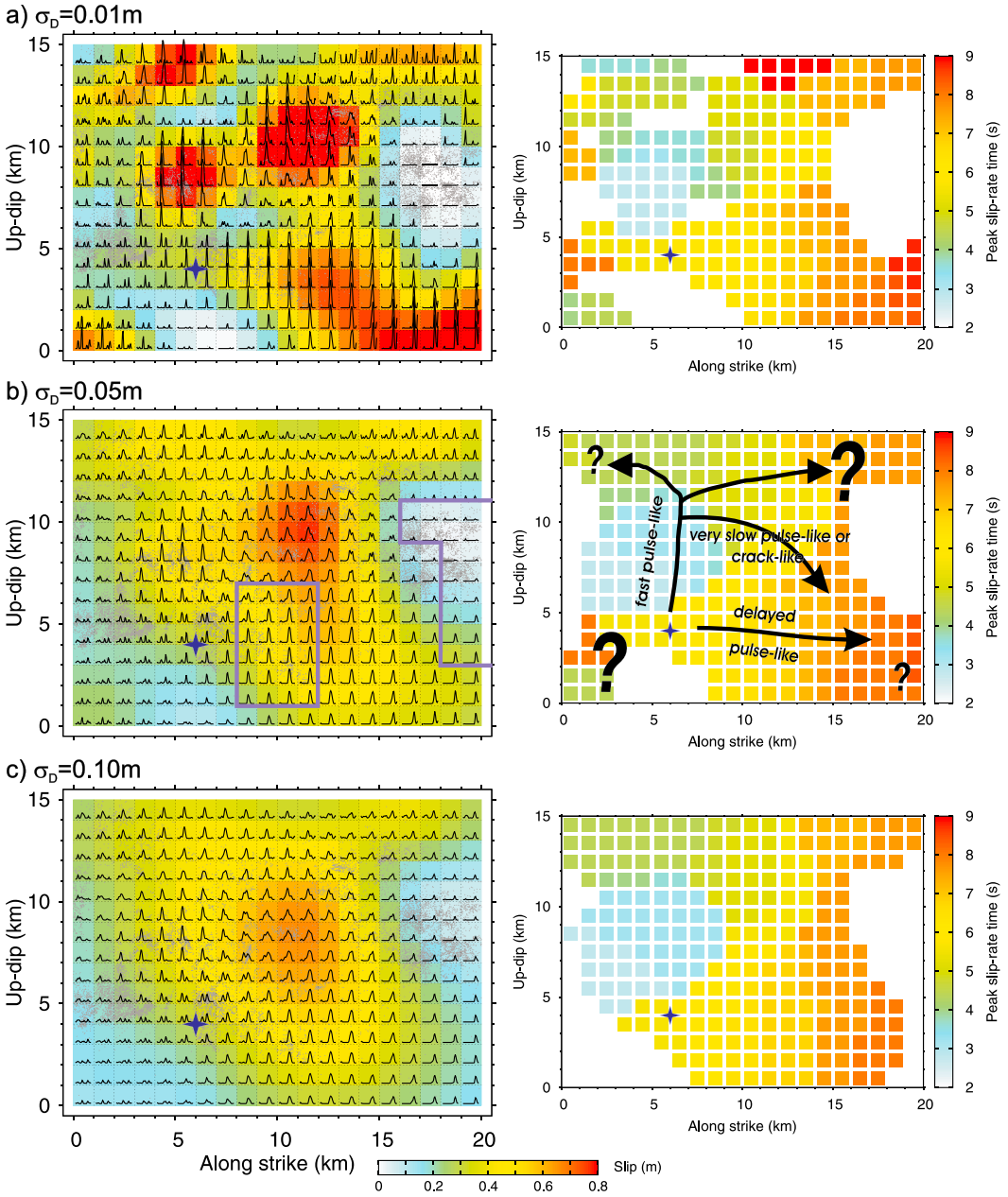

Figure 9. (a–c) Inversion of the L'Aquila earthquake real data set using 3-D GFs for crustal model C2 and assuming different smoothing strengths, plotted in terms of (left column) slip and slip rate functions along the fault and (right column) peak slip rate times. The duration of the slip rate functions in Figure 9 (left column) is 10 s, starting at the hypocentral time, thus covering the total rupture duration. For reference, the star denotes the hypocenter (not used in our inversion approach), small grey dots superimposed on the slip plots represent on-fault aftershocks (within 500 m from the fault plane) relocated by *Valoroso et al.* [2013], and the grey boxes depict major afterslip regions inferred by *Gualandi et al.* [2014]. The arrows and text in Figure 9b (right) refer to critical interpretation of the inverted model, see text for details.

rather slow but complex rupture propagation, suggesting asperity breakage with highly variable rupture velocity. Since both our and the Cirella models fit data well, this disagreement represents perhaps the "true" uncertainty of the slip inversion. Indeed, if the slow (and complex) propagation of the rupture is correct, the smoothing constraint (see discussion in section 6), would most likely smear out the inferred slip rates, thereby generating an apparently long duration (i.e., long risetime). Alternatively, one could argue that the result by *Cirella et al.* [2012] may be affected due to using constraints on the prescribed shape of the slip rate, and prescribed limits on the rupture velocity, risetime, etc. In particular, they limit risetime values to the range

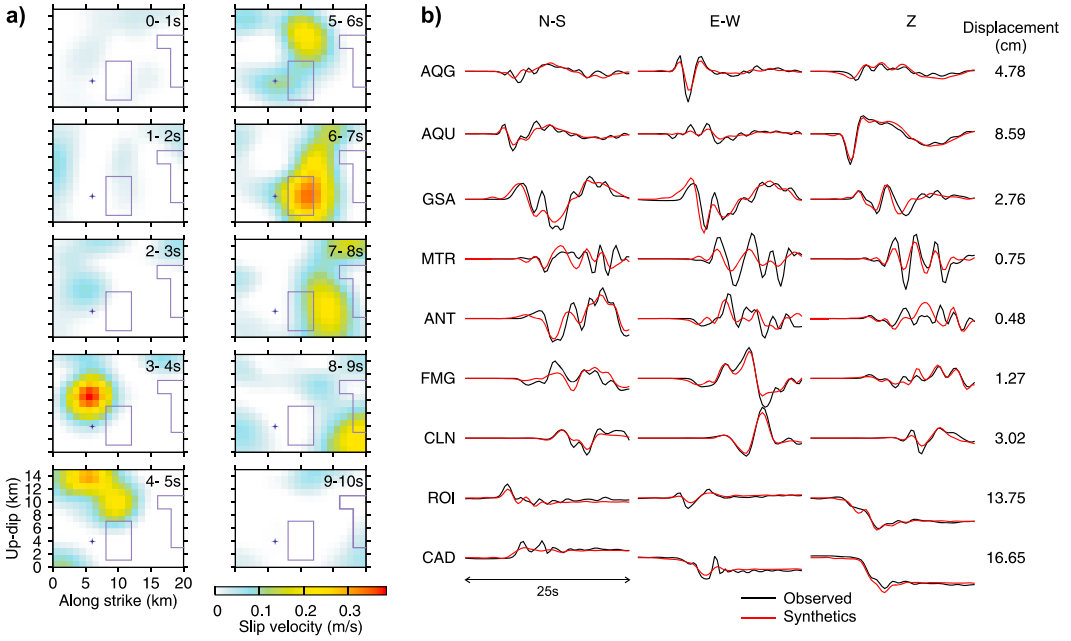

Figure 10. (a) Rupture evolution of the L'Aquila earthquake as revealed from the real data inversion (smoothing $\sigma_D = 0.05$ m in Figure 9) shown in form of snapshots at 1 s time intervals. The blue areas depict major afterslip regions by *Gualandi et al.* [2014], and star denotes the hypocenter (not used in our inversion). (b) Observed (black) and predicted (red) displacement waveform; variance reduction is 0.95.

0.75–3 s, finding a best value ~2.5 s, while our inverted model suggests risetime as long as ~5 s. Interestingly, *Cirella et al.* [2012] inferred rather small risetime uncertainty (variance coefficient of ~0.2). However, small variances are not necessarily a reliable indicator for correct result. Indeed, based on synthetic tests, *Razafindrakoto and Mai* [2014] and *Monelli and Mai* [2008] showed that in nonlinear slip inversions the true parameter values can lie at the tail of the posterior distribution, ascribing this effect to imperfect shape of the prescribed slip rate function.

Our inferred source models exhibit other areas with multiple slip rate peaks, especially at the shallow part of the fault. We point out that not only the first or secondary peak may not be real but that even all of the peaks might be artifacts. Indeed, as a consequence of an inadequate crustal structure, the artificial occurrence of slip rate peaks at shallow depths is observed in the spike-resolution analysis (section 6). In particular, when the tested slip rate spike is located in the area of maximum slip in the real-data inversion (see Figure 8 (middle)), a significant amount of slip is artificially mapped at the top right part of the fault. Thus, we conclude that the shallow slip is not well constrained in our inversion but rather may be an artifact due both smoothing and the use of imperfect GFs.

Besides the shallow slip, the aspects of our source inversion discussed above are related to rather minor features in the rupture models. They are basically not "visible" in the snapshots of rupture propagation in Figure 10a. Therefore, we believe that the general style of rupture propagation observed is reliable.

8. Discussion and Conclusions

In the present study, we employ a linear approach to slip inversion, a technique that recently regains attention as it allows for very flexible source parameterization. This is especially important if rupture propagation complexities (such as delays, multiple rupturing, rupture-propagation reversals, and supershear rupture propagation) are expected. In our inversion method, model parameters are samples of slip rate along the discretized fault, in a time window that spans the entire (assumed) rupture duration. The least squares inverse solution is regularized assuming spatial smoothing through an a priori covariance matrix composed of a k^{-2} covariance function and positivity constraint on slip rate samples. As such, the source description is very general with no constraints on the nucleation point, rupture velocity, or shape of the slip rate function.

However, due to the rather large number of model parameters, the inversion result must be carefully appraised given the general nonuniqueness of finite-fault source inversions, and the possibility of obtaining artifacts and biased solutions [*Zahradník and Gallovič*, 2010; *Gallovič and Zahradník*, 2011]. Thus, the resolving power of the proposed linear inversion approach is first examined by thorough synthetic testing. To correctly assess the performance of our inversion for the real-data application, we use the same data processing and inversion parameterization (e.g., fault discretization and smoothing) for the testing stage as in the later application to the L'Aquila earthquake. We note that our findings overviewed below are in some cases related to our specific inversion method and cannot be understood as universally valid.

8.1. Lessons Learned From the Synthetic Tests

Our synthetic tests aim to understand effect of 3-D crustal inhomogeneities and smoothing on linear slip inversions. Generally, when correct (3-D) Green's functions (GFs) are used in the inversion, near-fault recordings have resolution power for almost perfect model estimation (Figure 3). However, this is not the case when less precise (1-D) GFs are employed. In this case, smoothing constraint must be utilized to effectively damp the arising artificial small-scale heterogeneities.

To better understand this issue, we have analyzed effects of smoothing constraint and imperfect Green's functions through careful synthetic testing (sections 6.1 and 6.2, respectively), considering (i) a smooth slip model with a prescribed rupture delay on a part of the fault and (ii) a single slip rate spike localized on the fault plane (section 6.3). In addition, we have performed the inversion for the heterogeneous source model SIV inv1 of the Slip Inversion Validation (SIV) initiative [*Page et al*., 2011], which is based on a spontaneous dynamic simulation with heterogeneous initial stress (see Appendix A).

We show that the effects of smoothing are nontrivial. Indeed, the "averaging effects" occur on the true slip rates at each time instance, obtaining something like time-dependent local centroids at each time step. This effect is best visible in Figure A2 (compare the middle and right slip rate snapshots). Consequently, since slip rate at a given position on the fault and at a given time instance is affected by spatially distant points on the fault that are at different stages of slipping, the spatial smoothing is translated to the time domain as apparent temporal smoothing (see slip rates at points 3 and 4 in Figures 4c). The slip rates are thus broadened in time around their maxima; thus, the timing of peak slip rates is potentially better resolved than the rupture time and risetime (that trade-off with each other). However, the latter effect is even stronger if the true slip rate functions have strong onsets and/or the local rupture front is highly curved (such as observed in dynamic simulations; see Figure A3). In such case, both risetimes and peak slip rate times would become biased.

For the same reason, one can expect stronger artificial slip rate broadening in case of low rupture velocity in a real case, which would be indistinguishable from the case of true longer risetimes. In other words, in case of true pulse-like rupture propagating at low rupture velocity, the smoothing constraint would modify this slip image to apparently slow crack-like rupture. Qualitatively, similar trade-offs of rupture speed and risetime have been found by *Razafindrakoto and Mai* [2014]. Similarly, close to a delayed asperity, the inferred slip rates contain artificial slip pulses (see slip rates at points 1 and 2 in Figures 4c).

The spatial smoothing effect is also strongly controlled by station coverage and station weighting. One way to understand these effects is to examine the extreme case of a single-station inversion. The inferred slip model would have artificially amplified values close to the station location, and the inferred rupture evolution would look as if the rupture propagated toward that station [see also *Olson and Anderson*, 1988; *Gallovič and Zahradník*, 2011]. This prompts for azimuthally homogenous station coverage and careful station weighting. Regarding the latter, it is advisable to consider weights dependent on the station distance only. In this case, weights are used to compensate for the smaller amplitudes of far-distant stations due to the geometrical spreading (as considered in our synthetic tests based on the L'Aquila earthquake geometry). However, caution must be exercised because the quality of synthetic GFs generally decreases with increasing distance, which may lead to even stronger artifacts due to the imperfection of the GFs. Proper selection of a weighting scheme can be attained through spike-resolution tests (see section 6.3 and Figure 8). Reporting such test in the publication is a good practice for source inversion studies.

We have performed tests for which synthetics were calculated using 3-D GFs from a model with strong random heterogeneities combined with local tomography model [*Di Stefano et al*., 2011]. The waveforms were then inverted using (approximate) 1-D GFs from a crustal model composed of homogeneous layers.

The imperfections of the GFs give rise to artificial small-scale source heterogeneities not only in the final slip distribution on the fault but also in the slip rate functions in terms of multiple slip rate peaks (see Figure 5). Applied smoothing constraints effectively damp these artifacts in the deeper parts of the fault, but to a lesser extent in the shallow part. This confirms findings by *Ji et al*. [2002] and *Piatanesi et al*. [2007], who report that especially the near-surface slip estimate is strongly affected by the quality of the structural model.

The above mentioned problems obscure the estimation of the true rupture propagation since (i) the smoothing effect depends on the actual behavior of the rupture (ii) and the real effect of imprecise GFs is not perfectly predictable. Therefore, we stress that inversion results should not be taken at face value but instead require interpretation by questioning particular model features and seeking alternative models that may result in the same slip image after inverting their seismograms.

8.2. Real-Data Inversion

The lessons learned from the synthetic tests help to understand models inferred from the real data of the 2009 *Mw*6.3 L'Aquila earthquake. We have applied the inversion approach to real data of the 2009 *Mw*6.3 L'Aquila earthquake, utilizing 3-D GFs that considered tomography model and local topography. This real-data application represents an extension of previous work by *Gallovič and Zahradník* [2012], who considered a maximum frequency of 0.2 Hz, whereas in the present application the maximum frequency is set to 0.5 Hz. The authors considered a simplistic rupture parameterization by means of rectangular homogenous slip patches and 1-D GFs. Using the higher-maximum frequency allows us to infer more details of the rupture propagation. Nevertheless, the lessons learned from the synthetic tests must be taken into account to avoid misinterpretation of the inferred source model.

Our basic interpretation is discussed in Figure 9. The inferred slip model resembles previously published solutions using geodetic data, showing a large-slip asperity southeast of the hypocenter. In agreement with other studies, we find evidence for fast updip subshear rupture propagation, followed by a delayed propagation along strike. We speculate that the rupture was temporarily inhibited by a deep localized velocity-strengthening patch that then experienced afterslip.

Due to the smoothing effect and potential artifacts because of imprecise GFs, other potentially visible features of rupture complexity cannot be quantified unambiguously. For example, the inferred source model contains significant amount of slip in the top right part of the fault. However, the spike-resolution test has shown that this might be just an artifact due to the presence of significant amount of slip in the deeper part of the fault (Figure 8), as a consequence of improper crustal model. Indeed, *D'Agostino et al*. [2012] showed using DInSAR data that no or only very small coseismic slip occurred at shallow depths ($<$~2–3 km along the fault dip), while significant shallow postseismic slip has occurred there [*Cheloni et al*., 2010; *Gualandi et al*., 2014]. To fit near-source strong-motion recordings in a broad frequency range (0.5–10 Hz), *Ameri et al*. [2012] required slip to vanish at such depths. Thus, the shallow slip in our inversion is likely an artifact.

Our inverted source model comprises several other detailed features, some of which may be explained by theoretical (dynamic) models. Note that these features are conjectural at present, owing to potential artifacts due to smoothing and imprecise GFs. For example, especially if weak smoothing is applied, the inferred source image contains multiple slip pulses. Such slip rate multiples can be observed also in dynamic models [e.g., *Gabriel et al*., 2012; *Goto et al*., 2012; *Huang et al*., 2014]. However, the reliability of the inverted slip rate multiples can be hardly proven as they are a common artifact if imperfect GFs are used and/or if the true rupture includes complexities in rupture propagation (such as a time delay). Our experience is that the presence of multiple slip rate pulses suggests poor resolution at the respective part of the fault, rather than a true slip rate complexity. Another questionable feature of the inverted model is long risetime at the large-slip asperity (i.e., crack-like rupture evolution). We point out that it is impossible to discriminate whether this feature is real or a smoothing artifact of true pulse-like rupture propagating at low rupture speed. Given the available data and source inversion techniques, the precise rupture evolution remains inaccessible.

We believe that dynamic modeling of the L'Aquila earthquake will help to discriminate various proposed rupture-model solutions. This well-studied earthquake is characterized by unique lateral composition of parts of the fault that ruptured coseismically while other parts had mostly postseismic slip. This different slip behavior can be attributed to variations in rate-and-state frictional properties along the fault, with velocity strengthening and velocity weakening, respectively. Such a composition of fault has been previously

observed only on larger scales, such as in subduction zone settings [e.g., *Perfettini et al*., 2010]. The coexistence of these two frictionally distinct zones is mainly theoretically studied in terms of long-term loading, seismic cycle, aftershock triggering, and postseismic effects. *Kaneko et al*. [2008] analyzed the effect of velocity-strengthening zone below the surface on coseismic (strike-slip) rupture, showing inhibition of static slip and decrease of rupture velocity. However, to the best of our knowledge, effects of laterally inhomogeneous frictional parameters, including a distinct velocity-strengthening zone at depth, has not been studied for normal or thrust faulting earthquakes, thus posing an obvious avenue for future research.

Appendix A

A1. Target Model (SIV inv1) and Inversion Setup

Here we analyze the performance of our linear slip-inversion approach based on a synthetic test developed in the framework of the Source Inversion Validation project (SIV) [*Mai et al*., 2007; *Page et al*., 2011]. The particular model inv1 considered here has been recently utilized in synthetic tests by *Razafindrakoto and Mai* [2014] and *Fan et al*. [2014]. The source model is an 80° dipping right-lateral strike-slip fault of 35 × 20 km size, considered to be known. The target rupture model (SIV inv1, see http://equake-rc.info/SIV/ for details) is a result of a spontaneous dynamic rupture simulation, assuming random initial stress distribution. Its scalar seismic moment is $M_0 = 1.06 \times 10^{19}$ Nm. We use all 40 well-distributed stations for which seismic waveforms are available (Figure A1). The seismograms are processed using a Butterworth band-pass causal filter in the same range as in the case of the L'Aquila earthquake, i.e., between 0.05 and 0.5 Hz, and then integrated to displacements. The same processing is applied to Green's functions that are calculated in the same crustal model (homogeneous layers) as the one used to synthesize the target waveforms. The parameters are summarized in Table A1. No station weights are considered.

Figure A2 (middle row) shows the distribution of static slip and peak slip rate times, and snapshots of the true rupture propagation. The rupture starts at the largest slip patch at the bottom right of the fault and then propagates radially with slightly faster velocity along strike (in plane) than in the updip (antiplane) direction.

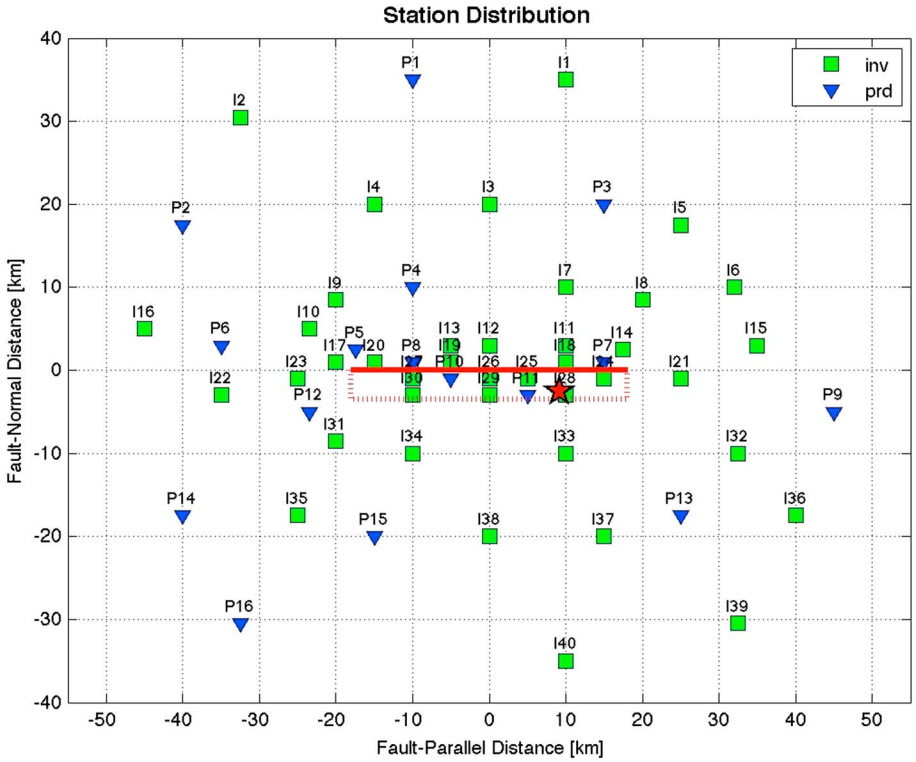

Figure A1. Fault and station geometry of the SIV test inv1. See http://equake-rc.info/SIV/ for details.

Table A1. Model and Computational Parameters Considered for the SIV inv1 Tests

Parameters	Values
Fault mechanism	Strike: 90°, dip: 80°, rake: 180°
Fault dimensions	Length: 35 km, width: 20 km
Focal depth	14.0 km
Nucleation point position (from NW fault edge)	Updip: 6 km, along strike: 27 km
Scalar seismic moment	1.06×10^{19} Nm
Spatial fault discretization	1 × 1 km
Time sampling	0.4 s
Duration of slip rate functions	10 s
Waveform frequency range (displacements)	0.05–0.5 Hz
Station weights	Equal for all stations

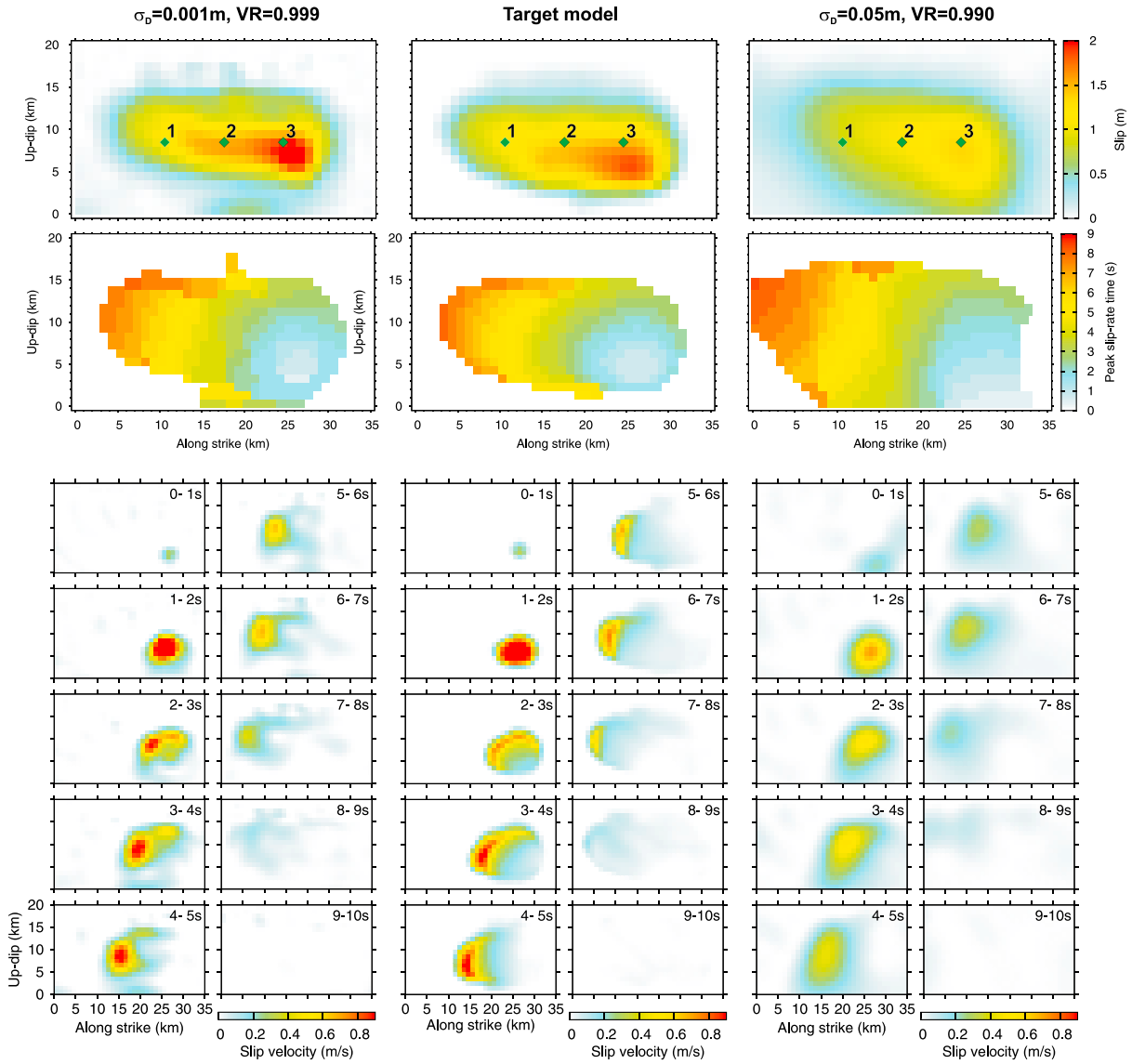

Figure A2. (left and right columns) Inversion of the SIV test inv1 for two values of smoothing, compared to the (middle column) target model. (top row) Final slip. Diamonds denote points, for which the slip rate functions are compared in Figure A3. (middle row) Comparison of peak slip rate times. (bottom rows) Snapshots (1 s time interval) of rupture evolution.

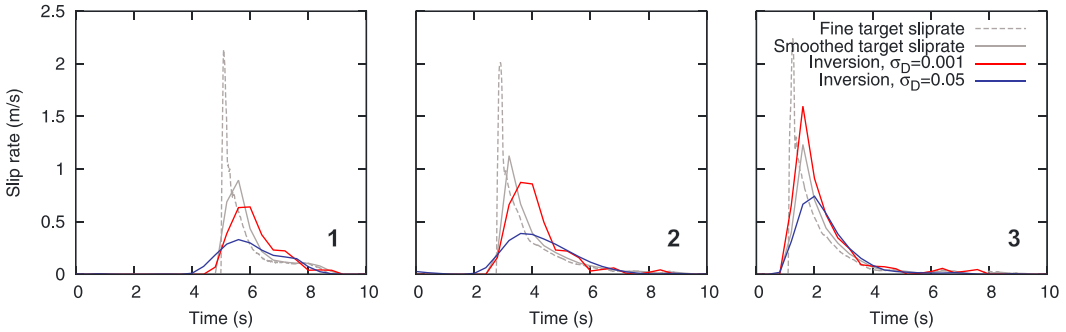

Figure A3. Comparison of slip rates at selected points on the fault (see Figure A2). Grey dashed and solid lines represent slip rates of the finely sampled model (taken directly from the dynamic simulation) and those calculated by averaging over a 1 km × 1 km subfault, respectively. The number in the bottom right of each panel refers to the slip rate location on the fault, depicted in Figure A2.

Figure A3 shows examples of slip rates (dashed grey curve) at three points on the fault (depicted in Figure A2). The target slip rates are characterized by sharp onsets due to the fast stress drop from static to dynamic frictional levels.

The inversions described below are performed on a fault that is discretized with 1 × 1 km large subfaults. Figure A3 shows the (averaged) target slip rates (solid grey curve). Note that the averaging distorts the fine slip rate function stemming from the dynamic simulation in the following way: the averaged slip rates are broader with smaller maxima; they have delayed onset and peak slip rate time by ~0.5 s with respect to the fine ones.

A2. Inversion Results

Figure A2 shows inversion result for two values of smoothing for the slip distribution, the peak slip rate times, and snapshots of the rupture propagation. In both cases, the general rupture characteristics are well recovered. In case of less smoothing (Figure A2, left column) both slip and peak slip rate time distributions are very similar to those of the target model, while the model inverted assuming stronger smoothing has smoother slip distribution and somewhat slower rupture propagation. These characteristics are also visible in Figure A3 that compares inferred slip rates with the target ones. Indeed, when increasing the smoothing, the inverted slip rates tend to be broader, with decreased peak amplitude and increased peak slip rate times. The effect is similar to averaging the target slip rates spatially (compare the dashed and solid grey lines in Figure A3); however, the effect is amplified due to the smoothing constraint that effectively results in spatial smoothing over larger distances.

The above-described discrepancies between the target and the inverted models can be understood when looking at the snapshots of the rupture propagation (Figure A2). Especially for the stronger smoothing, the inverted slip rate snapshots at each time instant resemble spatially smoothed image of the respective true snapshot. This leads not only to the (expected) decrease of peak slip rate but also to the apparent larger values of the peak slip rate times (see also Figure A3). In addition, there is an apparent elongation in the downdip direction due to the fact that all stations lay above the fault, which is then also responsible for the vertically elongated slip map (Figure A2, top row).

Acknowledgments
Observed waveforms were provided by the Italian Strong Motion Database (ITACA, http://itaca.mi.ingv.it/). The displacement waveforms obtained from HR-GPS stations were kindly provided by A. Avallone [*Avallone et al.*, 2011]. Map figures were prepared using the Generic Mapping Tools package (http://www.soest.hawaii.edu/gmt/). Financial support: Grant Agency of Czech Republic 14-04372S and Charles University project UNCE 204020/2012. This study was supported by the King Abdullah University of Science and Technology (KAUST), and numerical simulations were run on the BlueGene-P "Shaheen" of the KAUST Supercomputing Lab.

References

Aki, K., and P. G. Richards (2002), *Quantitative Seismology*, Univ. Sci, Sausalito, Calif.

Ameri, G., et al. (2009), The 6 April 2009, Mw 6.3, L'Aquila (central Italy) earthquake: Strong-motion observations, *Seismol. Res. Lett.*, *80*, 951–966.

Ameri, G., F. Gallovič, and F. Pacor (2012), Complexity of the Mw6.3 2009 L'Aquila (Central Italy) earthquake: 2. Broadband strong-motion modeling, *J. Geophys. Res.*, *117*, B04308, doi:10.1029/2011JB008729.

Andrews, D. J. (1980), A stochastic fault model: 1. Static case, *J. Geophys. Res.*, *85*, 3867–3877, doi:10.1029/JB085iB07p03867.

Avallone, A., M. Marzario, A. Cirella, A. Piatanesi, A. Rovelli, C. Di Alessandro, E. D'Anastasio, N. D'Agostino, R. Giuliani, and M. Mattone (2011), Very high rate (10 Hz) GPS seismology for moderate-magnitude earthquakes: The case of the M_w 6.3 L'Aquila (central Italy) event, *J. Geophys. Res.*, *116*, B02305, doi:10.1029/2010JB007834.

Avallone, A., A. Rovelli, G. Di Giulio, L. Improta, Y. Ben-Zion, G. Milana, and F. Cara (2014), Waveguide effects in very high rate GPS record of the 6 April 2009, M_w 6.1 L'Aquila, central Italy earthquake, *J. Geophys. Res. Solid Earth*, *191*, 490–501, doi:10.1002/2013JB010475.

Beresnev, I. A. (2003), Uncertainties in finite-fault slip inversions: To what extent to believe? (A critical review), *Bull. Seismol. Soc. Am.*, *93*, 2445–2458.
Bernauer, B., A. Fichtner, and H. Igel (2014), Reducing non-uniqueness in finite source inversion using rotational ground motions, *J. Geophys. Res. Solid Earth*, *119*, 4860–4875, doi:10.1002/2014JB011042.
Bindi, D., and A. Caponnetto (2001), Tomographic imaging of the earthquake source: Numerical validation in two-dimensional approximation, *J. Geophys. Res.*, *106*, 6643–6656, doi:10.1029/2000JB900433.
Cheloni, D., et al. (2010), Coseismic and initial post-seismic slip of the 2009 M_w 6.3 L'Aquila earthquake, Italy, from GPS measurements, *Geophys. J. Int.*, *181*, 1539–1546.
Cirella, A., A. Piatanesi, M. Cocco, E. Tinti, L. Scognamiglio, A. Michelini, A. Lomax, and E. Boschi (2009), Rupture history of the 2009 L'Aquila (Italy) earthquake from non-linear joint inversion of strong motion and GPS data, *Geophys. Res. Lett. 36*, L19304, doi:10.1029/2009GL039795.
Cirella, A., A. Piatanesi, E. Tinti, M. Chini, and M. Cocco (2012), Complexity of the rupture process during the 2009 L'Aquila, Italy, earthquake, *Geophys. J. Int.*, *190*, 607–621.
Clévédé, E., M.-P. Bouin, B. Bukchin, A. Mostinskiy, and G. Patau (2004), New constraints on the rupture process of the 1999 August 17 Izmit earthquake deduced from estimates of stress glut rate moments, *Geophys. J. Int.*, *159*, 931–942.
Cohee, B. P., and G. C. Beroza (1994), A comparison of two methods for earthquake source inversion using strong motion seismograms, *Ann. Geophys.*, *XXXVII*, 1515–1538.
D'Agostino, N., D. Cheloni, G. Fornaro, R. Giuliani, and D. Reale (2012), Space-time distribution of afterslip following the 2009 L'Aquila earthquake, *J. Geophys. Res. 117*, B02402, doi:10.1029/2011JB008523.
Das, S., and B. V. Kostrov (1994), Diversity of solutions of the problem of earthquake faulting inversion: Application to SH waves for the great 1989 Macquarie Ridge earthquake, *Phys. Earth Planet. Inter.*, *85*, 293–318.
Delouis, B., D. Giardini, P. Lundgren, and J. Salichon (2002), Joint inversion of InSAR, GPS, teleseismic, and strong-motion data for the spatial and temporal distribution of earthquake slip: Application to the 1999 İzmit mainshock, *Bull. Seismol. Soc. Am.*, *92*, 278–299.
Di Stefano, R., C. Chiarabba, L. Chiaraluce, M. Cocco, P. De Gori, D. Piccinini, and L. Valoroso (2011), Fault zone properties affecting the rupture evolution of the 2009 (M_w 6.1) L'Aquila earthquake (central Italy): Insights from seismic tomography, *Geophys. Res. Lett.*, *38*, L10310, doi:10.1029/2011GL047365.
Dunham, E. M., and R. J. Archuleta (2004), Evidence for a supershear transient during the 2002 Denali fault earthquake, *Bull. Seismol. Soc. Am.*, *94*(6), 256–268.
Fan, W., P. M. Shearer, and P. Gerstoft (2014), Kinematic earthquake rupture inversion in the frequency domain, *Geophys. J. Int.*, *199*, 1138–1160.
Frankel, A., and L. Wennerberg (1989), Rupture process of the Ms 6.6 Superstition Hills, California, earthquake determined from strong-motion recordings: Application of tomographic source inversion, *Bull. Seismol. Soc. Am.*, *79*, 515–541.
Gabriel, A. A., J.-P. Ampuero, L. A. Dalguer, and P. M. Mai (2012), The transition of dynamic rupture modes in elastic media, *J. Geophys. Res.*, *117*, B09311, doi:10.1029/2012JB009468.
Gallovič, F., and J. Zahradník (2011), Toward understanding slip-inversion uncertainty and artifacts II: Singular value analysis, *J. Geophys. Res.*, *116*, B02309, doi:10.1029/2010JB007814.
Gallovič, F., and J. Zahradník (2012), Complexity of the M6.3 2009 L'Aquila (central Italy) earthquake: 1. Multiple finite-extent source inversion, *J. Geophys. Res.*, *117*, B04307, doi:10.1029/2011JB008709.
Gallovič, F., J. Zahradník, D. Křížová, V. Plicka, E. Sokos, A. Serpetsidaki, and G.-A. Tselentis (2009), From earthquake centroid to spatial-temporal rupture evolution: Mw 6.3 Movri Mountain earthquake, June 8, 2008, Greece, *Geophys. Res. Lett. 36*, L21310, doi:10.1029/2009GL040283.
Goto, H., Y. Yamamoto, and S. Kita (2012), Dynamic rupture simulation of the 2011 off the Pacific coast of Tohoku Earthquake: Multi-event generation within dozens of seconds, *Earth Planets Space*, *64*(12), 1167–1175, doi:10.5047/eps.2012.06.002.
Graves, R., and D. Wald (2001), Resolution analysis of finite fault source inversion using one- and three-dimensional Green's functions. I—Strong motions, *J. Geophys. Res.*, *106*, 8745–8766, doi:10.1029/2000JB900436.
Gualandi, A., E. Serpelloni, and M. E. Belardinelli (2014), Space-time evolution of crustal deformation related to the Mw 6.3, 2009 L'Aquila earthquake (central Italy) from principal component analysis inversion of GPS position time-series, *Geophys. J. Int.*, *197*, 174–191.
Hartzell, S., and P. Lui (1995), Determination of earthquake source parameters using a hybrid global search algorithm, *Bull. Seismol. Soc. Am.*, *85*, 616–524.
Hartzell, S. H., and T. H. Heaton (1983), Inversion of strong ground motion and teleseismic waveform data for the fault rupture history of the 1979 Imperial Valley, California, earthquake, *Bull. Seismol. Soc. Am.*, *73*, 1553–1583.
Hartzell, S., P. Lui, and C. Mendoza (1996), The 1994 Northridge, California, earthquake: Investigation of rupture velocity, risetime and high-frequency radiation, *J. Geophys. Res.*, *101*, 20,091–20,108, doi:10.1029/96JB01883.
Hartzell, S. H., S. Harmsen, and A. Frankel (2010), Effects of 3D random correlated velocity perturbations on predicted ground motions, *Bull. Seismol. Soc. Am.*, *100*, 1415–1426.
Herrero, A., and P. Bernard (1994), A kinematic self-similar rupture process for earthquakes, *Bull. Seismol. Soc. Am.*, *84*, 1216–1228.
Huang, Y., J.-P. Ampuero, and D. V. Helmberger (2014), Earthquake ruptures modulated by waves in damaged fault zones, *J. Geophys. Res. Solid Earth*, *119*, 3133–3154, doi:10.1002/2013JB010724.
Imperatori, W., and M. P. Mai (2012), Broad-band near-field ground motion simulations in 3-dimensional scattering media, *Geophys. J. Int.*, *192*, 725–744.
Ji, C., D. Wald, and D. V. Helmberger (2002), Source description of the 1999 Hector Mine, California, earthquake, part I: Wavelet domain inversion theory and resolution analysis, *Bull. Seismol. Soc. Am.*, *92*, 1192–1207.
Kaneko, Y., N. Lapusta, and J.-P. Ampuero (2008), Spectral element modeling of spontaneous earthquake rupture on rate and state faults: Effect of velocity-strengthening friction at shallow depths, *J. Geophys. Res.*, *113*, B09317, doi:10.1029/2007JB005553.
Konca, O. A., Y. Kaneko, N. Lapusta, and J.-P. Avouac (2013), Kinematic inversion of physically plausible earthquake source models obtained from dynamic rupture simulations, *Bull. Seismol. Soc. Am.*, *103*, 2621–2644.
Lawson, C. L., and R. J. Hanson (1974), *Solving Least Square Problems*, vol. 340, Prentice-Hall, Upper Saddle River, N. J.
Lee, S. J., D. Komatitsch, B. S. Huang, and J. Tromp (2009), Effects of topography on seismic-wave propagation: An example from northern Taiwan, *Bull. Seismol. Soc. Am.*, *99*(1), 314–325.
Luo, Y., and R. Duraiswami (2011), Efficient parallel nonnegative least squares on multicore architectures, *SIAM J. Sci. Comput.*, *33*, 2848–2863.
Magnoni, F., E. Casarotti, A. Michelini, A. Piersanti, D. Komatitsch, D. Peter, and J. Tromp (2014), Spectral-element simulations of seismic waves generated by the 2009 L'Aquila earthquake, *Bull. Seismol. Soc. Am.*, *104*, 73–94.

Mai, P. M., and G. C. Beroza (2002), A spatial random field model to characterize complexity in earthquake slip, *J. Geophys. Res.*, *107*(B11), 2308, doi:10.1029/2001JB000588.
Mai, P. M., and K. K. S. Thingbaijam (2014), SRCMOD: An online database of finite-fault rupture model, *Seismol. Res. Lett.*, *85*, doi:10.1785/0220140077.
Mai, P. M., J. Burjanek, B. Delouis, G. Festa, C. Holden, D. Monelli, and T. Uchide (2007), Earthquake source inversion blindtest: Initial results and further developments, *Eos Trans. AGU*, *88*, 855–877.
Mello, M., H. S. Bhat, A. J. Rosakis, and H. Kanamori (2014), Reproducing the supershear portion of the 2002 Denali earthquake rupture in laboratory, *Earth Planet. Sci. Lett.*, *387*, 89–96, doi:10.1016/j.epsl.2013.11.030.
Menke, W. (1985), Imaging fault slip using teleseismic waveforms: Analysis of a typical incomplete tomography problem, *Geophys. J. R. Astron. Soc.*, *81*, 197–204.
Monelli, D., and M. P. Mai (2008), Bayesian inference of kinematic earthquake rupture parameters through fitting of strong motion data, *Geophys. J. Int.*, *173*, 220–232.
Monelli, D., M. P. Mai, S. Jónsson, and D. Giardini (2009), Bayesian imaging of the 2000 Western Tottori (Japan) earthquake through fitting of strong motion and GPS data, *Geophys. J. Int.*, *176*, 135–150.
Nilsson, S., A. N. Petersson, B. Sjögreen, and H. O. Kreiss (2007), Stable difference approximations for the elastic wave equation in second order formulation, *SIAM J. Numer. Anal.*, *45*(2), 1902–1936.
Olson, A. H., and J. G. Anderson (1988), Implications of frequency-domain inversion of earthquake ground motions for resolving the space-time dependence of slip on an extended fault, *Geophys. J. Int.*, *94*, 443–455.
Page, M., P. Mai, and D. Schorlemmer (2011), Testing earthquake source inversion methodologies, *Eos Trans. AGU*, *92*, 75, doi:10.1029/2011EO090007.
Perfettini, H., et al. (2010), Seismic and aseismic slip on the Central Peru megathrust, *Nature*, *465*, 78–81.
Petersson, N. A., and B. Sjögreen (2012), Stable and efficient modeling of anelastic attenuation in seismic wave propagation, *Comm. Comput. Phys.*, *12*, 193–225.
Piatanesi, A., A. Cirella, P. Spudich, and M. Cocco (2007), A global search inversion for earthquake kinematic rupture history: Application to the 2000 western Tottori, Japan earthquake, *J. Geophys. Res. 112*, B07314, doi:10.1029/2006JB004821.
Poiata, N., K. Koketsu, A. Vuan, and H. Miyake (2012), Low-frequency and broad-band source models for the 2009 L'Aquila, Italy, earthquake, *Geophys. J. Int.*, *191*, 224–242.
Razafindrakoto, H. N. T., and P. M. Mai (2014), Uncertainty in earthquake source imaging due to variations in source time function and earth structure, *Bull. Seismol. Soc. Am.*, *104*(2), doi:10.1785/0120130195.
Sekiguchi, H., K. Irikura, and T. Iwata (2000), Fault geometry at the rupture termination of the 1995 Hyogo-ken Nanbu earthquake, *Bull. Seismol. Soc. Am.*, *90*, 117–133.
Sekiguchi, H., K. Irikura, and T. Iwata (2002), Source inversion for estimating the continuous slip distribution on a fault—Introduction of Green's functions convolved with a correction function to give moving dislocation effects in subfaults, *Geophys. J. Int.*, *150*, 377–391.
Serpelloni, E., L. Anderlini, and M. E. Belardinelli (2012), Fault geometry, coseismic-slip distribution and Coulomb stress change associated with the 2009 April 6, Mw 6.3, L'Aquila earthquake from inversion of GPS displacements, *Geophys. J. Int.*, *188*, 473–489.
Shao, G., and C. Ji (2012), What the exercise of the SPICE source inversion validation BlindTest 1 did not tell you, *Geophys. J. Int.*, *189*, 569–590.
Somerville, P., K. Irikura, R. Graves, S. Sawada, D. Wald, N. Abrahamson, Y. Iwasaki, T. Kagawa, N. Smith, and A. Kowada (1999), Characterizing crustal earthquake slip models for the prediction of strong ground motion, *Seismol. Res. Lett.*, *70*, 59–80.
Spudich, P., and R. J. Archuleta (1987), Techniques for earthquake ground motion calculation with applications to source parameterization of finite faults, in *Seismic Strong Motion Synthetics*, edited by B. A. Bolt, pp. 205–265, Acad. Press, San Diego, Calif.
Takemura, S., and T. Furumura (2013), Scattering of high-frequency P wavefield derived by dense Hi-net array observations in Japan and computer simulations of seismic wave propagations, *Geophys. J. Int.*, *193*, 421–436.
Tinti, E., L. Scognamiglio, A. Cirella, and M. Cocco (2014), Up-dip directivity in near-source during the 2009 L'Aquila main shock, *Geophys. J. Int.*, *198*, 1618–1631.
Trasatti, E., C. Kyriakopoulos, and M. Chini (2011), Finite element inversion of DInSAR data from the Mw 6.3 L'Aquila earthquake, 2009 (Italy), *Geophys. Res. Lett.*, *38*, L08306, doi:10.1029/2011GL046714.
Valoroso, L., L. Chiaraluce, D. Piccinini, R. Di Stefano, D. Schaff, and F. Waldhauser (2013), Radiography of a normal fault system by 64,000 high-precision earthquake locations: The 2009 L'Aquila (central Italy) case study, *J. Geophys. Res. Solid Earth*, *118*, 1156–1176, doi:10.1002/jgrb.50130.
Yano, T. E., G. Shao, Q. Liu, C. Ji, and R. J. Archuleta (2014), Coseismic and potential early afterslip distribution of the 2009 Mw 6.3 L'Aquila, Italy earthquake, *Geophys. J. Int.*, *199*, 23–40.
Yoshida, S. (1989), Waveform inversion using ABIC for the rupture process of the 1983 Hindu Kush earthquake, *Phys. Earth Planet. Inter.*, *56*, 389–405.
Zahradník, J., and F. Gallovič (2010), Toward understanding slip inversion uncertainty and artifacts, *J. Geophys. Res.*, *115*, B09310, doi:10.1029/2010JB007414.
Zhang, Y., W. Feng, Y. Chen, L. Xu, Z. Li, and D. Forrest (2012), The 2009 L'Aquila Mw6.3 earthquake: A new technique to locate the hypocentre in the joint inversion of earthquake rupture process, *Geophys. J. Int.*, *191*, 1417–1426.

[P16]

Tectonophysics 656 (2015) 131–141

Contents lists available at ScienceDirect

Tectonophysics

journal homepage: www.elsevier.com/locate/tecto

Rupture process of the 2014 Cephalonia, Greece, earthquake doublet (Mw6) as inferred from regional and local seismic data

E. Sokos [a,*], A. Kiratzi [b], F. Gallovič [c], J. Zahradník [c], A. Serpetsidaki [a], V. Plicka [c], J. Janský [c], J. Kostelecký [d], G.-A. Tselentis [a]

[a] University of Patras, Department of Geology — Seismological Laboratory, Greece
[b] Aristotle University of Thessaloniki, Department of Geophysics, Greece
[c] Charles University in Prague, Faculty of Mathematics and Physics, Czech Republic
[d] Research Institute of Geodesy, Topography and Cartography, Geodetic Observatory Pecný, Ondřejov, Czech Republic

ARTICLE INFO

Article history:
Received 2 April 2015
Received in revised form 30 May 2015
Accepted 6 June 2015
Available online 26 June 2015

Keywords:
Cephalonia earthquake
Centroid moment tensor
Waveform inversion
Slip history
Fault complexity
Stress field

ABSTRACT

We study the 26 January and 3 February, 2014 (~Mw6) events in Cephalonia, combining weak and strong motion waveforms from regional and local stations. The hypocenter of the January 26 event is located at the southernmost tip of the Paliki Peninsula, at a depth of ~15 km. The centroid moment tensor (CMT) solution indicates rupture along a N20°E dextral strike-slip fault, dipping to the east. The hypocenter of the February 3 event is 10 km NNE of the first, at shallower depth (~5 km). The CMT solution of this event is highly uncertain. The kinematic slip model for the January 26 event indicates that the rupture was mainly confined to shallow depths, and it propagated upwards and towards NE. The major slip patches, when projected to the surface, cover the western part of the Paliki Peninsula and include the areas where surface ruptures were observed. Our preferred slip model for the event of February 3 is based on a published two-segment fault model. Although this is our preferred slip model, it is worth noting, that the single segment inversion provided a similar slip pattern. The rupture propagated predominantly southwards along both segments. The main slip episode on both segments occurred almost simultaneously. Total duration of the rupture propagation did not exceed 9 and 6 s, respectively. The 2014 Cephalonia doublet did not rupture the Cephalonia Transform Fault (CTF). The diffuse pattern of the aftershocks implies the activation of a network of faults on-shore the Paliki Peninsula, in accordance with the local stress field derived from aftershocks. The 2014 sequence has implications for the seismic hazard assessment: active faults in western Cephalonia exist on-shore; some have gentle dip angles; the strike-slip motions can be combined with thrust components; and the segmented ruptures may introduce time delays that increase the duration of strong ground shaking.

1. Introduction

Cephalonia (Greece) belongs to the Ionian Islands and is best known for its beautiful landscape and the strong and frequent earthquakes. The earthquake activity in 1953 benchmarks the history of Cephalonia, as the island was destroyed and more than 450 people lost their lives. This event was the startup point for the Hellenic Antiseismic Code whose provisions for the constructions in the Ionian Islands are the strictest over Greece (reference ground acceleration for ground type A (rock) equal to 0.36 g).

The focus of this work is the sequence that burst in Cephalonia Island on January 26, 2014 with an Mw6 earthquake and culminated on February 3 to another Mw6 event (Fig. 1). The reported epicenters of the two strong events and all aftershocks are spread along the western coast (Paliki Peninsula) of Cephalonia. No loss of life was reported and the constructions performed remarkably well (GEER/EERI/ATC report, 2014). The 2014 sequence attracted the attention of the scientific community and a number of publications are already available (Benekos et al., 2015; Boncori et al., 2015; Karakostas et al., 2014; Karastathis et al., 2015; Papadopoulos et al., 2014; Sakkas and Lagios, 2015; Valkaniotis et al., 2014). Despite the fact that the sequence was well recorded by the regional networks in Greece, there are still unresolved issues. Accurate location of earthquakes in Cephalonia is a challenge by itself, due to the absence of stations from the west and the sparse seismic coverage from the south. For example, in the west the closest seismic station is in Italy. As a result, in the related publications (Boncori et al., 2015; Karakostas et al., 2014; Papadopoulos et al., 2014), the location, the fault orientation and its dip polarity of the two strong events show considerable variability, reflecting the difficulties in the data analysis.

Another issue that further intrigued the scientists is the unclear, if any, connection of the sequence to the well-known dextral Cephalonia Transform Fault (CTF) that dominates along the western coast of the

* Corresponding author. Tel.: +30 2610 969369; fax: +30 2610 990639.
E-mail address: esokos@upatras.gr (E. Sokos).

http://dx.doi.org/10.1016/j.tecto.2015.06.013
0040-1951/

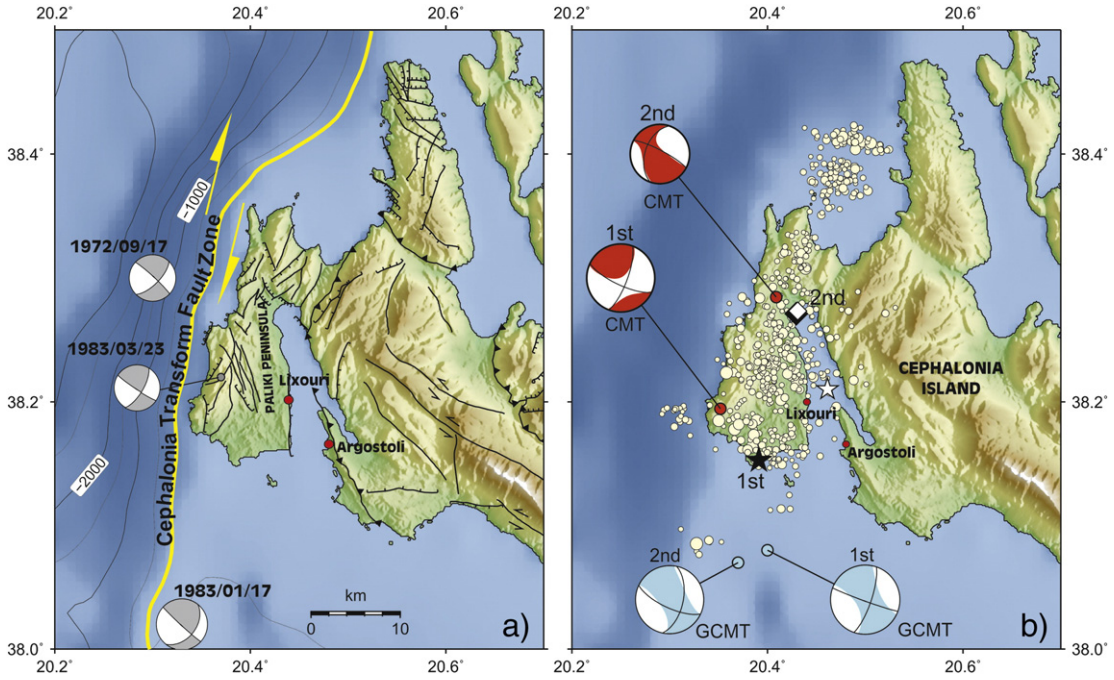

Fig. 1. a) Map of Cephalonia Island showing focal mechanisms of post-1966 earthquakes with Mw > 6 (beach-balls) and mapped faults on-shore (Lekkas et al., 2001); the Cephalonia Transform Fault (CTF) zone is highlighted, and black contours denote the sea bathymetry. b) Relocated epicenters of the two major events: the black star denotes the epicenter of the 1st event on Jan 26, 2014 and the black diamond denotes the epicenter of the 2nd event on Feb 3, 2014. For comparison we have included the relocated epicenters for the 1st (gray star) and 2nd (gray diamond) events reported in Karastathis et al. (2015). The CMT solutions for the two events, as calculated here and as reported in GCMT catalog are also shown (beach-balls marked accordingly). The relocated aftershocks (yellow circles) are scaled proportionally to their magnitude.

Ionian Islands (Louvari et al., 1999; Scordilis et al., 1985) and is rather described as a ramp in the bathymetry (Shaw and Jackson, 2010). Two branches were identified along CTF — the Cephalonia segment in the south, where the typical focal mechanisms have parameters: strike 38°, dip 63° and rake 172°, and the Lefkada segment in the north with: strike 14°, dip 65° and rake 167° (Louvari et al., 1999 and references therein). The strike-slip motions, often combined with a thrust component, are not confined along the CTF only. On the contrary, a broad zone, ~100 km wide, up to the western Peloponnese is characterized by strike-slip motions (Kiratzi, 2014; Louvari et al., 1999; Shaw and Jackson, 2010). The available fault databases include a few strike-slip fault segments offshore Cephalonia (Caputo et al., 2012), and a network of mapped faults onshore (Lekkas et al., 2001).

Below we briefly review the knowledge that has been accumulated so far. Prior to the 2014 sequence, a change in the long-term deformation of the Cephalonia Island was geodetically detected. It started in ~2003 and until 2010 the western peninsula of the Cephalonia Island (Paliki Peninsula, Fig. 1a) was uplifting at a rate of 1 cm/yr in an abrupt contrast with the subsidence of the rest of the Cephalonia Island (Lagios et al., 2012). Karakostas et al. (2014) relocated the sequence and concluded that the two major shocks were related to two adjacent fault segments, striking almost N–S and dipping to the east. Karastathis et al. (2015) relocated the sequence using the equal differential time and probabilistic non-linear approaches, accounting for the effects of the laterally varying crustal structure. They showed that the January 26 and February 3 events could be related with fault planes dipping to east and west, respectively. Papadopoulos et al. (2014) made a preliminary comprehensive analysis of the 2014 sequence. Their results support predominantly downward and upward rupture propagation for the January 26 and February 3 events, respectively. They concluded that the 2014 sequence ruptured a fault segment which is the SSW-wards continuation of the Lefkada segment as this was defined in Louvari et al. (1999).

Valkaniotis et al. (2014) analyzed geological effects, such as liquefaction, rock falls, and landslides, concluding that primary (co-seismic) fault surface ruptures were most probably not produced. The abundant surface cracks with cm-size offsets in the northern part of the Paliki Peninsula, ~38.29°N, were interpreted as due to close proximity of the ruptured fault to the earth surface (with unclear relation to either of the events). Boncori et al. (2015) inferred static ground displacements related to the event of 3 February from InSAR images. Their results were better modeled by a two-segment fault for this event.

Here we use weak and strong motion waveforms from local and regional stations to constrain kinematic rupture models of the two major events. For brevity, hereafter we refer to the January 26 and February 3 earthquakes as the 1st and 2nd event, respectively. In particular, we pay careful attention to the determination and consistency of their hypocenters, centroid moment tensors (location and faulting parameters), and fault plane geometries. We discuss the two events not only in terms of their source properties, but also in terms of the difficulties encountered during their source inversions. In this context, we discuss why the moment tensor solutions, as reported by different agencies, are quite similar for the 1st event, whereas those reported for the 2nd event vary significantly and include large non-double-couple components.

The paper is structured as follows: the data and methods used are briefly described; observed data of 1st and 2nd event are investigated, each following a hierarchic scheme (starting from the hypocenter location and calculation of the centroid moment tensor, continuing with specification of fault plane, ending with slip inversion). Finally, the two events are compared to each other, and to aftershocks, and they are collectively discussed in terms of the local stress field and seismic hazard.

2. Data and methods

Broad-band waveforms were retrieved from the Hellenic Unified Seismic Network (HUSN). We adopted the manual P and S phase picks from the Geodynamics Institute of the National Observatory of Athens and added manual picks from available local strong motion stations

for aftershock relocation. Stations in Italy were also picked manually for the two major shocks only. The strong motion records from the local stations were provided to us by the Institute of Engineering Seismology and Earthquake Engineering (ITSAK) and by the Geodynamics Institute of National Observatory of Athens (GI-NOA). DMLN strong motion station belongs to the seismic network of Patras University. The locations of the stations used are shown in Fig. S1.

2.1. Hypocenter locations

To locate the hypocenters of the two major events we primarily used the NonLinLoc code (Lomax et al., 2000). This approach is very suitable because it permits an uncertainty analysis considering the non-linearity of the problem. Hence, the error volume, as it is expressed by the probability density function, has a more general shape compared to the ellipsoids provided by the standard (linearized) approaches. Parallel to that, many trial locations were performed by four other codes: a) FASTHYPO (Herrmann, 1979), b) HYPOINVERSE (Klein, 2002), c) HYPO71PC (Lee and Valdes, 1985) and d) HYPODD (Waldhauser, 2001).

To locate the aftershocks we used HYPOINVERSE and HYPODD. The most suitable velocity model for the geometry of the problem was that of Haslinger et al. (1999). Other models were also tested, but the location uncertainties due to selection of station subsets were always greater than those due to the choice of the velocity model.

2.2. Centroid moment tensor (CMT) solutions

CMT solutions were inferred using the ISOLA code (Sokos and Zahradník, 2008, 2013) as further extended elsewhere (Fojtíková and Zahradník, 2014; Zahradník and Sokos, 2014). This approach is based on full waveform least-squares inversion, assuming a point- or multiple-point source representation. Green's functions were calculated by the discrete wavenumber and matrix methods (Bouchon, 1981; Coutant, 1989; Kennett and Kerry, 1979) for the 1D velocity model adopted for location (Haslinger et al., 1999). Here and subsequently for the slip inversions, we evaluate the seismogram fit in terms of the variance reduction percentage (VR) and/or correlation (corr), which are related simply by $VR/100 = corr^2$. The centroid position and centroid time are calculated by a grid search. A 3D spatial grid search is made for the two main events in order to infer not only the best-fitting centroid location and faulting parameters, but also to assess the uncertainty of the solution. The centroids of the aftershocks are grid-searched in vertical direction below their epicenters.

2.3. Finite fault slip inversions

To obtain the model of rupture propagation along the fault plane we adopted the linear slip inversion method of Gallovič et al. (2015). It has been extended, for the purpose of the present work, to perform the inversion simultaneously on multiple fault segments. In this approach, the rupture process is discretized in space and time along a given fault plane, and the model parameters are the spatial–temporal samples of the slip rate, spanning the whole rupture duration. Green's functions are calculated as previously. To stabilize the inverse problem in the least-square sense, we apply: (i) spatial smoothing by means of a prior covariance function with k^{-2} decay at large wavenumbers k and (ii) a positivity constraint on the slip rate by means of the non-negative-least squares (NNLS) approach (Lawson and Hanson, 1974). As such, the source description is very general with no a-priori constraints, as for example on the position of the nucleation point, the rupture velocity, and the shape of the slip-rate functions. Nevertheless, as in any multi-parameter inversion, the slip model is vulnerable to artifacts and biases due to the imperfect station distribution and smoothing, requiring careful appraisal. In view of the above, we interpret the inversion results with caution taking into account the previous resolution results from synthetic tests (Gallovič and Zahradník, 2011; Gallovič et al., 2015). All slip models were obtained using displacement waveforms from local strong motion stations, permanently or temporarily deployed on Cephalonia Island. For the strong motion stations CHV1, ARG2, and VSK1 accurate timing was not available, thus we corrected the timing using the relocated hypocenter of January 26 event and synthetic travel times calculated by ray-tracing.

2.4. Apparent source time functions

We were able to find a suitable aftershock for the 26 January (1st event) only, in order to calculate apparent source-time functions (ASTFs) using the method of Empirical Green's Functions (e.g. Courboulex et al., 1997; Roumelioti et al., 2009). The deconvolution process was stabilized following the approaches of Bertero et al. (1997) and Vallée (2004).

2.5. Stress inversion

We used aftershock mechanisms to examine the local stress field using the STRESSINVERSE code of Vavryčuk (2014). This is a modification of the method of Michael (1987), based on iterative joint inversion for direction of principal stress axes and fault orientations. The method resolves ambiguity of nodal planes for each studied event by applying the fault instability constraint, which leads to stabilization of the estimated shape ratio. The uncertainty estimates of the stress axes and shape ratio are provided by randomly perturbing the input mechanisms; here we use 200 variations, assuming $\pm 20°$ uncertainty in the orientation of the P–T axes. Using the Mohr's diagram the code allows us to verify whether the stress inversion is reasonable by means of checking whether the faults identified by the inversion are concentrated in the area of validity of the Mohr–Coulomb failure criterion.

3. Results

In the following sections we discuss the source properties of each event. Before doing so, in Fig. 1a we show surface fault traces on land Cephalonia, while in Fig. 1b we show our relative relocation of the sequence (630 events of $M > 3$). The aftershock distribution is diffused along the Paliki Peninsula, not allowing for any initial constraints on the fault planes.

3.1. The 26 January 2014 event

We exhaustively tested the variability in location by jack-knifing the stations, in terms of their proximity to the sequence i.e. local and distant. The epicenter location varied significantly, and this variability is well illustrated by the final NonLinLoc results, displayed in Fig. 2(a, b) and summarized in Table 1. Fig. 2a shows the location using only the stations deployed on Cephalonia Island. Fig. 2b shows the location using distant stations in Greece and Italy (shown in Fig. 2d), in an attempt to reduce the azimuthal gap inherent to the near stations. The first striking observation is the significantly different epicenters for this event.

Our preferred solution is the one obtained by the distant stations and not the local. This choice is based on the fact that this epicenter: a) is supported by the first-motion polarities at near station DMLN (Z+, N+, E+), which imply that the epicenter lies south-west of the station and b) is in agreement with the provisions imposed by the collocation of hypocenter and fault plane position (Zahradník et al., 2008). Our preferred solution is in disagreement with the relocations proposed by other authors (Karakostas et al., 2014; Karastathis et al., 2015), which are closer to our epicenter obtained from the local data.

The CMT solution was calculated by the full waveform inversion of relatively low-frequency regional data, assuming a single point-source model. Several frequency ranges and subsets of the stations were tested and the obtained source parameters varied as: strike (15°–30°), dip

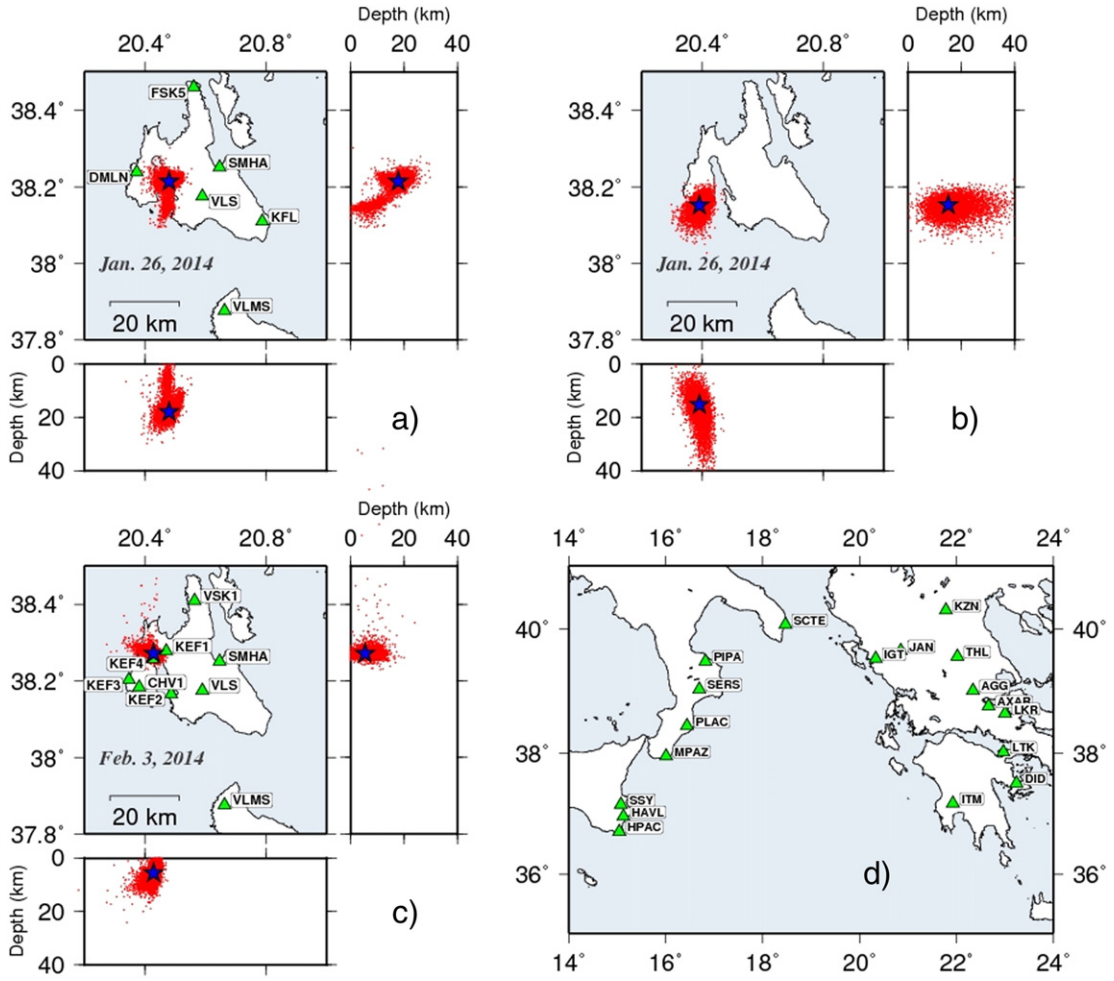

Fig. 2. Location of the two major shocks of the 2014 sequence by the NonLinLoc method (see also Table 1). The best-fitting hypocenter position is shown by a blue star, while scattered red dots demonstrate the probability density function. A map-view is supplemented by two vertical cross-sections, W–E (bottom panel) and N–S (right panel). a) 1st event location using only local stations (green triangles), b) our preferred 1st event location using distant stations (green triangles in panel d), c) 2nd event location using local stations (green triangles), d) stations used in panel b.

(70°–85°), rake (140°–180°), scalar moment (1.2–1.4 × 10^{18} Nm), and centroid depth (8–12 km).

The horizontal position of the centroid is also uncertain. A typical example of the spatial variability of the MT solution, for the depth of 10 km and for the frequency range 0.05–0.08 Hz, is shown in Fig. 3a. In particular, the centroid position is less certain in the SW–NE direction due to the distribution of the available stations. The best-fitting solution is found at the center of the trial source grid with 5 × 5 km increments. This solution was adopted as our preferred CMT solution (Table 2) and favors an eastward dipping nodal plane with strike/dip/rake equal to 20°/74°/162°. The global waveform match at this centroid position is very good (variance reduction 86%, Fig. S2a). However, the double-couple (DC) percentage is relatively low, 61%. Nevertheless, some near-by trial source positions (e.g., 7 km north-east of the centroid) provide similar strike/dip/rake angles and considerably higher DC ~90%, with just a slightly lower waveform correlation.

In order to perform the slip inversion, we used a single fault segment, a valid approach based on the large DC percentage near the centroid position. We chose the nodal plane striking at ~20° and dipping ~75° to the east as the fault plane, in accordance also with previous knowledge on the orientation of the main tectonic structures in the area (Louvari et al., 1999) and the directivity effects observed on the ASTFs as discussed later. However, the exact position of the fault in space is neither constrained by the (diffuse) aftershocks, nor by surface ruptures or other data. Therefore, we try to further constrain its position and the focal mechanism using finite-fault full waveform inversion of local seismic data.

To this goal we increase the maximum frequency to 0.2 Hz (e.g. frequency range 0.05–0.2 Hz). We assume a planar fault of 30 km × 30 km size (along strike and dip) and perform a grid search varying the position and orientation of the fault plane. In particular, the so-called fault origin (defined as a point situated 10 km along strike and 8 km down-dip from the top-left corner of the fault) is varied around the centroid within the range: 38.1945°–38.2445°N and 20.3519°–20.4119°E. The top of the fault is fixed at 0.5 km depth. We also vary the pure-shear mechanism in the vicinity of

Table 1
Hypocenter locations of the two events studied.

Arrivals used	Origin time	1st event: January 26, 2014 Latitude (°N)	Longitude (°E)	Depth (km)
Local stations[a]	13:55:42.91	38.2142	20.4804	18.0
Distant stations[b]	13:55:43.27	38.1522	20.3912	15.0
Arrivals used	**Origin time**	**2nd Event: February 3, 2014 Latitude (°N)**	**Longitude (°E)**	**Depth (km)**
Local stations	03:08:45.23	38.2712	20.4295	5.5

[a] Solution not supported by all data.
[b] Preferred solution.

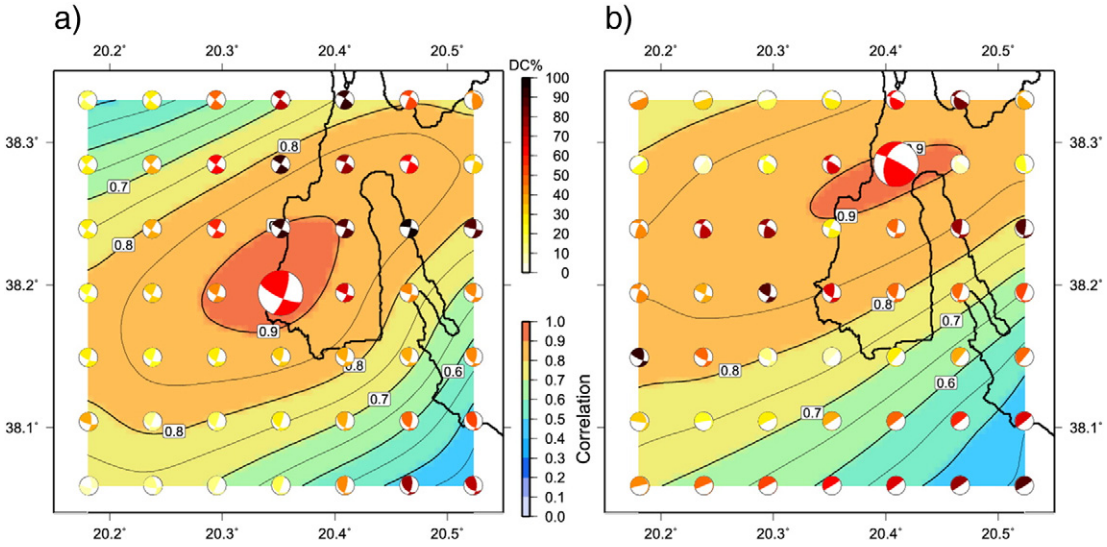

Fig. 3. Spatial variability of the MT solution on a horizontal grid with step size of 5 km for a) the 1st event and b) the 2nd event. The background color and isolines show the correlation between observed and synthetic waveforms, according to the scale. Beach balls at the trial source positions are color-coded according to their DC percentage. The largest beach ball is for the best-fitting solution (Table 2, Fig. 1b).

the preferred CMT parameters: strike 15–25°, dip 70–80° and rake 150–180°. For each trial fault location and mechanism (729 in total) we perform the NNLS linear slip inversion with a fixed smoothing weight.

The optimal solution was found for the fault origin 38.2195°N, 20.3819°E, depth 8 km, and for mechanism with strike 20°, dip 80°, and rake 180°. The fault plane agrees with our preferred epicenter position as calculated from the distant stations (Fig. 2b). Indeed, when we allowed the hypocenter depth to increase by less than 10 km, reflecting the location uncertainty, the orthogonal distance of the hypocenter to the fault plane became smaller than 1 km. This test also showed that the epicenter defined by the use of the local stations (Fig. 2a), close to that of Karastathis et al. (2015), is much less favored. This stems from the fact that even a large increase in the depth still leaves the hypocenter distance from the fault too large (~5 km) and, moreover, such a hypocenter would project closer to the conjugate WNW–ESE trending nodal plane.

Our calculated slip model, for the 1st event, is presented in Fig. 4 (and Fig. S3a). The slip patch covers almost the entire length of the fault (~25 km), being approximately 10 km wide. Slip distributed over such a relatively large area suggests rather small mean static stress drop of the order of 1 MPa. The locus of maximum slip (~25 cm) is depicted ~10 km away from the epicenter and ~6 km from the centroid position, towards NNE. The DMLN station is located close to this largest slip, and it should be noted that this close station might have controlled the location of the maximum slip (see for example the synthetic tests in Gallovič et al., 2015). However, still the maximum slip is well within the area of the largest correlations in the CMT solutions (Fig. 3) and in these solutions the data from DMLN station were not used.

Fig. 4b shows the snapshots of the slip rate on the fault plotted every 1 s. The largest values of the slip rate are attained ~15 km up-dip the hypocenter (recall that the hypocenter position was not prescribed in the slip inversion). The spatial distribution of the slip rate denotes that the rupture initially propagated up-dip from the hypocenter. It reached shallow depths in ~4 s (suggesting a relatively large rupture velocity of ~4 km/s) and continued to propagate along-strike (NE-wards) for another ~5 s at a rather slower velocity of ~2 to 3 km/s, perhaps reflecting the decrease of shear modulus with decreasing depth. It is worth noting that these absolute values might be obscured by the smoothing constraint imposed during the inversion, as well as affected by the imperfect station coverage (see also Gallovič et al., 2015).

Fig. S4a shows the comparison between the synthetic and observed displacement waveforms for the strong motion sites. The synthetics reproduce the observed records relatively well (VR 83%), with the exception of the fit to the E–W and N–S components of stations DMLN and SMHA, respectively. In summary, taking into account that the event might have contained more complex fault geometry and variable focal mechanisms, our slip model reproduces satisfactorily the observed strong motion displacement records. Attempts to account for the mentioned complexities would go beyond the resolution of the frequency range used and the crustal model available. It is also important to note that in our model the rupture propagated nearly to the surface, which might be in accordance with the surface ruptures, as marked in Fig. 4a, reported by Valkaniotis et al. (2014).

As previously mentioned, we were able to identify an event which could serve as an Empirical Green's Function, in order to obtain apparent source time functions (ASTFs) at regional stations. Thus, the waveforms of an Mw4.3 aftershock (2014/01/26 at 19:12 UTC, no. 4 in Table S1) were deconvolved from the mainshock waveforms. The inferred ASTFs (Fig. S5) have two distinct lobes. The duration of the first pulse is ~6 s and of the second is ~4 s. The second lobe is more pronounced at the stations east and south of the hypocenter. The narrower pulse at one station (e.g. IGT) which lies directly north of the epicenter

Table 2
Centroid moment tensor solutions of the two events studied.

Centroid time	Lat. (°N)	Lon. (°E)	Depth (km)	Mo (Nm)	Mw	Strike (°)	Dip (°)	Rake (°)	DC (%)	VR (%)
1st event: January 26, 2014										
13:55:47.06	38.1944	20.3519	10.5	1.4E + 18	6.1	20°	74°	163°	61	85
2nd event: February 3, 2014										
03:08:48.67	38.2845	20.4089	2.5	1.0E + 18	6.0	199°	49°	167°	63	82

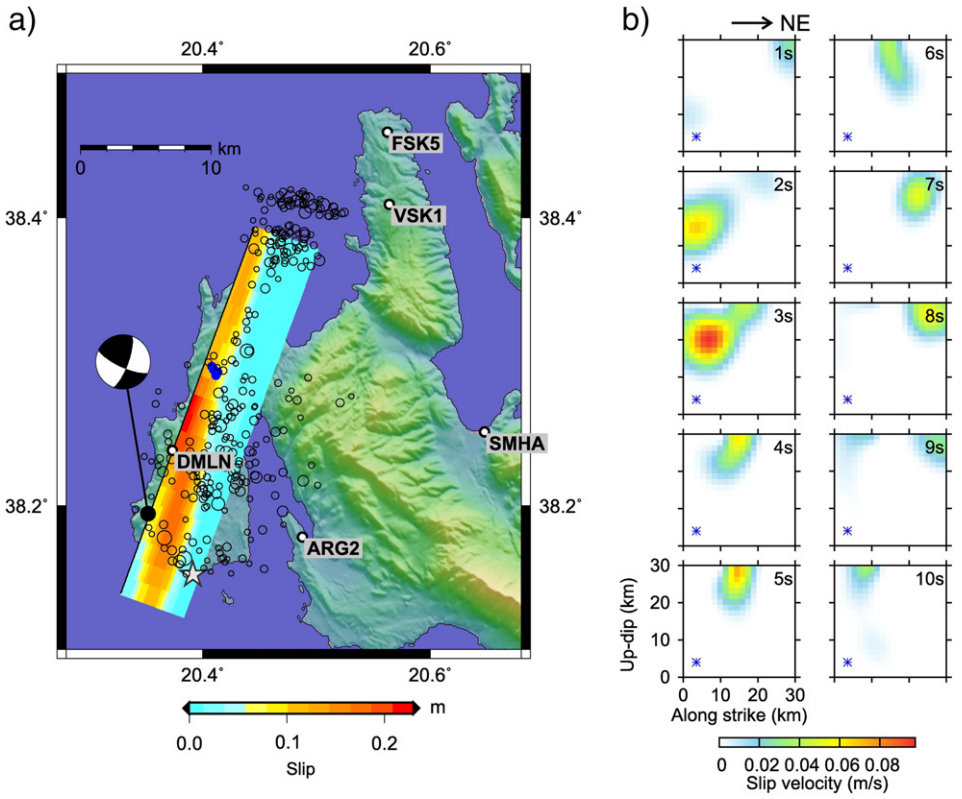

Fig. 4. Slip model for the January 26, 2014 event obtained using strong motion displacement waveforms from the stations depicted on the map. a) Surface projection of the slip distribution along the fault, according to the scale shown below. The epicenter (star) and the centroid location (black circle) together with the CMT solution are also depicted. The relocated aftershocks prior to the occurrence of the 2nd event are also plotted, showing that they are mainly confined off the major slip patches. Blue symbols denote the surface ruptures of Valkaniotis et al. (2014). The fault-top depth is 0.5 km. Coordinates of the fault corners as in Table S2. b) Snapshots every 1 s of the space–time evolution of the slip velocity on the fault. The blue asterisk denotes the vertical projection of the hypocenter on the fault. Note the initially up-dip rupture propagation, which continued to propagate along strike and towards NE.

indicates predominantly along-strike propagation of the rupture. The second pulse, which is of shorter duration and amplitude, and well lagged in time from the first pulse, probably reflects the shallower slip patch of the slip model (Figs. 4 and S3). A secondary subevent similar to the northern slip patch of Fig. 4 has been also indicated by multiple-point source models; these tests are not reported here because the secondary subevent had an unstable position and focal mechanism. The fact that the northern asperity is not clearly separated from the slip closer to the hypocenter can be attributed to the smoothing constraint applied in the slip inversion.

3.2. The 3 February 2014 event

After the occurrence of the 1st event temporary stations were deployed in Cephalonia Island by various agencies (e.g. Geodynamics Institute of the National Observatory of Athens, GINOA, Institute of Engineering Seismology and Earthquake Engineering, ITSAK, University of Patras Seismology Laboratory, UPSL) which greatly facilitated the location procedure. After jackknifing the stations, to test the location stability, we obtained similar epicenter positions for most of the station subsets tested. Thus, the NonLinLoc solution for this event, shown in Fig. 2c and Table 1, can be considered as a typical result. For this event we are in agreement, within error limits, with the relocation by Karastathis et al. (2015). This second event was considerably shallower (~5 km) than the 1st event, and its epicenter is shifted ~10 km towards NNE.

To find the point-source CMT approximation of the 2nd event, we used the same frequency range (i.e. 0.05–0.08 Hz) and initial tests as for the 1st event. The 3D grid search systematically indicated a relatively shallow centroid depth (~2.5–5.0 km). The centroid position was also systematically shifted northward with respect to the 1st event, analogously to the epicenter. However, the best-fitting centroid position and focal mechanism varied with station subsets more dramatically than for the 1st event. In particular, solutions with both east- and west-ward dipping nodal plane were obtained. Many solutions were characterized by strike ~200°, accompanied with dip and rake angles ranging between 60°–85° and 130°–180°, respectively.

Fig. 3b shows the correlation map at 2.5 depth, as an indicative example. Similarly to the pattern of the 1st event (Fig. 3a) the correlation isolines are elongated in the SW–NE direction due to the station azimuthal coverage. The best-fitting CMT solution (Table 2) has a west dipping nodal plane (strike/dip/rake equal to 199°/49°/167°) and DC = 63%. The waveform fit (variance reduction 82%) is shown in Fig. S2b. The spatial variability of the source mechanism (beach balls in Fig. 3b) is more pronounced compared to that of the 1st event (Fig. 3b). We emphasize that although the data are fitted almost equally well as in the case of the 1st event, the absence of the high-DC solutions near the best-fitting trial source points and the spatial variability of the moment tensor do not allow a straightforward interpretation. One possibility how to explain the MT variability is simply due to the shallow depth. As shown in Fig. 5, based on the analysis of theoretical MT resolvability (Zahradník and Custodio, 2012), from two hypothetical sources inverted in the same station network, velocity model and low-frequency range, the MT solution of the shallow source is much more uncertain; in particular, the east and west dipping nodal planes are hard to distinguish, and the DC percentage of the shallow source is poorly determined. The same shallow-source effect most likely caused the large variation of the MT agency reports of this event. Nevertheless, when interpreting the CMT variability, we

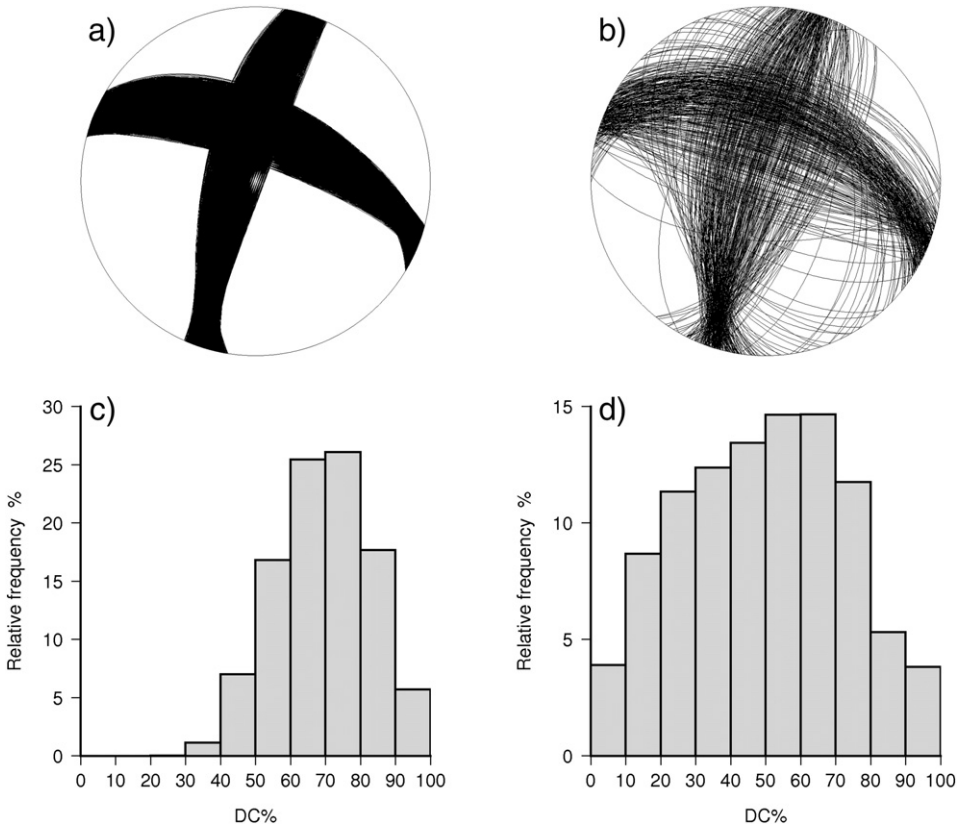

Fig. 5. Theoretical resolvability analysis of the moment tensor for a fixed configuration of the stations and two centroid depths, 8.5 km (left panels) and 2.5 km (right panels). Panels a) and b) show the uncertainty of the nodal lines. Panels c) and d) are the uncertainties of the DC percentage.

should count also with a possible source complexity, discussed in the following.

Definition of a fault for the slip inversion of this event was a challenge taking into account the spatial variability of our CMT solutions. Initial slip inversions considering various fault planes and mechanisms within the MT uncertainty limits did not provide robust space–time slip distributions. Thus, we adopted a fault geometry constrained by DInSAR data (Boncori et al., 2015). The authors showed in their analysis (in their Fig. 3c) that the uplift and subsidence regions, observed at the northern part of the Paliki Peninsula, are separated by a sharp north–south trending boundary. Along this line, the orientation of the horizontal motions changes abruptly, too. Thus, for our finite fault slip inversion, we adopted their two-segment fault model: segments 1 and 2 with strike/dip/rake equal to 180°/86°/147° and 33°/76°/164°, respectively (Boncori et al., 2015). This is also justified by the fact, that this fault model is consistent with our calculated hypocenter (Table 2) as it is situated close to the junction of the two segments (the orthogonal distance of the hypocenter from segments 1 and 2 is only 600 and 1400 m, respectively). Both segments are simultaneously included in the slip inversion. The data are the displacement waveforms at five strong motion stations (Fig. 6a), and both data and synthetics were filtered between 0.05 and 0.2 Hz.

There are some interesting features recovered in the space–time slip-rate history for the two segments (Figs. 6b and S4b for waveform fit with VR = 87%). Segment 1 ruptured mainly at shallow depths, and the rupture front propagated predominantly southwards, towards the town of Lixouri (shown in Fig. 1). After 4 s the rupture activated deeper part of the fault. In this nearly vertical segment, the northward rupture propagation is less pronounced, as indicated by the relatively small slip rate amplitudes north of the hypocenter (Fig. S3b). The slip patch covers approximately 15 km × 10 km large area, corresponding to static stress drop of ~1 MPa, i.e. the same order as for Event 1. The less steep eastward dipping segment 2 ruptured rather unilaterally, with less slip near the surface, compared to segment 1 (Fig. S3b). The two segments experienced the main slip episode almost simultaneously (see snapshots at 4–6 s in Fig. 5b–c). In view of the above, the 2nd event should be regarded as an earthquake that ruptured almost simultaneously the two fault segments, with a joint hypocenter, both involving minor thrust components. However, it should be noted that we have tested also slip inversion considering just segment 1. The rupture propagation is very similar to that obtained above (along segment 1), while the fit deteriorates only slightly (Fig. S4c, variance reduction 70%). Therefore, we cannot confirm the existence of segment 2 based on the available seismic data.

The seismically derived slip distributions of the two-segment and single-segment fault models were employed in forward modeling to simulate the horizontal and vertical static displacements using the closed-form solution of Okada (1992) for homogeneous half space. Both slip models are able to reproduce very well (see Fig. S6) the main features of the DInSAR data (Boncori et al., 2015), as previously mentioned.

Unfortunately, even though the sequence was rich in aftershocks, we were not able to find a suitable event as Empirical Green's Function to retrieve apparent source time functions (ASTFs) for the 2nd event.

3.3. Local stress field

We inverted the local stress field using the focal mechanisms of the aftershocks (Table S1) and the results are summarized in Table S3, Figs. 7 and S7. We have found that the best resolved parameter is the maximum horizontal compression axis σ_1 with azimuth 248° and plunge 7°. Almost identical orientation of the strain–tensor compression axis was reported by Ganas et al. (2013) for a broader central Ionian Sea region, based on continuous GPS data. The other two principal stress axes σ_2 and σ_3 are less stable when randomly perturbing the input focal mechanism within their expected uncertainties and/or when

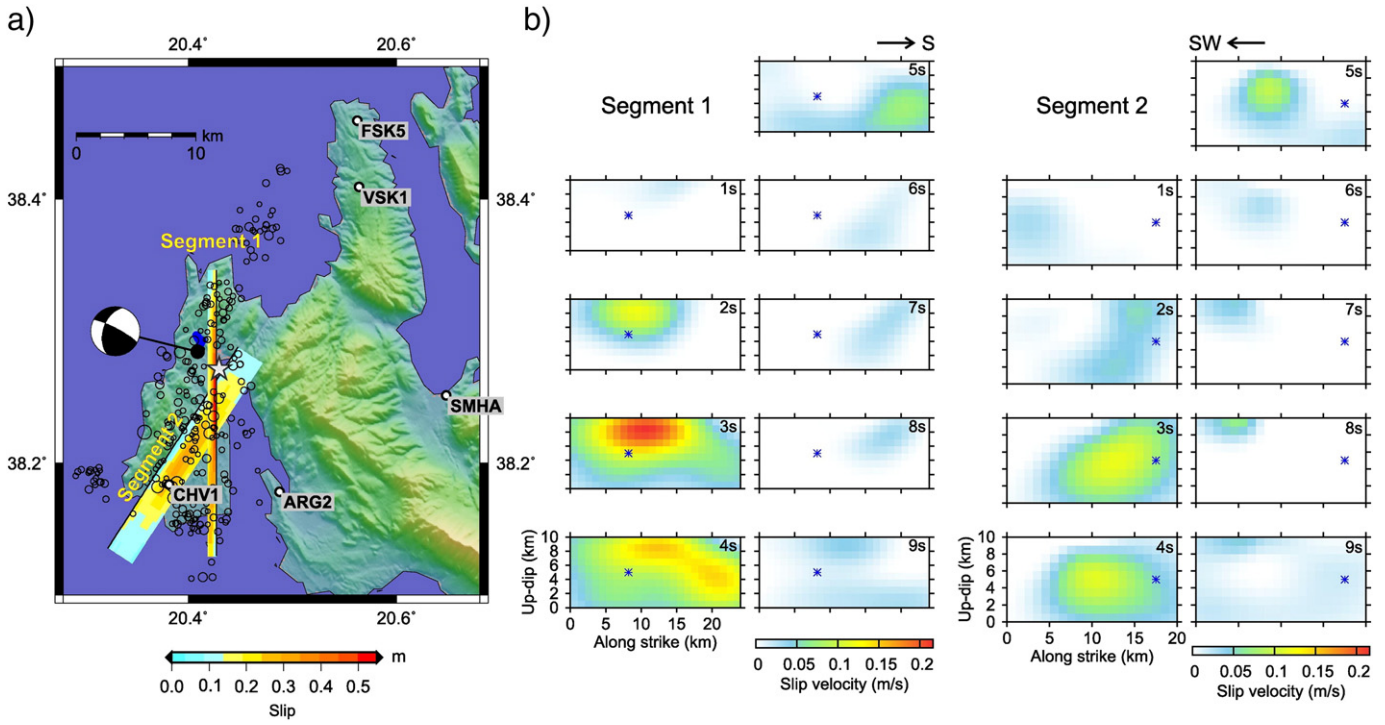

Fig. 6. Slip model for the February 3, 2014 event, obtained using displacement waveforms from the strong motion stations depicted in the map, and the two-segment fault geometry from Boncori et al. (2015). a) Surface projection of the slip of the two fault segments. The star denotes the epicenter (Table 1, Fig. 2b), the black dot and the beach-ball correspond to the centroid (Table 2, Fig. 3b). Relocated aftershocks after the occurrence of the 2nd event up to March 28 are shown. The fault-top depth is 0.5 km. Coordinates of the fault corners as in Table S2. Blue symbols denote the surface ruptures of Valkaniotis et al. (2014). b) Snapshots every 1 s of the space–time evolution of the slip velocity on segment 1 (left panels) and segment 2 (right panels). The blue asterisk in all panels denotes the horizontal projection of the hypocenter perpendicularly to the strike of the respective fault segment. Note that in segment 1 the rupture initiated at shallow depth, propagated mainly southwards, towards the town of Lixouri, activating a deeper asperity at 4 s.

constraining the friction coefficient at various values. In particular, according to the scatter plot in Fig. S7c the uncertainty pattern of axis σ_2 indicates that this axis is likely not vertical. The stress regime is not strictly strike-slip, which agrees with the observed co-existence of the strike-slip and reverse faults.

Interestingly, the shape ratio remains stable (0.8–0.9) when randomly perturbing the input mechanisms. The events are well distributed in the Mohr's diagram, covering only the left part of the upper and lower semicircles, which is the area of validity of the Mohr–Coulomb failure criterion. This indicates that the stress inversion results are reasonable (p. 75 of Vavryčuk, 2014).

4. Conclusions

We studied the January–February 2014 Cephalonia Island earthquake sequence, confined along the Paliki Peninsula. Two major events of M ~ 6 occurred on January 26 and February 3. We have exhaustively exploited the available local, regional and distant data in order to: locate the two events, calculate their centroid moment tensor solutions, determine their kinematic rupture models, relocate 569 aftershocks with M > 3 and calculate focal mechanisms for 31 of them. The main results of our work summarize as follows.

4.1. The 26 January 2014 earthquake

The hypocenter location of the January 26 event was very difficult. The local data (stations onshore Cephalonia) had a considerable gap in azimuth coverage. Our preferred hypocenter (38.1522°N, 20.3912°E; h ~ 15 km) was calculated using stations in Italy and regional stations in Greece. Our solution is consistent with the 3-component first-motion polarities at the near DMLN strong motion station. This epicenter is located at the southernmost tip of the Paliki Peninsula. The earthquake ruptured an on-shore strike-slip fault, steeply dipping to the east, roughly parallel to the major structure that dominates offshore the Cephalonia Island, the so called Cephalonia Transform Fault (CTF). From the two segments of CTF, the January 26 earthquake had roughly the orientation and the dip polarity of the Lefkada segment (Louvari et al., 1999).

We were able to retrieve the slip model for the January 26 event using data from the local strong motion stations. Although ruptures normally propagate in all directions (Gudmundsson, 2011), here, initially, the up-dip rupture propagation from the hypocenter prevailed, reaching shallow depths in ~4 s and continuing to propagate predominantly along-strike towards the north for another ~5 s. This along-strike rupture propagation scenario is in agreement with the shape of the apparent source time functions obtained from the Empirical Green's Function method. We cannot exclude the possibility that the rupture process along the entire fault had a more complex fault geometry and/or variable focal mechanism because the resolution capacity of our data does not permit the retrieval of such details. Our kinematic slip model for the 1st event differs from the preliminary model by Papadopoulos et al. (2014) due to the considerable difference in the assumed fault planes and since we use strong motion waveforms at local distances and different frequencies.

4.2. The 3 February 2014 earthquake

The epicenter location of the second major shock (February 3) was better constrained thanks to the temporary stations installed during the sequence. Its hypocenter (38.2712°N, 20.4295°E) is 10 km to the NNE of the 1st earthquake and considerably shallower (~5 km). The centroid position and MT of the 2nd event featured large uncertainties, accompanied by low double-couple (DC) percentage, similar to the variability among agency reports.

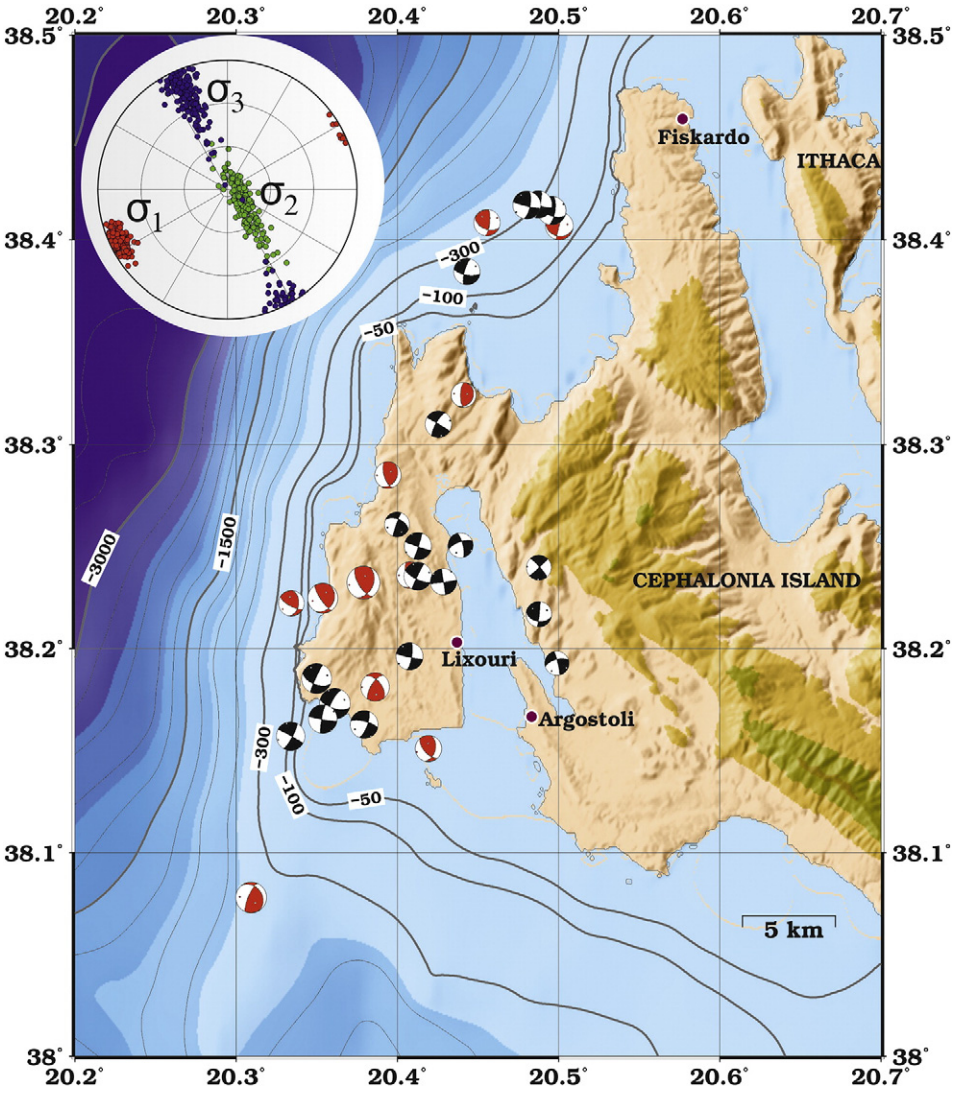

Fig. 7. Moment tensor solutions of 31 aftershocks with M > 4 (listed in Table S1). Black and red beach-balls denote the strike-slip and reverse faulting, respectively. Contours denote the sea bathymetry. The inset shows the principal axes of the stress field and their uncertainty derived from the aftershocks (see also Table S3 and Fig. S7).

As such, the MT solution did not provide enough clues for robust slip models with reasonable fit of the strong motion data. Therefore, we adopted the two-segment fault geometry proposed by Boncori et al. (2015) based on modeling the synthetic aperture radar (SAR) acquisitions. The two-segment fault model provided a kinematic slip model with satisfactory fit to the strong motion records. The rupture of the N–S trending and nearly vertical segment 1 (strike/dip/rake 180°/86°/147°) was confined at shallow depths. The rupture propagated basically along strike with a pronounced directivity southwards, towards the town of Lixouri, and with less pronounced northward propagation. The second, less steep, eastward dipping segment 2 (strike/dip/rake 33°/76°/164°) ruptured unilaterally, with less slip near the surface compared to the N–S segment. The two segments experienced the main slip episode almost simultaneously (~4–6 s after initiation). Moreover, even though our inversion technique does not require any prescribed hypocenter position, the results indicate that the two segments could have started their rupturing from a common hypocenter, situated at the junction of the two segments. It is worth mentioning that we have tested also slip inversion considering only segment 1, which provides by itself a reasonable model with just minor deterioration of the waveform fit.

Our seismically derived slip model was able, using forward modeling, to simulate the surface static displacements and dominant features of the DInSAR data (the sharp north–south trending discontinuity between the uplift and subsidence, as well as a dramatic change in the horizontal-motion direction). In this sense, our work extends the study by Boncori et al. (2015), because we not only confirmed their fault interpretation by seismic data, but also provided a kinematic space–time slip model consistent with the seismic and space-geodesy data.

4.3. Connection to regional tectonics

One question that arose after the occurrence of the 2014 Cephalonia sequence was its connection to the regional tectonics, and more specifically, to the Cephalonia Transform Fault that dominates the bathymetry along the western coasts of the Ionian Islands. We start by the fact that the 2014 sequence occurred on-land and that the aftershocks do not delineate a single fault structure (Fig. 1b). Instead, the rather diffuse pattern is more consistent with the activation of a network of minor faults that have been mapped on land (Lekkas et al., 2001). The focal mechanisms of the two major events clearly show dextral strike-slip motions

combined with a thrust component along faults that are approximately parallel to the strike of the Cephalonia Transform Fault, and more specifically to the strike of the Lefkada segment (Louvari et al., 1999). This sequence did not rupture CTF itself, but fault segments that are more or less parallel to it, on-shore Cephalonia. The shear motions in Cephalonia and the other Ionian Islands are not confined along the CTF only, but on the contrary there is a wide zone (~100 km) which extends in the east up to western Peloponnese (Kiratzi, 2014 and references therein). We estimated the local stress field and the best resolved stress axis is the maximum compression (azimuth 248°, plunge 7°), while the intermediate axis (less well resolved) is not strictly vertical, hence corresponding to a combination of the strike-slip and thrust regime. In view of the above, the 2014 Cephalonia sequence reflects the general stress field in the broader region and is in accordance with that.

The conclusions which, to our view, have important implications to the seismic hazard, can be summarized as follows: a) the active faults are not only confined to the CTF, but there are many on-shore faults the Cephalonia Island; b) the focal mechanisms are not pure dextral strike-slip but the thrust component could be significant; c) the dip angles of these faults are not always nearly vertical, and less steep faults affect broader regions on land; d) the seismogenic thickness seems to extend from the surface up to ~20 km in the region; and f) the fault ruptures seem to have a tendency to be segmented, which might introduce time delays between major patches; this effect may possibly prolong the duration of strong ground shaking (in time scale of seconds or minutes), and also increase the duration of the elevated seismic hazard (in a time scale of days or weeks).

Acknowledgments

Constructive comments of E. Burov (Editor), A. Gudmundsson (Reviewer) and an anonymous reviewer helped to improve the presentation of the results. We acknowledge the waveform data exchange within the Hellenic Unified Seismic Network (HUSN) for the broad band stations used in this work. Strong motion data (stations ARG2, VSK1, KRI1, ZAK2 and CHV1) were provided by the Institute of Engineering Seismology and Earthquake Engineering (ITSAK) and by the Geodynamics Institute of the National Observatory of Athens (station SMHA). Phase data for stations KEF1, KEF2, KEF3, and KEF4 were downloaded from GI-NOA web site (http://bbnet.gein.noa.gr/HL/). A. Kiratzi acknowledges support by the European Union (European Social Fund — ESF MIS377335), Greek national funds — Research Funding Program: Thales — Investing in knowledge society through the European Social Fund (ESF) (MIS377335) and the Earthquake Planning and Protection Organization (91138) for the network operation. Financial support in the Czech Republic: GACR 14-04372S and CzechGeo/EPOS LM2010008. A number of figures were constructed using Generic Mapping Tools (Wessel and Smith, 2013). Czech–Greek cooperation under Erasmus$^+$ Program (CZ Praha07 and G Patra01) is acknowledged.

Appendix A. Supplementary data

Supplementary data to this article can be found online at http://dx.doi.org/10.1016/j.tecto.2015.06.013.

References

Benekos, G., Derdelakos, K., Bountzouklis, C., Kourkouli, P., Parcharidis, I., 2015. Surface displacements of the 2014 Cephalonia (Greece) earthquake using high resolution SAR interferometry. Earth Sci. Inf. 1–7. http://dx.doi.org/10.1007/s12145-015-0205-7.

Bertero, M., Bindi, D., Boccacci, P., Cattaneo, M., Eva, C., Lanza, V., 1997. Application of the projected Landweber method to the estimation of the source time function in seismology. Inverse Prob. 13-2, 465–486.

Boncori, J.P.M., Papoutsis, I., Pezzo, G., Tolomei, C., Atzori, S., Ganas, A., Karastathis, V., Salvi, S., Kontoes, C., Antonioli, A., 2015. The February 2014 Cephalonia earthquake (Greece): 3D deformation field and source modeling from multiple SAR techniques. Seismol. Res. Lett. 86-1, 124–137. http://dx.doi.org/10.1785/0220140126.

Bouchon, M., 1981. A simple method to calculate Green's functions for elastic layered media. Bull. Seismol. Soc. Am. 71-4, 959–971.

Caputo, R., Chatzipetros, A., Pavlides, S., Sboras, S., 2012. The Greek database of seismogenic sources (GreDaSS): state-of-the-art for northern Greece. Ann. Geophys.-Italy 55-5, 859–894. http://dx.doi.org/10.4401/ag-5168.

Courboulex, F., Santoyo, M.A., Pacheco, J.F., Singh, S.K., 1997. The 14 September 1995 (M = 7.3) Copala, Mexico, earthquake: a source study using teleseismic, regional, and local data. Bull. Seismol. Soc. Am. 87-4, 999–1010.

Coutant, O., 1989. Program of Numerical Simulation AXITRA. Research Reports LGIT, University of Joseph Fourier, Grenoble, France.

Fojtíková, L., Zahradník, J., 2014. A new strategy for weak events in sparse networks: the first-motion polarity solutions constrained by single-station waveform inversion. Seismol. Res. Lett. 85-6, 1265–1274. http://dx.doi.org/10.1785/0220140072.

Gallovič, F., Zahradník, J., 2011. Toward understanding slip inversion uncertainty and artifacts: 2. Singular value analysis. J. Geophys. Res. Solid Earth 116 (B2), B02309. http://dx.doi.org/10.1029/2010JB007814.

Gallovič, F., Imperatori, W., Mai, P.M., 2015. Effects of three-dimensional crustal structure and smoothing constraint on earthquake slip inversions: case study of the Mw6.3 2009 L'Aquila earthquake. J. Geophys. Res. Solid Earth 120 (1), 2169–9356. http://dx.doi.org/10.1002/2014JB011650.

Ganas, A., Marinou, A., Anastasiou, D., Paradissis, D., Papazissi, K., Tzavaras, P., Drakatos, G., 2013. GPS-derived estimates of crustal deformation in the central and north Ionian Sea, Greece: 3-yr results from NOANET continuous network data. J. Geodyn. 67-0, 62–71. http://dx.doi.org/10.1016/j.jog.2012.05.010.

GEER/EERI/ATC, report, 2014. Earthquake Reconnaissance January 26th/February 2nd 2014 Cephalonia, Greece Events, Version 1: June 6, 2014. http://www.geerassociation.org/GEER_Post%20EQ%20Reports/Cephalonia_Greece_2014/GEER-EERI-ATC_Cephalonia-GREECE_v1.pdf.

Gudmundsson, A., 2011. Rock Fractures in Geological Processes. Cambridge University Press 978-0-521-86392-6 http://dx.doi.org/10.1017/CBO9780511975684.

Haslinger, F., Kissling, E., Ansorge, J., Hatzfeld, D., Papadimitriou, E., Karakostas, V., Makropoulos, K., Kahle, H.G., Peter, Y., 1999. 3D crustal structure from local earthquake tomography around the Gulf of Arta (Ionian region, NW Greece). Tectonophysics 304 (3), 201–218. http://dx.doi.org/10.1016/S0040-1951(98)00298-4.

Herrmann, R.B., 1979. Fasthypo — a hypocenter location program. Seismol. Res. Lett. 50-2, 25–38.

Karakostas, V., Papadimitriou, E., Mesimeri, M., Gkarlaouni, C., Paradisopoulou, P., 2014. The 2014 Kefalonia doublet (M w 6.1 and M w 6.0), central Ionian islands, Greece: seismotectonic implications along the Kefalonia transform fault zone. Acta Geotech. 1–16 http://dx.doi.org/10.2478/s11600-014-0227-4.

Karastathis, V.K., Mouzakiotis, E., Ganas, A., Papadopoulos, G.A., 2015. High-precision relocation of seismic sequences above a dipping Moho: the case of the January–February 2014 seismic sequence on Cephalonia Island (Greece). Solid Earth 6-1, 173–184. http://dx.doi.org/10.5194/se-6-173-2015.

Kennett, B.L.N., Kerry, N.J., 1979. Seismic waves in a stratified half space. Geophys. J. Int. 57-3, 557–583.

Kiratzi, A., 2014. In: Beer, M., Kougioumtzoglou, I., Patelli, E., Siu-Kui Au, Ivan (Eds.), Mechanisms of Earthquakes in Aegean, In: Encyclopedia of Earthquake Engineering. ISBN: 978-3-642-36197-5.

Klein, F.W., 2002. User's guide to HYPOINVERSE-2000, a Fortran program to solve for earthquake locations and magnitudes. U.S. Geol. Surv. Open File Rep. 02–171 (Version 1.0 (2002), 123 pp.).

Lagios, E., Papadimitriou, P., Novali, F., Sakkas, V., Fumagalli, A., Vlachou, K., Del Conte, S., 2012. Combined seismicity pattern analysis, DGPS and PSInSAR studies in the broader area of Cephalonia (Greece). Tectonophysics 524–525, 43–58. http://dx.doi.org/10.1016/j.tecto.2011.12.015.

Lawson, C.L., Hanson, R.J., 1974. Solving Least Square Problems. Prentice-Hall, Inc., New Jersey (340 pp).

Lee, W.H.K., Valdes, C.M., 1985. A personal computer version of the HYPO71 earthquake location program. U.S. Geol. Surv. Open File Rep. 85-749, 43.

Lekkas, E., Danamos, G., Mavrikas, G., 2001. Geological structure and evolution of Cephalonia and Ithaki Islands. Bull. Geol. Soc. Greece XXXIV (1), 11–17.

Lomax, A., Virieux, P., Berge, C., 2000. Probabilistic earthquake location in 3D and layered models: introduction of a Metropolis-Gibbs method and comparison with linear locations. In: Thurber, C.H., Rabinowitz, N. (Eds.), Advances in Seismic Event Location. Kluwer Academic Publishers.

Louvari, E., Kiratzi, A.A., Papazachos, B.C., 1999. The Cephalonia Transform Fault and its extension to western Lefkada Island (Greece). Tectonophysics 308 (1–2), 223–236. http://dx.doi.org/10.1016/S0040-1951(99)00078-5.

Michael, A.J., 1987. Use of focal mechanisms to determine stress: a control study. J. Geophys. Res. 92 (B1), 357–368. http://dx.doi.org/10.1029/JB092iB01p00357.

Okada, Y., 1992. Internal deformation due to shear and tensile faults in a half-space. Bull. Seismol. Soc. Am. 82-2, 1018–1040.

Papadopoulos, G.A., Karastathis, V.K., Koukouvelas, I., Sachpazi, M., Baskoutas, I., Chouliaras, G., Agalos, A., Daskalaki, E., Minadakis, G., Moshou, A., Mouzakiotis, A., Orfanogiannaki, K., Papageorgiou, A., Spanos, D., Triantafyllou, I., 2014. The Cephalonia, Ionian Sea (Greece), sequence of strong earthquakes of January–February 2014: a first report. Res. Geophys. 4-1. http://dx.doi.org/10.4081/rg.2014.5441.

Roumelioti, Z., Benetatos, C., Kiratzi, A., 2009. The 14 February 2008 earthquake (M6.7) sequence offshore south Peloponnese (Greece): source models of the three strongest events. Tectonophysics 471-3 (4), 272–284. http://dx.doi.org/10.1016/j.tecto.2009.02.028.

Sakkas, V., Lagios, E., 2015. Fault modelling of the early-2014 ~M6 Earthquakes in Cephalonia Island (W. Greece) based on GPS measurements. Tectonophysics 644–645, 184–196. http://dx.doi.org/10.1016/j.tecto.2015.01.010.

Scordilis, E.M., Karakaisis, G.F., Karacostas, B.G., Panagiotopoulos, D.G., Comninakis, P.E., Papazachos, B.C., 1985. Evidence for transform faulting in the Ionian Sea:

the Cephalonia Island earthquake sequence of 1983. Pure Appl. Geophys. 123, 388–397.
Shaw, B., Jackson, J., 2010. Earthquake mechanisms and active tectonics of the Hellenic subduction zone. Geophys. J. Int. 181-2, 966–984. http://dx.doi.org/10.1111/j.1365-246X.2010.04551.x.
Sokos, E.N., Zahradník, J., 2008. ISOLA a Fortran code and a Matlab GUI to perform multiple-point source inversion of seismic data. Compt. Rendus Geosci. 34-8, 967–977. http://dx.doi.org/10.1016/j.cageo.2007.07.005.
Sokos, E., Zahradník, J., 2013. Evaluating centroid moment tensor uncertainty in the new version of ISOLA software. Seismol. Res. Lett. 84-4, 656–665. http://dx.doi.org/10.1785/0220130002.
Valkaniotis, S., Ganas, A., Papathanassiou, G., Papanikolaou, M., 2014. Field observations of geological effects triggered by the January–February 2014 Cephalonia (Ionian Sea, Greece) earthquakes. Tectonophysics 630, 150–157. http://dx.doi.org/10.1016/j.tecto.2014.05.012.
Vallée, M., 2004. Stabilizing the empirical Green function analysis: development of the projected Landweber method. Bull. Seismol. Soc. Am. 94-2, 394–409. http://dx.doi.org/10.1785/0120030017.
Vavryčuk, V., 2014. Iterative joint inversion for stress and fault orientations from focal mechanisms. Geophys. J. Int. 199-1, 69–77. http://dx.doi.org/10.1093/gji/ggu224.
Waldhauser, F., 2001. hypoDD: a computer program to compute double-difference earthquake locations. U.S. Geol. Surv. Open File Rep. 01–113.
Wessel, P., Smith, W.H.F., Scharroo, R., Luis, J., Wobbe, F., 2013. Generic Mapping Tools: improved version released. Eos. Trans. AGU 94-45, 409–410. http://dx.doi.org/10.1002/2013EO450001.
Zahradník, J., Custodio, S., 2012. Moment tensor resolvability: application to southwest Iberia. Bull. Seismol. Soc. Am. 102-3, 1235–1254. http://dx.doi.org/10.1785/0120110216.
Zahradník, J., Sokos, E., 2014. The Mw 7.1 Van, Eastern Turkey, earthquake 2011: two-point source modelling by iterative deconvolution and non-negative least squares. Geophys. J. Int. 196-1, 522–538. http://dx.doi.org/10.1093/gji/ggt386.
Zahradník, J., Gallovic, F., Sokos, E., Serpetsidaki, A., Tselentis, A., 2008. Quick fault-plane identification by a geometrical method: application to the Mw 6.2 Leonidio earthquake, 6 January 2008, Greece. Seismol. Res. Lett. 79 (5), 653–662. http://dx.doi.org/10.1785/gssrl.79.5.653.

[P17]

A New Strategy to Compare Inverted Rupture Models Exploiting the Eigenstructure of the Inverse Problem

by F. Gallovič and J.-P. Ampuero

Online Material: List of inverted models with explanation of the applied inversion techniques, description of conversion of inverted models to a unified discretization, and figures of original and processed inversion results.

INTRODUCTION

Finite-fault-slip inversions provide crucial information on earthquake rupture phenomena. Many slip-inversion methods exist and differ in how the rupture model is parameterized and which regularizations or constraints are applied (e.g., Ide, 2007, and references therein). Some methods are utilized even routinely for large earthquakes and published online (e.g., the U.S. Geological Survey website http://earthquake.usgs.gov/, last accessed August 2015). However, the slip-inversion results obtained by various authors for the same event may differ (e.g., Clévédé *et al.*, 2004). There is currently no consensus about which slip-inversion method is preferable, and there are concerns about the reliability of the inferred source models due to the nonuniqueness or ill conditioning of the inverse problem (Hartzell *et al.*, 2007; Zahradník and Gallovič, 2010; Gallovič and Zahradník, 2011; Shao and Ji, 2012). Therefore, slip inversion is still a subject of active research.

A requisite to understand the variability of slip-inversion results across different methods is the characterization of their similarities and differences. Methods to compare spatial distributions of final slip have been previously developed and applied to synthetic and real cases (Clévédé *et al.*, 2004; Razafindrakoto *et al.*, 2015; Zhang *et al.*, 2015). Here, we propose an approach to compare the complete space–time evolution of rupture models.

The basic ideas behind our comparison technique are as follows. If the fault geometry is assumed, the forward problem of the slip inversion is a linear mapping from the model space (the spatial–temporal distribution of slip) to the data space (the seismograms) by means of the representation theorem (e.g., Aki and Richards, 2002). The spectral decomposition of the forward operator and its discrete counterpart, the singular value decomposition (SVD), provide a natural set of basis functions (singular vectors) in the model space. Any source model then can be decomposed into two parts made of linear combinations of singular vectors lying in the coimage and in the null space, which are associated with large and small (or even zero) singular values, respectively. Because only the coimage components provide significant signal, any slip-inversion method should resolve them correctly. The inversion results obtained by different methods may then differ in their null-space contributions, which are implicitly determined by the particular choices of source model parameterization and regularization of each method.

In the subsequent section, we introduce the principles of our comparison method, including an objective method to determine the boundary between the coimage and null spaces. We then briefly describe the Source Inversion Validation (SIV2a) benchmark problem conducted under the SIV (http://equake-rc.info/SIV/, last accessed August 2015) project. We use the SIV2a setup to illustrate the practical application of our method and compare SIV2a-inversion results obtained by various authors. We also assess how the conditioning of the slip inversion is affected by frequency band, station weighting, network coverage, and crustal model. Finally, we discuss the origin of slip-inversion bias and the implications of our results for the comparison of performance of source-inversion methods.

METHOD

Background of SVD

The forward modeling of the ground motions due to slip along a fault of known geometry is a linear mapping from the model space to the data space by means of the representation theorem (Aki and Richards, 2002),

$$u_i(\mathbf{r},t) = \iint G_{ij}(\mathbf{r},\boldsymbol{\xi},t-\tau)\Delta v_j(\boldsymbol{\xi},t)d\boldsymbol{\xi}d\tau, \quad (1)$$

in which $u_i(\mathbf{r},t)$ is the ith component of the ground displacement at position $\mathbf{r}$ and time t, $\Delta v_j(\boldsymbol{\xi},t)$ is the jth component of the slip rate at position $\boldsymbol{\xi}$ on the fault and at time t, and $G_{ij}(\mathbf{r},\boldsymbol{\xi},t)$ is the ground displacement in the direction i at location $\mathbf{r}$ due to sudden, unit slip in direction j at position $\boldsymbol{\xi}$. In the following, we refer to G_{ij} as the Green's function (GF).

doi: 10.1785/0220150096

Detailed presentations of the role of the SVD in understanding the properties of linear-inverse problems can be found in textbooks on geophysical inverse problems (Menke, 2012), or, for example, Olson and Apsel (1982) and Gallovič and Zahradník (2011) in the context of the slip inversions. The SVD approach implicitly assumes as the objective function the L2 norm of data residuals relative to model predictions. Weights can be included to emphasize or depreciate certain aspects of the data (stations, seismic phases, frequency ranges, etc.; note the choice between velocity and displacement data is equivalent to a choice of frequency-dependent weights) or to account for data and model prediction uncertainties (Duputel *et al.*, 2014). Weights generally affect the eigenstructure of the problem as shown later. Approaches to objectively determine these weights are under development (e.g., Duputel *et al.*, 2014) and could be incorporated in our analysis in the future.

We aim to perform a spectral decomposition of the continuum operator in equation (1) by means of a singular value expansion (Hori, 2001; Hansen, 2010). In practice, we achieve this computationally, considering a discretized version of the representation theorem with spatial and temporal sampling dense enough to accurately approximate the singular value expansion of the continuum problem.

After sufficiently fine discretization in time and space, the representation in theorem (1) is written in matrix form,

$$\mathbf{d} = \mathbf{G}\mathbf{m}, \tag{2}$$

in which $\mathbf{d}$ is a data vector of size N that contains the displacements waveforms of all stations and components, $\mathbf{m}$ is a model vector of size M that encompasses all spatial and temporal samples of slip rate, and $\mathbf{G}$ is a design matrix of size $N \times M$ that contains the responses to unit-step slip at each subfault and at each time represented by the elements of $\mathbf{m}$.

The SVD of matrix $\mathbf{G}$ is

$$\mathbf{G} = \mathbf{U}\mathbf{\Lambda}\mathbf{V}^T, \tag{3}$$

in which T represents matrix transpose, $\mathbf{U}$ and $\mathbf{V}$ are orthonormal matrices ($\mathbf{U}^T\mathbf{U} = \mathbf{I}, \mathbf{V}^T\mathbf{V} = \mathbf{I}$) of size $N \times N$ and $M \times M$, respectively, and $\mathbf{\Lambda}$ is a diagonal matrix of size $N \times M$ consisting of positive singular values λ_i, $i = 1, ..., \min(M, N)$, sorted in descending order. The columns $\mathbf{V}_{(i)}$ of matrix $\mathbf{V}$ are right-singular vectors. They are also eigenvectors of matrix $\mathbf{G}^T\mathbf{G}$ (size $M \times M$), forming an orthonormal basis system in the model space and are associated with eigenvalues λ_i^2. The columns $\mathbf{U}_{(i)}$ of matrix $\mathbf{U}$ are left-singular vectors, representing orthogonal basis in the data space. The first $\min(M, N)$ vectors $\mathbf{U}_{(i)}$ are projections of model-space basis vectors $\mathbf{V}_{(i)}$ into the data space:

$$\mathbf{U}_{(i)} = \mathbf{G}\mathbf{V}_{(i)}/\lambda_i, \qquad i = 1, ... \min(M, N), \tag{4}$$

that is, normalized seismograms generated by the individual model-space singular vectors.

The generalized solution of the inverse problem is defined as $\tilde{\mathbf{m}} = \mathbf{G}^{\#}\mathbf{d}$, in which $\mathbf{G}^{\#}$ is the pseudoinverse of $\mathbf{G}$ (i.e., $\mathbf{G}^{\#} = \mathbf{V}\mathbf{\Lambda}^{\#}\mathbf{U}^T$), in which $\mathbf{\Lambda}^{\#}$ is formed by replacing every nonzero diagonal entry of $\mathbf{\Lambda}$ by its reciprocal and transposing the resulting matrix. This is equivalent to expressing $\tilde{\mathbf{m}}$ as a linear combination of basis vectors $\mathbf{V}_{(i)}$,

$$\tilde{\mathbf{m}} = \sum_{i=1... \min(M,N)} \tilde{m}_i \mathbf{V}_{(i)}, \tag{5}$$

in which the ith spectral component of the singular vector expansion of the model is

$$\tilde{m}_i = \mathbf{U}_{(i)} \cdot \mathbf{d}/\lambda_i, \qquad i = 1, ..., \min(M, N), \tag{6}$$

in which the centered dot represents the scalar product. Similarly, the data vector can be expressed as $\mathbf{d} = \sum_{i=1...N} \tilde{d}_i \mathbf{U}_{(i)}$, in which the ith spectral component of the data is $\tilde{d}_i = \mathbf{U}_{(i)} \cdot \mathbf{d}$. The first $\min(M, N)$ spectral components of data and model are thus related by $\tilde{d}_i = \lambda_i \tilde{m}_i$. Therefore, the smaller is the singular value, the less sensitive is the data component to a given change of the corresponding model component; in other words, the singular value bears information about the sensitivity of the data to the particular basis function in the model space. Moreover, the relation $\tilde{m}_i = \tilde{d}_i/\lambda_i$ shows that noise in a data component associated with a small λ_i is amplified by the inversion; the singular value also bears information about the sensitivity of the model to additive data noise. The singular vectors thus can be divided into those lying in either the coimage space or the null space, associated with large and small (or even zero) singular values, respectively.

Comparison Metric

One can quantify the similarity between an inverted source model $\mathbf{m}$ and a target model by the model variance reduction (MVR), defined as

$$\text{MVR} = 1 - ||\mathbf{m} - \bar{\mathbf{m}}||/||\bar{\mathbf{m}}||, \tag{7}$$

in which $||\cdot||$ denotes the L2 norm. This metric compares the complete rupture evolutions because $\mathbf{m}$ and $\bar{\mathbf{m}}$ contain samples of the spatial–temporal slip-rate distributions. It is based on the full spectrum of the target and inverted models (i.e., includes contributions from all the singular vectors of $\mathbf{G}$). Here we propose to compare the models after expanding them in terms of the (approximate) singular vectors of the continuum problem, then truncating their expansion at a common cutoff singular value λ_c sufficiently large to contain only components that, in principle, can be well resolved. For any model $\mathbf{m}$, we define a truncated model $\mathbf{m}_T$ by

$$\mathbf{m}_T = \Sigma_{i=1...K}(\mathbf{V}_{(i)} \cdot \mathbf{m})\mathbf{V}_{(i)}, \tag{8}$$

in which K is the index of the smallest singular value larger than λ_c (Jackson, 1972; Wiggins, 1972; Gallovič and Zahradník, 2011). After truncating both the inverted and the target model, we evaluate the MVR using the following variant of

equation (7), which we refer to as the truncated model variance reduction (TMVR):

$$\mathrm{TMVR} = 1 - ||\mathbf{m}_T - \tilde{\mathbf{m}}_T||/||\tilde{\mathbf{m}}_T||. \quad (9)$$

The choice of λ_c is crucial. Here it is defined by a departure from the discrete Picard condition, a fundamental condition for stability of regularized solutions of the inverse problem, which requires the spectral amplitudes of the data $\tilde{d}_i$ to decay faster than the singular values λ_i (Hansen, 1990, 2010; Visser, 2004). In particular, the Picard condition ensures that a truncated SVD solution ($\Sigma_{i=1\ldots K}\tilde{d}_i/\lambda_i\mathbf{V}_{(i)}$) converges as more eigenvalues are included (as K is increased). As illustrated later (Fig. 2b), inaccuracies in GFs due to uncertainties in the velocity model or fault geometry cause $\tilde{d}_i$ to stagnate or even increase at small λ_i. This departure from the decay behavior of the data spectrum is usually clear enough to provide an objective choice of cutoff for truncated SVD solutions (Hansen, 1990; Visser, 2004). Here, we use that same rationale to set the cutoff singular value λ_c for our TMVR comparison metric.

TEST CASE: SIV2A MODEL

Here we present the main features of the SIV2a benchmark problem. A complete description can be found at the SIV web portal (http://equake-rc.info/SIV, last accessed August 2015). A complex kinematic rupture model with oblique mechanism on a dipping fault plane is considered. The fault is 40 km long (along strike) and 20 km wide (along dip), and the seismic moment is 3.5×10^{19} N·m (M_w 7.0). The source model is kinematic and adopts the regularized Yoffe slip-rate function (Tinti *et al.*, 2005) with variable rise time and rupture speed along the fault. The rake and dip angles are constant, but only approximate value ranges are provided (230°–250° and 40°–50°, respectively). The hypocentral depth is also given only approximately, ranging between 9 and 11 km. Here we adopt the middle values of the provided intervals: dip 45°, rake 240°, and depth 10 km.

The SIV2a rupture model (hereafter referred to as the target model) was initially unknown to the participants of the source-inversion blind test but is presently available upon request. Figure 1a shows the spatial distribution of slip of the target model and slip-rate snapshots showing the temporal evolution of the rupture. The model was originally provided at a fine spatial–temporal discretization. Ⓔ We downsampled it as described in the electronic supplement to this article, at a sampling rate sufficient for the maximum frequency we considered (see below).

The fault is embedded in a layered isotropic velocity–density structure, the parameters of which were given to the modelers. Synthetic waveforms evaluated at 40 receivers distributed from above the fault to approximately 30 km distance to the fault (see Fig. 1b) were available as data for the source inversion.

We calculate GFs with the Axitra code (Coutant, 1989) based on the discrete wavenumber method by Bouchon (1981). The waveforms are band-pass filtered between 0.05 and 0.5 Hz using a causal four-pole Butterworth filter. These GFs are not those used to compute the disseminated benchmark waveform data. Indeed, the variance reduction (VR) between our synthetics for the target model and the benchmark data is VR = 0.95. This minor mismatch can be attributed to the use of slightly different fault-plane position and orientation, a rake angle, or to minor numerical inaccuracies and different choices of algorithmic parameters in wave propagation codes. Similar differences can be expected for the other benchmark participants.

RESULTS

Figure 1c shows the spectrum of the design matrix (i.e., the distribution of its singular values). The spectrum decays approximately exponentially with the increasing index. This decay is steady, without sharp break, and hence there is no obvious definition of the boundary between coimage and null spaces. We propose to define an effective boundary, that is, a cutoff singular value λ_c that separates resolved from unresolved source features, using the discrete Picard condition.

SIV2a Test Case with Precise GFs

We perform the first tests on the inversion results obtained with the method of Gallovič *et al.* (2015), a linear-inversion method with multitime window parameterization, unconstrained rupture speed and rise time, constrained total rupture duration (12 s or less), and two regularization constraints: a k^{-2} slip covariance function (k being the wavenumber) and positivity of slip rate (see also Sokos *et al.*, 2015). The degree of smoothing is controlled by a parameter σ_D defined by Gallovič *et al.* (2015). A value of $\sigma_D = 0.1$ m is adequate for real-data applications with imperfect GFs, but in this controlled experiment we use weaker smoothing with $\sigma_D = 0.01$ m. Exact GFs are used in this test: we apply the inversion procedure to data evaluated using our own version of the target model and our own computed GFs (the disseminated waveforms are not used at this point).

The resulting source model has MVR = 0.75 (without truncation). Its TMVR decreases toward the MVR value as a function of decreasing λ_c (Fig. 2a). It is close to 1 when $\lambda_c > \lambda_{max}/20$, in which λ_{max} is the largest singular value. The spectral amplitudes of the data $\tilde{d}_i$ (red curve in Fig. 2b) decay slightly faster than the singular values (black line), which shows that the discrete Picard condition is satisfied.

SIV2a Test Case with Imprecise GFs

We now consider a case in which the GFs used in the forward and inverse modeling are not identical: we invert the disseminated benchmark data using the method of Gallovič *et al.* (2015) based on our GFs. The obtained model is denoted as Gallovic0.01 (see Ⓔ Table S1). Its final slip and slip-rate snapshots are shown in Figure 3 (left-most column). Its MVR is 0.66, lower than in the case of precise GFs. Its TMVR (Fig. 2a) decreases as a function of decreasing λ_c, from relatively large values ~0.95 to 0.66, with faster decay at $\lambda_c < 1/10 \sim 1/20\lambda_{max}$. The

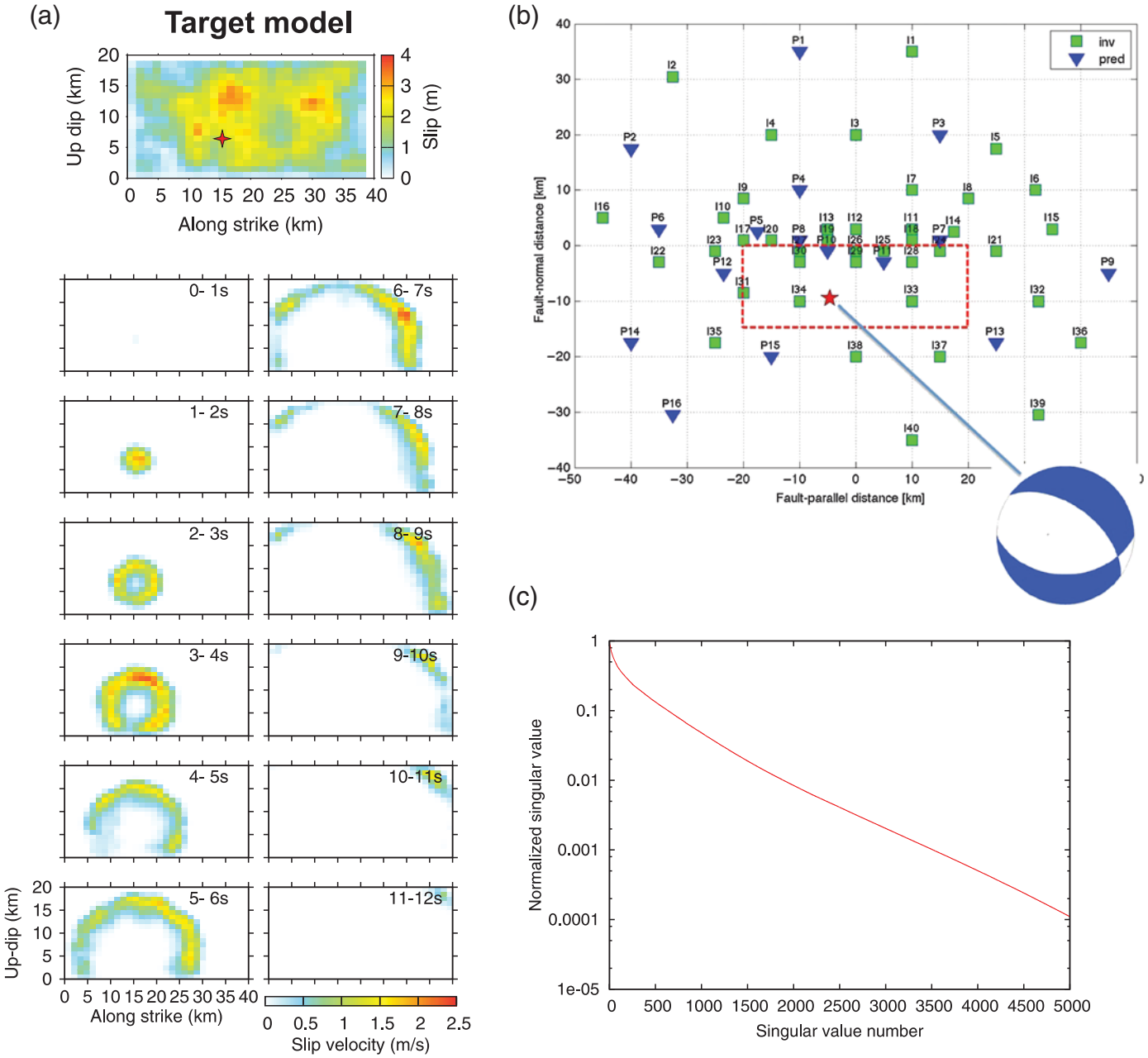

▲ **Figure 1.** Properties of the Source Inversion Validation (SIV2a) benchmark. (a) (top-most panel) Slip distribution and (bottom panels) slip-rate snapshots of the target rupture model. (b) Distribution of stations, surface projection of the fault (red rectangle), and the source mechanism (focal mechanism plot). (c) Normalized singular values of the **G** matrix. Because the discretization is very fine relative to the considered frequency range, the spectrum very closely approximates the spectrum of the continuum forward operator.

spectral amplitudes of the data (green in Fig. 2b) decay as a function of decreasing λ_i like those obtained with perfect GFs when $\lambda_i > 1/10 \sim 1/20\lambda_{max}$, but stagnate at smaller λ_i. This clear transition of the decay behavior of the data spectrum is caused by the use of imprecise GFs in the inversion and signals a departure from the discrete Picard condition. This suggests that, in the present case, a reasonable choice for the cutoff in model comparisons based on TMVR is $\lambda_c \sim 1/10\lambda_{max}$. This level corresponds to a coimage subspace dimension of 637. This number does not depend on the discretization, provided it is fine enough to accurately approximate the continuum formulation of the problem.

Comparison of Inverted Models from the SIV2a Solution Database

Several other modelers have made their solutions of the SIV2a benchmark available. Ⓔ Table S1 lists the model names and provides brief descriptions of their inversion methods and data preprocessing. The methods include the linear-inversion method by Sekiguchi *et al.* (2000) (Asano model provided by

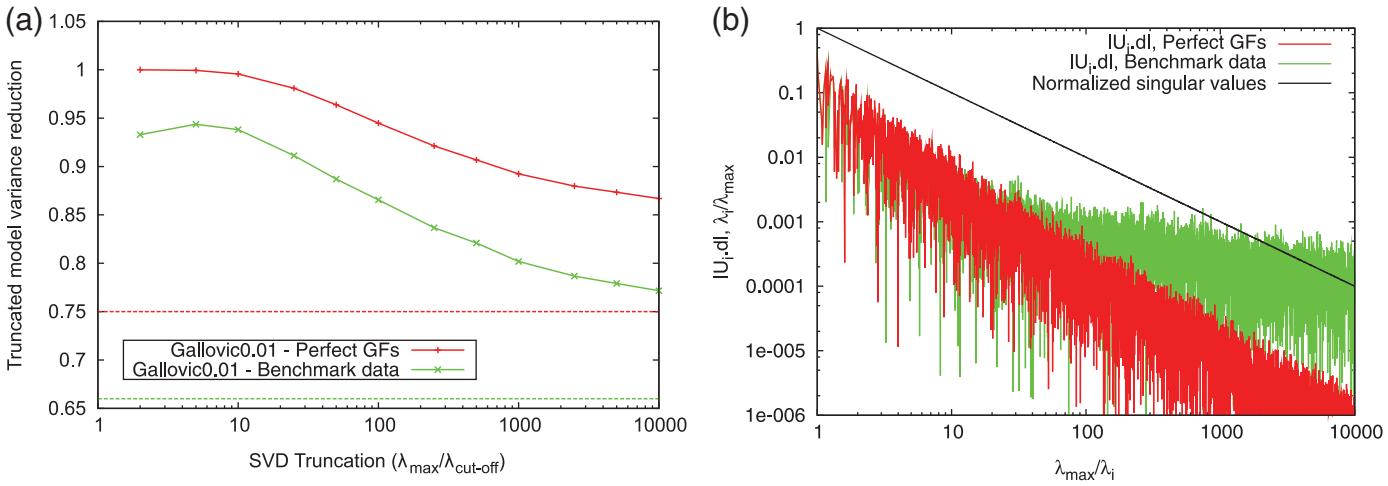

▲ **Figure 2.** Role of the precision of the Green's functions (GFs) on the inversion results for the SIV2a benchmark. (a) Model variance reduction (MVR) between the truncated true model and the truncated solution Gallovic0.01 as a function of the cutoff singular value (solid lines) when perfect (red line) or imprecise (green line) GFs are considered. MVRs between the inverted and true models without truncation are indicated by dashed lines (same color scheme). (b) Spectral components of the data for perfect (red) and imperfect (green) GFs as a function of (inverse) singular values. A decay faster than the black solid line indicates satisfaction of the discrete Picard condition for stability of regularized solutions of the inverse problem.

K. Asano see Asano and Iwata, 2011), a nonlinear formulation by Razafindrakoto and Mai (2014) (Hoby model provided by H. Razafindrakoto), and the method by Twardzik *et al.* (2012) based on a simplified source parameterization comprising two elliptical subfaults with constant rupture velocities (model CedricT3 provided by C. Twardzik).

Ⓔ We resampled these solutions to a common discretization as described in the electronic supplement. Figure 3

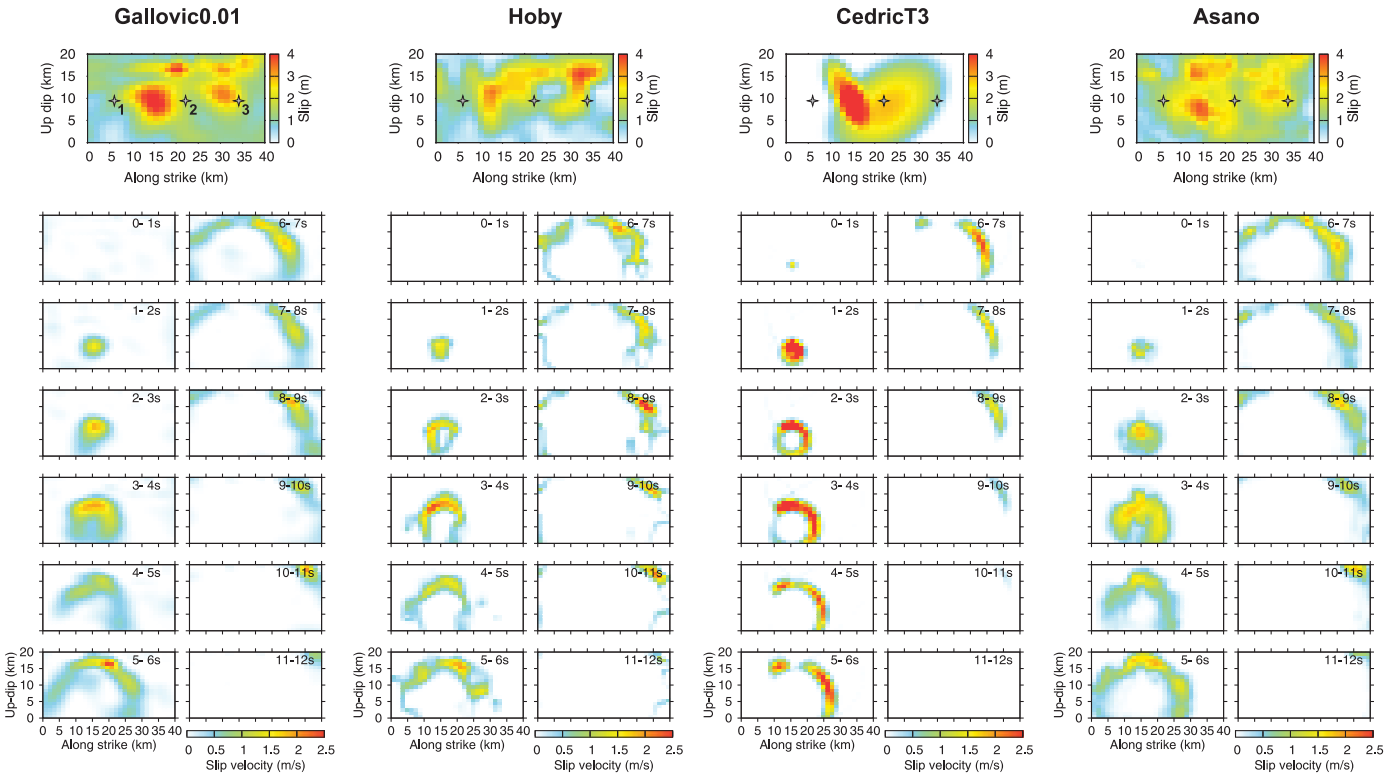

▲ **Figure 3.** Selected inversion results of the SIV2a benchmark obtained by various authors (see Ⓔ Table S1): slip distributions (top-most panels) and slip-rate snapshots (bottom panels). Stars in the slip plots denote locations for which slip rates are shown in Figure 4a. Ⓔ More models are shown in the electronic supplement.

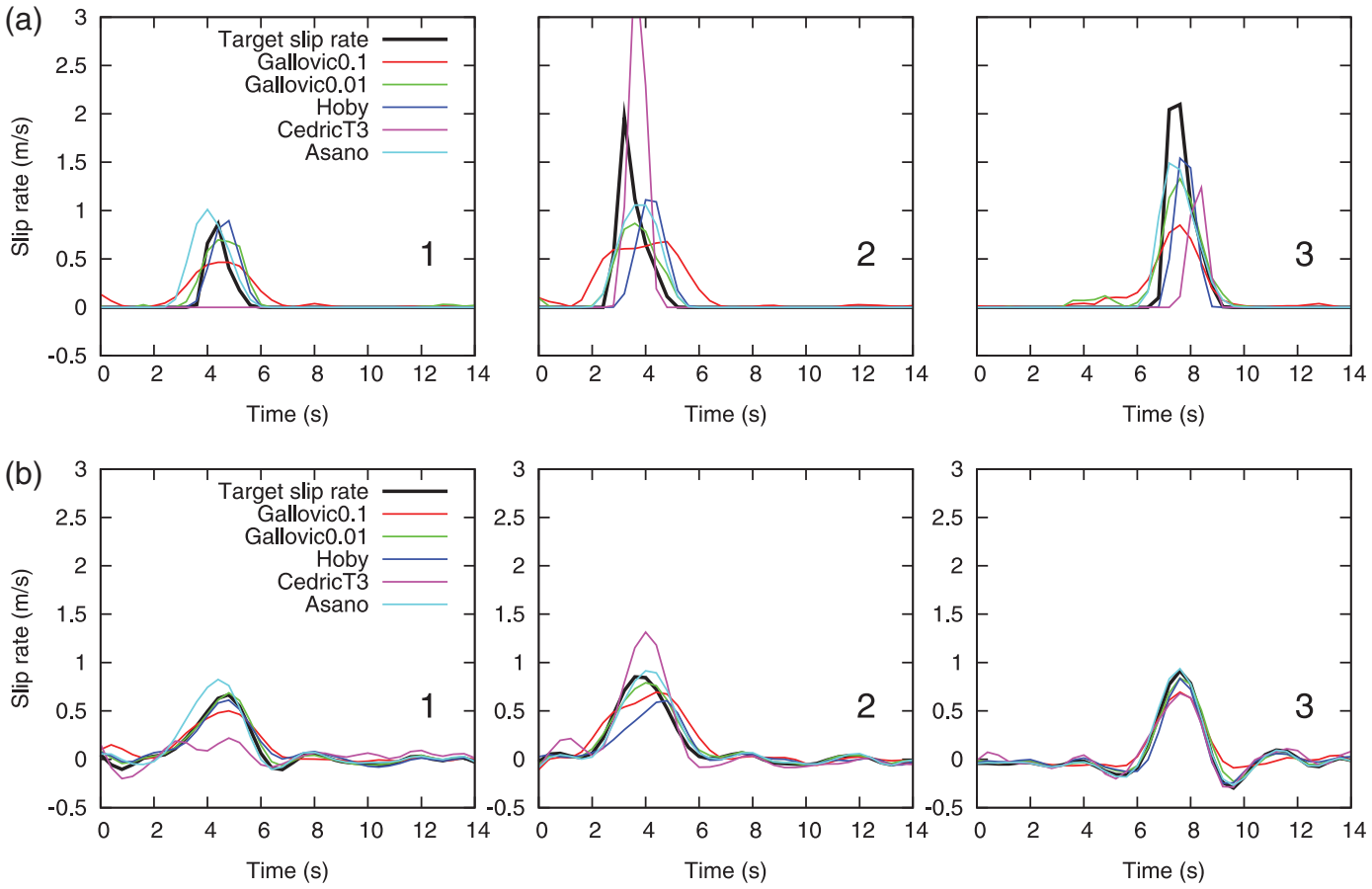

▲ **Figure 4.** (a) The comparison of slip-rate functions from inverted and target models at three selected points on the fault indicated in Figure 3. (b) Same as (a) but after truncation at one-tenth of the largest singular value. After truncation, the slip rates become much more similar to each other.

shows the final slip distribution and slip-rate snapshots for selected models (Ⓔ all models are shown in the electronic supplement). These are to be compared with the target model in Figure 1a. Figure 4a shows a comparison of the inferred slip rates at three selected points on the fault depicted in the slip maps of Figure 3. The MVR of each model is listed in Table 1.

All the models resolve well the basic character of the rupture propagation (see the snapshots in Fig. 3). However, at a more detailed level, differences among the methods become evident, as in the slip-rate functions shown in Figure 4a. For example, in the CedricT3 solution, point 1 has zero slip rate, whereas point 2 has an exaggerated peak slip-rate amplitude. Solution Gallovic0.1 (with stronger smoothing than in the

Table 1
Data and Model Variance Reductions for the Various Inversion Solutions and the Target Model of the SIV2a Benchmark

	Model VR		Data VR	
Model Name	**Complete**	**Truncated**	**Complete**	**Truncated**
Gallovic0.01	0.66	0.94	0.997	0.995
Gallovic0.1	0.53	0.84	0.981	0.980
Hoby	0.50	0.83	0.825	0.824
Cedrict3	−0.20	0.65	0.700	0.699
Asano	0.61	0.86	0.960	0.959
Target (with perfect GFs)	—	—	1.000	0.996

The truncation is performed with cutoff at one-tenth of the largest singular value and is applied to both models under comparison. SIV, Source Inversion Validation; VR, variance reduction; GF, Green's function.

Gallovic0.01 model discussed previously) provides broader slip-rate functions centered at the true maximum.

Figure 3 also shows a comparison of the final slip maps (top panels). The most dissimilar solution is model CedricT3. This model has a simple parameterization comprising two ellipses (see Ⓔ Table S1) with clearly visible contributions in the retrieved slip map. The ellipse with the largest amount of slip is located around the true hypocenter. Nevertheless, a similar concentration of slip at the hypocenter is common to all the other models, although in the target model the maximum slip is located ~5 km above the hypocenter. Other details of the slip distribution are also resolved imperfectly; for example, the location of subsurface asperities is biased toward shallower depths. The deficiencies in the recovery of final slip should come as no surprise, given the limited frequency band of the data considered and the inherent nonuniqueness of the inverse problem. In particular, the applied high-pass filter above 0.05 Hz effectively downweights the static deformation.

We analyze these four models in the same way as for model Gallovic0.01. Figure 5 shows their TMVR as a function of the truncation cutoff λ_c. Dashed lines indicate their MVR without truncation (see also Table 1). Similarly to the Gallovic0.01 model, most truncated solutions agree well with the truncated target model (TMVR > 0.8) if $\lambda_c > \sim 1/10\lambda_{max}$. The exception is model CedricT3, although it still has a much higher agreement after truncation (TMVR = 0.6) than without it (MVR = −0.2).

Figure 6 shows the final slip and slip-rate snapshots of some of the analyzed models truncated at $\lambda_c = 1/10\lambda_{max}$ (for a plot with all the models, Ⓔ see the electronic supplement). There is a striking visual similarity between the truncated models, consistent with the large TMVR values presented above. Figure 4b shows slip rates after truncation at three selected points on the fault indicated in Figure 3. The similarity of slip rates among different methods is significantly higher with truncation than without it (Fig. 4a). Even though at point 1, the CedricT3 solution has zero slip rates, after truncation the slip rates become nonzero. Although this model is the least similar to the target model, after truncation the similarity improves significantly. Thus, we conclude that all the inverted models agree within the coimage subspace associated with singular values $> \sim 1/10\lambda_{max}$. This boundary thus defines the effective range of the problem, which encapsulates the source features that are resolvable, and agrees with the bound indicated by the discrete Picard plot (Fig. 2b).

We also evaluate the contribution from the null-space in terms of the data fit. Table 1 lists the variance reduction in the data space (DVR). There is a very small difference (~0.1%) in DVR between the truncated models and those without truncation. This confirms that the contribution of the truncated singular vectors to the signal is very weak. This, in turn, means that the contribution of these singular vectors to the inverse solutions is highly vulnerable to any inconsistency in the fault geometry or velocity model considered.

Finally, we compare the original target model (without truncation) with the truncated one. Both models are shown with the same color scale in the two left-most columns in Figure 6. The truncated model captures well the general rupture propagation characteristics, which is expressed by the relatively high MVR (0.58) between the two models. Nevertheless, the final slip distributions are significantly different (compare the two top left panels in Fig. 6). The slip distribution of the truncated model is biased, having exaggerated slip values in relatively small areas near the projection of the stations on the fault. This is a manifestation of the nonuniform resolution of the inverse problem. In terms of waveform fit, the truncated target model reproduces the original data very well up to 0.5 Hz (DVR = 0.996).

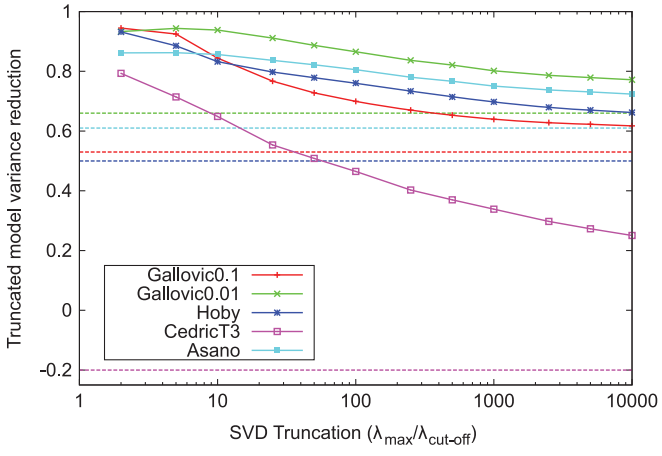

▲ **Figure 5.** MVR as a function of the cutoff singular value for all the analyzed models from the SIV database (solid lines). Dashed lines denote MVRs between inverted and true models without truncation.

Factors Controlling the Spectrum of the G Matrix

The steepness of the decay of the spectrum of the forward operator (in the discrete form represented by the **G** matrix) determines the conditioning of the inverse problem, which is defined here as the number of singular values larger than the given cutoff λ_c. Here we analyze the effect of various features of the slip-inversion setup on the **G** matrix spectrum. For this test, we utilize the geometry and parameters of a real earthquake study, the 2009 M_w 6.3 L'Aquila earthquake (Gallovič *et al.*, 2015), including additional phantom stations denoted as EX_.

As a reference-inversion setup, we assume nine real stations near L'Aquila (see Fig. 7a, excluding the EX_ stations), a 1D layered crustal model, maximum frequency $F_{max} = 0.5$ Hz, and distance-independent weights. The bold black line in Figure 7b shows the spectrum of singular values of the corresponding **G** matrix normalized by their maximum.

We then perform tests, in which the model features are altered one at a time. Colored curves in Figure 7 show the resulting spectra of **G**. In the first test, we decrease the maximum frequency to 0.3 Hz. This leads to faster decay of the spectrum of **G**, and thus its conditioning worsens significantly. The reason is that decreasing the maximum frequency decreases the

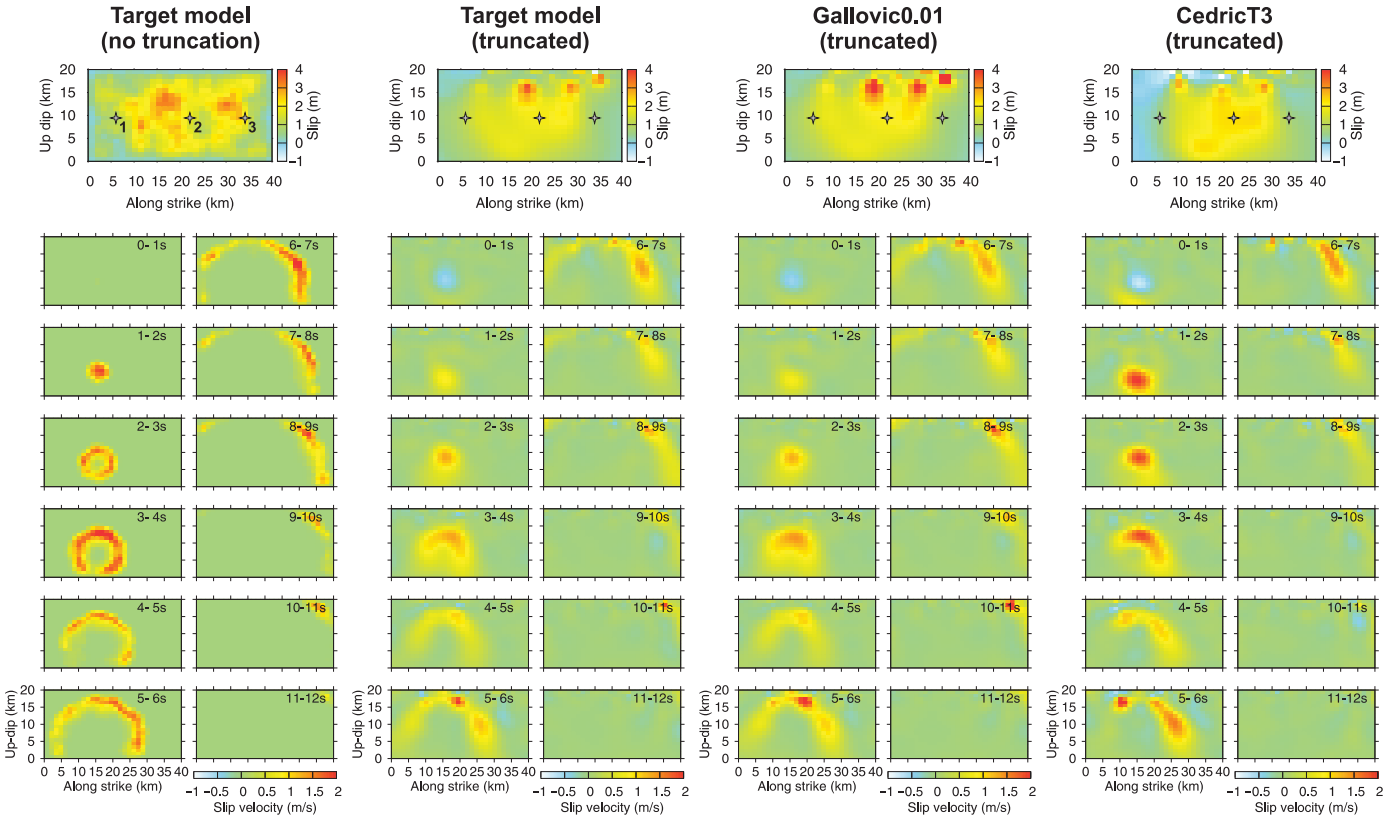

▲ **Figure 6.** Target model and two selected inversion results (columns) truncated with cutoff at one-tenth of the largest singular value: slip distributions (top-most panels) and slip-rate snapshots (bottom panels). The original target model is shown on the left, for reference, in the same color scale. Note the very good agreement between the inverted models and the target model after truncation. Stars in the slip plots denote locations for which slip rates are shown in Figure 4a. Ⓔ All the models are shown in the electronic supplement.

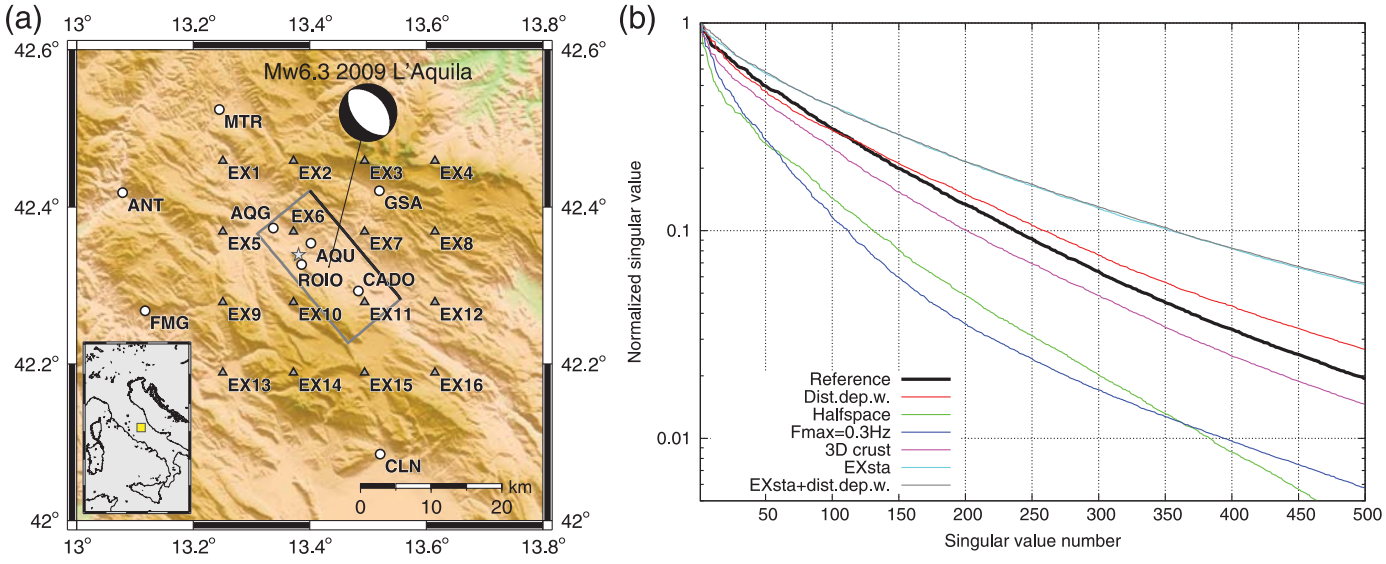

▲ **Figure 7.** An assessment of factors controlling the spectrum of the forward operator (i.e., of the **G** matrix after discretization). (a) Real (circles) and phantom (triangles, EX_) stations and fault of the L'Aquila earthquake (gray rectangle with the top denoted by the black line); the yellow rectangle in the inset marks the study area. (b) Normalized singular values of the forward **G** matrix and their dependence on various features and parameters of the inversion setup (see text for explanation).

variability of the GFs along the fault and hence their information content, which makes the inversion less constrained.

As a next test, we apply distance-dependent weights equal to $\max(4R/L, 1)$, in which L is the fault length and R is the Joyner–Boore fault distance. This weighting scheme strengthens the role of the distant stations, and the conditioning of **G** improves, although its effect is less significant than that of changing the frequency range (Fig. 7b). We then add stations to the inversion (denoted as EX_ in Fig. 7a). Figure 7b shows how the conditioning of **G** improves. The figure also demonstrates that there is not much difference whether the distance-dependent weights are considered or not.

We further test the effect of the crustal model on the inversion. To avoid confusion, we note that this analysis does not depend on any data, so we do not analyze effects of imprecise GFs here. We consider two additional crustal models: a half-space and a smooth 3D tomographic velocity model by Di Stefano *et al.* (2011). Details on the velocity model and the GF calculations are provided by Gallovič *et al.* (2015). In both cases, the conditioning of **G** worsens, but it is more severe in the former case. We attribute this to the decreased variability of GFs along the fault due to the smoothness of these two models and hence to the decrease of the wavefield information content. In contrast, the layered crustal model contains strong velocity interfaces that make the wave propagation more complex (reflected and transmitted waves, multiples, dispersion of surface waves, etc.).

The behavior of the conditioning of **G** presented here must be considered only qualitatively. The exact behavior is case dependent, and the presented results are only intended to provide general trends. Moreover, the changes of the inversion setup not only change the spectrum of **G**, but also the shapes of the singular vectors. A synoptic quantification of such changes is difficult, mostly because the singular vectors are 3D, but deserves further study.

DISCUSSION

Effect of Station Distribution on Final Slip Bias

Although the inverted models explain 99% of the data and reproduce the general space–time characteristics of rupture propagation of the true source reasonably well after projection on the effective coimage subspace, their final slip distribution is significantly biased, consisting of a few peaks below the stations overlying the rupture area (see Fig. 6). This nonuniform resolution (implicitly included in the design matrix **G**) indicates that the minimum resolvable length scale is not completely determined by the maximum frequency considered (related with a minimum wavelength), but also depends on station coverage. This arises generally if near-field data are used in the source inversion. The sensitivity of far-field waves can be intuitively characterized by their frequency-dependent wavelength. However, the near-field part of the wavefield is composed of evanescent waves that decay with distance from the fault, with a characteristic decay distance comparable to the wavelength of the slip source (e.g., Somala *et al.*, 2014). Hence, each station has enhanced sensitivity in its vicinity. This example highlights the abstract nature of the coimage subspace: a truncated model, although robust, may display source patterns that are not directly amenable for physical interpretation. The enhanced sensitivity of the near-field observations is particularly visible when considering static displacement data, such as Interferometric Synthetic Aperture Radar data (e.g., Fukahata and Wright, 2008).

Assessment of Inversion Methods Performance

The inverted models agree with the target model after truncation generally well but not perfectly. The particular inversion methods also alter the resolvable (coimage) part of the solution. This could motivate a ranking of the inversion methods. However, further considerations are needed to generalize the present model comparison in this way. Indeed, the analysis is based on the GF matrix, which in practice is always affected by inaccuracies in the assumed fault-plane geometry, choice of station weights and frequency band of data filters, numerical issues in the evaluation of the GFs, and so on. All these factors affect the **G** matrix spectrum, and thus the comparison among different methods can be biased toward the one with the exact GFs. In other words, exact comparison can be made only if all the models use exactly the same GFs and the same inversion setup. One could also extend the comparison metric using multiple **G** matrices computed for a reasonable range of velocity models.

The comparison of SIV2a benchmark solutions presented here suggests that the linear methods perform better than the nonlinear ones. That might be true in this particular case where the fault-plane geometry and the GFs are almost exact. However, nonlinear methods can be potentially less sensitive to imperfections in the GFs, thus providing more robust (albeit less precise) solutions. They can also work with other objective functions than the L2 norm considered here, putting emphasis on different aspects of the wavefield and potentially leading to different solutions (Hartzell *et al.*, 1991). Moreover, the nonlinear methods have the advantage of working with generally lower number of parameters, which enables effective uncertainty analysis.

Inversions that use only few parameters (represented here by model CedricT) are the most extreme cases, with just ∼20 parameters. Their results compared with the target model after truncation at the twentieth singular value gives TMVR = 0.82. Thus, from this perspective, the CedricT model is successful. However, such a severely truncated model does not even resemble the rupture propagation; hence, inferences on rupture processes cannot be readily extracted from it.

CONCLUSIONS

We introduced a new comparison technique based on an SVD of the design matrix of the continuum inverse problem. We propose to separate the coimage and null subspaces (representing resolved and unresolved features, respectively) by a selected cutoff singular value and compare different inverted models

with the target (exact) model after projecting them on the coimage subspace (i.e., after truncation). This procedure effectively quantifies the ability of an inversion result to reproduce the resolvable features of the source.

As an example, we applied this technique to the SIV2a benchmark exercise within the SIV project (http://equake-rc.info/SIV/). The design matrix **G** of the SIV2a slip-inversion benchmark case has a smoothly decaying spectrum (see Fig. 1c) without a clear boundary between the coimage and the null space. The tests performed here (Picard plot and comparison of inversions from various authors) indicate that due to the use of imperfect GF the effective rank of **G** is limited to the subspace associated with singular values larger than one-tenth of the maximum singular value.

By applying our approach to the SIV2a benchmark results from various authors (see Ⓔ Table S1), we show that the inferred source images are very similar to the target model after they all are truncated with cutoff at approximately one-tenth of the largest singular value. The models thus mainly differ in their respective contribution from the null-space, which is determined by the particular priors implied by their choices of regularization or parameterization and affected by the imperfections of the GFs. Although the truncated models capture the overall rupture propagation, their final slip distributions are biased significantly, showing distinct peaks below the stations lying above the rupture. This suggests that although the overall characteristics of the rupture propagation can be retrieved relatively well, the static slip distribution is not very well constrained. It also illustrates that the coimage subspace may contain abstract source patterns that are not directly amenable for interpretation.

Application of the comparison technique to inversions of a real event, with limited station coverage and imperfect knowledge of the fault geometry and GFs, would provide further insight into the quality of inferred source images. For such a comparative study, a well-studied event would have to be selected and all the modelers would have to consider the same basic setup (fault, mechanism, GFs, data processing, etc.) to carry out a fair comparison. ◪

ACKNOWLEDGMENTS

We are grateful to all the participants in the Source Inversion Validation (SIV) benchmarks and to Martin Mai for his leadership in the SIV project, without whom this study would have been impossible. The article benefited from comments and suggestions by two anonymous reviewers. We acknowledge financial support from the Czech Science Foundation project 14-04372S, the Charles University project UNCE 204020/2012, the National Science Foundation (NSF) CAREER Award EAR-1151926, and the Southern California Earthquake Center (which is funded by NSF Cooperative Agreement EAR-1033462 and U.S. Geological Survey Cooperative Agreement G12AC20038).

REFERENCES

Aki, K., and P. G. Richards (2002). *Quantitative Seismology*, University Science Books, Sausalito, California.

Asano, K., and T. Iwata (2011). Source rupture process of the 2007 Noto Hanto, Japan, earthquake estimated by the joint inversion of strong motion and GPS data, *Bull. Seismol. Soc. Am.* **101,** 2467–2480.

Bouchon, M. (1981). A simple method to calculate Green's functions for elastic layered media, *Bull. Seismol. Soc. Am.* **71,** 959–971.

Clévédé, E., M.-P. Bouin, B. Bukchin, A. Mostinskiy, and G. Patau (2004). New constraints on the rupture process of the 1999 August 17 Izmit earthquake deduced from estimates of stress glut rate moments, *Geophys. J. Int.* **159,** 931–942.

Coutant, O. (1989). Program of numerical simulation AXITRA, Research Report, Laboratoire de Géophysique Interne et Tectonophysique, Grenoble, France.

Di Stefano, R., C. Chiarabba, L. Chiaraluce, M. Cocco, P. De Gori, D. Piccinini, and L. Valoroso (2011). Fault zone properties affecting the rupture evolution of the 2009 (M_w 6.1) L'Aquila earthquake (central Italy): Insights from seismic tomography, *Geophys. Res. Lett.* **38,** L10310, doi: 10.1029/2011GL047365.

Duputel, Z., P. S. Agram, M. Simons, S. E. Minson, and J. L. Beck (2014). Accounting for prediction uncertainty when inferring subsurface fault slip, *Geophys. J. Int.* **197,** no. 1, 464–482.

Fukahata, Y., and T. J. Wright (2008). A non-linear geodetic data inversion using ABIC for slip distribution on a fault with an unknown dip angle, *Geophys. J. Int.* **173,** 353–364.

Gallovič, F., and J. Zahradník (2011). Toward understanding slip-inversion uncertainty and artifacts: 2. Singular value analysis, *J. Geophys. Res.* **116,** no. B02309, doi: 10.1029/2010JB007814.

Gallovič, F., W. Imperatori, and P. M. Mai (2015). Effect of three-dimensional velocity heterogeneities and topography on slip inversions: Case study of the M_w 6.3 2009 L'Aquila earthquake, *J. Geophys. Res.* **120,** 428–449.

Hansen, P. Ch. (1990). The discrete Picard condition for discrete ill-posed problems, *BIT* **30,** 658–672.

Hansen, P. Ch. (2010). *Discrete Inverse Problems: Insight and Algorithms*, Fundamentals of Algorithms Series , doi: 10.1137/1.9780898718836.

Hartzell, S., P. Liu, C. Mendoza, C. Ji, and K. M. Larson (2007). Stability and uncertainty of finite-fault slip inversions: Applications to the 2004 Parkfield, California, earthquake, *Bull. Seismol. Soc. Am.* **97,** no. 6, 1911–1934.

Hartzell, S. H., G. S. Stewart, and C. Mendoza (1991). Comparison of L1 and L2 norms in a teleseismic waveform inversion for the slip history of the Loma Prieta, California, earthquake, *Bull. Seismol. Soc. Am.* **81,** 1518–1539.

Hori, M. (2001). Inverse analysis method using spectral decomposition of Green's function, *Geophys. J. Int.* **147,** 77–87.

Ide, S. (2007). Slip inversion, in *Treatise on Geophysics*, G. Schubert (Editor-in-Chief), H. Kanamori (Editor), Vol. 4, Elsevier, Amsterdam, The Netherlands, 193–223.

Jackson, D. D. (1972). Interpretation of inaccurate, insufficient, and inconsistent data, *Geophys. J.* **28,** 97–109.

Menke, W. (2012). *Geophysical Data Analysis: Discrete Inverse Theory*, Third Ed., Academic Press, Boston, Massachusetts.

Olson, A. H., and R. J. Apsel (1982). Finite faults and inverse theory with applications to the 1979 Imperial Valley earthquake, *Bull. Seismol. Soc. Am.* **72,** no. 6A, 1969–2001.

Razafindrakoto, H. N. T., and M. P. Mai (2014). Uncertainty in earthquake source imaging due to variations in source time function and earth structure, *Bull. Seismol. Soc. Am.* **104,** 855–874.

Razafindrakoto, H. N. T., P. M. Mai, M. G. Genton, L. Zhang, and K. K. S. Thingbaijam (2015). An embedding method to quantify rupture model variability: Stability analysis and application to the 2011 M 9 Tohoku earthquake, *Geophys. J. Int.* **202,** 17–40.

Sekiguchi, H., K. Irikura, and T. Iwata (2000). Fault geometry at the rupture termination of the 1995 Hyogo-ken Nanbu earthquake, *Bull. Seismol. Soc. Am.* **90,** 117–133.

Shao, G. F., and C. Ji (2012). What the exercise of the SPICE source inversion validation BlindTest 1 did not tell you, *Geophys. J. Int.* **189,** 569–590.

Sokos, E., A. Kiratzi, F. Gallovič, J. Zahradník, A. Serpetsidaki, V. Plicka, J. Janský, J. Kostelecký, and G.-A. Tselentis (2015). Rupture process of the 2014 Cephalonia, Greece, earthquake doublet (M_w 6) as inferred from regional and local seismic data, *Tectonophysics* **656,** 131–141.

Somala, S. N., J.-P. Ampuero, and N. Lapusta (2014). Resolution of rise time in earthquake slip inversions: Effect of station spacing and rupture velocity, *Bull. Seismol. Soc. Am.* **104,** 2717–2734.

Tinti, E., E. Fukuyama, A. Piatanesi, and M. Cocco (2005). A kinematic source-time function compatible with earthquake dynamics, *Bull. Seismol. Soc. Am.* **95,** 1211–1223.

Twardzik, C., R. Madariaga, S. Das, and S. Custódio (2012). Robust features of the source process for the 2004 Parkfield, California, earthquake from strong-motion seismograms, *Geophys. J. Int.* **191,** 1245–1254.

Visser, R. (2004). A boundary element approach to acoustic radiation and source identification, *Ph.D. Thesis*, University of Twente, Enschede, the Netherlands.

Wiggins, R. (1972). The general linear inverse problem: Implications of surface waves and free oscillations on earth structure, *Rev. Geophys. Space Phys.* **10,** 251–285.

Zahradník, J., and F. Gallovič (2010). Toward understanding slip-inversion uncertainty and artifacts, *J. Geophys. Res.* **115,** no. B09310, doi: 10.1029/2010JB007814.

Zhang, L., P. M. Mai, K. K. S. Thingbaijam, H. N. Razafindrakoto, and M. G. Genton (2015). Comparing earthquake slip models with the spatial prediction comparison test, *Geophys. J. Int.* **200,** 185–198.

F. Gallovič
Charles University in Prague
Faculty of Mathematics and Physics
Department of Geophysics
V Holešovičkách 2
Prague 181 00, Czech Republic
gallovic@karel.troja.mff.cuni.cz

J.-P. Ampuero
Seismological Laboratory
California Institute of Technology
1200 East California Boulevard
Pasadena, California 91125 U.S.A.

Published Online 16 September 2015

[P18]

Modeling Velocity Recordings of the M_w 6.0 South Napa, California, Earthquake: Unilateral Event with Weak High-Frequency Directivity

by František Gallovič

ABSTRACT

On 24 August 2014, an M_w 6.0 earthquake struck the Napa area in the north San Francisco Bay region, causing one fatality and damaging many older buildings in the Napa area. First, I employ low-frequency data (0.05–0.5 Hz) from 10 near-fault strong-motion stations to perform slip inversion, revealing (in agreement with other studies) rupture propagating up-dip and unilaterally along the fault with a dominant shallow asperity. Then I generate broadband synthetics (0.05–5 Hz) using an advanced Ruiz integral kinematic (RIK) source model (Ruiz *et al.*, 2011) and a 1D velocity model. The RIK model is composed of randomly distributed overlapping subsources with a fractal number–size distribution. The particular distribution of the RIK subsources is constrained by the low-resolution slip model from the inversion. Besides providing stable omega-squared spectral decay at high frequencies, the RIK model is able to reproduce the frequency-dependent directivity effect with adjustable strength. Comparison of the synthetic velocity waveforms with the observed data shows that the smallest modeling bias and variance is achieved by a rupture model with complex rupture propagation and thus weak high-frequency directivity. I link my findings with other studies, including analog experiments by Day *et al.* (2008), suggesting that this feature is rather common to earthquake sources.

Online Material: Tables of station locations and crustal model, and figures of synthetic seismograms and their smoothed Fourier spectra for all directivity models.

INTRODUCTION

The South Napa earthquake occurred on 24 August 2014 at 10:20:44 UTC in California, 6 km northwest of American Canyon and 9 km southwest of Napa. The event triggered ShakeAlert and G-larmS early warning systems, sending an alert to San Francisco about 10 s prior to the start of the strongest shaking (Grapenthin *et al.*, 2014). Quick estimates of the ground motions (ShakeMap) and the impact on the population (PAGER) were released 11 and 13 min after the earthquake, respectively. The earthquake caused one fatality and damaged many older buildings in the Napa area (Brocher *et al.*, 2015).

Routine seismological and geodetical analyses were performed by world agencies, including several United States institutions. Basic parameters of the event are summarized (e.g., at the U.S. Geological Survey [USGS] website; http://earthquake.usgs.gov, last accessed October 2015), including the location and the centroid moment tensor (CMT). The event ruptured the West Napa fault belonging to the San Andreas fault system. The fault is known to be active; the USGS National Seismic Hazard Maps depicts the epicentral region to likely experience strong shaking in the future. Quick slip inversions were provided at the USGS webpage by D. Dreger (University of California, Berkeley) using regional seismic data and by W. Barnhart (USGS National Earthquake Information Center) using the Global Positioning System and Interferometric Synthetic Aperture Radar data. Those preliminary results have been refined and published in an *SRL* focus section (Barnhart *et al.*, 2015; Dreger *et al.*, 2015). Together with other models published so far (Ji *et al.*, 2015; Melgar *et al.*, 2015; Wei *et al.*, 2015) show, generally speaking, that the event was unilateral northward toward the city of Napa, having significant asperity at shallow depths (<5 km) with longer rise times at the place where 40–46 cm surface fault slip was observed (Brocher *et al.*, 2015).

Such a unilateral event is expected to exhibit a strong source directivity effect, amplifying the ground motions in the direction of the rupture propagation (northward) and broadening of velocity pulses, especially at the fault-normal (F-N) components (e.g., Somerville *et al.*, 1997). Therefore, the directivity effect is of great interest for earthquake engineers. Baltay and Boatwright (2015) have analyzed residuals of the South Napa earthquake observed data with respect to ground-motion prediction equations (GMPEs). They have shown that while the residuals of pseudospectral acceleration (PSA) at 3 s exhibit clear amplification due to the directivity

 doi: 10.1785/0220150042

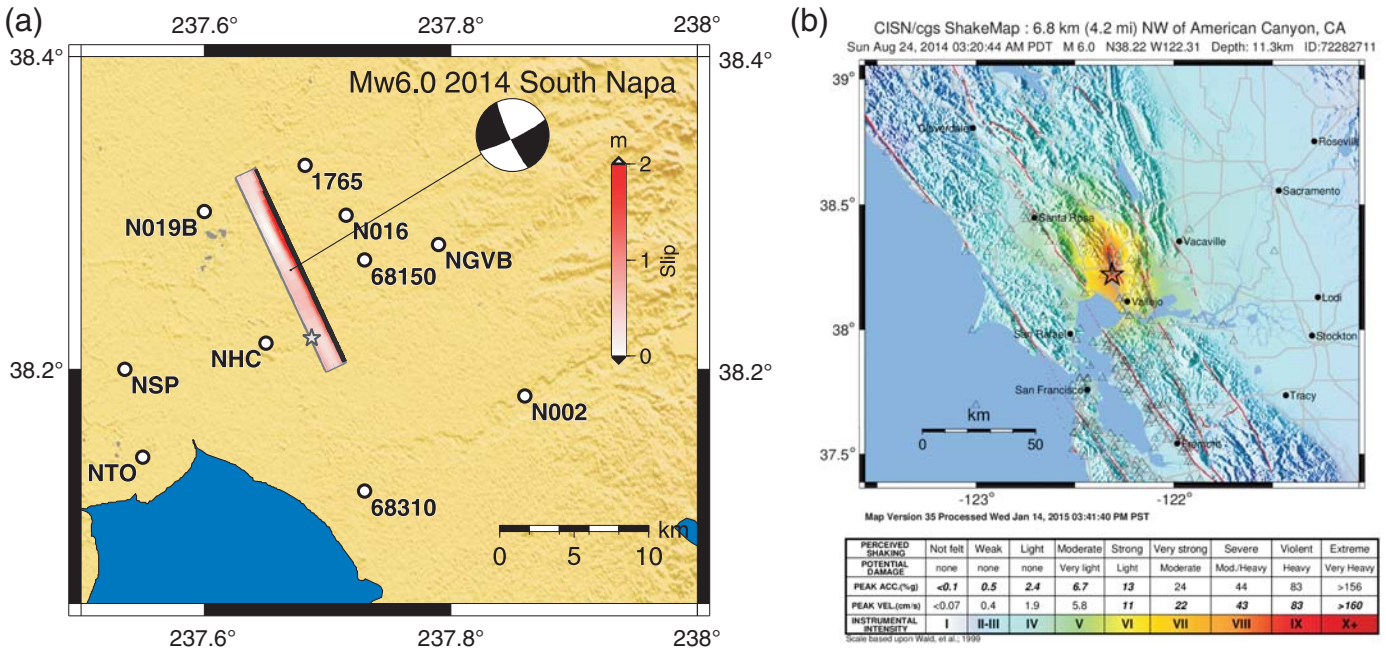

▲ **Figure 1.** (a) Map of the Napa earthquake epicentral area showing stations (circles), the event hypocenter (star), focal mechanism (beachball), and the fault model (rectangle) with the top (black line) reaching 400 m below the surface. Stations 1765, N016, and 68150 are located in the city of Napa. The slip model from inversion (see also Fig. 2) is shown on the fault in the shaded scale. (b) Instrumental intensity ShakeMap (see Data and Resources) with apparently no directivity effect, except for the elongation related to the finite extent of the fault (gray line).

effect, those at 0.3 s and the peak ground accelerations (PGAs) do not. This suggests that the source directivity effect is reduced at higher frequencies. At midfrequencies, the residuals of PSA at 1 s and peak ground velocities (PGVs) show indeed a less-pronounced directivity effect, being also perhaps overlaid by a fault-zone-guided wave effect (Baltay and Boatwright, 2015). Instrumental intensity ShakeMaps, obtained by interpolating recorded ground motion, do not exhibit clear manifestation of the northward source directivity effect, being characterized only by elongation due to the finite extent of the fault (Fig. 1). Stations NHC and N019B, located at similar distance from the largest slip patch (Fig. 1) but at opposite directions with respect to the rupture propagation, experienced almost the same PGV (0.58 and 0.63 m/s, respectively) and PGA (0.40*g* and 0.34*g*, respectively). Moreover, although the F-N component at the directive stations N019B and 1765 exhibit broader velocity pulses due to the strong low-frequency directivity effect, their amplitudes (related to the perhaps weaker high-frequency directivity) are comparable or only slightly larger than those at the respective fault-parallel (F-P) components. I emphasize that this is in contradiction to the classical source directivity models that predict amplification of the motion up to 5–10 times at all frequencies larger than the corner frequency, which is definitely not observed for this particular event. Although wave-propagation effects could have contributed to some extent to the amplification of the ground shaking south from the event (e.g., NHC is situated in deeper sediments than N019B), it is very likely that the source effect also had to contribute in the almost full removal of the directivity effect at high frequencies. Proper modeling of such frequency-dependent directivity effect is the key point of this article.

Because many high-quality recordings were written by stations at near-fault distances for this earthquake, it is a unique opportunity to test source models with various directivity strengths. The article consists of two parts. In the first one, I perform slip inversion by the recently introduced technique by Gallovič *et al.* (2015) using local strong-motion data at relatively low frequencies (0.05–0.5 Hz). In the second part, I generate broadband synthetics (0.05–5 Hz) using an advanced kinematic source model introduced by Ruiz *et al.* (2011), hereinafter denoted as the Ruiz integral kinematic (RIK) model. High-frequency ground-motion modeling requires a stochastic component. In RIK, it is represented by a random distribution of overlapping subsources with fractal number-size distribution that compose the source model. The particular distribution of the RIK subsources is constrained by the retrieved low-frequency slip model from the inversion. Besides the fact that the RIK model provides consistently omega-squared spectral decay at high frequencies, it allows for modeling the frequency-dependent directivity effect with various strengths. The model with the weakest (high-frequency) directivity, being characterized by complex rupture propagation along the fault, is demonstrated to provide synthetics with the smallest modeling bias and variance when compared with the velocity recordings.

Table 1
Parameters of the Earthquake Source Model Including Details of the Model Setup for the Low-Frequency Slip Inversion and the Ruiz Integral Kinematic (RIK) Model Used in the Broadband Modeling

	Parameter	Definition
General Source Parameters	Origin time	24 August 2014, 10:20:44
	Epicenter location	38.220° N, 122.313° W
	Hypocentral depth	10 km
	Fault size	15 km × 10 km
	Fault mechanism	Strike 155°, dip 82°, rake −172°
	Scalar seismic moment	1.6×10^{18} N·m
	Location of hypocenter on the fault	12.5 km along strike, 0 km from the fault bottom
Parameters Specific to the Slip Inversion	Fault discretization	750 m × 625 m
	Smoothing parameter (σ_D)	0.1 m (see Gallovič *et al.*, 2015)
Parameters Specific to the RIK Model	Fault discretization	100 m × 100 m
	Slip pulse width (L_0)	3 km (weak- and moderate-directivity model); 0.75 km (Strong-directivity model)
	Number of subsources	925
	Subsource radii	2.5–0.2 km
	Earthquake stress drop	1 MPa
	Parameter *a* (see equation 2)	0.5
	Rupture velocity	$0.8 \times V_S$ (V_S follows the velocity depth profile; Ⓔ see Table S2)

DATA AND CRUSTAL MODEL

I have downloaded the raw accelerometric data from the database of the Center for Engineering Strong Motion Data (CESMD, see Data and Resources) recorded at stations distant up to 15 km from the fault. Figure 1a shows the station distribution together with the earthquake hypocenter and fault. The stations are also listed in Ⓔ Table S1 (available in the electronic supplement to this article), together with the network and site information as available in the CESMD database. Unfortunately, only two stations have been assigned National Earthquake Hazards Reduction Program (Dobry *et al.*, 2000) site classes, namely stations 68150 (class D) and 68310 (class C). Regarding the latter station, it is the deepest station from a geotechnical array (at 44.5 m) in Vallejo. I note that there are other two nearby stations available in Vallejo (California Geological Survey station 68294, Broadway and Sereno, and USGS station 1759, Fire Station). However, because for my purpose the recordings are very similar with each other, I prefer to use only the borehole station as being least affected by the site effects.

The acceleration data were detrended, band-pass filtered using one-way (causal) Butterworth filter of the fourth order, once- or double-integrated to velocity or displacements, respectively, and eventually undersampled. The high-pass filtering at 0.05 Hz removes the low-frequency part of the wavefield that is corrupted by the instrumental noise. The low-pass filter depends on the particular application. In the slip inversion, I assume the filtering frequency at 0.5 Hz because the 1D crustal model considered (see below) is not able to model Green's functions (GFs) at higher frequencies with the required accuracy. For the broadband modeling, I consider filtering frequency at 5 Hz as sufficient for the velocity recordings and to limit the computational expense. The horizontal components were rotated to the F-P and F-N components. No time shifts were applied.

For the wave-propagation modeling, I use a modification of the 1D layered velocity model GIL7 (Stidham *et al.*, 1999; see Ⓔ Table S2). The original model has 1-km-deep subsurface layer with *S*-wave velocity of 1.5 km/s. Because the station sites have lower subsurface velocities, I have introduced two additional layers with subsurface velocity representing soft-rock site properties (see Ⓔ Table S2). Nevertheless, I note that, in the 1D modeling, such modifications lead to just minor amplification at higher frequencies and thus are not critical in the modeling. Full wavefield GFs are calculated using the discrete wavenumber technique (Axitra code, Kennett and Kerry, 1979; Bouchon, 1981; Coutant, 1989). No stochastic GFs are used throughout the whole study.

SLIP INVERSION

Basic source parameters are listed in Table 1. I adopt the USGS location parameters (see Data and Resources) and the mechanism from the Northern California Earthquake Data Center (see Data and Resources). The planar fault is 15 km × 10 km,

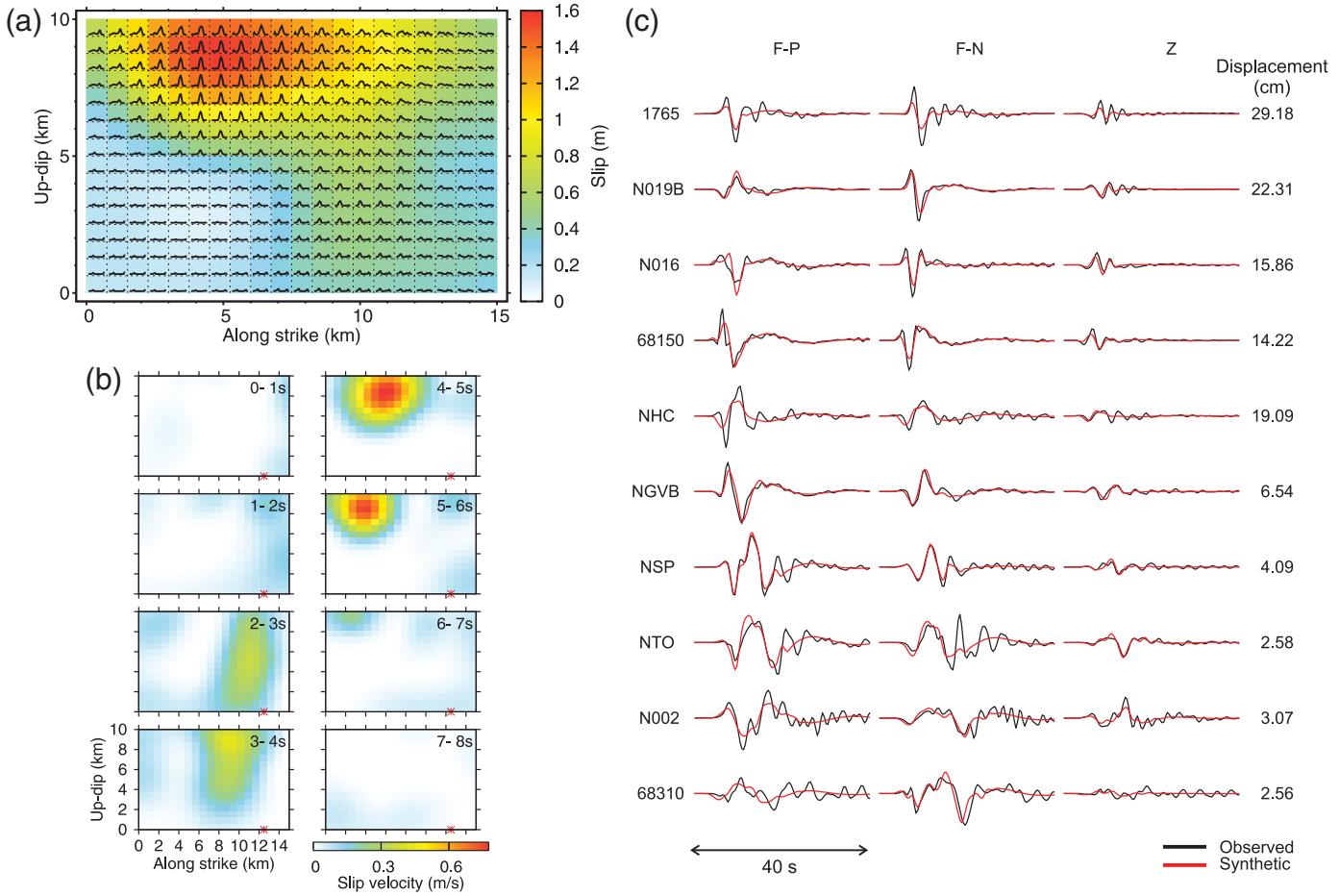

▲ **Figure 2.** Result of the linear slip inversion by the Gallovič *et al.* (2015) method considering slip-rate positivity and spatial smoothing by means of a prior covariance matrix. (a) Final slip is shown using the shaded scale, with superimposed slip rates as inferred from the inversion; the duration of the slip rates cover 0–8 s after the hypocentral time. (b) Snapshots of the rupture propagation suggesting up-dip and against-strike propagation (northward). Asterisks denote the hypocenters (not considered in the inversion). (c) Comparison of observed and synthetic displacement waveforms (0.05–0.5 Hz) corresponding to the inverted source model (variance reduction 61%). (F-P, fault-parallel component; F-N, fault-normal; and Z, vertical component.) Station names are to the left (see Fig. 1 for their location).

with the hypocenter located at its bottom edge at a depth of 10 km.

I use the recently introduced slip inversion technique by Gallovič *et al.* (2015) exploiting the linear formulation of the forward problem. The method has been recently tested on a source inversion validation benchmark test (Gallovič and Ampuero, 2015) and applied to the 2014 Cephalonia earthquake doublet (Sokos *et al.*, 2015). Parameters of the inverse problem are the slip-rate functions discretized in time and along the fault. The slip rates span an 8-s-long time window, starting at the hypocentral time; the nucleation point is not prescribed in the inversion. The inverse solution is regularized by (1) spatial smoothing by means of a prescribed prior covariance function with the k^{-2} spectral decay (k being the wavenumber) and (2) positivity constraint by means of using the nonnegative least-squares approach by Lawson and Hanson (1974) to minimize the L2 misfit function in displacements filtered between 0.05 and 0.5 Hz. The weight of the smoothing constraint is set to $\sigma_D = 0.1$ m (for the formal definition of σ_D, see Gallovič *et al.*, 2015), which corresponds to rather stronger smoothing. Gallovič *et al.* (2015) demonstrated by means of synthetic tests in a very similar setting (source–station geometry, frequency range, etc.) that the use of low-frequency waveforms together with the stronger smoothing prevents the occurrence of artificial slip-rate peaks when the 3D structural model is approximated by a 1D velocity model. This suggests that the inversion does not require any temporal alignment of the GFs, thus providing a robust inversion result. This is important because, especially at near-source stations, such alignments should, in principle, vary along the fault as the propagating wavefields sample different volumes of the velocity structure.

The result of the inversion is shown in Figure 2. In particular, Figure 2a shows the final slip distribution overlaid by the individual slip-rate functions from the inversion. The slip distribution is characterized by a large slip patch at rather shallow depths. Figure 2b displays the evolution of the inverted

rupture model in terms of slip-rate snapshots. I note that the inversion result cannot be taken at face value as discussed by Gallovič *et al.* (2015) due to the generous model parameterization, applied smoothing, and limited frequency range. Regarding the former, because the rupture can generally occur at any place at any time, the inferred model contains some "ghost" features, presumably due to imperfections in GFs. Despite this issue, the general feature of the result is that the rupture propagated from the hypocenter upward and against the fault strike (northward). Unfortunately, further details are hard to reveal. Indeed, the inferred source model represents the true model after spatial smoothing applied at each time instance (see the synthetic tests by Gallovič *et al.*, 2015), requiring careful interpretation of the inferred rupture image. The large asperity is rather biased toward too-shallow depths (note that the surface fault traces showed 40–46 cm large displacements). Inspecting the snapshots in Figure 2b, the slip rates seem negligible during the first 2 s, suggesting rather low slip or slip rates at the hypocenter. Larger slip rates then occur ~5 km from the hypocenter. After another 3 s, the shallow asperity located ~12 km from the hypocenter is slipping at larger slip velocities. These observations can help to roughly estimate that the rupture speed is approximately ~2.5 km/s, noting that this value is rather underestimated due to the severe spatial smoothing as shown by Gallovič *et al.* (2015) using synthetic tests. Figure 2c shows the comparison between the observed and synthetic displacements. The fit is best at the near-fault stations. At the distant stations the 1D model does not explain the short-period oscillations and later arrivals, being presumably related to the complexity in the wave propagation in the heterogeneous crust.

The inferred slip model is close to the model by Wei *et al.* (2015) and geodetic model by Melgar *et al.* (2015). Seismic and seismogeodetic model by Melgar *et al.* (2015), as well as models by Barnhart *et al.* (2015) and Dreger *et al.* (2015), are characterized by a deeper main asperity (3–8 km). Ji *et al.* (2015) inferred a model with an ellipsoidal slip of approximately 12 km × 5 km oriented toward top left from the hypocenter. The slip rates inferred by Melgar *et al.* (2015) are of similar shape as those retrieved in this study but with rise time approximately two times shorter (1 s). All the models consistently show up-dip and northward rupture propagation. I note that while the source model derived here is smoother than the others, it is not sensitive to minor changes of the crustal model (i.e., no artificial time shifts of the GFs are required).

RUIZ INTEGRAL KINEMATIC (RIK) SOURCE MODEL

Model Description

Here, I use an advanced kinematic source model introduced by Ruiz *et al.* (2011), the RIK model. It was developed for earthquake ground-motion simulations utilizing the representation integral in the full frequency band (no composite or stochastic modeling needed) and providing omega-squared spectral decay at high frequencies. I applied some simplifications and minor modifications to the original method, following specific properties of my particular application (see below). The RIK model is composed of randomly distributed circular subsources with fractal number-size distribution with dimension $D = 2$, which is the same as considered in other kinematic models (e.g., Zeng *et al.*, 1994; Gallovič and Brokešová, 2007). In the present model, kinematic properties (including the rupture propagation) are prescribed individually to each of the subsources, and thus each subsource is characterized by its own slip-rate functions along its areal extent. The total slip rates of the RIK model are eventually evaluated on a dense regular discretization grid along the fault by summing up slip-rate contributions from all the subsources.

Regarding the subsource distribution, I introduce a minor simplification to the original Ruiz *et al.* (2011) approach, considering that subsource radii R are equal to integer fractions n of the fault width W, that is, $R = W/n$. For the particular number-size distribution, the number of subsources at level n is equal to $2n - 1$. The subsources are distributed randomly along the fault, following a prescribed spatial probability density function (PDF), which is considered equal to the normalized slip distribution from the inversion (see above). The subsources have the crack-model slip distributions Δu^R, that is,

$$\Delta u^R(\rho) \sim \sqrt{R^2 - \rho^2} \quad \text{if } \rho < R \quad \text{and}$$
$$\Delta u^R(\rho) = 0 \text{ otherwise,} \tag{1}$$

in which ρ is the distance from the subsource center. The constant of proportionality in equation (1) is determined so that the total seismic moment fits the prescribed scalar seismic moment M_0. This fractal decomposition of the source model implies that the slip decays with k^{-2} at high wavenumbers k (Gallovič and Brokešová, 2007; Ruiz *et al.*, 2011), implying k^{-1} decay of the stress distribution, which was shown by means of theoretical considerations as physically plausible (Andrews, 1980).

The rupture is assumed to propagate in the form of a slip pulse of width L_0 with the Brune's pulse (Brune, 1970) as the slip-rate function. I note that if rise time was constant, the source spectrum would decay as omega squared only up to the reciprocal of the rise time, after which the spectrum would decay faster due to the low-pass filtering effect of the consider slip-rate function. To correct for this, Bernard *et al.* (1996) introduced the concept of the wavenumber-dependent rise time. In particular, in the RIK model, the rise time depends on subsource radius R as

$$\tau(R) = \tau_{\max} = aL_0/v_r \quad \text{if } 2R > L_0 \quad \text{and}$$
$$\tau(R) = a(2R)/v_r \text{ otherwise,} \tag{2}$$

in which $a \sim 1$ is a free parameter and v_r is the rupture velocity equal to a prescribed fraction of the local S-wave velocity following the crustal model considered. Consequently, one avoids unrealistically strong ground motions when dealing with subsurface rupture because the rise time generally increases with

the decreasing depth (Graves and Pitarka, 2010). Furthermore, the dependence of the rise time on the subsource radii (also called the k-dependent rise time) also has implications for the strength of the directivity effect. As discussed by Bernard *et al.* (1996) and Gallovič and Brokešová (2004), the source spectral amplitudes between roughly the corner frequency and the reciprocal of the maximum rise time ($1/\tau_{max}$) are proportional to C_d^2, in which $C_d = 1/(1 - \alpha \cos\theta)$ is the classical directivity coefficient, with α representing the ratio of rupture and shear wavespeeds and θ being the station angle from the rupture direction. At frequencies larger than $\sim 1/\tau_{max}$, the directivity effect is reduced to C_d^1, while preserving the omega-squared spectral decay. I also note that the use of the k-dependent rise time implies a positive correlation between the slip and the rise time as found in dynamic source simulations (Schmedes *et al.*, 2010).

In terms of the rupture propagation, Ruiz *et al.* (2011) introduced a concept of small- and large-scale rupture fronts. In particular, each point on subsources with radius $R > L_0$ starts to slip upon arrival of the macroscopic rupture front from the hypocenter. Contrarily, each smaller subsource has its own random point, from which a small-scale rupture is initiated after the random point is reached by the macroscopic rupture front. In other words, rupture time at a given point on the small subsource is a sum of the arrival time of the macroscopic rupture front to the random point and the time delay corresponding to the small-scale rupture propagation from the random point. This way, the directivity effect is weakened even further, to effectively $C_d^0 = 1$ (i.e., is isotropic).

All source parameters describing the RIK model are listed in Table 1. The values of the rupture velocity, slip pulse width, and rise-time parameter a of equation (2) were found by trial-and-error modeling to best fit the observed duration of the major velocity pulses, their peak values, and the spectral content at all the stations. In particular, the rupture velocity is equal to $0.8V_S$, which is consistent with other studies (Dreger *et al.*, 2015; Wei *et al.*, 2015). Because of the large uncertainty of the strongly smoothed source model obtained by the low-frequency inversion, I employ only the final slip distribution (Fig. 2a) as the PDF function for the random distribution of the subsources along the fault plane. Figure 3a shows the distribution of just the largest subsources (for clarity), together with the resulting slip distribution. I note that the RIK model has much smaller slip values at the surface than the slip model from the low-frequency inversion (compare Fig. 3a and 2a). Conclusions regarding the directivity effect (as drawn below) are based exclusively upon the RIK model and are thus not compromised by the rather biased surface slip values from the slip inversion.

In the following, I test three models with various strengths of the directivity effect. The first one, the weak-directivity model, is the one described above. The moderate-directivity model differs in that the small-scale rupture front on the subsources is the same as the large-scale front, which makes the model close to the classical kinematic models with a single rupture front. The third model, with the strong directivity, has a narrower slip pulse width, that is, shorter maximum rise time (see Table 1).

Moment rate functions corresponding to the three directivity models are displayed in Figure 3b in both the temporal and spectral domains. The Fourier spectrum of the source time functions is well fitted by the Brune model (Brune, 1970) with stress drop of 1 MPa (Fig. 3b), which is close to the typical regional value of 5 MPa as determined by Baltay and Hanks (2014). Figure 3c shows examples of slip rates at two time instances to visualize the difference between the rupture propagation of the three models. Basically, in the weak-directivity model, the instantaneous slip-rate maxima are less coherently aligned along the rupture front than in the other two models. The strong-directivity model has a narrower pulse width with larger slip-rate maxima. Figure 3d displays also the apparent moment rate functions at two stations, one in the forward (N019B) and one in the backward (68310) directivity area. Although the apparent time functions of the three models are similar at long periods, they differ in the strength of the short-period oscillations (especially in the forward-directivity station N019B) owing to the different style of the rupture propagation. This is clearly visible in the apparent acceleration source spectra in Figure 3d. Because of the short maximum rise time, the strong-directivity model has the C_d^2 spectral amplification in a broad range of frequencies. Although the difference between the weak- and moderate-directivity models is not large, the former has slightly smaller and larger amplitudes at the forward- and backward-directivity stations, respectively, due to the additional random propagation inside the individual subsources. A similar effect is achieved when considering radiation from the centers of the subsources, as considered in the composite source models (e.g., Zeng *et al.*, 1994; Gallovič and Brokešová, 2007).

Modeling Results (Weak-Directivity Model)

Figure 4 shows comparisons between the observed and synthetic velocity waveforms in the frequency range 0.05–5 Hz for the weak-directivity model. Because of the fact that at such large frequencies both the source and propagation medium have a fractal (random) nature, a model cannot capture all details of the velocity records. Thus the point is not to fit the observed waveforms in detail (i.e., wiggle for wiggle), but rather to match their basic characteristics in the temporal domain and their spectral response. Below, I discuss that this is the case of the model presented here.

In particular, at the Z component, the peak values and the dominant period of the first arrivals are correctly captured by the model, except for station 68310, the amplitude of which is underestimated significantly. At the F-N component, the forward-directivity velocity pulse is fit very well at station N019B. Interestingly, the model captures (although not perfectly) the more complex shape of the pulse at station 1765, lying just on the opposite side of the fault (Fig. 1) and thus being a consequence of the up-dip directivity. Stations N016 and 68150, lying close to the central part of the fault, exhibit two-sided pulses at the F-N component, which are explained relatively

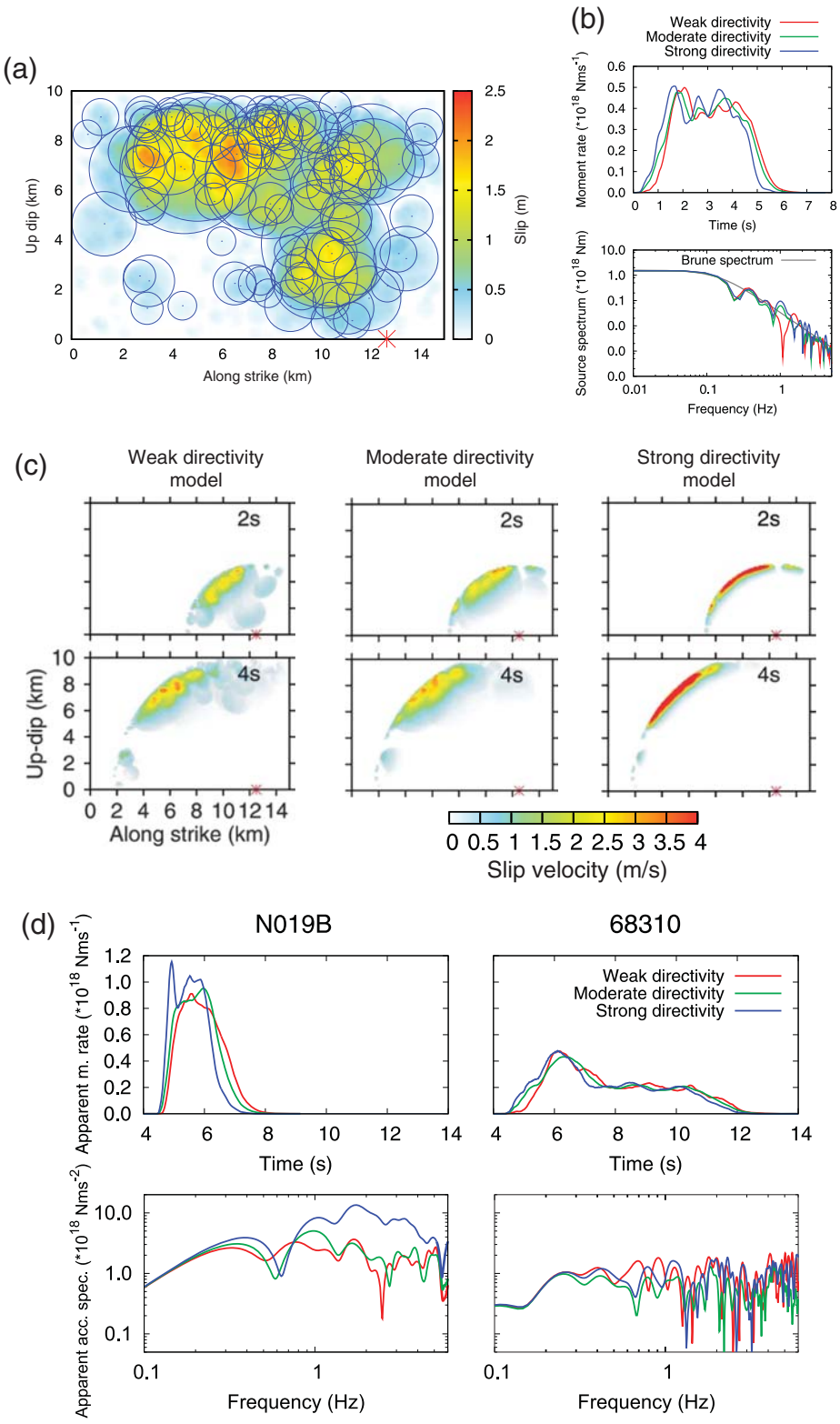

▲ **Figure 3.** Properties of the Ruiz integral kinematic (RIK) model used in the velocity waveform modeling (0.05–5 Hz). (a) Slip model (shaded scale) built by randomly distributing subsources (circles) with fractal number-size distribution (see the Model Description section for details); only the largest subsources are plotted for the sake of clarity. The red asterisk denotes the hypocenter. (b) Moment rates and their Fourier spectra are shown for the three directivity models (considering the same subsource distribution). In the spectral plot, the Brune's model spectrum (Brune, 1970) with stress drop of 1 MPa is shown. (c) Snapshots of the rupture propagation at two time instances for the three directivity models. (d) Apparent moment rate functions (top) and apparent source acceleration spectra (bottom) for the three directivity models at two stations lying in the forward (left) and backward (right) directivity regions.

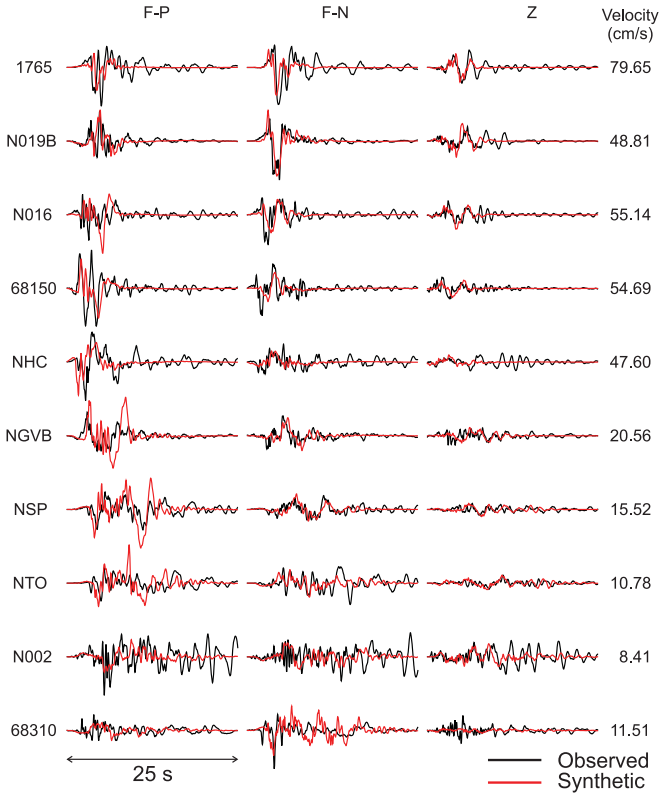

▲ **Figure 4.** Comparison of observed and synthetic velocity waveforms in broad frequency range (0.05–5 Hz) as obtained by the RIK model in the weak-directivity mode (see the Model Description section for details). For the other directivity models, see Ⓔ Figure S1. Station names are to the left (see Fig. 1 for their location).

well by the model. The shorter-period content of the F-P components at stations 1765, N019B, N016, and 68150 is predicted as well. Interestingly, the model also correctly captures the presence of the dominant broad pulse at the F-P component and weaker F-N component at station NHC, which lies nearest to the hypocenter.

The more distant stations NGVB, NSP, and NTO have longer duration of the strong-motion phase and more rich spectral content at all components. Again, the model fits these recordings relatively well, despite the fact that these stations are more affected by the complexity of the wave propagation (see the overestimated later phases at the F-P components). Unfortunately, the stations in the backward-directivity zone (N002 and 68310) lie at relatively large distances. In particular, station N002 is dominated by the long duration of almost monochromatic oscillations clearly related to some basin effects. Nevertheless, the model fits the duration of the earlier part with higher frequency content. At station 68310 the model captures the position of the maximum peak at the F-N component, while it exceeds the amplitudes of the later long-period arrivals.

Figure 5a shows the comparison of the synthetics (red curves) with the observed data (black curves) in terms of the Fourier spectrum. The observed data were tapered at 20 s after the hypocentral time to effectively remove spectral contributions due to the later low-frequency oscillations related to the unmodeled propagation effects. For clarity of the presentation, the spectra are smoothed by the Konno and Omachi (1998) method. In Figure 5a, I show only the vertical component as an example; for the other components, see Ⓔ Figure S2. With few exceptions, one can see that, generally, the modeled spectrum (red) follows the observed spectral fall-off. At some cases, the synthetic spectra underestimate the observed ones at frequencies >1 Hz (e.g., N68150, NGVB). The worst situation is at station 68310, where the observed spectrum is significantly underestimated at frequencies >0.5 Hz, although at low frequencies the model performs relatively well. I ascribe this problem to the radiation pattern effect that is in reality weakened at higher frequencies due to the 3D wave-propagation effects as suggested by numerical modeling in random media (e.g., Gallovič *et al.*, 2010; Imperatori and Mai, 2012).

Figure 5b shows the modeling bias (red crosses) in terms of PGV defined as the natural logarithm of the ratio between the observed and modeled PGV. The figure also shows mean values and standard deviations evaluated over the stations for the individual components (the outlying large bias at vertical component of the 68310 station has been removed from this calculation). I emphasize that the bias is close to the zero line (corresponding to perfect fit) with very low standard deviation (0.02–0.26). Figure 6 (left column) then displays the modeling bias in terms of the acceleration response spectra at the individual components. The mean bias (black curve) is close to zero at the F-N component. At the others, the bias suggests minor underestimation (−0.3). The variance of the bias is also rather low (0.2–0.4), especially at the F-N component.

Modeling the Strength of the Observed Directivity Effect

Here, I discuss the modeling bias when the other two strengths of the directivity effect are considered. I remind the reader that Figure 3 shows properties of the three directivity models in terms of the moment rate functions, rupture propagation snapshots, and the apparent source time functions. Ⓔ Figures S1 and S2 display all simulated velocity waveforms and their smoothed Fourier spectra, respectively, for all the directivity models.

Figure 5a illustrates the effects of the directivity strength on the Fourier spectra. Major differences between the directivity models are visible mostly at the forward-directivity stations (top four panels in Fig. 5a), where the strong directivity leads to clear overestimation of the observed spectra at frequencies >1 Hz. This is also evident in Ⓔ Figure S1c as too-strong high-frequency oscillations. At the other stations, the differences are also significant. At the backward-directivity station N002, the strongest amplitudes are predicted by the strong-directivity model. I assign this to the up-dip rupture propagation that amplifies the N002 synthetics. Indeed, at station 68310, which is not affected by the up-dip propagation, the largest Fourier amplitudes are obtained by the model with the weakest directivity. Overall, both the weak- and moderate-directivity models perform similarly well.

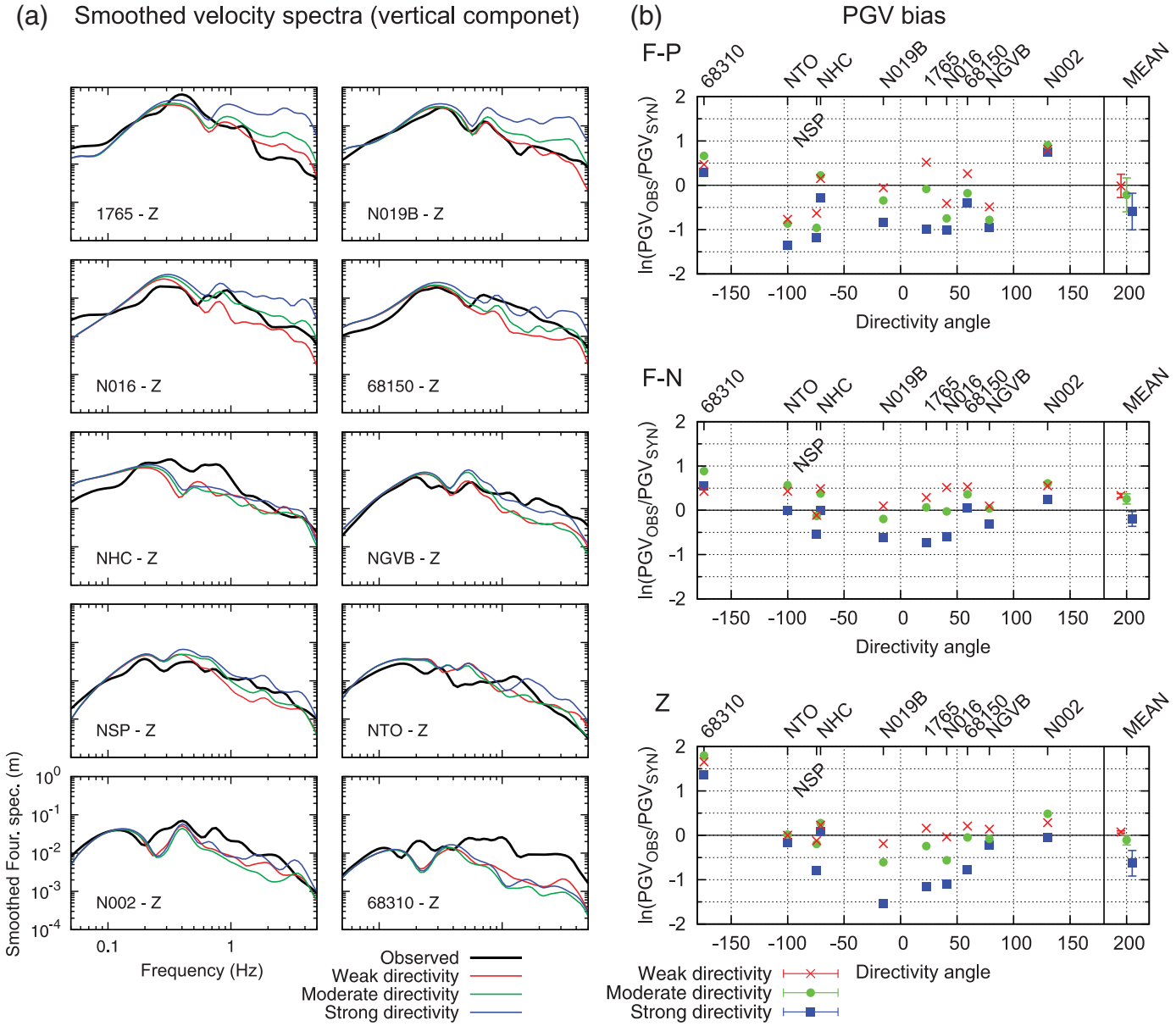

▲ **Figure 5.** Result of the broadband velocity waveform modeling using the RIK model in the three directivity modes (see legend). (a) Comparisons of the directivities in terms of the smoothed Fourier spectra at the individual stations (vertical component) are shown. For the other components, see Ⓔ Figure S2. (b) Modeling bias is shown in terms of peak velocities (PGV), defined as the natural logarithm of the ratio of the observed and synthetic PGV plotted as a function of the directivity angle (i.e., clockwise-positive angle from the antistrike direction) for the three directivity models (shaded). The mean and standard deviation evaluated over each station component are shown with error bars (denoted as MEAN). The *Z* component of station 68310 has been removed from the mean and variance calculations as an outlier.

Figures 5b and 6 display the modeling bias for all the directivity models in terms of PGV and response spectra, respectively. As one can see, especially the strong-directivity model clearly overestimates the observed data, which is expressed by the negative values of the mean bias. The moderate- and weak-directivity models perform better in this sense. In particular, the moderate-directivity model shows slightly better fit at F-N and *Z* components, whereas the F-P component is fitted better by the weak-directivity model. I point out that underprediction at high frequencies is preferable because the site effects are rather underestimated here, considering only a generic soft-rock properties.

I emphasize that when discussing the performance of the individual models in modeling the directivity effect, one needs to consider mainly the variability of the bias (modeling variance) over the stations, keeping in mind that the directivity affects the waveforms systematically in the azimuthal sense. Although site effects would also contribute to the modeling variance, their involvement in the modeling would (statistically speaking) decrease the modeling variances but almost equally

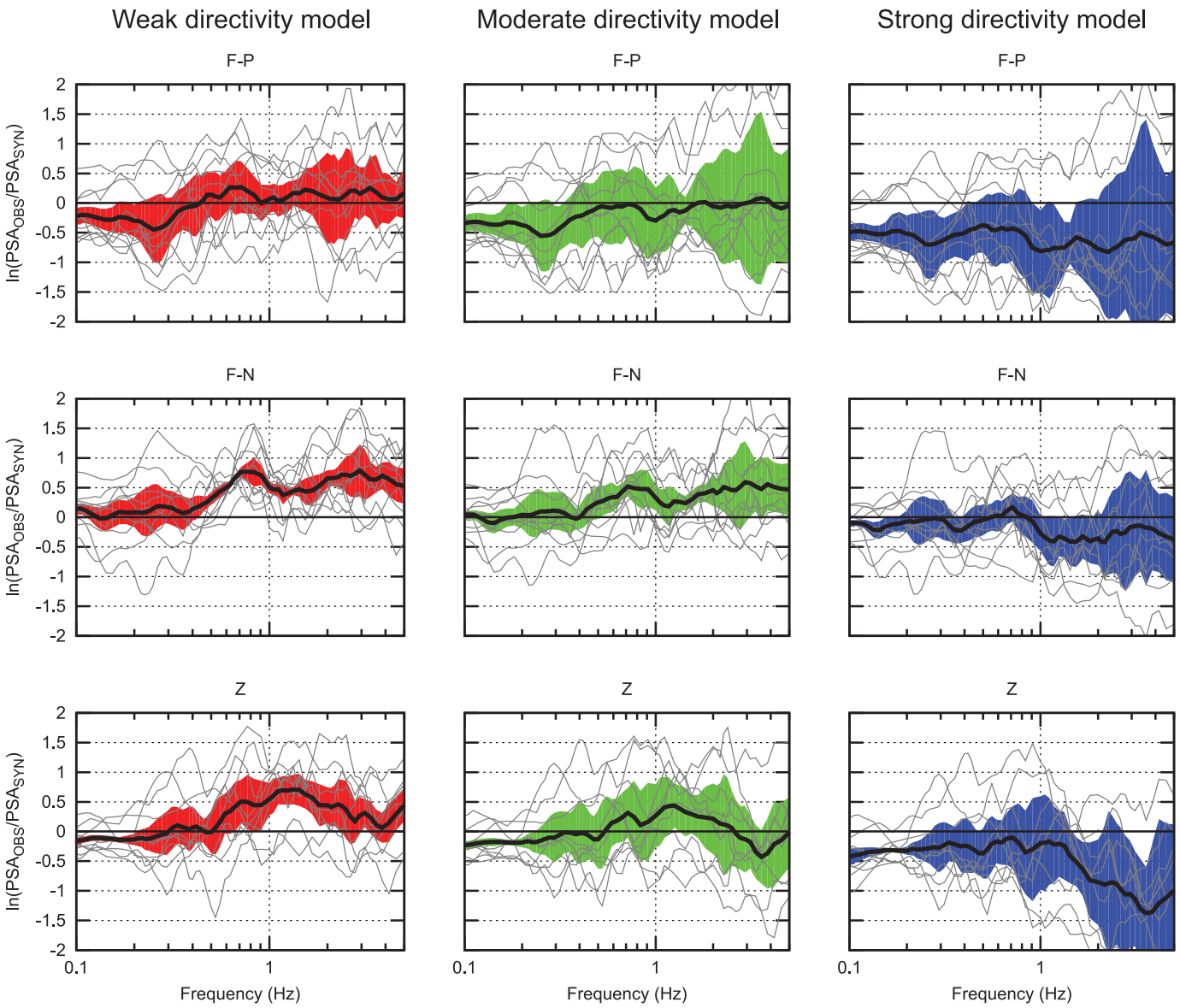

▲ **Figure 6.** Modeling bias in terms of acceleration response spectra, defined as the natural logarithm of the ratio of the observed and synthetic pseudospectral acceleration (PSA) plotted as a function of frequency for the three directivity models (columns) and individual components (rows). Gray lines correspond to the modeling bias at the individual stations. The black line and shaded strip denote the mean over stations and ±1 standard deviation, respectively. Shades distinguish the directivity models as in Figure 5. The *Z*-component for station 68310 was removed from the mean and variance calculations as an outlier. (Abbreviations are as in Fig. 2.)

for all the directivity models. In particular, the variability of the modeling bias across the stations (expressed by the error bars in Fig. 5b and shaded strips in Fig. 6) is consistently smallest for the weak-directivity model. The moderate-directivity model provides the bias variance similar to the weak-directivity model but only at the F-N component. The strong-directivity model clearly overestimates the directivity as expressed by the largest modeling variance. I note that the strong-directivity model cannot be improved by decreasing the rupture velocity. Indeed, the required reduction of the rupture velocity to diminish the forward-directivity effect would lead to significant overestimation of the durations of the observed velocity pulses. Thus, I conclude that the strong-directivity model can be considered unrealistic. Although, of the three models, the weak-directivity model best explains the data in terms of modeling variance, the performance of the moderate-directivity model is also satisfactory. I emphasize that both the latter two models are characterized by a directivity effect that weakens with increasing frequency, which is a crucial feature to fit the observed records.

DISCUSSION AND CONCLUSIONS

In the present article, I performed a seismological analysis of the 2014 South Napa earthquake with the emphasis on its

directivity effect. Using the near-fault high-quality recordings, a slip inversion was performed (in the 0.05–0.5 Hz frequency range), retrieving up-dip and against-strike (northward) rupture propagation. The rupture is characterized by a major slip patch located at depths shallower than 5 km. I note that, although the source model is rather smooth with respect to the other published models (Dreger *et al.*, 2015; Ji *et al.*, 2015; Wei *et al.*, 2015), it is robust in terms of quality of the crustal model considered, not requiring use of any artificial time shifts of the GFs. The inferred slip model is used to constrain a broadband (0.05–5 Hz) source model to predict the velocity waveforms. Specifically, I have considered the RIK model introduced by Ruiz *et al.* (2011). It is characterized by the k^{-2} slip distribution and the k-dependent rise time, correctly providing the omega-squared spectral decay at high frequencies (see Ruiz *et al.*, 2011). The advantage of this model is that one may control the strength of the directivity effect, including its frequency dependence by considering the rupture propagation as more (or less) coherent. In particular, I have considered three models with weak-, moderate-, and strong-directivity effects. The first two models are characterized by decreasing strength of the directivity effect with increasing frequency.

The weak- and moderate-directivity models are shown to best fit the observed velocity waveforms in both the temporal domain (Fig. 4), including the peak values (Fig. 5b), and in terms of the response spectra (Fig. 6). Those two models explain the observed data with both the smallest modeling bias and modeling variance (variability of the bias over stations). This is particularly important because any mismodeling of the directivity effect of this unilateral event introduces a systematic azimuthally dependent variability in the modeling bias, thus increasing the modeling variance. In this sense, the weak-directivity model fits the data slightly better than the moderate-directivity model. Because of the very large modeling variance, the strong-directivity model can be confidently considered as unrealistic.

All three models have rise time proportional to the reciprocal to the local rupture velocity and to the spatial scale of slip. Therefore, rise times are largest at the shallow asperity, as also observed by Ji *et al.* (2015) and Wei *et al.* (2015). However, this feature alone cannot explain the observed weak high-frequency directivity, because only the weak- and moderate-directivity models are able to model correctly the low-frequency directivity pulses observed at the forward-directivity stations while not overpredicting the high-frequency spectral content. The models have rupture speed corresponding to 80% of the depth-dependent shear-wave velocity (see Table 1), which is almost the same value as inferred by other authors (e.g., Dreger *et al.*, 2015; Wei *et al.*, 2015). Such a large rupture velocity would lead to very strong amplification at high frequencies if a coherent rupture is considered as illustrated by the strong-directivity model. The weak- and moderate-directivity RIK source models are characterized by complex style of rupture propagation at short wavelengths, leading to the weakening of the directivity effect at high frequencies. The weak high-frequency directivity model thus explains the weak imprint of the rupture directivity in the ShakeMaps, despite the mostly unilateral character of the rupture propagation. Furthermore, it also potentially explains the observed frequency dependence of the residuals with respect to GMPEs analyzed by Baltay and Boatwright (2015); see also the Introduction.

The modeling is based on a relatively complex source model embedded in a 1D wave-propagation medium. I admit that the 1D wave-propagation model is a significant simplification, which, on the other hand, allows for extensive tests because the computational cost is rather small (approximately three days to calculate GFs on a common personal computer, and then just minutes to generate the RIK slip rates and evaluate the representation integral for each source model). This way, because the source model is built upon characteristics inferred by the slip inversion, the modeling allows for identification of features in the broadband observed waveforms that can be ascribed to the source effects. Indeed, while the later arrivals are not captured by the model (being presumably induced by 3D crustal heterogeneities), the early parts of displacement and velocity waveforms are explained relatively well. Indeed, Dreger *et al.* (2015) and Wei *et al.* (2015) analyzed effects of the 3D medium on the South Napa earthquake synthetics (up to 1 Hz), demonstrating mostly amplification of the vertical components (up to approximately two to three times) and occurrence of later phases at more distant stations. At the near-fault stations, the first pulses at most of the horizontal components are not altered significantly. In some cases (e.g., station 1765), the 3D velocity model slightly improves the fit, whereas at others the 3D medium does not help to explain the data. Because these effects are dependent on the actual source model, in a future study I plan to combine the source model developed here with the wave propagation in a complex 3D crustal model (including random heterogeneities and topography at short scales) to explore its effects on the present source model. Nevertheless, although I expect that taking into account the complexity of the velocity structure will improve the modeling bias, the modeling variance will change for all the three models in the same way, thus preserving my conclusions regarding the frequency dependence of the directivity.

Another simplified aspect of the source models of this study is related to the simplified west-dipping planar fault model geometry as adopted from the CMT solution of Berkeley. Other authors use different fault geometries, including those dipping east and/or consisting of two segments, as suggested by the observed surface ruptures (Wei *et al.*, 2015). We tested other fault geometries in the slip inversion, always obtaining a similar data fit but with more pronounced ghost features in the inferred slip rates. The impact on the RIK modeling has not been extensively studied yet. Although the fault geometry will have some effect on the velocity synthetics (perhaps eventually improving the modeling bias), I expect that it will affect the modeling variance of all three models in the same way, thus preserving the directivity-related conclusions as discussed also above in the case of the 3D velocity model. Nevertheless, this aspect also deserves further study.

The RIK source model is characterized by complex style of rupture propagation especially at short wavelengths, which leads to weakening of the directivity effect at high frequencies. I note that the present model is not unique in providing synthetics with the weak high-frequency directivity effect. Widely and successfully used source models for strong-motion simulations utilizing the so-called composite modeling at high frequencies (Zeng *et al.*, 1994; Pitarka *et al.*, 2000; Gallovič and Brokešová, 2007) implicitly consider no or very weak directivity effect at high frequencies (Gallovič and Burjánek, 2007). Analysis of observed spectra by Somerville *et al.* (1997) suggested that the strength of the directivity effect decreases with increasing frequency. Fletcher (2014) observed such a frequency-dependence of the directivity in the USGS Parkfield Seismic Array recordings of the 2004 Parkfield earthquake. By means of broadband modeling of the 2009 M_w 6.3 L'Aquila earthquake recordings, Ameri *et al.* (2012) showed that the observed directivity effect is reduced significantly already at frequencies >0.5–2 Hz (depending on the station fault distance). All this thus suggests that the feature of the rather weak source directivity is not unique to the 2014 South Napa, but is perhaps common to other earthquakes. Interestingly, similar behavior of the frequency-dependent directivity effect was observed by Day *et al.* (2008) in laboratory foam rubber experiments simulating earthquake with a unilateral rupture propagation. Day *et al.* (2008) discussed possible rheological features that may be responsible for considerable complexity of the rupture propagation. Those are, for example, localized strong barriers that initially withstand the main rupture front arrival and break later with rupture propagation direction even different from that of the main rupture front, as in the RIK model (see also laboratory experiments by Latour *et al.*, 2013). Such barriers can be also formed by irregularities in the fault geometry (Shi and Day, 2013) that are not included in our simulations and might represent another extension of the present work.

DATA AND RESOURCES

Accelerometric data were downloaded from the freely available online repository, Center for Engineering Strong Motion Data (CESMD, http://strongmotioncenter.org, last accessed October 2015). The ShakeMap shown in Figure 1 was downloaded from its archive (http://www.quake.ca.gov/shake/archive/, last accessed October 2015). Location parameters were taken from the U.S. Geological Survey Earthquake Location Archive (http://earthquake.usgs.gov, last accessed October 2015). Earthquake mechanism was adopted from the Northern California Earthquake Data Center (http://www.ncedc.org/, last accessed October 2015).

ACKNOWLEDGMENTS

The reviews provided by A. Rodgers, D. Melgar, and two anonymous reviewers helped to improve the manuscript. I acknowledge financial support from the Czech Science Foundation project 14-04372S and the Charles University project UNCE 204020/2012.

REFERENCES

Ameri, G., F. Gallovič, and F. Pacor (2012). Complexity of the M_w 6.3 2009 L'Aquila (central Italy) earthquake: 2. Broadband strong motion modeling, *J. Geophys. Res.* **117,** no. B04308, doi: 10.1029/2011JB008709.

Andrews, D. J. (1980). A stochastic fault model: 1. Static case, *J. Geophys. Res.* **85,** 3867–3877.

Baltay, A., and J. Boatwright (2015). Ground motion observations of the 2014 South Napa earthquake, *Seismol. Res. Lett.* **86,** 355–360.

Baltay, A. S., and T. C. Hanks (2014). Understanding the magnitude dependence of PGA and PGV in NGA-West2 data, *Bull. Seismol. Soc. Am* **104,** 2851–2865.

Barnhart, W., J. R. Murray, S.-H. Yun, J. L. Svarc, S. V. Samsonov, E. J. Fielding, B. A. Brooks, and P. Milillo (2015). Geodetic constraints on the 2014 M 6.0 South Napa earthquake, *Seismol. Res. Lett.* **86,** 335–343.

Bernard, P., A. Herrero, and C. Berge (1996). Modeling directivity of heterogeneous earthquake ruptures. *Bull. Seismol. Soc. Am.* **86,** 1149–1160.

Bouchon, M. (1981). A simple method to calculate Green's functions for elastic layered media, *Bull. Seismol. Soc. Am.* **71,** 959–971.

Brocher, T. M., A. S. Baltay, J. L. Hardebeck, F. F. Pollitz, J. R. Murray, A. L. Llenos, D. P. Schwartz, J. L. Blair, D. J. Ponti, J. J. Lienkaemper, *et al.* (2015). The M 6.0 24 August 2014 South Napa earthquake, *Seismol. Res. Lett.* **86,** 309–326.

Brune, J. N. (1970). Tectonic stress and the spectra of seismic shear waves from earthquakes, *J. Geophys. Res.* **75,** 4997–5009.

Coutant, O. (1989). Program of numerical simulation AXITRA, *Research Report*, Laboratoire de Géophysique Interne et Tectonophysique, Université Joseph Fourier, Grenoble, France.

Day, S. M., S. H. Gonzalez, R. Anooshehpoor, and J. N. Brune (2008). Scale-model and numerical simulations of near-fault seismic directivity, *Bull. Seismol. Soc. Am.* **98,** no. 3, 1186–1206.

Dobry, R., R. D. Borcherdt, C. B. Crouse, I. M. Idriss, W. B. Joyner, G. R. Martin, M. S. Power, E. E. Rinne, and R. B. Seed (2000). New site coefficients and site classification system used in recent building seismic code provisions, *Earthq. Spectra* **16,** 41–67.

Dreger, D. S., M.-H. Huang, A. Rodgers, T. Taira, and K. Wooddell (2015). Kinematic finite-source model for the 24 August 2014 South Napa, Califonia, earthquake from joint inversion of seismic, GPS and InSAR data, *Seismol. Res. Lett.* **86,** 327–334.

Fletcher, J. B. (2014). Frequency-dependent effects of rupture for the 2004 Parkfield main shock, results from UPSAR, *J. Geophys. Res.* **119,** 7195–7208.

Gallovič, F., and J.-P. Ampuero (2015). A new strategy to compare inverted rupture models exploiting the eigen-structure of the inverse problem, *Seismol. Res. Lett.* **86,** doi: 10.1785/0220150096.

Gallovič, F., and J. Brokešová (2004). On strong ground motion synthesis with k^{-2} slip distributions, *J. Seismol.* **8,** 211–224.

Gallovič, F., and J. Brokešová (2007). Hybrid *k*-squared source model for strong ground motion simulations: Introduction, *Phys. Earth Planet. In.* **160,** 34–50.

Gallovič, F., and J. Burjánek (2007). High-frequency directivity in strong ground motion modeling methods, *Ann. Geophys.* **50,** 203–211.

Gallovič, F., W. Imperatori, and P. M. Mai (2015). Effects of three-dimensional crustal structure and smoothing constraint on earthquake slip inversions: Case study of the M_w 6.3 2009 L'Aquila earthquake, *J. Geophys. Res.* **120,** 428–449.

Gallovič, F., M. Käser, J. Burjánek, and Ch. Papaioannou (2010). Three-dimensional modeling of near-fault ground motions with nonplanar rupture models and topography: Case of the 2004 Parkfield earthquake, *J. Geophys. Res.* **115,** no. B03308, doi: 10.1029/2008JB006171.

Grapenthin, R., I. Johanson, and R. M. Allen (2014). The 2014 M_w 6.0 Napa earthquake, California: Observations from real-time GPS-enhanced earthquake early warning, *Geophys. Res. Lett.* **41,** 8269–8276.

Graves, R. W., and A. Pitarka (2010). Broadband ground-motion simulation using a hybrid approach, *Bull. Seismol. Soc. Am.* **100,** 2095–2123.

Imperatori, W., and M. P. Mai (2012). Broad-band near-field ground motion simulations in 3-dimensional scattering media, *Geophys. J. Int.* **192,** 725–744.

Ji, Ch., R. Archuleta, and C. Twardzik (2015). Rupture history of 2014 M_w 6.0 South Napa earthquake inferred from near fault strong motion data and its impact to the practice of ground strong motion prediction, *Geophys. Res. Lett.* **42,** 2149–2156.

Kennett, B. L. N., and N. J. Kerry (1979). Seismic waves in a stratified half space, *Geophys. J. Int.* **57,** 557–583.

Konno, K., and T. Omachi (1998). Ground-motion characteristics estimated from spectral ratio between horizontal and vertical components of microtremor, *Bull. Seismol. Soc. Am.* **88,** 228–241.

Latour, S., C. Voisin, F. Renard, E. Larose, S. Catheline, and M. Campillo (2013). Effect of fault heterogeneity on rupture dynamics: An experimental approach using ultrafast ultrasonic imaging, *J. Geophys. Res.* **118,** 5888–5902.

Lawson, C. L., and R. J. Hanson (1974). *Solving Least Square Problems*, Prentice-Hall, Upper Saddle River, New Jersey, 340 pp.

Melgar, D., J. Geng, B. W. Crowell, J. S. Haase, Y. Bock, W. C. Hammond, and R. M. Allen (2015). Seismogeodesy of the 2014 M_w 6.1 Napa earthquake, California: Rapid response and modeling of fast rupture on a dipping strike-slip fault, *J. Geophys. Res.* **120,** 5013–5033.

Pitarka, A., P. G. Somerville, Y. Fukushima, T. Uetake, and K. Irikura (2000). Simulation of near-fault ground motion using hybrid Green's functions, *Bull. Seismol. Soc. Am.* **90,** 566–586.

Ruiz, J. A., D. Baumont, P. Bernard, and C. Berge-Thierry (2011). Modeling directivity of strong ground motion with a fractal, k^{-2}, kinematic source model, *Geophys. J. Int.* **186,** 226–244.

Schmedes, J., R. J. Archuleta, and D. Lavallée (2010). Correlation of earthquake source parameters inferred from dynamic rupture simulations, *J. Geophys. Res.* **115,** no. B03304, doi: 10.1029/2009JB006689.

Shi, Z., and S. M. Day (2013). Rupture dynamics and ground motion from 3-D rough-fault simulations, *J. Geophys. Res.* **118,** 1122–1141.

Sokos, E., A. Kiratzi, F. Gallovič, J. Zahradník, A. Serpetsidaki, V. Plicka, J. Janský, J. Kostelecký, and G.-A. Tselentis (2015). Rupture process of the 2014 Cephalonia, Greece, earthquake doublet (M_w 6) as inferred from regional and local seismic data, *Tectonophysics* **656,** 131–141.

Somerville, P., N. F. Smith, W. Graves, and N. Abrahamson (1997). Modification of empirical strong ground motion attenuation relations to include the amplitude and duration effects of rupture directivity, *Seismol. Res. Lett.* **68,** 199–222.

Stidham, C., M. Antolik, D. Dreger, S. Larsen, and B. Romanowicz (1999). Three-dimensional structure influences on the strong motion wavefield of the 1989 Loma Prieta earthquake, *Bull. Seismol. Soc. Am.* **89,** 1184–1202.

Wei, S., S. Barbot, R. Graves, J. J. Lienkaemper, T. Wang, K. Hudnut, Y. Fu, and D. Helmberger (2015). The 2014 M_w 6.1 South Napa earthquake: A unilateral rupture with shallow asperity and rapid afterslip, *Seismol. Res. Lett.* **86,** 344–354.

Zeng, Y., J. Anderson, and G. Yu (1994). A composite source model for computing realistic synthetic strong ground motions, *Geophys. Res. Lett.* **21,** 725–728.

František Gallovič
Charles University in Prague
Faculty of Mathematics and Physics
Department of Geophysics
V Holešovičkách 2
180 00 Praha 8, Czech Republic
gallovic@karel.troja.mff.cuni.cz

Published Online 25 November 2015

[P19]

SCENARIO MODELING OF THE 2014 Mw6.0 SOUTH NAPA, CALIFORNIA, EARTHQUAKE USING AN ADVANCED BROADBAND KINEMATIC SOURCE MODEL

F. GALLOVIČ[1]

[1] Charles University in Prague, Faculty of Mathematics and Physics, Dept. of Geophysics, V Holešovičkách 2, Praha 8, 180 00

E-mail contact: gallovic@karel.troja.mff.cuni.cz

Abstract

Strong ground motion simulations require physically plausible earthquake source model. Here we present application of such a kinematic model introduced by Ruiz et al. (2011). The model is constructed to inherently provide desired omega-squared spectral decay at high frequencies. The source is composed of randomly distributed overlapping subsources with fractal number-size distribution. Position of the subsources can be constrained by prior knowledge of major asperities (stemming, e.g., from slip inversions), or can be completely random. From earthquake physics point of view, the model includes positive correlation between slip and rise time as found in dynamic source simulations. Rupture velocity and rise time follows local S-wave velocity profile, so that the rupture slows down and rise times increase close to the surface, avoiding unrealistically strong ground motions. Rupture velocity can also have random variations, which results in irregular rupture front while satisfying the causality principle. This advanced kinematic broadband source model can be easily incorporated in any numerical wave propagation code as the source is described by spatially distributed slip rate functions, not requiring any stochastic Green's functions. Here we present a simple parametric study to illustrate the role of individual model parameters. Performance of the source model is shown on the very shallow unilateral 2014 Mw6 South Napa, California, earthquake. The model reproduces well the observed data including the near fault directivity, suggesting that main features of the earthquake rupture are correctly captured (Gallovič, 2015). We also present scenario simulation maps for this event, and comparison with existing ground motion prediction equations.

Key Words: 2014 Mw6 South Napa earthquake, kinematic strong ground motion modeling, scenario modeling, between-event ground motion variability, single-station sigma.

1. Introduction

Strong ground motion simulations require physically plausible earthquake source model. The method must be able to provide omega-square source spectrum in a broad frequency range, which is commonly observed in the real data. Moreover, the model must be compatible with basic characteristics observed in earthquake source studies of real events and with properties suggested by earthquake source dynamics.

For the strong ground motion modeling generally kinematic models are preferred to their dynamic counterpart for much better numerical efficiency. Here we apply one of the kinematic methods, which is based on evaluation of the representation theorem [1]. The source process is prescribed in terms of spatial-temporal evolution of slip along the fault. Numerically, the fault is discretized and the representation integral is substituted by a sum, so that the finite extent source is represented as a coherent superposition of point sources distributed regularly along the fault with spatial spacing small enough to avoid numerical problems in the integration. We note that this approach differs from the so-called composite modeling, which is based on

assumption that the modeled event can be described as a discrete sequence of individually-rupturing subevents that are treated as point-sources (e.g., [2]). Another viable approach to strong motion modeling is a hybrid combination of the latter two methods (e.g., [3], [4]). However, the disadvantage of such combination is the need for cross-over filtering of the synthetics simulated by the two techniques, which is typically performed ad-hoc.

Here we utilize method introduced by [5] (hereafter denoted as Ruiz Integral Kinematic, RIK, model) with some minor modifications. It has been recently applied to the broadband modeling of the observed velocity waveforms written by the 2014 Mw6 South Napa earthquake ([6]). We first explain basic characteristics of the source model, taking newly into account random variations of the rupture speed along the fault. We employ full-wavefield Green's functions calculated in a 1D velocity model. We validate the earthquake model against the observed data. Eventually, we perform scenario simulations to predict possible variability of ground motions due to varying hypocenter location, mean rupture speed and slip distribution. We compare the results with ground motion prediction equations (GMPEs) and discuss spatial distribution of the between-event ground motion variability.

2. RIK Source model description

The RIK model has been developed by [5] for earthquake ground-motion simulations in order to provide omega-squared spectral decay at high frequencies. It utilizes the representation integral in the full frequency range (no composite modeling needed). In [6] some simplifications and minor modifications of the method have been introduced, such as taking into account the depth-dependence of the rupture velocity. Here we additionally introduce random variations of the rupture speed as discussed further.

The RIK model is composed of randomly distributed circular subsources with fractal number-size distribution with dimension D=2, which is considered also in other kinematic source models (e.g., [2], [4]). Kinematic properties (including the rupture propagation) are prescribed individually to each of the subsources, and thus each subsource is characterized by its own slip rate functions along its areal extent. The total slip rates of the RIK model are eventually evaluated on a regular discretization grid along the fault by summing up slip rate contributions from all the subsources.

In particular, we consider that radii of the subsources, R, are integer fractions of the fault width W, i.e. $R=W/n$. For our number-size distribution the number of subsources at level n is then $2n-1$. The subsources are distributed randomly along the fault. In the scenario modeling we consider uniform distribution, but in the real data modeling we use slip distribution obtained from inversion of low-frequency data as a spatial probability density functions, see further.

The individual subsources have slip distributions corresponding to the crack model, i.e.

$$\Delta u^R(\rho) \sim \sqrt{R^2-\rho^2} \text{ if } \rho < R; \quad \Delta u^R(\rho) = 0 \text{ otherwise,} \qquad (1)$$

where ρ is the distance from the subsource center. The constant of proportionality in (1) is determined so that the total seismic moment fits the prescribed scalar seismic moment M_0. This fractal decomposition of the source model implies that the slip decays as k^{-2} at high wavenumbers k ([4], [2]). It implies physically plausible k^{-1} spectral decay of the stress distribution ([7]).

The rupture is assumed to propagate in form of a slip pulse of width L_0 with the Brune's pulse ([8]) as the slip rate function. If rise time were constant, the source spectrum would decay as omega-squared only up to the reciprocal of the rise time, decaying then faster due to the low-pass filtering effect of the slip rate function. To correct for this, [9] introduced the concept of

the *k*-dependent rise time. In the RIK model with subsources of varying sizes, the rise time is considered to depend on subsource radius *R* as

$$\tau(R) = \tau_{max} = aL_0/v_r \text{ if } 2R > L_0; \quad \tau(R) = a(2R)/v_r \text{ otherwise,} \qquad (2)$$

where a is a free parameter (of the order of 1). Rupture speed v_r follows the S-wave velocity profile, keeping the rupture speed to S-wave velocity ratio constant. This way we avoid too fast (even supershear) rupture propagation close to the surface and thus enhanced source radiation. The rise-time dependence on the subsource radii (2) also implies a positive spatial correlation between the slip and the rise time as it is observed in dynamic rupture simulations (e.g., [10]).

[2] introduced a concept of small- and large-scale rupture fronts to decrease the coherency of the rupture front. [6] showed that taking this feature into account improved slightly the model performance in terms of explaining the azimuthal variability of the observed data. Instead, here we consider random variations of the rupture speed following a k^{-1} distribution. The rupture times are numerically evaluated using the solver of the eikonal equation by [11].

3. Application to the 2014 South Napa earthquake

The South Napa earthquake occurred on 24 August 2014 at 10:20:44 UTC in California, 6km NW of American Canyon and 9km SW of Napa ([12]). For this earthquake many high-quality recordings were written by many stations located at near-fault distances (see Fig. 1).

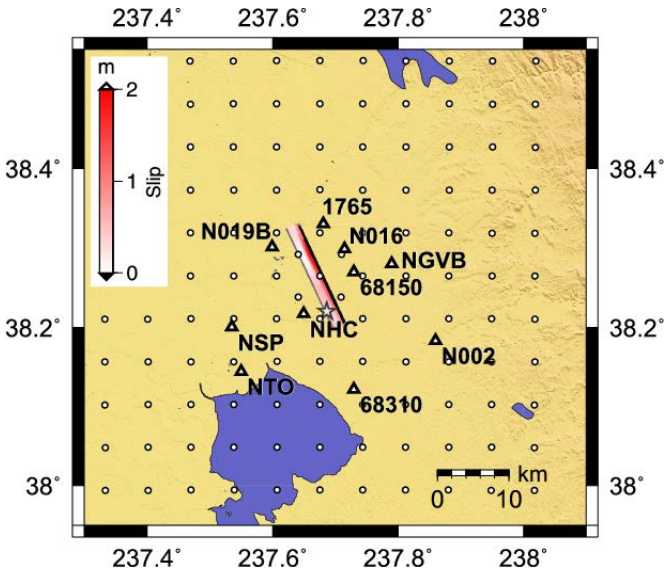

FIG. 1. Distribution of near-fault stations (triangles) that recorded the 2014 South Napa earthquake. Box represents the surface projection of the fault with superimposed slip distribution by [6]. Star denotes the nucleation point of the event. Small circles show position of phantom stations considered in the scenario simulations.

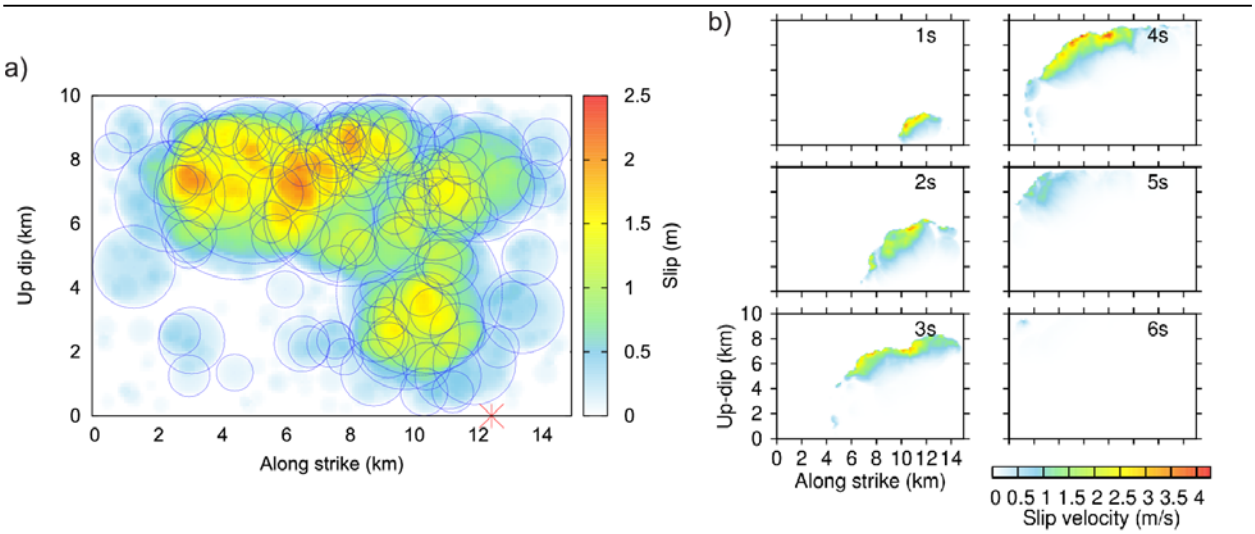

FIG. 2. Setup of the RIK model for simulation of the observed data. a) Distribution of RIK subsources (circles) composing the final slip distribution (color coded). Only the largest subsources are plotted for lucidity. b) Rupture evolution snapshots every 1s. Note the irregular rupture front due to the random variations of the rupture velocity.

[6] present a slip inversion of the South Napa earthquake utilizing method by [13] and near-fault stations (Figure 1). The model is in agreement with other models published so far ([14]; [15]; [16]; [17]), showing a unilateral northward rupture propagation towards the city of Napa, having significant asperity at shallow depths (<5 km) with longer rise times at the place where 40-46cm slip was observed at the surface ([12]).

3.1. Modeling the observed data

Raw accelerometric data from stations located within 15km from the fault were downloaded from the database of the Center for Engineering Strong Motion Data (Fig. 1). After detrending, bandpass filtering using one-way (causal) Butterworth filter of the 4th order, the data were integrated to velocity and eventually undersampled. The high-pass filtering at 0.05Hz removes the low-frequency part of the wavefield that is corrupted by the instrumental noise. The low-pass filter at 5Hz is sufficient for the velocity recordings, while limiting the computational expense. The horizontal components were rotated to the fault-parallel (F-P) and fault-normal (F-N) components.

We adopt RIK model parameters from [6]. In particular, the distribution of the subsources of the RIK model is constrained by slip model from the low-frequency data inversion by [6], see Fig. 2a. The mean rupture velocity is considered also as 0.8 times the local rupture velocity. We add random variations to the rupture speed to distort the coherent rupture front obtained when a constant rupture velocity is considered. Fig. 2b shows snapshots of the slip rates along the fault illustrating the irregular shape of the rupture front.

The model is used to simulate ground motions at all the receiver sites (Fig. 1). For the wave propagation modeling we use a modification of the 1-D layered velocity model GIL7 ([18]), with two additional layers with subsurface velocity representing soft-rock site properties (see Table S2 in [6]). Full wavefield Green's functions (GFs) are calculated using the discrete wavenumber technique (Axitra code, [19]; [20]). No stochastic GFs are used throughout the whole study.

Fig. 3 shows comparison between observed and synthetic velocity waveforms, showing relatively good fit despite the simplicity of the modeling, especially in terms of the wave propagation modeling (considering just a 1D velocity model in the full-frequency range). Generally, both the shapes of the waveforms and their peak values are correctly reproduced. In particular, the model successfully explains the long-period directivity pulses observed at the F-N components of the stations located in the forward direction from the rupture propagation (N019B, N016). Interestingly, it also reproduces the double peak character of the F-N component observed at station 1765, located just across the fault from station N019B.

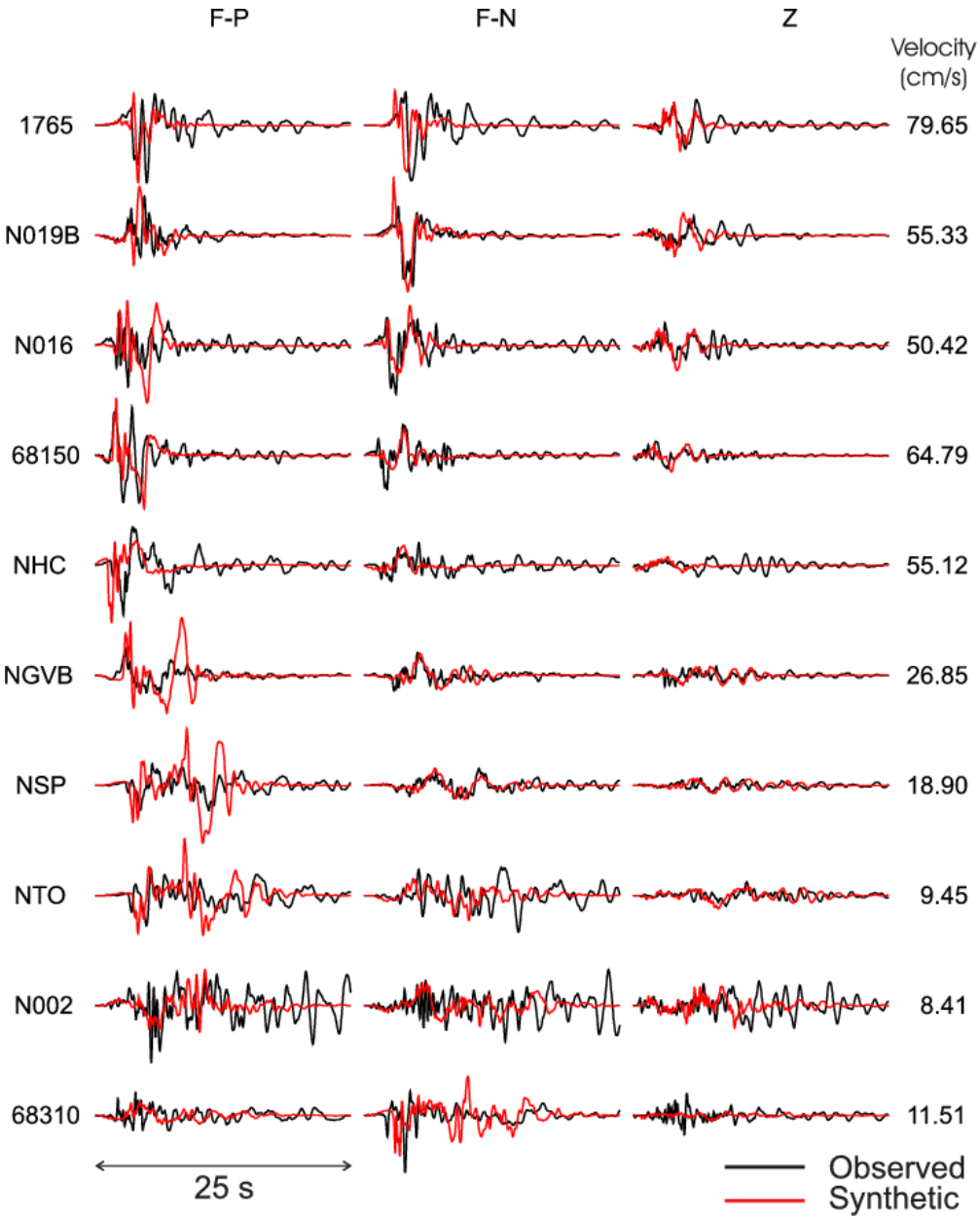

FIG. 3. Comparison between observed and synthetic velocity data simulated by the RIK model (frequency range 0.05-5Hz).

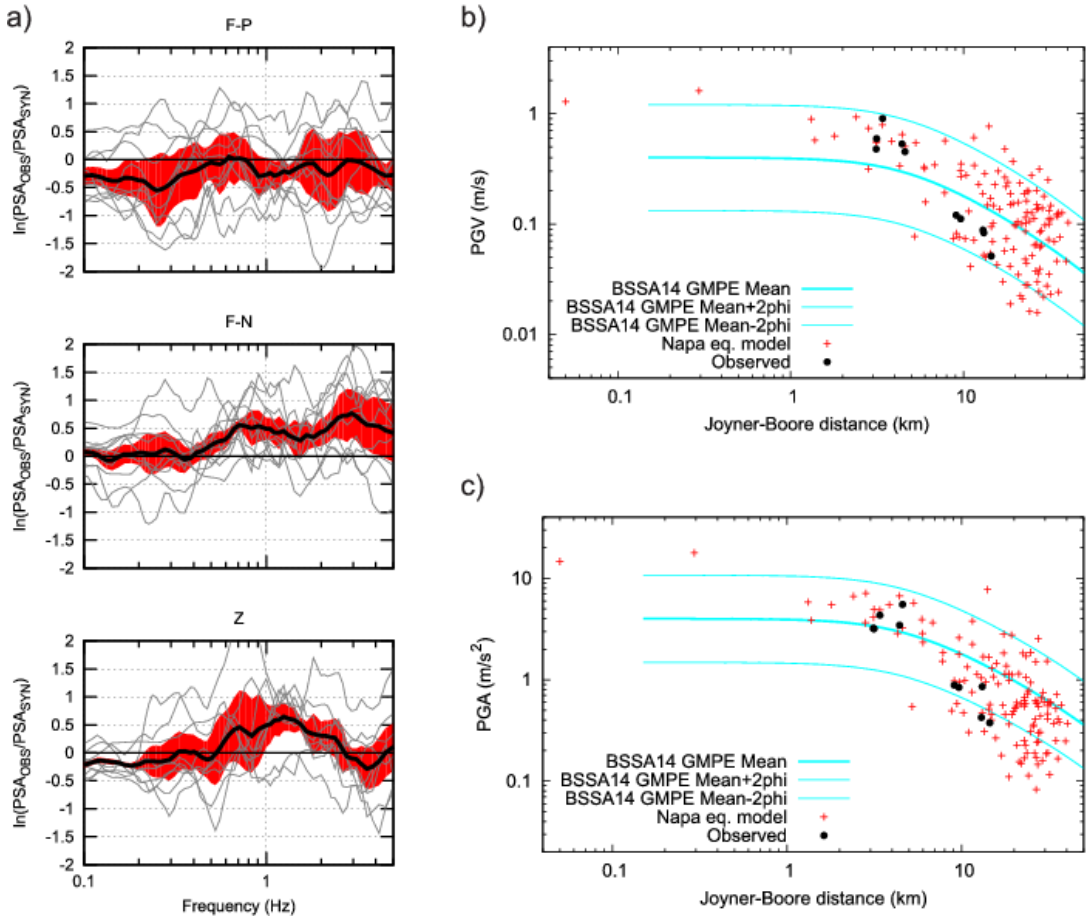

FIG. 4. a) Modeling bias in terms of the response spectra. b) Comparison between simulated (red points) and observed (black points) PGV values collected from all the real and phantom stations (Fig. 1). Lines represent mean (thick) and mean±2ϕ (thin), where ϕ is the within-event standard deviation of the GMPE ([21]). c) Same as b) but for PGA.

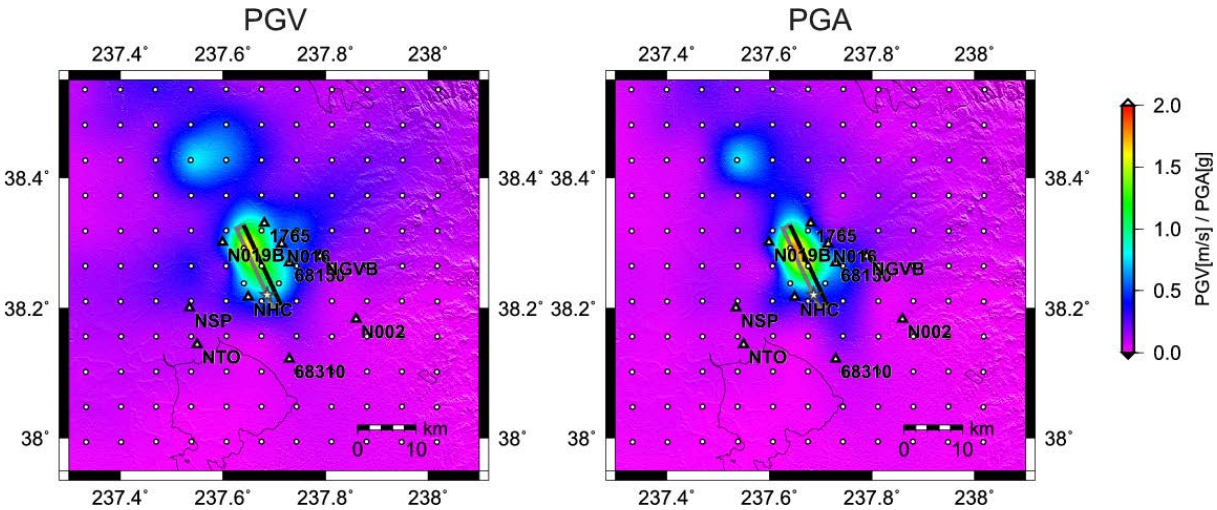

FIG. 5. Map view of the simulated PGV and PGA values interpolated from all the real and phantom stations (triangles and circles, respectively).

Fig. 4a displays the modeling bias in terms of the acceleration response spectra at the individual components. The mean bias (black curve) is generally close to zero, suggesting minor overestimation (-0.2) and underestimation (0.3) at the F-P and F-N components, respectively. The variance of the bias is also rather low (0.2-0.4).

The simulations are carried out not only for the real stations, but also for a regular distribution of phantom stations (see Fig. 1). Fig. 5 shows map view of the simulated PGA and PGV values. Red points in Fig. 4b and 4c show the simulated PGV and PGA values, respectively, as a function of the Joyner-Boore distance. The plots are complemented by the real-data peak values and GMPEs adopted from [21]. Note that the real data overshoot the mean GMPE curves, especially in terms of PGV, while at larger distance the observed values are smaller than those predicted by GMPEs. This behavior, which results in a seemingly stronger attenuation with distance than suggested by the GMPE curves, is well captured by the strong motion simulations. We ascribe this particular behavior to the very shallow location of the major asperity, which is a rather peculiar feature of the present event (Fig. 2).

3.2. Scenario modeling

In deterministic seismic hazard assessment one is typically interested in strong ground motion prediction for a hypothetical earthquake on an assumed fault. Typically, mechanism and geometry of a causative fault can be estimated a priori with some epistemic uncertainty. However, details of the rupture process, such as position of the nucleation point, asperity, or rupture velocity, are generally not known in advance, representing source of aleatoric uncertainty. In such a case, scenario simulations are performed to take into account possible variations of the source parameters.

To estimate the variability related to the a priori unknown rupture scenario, we assume the following variations of the source parameters: two ratios between the mean rupture speed and S-wave velocities (0.6 and 0.8), six positions of the nucleation point on the fault and six slip distributions, see Fig. 6a. Regarding the latter, we actually consider three different slip distributions as shown in Fig. 6a and then their horizontal mirror image to improve the symmetry of the simulated scenarios. Considering all combinations of the rupture parameters, we thus generate 72 rupture scenarios in total. For each of the scenarios we consider a unique distribution of the rupture speed variations. Fig. 6b shows examples of three of source scenarios in terms of rupture evolution snapshots. The rupture propagation is characterized by similar complexity as the model used for modeling the observed data (see above).

Fig. 7 displays the resulting PGV and PGA values picked from the simulated seismograms (red dots) against the Joyner-Boore distance. For reference, the GMPEs and real data are plotted as well. Scatter of the simulated values is relatively large, having standard deviation of approximately 1.0 (in natural log units). This value is much larger than the standard deviation of the GMPEs (including both within- and between- event variability), which is approximately 0.6-0.65 and roughly constant for our distance range ([21]). We ascribe this discrepancy to the abundant number of earthquake scenarios and seismic station density considered in the simulations, which by far exceeds any standard number of observations in real cases. We suppose that scarce real observations might not capture all systematic features of the earthquake ground motions as suggested by the simulations (see also further).

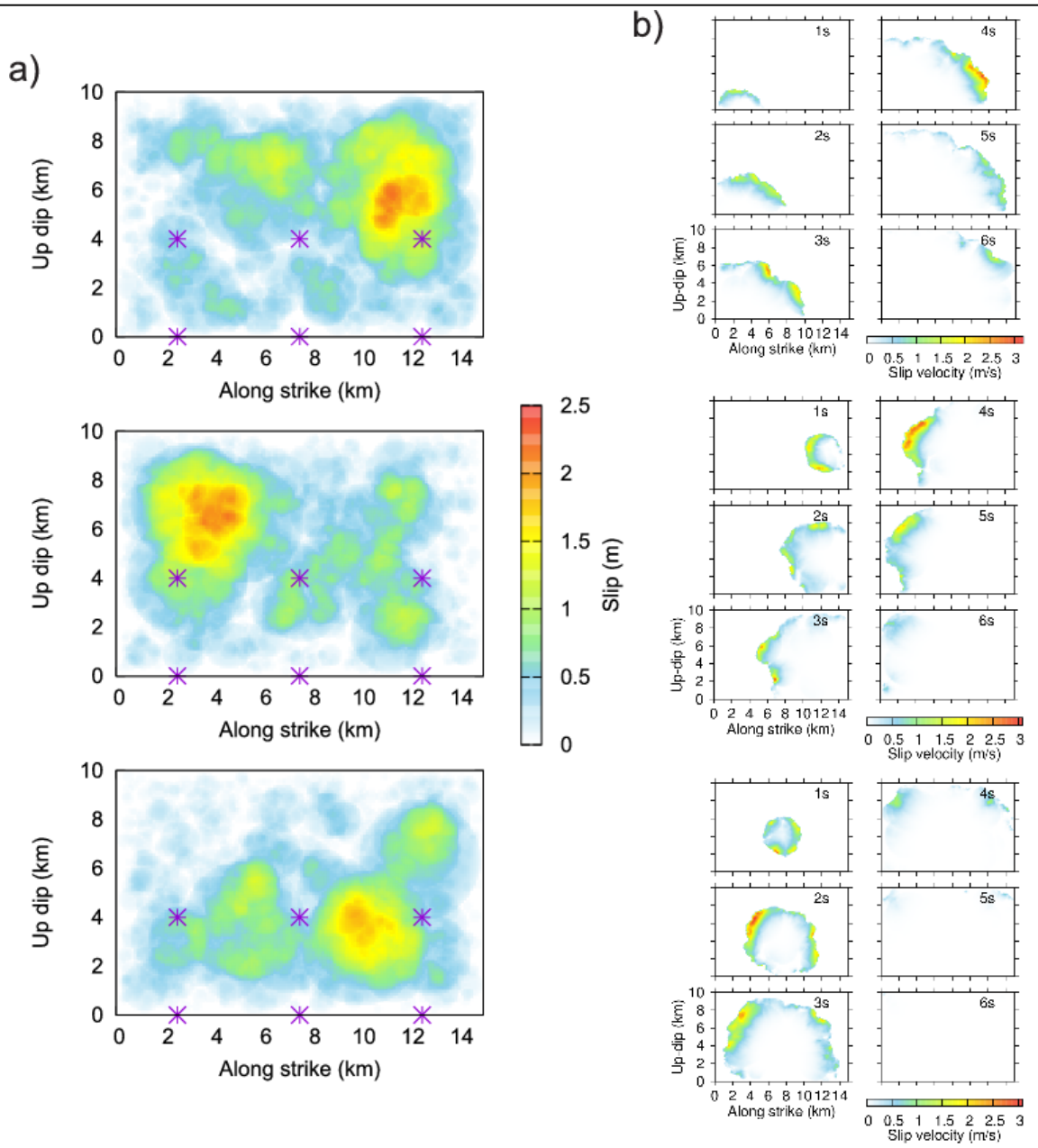

FIG. 6. Setup of the scenario modeling. a) Three slip distribution models with considered positions of nucleation points (stars). b) Three examples of the rupture propagation scenarios.

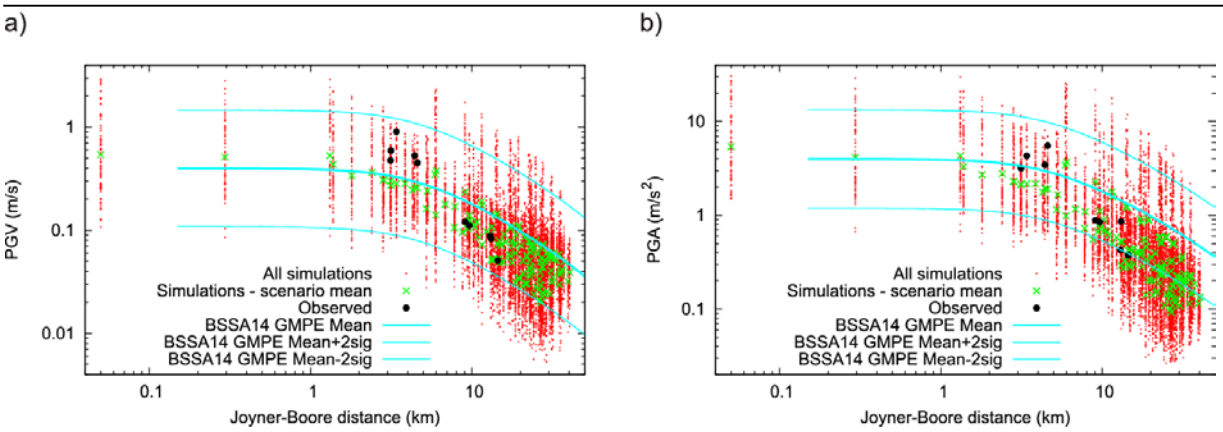

FIG. 7. Results of the scenario simulations. Red points are simulated PGV (a) and PGA (b) from all scenarios and stations. Lines represent mean (thick) and mean±2σ (thin), where σ is the complete standard deviation of the GMPE ([21]) including within- and between-event variabilities. Green crosses show mean values over scenarios for each of the stations considered.

Fig. 7 shows also mean values of the peak values evaluated at each of the stations over all the scenarios. The mean peak values have smaller scatter. They decay slightly faster with distance (especially in terms of PGA), which resembles the faster decay of the observed data. In the case of modeling the real data we have ascribed it to the superficial character of the slip distribution. In this case we cannot use this argument although there is a larger number of models having shallower slip (see Fig. 6). Instead, the 1D velocity model seems to attenuate the seismic waves more strongly than what is suggested by the empirical data (GMPEs). It is also possible that our velocity model lacks some superficial structure that would enhance the seismic waves at larger distances.

Fig. 8 shows spatial distribution of the simulated PGV and PGA values in terms of their mean and standard deviations (in natural log units). The mean values have elongated shape following the geometry of the fault. In the along strike direction at larger distances the mean values are larger than at perpendicular direction. Minor effect of the radiation pattern can be also seen, being expressed by the cross-like character of the peak-value maps.

Regarding the ground motion variability, the simulations suggest spatially inhomogeneous standard deviation (also called single-station between-event sigma) ranging from approximately 0.35 to 1.1. Indeed, the corresponding maps in Fig. 8 have fan-like shape with the largest values located in the along the directions of the fault. This is due to the directivity effect, which is mostly pronounced in the along-fault direction. Indeed, the variability is lowest in the directions perpendicular to the fault, where the ground motions are not much affected by the direction, in which the rupture front propagates. Root-mean-square of the variability over all the stations is 0.65 and 0.75 for PGV and PGA, respectively.

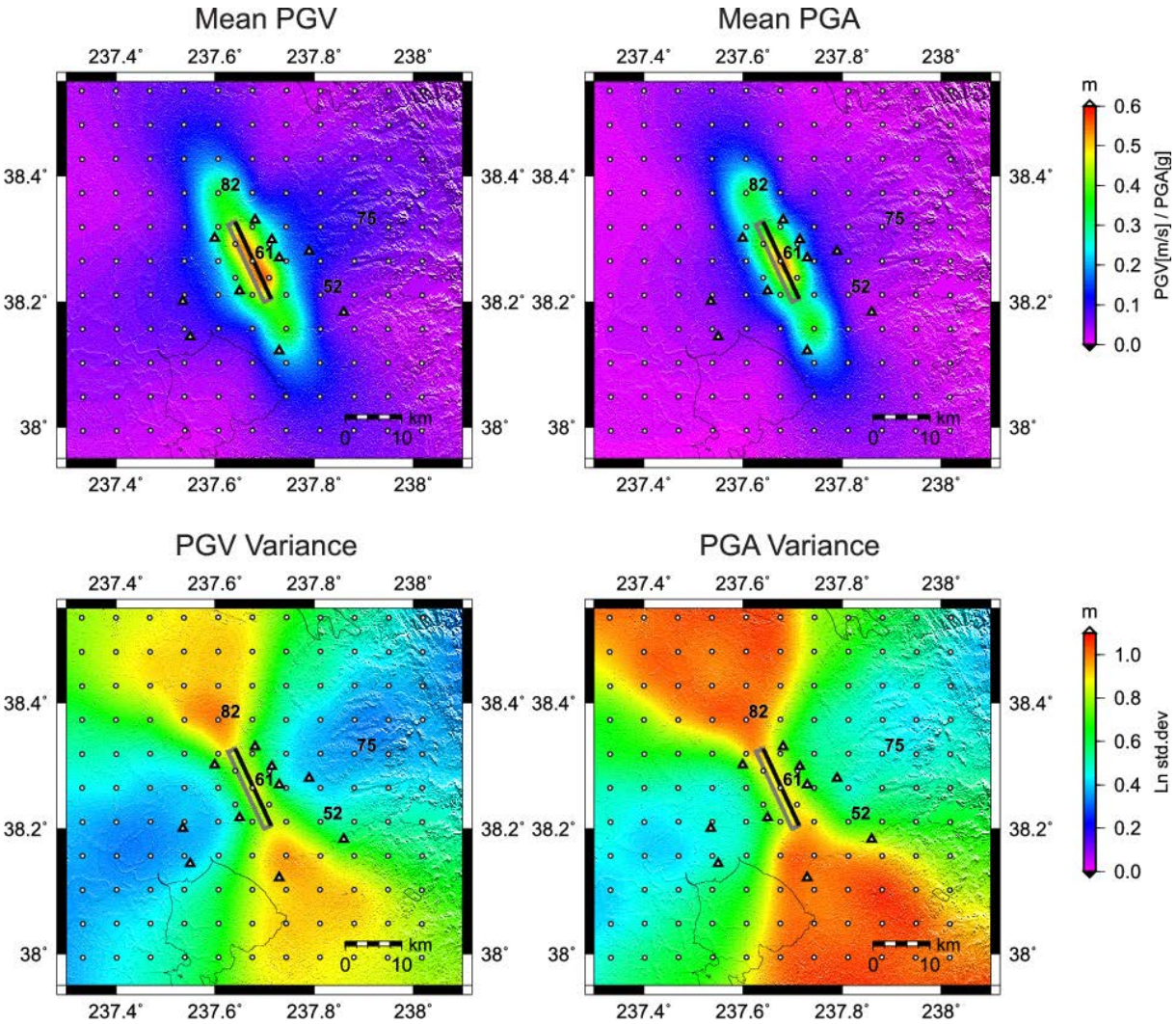

FIG. 8. Results of the scenario simulations plotted in terms of mean values of PGA and PGV evaluated over all the scenarios and their variability. Triangles and small circles denote real and phantom stations, respectively. For the numbered phantom stations Fig. 9 shows histograms of PGA values.

For four selected phantom stations depicted in Fig. 8, we show histograms of the simulated PGA values in Fig. 9. The histograms have varying shape, resembling normal distribution (e.g., station 75). In some cases (stations 82 and 52) they have a bimodal character, having more than one peak. We observe the bimodal shape generally at stations lying in the along-strike direction. They are perhaps imprints of the significant difference between the peak values simulated in the forward and backward directivity directions.

The plots in Fig. 9 show also PGA values obtained considering the source model used to simulate the observed data (crosses). They fall within the histograms from the scenario simulations. However, one can see that the values obtained for the constrained source model do not fall to the same part of the histograms for various stations; in some cases they fall at the margin of the distribution (stations 75 and 61), while in other cases they are located approximately in their centers (stations 82 and 52).

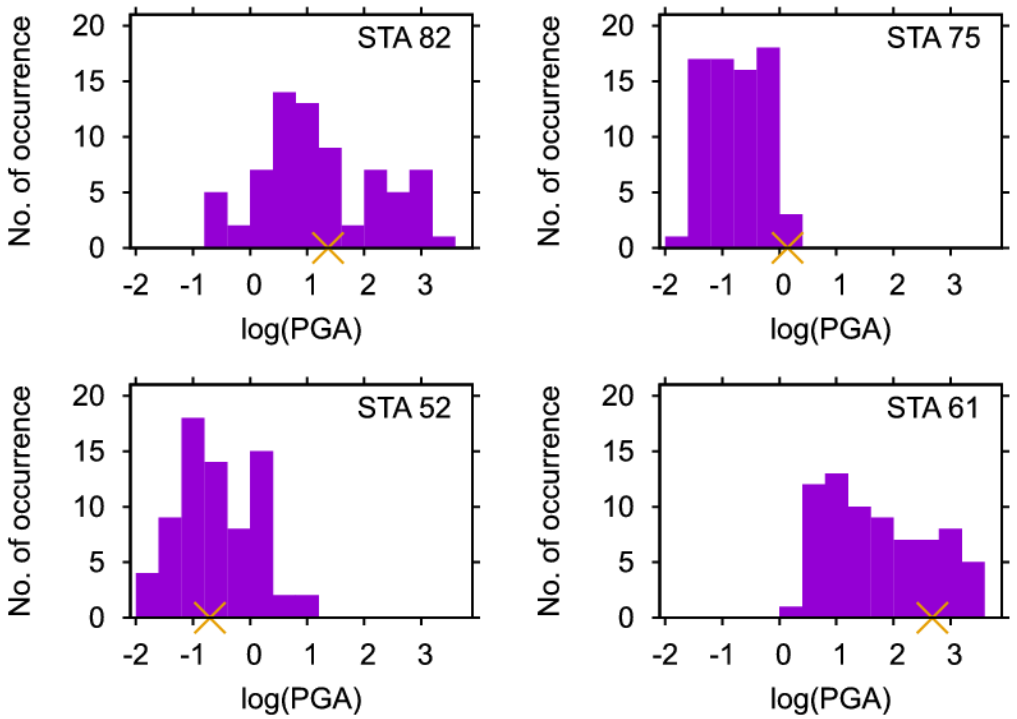

FIG. 9. Histograms of (natural log) PGA values corresponding to the numbered phantom stations in Fig. 8. Crosses denote values obtained from the model used to simulate the observed data.

4. Discussion and Conclusions

In this study we have employed an advanced broadband kinematic source model originally introduced by [5]. It is characterized by k^{-2} slip distribution and k-dependent rise time, providing correctly omega-squared source spectrum in a broad frequency range. We have introduced several minor modifications, such as dependence of the rupture speed on the 1D velocity profile to avoid too fast (even supershear) rupture propagation close to the surface. We have also included random variations of the rupture speed to distort the otherwise too coherent rupture front.

The approach is validated against near-fault high-quality recordings of the 2014 Mw6 South Napa earthquake. Slip model inferred by [6] (having a major slip patch located at depths shallower than 5km) is used to constrain a source model to predict the velocity waveforms (0.05-5Hz). Full-wavefield Green's functions calculated in a 1D velocity model roughly corresponding to a hard-rock site are taken into account in the whole frequency range (no stochastic Green's functions were utilized). The model correctly reproduces the major characteristics of the observed data including their peak values and broad directivity pulses in the velocity waveforms.

We have performed scenario simulations for the South Napa causative fault. To this end, we have generated 72 source models varying rupture speed, nucleation point position and slip distribution in order to evaluate within-event uncertainty of the ground motions. The resulting maps of the average peak motions have elongated shape due to the finite extent of the fault.

PGA and PGV values decay slightly more rapidly with increasing distance than suggested by the empirical GMPEs ([21]). The variability of the ground motions (in terms of single-station between-event standard deviation) show a peculiar fan-like shape with largest values in the along-strike directions. We ascribe this to the effect of directivity, which is most pronounced in those directions. The directivity effect is also imprinted in the histograms of the peak values at stations in the along strike-directions, having rather a bimodal character.

The simulated single-station between-event standard deviations range from 0.35 to 1.1 with root-mean-square value (over all stations) of 0.65-0.75, which is larger than the between-event standard deviations of GMPEs (0.35). We note that the standard GMPEs take into account only distance-dependence of the observed motion, and thus do not capture the systematic azimuthal dependence of the ground motion variability as suggested by the simulations.

Although the present application utilizes just a 1D velocity model to evaluate ground motions, the source model can be easily implemented in any code simulating wave propagation in generally 3D media. In terms of scenario simulations, we expect that the 3D model would mainly affect the mean ground motions and perhaps also the variability at further distances in directions perpendicular to the fault. Contrarily, we suppose that close to the fault and in the along-strike directions the source effect plays a dominant role in controlling the within-event ground-motions variability. The simulations may thus help to introduce new types of functional forms of GMPEs that would take into account the ground motion variability due to the source effect.

5. Acknowledgement

Financial support: Grant Agency of Czech Republic 14-04372S.

REFERENCES

[1] AKI, K., and P. G. RICHARDS, “Quantitative Seismology”, Univ. Sci., Sausalito, California (2002).

[2] ZENG, Y., et al., “A composite source model for computing realistic synthetic strong ground motions”, Geophys. Res. Lett. 21 (1994), 725–728.

[3] GRAVES, R. W., and PITARKA, A., “Broadband ground-motion simulation using a hybrid approach”, Bull. Seismol. Soc. Am. 100 (2010), 2095-2123.

[4] GALLOVIČ, F., and BROKEŠOVÁ, J., “Hybrid k-squared Source Model for Strong Ground Motion Simulations: Introduction”, Phys. Earth Planet. Interiors 160 (2007), 34-50.

[5] RUIZ, J. A., D., et al., “Modeling directivity of strong ground motion with a fractal, k^{-2}, kinematic source model”, Geophys. J. Int. 186 (2011), 226–244.

[6] GALLOVIČ, F. “Modeling velocity recordings of the Mw6.0 South Napa, California, earthquake: unilateral event with weak high-frequency directivity”, Seism. Res. Lett. (2015), in press.

[7] ANDREWS, D. J., A stochastic fault model: 1. Static case, J. Geophys. Res. 85 (1980), 3867-3877.

[8] BRUNE, J. N., "Tectonic stress and the spectra of seismic shear waves from earthquakes", J. Geophys. Res. 75 (1970), 4997-5009.
[9] BERNARD, P., et al., "Modeling directivity of heterogeneous earthquake ruptures". Bull. Seism. Soc. Am. 86 (1996), 1149-1160.
[10] SCHMEDES, J., et al., "Correlation of earthquake source parameters inferred from dynamic rupture simulations", J. Geophys. Res. 115 (2010), B03304.
[11] PODVIN, P., and I. LECOMTE, "Finite difference computation of traveltimes in very contrasted velocity models: a massively parallel approach and its associated tool", Geophys. J. Intern. 105 (1991), 271-284.
[12] BROCHER, T. M., et al., "The M 6.0 24 August 2014 South Napa Earthquake", Seismol. Res. Lett. 86 (2015), 309-326.
[13] GALLOVIČ, F., et al., "Effects of three-dimensional crustal structure and smoothing constraint on earthquake slip inversions: case study of the Mw6.3 2009 L'Aquila earthquake", J. Geophys. Res. 120 (2015), 428-449.
[14] DREGER, D. S., et al., "Kinematic finite-source model for the 24 August 2014 South Napa, Califonia, earthquake from joint inversion of seismic, GPS and InSAR data", Seismol. Res. Lett. 86 (2015), 327-334.
[15] JI, Ch., et al., "Rupture history of 2014 Mw 6.0 South Napa earthquake inferred from near fault strong motion data and its impact to the practice of ground strong motion prediction", Geophys. Res. Lett. 42 (2015), 2149-2156.
[16] MELGAR, D., et al., "Seismogeodesy of the 2014 Mw6.1 Napa earthquake, California: Rapid response and modeling of fast rupture on a dipping strike-slip fault", J. Geophys. Res. Solid Earth 120 (2015), 5013-5033.
[17] WEI, S., et al., "The 2014 Mw 6.1 South Napa earthquake: A unilateral rupture with shallow asperity and rapid afterslip", Seismol. Res. Lett. 86 (2015), 344-354.
[18] STIDHAM, C., et al., "Three-dimensional structure influences on the strong motion wavefield of the 1989 Loma Prieta earthquake", Bull. Seismol. Soc. Am. 89 (1999), 1184–1202.
[19] BOUCHON, M., "A simple method to calculate Green's functions for elastic layered media", Bull. Seismol. Soc. Am. 71 (1981), 959-971.
[20] COUTANT, O., "Program of numerical simulation AXITRA", research report (1989), Lab. de Geophys. Interne et Tectonophys., Grenoble, France.
[21] BOORE, D.M., et al., "NGA-West 2 equations for predicting PGA, PGV, and 5%-damped PSA for shallow crustal earthquakes", Earthquake Spectra 30 (2014), 1057-1085.